UNIVERSITAT DE BARCELONA

Towards the development of biomimetic *in vitro* models of intestinal epithelium derived from intestinal organoids

Gizem Altay

UNIVERSITAT DE BARCELONA

IBEC
Institute for Bioengineering of Catalonia

UNIVERSITY OF BARCELONA
FACULTY OF PHARMACY AND FOOD SCIENCES

Towards the development of biomimetic *in vitro* models of intestinal epithelium derived from intestinal organoids

---

DOCTORAL THESIS

by
Gizem ALTAY

Supervisor:
Dr. Elena MARTÍNEZ FRAIZ

Tutor:
Prof. Josep SAMITIER MARTÍ

A thesis submitted in partial fulfillment of the requirements for the degree of ***Doctor of Philosophy in Biomedicine***

Doctoral Programme in Biomedicine

Barcelona, 2018

To Berat and Mehmet Dilaver Altay...

Acknowledgements

Going ahead with this project required a lot of effort and determination. In this path, I have passed through many different moments. Moments of frustration and exhaustion and moments of pure joy. I saw myself grow and become more resilient day by day. In this difficult path, I was accompanied by wonderful people that always offered me their help and support, without whom this work wouldn't have been possible.

In the first place, I would like to express my sincere gratitude to my thesis supervisor Elena Martínez. Thank you for your confidence, for providing guidance through this long journey and for supporting me through my professional growth. In the second place, I would like to thank to my tutor and the director of IBEC Josep Samitier, for giving me the opportunity to be a part of this institute with exceptional facilities. Then, I would like to thank to Vanesa Fernández and Albert García for their scientific contributions and for the fruitful discussions in the laboratory. And, of course to the rest of the 'Elenos'... Thank you Vero, María and Albert for making me part of the family. Thank you Enara for the emotional support that you offered me during this period. Thank you María García-Díaz and Núria for your crucial contributions in the optimization of the microfabrication protocol. Thank you Javi and Jordi for your useful advices. Thank you Tere for transmitting your good energy and for the great moments we shared outside work. Thank you, Raquel, Anna, Aina y Jon for your support in the lab. I express my warmest thanks to all the members of Biomimetics group for their help and encouragements throughout all these years.

During this work, I have got the chance to collaborate with many valuable scientists that made crucial contributions and for whom I have great regard. First, I would like to express my sincere gratitude to Eduard Batlle from IRB for providing us the mouse intestine tissue and his scientific advice without which this work wouldn't have been possible. Also, I would like to thank to Francisco Barriga for performing the isolation of the mouse intestinal crypts at the initial stages of the project and for the ideas that he gave me that were helpful in the development of this work. In addition, I would like to acknowledge the technical support of Marta Sevillano and Xavier Hernando. Then, I would like to express my warmest thanks to Emilio Gualda from ICFO for performing the light-sheet fluorescence microscopy experiments and for his help in the data analysis. Thank you, Emilio, for believing in the project! In addition, I acknowledge the help provided by the Advanced Digital Microscopy Unit of IRB. Especially, I would like to thank

to Sébastien Tosi for his strong help on the bioimage analysis by providing image analysis macros and helping interpret the light-sheet microscopy data and for all the fruitful discussions on the physics of diffusion. I would also like to thank to the IBEC MicroFabSpace staff for the technical support they provided. And finally, I would like to gratefully acknowledge the Agència de Gestió d'Ajuts Universitaris i de Recerca (AGAUR) for the funding of my PhD through FI-DGR 2014.

Furthermore, I would like to express my sincere appreciation to all my colleagues and friends in the Nanobioengineering Laboratory: Miriam, David Izquierdo, Ana Lagunas, Luis, Coco, Rossella, Marta, Juan Pablo, Bogaçhan, Reyes, Marga, Monica, Tommy, Marilia, Roberto, Maria Jose, Andrea y Maider for making the time that I spent in their lab very pleasant and providing help whenever needed. Especially, I would like to thank to Mateu Pla for all the scientific knowledge he taught me and to David Caballero for the valuable discussions on my work.

I would also like to acknowledge the indispensable role of the entire IBEC community. I would like to thank to the support services staff for providing help in all matters regarding non-scientific issues. And, I would like to thank to all my friends in the IBEC PhD committee, the people with whom I shared the same values. I enjoyed every meeting, every social activity that we did together, and you are an important part of the whole that has made this experience great.

Next, I would like to thank to all my friends, especially to Işıl, Üstün, Beste, İbrahim, Emre, İdil, Vesna, and Zeynep. Throughout all these years, you have been there for me always. You have listened to me, cheered me up and offered help in different ways. Thank you all for the love and understanding you showed me. I am very lucky to have such great people in my life.

Last but foremost, I would like to express my sincere gratitude to my family. To my parents, Berat and Mehmet Dilaver Altay, who love and support me unconditionally... It was a great sacrifice on their side accepting to see me only once a year so that I can work and advance in this project. I thank you from the bottom of my heart for believing in me in the moments that even I wasn't capable of do so. And, to my partner, companion, and friend, Sébastien... I cannot possibly thank you enough. Thank you for cherishing, loving and respecting me. Thank you for the emotional support and the patience you showed. Thank you for being such a wonderful person! Merci pour tout!

Contents

List of Abbreviations

2D	Two dimensional
3D	Three dimensional
AA	Acrylic acid
ATC	Area of a truncated cone
AU	Airy unit
ISC	Intestinal stem cell
Caco-2	Human epithelial colorectal adenocarcinoma cells
BCA	Bicinchonic acid
BSA	Bovine serum albumin
BSA_TxRED	Texas red conjugated bovine serum albumin
BMP	Bone morphogenic protein
CA	Carbonic anhydrase
CK20	Cytokeratin 20
CLSM	Confocal laser scanning microscope
DAPI	4′,6-diamidino-2-phenylindole
DMEM	Dulbecco's modified eagle medium
DMA	Dynamic mechanical analysis
ECM	Extracellular matrix
EDC	N-(3-Dimethylaminopropyl)-N′ -ethylcarbodiimide
EDTA	Ethylenedinitrilo-tetraacetic acid
EdU	5-ethynyl-2-deoxyuridine
EGF	Epidermal growth factor
FBS	Fetal bovine serum
FEM	Finite element method
GFP	Green fluorescence protein
HBSS	Hank's balanced salt solution
HEPES	N-2-hydroxyethylpiperazine-N-2-ethane sulfonic acid
hInEpC	Human intestinal epithelial cells
HIO	Human intestinal organoids
hiPSC	Human induced pluripotent stem cell

I2959	2-hydroxy-1-[4-(2-hydroxyethoxy) phenyl]-2-methyl-1-propanone
ISEMF	Intestinal subepithelial myofibroblast
ISEMF_CM	Intestinal subepithelial myofibroblast conditioned medium
LGR5	Leucine-rich repeat-containing G-protein coupled receptor 5
LSFM	Light-sheet fluorescence microscopy
Lyz	Lysozyme
MES	2-(N-morpholino)ethanesulfonic acid
NHS	N-Hydroxysuccinimide
PBS	Phosphate buffered saline
PDMS	Polydimethylsiloxane
PEG	Poly (ethylene glycol)
PEGDA	Poly (ethylene glycol) diacrylate
PEGMA	Poly (ethylene glycol) monoacrylate
PET	Polyethylene terephthalate
PI	Photoinitiator
PLGA	Poly (lactic-co-glycolic acid)
PAS	Periodic acid-Schiff base
RT	Room temperature
RFI	Relative fluorescence intensity
ROI	Region of interest
SA_TxRED	Texas RED conjugated Streptavidin
SEM	Scanning electron microscopy
TA	Transit amplifying
TEER	Transepithelial electrical resistance
TSA	True surface area
UV	Ultraviolet light
Wnt	Wingless/Int
Wnt3a_CM	Wnt3a conditioned medium
ZO-1	*Zonula occludens-1*
α-SMA	α-Smooth muscle actin

General introduction

The small intestine is the organ where the most digestion and absorption of nutrients take place. It is a long tube with an average diameter of 2,5 cm and a length of 3 m in a living person [1]. With these dimensions it is the largest component of the gastrointestinal tract. The small intestine begins after the stomach, coils through the abdominal cavity, and eventually opens into the large intestine (Figure 1 A). It is comprised of three regions: the duodenum, jejunum and ileum [1, 2]. The structure of the small intestine is highly adapted for its functions. On top of its length, the inner wall of small intestine is formed into circular folds, which contain finger-like protrusions called villi that are covered with cells that have membrane projections called microvilli [1]. All these features increase the total surface area in contact with the inner cavity up to 400 m^2 for the digestion and absorption to take place [3]. The wall of the small intestine is made up of four layers: mucosa, submucosa, *muscularis*, and serosa (Figure 1 B, C). The mucosa is the innermost layer of the intestinal wall. It covers the surface of the lumen (intestinal cavity) and it is in direct contact with lumenal contents. The submucosa is a layer of dense irregular connective tissue, which provides structural support to the mucosa and connects it to the underlying *muscularis*. Also, it contains blood and lymphatic vessels, and nerves that are distributed into the mucosa. The *muscularis* is made up of an inner, thicker layer with circular muscle fibers and an outer, thinner layer with longitudinal muscle fibers. The *muscularis* is responsible for the movement of the digested food through the small intestine by creating waves of contractions called peristalsis. Finally, the serosa is the smooth tissue membrane that completely surrounds the small intestine [1, 2].

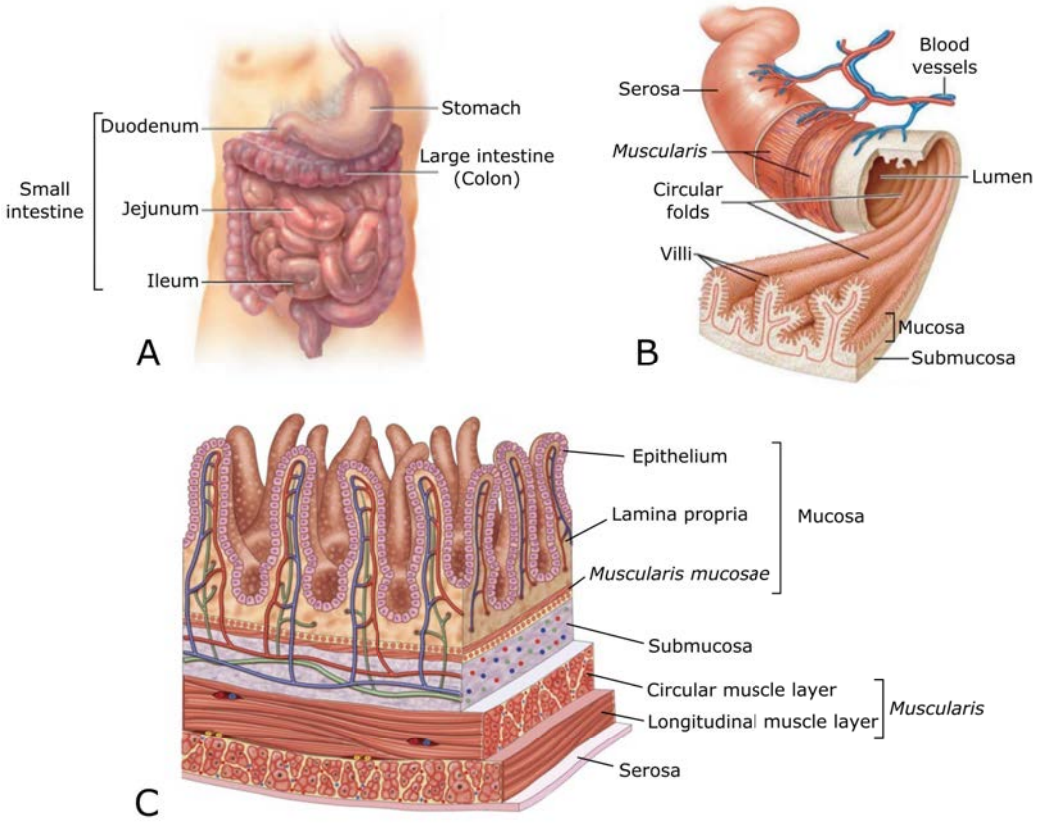

Figure 1: *Illustrations of the gastrointestinal tract (A), adapted from Tortora et al. [1], anatomy of the small intestine (https://www.slideshare.net/brissomathewarackal/small-intestine) (B), and detailed drawing of the four layers of small intestinal wall (https://www.ck12.org/biology/small-intestine/lesson/Small-Intestine/) (C).*

The intestinal mucosa is also a multilayered tissue. It is composed of the epithelium, lamina propria, and *muscularis mucosae* (Figure 1 C). The epithelial layer consists of a simple columnar epithelium that forms a highly selective biochemical and physical barrier separating the luminal contents and the microbes from the underlying tissue, while permitting digestive absorption of the nutrients, electrolytes and water. It is also responsible for the secretion of mucus, antimicrobial proteins and hormones that regulate digestive functions. Furthermore, the epithelium participates in the coordination of appropriate immune responses [3]. The lamina propria of the small intestinal mucosa is a connective tissue underlying epithelium and contains blood and lymphatic vessels that constitute the routes through which the absorbed nutrients are distributed to the other parts of

the body [1]. In the lamina propria reside the stromal cells (e.g. subepithelial myofibroblasts) that help maintain epithelial homeostasis and the immune system related cells (e.g. macrophages, dendritic cells, and lymphoid cells) that are crucial in the host-microbial interactions [3]. The *muscularis mucosae* of mucosa consists of a thin layer of smooth muscles cells, which provides constant movement to the mucosal surface and underlying glands to enhance the contact between the epithelial cells and the lumenal content [4].

The small intestinal epithelium is organized into finger-like protrusions, called villi that are surrounded by multiple invaginations called crypts of Lieberkühn (Figure 2 A) [5, 6]. Villi dimensions are 0,2-1 mm in height [1, 7] and 100-150 μm in diameter [7, 8]. They are found at a density of 20-40 villi.mm^{-2} [1]. Villi morphology is crucial in increasing the surface area of the small intestine to maximize nutrient breakdown and absorption. Each villus has a core of lamina propria that is mainly composed of collagen type I and type III forming a scaffolding for the villus (Figure 2 B) [9]. Inside the lamina propria there is a network of blood and lymphatic capillaries that are responsible for taking the absorbed nutrients into direct circulation. Between the lamina propria and the epithelium there is the basement membrane. This is a specialized structure composed of extracellular matrix (ECM) components, predominantly collagen type IV and laminin [10]. It provides structural support to the epithelium and separates it from the underlying lamina propria, but also it influences adhesion, migration, proliferation, and differentiation of the epithelial cells [10]. Attached on the basement membrane, epithelial cells form a tightly joined, continuous monolayer called columnar epithelium [11]. Thanks to strongly joined epithelial cells, the epithelium avoids the entrance of harmful agents such as pathogens, while performing the digestive absorption of the nutrients [3]. In addition to the tightly joined epithelial cells there is a highly hydrated layer called mucus ($500\,\mu m$ in thickness in ileum) that covers the epithelial surface. It traps the pathogenic agents and keeps them from reaching the underlying tissue [12]. The mucus is secreted by the specialized epithelial cells and is mainly composed of glycoproteins called mucins that are found either free in the mucus (MUC2) or bound to the epthelial membrane (MUC1, MUC3, MUC17) [13]. The epithelial mucus layer is the first line of defense of the body against pathogenic invasion. In fact, the epithelium is in close contact with the immune system (Figure 2 C). In the underlying lamina propria reside number of different immune cells: lymphocytes (B cells and T cells), dendritic cells, macrophages, and mast cells [3, 14]. In addition, there are T cells present between the epithelium and the

basal membrane [15]. Epithelial cells express antimicrobial proteins and innate immune receptors that help coordinate proper responses within the underlying immune system. This limits the quantity and diversity of bacteria that can access the epithelium allowing the colonization of commensal bacteria, while keeping away the pathogenic ones [3, 14]. The loss of epithelial barrier integrity causes pathogens to reach the underlying tissue leading to conditions such as inflammation, infections, autoimmune diseases or cancer [16].

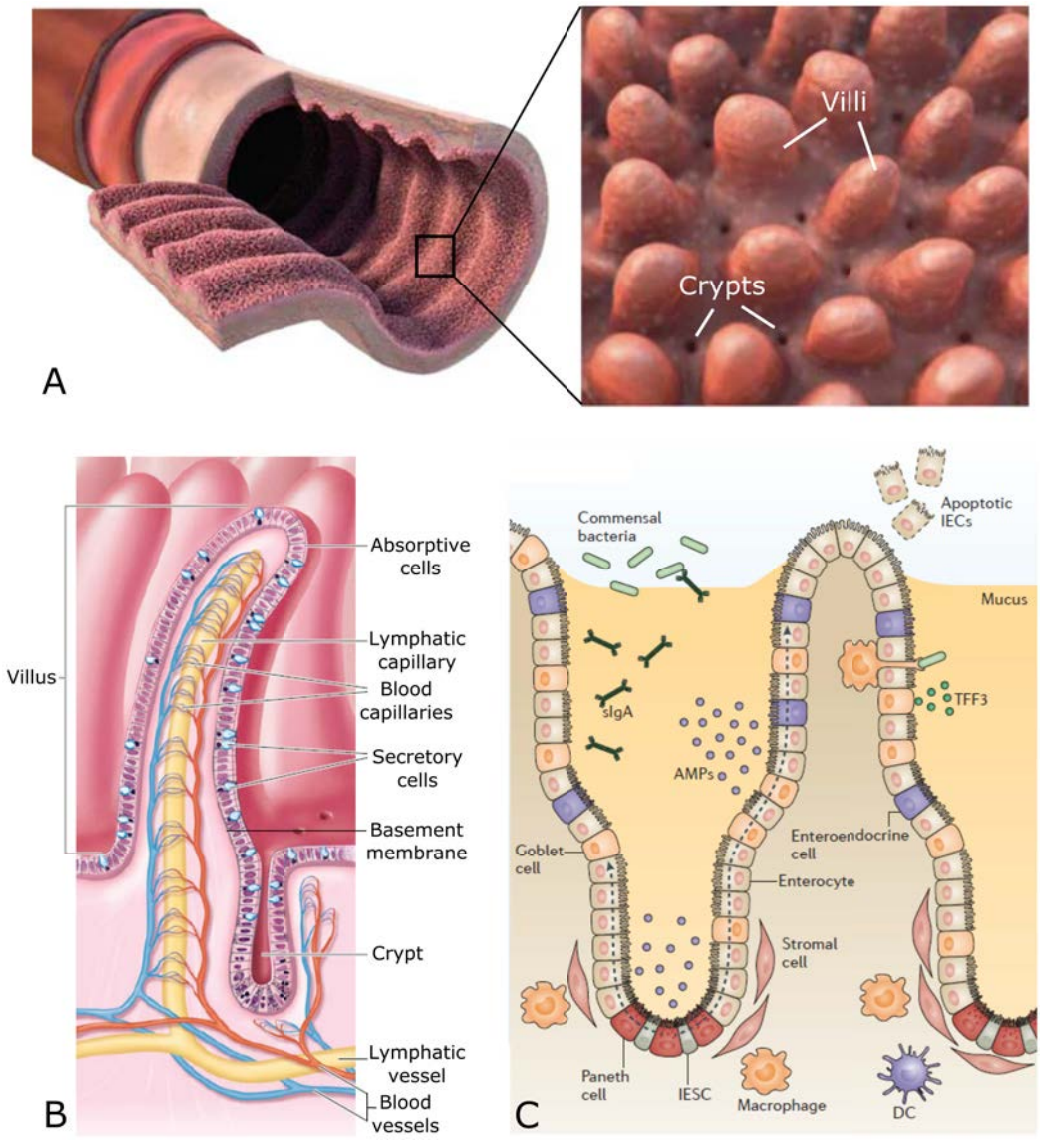

Figure 2: *Illustration showing the crypt-villus architecture of the inner wall of the small intestine (A). Adapted from Schuijers et al. [17]. Schematic representation of the cross-section of the villi (B). Adapted from Barret et al. [18]. Illustration of the intestinal mucosa and its immune apparatus (C). Adapted from Peterson and Artis [3]. IESC: intestinal epithelial stem cells, DC: dendritic cells, AMPs: antimicrobial peptides, sIgA: secretory immunoglobulin A,IECs: intestinal epithelial cells.*

The small intestinal epithelium is continuously renewed as it endures continuous mechanical and chemical stress. It is the fastest proliferating tissue in the body with a turnover rate of 4-6 days [17]. The active proliferation takes place at the crypts of Lieberkühn, that are located at the base of the villi embedded within

the underlying connective tissue (lamina propria). Epithelial renewal is driven by the adult intestinal stem cells (ISCs) that reside at the crypt bottoms (Figure 3). ISCs give rise to different types of specialized epithelial cells: absorptive cells (enterocytes), Paneth cells, Goblet cells, and enteroendocrine cells [19]. Enterocytes are the predominant cell type within the epithelium and they transport selected nutrients across the epithelium, from the lumen into the connective tissue underneath. They also secrete enzymes that help the efficient breakdown of partially digested food and the absorption of nutrients. Goblet cells are secretory cells that produce the mucus [6]. They are most common in the ileal epithelium, where they provide the extra lubrication necessary for the passage of increasingly compact stool toward the large intestine (colon) [19]. Enteroendocrine cells form 1% of the total cell population in the epithelium and produce hormones that regulate digestive functions [20]. Paneth cells secrete protective antimicrobial proteins and they are intercalated among the ISCs providing biochemical signals to preserve the stem cell niche [5]. Within the epithelium there are three other cell types with not very well defined functions: tuft cells, Peyer's patch-associated M cells and cup cells [19].

Intestinal epithelial regeneration relies on the existance of the ISCs at the crypt base. ISCs divide to produce highly proliferative progenitors known as transit-amplifying (TA) cells. TA cells divide a couple of times and migrate upwards along the villi while gradually differentiating into different types of specialized epithelial cells with the exception of Paneth cells that stay within the stem cell niche at the bottom of the crypts (Figure 3) [5, 6, 19, 20]. ISCs are identified by the Wingless/Int (Wnt) target gene leucine-rich repeat-containing G-protein coupled receptor 5 (Lgr5) [21]. There are approximately 14 $Lgr5^+$ ISCs at each crypt base [22] and they divide every 24 h feeding the epithelium with new progeny [17]. A second pool of stem cells found right above the Paneth cells at +4 position from the crypt base, was also described (Figure 3) [5, 6]. It has been seen that, these cells are relatively quiescent and responsible for injury-induced regeneration [23]. It was proposed that the epithelial regeneration relies on $Lgr5^+$ ISCs during homeostasis (physiological epithelial renewal), and on +4 ISC upon injury [23].

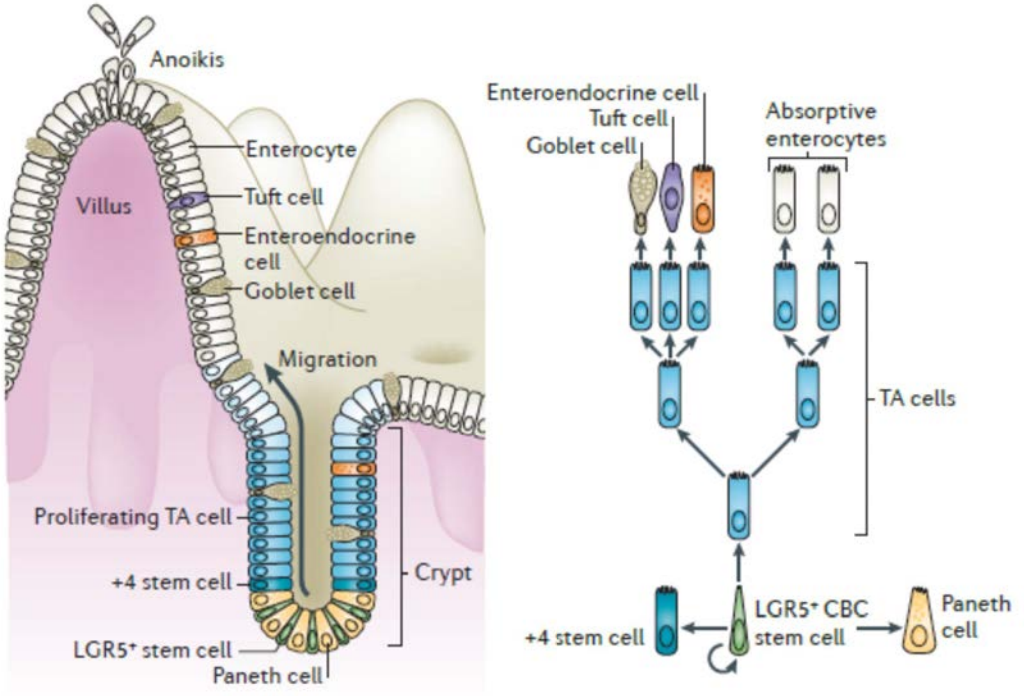

Figure 3: *Schematics of the distribution different epithelial cell types in the small intestinal epithelium (left panel). Lgr5⁺ stem cells located at the crypt base, intercalated with Paneth cells, continuously divide to produce highly proliferative transit-amplifying (TA) cells, which occupy the rest of the crypt. TA cells migrate up and differentiate into the various cell types (enterocytes, tuft cells, goblet cells and enteroendocrine cells) to replace the epithelial cells being lost at the villus tip. The +4 'reserve' stem cells can restore Lgr5⁺ stem cell compartment following injury. This differentiating hierarchy is given in the scheme on the right panel. Adapted from Barker [19].*

The ISC maintenance and so the epithelial renewal, is tightly controlled by well-characterized signaling pathways of epidermal growth factor (EGF), Wingless/Int (Wnt), Notch and bone morphogenetic protein (BMP) signaling [24]. With the exception of membrane-bound Notch, these biochemical factors create gradients from the crypt base to the villus tips and control the growth, migration and differentiation of the ISCs (Figure 4 A) [24]. The principle driver of the epithelial regeneration is the Wnt signaling. Cell secreted Wnt ligands bind their cell surface receptors leading to the accumulation of β-catenin proteins in the nucleus, which drives a transcriptional programme that maintains the ISC pool [25]. R-Spondins, physiological ligands of Lgr5, enhance the signal initiated by the Wnt ligands [26, 27]. EGF signals exert strong mitogenic effects on ISCs and TA cells upon binding to their EGF receptors [24]. Notch signals inhibit differentiation through membrane-bound proteins and control

the enterocyte-secretory cell fate decisions [6]. Finally, BMP signals are active in the villus compartment and drive the differentiation of TA cells as they migrate up along the villi. Therefore, it is inhibited in the ISC compartment [28–30]. In the epithelium, Paneth cells secrete Wnt3 and EGF, and also they provide neigboring ISCs with membrane-bound Notch ligands, Dll1/Dll4 (Figure 4 B, C) [31]. However, they are not the only source for Wnts and EGF. These factors are also produced by the underlying mesenchyme [32]. R-Spondins are also provided by nonepithelial sources such as intestinal subepithelial myofibroblasts [24].

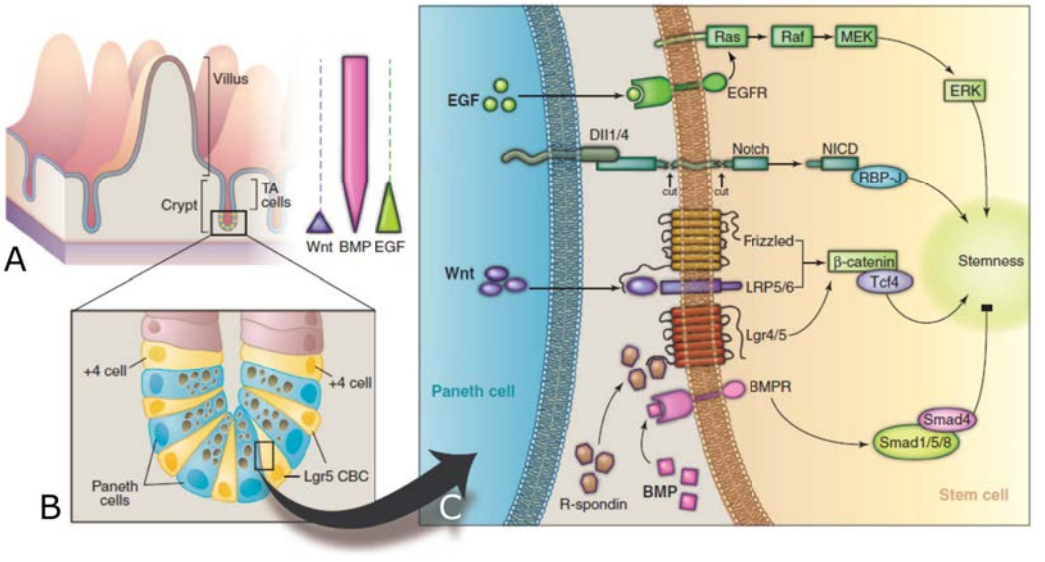

Figure 4: *Scheme showing the spatial gradients of Wnt, BMP, and EGF signals formed along the crypt axis (A). Scheme showing the stem cell niche with Lgr5⁺ intestinal stem cells adhered to Paneth cells that provide necessary signals for stem cell maintenance (B). Detailed representation of the three signals (EGF, Notch, and Wnt) that are essential for intestinal epithelial stemness, while BMP inhibits the stemness (C). R-Spondin–Lgr4/5 signal enhances the Wnt activation in the intestinal epithelium. Adapted from Sato and Clevers [24].*

The evidence pointing to nonepithelial sources of ISC niche factors drove the attention to the involvement of mesenchymal cells in the stem cell niche function. Right below the basement membrane within the lamina propria there is an extensive network of fibroblast-like cells [30]. The fibroblast-like cells form a basket-like network around the crypts and are tightly arranged beneath villi (Figure 5) [33]. These subepithelial cells are mainly two types: ECM secreting, non-contractile fibroblasts and contractile myofibroblasts [30]. The intestinal subepithelial myofibroblasts (ISEMFs) are primarily located around

the crypts right below the epithelial cells [34] and characteristically stained positive for α-smooth muscle actin (α-SMA) and vimentin and negative for the smooth muscle cell marker desmin [35]. An increasing number of studies have demonstrated that ISEMFs contribute to the ISC niche function. In colon, ISEMFs were shown to secrete BMP inhibitors [29]. These inhibitors form a gradient from the crypt base toward the villus where BMPs are active and progenitor cells differentiate [29]. Intestinal subepithelial fibroblast-like cells were shown to express non-canonical Wnt signals, such as Wnt-2b, Wnt-4, Wnt-5a, and Wnt-5b [36]. In fact, Wnt2b secreted by these cells was demonstrated to be enough to restore epithelial homeostasis after epithelial Wnt3 deletion [32]. In other studies, ISEMFs were shown to produce a number of Wnts, R-Spondin 3 [37], BMP inhibitor Noggin [38], and R-Spondin 2 [39]. Altogether, these findings demonstrate that the mesenchymal cells, primarily ISEMFs, form part of the ISC niche by secreting key biochemical niche factors: Wnts, R-Spondins, and BMP inhibitors (Figure 5).

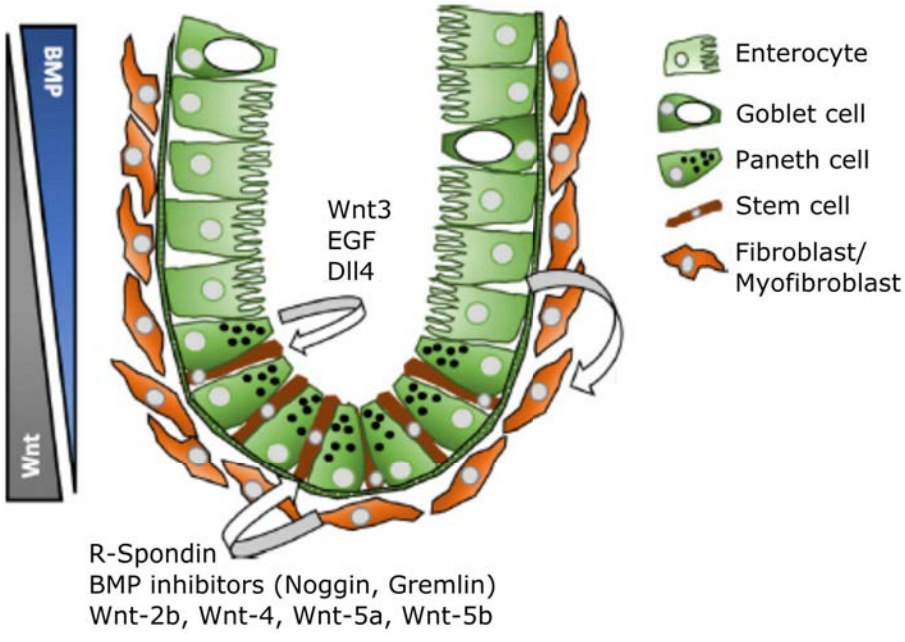

Figure 5: *Scheme describing the intestinal subepithelial fibroblast/myofibroblasts forming part of the ISC niche. These mesenchymal cells secrete BMP inhibitors (Noggin, Gremlin 1 and 2), Wnt enhancer R-Spondins, and non-canonical Wnt ligands: Wnt-2b, Wnt-4, Wnt-5a, and Wnt-5b. Adapted from Roulis and Flavell [30].*

The epithelial homeostasis (physiological epithelial renewal) is maintained by

tightly controlled mechanisms for the tissue to have proper barrier and absorption functions. There are number of diseases that affect the epithelial homeostasis, altering its morphology and proper functioning. These diseases can be classified as infections, food intolerances, obstructions, inflammation and autoimmune diseases and cancer [40–45]. These diseases affect large populations worldwide. Enteric infections, for instance, are among the leading cause of illness and death in children under the age of 5, especially in developing countries [41]. Only in 2010 there were over one million reported deaths [41]. Food intolerances such as celiac disease is one of the most common diseases with an estimated prevalence of 0,5-1% in different parts of the world [42]. Inflammatory bowel diseases, ulcerative colitis (UC) and Crohn's disease are common among westernized nations. In Europe, reported incidences were 24,3 and 12,7 for 100.000 person per year, respectively [44]. Cancers of the small intestine are not common; however, colorectal cancer is the third most commonly diagnosed cancer in males and the second in females [46]. Nearly 1,4 million new cases and 694.000 deaths were estimated to have occurred in 2012 [47]. The high prevalence of intestinal diseases and the lack of proper treatments raises the need to develop better therapeutics. To be able to improve the treatments, model diseases and investigate new drug candidates, a better understanding of epithelium physiology and pathology is required. To this end, there is a growing interest in the field of tissue engineering and regenerative medicine to developed predictive models of the small intestinal epithelium [48, 49].

A wide variety of *in vivo* mammalian models, from mouse to pig, are used in the study of intestinal diseases. Mouse is the most commonly used species due to the similarities in the intestinal development between mice and human. Mice models were proven useful for the study of gastroenteritis [50], celiac disease [51], intestinal inflammation [52], inflammatory bowel disease [53], autoimmune gastritis [54], intestinal and colorectal cancer [55, 56], and also intestinal drug transport [57]. Animal models provide useful *in vivo* information as they better represent the complex physiology of the intestinal epithelium. However, there is little control over the individual contributions of the complex microbiota, intestinal epithelium, and immune system. In additions, there are physiological differences between humans and the animal models. Moreover, these models are very costly and raise ethical concerns. Alternatively, small intestinal tissue explants are used, referred as *ex vivo* models, especially for the studies of mechanisms and kinetics of drug absorption [58–60]. Tissue explants have the advantage of using

native tissue environment and cell populations while providing access for the manipulation and inspection of it, which would otherwise be hindered in the body. However, the tissue viability, which is limited by couple of hours in most of the cases, is the main restriction of the explant models.

Cell-based *in vitro* culture models of intestinal epithelium are valuable tools and have a wide range of applications from understanding of the basic biology of intestinal epithelium, investigating intestinal diseases and searching for new therapeutics. Long-term propagation of the primary cultures of intestinal epithelial cells was not feasible due to their short lifespan. This imposed a problem to find reliable cell-based *in vitro* models of this tissue. Traditional models rely on cultures of human colorectal tumor derived cell line, Caco-2, to study drug transport processes through the epithelium due to their functional and phenotypical similarity to human enterocytes [61, 62]. Typically, Caco-2 cells are seeded on porous membrane inserts that separate the culture well into two compartments mimicking the luminal (apical) and stromal (basolateral) sides of the tissue barrier. The Caco-2 cells grow to form a confluent differentiated epithelial cell monolayer with mature tight-junctions [61]. Caco-2 cell model is considered as the gold standard in the pharmaceutical industry and extensively used to study the transport properties of drug molecules through the epithelium. However, Caco-2 cells' tight junctions are markedly stronger than those of the native small intestinal epithelium causing the underestimation of the permeability of many small molecules, especially that of the slowly absorbed drugs [63, 64]. Moreover, these cells have altered metabolism and show inconsistent expression of metabolic proteins and transporters [63, 64]. The model also lack the mucus layer as these enterocyte-like cells do not produce mucins. Furthermore, the absence of ISCs and their diverse progeny limits the relevance of this Caco-2 cell model. As in native intestinal epithelium, multicellularity creates differences in the tight junction properties along the crypt-villus axis, resulting in a leakier barrier [65] than what is represented by the oversimplified Caco-2 cell model.

Identification of the exquisite stem cell marker Lgr5 made it possible the isolation of ISCs [21]. Sato *et al.* showed that when single $Lgr5^+$ stem cells were grown in a drop of support matrix that resembled basement membrane, they formed 'miniguts' or 'intestinal organoids' that contained all different cell types and the multicellular hierarchy with crypt-like and villus-like domains, very much like *in vivo* intestinal epithelium [66]. The organoids had a central cavity into which terminally differentiated cells were expelled recapitulating the homeostatic cycle *in vivo*. Long-term propagation of these cultures was possible without any change

in the phenotype and genotype [66]. Organoids could be obtained from isolated intestinal crypts together with the underlying mesenchyme [67] and from human induced pluripotent stem cells (hiPSCs) [68]. Organoid technology has provided useful *in vitro* models in a wide range of applications from the study of basic biology of the intestine to *in vitro* screening of drug candidates [69–73]. However, their three-dimensional (3D) closed form prevents access to the apical side of the epithelium, making them unsuitable for standard functionality assays that are typically performed on epithelial monolayers grown on planar surfaces. Very recently, some works have been published reporting monolayers obtained from intestinal crypts or dissociated cells from organoids. However, either they lacked *in vivo*-like crypt-villus organization [74–77] or formation of an effective tissue barrier with tight junction integrity similar to that of the native intestinal epithelium [76, 78].

Another important consideration is the 3D architecture of the small intestine that is involved in nutrient absorption, cellular organization and epithelial homeostasis. Cultures grown on flat surfaces and porous membranes or embedded into a support matrix lack the crypt-villus architecture of the native intestinal tissue. To overcome the limitations of these cultures, new strategies have been developed to establish more complex models of small intestine using biomaterials and microtechnologies. These models incorporated the 3D structural features of the small intestine by special molds prepared by microfabrication techniques to replicate the characteristic villus-like forms on a variety of biomaterials [79–82]. The 3D architecture was shown to improve the correlation between the *in vitro* models and the native human small intestine in tight junction permeability [80] and induced differentiation [82, 83]. However, these models were developed with Caco-2 or other intestinal epithelial cell lines; therefore, they lacked the multicellular composition and distribution of the native intestinal epithelium.

Very recently, a couple of studies reported biomaterial based models that had 3D features mimicking the intestinal architecture and used intestinal cells derived from organoids [82, 84]. Nevertheless, these models required complex fabrication strategies and the critical mechanical and physicochemical properties of the biomaterials chosen could not be tuned easily. Furthermore, multicellular distribution, and therefore, the performance of the epithelium functionality was not demonstrated. In a representative model of intestinal epithelium, not only mimicking the mechanical and network properties of the basement membrane and the 3D architecture is relevant, but also it might be beneficial to guide cell position and functionality through the delivery of gradients of ISC niche biochemical

factors as they are existing *in vivo*. Only a couple of studies has been reported culturing organoids under gradients of ISC niche biochemical factors [85, 86]. It was demonstrated that proliferative cell compartments were formed towards the higher concentration regions of the ISC niche factors. These models lacked the 3D structural features of the small intestine and the gradients were generated across the organoids embedded within the support matrix, far away from the *in vivo* scenario. Nevertheless, they demonstrated that biochemical gradients of ISC niche factors could be used to guide cellular organization in organoids. Indeed, in a very recent study, basolateral delivery of ISC niche factors was shown to lead to *in vivo*-like crypt-villus cellular distribution along microstructured collagen scaffolds [87]. The state of the art proves the benefits of the use of soft biomaterials as substitutes of basement membranes, microfabricated 3D villus-like structures, ISCs or organoids, and the presence of gradients of ISC niche biochemical factors in the growth and functionality of intestinal epithelium. To the best of our knowledge, a microengineered system combining these features have not been reported.

References

[1] Gerard Tortora and Bryan Derrickson. *Principles of Anatory and Physiology*. 12th ed. John Wiley and Sons, Inc., 2010.

[2] Last Guyton et al. *Guyton and Hall Textbook of Medical Physiology*. 1. 2014, p. 1129. ISBN: 9780874216561.

[3] Lance W. Peterson and David Artis. "Intestinal epithelial cells: Regulators of barrier function and immune homeostasis". In: *Nature Reviews Immunology* 14.3 (2014), pp. 141–153.

[4] Barbara Young et al. *Wheater's Functional Histology*. 5th ed. Elsevier, 2006. ISBN: 9780443068508.

[5] Hans Clevers. "The intestinal crypt, a prototype stem cell compartment." In: *Cell* 154.2 (2013), pp. 274–84.

[6] Marc Leushacke and Nick Barker. "Ex vivo culture of the intestinal epithelium: Strategies and applications". In: *Gut* 63.8 (2014), pp. 1345–1354.

[7] John Louis Auguste et al. "High dose multiple micronutrient supplementation improves villous morphology in environmental enteropathy without HIV enteropathy: Results from a double-blind randomised placebo controlled trial in Zambian adults". In: *BMC Gastroenterology* 14.1 (2014), pp. 1–10.

[8] Paul Kelly et al. "Responses of small intestinal architecture and function over time to environmental factors in a tropical population". In: *Am. J. Trop. Med. Hyg.* 70 (2004), pp. 412–419.

[9] Dany Muñoz-Pinto, Peter Whittaker, and Marian S. Hahn. "Lamina propria cellularity and collagen composition: An integrated assessment of structure in humans". In: *Annals of Otology, Rhinology and Laryngology* 118.4 (2009), pp. 299–306.

[10] A C Y Li and A Li. "Basement membrane components". In: *Journal of Clinical Pathology* 56.12 (2003), pp. 885–887.

[11] Alexander Alberts, BruceJohnson et al. *Molecular Biology of the Cell*. Vol. 53. 9. 2008, pp. 1689–1699. ISBN: 9788578110796.

[12] C. Atuma et al. "The adherent gastrointestinal mucus gel layer: thickness and physical state in vivo". In: *American Journal of Physiology-Gastrointestinal and Liver Physiology* 280.5 (2001), G922–G929.

[13] Young S. Kim and Samuel B. Ho. "Intestinal goblet cells and mucins in health and disease: Recent insights and progress". In: *Current Gastroenterology Reports* 12.5 (2010), pp. 319–330.

[14] Allan M. Mowat and William W. Agace. "Regional specialization within the intestinal immune system". In: *Nature Reviews Immunology* 14.10 (2014), pp. 667–685.

[15] L. Liu and G. Talmon. "Quantification of intraepithelial lymphocytes in normal pediatric small intestinal allograft and native ilea". In: *Transplantation Proceedings* 43.5 (2011), pp. 1831–1835.

[16] June L. Round and Sarkis K. Mazmanian. "The gut microbiota shapes intestinal immune responses during health and disease". In: *Nature Reviews Immunology* 9.5 (2009), pp. 313–323.

[17] Jurian Schuijers and Hans Clevers. "Adult mammalian stem cells: the role of Wnt, Lgr5 and R-spondins". In: *The EMBO Journal* 31.12 (2012), pp. 2685–2696.

[18] K. Barret et al. *Ganong's Review of Medical Physiology*. 23rd ed. New York: NY McGraw-Hill, 2010. ISBN: 978-0-07-160568-7.

[19] Nick Barker. "Adult intestinal stem cells: critical drivers of epithelial homeostasis and regeneration". In: (2013).

[20] Shahid Umar. "Intestinal Stem Cells". In: *Curr Gastroenterol Rep* 12.5 (2011), pp. 340–348.

[21] Nick Barker et al. "Identification of stem cells in small intestine and colon by marker gene Lgr5." en. In: *Nature* 449.7165 (2007), pp. 1003–7.

[22] Hugo J. Snippert et al. "Intestinal crypt homeostasis results from neutral competition between symmetrically dividing Lgr5 stem cells". In: *Cell* 143.1 (2010), pp. 134–144.

[23] Ks Yan, La Chia, and Xingnan Li. "The intestinal stem cell markers Bmi1 and Lgr5 identify two functionally distinct populations". In: *Pnas* 109.2 (2012), pp. 466–471.

[24] Toshiro Sato and Hans Clevers. "Growing self-organizing mini-guts from a single intestinal stem cell: mechanism and applications." In: *Science (New York, N.Y.)* 340.6137 (2013), pp. 1190–4.

[25] Hans Clevers and Roel Nusse. "Wnt/β-catenin signaling and disease". In: *Cell* 149.6 (2012), pp. 1192–1205.

[26] W de Lau et al. "Lgr5 homologues associate with Wnt receptors and mediate R-spondin signalling." In: *Nature* 476.7360 (2011), pp. 293–7.

[27] K. S. Carmon et al. "R-spondins function as ligands of the orphan receptors LGR4 and LGR5 to regulate Wnt/beta-catenin signaling". In: *Proceedings of the National Academy of Sciences* 108.28 (2011), pp. 11452–11457.

[28] Anna Pavlina G Haramis et al. "De Novo Crypt Formation and Juvenile Polyposis on BMP Inhibition in Mouse Intestine". In: *Science* 303.5664 (2004), pp. 1684–1686.

[29] C. Kosinski et al. "Gene expression patterns of human colon tops and basal crypts and BMP antagonists as intestinal stem cell niche factors". In: *Proceedings of the National Academy of Sciences* 104.39 (2007), pp. 15418–15423.

[30] Manolis Roulis and Richard A. Flavell. "Fibroblasts and myofibroblasts of the intestinal lamina propria in physiology and disease". In: *Differentiation* 92.3 (2016), pp. 116–131.

[31] Toshiro Sato et al. "Paneth cells constitute the niche for Lgr5 stem cells in intestinal crypts." In: *Nature* 469.7330 (2011), pp. 415–418.

[32] Henner F. Farin, Johan H. Van Es, and Hans Clevers. "Redundant Sources of Wnt Regulate Intestinal Stem Cells and Promote Formation of Paneth Cells". In: *Gastroenterology* 143.6 (2012), 1518–1529.e7.

[33] Junzo Desaki and Maki Shimizu. "A re-examination of the cellular reticulum of fibroblast-like cells in the rat small intestine by scanning electron microscopy". In: *Journal of Electron Microscopy* 49.1 (2000), pp. 203–208.

[34] R. C. Mifflin et al. "Intestinal myofibroblasts: targets for stem cell therapy". In: *American Journal of Physiology-Gastrointestinal and Liver Physiology* 300.5 (2011), G684–G696.

[35] I. V. Pinchuk et al. “Intestinal Mesenchymal Cells”. In: *Current Gastroenterology Reports* 12.5 (2010), pp. 310–318.

[36] Alex Gregorieff et al. “Expression Pattern of Wnt Signaling Components in the Adult Intestine”. In: *Gastroenterology* 129.2 (2005), pp. 626–638.

[37] Z. Kabiri et al. “Stroma provides an intestinal stem cell niche in the absence of epithelial Wnts”. In: *Development* 141.11 (2014), pp. 2206–2215.

[38] Xi C He et al. “BMP signaling inhibits intestinal stem cell self-renewal through suppression of Wnt–β-catenin signaling”. In: *Nature Genetics* 36.10 (2004), pp. 1117–1121.

[39] Nan Ye Lei et al. “Intestinal subepithelial myofibroblasts support the growth of intestinal epithelial stem cells”. In: *PLoS ONE* 9.1 (2014).

[40] Glynis Kolling, Martin Wu, and Richard L. Guerrant. “Enteric pathogens through life stages”. In: *Frontiers in Cellular and Infection Microbiology* 2.August (2012), pp. 1–8.

[41] Martyn D. Kirk et al. “World Health Organization Estimates of the Global and Regional Disease Burden of 22 Foodborne Bacterial, Protozoal, and Viral Diseases, 2010: A Data Synthesis”. In: *PLoS Medicine* 12.12 (2015), pp. 1–21.

[42] Naiyana Gujral, Hugh J. Freeman, and Alan B.R. Thomson. “Celiac disease: Prevalence, diagnosis, pathogenesis and treatment”. In: *World Journal of Gastroenterology* 18.42 (2012), pp. 6036–6059.

[43] Marian Rewers. “Epidemiology of celiac disease: What are the prevalence, incidence, and progression of celiac disease?” In: *Gastroenterology* 128.4 SUPPL. 1 (2005), pp. 47–51.

[44] Natalie A. Molodecky et al. “Increasing incidence and prevalence of the inflammatory bowel diseases with time, based on systematic review”. In: *Gastroenterology* 142.1 (2012), 46–54.e42.

[45] Makoto Naganuma et al. “Characterization of structures with T-lymphocyte aggregates in ileal villi of Crohn’s disease”. In: *American Journal of Gastroenterology* 97.7 (2002), pp. 1741–1747.

[46] Ahmedin Jemal et al. “Global Cancer Statistics: 2011”. In: *CA Cancer J Clin* 61 (2011), pp. 69–90.

[47] World Health Organization. *globocan 2012: Estimated cancer incidence, mortality and prevalence worldwide in 2012*.

[48] Ryan G. Spurrier and Tracy C. Grikscheit. “Tissue engineering the small intestine”. In: *Clinical Gastroenterology and Hepatology* 11.4 (2013), pp. 354–358.

[49] Mitchell R. Ladd et al. “Generation of an artificial intestine for the management of short bowel syndrome”. In: *Current Opinion in Organ Transplantation* 21.2 (2016), pp. 178–185.

[50] Martin Stahl et al. “A Novel Mouse Model of Campylobacter jejuni Gastroenteritis Reveals Key Pro-inflammatory and Tissue Protective Roles for Toll-like Receptor Signaling during Infection”. In: *PLoS Pathogens* 10.7 (2014), pp. 9–11.

[51] E. V. Marietta, C. S. David, and J. A. Murray. “Important lessons derived from animal models of celiac disease”. In: *International Reviews of Immunology* 30.4 (2011), pp. 197–206.

[52] Janelle A. Jiminez et al. "Animal models to study acute and chronic intestinal inflammation in mammals". In: *Gut Pathogens* 7.1 (2015), p. 29.

[53] Nidhi Goyal et al. "Animal models of inflammatory bowel disease: A review". In: *Inflammopharmacology* 22.4 (2014), pp. 219–233.

[54] Frank Alderuccio et al. "Animal models of human disease: Experimental autoimmune gastritis - A model for autoimmune gastritis and pernicious anemia". In: *Clinical Immunology* 102.1 (2002), pp. 48–58.

[55] Robert L. Johnson and James C. Fleet. "Animal models of colorectal cancer". In: *Cancer and Metastasis Reviews* 32.1-2 (2013), pp. 39–61.

[56] Rene Jackstadt and Owen J. Sansom. "Mouse models of intestinal cancer". In: *Journal of Pathology* 238.2 (2016), pp. 141–151.

[57] Hartmut Glaeser and Martin F Fromm. "Animal models and intestinal drug transport." In: *Expert opinion on drug metabolism and toxicology* 4.4 (2008), pp. 347–61.

[58] Esther G. Van De Kerkhof et al. "Innovative methods to study human intestinal drug metabolism in vitro: Precision-cut slices compared with Ussing chamber preparations". In: *Drug Metabolism and Disposition* 34.11 (2006), pp. 1893–1902.

[59] Kevin J. Randall, John Turton, and John R. Foster. "Explant culture of gastrointestinal tissue: A review of methods and applications". In: *Cell Biology and Toxicology* 27.4 (2011), pp. 267–284.

[60] Mohd Aftab Alam, Fahad Ibrahim Al-Jenoobi, and Abdullah M. Al-Mohizea. "Everted gut sac model as a tool in pharmaceutical research: Limitations and applications". In: *Journal of Pharmacy and Pharmacology* 64.3 (2012), pp. 326–336.

[61] I J Hidalgo, T J Raub, and R T Borchardt. "Characterization of the human colon carcinoma cell line (Caco-2) as a model system for intestinal epithelial permeability." In: *Gastroenterology* 96.3 (1989), pp. 736–49.

[62] P. Shah et al. "Role of Caco-2 Cell Monolayers in Prediction of Intestinal Drug Absorption". In: *Biotechnology Progress* 22.1 (2006), pp. 186–198.

[63] Y. Sambuy et al. "The Caco-2 cell line as a model of the intestinal barrier: influence of cell and culture-related factors on Caco-2 cell functional characteristics". In: *Cell Biology and Toxicology* 21.1 (2005), pp. 1–26.

[64] Huadong Sun et al. "The Caco-2 cell monolayer: usefulness and limitations". In: *Expert Opinion on Drug Metabolism and Toxicology* 4.4 (2008), pp. 395–411.

[65] BrittMarie M. Fihn, Anders Sjoqvist, and Mats Jodal. "Permeability of the rat small intestinal epithelium along the villus-crypt axis: Effects of glucose transport". In: *Gastroenterology* 119.4 (2000), pp. 1029–1036.

[66] Toshiro Sato et al. "Single Lgr5 stem cells build crypt-villus structures in vitro without a mesenchymal niche." In: *Nature* 459.7244 (2009), pp. 262–5.

[67] Akifumi Ootani et al. "Sustained in vitro intestinal epithelial culture within a Wnt-dependent stem cell niche." In: *Nature medicine* 15.6 (2009), pp. 701–6.

[68] Jason R. Spence et al. "Directed differentiation of human pluripotent stem cells into intestinal tissue in vitro". en. In: *Nature* 470.7332 (2010), pp. 105–109.

[69] Johanna F Dekkers et al. "A functional CFTR assay using primary cystic fibrosis intestinal organoids". In: *Nature Medicine* 19.7 (2013), pp. 939–945.

[70] Adrian Ranga, Nikolche Gjorevski, and Matthias P Lutolf. "Drug discovery through stem cell-based organoid models." In: *Advanced drug delivery reviews* 69-70 (2014), pp. 19–28.

[71] Stacy R. Finkbeiner et al. "Transcriptome-wide Analysis Reveals Hallmarks of Human Intestine Development and Maturation In Vitro and In Vivo". In: *Stem Cell Reports* 4.6 (2015), pp. 1140–1155.

[72] Mami Matano et al. "Modeling colorectal cancer using CRISPR-Cas9–mediated engineering of human intestinal organoids". In: *Nature Medicine* 21.3 (2015), p. 256.

[73] Shiro Yui et al. "Functional engraftment of colon epithelium expanded in vitro from a single adult Lgr5+ stem cell." en. In: *Nature medicine* 18.4 (2012), pp. 618–23.

[74] C. Moon et al. "Development of a primary mouse intestinal epithelial cell monolayer culture system to evaluate factors that modulate IgA transcytosis". In: *Mucosal Immunology* 7.4 (2014), pp. 818–828.

[75] Kelli L. VanDussen et al. "Development of an enhanced human gastrointestinal epithelial culture system to facilitate patient-based assays". In: *Gut* 64.6 (2015), pp. 911–920.

[76] Yuli Wang et al. "Self-renewing Monolayer of Primary Colonic or Rectal Epithelial Cells". In: *Cellular and Molecular Gastroenterology and Hepatology* 4.1 (2017), 165–182.e7.

[77] Kenji Kozuka et al. "Development and Characterization of a Human and Mouse Intestinal Epithelial Cell Monolayer Platform." In: *Stem cell reports* 9.6 (2017), pp. 1976–1990.

[78] Curtis A. Thorne et al. "Enteroid Monolayers Reveal an Autonomous WNT and BMP Circuit Controlling Intestinal Epithelial Growth and Organization". In: *Developmental Cell* 44.5 (2018), 624–633.e4.

[79] Jong Hwan Sung et al. "Microscale 3-D hydrogel scaffold for biomimetic gastrointestinal (GI) tract model." en. In: *Lab on a chip* 11.3 (2011), pp. 389–92.

[80] Jiajie Yu et al. "In vitro 3D human small intestinal villous model for drug permeability determination." In: *Biotechnology and bioengineering* 109.9 (2012), pp. 2173–8.

[81] Ying Chen et al. "Robust bioengineered 3D functional human intestinal epithelium". In: *Scientific Reports* 5 (2015), p. 13708.

[82] Cait M Costello et al. "Synthetic small intestinal scaffolds for improved studies of intestinal differentiation." In: *Biotechnology and bioengineering* 111.6 (2014), pp. 1222–32.

[83] Si Hyun Kim et al. "Three-dimensional intestinal villi epithelium enhances protection of human intestinal cells from bacterial infection by inducing mucin expression." en. In: *Integrative biology : quantitative biosciences from nano to macro* 6.12 (2014), pp. 1122–31.

[84] Ying Chen et al. "In vitro enteroid-derived three-dimensional tissue model of human small intestinal epithelium with innate immune responses". In: *PLoS ONE* 12.11 (2017), pp. 1–20.

[85] Asad A. Ahmad et al. "Optimizing Wnt-3a and R-spondin1 concentrations for stem cell renewal and differentiation in intestinal organoids using a gradient-forming microdevice". In: *RSC Advances* 5.91 (2015), pp. 74881–74891.

[86] Peter J. Attayek et al. "In vitro polarization of colonoids to create an intestinal stem cell compartment". In: *PLoS ONE* 11.4 (2016), pp. 1–23.

[87] Yuli Wang et al. "A microengineered collagen scaffold for generating a polarized crypt-villus architecture of human small intestinal epithelium". In: *Biomaterials* 128 (2017), pp. 44–55.

Objectives

The developments in intestinal stem cell (ISC) culture methods have made it possible to use primary intestinal epithelial cells to create near-physiological tissues called 'organoids' *in vitro*. Nevertheless, the three-dimensional (3D) closed form of organoids presents severe limitations in many applications. Therefore, there is a need for engineering culture platforms that overcome this limitation and provide a physiologically relevant environment, while preserving the stem and differentiated cells present. The current engineered culture platforms of intestinal epithelium are limited as they lack to combine all the key features of intestinal epithelium, such as distinct stem/proliferative and differentiated cell types, 3D architectural features, and gradients of ISC niche biochemical factors.

This thesis, entitled "**Towards the development of biomimetic *in vitro* models of intestinal epithelium derived from intestinal organoids**", aims to contribute to the development of complex *in vitro* models of intestinal epithelium by considering the novel advancements in cell biology, biomaterials and microfabrication technologies. The main **objective** of this study is to generate a small intestinal epithelial model on microengineered villus-like soft porous scaffolds by guiding the growth and differentiation of organoid-derived intestinal epithelial cells through establishing gradients of key ISC niche biochemical factors on these scaffolds. Towards this general objective, the specific objectives are defined as:

1) Generation of small intestinal epithelial monolayers derived from mouse intestinal organoids with an accessible lumen and *in vivo*-like cellular organization. Establishment of proper culture conditions to obtain epithelial monolayers with effective tissue barrier properties.

2) Development and characterization of hydrogel-based basement membrane substitute that mimic the villus-like architecture with proper biochemical, mechanical and physicochemical properties for its successful bioactivity. Optimization of material properties and culture conditions for successful engraftment of intestinal cells derived from organoids.

3) Development and characterization of spatio-chemical gradients of ISC niche biochemical factors within 3D villus-like hydrogel scaffolds. Study of intestinal epithelial cell response over these spatio-chemical gradients.

This thesis is structured in three experimental chapters each of them targeting one specific objective contributing to the final aim and described in what follows.

In **Chapter 1**, we describe a method taking the advantage of the substrate stiffness for the generation of the epithelial monolayers. The cell types and their distributions within the monolayers were characterized by immunofluorescence. The monolayer formation and cell death were followed by time-lapse microscopy. Confluent monolayers were obtained on porous membranes with the use of factors secreted by intestinal subepithelial myofibroblasts (ISEMFs) that are rich in ISC niche proteins, and Wnt3a. The barrier integrity was evaluated by monitoring the transepithelial electrical resistance of the monolayers. Overall, the intestinal epithelial monolayers demonstrated *in vivo*-like crypt-villus cellular organization and formed effective tissue barriers with physiologically relevant transport properties. The 2D intestinal epithelial model has an advantage over the current 3D organoid model for studies that require an accessible lumen compartment such as drug testing and host-microbe interactions. The knowledge we acquired here on the optimal cell culture conditions was used in the following chapters.

In **Chapter 2**, we describe development of microengineered hydrogel scaffolds with villus-like architecture and proper biochemical, mechanical and physicochemical properties that support the growth of intestinal epithelial cells derived from organoids. The scaffold material used for the purpose was poly(ethylene glycol) diacrylate (PEGDA), a photocrosslinkable hydrogel that can be biochemically and topographically modified. PEGDA-based hydrogels were microstructured using a simple photolithographic approach and characterized by microscopic techniques. The mechanical and swelling properties and their dependence on fabrication conditions were assessed. Bioactive functionalization of PEGDA hydrogels was optimized for the growth of intestinal organoid-derived cells by screening different cell adhesion ligands. The effects of microstructure dimensions, hydrogel stiffness and factors secreted by ISEMF on intestinal cell growth were studied by microscopic and image analysis techniques. The proliferative and differentiated cell type distributions were characterized by immunofluorescence. The 3D villus-like scaffold model reported here, developed using a simple photolithographic approach provides the cells

with a more realistic cellular microenvironment. The simplicity of the fabrication method allows to routinely incorporate 3D architectures in cell culture systems of primary intestinal epithelial cells derived from organoids. In the following chapter, the gradients of ISC niche biochemical factors were established on these microengineered villus-like hydrogel scaffolds.

In **Chapter 3**, we describe development and characterization of spatio-chemical gradients of ISC niche biochemical factors within PEGDA-based hydrogel scaffolds. The pore sizes of PEGDA hydrogels were determined using well established equilibrium swelling theory to assess the difusivity of the factors through the hydrogels. *In silico* models were developed to simulate the spatio-chemical gradients of ISC niche biochemical factors and to gain an insight on their diffusion times, gradient profiles and surface concentrations. A microfluidic chip allocating the hydrogel was designed and fabricated to be able to visualize gradients by microscopic techniques. The gradients were generated based on the free diffusion of the factors from a source to a sink chamber. Stable profiles could be obtained by periodically replenishing the chambers. Light-sheet fluorescence microscopy was used to characterize the stable gradients formed by a fluorescently labeled model protein. The PEGDA-based hydrogels with villus-like architecture were fabricated on porous membranes and the fabrication parameters were optimized. The hydrogels were successfully incorporated into standard cell culture inserts that permitted access to both sides of the hydrogel. Spatio-chemical gradients were generated in this setup using the below compartment as the source and upper compartment as the sink. The effect of such gradients on the growth and differentiation of the organoid-derived intestinal epithelial cells was tested. This platform presents a physiologically relevant experimental mimic of intestinal epithelium in combining a 3D villus-like soft basement membrane substitute, organoid-derived primary intestinal epithelial cells, and the gradients of ISC niche biochemical factors as they are found *in vivo*.

Within the three experimental chapters, an introductory section is included with the current state of the art relevant to their specific objectives to help the reader contextualize the research subject. The results obtained are explained in the following section and they are discussed in detail showing their contribution to the current state of the art in a separate discussion section. The main findings of each chapter are summarized in the conclusions section. The thesis ends with general discussion and general conclusions sections in which the global achievements from the performed studies are given.

Finally, four **appendix** sections describing a method developed for the embedding and sectioning of microstructured hydrogels for improved imaging, the image analysis macro codes used, and the journal articles, published, under review or to be submitted, can be found.

Chapter 1

Organoid-derived 2D model of intestinal epithelium

1.1 Introduction

The small intestinal epithelium is composed of a monolayer of tightly packed polarized columnar epithelial cells with a variety of functions. These include formation and maintenance of a barrier to separate the luminal contents and the microbes from the underlying tissue, digestion and absorption of the nutrients, and participation in host immune response [1]. The epithelial monolayer is organized into invaginations called crypts, and finger-like protrusions, called villi, to maximize nutrient breakdown and absorption [2, 3]. The villi are mainly constitute of terminally differentiated absorptive cells (enterocytes) and secretory cells (Goblet and enteroendocrine cells), while the crypts are constituted by the intestinal stem cells, neighboring Paneth cells and transit-amplifying progenitors [1]. Intestinal stem cells (ISCs) divide every 24 h, feeding the monolayer with new cells that migrate up along the villi, differentiate, and eventually shed off at the villus tips [2, 4]. This mechanism leads to the renewal of the whole epithelium every 4-5 days, the highest self-renewal rate among all other mammalian tissues [1]. Perturbations of the epithelial homeostasis lead to gastrointestinal tract disorders such as infections [5], Celiac disease [6], inflammatory bowel disease [7] and cancer [8].

In vitro intestinal epithelial models are needed in a wide range of applications encompassing the improvement of the understanding of the intestinal epithelium basic biology, investigating intestinal disorders and mainly the accurate prediction of the *in vivo* absorption of orally administered drugs. Traditional models rely on 2D cultures of human colon cancer-derived cell line, Caco-2, to evaluate the drug and nutrient absorption because of their morphological and functional similarity to human enterocytes [9, 10]. Typically, Caco-2 cells are seeded on

porous membranes, grown to confluency forming a barrier acting as a semipermeable membrane with mature tight junctions [9]. For that reason, the Caco-2 model has been widely used to evaluate the permeability and the transport of drug candidates through the intestinal epithelium. However, its tight junctions are markedly tighter than those of the native small intestine, leading to the underestimation of transport parameters of mainly slowly absorbed drugs [11, 12]. In addition, these cells contain somatic mutations, altered metabolism, and aberrant proliferation and differentiation characteristics [11, 12]. Altogether, Caco-2 cell line does not accurately represent intestinal epithelium and its diverse cell lineages.

The use of primary human intestinal epithelial cells (hInEpCs) was expected to be a solution for the aforementioned limitations of the Caco-2 cell line model. However, due to limited donors, and poor viability and short life span of the cultures, their applications remained limited [13]. Recently, numerous companies have started to provide hInEpCs (e.g. Cell Systems, Lonza, MatTek Corporation), which has greatly facilitated obtaining of the primary cell stocks. Primary hInEpCs are shown to have the capacity to form epithelial monolayers, express general epithelial markers, and form proper tight junctions. However, interdonor variability in permeability of compounds continue to be a problem [13]. Moreover, primary intestinal cells are shown to transiently divide, but stop proliferation within 1-2 weeks [3]. Therefore, it was assumed that the long-term propagation of primary cultures of intestinal epithelial cells was not possible without introducing genetic transformations [14].

Recently, major advances have been made in establishing mouse [15, 16] and human [17] cell culture methods for the long-term propagation of intestinal epithelial cells *in vitro*. Ootani *et al.* developed a methodology supporting long-term proliferation and multilineage differentiation for mouse intestinal culture [15]. They used intestinal fragments containing both the epithelium and the underlying mesenchyme of neonatal mice, cultured in collagen gel at air-liquid interface. The intestinal cells grew into cystic structures formed of an inner monolayer of polarized epithelial cells containing all major cell types surrounded by the mesenchymal cells. The cultures were able to be propagated up to 350 days. Even though the culture system was promising in long-term maintenance of the intestinal tissue, it lacked the characteristic crypt-villus morphology of the native tissue.

Identification of the exquisite stem cell marker Lgr5 and generation of the Lgr5^{+}-GFP-Ires-creERT2 mice [18] facilitated the isolation of intestinal stem cells.

In a follow-up study, Sato and colleagues showed that when single Lgr5$^+$ stem cells were seeded into a drop of basement membrane-like support matrix, they grew into so-called 'miniguts' or 'organoids' that highly resembled the intestinal epithelium *in vivo* with all its different cell types and correct positioning (Figure 1.1 A, B) [16]. In the organoids, the finger-like protrusions are the crypt domains, where Lgr5$^+$ stem cells, neighboring Paneth cells and highly proliferative transit-amplifying cells reside. The regions in between protrusions are comprised of the differentiated cell types, i.e. absorptive enterocytes, secretory Goblet cells, and enteroendocrine cells, and are referred as the villus domains (Figure 1.1 A, B). These miniguts also have a central cavity which resembles the intestinal lumen into which terminally differentiated cells shed off displaced by the newcomer cells, faithfully recapitulating the *in vivo* situation. The organoid cultures require the use of soluble growth factors including R-Spondin, Noggin, and epidermal growth factor (EGF) to mimic the intestinal stem cell (ISC) niche; and Matrigel®, a laminin and collagen rich matrix, as support for 3D growth [16]. Matrigel® is a gelatinous protein mixture derived from Engelbreth-Holm-Swarm (EHS) mouse sarcoma cells commonly used as support matrix in cultures of many cell types due to its resemblance of the extracellular matrix of *in vivo* tissues [19]. Long-term propagation of the organoid cultures was possible for up to 1,5 years with the phenotype and karyotype being unchanged [16].

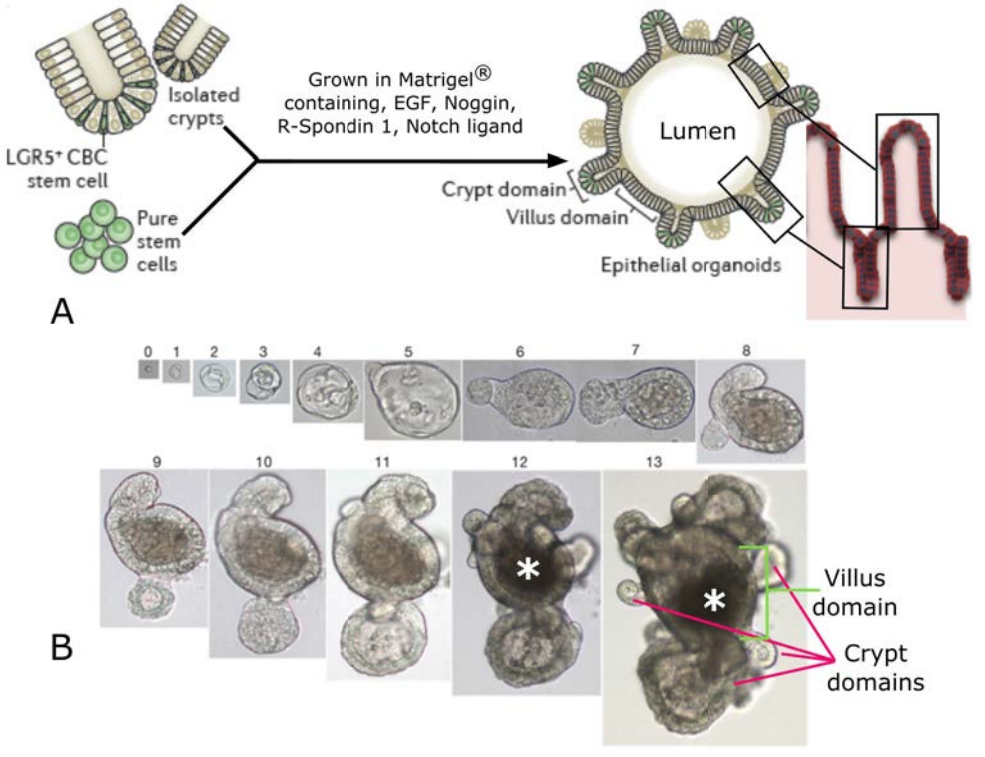

Figure 1.1: *Scheme showing the structure of the intestinal epithelial organoids obtained from isolated crypts and Lgr5⁺ stem cells (A). The finger-like protrusions are the crypts and the monolayers surrounding the cysts are the villus domains. Adapted from Barker [1]. Bright field image showing the development of an organoid from a single sorted Lgr5⁺ stem cell (B). White asterisk marks the dead cells accumulated in the lumen of the organoids. Adapted from Sato et al. [16].*

In an another study by Miyoshi and Stappenbeck, mouse intestinal crypts were cultured with Wnt3, R-Spondin, and Noggin enriched media, and shown to grow into 3D cystic structures called spheroids [20]. These spheroids were enriched in Lgr5 stem cells and could be cultured up to at least 3 months [20, 21]. In a following study from the same group, a culturing method for human intestinal spheroids was reported [22]. Human spheroids were successfully obtained from patient biopsies, expanded and propagated for numerous passages, and further tested for epithelial-microbiome interaction [22]. Spheroid-based culture systems can be developed relatively rapidly [20, 21], and the use of individuals own cells permit the development of patient-based assays [22]. However, these cultures were enriched for stem cells and did not contain differentiated cell types (enterocytes, Goblet, and enteroendocrine cells) [20]. Diluted Wnt3, R-Spondin, and

Noggin enriched media and small molecule inhibitors of Notch signaling pathway had to be used in order to obtain some proportion of differentiated cells [22]. Therefore, they did not represent the *in vivo* cell types and distributions of the intestinal epithelium.

In an alternative approach to obtain long-term cultures of intestinal tissue *in vitro*, Spence *et al.* showed that human induced pluripotent stem cells (hiPSCs) could be directed to differentiate into intestinal organoids by sequential exposure to growth factors specific to each stage of embryonic intestinal development [23]. Such induced human intestinal organoids (HIOs) contained mature intestinal stem cells and all major cell types of intestinal epithelium and mesenchymal cells. Such a stem cell source provides an important therapeutic potential in personalized medicine, as patient-specific somatic cells can be reprogrammed into pluripotent stem cells that can be further differentiated into the intestinal tissue (the epithelium and the mesenchyme) [24]. HIOs is a powerful tool for studies of embryonic intestinal development [25]. However, the prolonged times required to generate mature intestinal tissue may limit its use for patient-based assays; especially when the protocols to isolate and culture $Lgr5^+$ stem cells from human biopsies are very well established and much more straight forward.

Organoids, and other 3D culture systems reported (HIOs, spheroids), have proven to be very useful *in vitro* tools for studies of basic biology and development of the intestine, *in vitro* screening of possible drug candidates, and functional engraftments for regenerative medicine applications. However, the 3D closed spherical structure of organoids prevents access to the apical region of the epithelium (lumen) (Figure 1.2 A), making them unsuitable for standard functionality assays that are typically done in 2D Transwell® culture setup, which separates the culture well into two compartments through a monolayer of cells cultured on a porous membrane. Complicated techniques such as microinjection has to be utilized to deliver the drug molecules to the lumen-like regions [26]. Therefore; it is of great interest developing technique to obtain *in vitro* intestinal epithelium with an accessible apical surface (Figure 1.2 B).

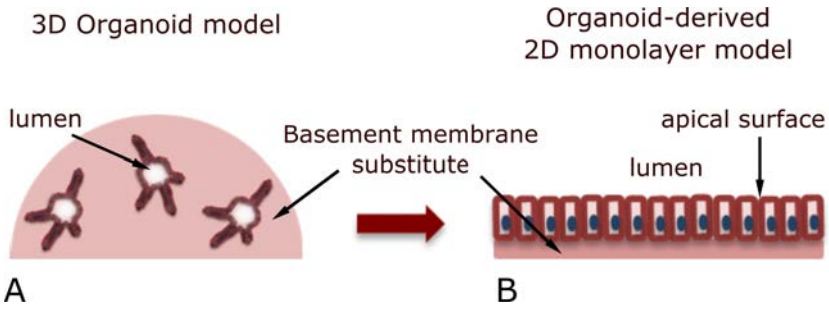

Figure 1.2: *Schematic representation of intestinal organoids cultured in a Matrigel® drop (A) or in a hypothetical 2D epithelial monolayer model with accesible apical surface (B).*

Recently, there has been some efforts to develop 2D culture systems derived from intestinal stem cells. Stappenbeck and colleagues developed a 2D epithelial monolayer model derived from mice [27] and human [22] intestinal spheroids. These monolayers were used in transcytosis assays [27] and in the evaluation of adhesion of certain pathogenic bacteria to the epithelium [22]. Even though proven useful in the applications tested, these monolayers were not very well characterized. All the characterizations were done at day 3 of culture, and no further data was provided on the evolution of the cultures at further times points. Although, immunofluorescence revealed the presence of different epithelial cell types, they were not organized in *in vivo*-like crypt-villus distribution. Altogether, these models might not have the features to faithfully recapitulate the phenotype and physiology of *in vivo* intestine.

In another study, a 2D epithelial monolayer model was developed from freshly isolated mouse colonic and human rectal crypts [28]. Intestinal epithelial monolayers could be propagated for up to 10 months by sequential passing and gave rise to 3D organoids/spheroids *de novo* when seeded back into Matrigel® drops [28]. The monolayers were shown to contain proliferative cells at the epithelial borders and secretory Goblet cells at the center [28], a cell-type distribution different of that found *in vivo*. Very recently, intestinal epithelial monolayers with an improved, physiologically relevant cell distribution have been generated from mouse crypts. These contained proliferative domains and differentiated zones resembling crypt-villus cellular organization found *in vivo* [29]. However, these monolayer models lacked total surface coverage, characteristic of a healthy *in vivo* epithelium. *In vitro* functional assays such as; cellular transport and secretion, can only be performed on a monolayer model that has the barrier properties of the native intestine.

One of the most important indication of the epithelial model viability and function is the state of the barrier permeability. Evaluation of the Transepithelial electrical resistance (TEER) is a quantitative and non-invasive technique, widely accepted to measure the integrity of the tight junctions in epithelial monolayers [30, 31]. Conventionally, the intestinal epithelial cells are cultured in the so-called Transwell® inserts (Figure 1.3 A), porous membranes that separate the cell culture well into two compartments; upper (apical side) and lower (basolateral side), and the epithelial resistance is measured by using a Voltohmmeter and an electrode pair placed on both sides of the porous membrane [31] (Figure 1.3 B). A voltage difference (12,5 Hz square-wave AC signal) is applied to both sides and the resulting current is represented as an ohmic resistance. The measured resistance is composed of the transcellular and paracellular resistance (Figure 1.3 C). Since the cell membranes found in the transcellular path show high resistance, the current predominantly flows through the paracellular path. Thus, TEER values measured describe the resistance associated to cell tight junctions. Therefore, TEER is a strong indicator of the level of maturation of the tight junctions and the formation of a cellular barrier. The resistances contributed by the culture medium, porous membrane and the electrode-medium interface are removed by subtracting the resistance of the system without the cell monolayers.

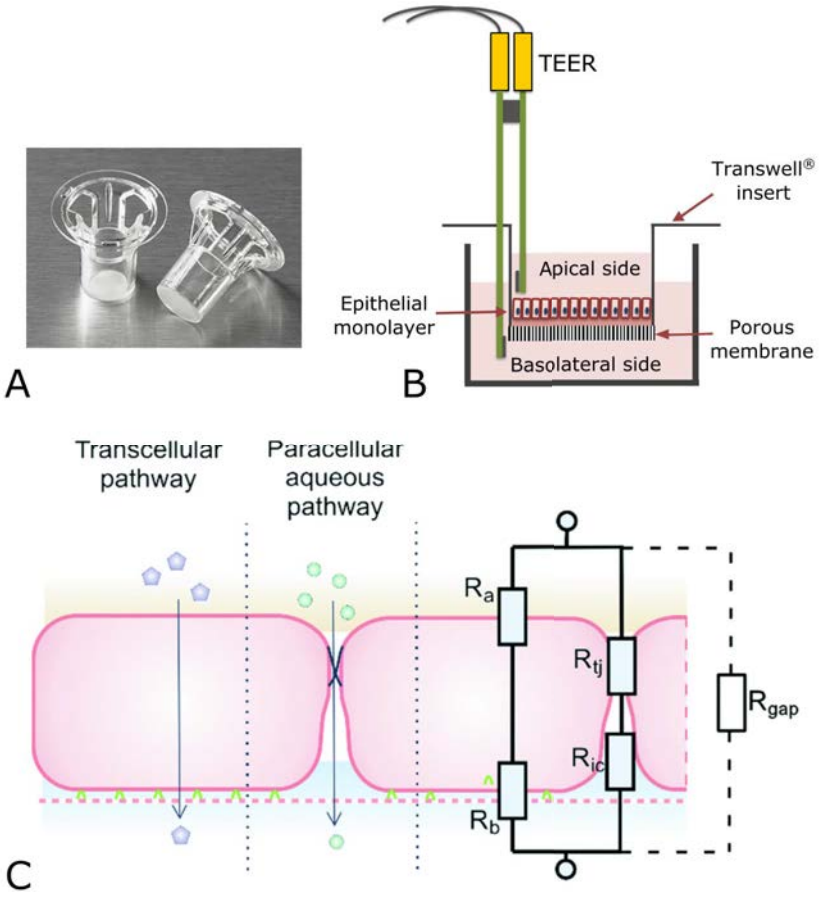

Figure 1.3: *Image of a standard 24 well plate Transwell® insert (Corning) (A). Schematic representation of an in vitro 2D Transwell® assay (B). Epithelial monolayer is grown on the porous membrane and TEER measurements are performed by an electrode pair inserted one to the apical and the other to the basolateral side of the monolayer. Scheme showing the electrical resistances associated to the epithelial monolayer consisting of the transcellular route (R_a + R_b) and the paracellular route (R_{tj} + R_{ic}) (C). R_a: apical membrane resistance, R_b: basolateral membrane resistance, R_{tj}: resistance of tight junctions, R_{ic}: resistance of intercellular space, R_{gap}: resistance of the gap. Adapted from Odijk et al. [32].*

Commonly used Caco-2 cell line has limited physiological accuracy due to altered expression of structural proteins, mainly those found in the tight junctions, resulting in much higher TEER values, greater than 300 $\Omega.cm^2$, relative to the native small intestine, which is 40-100 $\Omega.cm^2$ [30, 33, 34]. In a study reported by Kauffman *et al.*, commercially available hInEpCs showed interdonor variability and very high TEER values, greater than 1500 $\Omega.cm^2$ [13]. In the same study, human iPSCs were differentiated in a Transwell® system; however, the TEER

values reported were also very high (greater than 900 $\Omega.cm^2$) and required prolonged times for differentiation [13]. Spheroid-derived monolayers from mouse colon [27] and human ileum [22] were reported to have a TEER of approximately 3000 $\Omega.cm^2$ and 400 $\Omega.cm^2$, respectively. In all of these studies, the TEER values reported were substantially higher than that of the native small intestine, 40-100 $\Omega.cm^2$ [30, 34], poorly mimicking its paracellular transport behavior.

In a recent study, Kozuka *et al.* reported intestinal monolayers obtained from freshly isolated mouse crypt cells and human organoid-derived cells [35]. The monolayers contained all major intestinal cell types and shown to have absortive and secretory functions [35]. They performed a comparative gene expression study to optimize the cell culture media components [35]. To obtain confluent monolayers of small intestinal epithelium very high concentrations of Wnt3a, principle activator of Wnt pathway hence ISC proliferation, was needed and to further differentiate the cultures high concentrations of bone morphogenic proteins (BMPs), inhibitors of Wnt pathway, were needed. The TEER values reported were in the order of couple of hundreds of $\Omega.cm^2$, higher than that of the native small intestine [30, 33, 34], and no findings were reported on *in vivo* like crypt-villus cellular distribution. Even though, this platform was proven useful to identify a potential candidate for minimally absorbed drugs [35], it might be short in faithfully mimicking *in vivo*-like cellular organization and paracellular transport.

Altogether, current models either lack *in vivo*-like crypt-villus cell type composition and distribution or tissue barrier integrity representative of the native intestinal epithelium.

In this chapter, we describe a method that utilizes mouse-derived small intestinal organoids to obtain intestinal epithelial monolayers that self-organized into *in vivo*-like crypt-villus domains and show effective barrier function. Organoids were grown on substrates coated with thin films of Matrigel®, which provided the proper mechanical properties to induce the formation of epithelial 2D monolayers. Live-imaging of intestinal stem cells marked with green fluorescent protein (GFP) obtained from Lgr5-EGFP-ires-Cre ERT2 mice demonstrated that organoid-derived cells first organize into stem cell-containing crypt-like domains. Then, cells migrated out to form non-proliferating and differentiated monolayers, resembling the villus-like regions. The formation of epithelial monolayers that fully cover the substrate surface was accomplished by adding to the cell culture medium exogenous ISC niche biochemical factors such as Wnt3a, and the ones produced by the intestinal subepithelial myofibroblast cells, which helped maintaining the stem cell population within the crypt bases. Epithelial

monolayers with crypt-villus organization were obtained on Transwell® inserts coated with thin films of Matrigel®, upon basolateral delivery of ISC niche factors. Organoid-derived intestinal epithelial monolayers cultured in this setup, showed physiologically relevant TEER values, indicating formation of a mature epithelial barrier.

1.2 Materials and Methods

1.2.1 Mouse model

Lgr5-EGFP-IRES-creERT2 mice have been previously described [18]. Briefly, Lgr5-EGFP-IRES-creERT2 mice were generated by homologous recombination in embryonic stem cells targeting the EGFP-IRES-creERT2 cassette to the ATG codon of the stem cell marker Lgr5 locus, allowing the visualization of $Lgr5^{+}$ stem cells with a green fluorescent protein (GFP). The Lgr5-EGFP-IRES-creERT2 mice were provided by the Laboratory of Prof. Eduard Batlle at Institute for Research in Biomedicine (IRB, Barcelona, Spain).

1.2.2 Intestinal crypt isolation and organoid culture

The intestinal crypts from Lgr5-EGFP-IRES-creERT2 mice were isolated as previously described [36, 37]. Briefly, the intestines were harvested, cut open longitudinally, and washed with phosphate buffered saline (PBS) (Gibco) to remove luminal content. Then, villi were mechanically removed by scraping with the help of a glass coverslip (Deltalab). Intestinal crypts were isolated by incubating the tissue with PBS containing 2 mM Ethylenediaminetetraacetic acid (EDTA) (Sigma) for 30 min at 4°C. The digestion content was filtered through a 70 μm pore cell strainer (Biologix Research Co.) to obtain the crypt fractions and centrifuged at 55 g for 5 min. The crypts were resuspended and plated in Matrigel® (BD Bioscience) drops (Figure 1.4 A) and cultured with organoid growth media: Advance DMEM/F12 (Invitrogen) supplemented with 1% v/v Glutamax (Gibco), 1% v/v HEPES (Sigma), Normocin (1:500, Invitrogen), 2% v/v B27 (Gibco), 1% v/v N2 (Gibco), N-acetylcysteine (1,25 mM, Sigma), murine epidermal growth factor (EGF) (100 $ng.mL^{-1}$, Gibco), recombinant human R-Spondin 1 (200 $ng.mL^{-1}$, R & D Systems), recombinant murine Noggin (100 $ng.mL^{-1}$, Peprotech). The medium containing EGF, Noggin, and R-Spondin 1 is referred as ENR in what follows. The medium was changed every 2 to 3 days. The first 4 days the Rho kinase inhibitor, Y-27632, (Sigma) was added to the medium on daily bases to inhibit cell death due to anoikis [38]. Figure 1.4 B shows the freshly isolated crypts in a Matrigel® drop and the nascent organoids already after day 1 of culture (Figure 1.4 C).

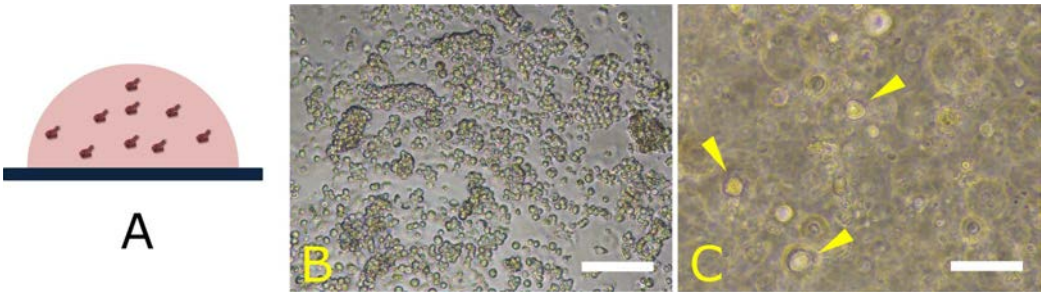

Figure 1.4: *Scheme showing the crypt pieces seeded in a Matrigel® drop (A). The bright-field image of freshly isolated crypts (B) and after 1 day in culture (C). Yellow arrowheads indicate the nascent organoids. Scale bars: 100 μm.*

The organoids grew from small, roundish structures (Figure 1.5 A) to fully grown organoids (Figure 1.5 B) within about a week. When the organoids reached that state the cultures were passed by a mild trypsinization protocol. Briefly, the medium was removed and 150 μL of TrypLE Express, 1X, (Gibco) was added to each well. The Matrigel® drops containing the organoids were mechanically disrupted with the help of a pipette and transferred to a falcon cooled on ice. The organoids were further broken with a 23 G 1" needle (BD Microlance 3) by syringing 3 to 4 times. Working on ice slows down the trypsin activity and avoids breaking down the organoids more than what is desired. Then, 500 μL of 2% v/v Fetal bovine serum (FBS; Gibco) in PBS was added to stop the organoid digestion reaction. The crypt suspension was centrifuged at 55 g at 8°C for 5 min. The pellet was resuspended in fresh Matrigel®. The drops were let to gel at 37°C for 15 min and 400 μL of organoid growth media (ENR) were added to each drop. The medium was changed every 2 to 3 days. The organoid stocks were maintained in ENR up to 3 to 4 months and after that fresh crypts were isolated again from Lgr5-EGFP-IRES-creERT2 mice.

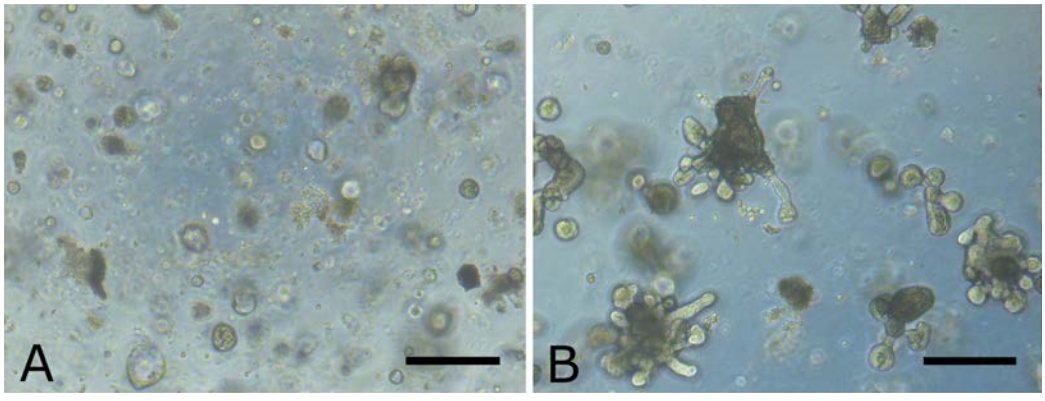

Figure 1.5: *Representative bright field images showing organoids grown under ENR at the initial growth (A), and at the fully grown (B) stage. The cultures were passed when they reached this state. Scale bars: 500 μm.*

The organoid cultures were enriched with stem cells by culturing them with CHIR99021 (3 μM, Stemgent) and valproic acid (1 mM, Sigma) small molecules in addition to EGF, Noggin, R-Spondin 1 during a couple of passages (maximum 3) before seeding. It has been previously shown that the addition of these small molecules (CHIR99021 and valproic acid) increases the stem cell percentage with respect to the total cell population in the organoid cultures up above 90% compared to 20% stem cells found in the organoids cultured with ENR medium [39]. The medium containing EGF, noggin, R-Spondin 1, CHIR99021 and valproic acid is referred as ENR_CV in what follows.

1.2.3 Generating and passing monolayers of epithelial cells

In this study, two culturing setups were used to obtain epithelial monolayers: standard 2D tissue culture plates (ibidi GmbH), and Transwell® inserts (Corning). The overview of the culturing methodology is shown in Figure 1.6. Both setups were coated with Matrigel® forming a thin film as support matrix for monolayer growth. The preparation and characterization of the Matrigel® thin film coating is explained in the following section.

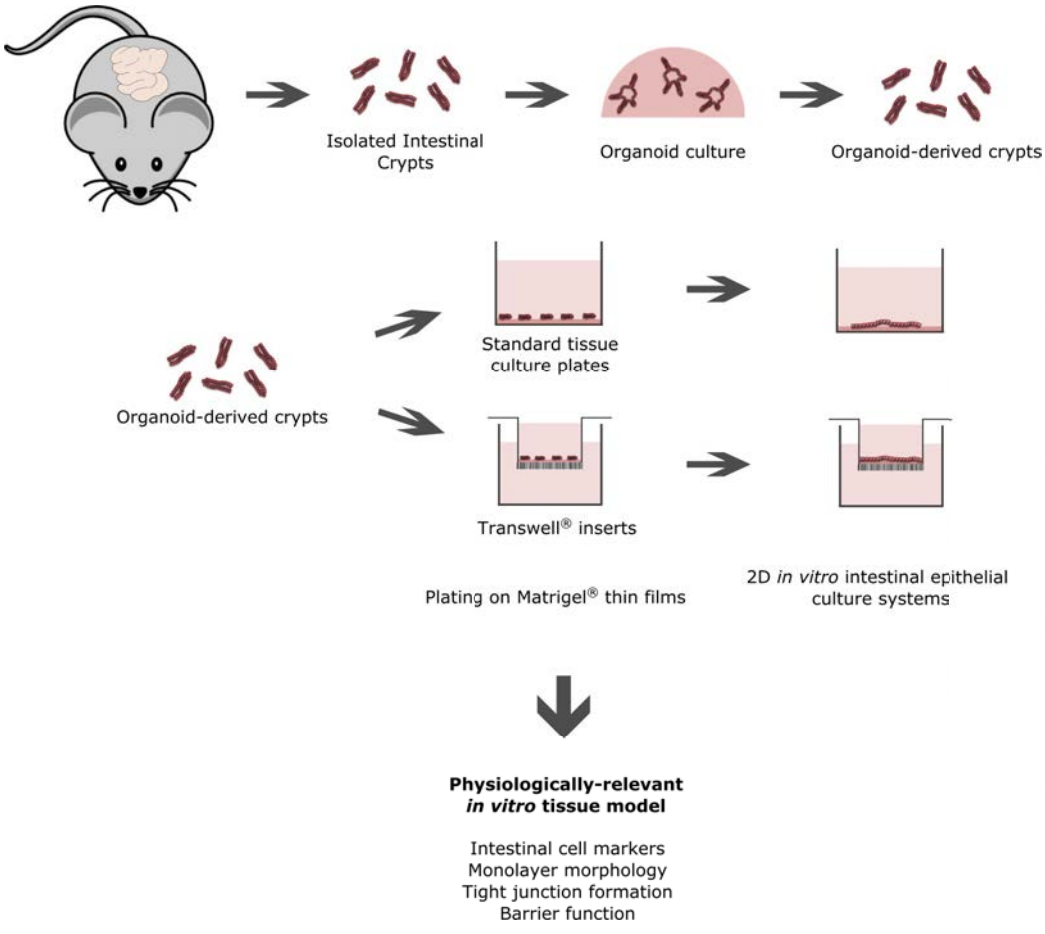

Figure 1.6: *Overview of culturing methodology to obtain organoid-derived epithelial monolayers. Intestinal stem cell-containing crypts were isolated from Lgr5-EGFP-Ires-creERT2 mice and cultured in Matrigel® drops to obtain organoid culture. Organoids were dissociated into crypt pieces and seeded on standard tissue culture plates or Transwell® inserts coated with a thin film of Matrigel®. The intestinal epithelial model obtained in this fashion was evaluated for its physiological relevance.*

1.2.3.1 Preparation and characterization of the Matrigel® thin film coating

The ibidi μ-Slides (1 cm^2, polymer coverslip bottom, ibidi GmbH) or Transwell® inserts (6,5 mm diameter, 0,4 μm pore size, Corning) were coated with Matrigel® (BD Biosciences) by pipetting 10 μL undiluted Matrigel® solution into the wells, spreading it to the whole surface and incubating at 37°C for at least 15 min. Matrigel® is a solubilized basement membrane substitute obtained from Engelbreth-Holm-Swarm (EHS) mouse sarcoma, mainly consisting of laminin and collagen [19], and it is routinely used for 3D support matrix for *in vitro*

cultures of intestinal stem cells [16, 20]. The Matrigel® coating prepared on ibidi plates was visualized by immunostaining with an antibody against laminin with a modified immunostaining protocol. After making the coating, the layer was fixed with 10% neutralized formalin (Sigma) for at least 30 min, washed thoroughly with PBS and blocked with a blocking buffer containing 1% w/v BSA (Sigma), 3% v/v donkey serum (Millipore), and 0,2% v/v Triton X-100 (Sigma) in PBS for two hours. Then, the samples were incubated with an anti-laminin antibody (1:500) raised in rabbit (Abcam) overnight at 4 °C. The secondary antibody used was Alexa Fluor® 488 donkey anti-rabbit diluted at 1:500 (Invitrogen).

Images of the matrigel coating were acquired by a Leica SP5 Confocal Laser Scanning Microscope (CLSM) equipped with a 20x dry objective (NA = 0,7) and hybrid detectors. The laser excitation and emission light spectral collection were both optimized for GFP fluorophore. The pinhole was set to 1 Airy unit and a stack of 22 μm (z-step of 1 μm) was acquired for each sample. The acquired stacks were post-processed by deconvolution following a theoretical model of the objective (fixed PSF, constrained iterative, 10 iterations) using Autoquant X3 software version 3.0.2 (Media Cybernetics). This helped mitigating the axial spread of the point spread function of the instrument. We analyzed three technical replicas and the thicknesses were estimated using ImageJ free software (http://rsb.info.nih.gov/ij, National Institutes of Health). To assess the sample uniformity and improve the estimates, for each image 20 randomly selected intensity axial profiles were extracted along 32 pixel thick lines covering the whole extension of the stack (ImageJ TransformJ Turn plugin + Plot profile). Since the extracted intensity profiles closely resembled Gaussian functions, we fitted them with a Gaussian plus offset function to estimate both the background and the standard deviation of the function (ImageJ Curve Fitting). For each intensity profile, an estimate of the layer thickness was obtained as the full width at half height of the fitted Gaussian function (FWHM $\approx$ 2,355 σ). In total, 3 different samples were characterized. The estimates of the layer thickness were averaged over each region and sample, and presented as the mean $\pm$ standard deviation.

1.2.3.2 Intestinal crypt seeding and passing

The ibidi plate wells were coated with a thin layer of Matrigel®, as explained in the previous section. Substrates with a thick layer of Matrigel® were also prepared by adding 80 μL for Transwell® inserts and 200 μL for ibidi μ-Slides to

yield a layer with a thickness of ≈ 2 mm. The volumes required to obtain this thickness was calculated by multiplying the surface area of the substrate (1 cm^2 for ibidi plates and 0,33 cm^2 for Transwell® inserts) by the height we wanted to obtain (i.e. 2 mm). It is reported that when gel thickness is less than 20 μm, the apparent stiffness of the material is reaching that of the underlying substrate [40]. The volume used for the preparation of the thin coating was selected such that the thickness would be less than 20 μm. Therefore, the substrates with a thin coating are referred as "Hard" and the ones with a thick layer as "Soft". To obtain a preparation of crypt pieces with homogeneous size, full-grown organoids were subjected to a mild digestion protocol as explained in Section 1.2.2. The total crypt number in the suspension was estimated by sampling 5 μL volume with a 20 μL pipette tip and counting the crypts within the sample volume under a bright field microscope (Eclipse Ts2, Nikon). From the counted crypt number in 5 μL volume, the total crypts in the suspension were estimated. At least three samples were used to do the estimations. A 20 μL pipette tip was used to not exclude any crypt pieces due to their size. Crypts were seeded at a density of 1000-1500 crypts.cm^{-2} on the standard 2D tissue culture plates using an initial volume of 30-50 μL. The cells were let attach to the substrate for 3-4 hours and then more medium was added. The monolayers were cultured with ENR_CV medium for different time periods ranging from 5 days to 4 weeks depending on the experiment indicated for each experiment (indicated in the corresponding figure legends). The passing of the cultures was done by mechanically disrupting the monolayers with the help of a pipette. Collected cell mixtures were reseeded into new wells freshly coated with Matrigel®.

1.2.4 The effect of different conditioned cell culture media on epithelial monolayer growth

The effect of exogenous sources of Wnt pathway activators added to culture medium on the epithelial monolayer growth was studied. For that, the conditioned media was produced from primary intestinal subepithelial myofibroblasts (ISEMFs) isolated from mouse colon and a Wnt3a producing cell line. ISEMFs are an important source of Wnt pathway activators and enhancers [41–43] (see General introduction for detailed information). The details of the procedures are explained in the following sections.

1.2.4.1 Preparation of intestinal subepithelial myofibroblast conditioned medium

ISEMFs were isolated from mouse colon by adapting a previously published protocol [44]. Briefly, once the epithelial cells were removed (Section 1.2.2), the intestine tissue was further digested using collagenase (100 U per mL of culture medium) (Sigma) by incubating at 37°C for up to 60 min under shaking. Then, the tissue was pelleted by centrifuging at 200 g for 5 min at 4°C. The pellet was resuspended in ACK lysis buffer (Gibco) at 47°C and centrifuged again at 200 g for 5 min at 4°C. Then, the pellet was resuspended in Dulbecco's modified medium (DMEM; Life Technologies) containing 10% v/v FBS, 1% v/v Penicillin/streptomycin (Sigma), and 1% v/v minimum essential medium-non-essential amino acids (MEM-NEAA; Gibco); and cultured in tissue culture plates. After 3 h the non-adherent cells were removed and the culture medium was renewed. Remaining adherent cells are initially composed of epithelial cells, macrophages, and myofibroblasts. However, one week post seeding only myofibroblasts divide, and therefore are passed. When the culture reached confluency it was passed up to a maximum of 8 passages (after that cells stopped division and started to die). The culture medium, referred as ISEMF conditioned medium, was collected every 4-6 days and replaced with fresh media. The collected medium was centrifuged and filtered with a 0,22 μm pore size filter (Merck-Millipore) in order to get rid of the debris and stored at – 20°C. After each isolation, some the cells were used to characterize the subepithelial intestinal myofibroblast phenotype by checking as markers: α-smooth muscle actin, vimentin, and fibronectin positive and desmin negative. The immunostaining protocol and the antibodies used are reported in the Section 1.2.6. Before use, ISEMF conditioned medium (ISEMF_CM) was supplemented with 1% v/v Glutamax, 1% v/v HEPES, Normocin (1:500), 2% v/v B27, 1% v/v N2, EGF (100 $ng.mL^{-1}$), human R-Spondin 1 (200 $ng.mL^{-1}$), Noggin (100 $ng.mL^{-1}$), CHIR99021 (3 μM), valproic acid (1 mM).

1.2.4.2 Preparation of Wnt3a conditioned medium

Wnt3a conditioned medium was obtained from L-Wnt3a cell line (American Type Culture Collection, ATCC® CRL-2647™). These mouse fibroblasts obtained from subcutaneous connective tissue were genetically engineered to produce Wnt3a. The cells were cultured on standard tissue culture flasks (Thermo Scientific) with

Dulbecco's modified medium (DMEM) containing 10% v/v FBS, 1% v/v Penicillin/streptomycin, and 1% v/v Glutamax. The Wnt3a conditioned medium (Wnt3a_CM) was collected and replaced with fresh medium every 4 days. As for ISEMF_CM, the collected medium was centrifuged and filtered with a 0,22 μm pore size filter in order to get rid of the debris and stored at –20°C. Before use, Wnt3a_CM was supplemented with 1% v/v Glutamax, 1% v/v HEPES, Normocin (1:500), 2% v/v B27, 1% v/v N2, EGF (100 ng.mL^{-1}), human R-Spondin 1 (200 ng.mL^{-1}), Noggin (100 ng.mL^{-1}), CHIR99021 (3 μM), valproic acid (1 mM). As control, conditioned medium was also obtained from L-cell line (ATCC® CRL-2648™), mouse fibroblasts from subcutaneous connective tissue, the parental line that doesn't produce Wnt3a. The medium obtained from the culture of L-cell line is referred as L-cell conditioned medium (L-cell_CM). Both of the cell lines were provided by the Laboratory of Prof. Eduard Batlle at Institute for Research in Biomedicine (IRB, Barcelona, Spain).

1.2.4.3 Culturing of intestinal epithelial monolayers with conditioned cell culture media (ISEMF_CM and Wnt3a_CM)

The ibidi μ-Slides were first coated with a thin layer of Matrigel®, and seeded with crypt pieces obtained from the organoid cultures (Section 1.2.3). The seeding density range used was 700-1500 crypts.cm^{-2}. Each sample was cultured with a different conditioned medium and maintained for up to 10 days. The combined effect of ISEMF_CM and Wnt3a_CM was tested by mixing these media in 1:1 ratio. Besides the Wnt3a_CM, commercially available recombinant Wnt3a (50 ng.mL^{-1}, Abcam) was also tested in order to better control the amount of Wnt3a added. The surface coverage was measured from bright field images obtained from 12 randomly selected regions for each sample in a total of three samples for each condition (n = 3) by manually delimiting the monolayer area using ImageJ software. The data were processed and plotted with OriginPro 8.5 software.

1.2.5 The effect of asymmetric administration of ISC niche factors and substrate rigidity on cellular phenotype

In a standard 2D tissue culture plate, intestinal cells receive the ISC niche biochemical factors only from the apical side and they are attached to the substrate at the basolateral side. Having an access to both apical and basolateral sides of the cell monolayer permits the study of the effects of asymmetric administration of

ISC niche biochemical factors on the intestinal cell phenotype. By asymmetric administration we mean the delivery of the ISC niche biochemical factors from the basolateral side like *in vivo*. To achieve that, Transwell® setup was adopted since it separates the cell culture well into two parts permitting access to both sides of the cell monolayer. The inserts were coated with 10 µL of Matrigel® to yield thin layers of less than 20 µm in thickness (referred as "Hard"), and with 80 µL of Matrigel® to yield thick layers of ≈ 2 mm in thickness (referred as "Soft"). The ISC niche biochemical factors were added only to the basolateral side in the case of asymmetric administration and both to the basolateral and apical sides in the case of uniform administration (Figure 1.7). A generic term 'ISC niche biochemical factors' is used to refer to the essential ingredients of the organoid growth medium. The detailed medium contents can be found in the corresponding figure captions.

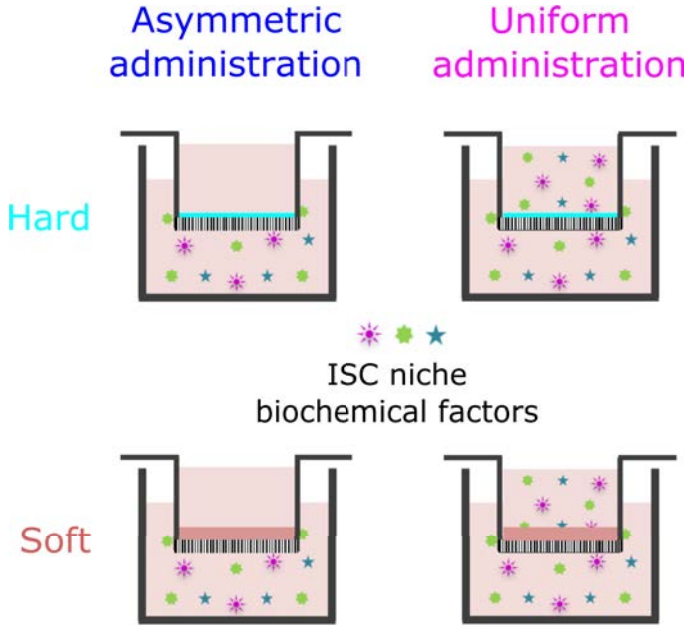

Figure 1.7: *Overview of the culturing methodology used to investigate the effect asymmetric administration of the stemness factors and the substrate rigidity.*

Organoid-derived crypt suspension was prepared by a mild digestion protocol as explained previously (Section 1.2.2). Crypts were seeded at a density of 3000-3500 crypts.cm^{-2} using an initial volume of 30-50 µL on the Transwell® inserts coated with Matrigel® as explained above. 500 µL of culture medium containing ISC niche biochemical factors was added to the basolateral side (bottom

compartment) and after letting cells attach for couple of hours more medium was added to the upper compartment completing it to a total of 200 μL. Under asymmetric administration, the ISC niche factors were added only to the basolateral side, while under uniform administration they were added both to the apical and basolateral side. The medium added to the upper compartment in asymmetric condition was standard organoid growth medium without the ISC niche factors and it was changed everyday to remove the factors diffused to the upper chamber with time of culture. The culture medium containing ISC niche biochemical factors was either ENR_CV medium, or ISEMF_CM containing ENR_CV and Wnt3a. The intestinal cells were cultured for 10 or 20 days depending on the experiment and indicated in the corresponding figure legends.

1.2.6 Histological characterization

The cells were fixed with 10% neutralized formalin, permeabilized with 0,5% v/v Triton X-100, and blocked with a blocking buffer containing 1% w/v BSA, 3% v/v donkey serum, and 0,2% v/v Triton X-100 in PBS for at least two hours. Primary antibodies used were: rabbit anti-GFP (1:100, Life Technologies), goat anti-GFP (1:100, Abcam), rabbit anti-Ki67 (1:100, Abcam), mouse anti-Ki67 (1:100, BD Biosciences), rabbit anti-lysozyme (Lyz) (1:100, Dako), goat anti-*zonula occludens 1* (ZO-1) (1:100, Abcam), mouse anti-cytokeratin 20 (CK20) (1:100, Dako), rabbit anti-Cleaved Caspase-3 (1:200, Cell Signaling Technology), goat anti-EPHB2 (1:200, R&D Systems). All samples were incubated with the primary antibody overnight at 4°C followed by 1 h incubation at RT with secondary antibodies: Alexa Fluor® 568 and Alexa Fluor® 488 donkey anti-goat, Alexa Fluor® 647 donkey anti-rabbit (Jackson ImmunoResearch), and Alexa Fluor® 488 donkey anti-mouse diluted at 1:500. Nuclei were stained with 4',6-diamidino-2-phenylindole (DAPI) (1:1000). Alexa Fluor® 568 phalloidin was used to stain filamentous actin (F-actin). The samples were mounted with Fluoromount-G® (SoutherBiotech). For the detection of mucus, the samples were washed thoroughly with tap water and stained with periodic acid-Schiff (PAS) (Sigma) following the manufacturer's protocol. The Matrigel® layer was detected with an antibody against laminin raised in rabbit (1:500, Abcam). For the characterization of ISEMFs, antibodies against α-smooth muscle actin (α-SMA) (1:100, Sigma), desmin (1:100, Abcam) and fibronectin (1:100, Sigma) all raised in rabbit, and anti-vimentin raised in mouse (1:100, Developmental Studies Hybridoma Bank) were used. All the

reagents were obtained from Invitrogen unless stated otherwise. The fluorescence images were acquired using confocal laser scanning microscopy (CLSM) (TCS SP5, Leica) with 10x dry (N.A. = 0,40), 20x dry (N.A. = 0,70) and 40x oil (N.A. = 1,25) objectives at randomly selected locations. The laser excitation and emission light spectral collection were optimized for each fluorophore. For the four color scans the emission bands were adjusted to avoid overlapping of the channels. The pin hole diameter was set to 1 Airy Unit (AU). For images acquired at 10x and 20x, a z-step of 1 μm, and for images acquired at 40x a z-step of 0,5 μm were used. The cross-section images of the monolayer was obtained from the orthogonal views of the stacks acquired at 40x. The cell heights were measured from the orthogonal views of the stacks at 40x magnification at 10 randomly selected locations for each sample (n = 3). The bright field images were obtained by an inverted microscope (Eclipse Ts2, Nikon).

1.2.7 EdU pulse-chase experiment for evaluating the monolayer formation

5-ethynyl-2-deoxyuridine (EdU) is a nucleoside analog of thymidine and is incorporated into DNA during active DNA synthesis [45]. When introduced into the culture medium (EdU-pulse) cells incorporate EdU into its DNA and once it is removed from the media, it remains incorporated into DNA and it is transferred to the progeny if the cells are actively dividing. Therefore, we hypothesized that by analyzing the cultures at specific time points after the EdU pulse was removed, we could evaluate the origin of the cells forming the monolayer. EdU staining was performed following the manufacturer's protocol (Click-iT® Plus EdU imaging kit, Invitrogen). Briefly, crypts were cultured on ibidi μ-Slides functionalized with a thin coating of Matrigel®, as explained previously. After 1 day in culture, cells were incubated with EdU (10 μM) for 2,5 h. After the removal of the pulse one of the plates was fixed immediately with 3,7% formaldehyde (Electron Microscopy Science) for 15 min at RT. The other plates were fixed after 1 day following the removal of the EdU pulse. The samples were permeabilized with 0,5% v/v Triton X-100 in PBS for 20 min and EdU was detected using Click-iT Plus EdU Alexa Fluor 488 imaging kit. Subsequently, the samples were washed with 3% w/v BSA in PBS and incubated with primary antibodies against Ki67 raised in rabbit (1:100) and ZO-1 raised in goat (1:200) overnight at 4°C. Ki67 was used to mark the proliferative cells at the moment of fixation and ZO-1 to assess the maturation of the epithelial cells. Later, the samples were stained with the secondary antibodies,

donkey anti-rabbit Alexa Fluor® 647 and donkey anti-goat Alexa Fluor® 568, for 1 h at RT. Nuclei were stained with Hoechst 33342 (10 μg.mL^{-1}, Click-iT, invitrogen) for 30 min at RT.

1.2.8 Image analysis

The quantification of the intestinal epithelial cell markers GFP (for stem cells), Ki67 (for proliferative cells), and cytokeratin 20 (CK20) (for terminally differentiated enterocytes and Goblet cells), with respect to the total cell number was estimated by a custom ImageJ macro provided by the Advanced Digital Microscopy (ADM) Unit of Institute for Research in Biomedicine (IRB) (see Appendix B for the macro code). The sequence of operations performed in the macro is reported below:

1) Compute maximum intensity Z-projection (all channels).

2) Apply Laplacian of Gaussian filter to DAPI channel image.

3) Detect salient regional intensity minima in filtered DAPI image.

4) For each marker, measure mean intensity in corresponding channel inside disks (r = 3 pixels) centered on detected minima; for disks with mean intensity above user defined threshold, count nucleus as positive for this label.

When the whole field of view was not covered by the monolayer, an additional step was applied after step 3 to discard nuclei falling outside the cell monolayer. To do so, a segmentation mask was obtained by Gaussian filtering the actin channel image and thresholding at a fixed level. All filters' radii were adjusted according to estimated nuclei size (r $\approx$ 6 pixels) at the imaging magnification. Nuclei detection sensitivity (noise tolerance) was adjusted empirically to lead to most accurate detection. All thresholds were adjusted to local intensity estimates performed inside user selected regions (actin channel, inside monolayer; weakest positive cell in label channels). The accuracy of the results was validated from summary images displaying colored markers at negative/positive nuclei positions overlaid over the projected image stacks. For each sample, the CLSM stacks were acquired at five to eight randomly selected locations within the same monolayer and were quantified. The data were processed and plotted with OriginPro 8.5 software.

1.2.9 Time-lapse microscopy for evaluating the monolayer formation

Digested intestinal epithelial crypts were seeded on ibidi μ-Slides coated with Matrigel®, as previously explained (Section 1.2.3). Formation of the epithelial

monolayer was monitored by time-lapse microscopy experiments, conducted at 10x magnification with Axio Observer 7 epifluorescence inverted microscope (Zeiss) with temperature (37°C), humidity and CO_2 (5%) regulation. Phase contrast and GFP channels were used and images were acquired every 5 minutes up to first 60 hours of the culture to evaluate the monolayer formation. The time-lapse videos and fluorescence images were processed with ImageJ software.

1.2.10 Transepithelial electrical resistance (TEER) measurements of epithelial monolayers

Transepithelial electrical resistance (TEER) is a quantitative, non-invasive technique to assess barrier tissue integrity *in vitro* [30, 31]. The standardized setup for TEER measurement consists of culturing epithelial monolayers on semipermeable membrane inserts (Transwell®) that create two separate compartments (apical and basolateral compartment). Then, by placing an electrode on each of these compartments, the electrical resistance across the cell layer is measured (Figure 1.8 A). In this study, an EVOM2 epithelial voltohmmeter (World Precision Instruments) (Figure 1.8 B) that uses a 12,5 Hz square-wave alternating current (AC) signal, together with STX3/"chopstick" electrodes (World Precision Instruments) (Figure 1.8 C) was used to measure TEER.

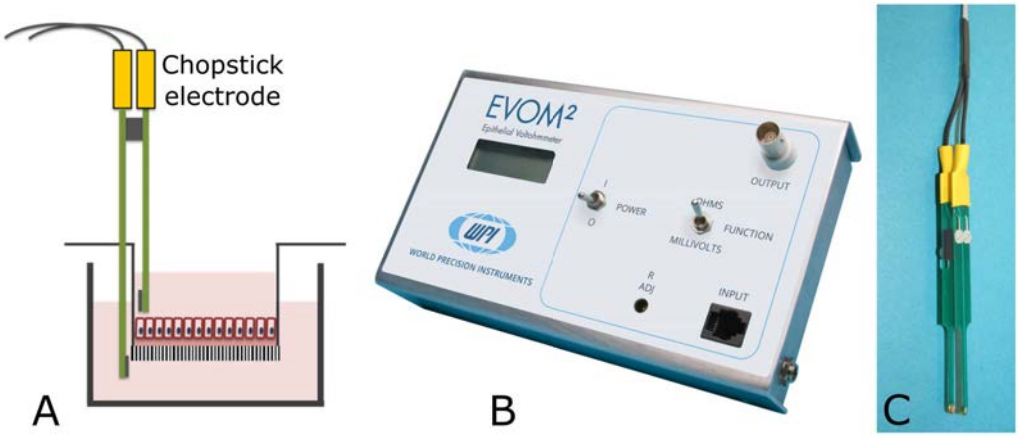

Figure 1.8: *Scheme showing the standardized setup for TEER measurements by voltohmmetry (A). EVOM2 epithelial voltohmmeter (B), and STX3/"chopstick" Ag/AgCl electrode pair (C) used.*

The Transwell® inserts (6,5 mm diameter, 0,4 μm pore size) were coated with a thin Matrigel® layer and were seeded with intestinal organoid-derived crypts,

as explained in section 1.2.3. The seeding density range used was 3000-3500 crypts.cm^{-2}. ISEMF_CM supplemented with ENR_CV and Wnt3a (25 ng.mL^{-1}) was added only to the basolateral side in the case of asymmetric administration of ISC niche biochemical factors and both to the basolateral and apical sides in the case of uniform administration. To measure TEER the electrodes were placed on the apical and basolateral sides of the inserts. The monolayer electrical resistance, $R_{monolayer}$, was obtained by subtracting the intrinsic resistance (membrane-Matrigel®, R_{blank}) from the total resistance measured (membrane-Matrigel®-cells, R_{total}) (Eqn. 1.1) and corrected for total surface area (TSA), which is 0,33 cm^2, to be expressed as ohm.cm^2 ($TEER_{monolayer}$) (Eqn. 1.2). The data were processed and plotted with OriginPro 8.5 software.

$$R_{monolayer} = R_{total} - R_{blank} \tag{1.1}$$

$$TEER_{monolayer} = R_{monolayer} \, . \, TSA \tag{1.2}$$

1.2.11 Statistical analysis

The statistical comparison was performed using two tailed, unequal variances Student's t-test and $p<0,05$ was considered significant. The error bars in the figures represent the standard deviations of at least two independent experiments with three technical replicas. The data were processed and plotted with OriginPro 8.5 software.

1.3 Results

1.3.1 Generation of epithelial monolayers from organoid-derived crypts

Small intestinal crypts were obtained by a mild digestion of the organoids and were seeded on top of either a thin film or a thick layer of Matrigel®. Two extreme conditions in thickness were selected to compare the intestinal cell growth phenotype. In order to obtain a thin film a 10 μL of Matrigel® was used. Matrigel® is a gelatinous protein mixture commonly used as basement membrane substitute for *in vitro* cultures of intestinal stem cells [16, 20, 23, 46] and mainly consists of laminin, a key protein in cell anchorage to the extracellular matrix [47]. To be able to visualize the Matrigel®, the films were stained with an antibody against laminin and from the confocal microscopy stacks their thicknesses were estimated. Uniform coatings were obtained as seen in Figure 1.9 and the average thickness was estimated to be 2,9 $\pm$ 0,1 μm using proper image analysis techniques (see Section 1.2.3.1). Matrigel® thick layers, on the other hand, were obtained by adding sufficient amount of volume to yield a gel of $\approx$ 2 mm height. The volumes needed to obtain this thickness was calculated by multiplying the surface area of the substrate by the height we wanted to obtain, i.e. 2 mm. The gels formed using large volumes (see Section 1.2.3.2 for details) were visibly thick and their thickness could be measured with the help of a ruler.

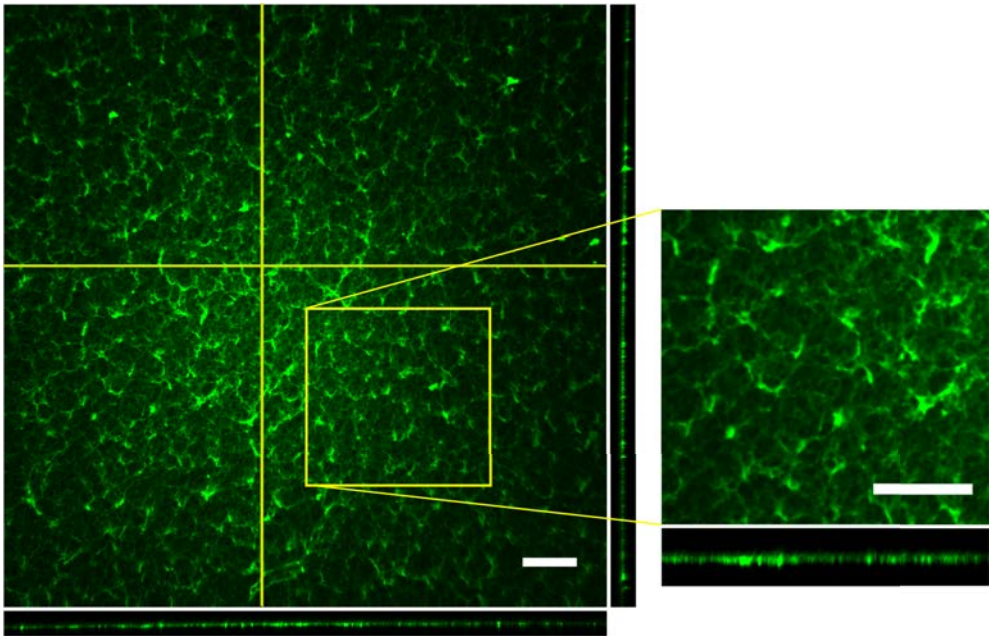

Figure 1.9: *Laminin immunofluorescence showing the top view of a Matrigel® thin film and two representative orthogonal sections taken along the corresponding yellow lines (Left panel). Zoomed image of the Matrigel® thin film and an orthogonal section (right panel). Film thickness value (2,9 ± 0,1 μm) is the mean of the thickness values measured at 20 different regions for each of three technical replicas (n = 3). Scale bars: 50 μm.*

It was previously demonstrated that when the gel thickness was less than 20 μm the apparent stiffness of the material was reaching that of the underlying substrate [40]. In our experimental setup, the thin film thickness is much less than that value. Therefore, the apparent stiffness for the cells is much closer to that of the underlying polystyrene. Polystyrene is the most commonly used 2D tissue culture substrate and it is reported to have a Young's modulus of ≈ 3 GPa [48]; whereas, Matrigel® itself is a much softer material (Storage modulus ≈ 50 Pa [49]). Consequently, the substrates coated with a thin film of Matrigel® were apparently 'Hard', while the ones coated with a thick layer were 'Soft'. This duality was found to be dictating the intestinal cell growth phenotype (Figure 1.10 A). Organoid-derived crypt pieces formed monolayers when cultured on hard substrates (Figure 1.10 B); while on soft substrates they grew into intestinal organoids (Figure 1.10 C). In addition, immunofluorescence for Ki67, a cellular marker for proliferation [50], revealed that intestinal epithelial monolayers grown on 'Hard'

substrates contained proliferative (Ki67$^+$) and non-proliferative cells found in distinct domains. Samples were covered by foci of packed proliferating cells separated by non-proliferating areas in accordance with recently published results [29]. Therefore, hard Matrigel®-coated substrates seem to provide a suitable environment that favors both ISC division and epithelial monolayer formation.

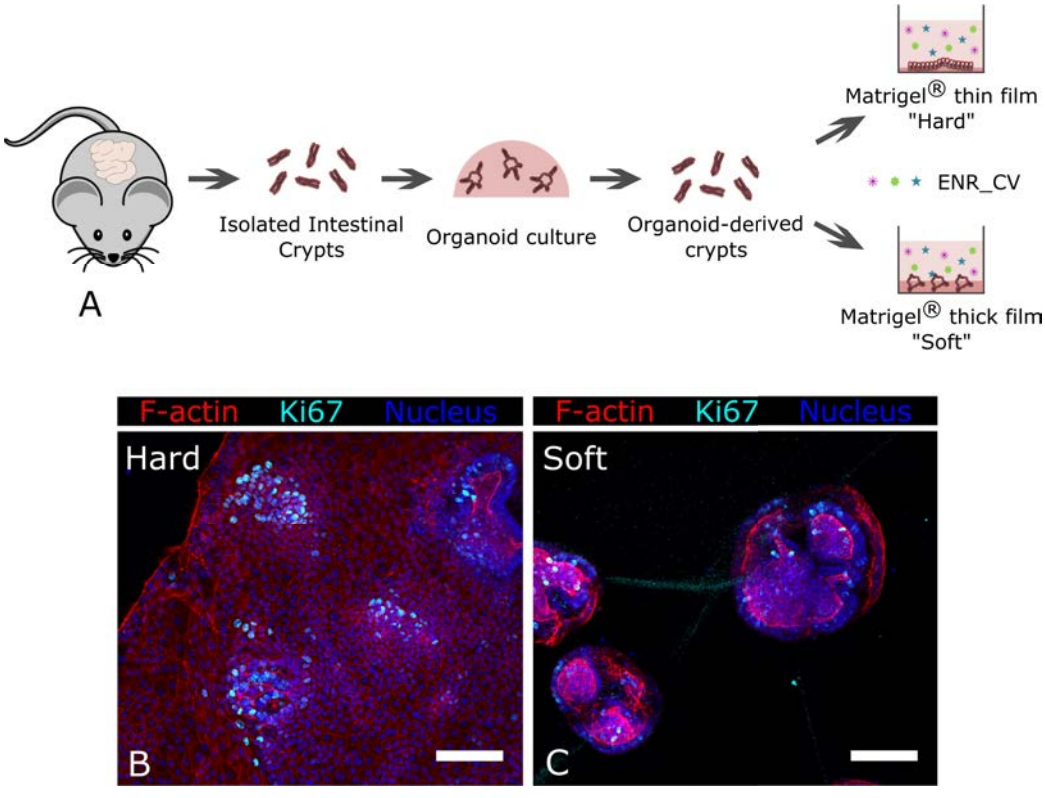

Figure 1.10: *Scheme depicting the experimental protocol used (A). Immunostaining of mouse organoid-derived crypts cultured on a thin layer (2,9 $\pm$ 0,1 μm) (B), and a thick layer ($\approx$ 2 mm height) of Matrigel® (C) after 5 days of culture. Hard substrates facilitate the formation of intestinal epithelial cell monolayers while in soft substrates intestinal epithelial cells grow as intestinal organoids. Scale bars: 100 μm.*

To investigate epithelial monolayer formation on Matrigel®-coated hard substrates, we used cells derived from Lgr5-EGFP-ires-CreERT2 intestinal organoids [18]. These organoids express GFP under the control of the stem cell marker Lgr5, which allows ISC tracking. Time-lapse microscopy experiments showed that organoid-derived crypt pieces, containing ISCs marked by GFP, rapidly self-organized to acquire crypt base columnar phenotype, intercalated by presumably

Paneth cells, and formed the crypt-like domains (Figure 1.11 A). Then, the intestinal epithelial cells started to migrate out forming the monolayer. The GFP signal was absent in the migrating monolayer, indicating the loss of Lgr5 expression; and therefore, suggesting the differentiation of the Lgr5 stem cells (Figure 1.11 B). Clearly, the epithelial cultures had two distinct regions: $Lgr5^+$ crypt-like domains and $Lgr5^-$ migrating monolayers.

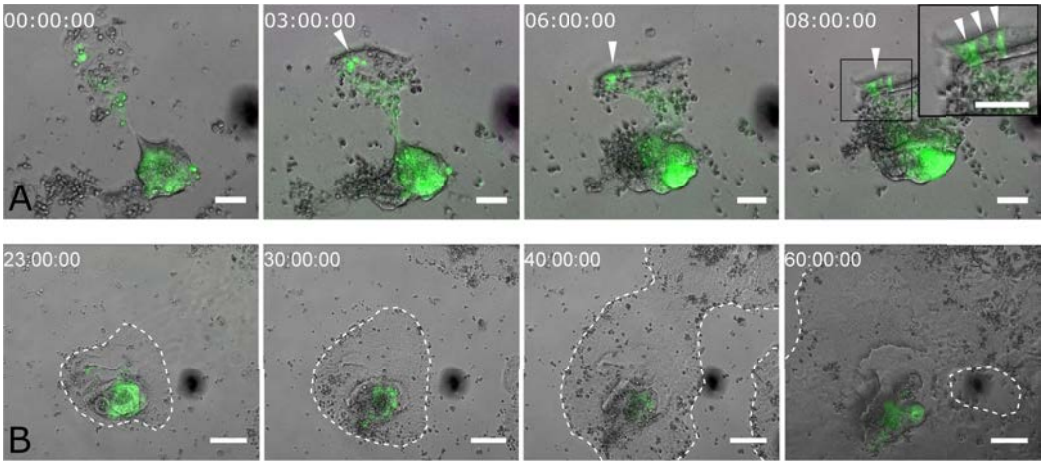

Figure 1.11: *Time-lapse image sequence showing the self-organization of the GFP^+ Lgr5 stem cells (indicated by white arrowheads) into crypt base columnar phenotype and the formation of the crypt-like domain (A). Scale bars: 50 μm. Image sequence showing the intestinal cells migrating out of the GFP^+ crypt-like domain and generating the monolayer (B). Scale bars: 100 μm. The time scales, indicated in hours, marked at the upper-left corners of the images.*

The results of the EdU pulse-chase experiment also supported the findings of live-imaging. The EdU^+ proliferative cells that were initially at the crypt-like region (Figure 1.12 A) generated the monolayer after 1 days of chase (Figure 1.12 B). A part of EdU^+ cells were $Ki67^-$, indicating that despite they were originated from proliferative cells (EdU^+) present at the crypt-like domain, they stopped dividing ($Ki67^-$), and presumably committed to differentiate into mature intestinal epithelial cells. The $Ki67^-$ cells also showed marked accumulation of the tight junction protein *zonula occludens 1* (ZO-1) at the cell membrane (Figure 1.12 B) as an evidence of tight junction maturation [51]. Overall, both the time-lapse microscopy analysis and EdU pulse-chase experiment demonstrated that, when seeded on hard substrates, organoid-derived crypt pieces self-organized into crypt-like domains where GFP^+ Lgr5 stem cells and $Ki67^+$ proliferative transit-amplifying cells were present. Then, the intestinal cells migrated out to generate the epithelial

monolayer while losing their proliferative state. This suggests that the 2D intestinal epithelial model we describe here recapitulates the intestinal epithelial physiology *in vivo*, where the Lgr5 stem cells present in the crypts divide to produce highly proliferative transit-amplifying cells that migrate up along the villi and gradually differentiate into the specific intestinal lineages [1, 2]. In a recent study, Thorne *et al.* reported similar findings. They demonstrated that the $Ki67^{+}$ proliferative cells self-organized to form the crypt-like domains, and then, the progeny of these cells formed to monolayer over a period of 3 days [29]. Such *in vitro* models that reproduce *in vivo* intestinal epithelial physiology can be powerful tools in the studies of basic biology of the epithelium and microbe-epithelium interaction. The fact that they provide access to the apical surface without the need for labor-intensive techniques (like microinjection) is a great advantage as most of the physiologically relevant assays require the access to the apical side. Also, these monolayers obtained on 2D flat surfaces in well-plate format can be used in high-throughput imaging assays and automated quantification of both cell- and tissue-level properties.

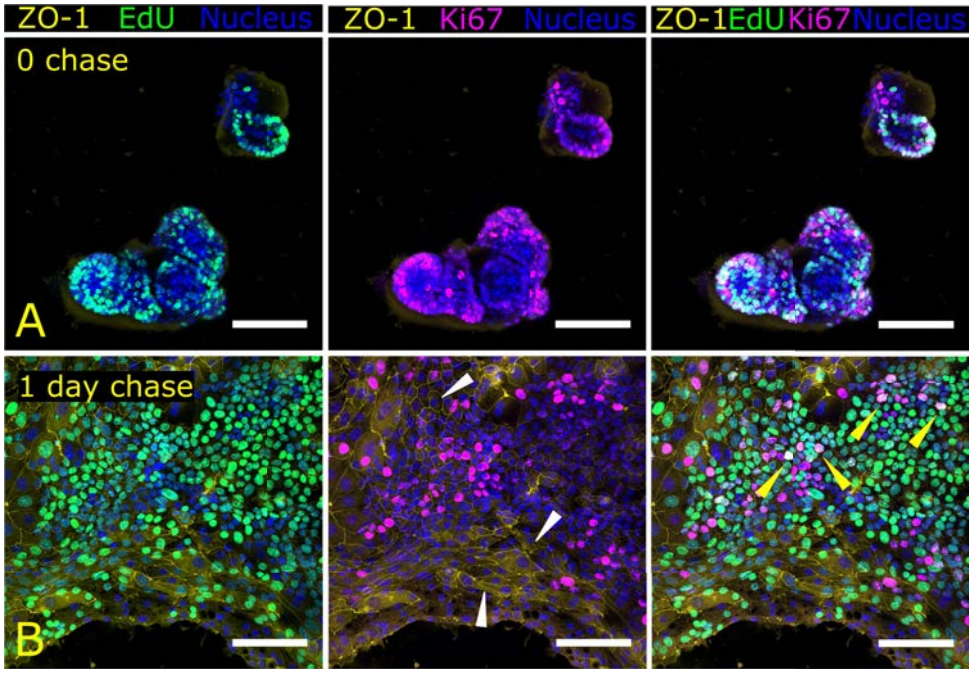

Figure 1.12: *Immunofluorescence images of EdU pulse-chase experiment co-stained for Ki67 and ZO-1 at 0 chase (A), and after 1 day chase (B). The intestinal cells were pulsed with EdU for 2,5 hours 1 day after the seeding. White arrowheads point at the marked accumulation of the ZO-1 signal. Yellow arrowheads indicate the double positive cells for Ki67 and EdU. Scale bars: 50 μm. Images are representative of two independent experiments (n = 2).*

In order to test the regenerative capacity of the 2D intestinal epithelial model, the monolayers were mechanically disrupted and passed to freshly coated new wells after one week in culture. The intestinal epithelial cells were able to regenerate monolayers and acquire similar phenotypes, i.e. crypt-like domains and non-proliferative spreading monolayers, even after passages. Figure 1.13 shows the monolayers at passage 0 (P0) (A) and at passage 2 (P2) (B). The fact that the passed cells can regenerate a monolayer suggests that a proportion of proliferative cells is maintained throughout the culture period, supported by the immunofluorescence for Ki67 revealing numerous Ki67^{+} crypt-like domains after passage 2 (Figure 1.13 B). This finding demonstrates that our 2D intestinal epithelial model could be propagated *in vitro*. In a work published by Wang *et al.* the epithelial monolayers obtained from freshly isolated crypts were also shown to have regenerative capacities [28]. The possibility of long-term propagation of primary intestinal epithelial cells as 2D monolayers in a format that allows facile access to the luminal surface, in contrast to 3D organoid culture systems, empowers their use as *in vitro* tools in studies that require exposed apical surfaces.

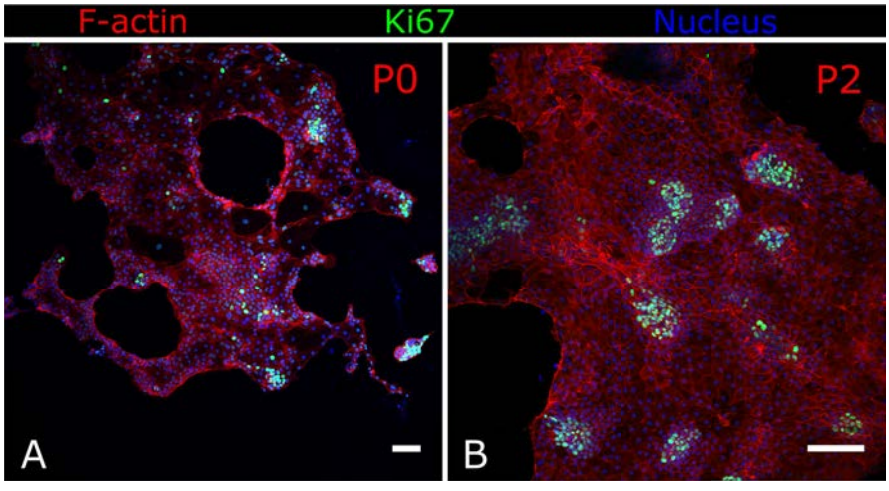

Figure 1.13: *Immunofluorescence for Ki67 showing intestinal epithelial monolayers at passage 0 (P0) at day 7 (A) and at passage 2 (P2) at day 11 (B). Monolayer phenotype, crypt-like domains and non-proliferative spreading monolayer, was still maintained after passages. Scale bars: 100 μm. The findings are representative of three independent experiments.*

The cell death in the 2D intestinal epithelial model was studied by immunofluorescence and time-lapse microscopy analysis. Immunofluorescence for cleaved caspase-3 (CC-3), a protein that plays a central role in cell apoptosis (cell death) [52], showed that the cells were undergoing apoptosis mainly at the epithelial

borders (Figure 1.14 A). Time-lapse microscopy analysis also supported this finding. Figure 1.14 B shows an image sequence of a cell extruded near the epithelial border, very much like *in vivo* intestine, where the epithelial cells shed off at the tips of the villi into the lumen [53]. In a recent study similar observations were made on epithelial monolayers derived from organoids, where apoptotic cells were identified at the epithelial border [29]. Whether apoptosis precedes or follows intestinal epithelial cell shedding is a matter of debate [54]. Similar to what we report here, *in vitro* studies showed that majority of the cells that were being extruded from epithelial monolayers expressed apoptosis markers, such as CC-3 [55]. On the other hand, live cell extrusion activated by stretch sensitive ion channels was also reported [54]. The extruded cells subsequently underwent anoikis [56]. However, in this scenario apoptosis may have already begun prior to extrusion and may have signaled extrusion itself. Either way, intestinal cell shedding occurs predominantly at the villus tip in the small intestine, similar to what we observe in the 2D intestinal epithelial monolayer model.

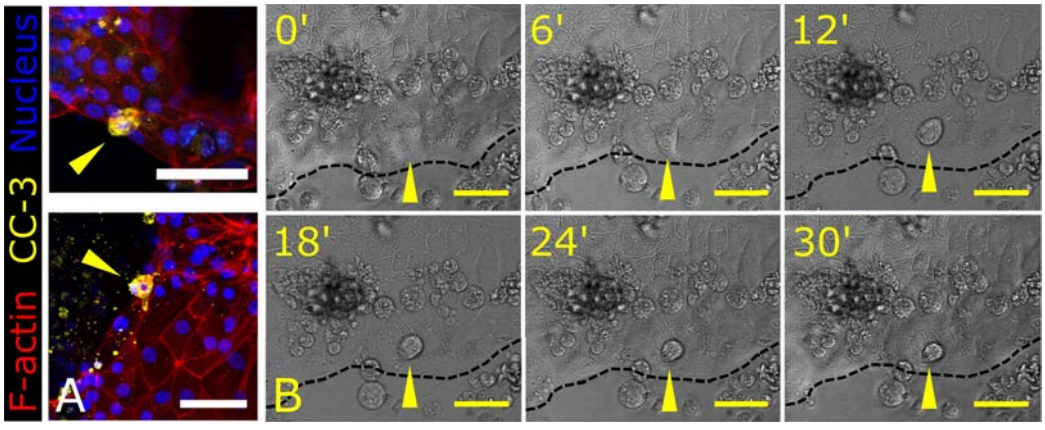

Figure 1.14: *Immunofluorescence for CC-3 of epithelial monolayers after 7 days in culture showing cell death at the epithelial border (A). Yellow arrowheads mark apoptotic cells. Images are representative of three technical replicas (n = 3). CC-3: Cleaved Caspase-3. Time-lapse image sequence of epithelial monolayers cultured for 7 days showing a cell dying off at the epithelial border (B). Images are representative of two independent experiments. Scale bars: 50 μm.*

Overall, time-lapse microscopy analysis and immunofluorescence characterizations demonstrated that in our 2D intestinal epithelial model Lgr5 stem cells at the crypt-like domain divide to give rise to an epithelial monolayer. As the intestinal cells divide and migrate out of the crypt-like domains, they lose their proliferative state and eventually die at the epithelial border very much like *in vivo* intestine.

1.3.2 Histological characterization of the monolayers

In order to better identify the different cell types constituting the intestinal epithelial monolayers, several markers were checked. CK20, a marker for mature enterocytes and Goblet cells [57], was present in the cells near the epithelial border (Figure 1.15 A), demonstrating that the major part of the non-proliferative spreading monolayer was, in fact, consisting of terminally differentiated cells. Therefore, it will be referred as the 'villus-like domain'. The villus-like and crypt-like domains occupied distinct regions within the monolayer (Figure 1.15 A). The crypt-like domains were formed by a pool of cells double positive for GFP and Ki67, corresponding to actively dividing Lgr5+ stem cells (Figure 1.15 B). Also, GFP^+ Lgr5 stem cells, and Lyz^+ Paneth cells were both positioned at the crypt-like domains (Figure 1.15 C) suggesting that, like *in vivo* intestine, in the 2D model Paneth cells formed part of the stem cell niche. Accumulation of the tight junction protein ZO-1 at the cellular membrane (Figure 1.15 D), specifically at the apical tips (Figure 1.15 D') and the F-actin at the apical side (Figure 1.15 E, E') demonstrated correct apical basal polarization of the cells as an indicator of mature differentiated cells found in the monolayer. The cells forming the monolayer displayed a polygonal morphology (F-actin staining) typical of epithelial cell layers. Moreover, PAS staining showed the presence of mucus secreting Goblet cells close to the epithelial border (Figure 1.15 F). Altogether, the histological characterization of the cultures demonstrated that the 2D intestinal epithelium model was formed of crypt-like domains containing Lgr5 stem, Paneth and proliferative transit-amplifying cells, and villus-like domains containing mature enterocytes and Goblet cells with the correct apical polarization of the tight junction protein ZO-1 and F-actin. This characterization also showed that in terms of tissue organization (crypt-villus domains) and cell-type composition our 2D intestinal epithelial model resembled very much the *in vivo* intestinal epithelium. Previously, epithelial monolayers derived from intestinal organoids [29] were also shown to contain all major intestinal cell types organized into crypt-villus units. Such *in vitro* systems are physiologically more relevant in better representing the multicellular heterogeneity and tissue organization, to be used in novel assays, pharmaceutical and dietary compounds' screens that are otherwise performed with colon cancer cell lines, such as Caco-2.

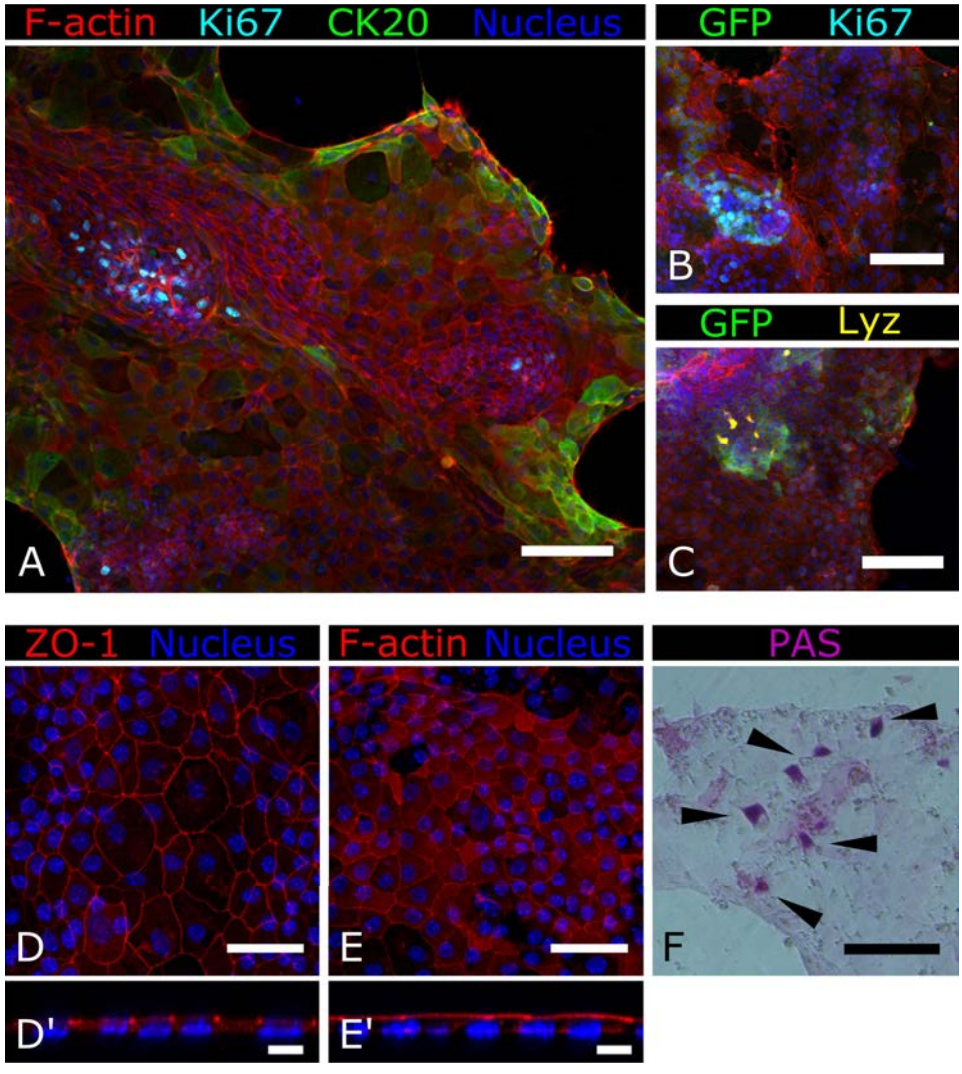

Figure 1.15: *Immunofluorescence for Ki67 and CK20 showing distinct compartments of the crypt-like domain (Ki67$^+$) and the villus-like (CK20$^+$) (A); for GFP and Ki67 showing the Lgr5 stem (GFP$^+$) and proliferative TA cells (Ki67$^+$) localized at the crypt-like domain (B); and for Lyz and GFP showing the presence of Paneth (Lyz) and Lgr5 stem cell (GFP) couples within the crypt-like domain (C). Scale bars: 100 μm. Immunofluorescence of the monolayers for tight junction protein ZO-1 showing its membrane localization (D). Monolayer side view showing ZO-1 concentrated at the cell junctions (D'). F-actin staining revealing the poligonal morphology (E), and the monolayer side view showing appropriate apical basal polarity with actin concentrated at the apical surface (E'). Scale bars: D, E: 50 μm, D', E': 10 μm. PAS staining confirming the presence of Goblet cells at the epithelial border (F). Scale bar: 100 μm. ZO-1: zona occludens 1, CK20: cytokeratin 20, Lyz: lysozyme, PAS: Periodic acid-Schiff base.*

1.3.3 Obtaining epithelial monolayers with functional tissue barrier properties

Intestinal epithelium is one of the most important tissue barriers in the body. Obtaining an *in vitro* epithelium model from intestinal organoid-derived crypts with functional tissue barrier properties is of great interest as it would allow the use of patient's own intestinal epithelial cells to screen for novel therapies, and perform clinical testing to assess the efficacy of a particular therapy. Recent studies reported the development of 2D cultures of intestinal epithelium with tissue barrier properties with the use of cell culture media rich in ISC niche factors such as Wnt pathway activators [22, 27, 35]. Here, we also tested different cell culture medium compositions (e.g. ISEMF_CM, Wnt3a_CM, and recombinant Wnt3a) and also the culturing time in the pursuit of determining the parameters necessary to obtain an intact *in vitro* epithelium.

1.3.3.1 Effect of the culturing time on epithelium growth and integrity

To achieve epithelial monolayers with functional tissue barrier properties, as a first approach, culturing the intestinal cells for prolonged periods of time was tried. However, even though cells were viable for up to 28 days, monolayers with full surface coverage were not obtained (Figure 1.16). Moreover, compared to the epithelium formed at day 7 and day 14 (Figure 1.16 A, B), significant changes in the cellular morphology were noted at day 21 and 28 (Figure 1.16 C, D). The polygonal phenotype, characteristic of the epithelial cells, was lost and aberrations in actin cytoskeleton were observed. Therefore, it was concluded that not only it was not possible to obtain intact monolayers by only culturing them for prolonged times but also it was not desired since the epithelial phenotype was lost at longer time points. The studies in which the epithelial monolayers derived from intestinal crypts or organoids were assayed, the culture times used were short (from 3 days to a maximum of 8 days) [22, 27, 35]. This might be due to the undesired effects of prolonged culturing times as we demonstrated here. Instead, in these studies cell culture media enriched for ISC niche biochemical factors were used to obtain epithelial monolayers that cover the entire substrate surface [22, 27, 35]. In what follows, we present the study we performed on the effects of such cell culture media enriched for ISC niche biochemical factors in the effort of forming epithelial monolayers with effective tissue barrier properties.

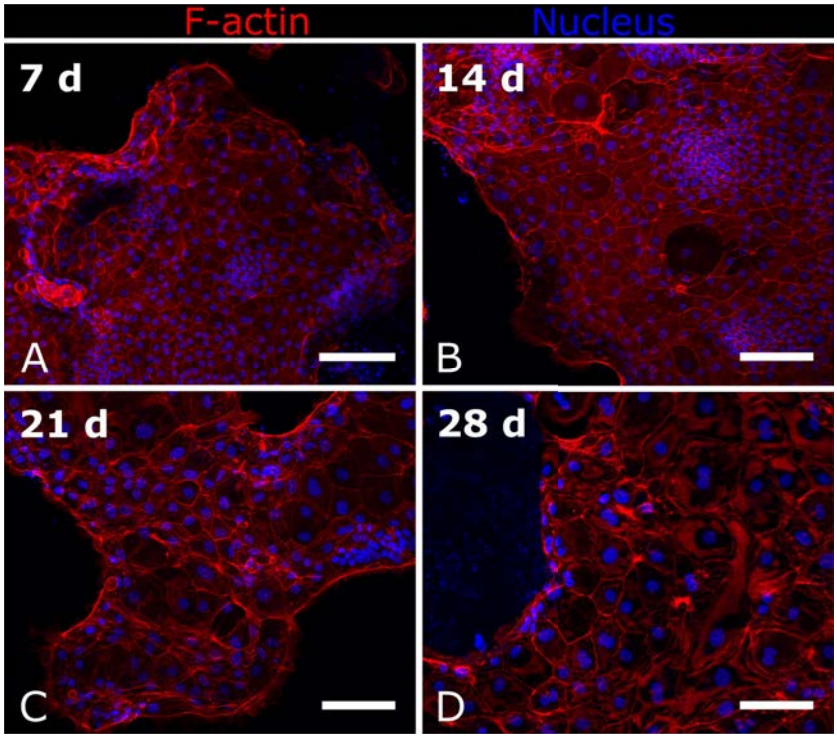

Figure 1.16: *Fluorescence staining for F-actin and nucleus showing the epithelial morphology after 7 (A), 14 (B), 21 (C), and 28 (D) days of culture. Morphological changes can be noted due to prolonged periods of culture time. Images are representative of three technical replicas (n = 3). Scale bars: 100 μm.*

1.3.3.2 Effects of conditioned cell culture medium (ISEMF_CM and Wnt3a_CM) on the growth of epithelial monolayers

The principal driver of the stem and transit-amplifying cells' proliferation in the intestinal epithelium is the canonical Wnt pathway [2, 58]. The main sources of Wnts *in vivo* are Paneth cells that produce Wnt3 [59], and intestinal subepithelial myofibroblasts (ISEMFs) that produce Wnt pathway activators, including Wnt2, Wnt2b, Wnt4, Wnt-5a, and Wnt9b [41–43], and the enhancers of the Wnt pathway, R-Spondin 2 and R-Spondin 3 [43, 60, 61]. It has been shown that the ISEMFs supported and enhanced the growth of organoids obtained from intestinal crypts [60, 62]. Here, we studied the effect of exogenous sources of Wnt pathway activators (like the ones found in the conditioned cell culture media obtained from ISEMF and Wnt3a producing cell line) added to culture medium on the epithelial monolayer growth and barrier formation. For that, the conditioned media was

produced from primary intestinal subepithelial myofibroblasts (ISEMFs) isolated from mouse colon and a Wnt3a producing cell line.

First, isolated ISEMFs (Section 1.2.4.1) were characterized by immunofluorescence in order to be sure that the isolated cells had the correct phenotype. ISEMFs are found right below the epithelium in the lamina propria (mesenchyme) surrounding the crypts and they are fibroblasts that exhibit contractile behavior with a central role in the restoration of the damaged epithelium (see General introduction) [63]. These cells express α- smooth muscle actin (α- SMA), a common marker for myofibroblasts [64, 65], and vimentin, a type III intermediate filament found in mesenchymal cells [66], but they are negative for desmin, a type III intermediate filament only found in muscle cells [66]. Immunofluorescence for these markers revealed that, indeed, isolated ISEMFs were positive for α- SMA and vimentin (Figure 1.17 A, B), and negative for desmin (Figure 1.17 C). This characteristic staining (α- SMA$^+$, vimentin$^+$, desmin$^-$) confirmed the phenotype of isolated ISEMFs [60, 62].

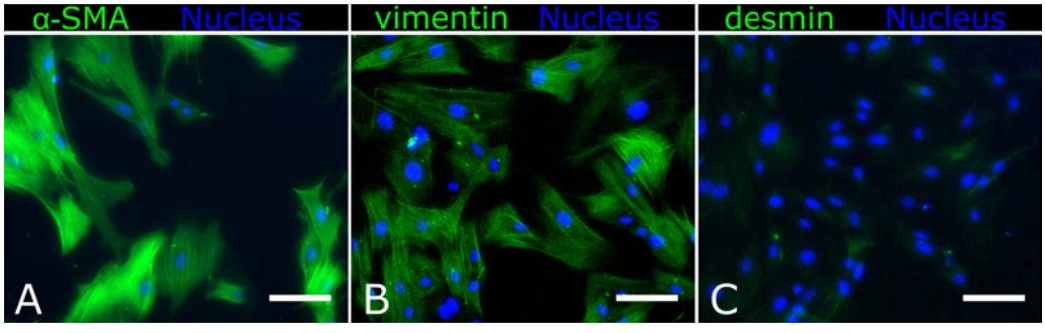

Figure 1.17: *Immunofluorescence of ISEMFs stained characteristically positive for α-smooth muscle actin (α-SMA) (A), and vimentin (B), and negative for desmin (C). Counterstaining was done with Hoechst 33342. Scale bars: 50 μm.*

ISEMF_CM was collected from isolated ISEMFs as explained in section 1.2.4.1. Wnt3a_CM and L-cell_CM were collected from the cultures of commercially available L-Wnt3a producing and parental L-cell line, respectively (Section 1.2.4.2). Organoid-derived crypts were cultured with the different conditioned media supplemented with ENR_CV. As controls, conditioned media not supplemented with ENR_CV were also tested. At dat 4 of culture, ISEMF_CM (Figure 1.18 A) had a pronounced effect on improving the surface coverage of the monolayer compared to the ENR_CV control (Figure 1.18 C); while there was no obvious difference in monolayer surface coverage between Wnt3a_CM, L-cell_CM (Figure 1.18 D, F) and ENR_CV control. Monolayers

grew only when the conditioned media were supplemented with ENR_CV; otherwise cells died in clumps (Figure 1.18 B, E). Some of the adherent cells found in the first days of culture were very short-lived (Figure 1.18 B). This suggested that, by itself, the ISC niche factors found in the conditioned media tested here were not sufficient in supporting the growth of the organoid-derived crypts. Therefore, the conditioned media had to be supplemented with ENR_CV prior to use. On the other hand, we observed a synergistic effect in the case of ISEMF_CM. When supplemented with ENR_CV, the monolayer growth was significantly improved with respect to ENR_CV alone (Figure 1.18 A, C). Wnt2b (secreted by ISEMFs *in vivo*) was shown to rescue organoids derived from $Wnt3^{fl}$ mice (Wnt3 allele deleted upon induction) compensating the loss of Wnt3 [42]. R-Spondin 2 secreting ISEMFs were shown to support organoid growth even in the absence of exogenous R-Spondin 1 [60]. These findings reported in the literature might explain the monolayer growth induction we observed with the use of ISEMF_CM. The fact that there was no obvious effect of the Wnt3a_CM with respect to ENR_CV alone was unexpected, since Wnt3a is the effector of the canonical Wnt pathway, the principal driver of Lgr5 stem cell proliferation *in vivo*. Yet, fast degradation of the cell line produced Wnt3a due to storage conditions of the conditioned medium, i.e. freeze-thaw cycles, prolonged storage at 4°C might explain why there was no obvious effect on monolayer growth [67]. The standard growth media of the parental L-cell line contains 10% FBS so does the L-cell_CM. However, there was no obvious effect of the FBS (L-cell_CM *vs.* ENR_CV) on the monolayer growth either (Figure 1.18 C, F). Cell culture medium containing both ISEMF_CM and Wnt3a_CM was also tested (Figure 1.18 G) in order to check for the synergistic effects of the factors secreted by the myofibroblasts, i.e. Wnt2b and R-Spondin 2, and the Wnt3a. There was a pronounced increase in surface coverage compared to the ENR_CV control. However, most likely this increase was due to the ingredients provided by ISEMF_CM since Wnt3a_CM alone did not show a proliferative effect (Wnt3a_CM *vs.* ENR_CV). Moreover, the quantification of the surface coverage of the monolayers revealed that both ISEMF_CM and ISEMF_CM + Wnt3a_CM conditions induced $\approx$ 2,5 fold increase.

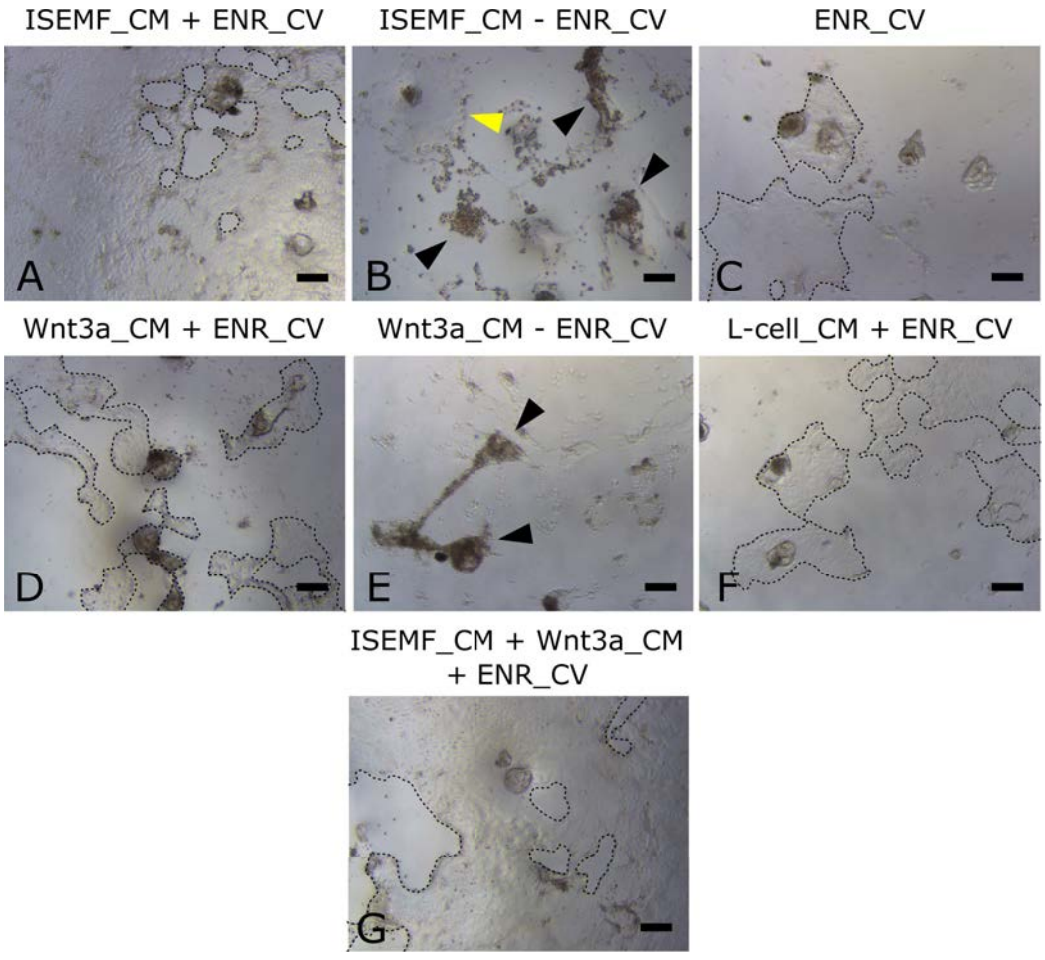

Figure 1.18: *Representative bright field images of the epithelial monolayers cultured with ISEMF_CM + ENR_CV (A), ISEMF_CM - ENR_CV (B), ENR_CV (C), Wnt3a_CM + ENR_CV (D), Wnt3a_CM -ENR_CV (E), L-cell_CM + ENR_CV (F), and ISEMF_CM + Wnt3a_CM + ENR_CV (G) after 4 days of culture (n = 2). Cells died when the culture media wasn't supplemented with ENR_CV (indicated by black arrowheads). Some cells adhered even in the absence of ENR_CV (indicated by yellow arrowhead); however, they were very short-lived. Black dashed lines mark the epithelial border. Images are representative of two technical replicas (n = 2). Scale bar: 100 μm.*

This preliminary assessment showed that it was possible to improve the surface coverage of epithelial monolayers derived from organoids by using ISEMF_CM at 4 days of culture. Then, the cultures were further continued until day 9 to see if the monolayer growth advanced with more time; however, no significant increase in the monolayer expansion was observed. Immunofluorescence images of cultures fixed at day 9 clearly showed that full surface coverage wasn't reached with prolonged culturing times (Figure 1.19). In addition, significant

changes in the cellular morphology were noted at the samples cultured with conditioned media (Figure 1.19 A, B) with respect to controls (Figure 1.19 C). The polygonal phenotype, characteristic of the epithelial cells, was lost and multilayers of cells were observed. However, one can still appreciate the formation of the $Ki67^{+}$ crypt-like domains and the non-proliferative spreading monolayer at day 9, when organoid-derived crypts were cultured with only ENR_CV (Figure 1.19 C).

Obtaining epithelial monolayers covering the entire surface of the substrate is indispensable in its proper barrier functionality. Our findings demonstrated that the use of ISEMF_CM (supplemented with ENR_CV) could be used to improve the surface coverage of the epithelial monolayers. Further ingredients such as Wnt3, principle activator of the Wnt pathway, can be tested in the effort of finding the optimal conditions.

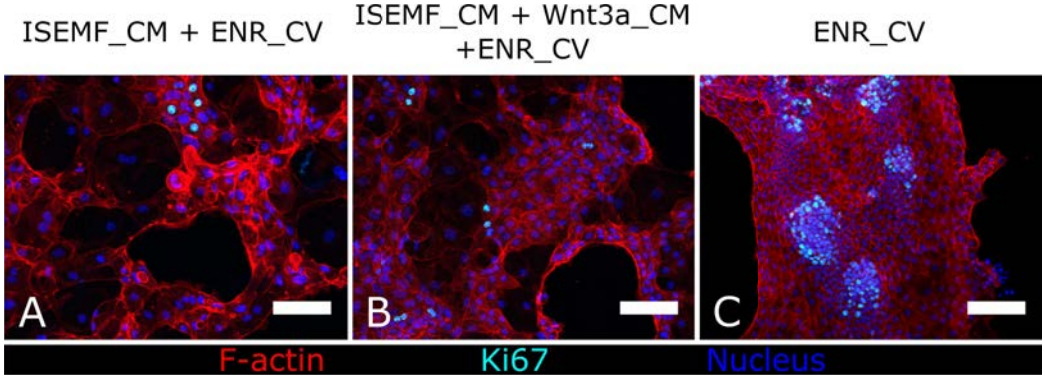

Figure 1.19: *Immunofluorescence images of epithelial monolayers obtained from organoid-derived crypts cultured with ISEMF_CM + ENR_CV (A), ISEMF_CM + Wnt3a_CM + ENR_CV (B), and ENR_CV (C) at day 9. Images are representative of two technical replicas (n = 2). Scale bar: 100 μm.*

In native intestine, the stem cell proliferation is mainly driven by the Wnt pathway. The major effector of this pathway is Wnt3 produced by the Paneth cells [59]. It, then, follows naturally that a medium containing Wnt3a (Wnt3a_CM) should increase the proliferative capacity of the ISCs *in vitro*. However, our results with Wnt3a_CM showed otherwise, no significant increase in epithelial monolayer growth was observed with respect to the control. We thought that one possible explanation of this could be the fast degradation of the cell line produced Wnt in the medium. Therefore, to better control the amount of active Wnt3a within the cell culture medium, commercially available Wnt3a was added in controlled

amounts. The effect of added Wnt3a was evident (Figure 1.20) with surface coverage values being 69,6% ± 2,7% for ISEMF_CM + Wnt3a + ENR_CV after 5 days of culture, while for ISEMF_CM + ENR_CV and ENR_CV only, it was 50,0% ± 13,3% and 24,0% ± 4,1%, respectively (n = 3). Even though the combined effect of Wnt3a and ISEMF_CM on the monolayer growth was significant, 100% surface coverage still was not attained. Cultures were not prolonged for further time points since previous trials showed that after 4-6 days in culture monolayers did not significantly expand more. Even so, the results demonstrate that ISEMF_CM supplemented with Wnt3a and ENR_CV can be used in further trials to boost the epithelial monolayer growth. In literature, similar strategies such as incorporating to the cell culture medium exogenous ISC niche biochemical factors, were adopted to generate epithelial monolayers with tissue barrier functionality in Transwell® setup [22, 27, 35]. This experimental setup provides access to both apical and basolateral side of the cell monolayer that allows performing of functional assays. In what follows, we present how we transfer our 2D epithelial monolayer model generated on 2D tissue culture plates to Transwell® format.

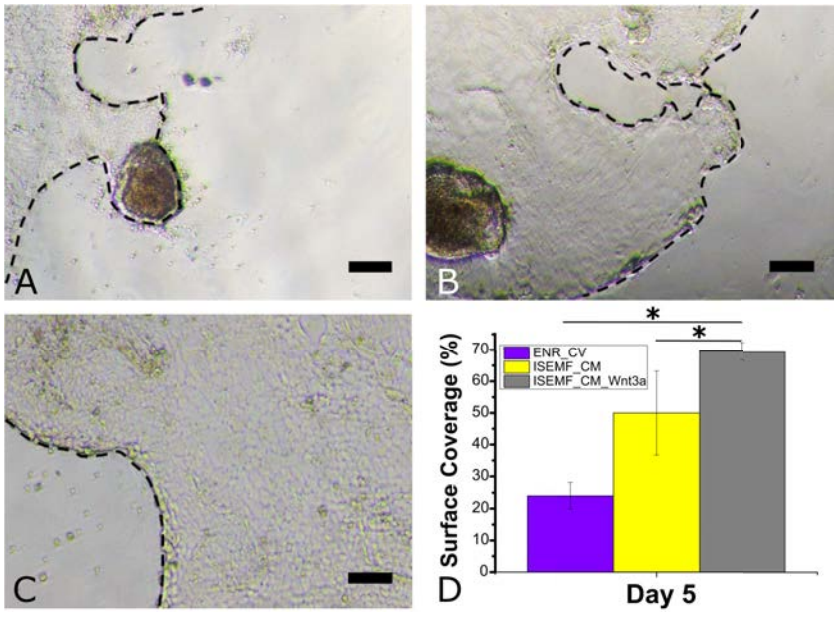

Figure 1.20: *Representative bright field images of the epithelial monolayers cultured with ENR_CV (A), ISEMF_CM + ENR_CV (B), and ISEMF_CM + Wnt3a + ENR_CV (C) after 5 days of culture. Graph showing the surface coverage measured from bright field images acquired at 12 randomly selected regions for each of three technical replicas (n = 3). The data are presented as mean ± standard deviation. *p<0,01 by Student's t test. Scale bars: 100 μm.*

1.3.4 Culturing organoid-derived crypts on Transwell® inserts

Intestinal epithelium is a semipermeable tissue, efficiently absorbing nutrients and small drug molecules, while blocking the lethal organisms and harmful compounds present in the lumen passing to the underlying tissue (mesenchyme). This is due to the presence of the tightly packed enterocytes, the dominant cell lineage (80%) within the epithelium [68]. Therefore, a physiologically relevant *in vitro* intestinal epithelial model must demonstrate a proper barrier functionality. The common way of verifying the barrier integrity of such models is growing the cells on the so-called Transwell® insert. The insert has a porous membrane at its base and separates the medium into two compartments, apical and basolateral, with the cell monolayer in between. This configuration permits the access to both apical and basolateral sides (luminal and mesenchymal) and enables to test the barrier properties regarding selective permeability. In this setup, the monolayer formation and tight junction integrity can be monitored by the measurement of a quantitative parameter called Transepithelial electric resistance (TEER). Moreover, by permitting access to both luminal and mesenchymal sides , Transwell® setup allows better mimicking of asymmetric condition found *in vivo*, where the ISC niche biochemical factors are delivered from the mesenchyme. Therefore, Transwell® setup was adopted in our work to improve our *in vitro* monolayer model.

1.3.4.1 Effects of asymmetric administration of ISC niche biochemical factors

Organoid-derived crypts were then seeded on Transwell® inserts coated with a thin layer of Matrigel® yielding a 'Hard' surface and cultured with the ISC niche factors delivered only at the basolateral compartment for the asymmetric condition and both at the basolateral and apical compartments for the uniform condition. As a control, inserts were coated with a thick layer of Matrigel® to yield a 'Soft' surface. Experimental setup used is depicted in section 1.2.5 figure 1.7. The cell culture medium containing ISC niche factors was selected to be ENR_CV medium, to be able to distinguish the effects of the asymmetric administration from the additional effects of the cell culture composition. Intestinal cells formed monolayers on 'Hard' surfaces with the asymmetric administration of the ENR_CV in all the independent experiments tried (n = 4) (Figure 1.21 A); while under uniform administration of the factors half of the times tested they formed organoid-like structures (2 in total of 4 independent experiments) and in the other half, monolayers (Figure 1.21 B, B'). On the other hand, when we have organoid

forming conditions, that is the 'Soft' surfaces, the asymmetric delivery of the factors does not play any role (Figure 1.21 C, D). The fact that only 'Hard' surfaces supported the formation of the monolayers, extends the findings of our previous trials on 2D tissue culture plates (Figure 1.10) to the Transwell® setup and suggests that the mechanical properties of the underlying substrate trigger the monolayer formation rather than the type of the substrate material itself (polystyrene plates *vs.* polycarbonate membranes).

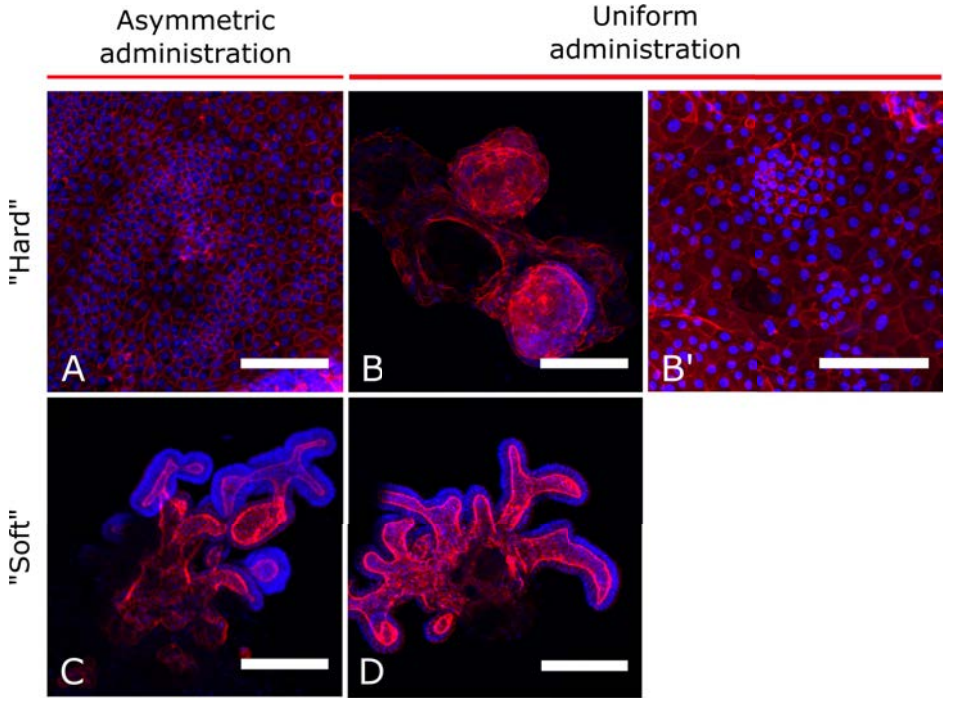

Figure 1.21: *Representative fluorescence images marking F-actin (red) and nuclei (blue) showing different growth phenotypes of the intestinal epithelial cells when cultured on 'Hard' surfaces under asymmetric (A), and uniform administration (B, B') (Scale bars: 100 μm); and on 'Soft' surfaces under asymmetric (C), and uniform administration (D) (Scale bars: 150 μm) of ENR_CV after 10 days of culture. Images are representative of at least three independent experiments (n = 3).*

The asymmetric administration of the ENR_CV (Lgr5 ISC niche factors) might have a synergistic effect with the mechanical properties of the surface assuring the formation of the monolayers since half of the times tested under uniform condition, intestinal cells only formed organoid-like structures. One possible explanation to these observations is that when the intestinal cells receive the ISC niche factors from all possible directions (uniform condition) they might prefer to grow as organoids; while when they receive them only from the basolateral side (*in*

vitro counterpart of the mesenchyme) they spread out on the surface to access the necessary growth factors. Although, in the previously published reports, same culture medium composition was reported to be used for both compartments for the generation of organoid-derived epithelial monolayers on porous membranes [22, 27, 69]; the air-liquid interface (ALI), basolateral delivery of the ISC niche factors, was shown to induce proper differentiation of monolayers obtained from ISCs [70]. *In vivo* intestine, the ISCs receive the niche factors to divide to fuel the epithelial regeneration from the neigboring Paneth cells and the underlying mesenchyme (basolateral side) [59]. In this respect, asymmetric administration of the ISC niche factors (ENR_CV) is more physiologically representative and among the conditions we tested, it assured the formation of the monolayers (Figure 1.21 A).

Once we established the necessary conditions to obtain monolayers on Transwell® setup ('Hard' substrate and asymmetric administration of ISC niche factors), we characterized the cellular phenotype of the monolayers formed in this setup.

1.3.4.2 Characterizing the monolayer cell phenotype on Transwell® setup

The cell-type distribution of the monolayers formed under the asymmetric administration of ENR_CV in Transwell® setup was characterized by immunofluorescence for Ki67, ephrin type-B receptor 2 (EPHB2), and GFP (Figure 1.22). EPHB2 is a receptor protein that is highly expressed in ISCs, and becomes gradually silenced as the cells differentiate [71]. A gradient in the expression patterns of the EPHB2 is observed from crypt bottoms towards villi *in vivo* [71].

As in 2D tissue culture plate setup, the monolayers were comprised of crypt-like domains, marked positive for Ki67, EPHB2 and GFP (Figure 1.22 A, B, C), and spreading non-proliferative monolayer. Numerous islets of $EPHB2^+$ cells were present in the monolayers (Figure 1.22 B) marking the crypt-like domains. The EPHB2 fluorescence was gradually faded moving out of these domains forming a gradient (Figure 1.22 B'), which suggested the differentiation of the intestinal cells as they moved out of the crypt-like domains very much like *in vivo* [71]. GFP^+ Lgr5 ISCs were found to be confined to the crypt-like domains, but not all of the cells in the domain were positive for GFP (Figure 1.22 C, C'). This suggests the presence of other types of cells, presumably Paneth and transit-amplifying progenitor cells. In this respect, the cell-type distribution of the monolayers in Transwell® setup, like in 2D tissue culture plate setup, was similar to that of the

in vivo intestine. However, the monolayers did not grow enough to form intact monolayers (100% surface coverage) (Figure 1.22 A, C).

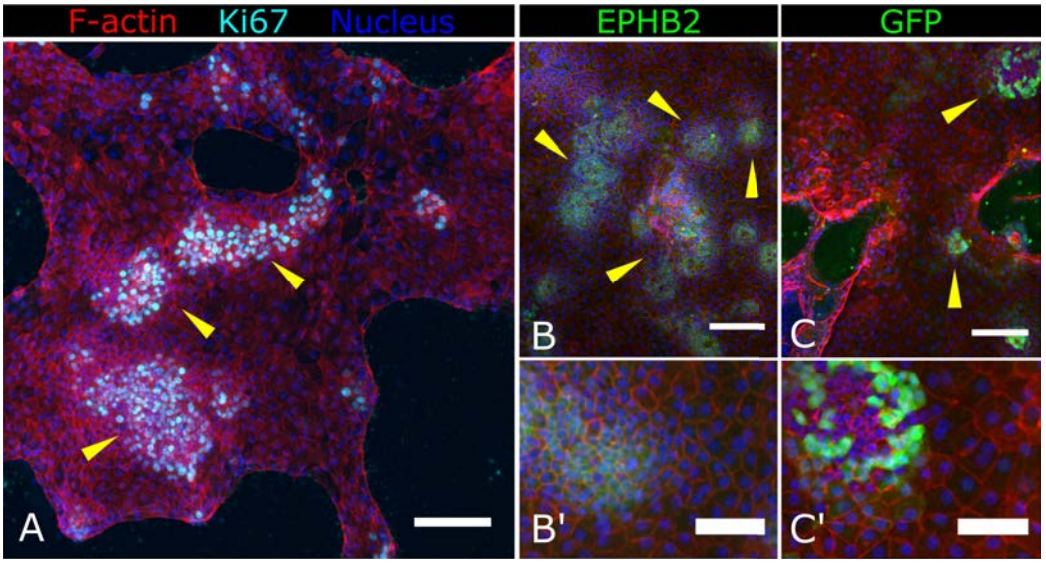

Figure 1.22: *Immunofluorescence of epithelial cultures obtained from Lgr5-EGFP-Ires-CreERT2 mice organoid-derived crypts in Transwell® setup showing Ki67 (A), EPHB2 (B), and GFP (C) positive crypt-like regions (indicated by yellow arrowheads) at day 10. Epithelial intestinal monolayer maintained its particular cell-type distribution when grown on a thin layer of Matrigel® in the Transwell® setup. Scale bars: 100 μm. Zoomed images showing the EPHB2 gradient (B'), and the presence of GFP$^-$ region (C') suggesting the differentiation of the progenitors. Scale bars: 50 μm.*

The methodology we present here for the formation of the monolayers in Transwell® setup succeeds in recapitulating the main cellular and organizational features of 3D organoids in 2D systems, in accordance with our previous findings on the monolayers formed on 2D tissue culture plates. The advantage of using Transwell® inserts is the possibility of accessing both sides of the monolayer. This not only allows the asymmetric delivery of ISC niche factors but also the performing of the functional assays related to epithelial barrier permeability. However, the cell culture medium used here, ENR_CV medium, does not promote the formation of monolayers that cover the entire surface of the substrate. For that reason, the medium composition was revised to include factors that would increase the proliferative capacities of ISCs. In the light of our previous findings on the beneficial effects of ISEMF_CM and Wnt3a on the monolayer growth (Section 1.3.3.2), we decided to incorporate these factors into the cell culture cocktail.

1.3.4.3 Effects of conditioned cell culture media on the formation of an epithelial barrier on Transwell® setup

The synergistic effect of ISEMF_CM and Wnt3a added to the cell culture medium supplemented with ENR_CV led to a significant increase in the surface coverage of the monolayer in standard 2D tissue culture plate setup, as shown in Section 1.3.3.2. We then hypothesized that the use of this culture medium composition in Transwell® setup would increase the surface coverage and lead to generation of epithelial monolayers fully covering the membranes of the Transwell® inserts. The inserts were coated with a thin layer of Matrigel® yielding a 'Hard' surface and organoid-derived crypts were cultured on these substrates under asymmetric (only basolateral delivery) or uniform administration (both basolateral and apical delivery) of ISEMF_CM + Wnt3a + ENR_CV. As a control, inserts were coated with a thick layer of Matrigel® to yield a 'Soft' surface (see Section 1.2.5 Figure 1.7 for experimental setup). The monolayer growth was monitored over the cell culture time, 20 days, by TEER (Figure 1.23).

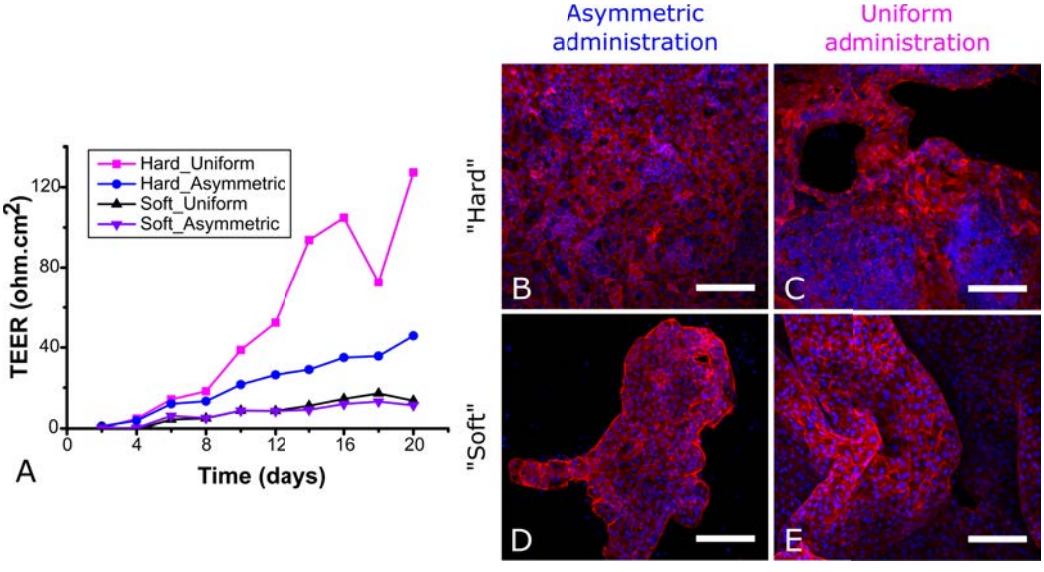

Figure 1.23: *Graph showing the TEER profiles (A) and representative fluorescence images for F-actin (red) and nuclei (blue) showing different growth phenotypes of the intestinal epithelial cells under the conditions; 'Hard' (B, C) and 'Soft' surfaces (D, E), and asymmetric (B, D), and uniform administration (C, E) of ISEMF_CM + Wnt3a + ENR_CV. Fluorescence images were acquired from samples fixed at day 20. Intestinal epithelial cells grown on 'Hard' surface with asymmetric administration of the factors had near physiological TEER values of small intestine, i.e. 40-100 $\Omega.cm^2$ [30, 33, 34]. Scale bars: 100 μm.*

The cell culture medium composition tested, ISEMF_CM + Wnt3a + ENR_CV,

led to the formation of monolayers with barrier properties on 'Hard' Transwell® inserts as indicated by increasing TEER profiles (Figure 1.23 A). Monolayers grown on 'Hard' surfaces under both asymmetric and uniform administration showed steadily growing TEER profiles; however, only the former (asymmetric) maintained the growth profile until day 20 (Figure 1.23 A). F-actin staining of the condition 'Hard-Asymmetric' revealed that the monolayer had covered the entire surface of the Transwell® insert (Figure 1.23 B). The TEER values of the uniform condition were very variable after day 12 (Figure 1.23 A), and F-actin staining showed that there were holes in the monolayer (Figure 1.23 C). The evolution of the TEER values under uniform condition suggested that cell growth was faster, presumably leading to the rupture of the monolayer. On the substrate condition leading to the formation of organoids ('Soft' surfaces), TEER profiles did not evolve indicating the absence of an epithelial barrier (Figure 1.23 A) and F-actin stainings confirmed this finding (Figure 1.23 D, E). However, intestinal cells grew in sheet-like forms with this cell culture media composition (ISEMF_CM + Wnt3a + ENR_CV) as oppose to the formation of the organoids when cultured only with ENR_CV on Transwell® inserts with 'Soft' surfaces (Section 1.3.4.1).

Overall, among the conditions tested, 'Hard' surfaces and the basolateral delivery (asymmetric condition) of cell culture medium containing ISEMF_CM + Wnt3a + ENR_CV promoted the formation of epithelial barriers revealed by the increasing TEER values. We selected these conditions as optimal and further studied the integrity and morphology of the epithelial monolayers cultured under these conditions at two different time points: day 10 and day 20. Representative images of the epithelial monolayers stained with F-actin showing the full area of the Transwell® inserts (6,5 mm in diameter) demonstrated that 10 days were enough time for the epithelial monolayer to fully cover the whole surface (Figure 1.24, upper left panel) and the intestinal epithelial monolayer with a characteristic epithelial cell cobblestoned disposition was properly formed (Figure 1.24, upper panel). The morphology of these monolayers was preserved and the surface coverage was still complete at day 20 (Figure 1.24, bottom panel and Figure 1.23 B). These results confirmed that adding exogenous ISC niche biochemical factors (derived from ISEMFs and added Wnt3a) to the standard ENR_CV medium boosted the monolayer growth and led to the formation of monolayers that covered the entire surface of the substrate. Therefore, this new cell culture medium composition and method will be adopted for further functional assays and cell-type composition characterizations performed on the epithelial monolayers.

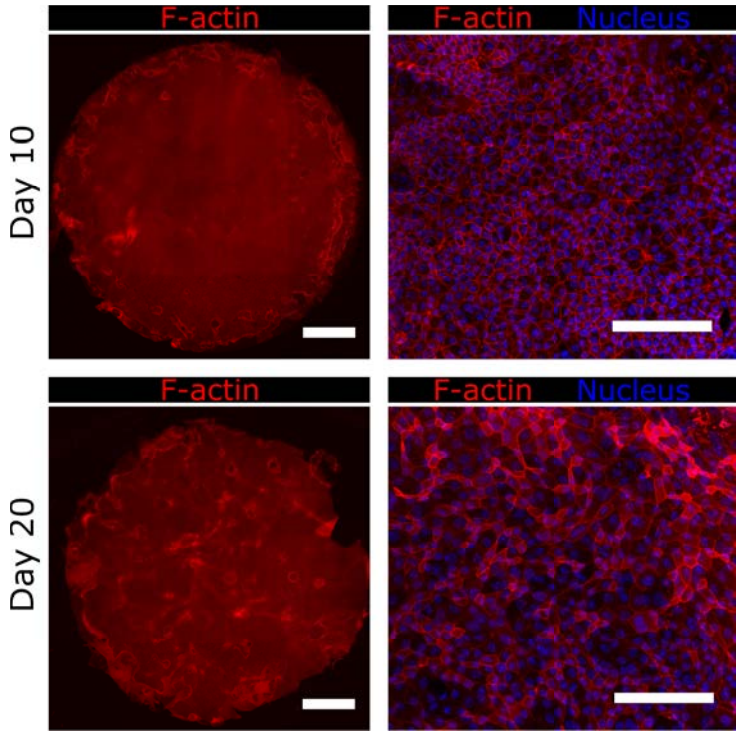

Figure 1.24: *Fluorescence of F-actin and nucleus of the monolayers cultured in transwell setup under asymmetric administration of ISEMF_CM + ENR_CV + Wnt3a medium at day 10 (n = 6) and day 20 (n = 4). Left panel shows the F-actin staining of the entire sample surface and right panel shows F-actin and nucleus staining at a higher magnification. Scale bars: 1 mm (left panel); 100 μm (right panel).*

1.3.4.4 Assessment of the barrier function of the epithelial monolayers

Organoid-derived crypts were seeded on 'Hard' surfaces and cultured under basolateral delivery of ISEMF_CM + Wnt3a + ENR_CV (asymmetric administration). Standard organoid growth medium that did not contain the ISC niche factors (ISEMF_CM + Wnt3a + ENR_CV) was added to the apical compartment. Cell-type distribution and quantification, and monolayer growth and tight junction integrity were assessed over time. Immunofluorescence for GFP revealed that GFP^+ stem cells were clustered in specific domains, indicating the formation of crypt-like domains containing $Lgr5^+$ ISCs both at day 10 (Figure 1.25 A) and 20 of culture (Figure 1.25 B). Therefore, in these conditions, the stem cell distribution previously observed on Matrigel®-coated hard substrates and Transwell® inserts was maintained. Contrarily, $Ki67^+$ proliferative cells were not as clustered as GFP^+ stem cells, but rather dispersed throughout the monolayer both at

day 10 and day 20 (Figure 1.25 C, D). This difference can be due to the new culture medium composition (ISEMF_CM + Wnt3a + ENR_CV). In a recent study Thorne *et al.* reported that adding Wnt3a disrupted the organization of crypt-like domains in a way that the proliferative regions were greatly expanded and had lost circularity [29]. On the other hand, $CK20^+$ differentiated cells were accumulated in non-proliferative areas ($Ki67^-$) both at day 10 and 20 (Figure 1.25 C, D). The amount of $Lgr5^+$ ISCs remained constant throughout the cell culture period, indicating that the pool of $Lgr5^+$ ISCs was maintained over time (Figure 1.25 E).

Contrarily, the amount of proliferative $Ki67^+$ in the monolayer was substantially lowered from day 10 to day 20. At day 10, only about 25% of the total percentage of proliferative cells (15,8% $\pm$ 4,8%) were $Lgr5^+$ ISCs (3,9% $\pm$ 1,4%), suggesting that the rest of the proliferative population was consisting of transit-amplifying cells. However, at day 20, the percentages of GFP^+ (3,8% $\pm$ 0,8%) and $Ki67^+$ cells (2,4% $\pm$ 1,2%) were not statistically different (Figure 1.25 E). This might be explained by the lowered amounts of transit-amplifying cells due to the maturation of the culture with time. Interestingly, the decrease in proliferative cell population over time correlated with an increase of differentiated $CK20^+$ cells (Figure 1.25 E). Moreover, F-actin was accumulated at the apical surface of the monolayer already at day 10 (Figure 1.25 F) and the cell height was increased significantly from day 10 to day 20 (Figure 1.25 F), indicating proper apical basal polarization of the epithelial cells forming the monolayer that was enhanced with time. These results suggest that the intestinal epithelial monolayer grown on Matrigel®-coated porous membranes with a basolateral administration of ISC niche biochemical factors is proliferative initially, while after reaching confluency epithelial cell differentiation increases and proliferation decreases.

Monitoring of transepithelial electric resistance (TEER), allows to evaluate epithelial monolayer formation and tight junction integrity, both indicators of epithelial barrier function [30, 31]. The increase of cell differentiation and polarization over time correlates with increasing TEER values throughout the culture time (Figure 1.25 G). During the initial stages of the culture, when epithelial monolayer is forming, TEER values were found to be low. From day 16 to day 20 of culture, coinciding with an increase in the differentiation of the monolayer, TEER values started to fall into the physiologically relevant range reported to be between 40 and 100 $\Omega.cm^2$ for the native small intestine [30, 33, 34].

As oppose to other studies in which differentiation was accomplished by the removal of the Wnt pathway activators and addition of the inhibitors of the Wnt

pathway [22, 35, 72] or by the use of air-liquid interface [70], in our model epithelial monolayer differentiation was achieved by prolonged culture times.

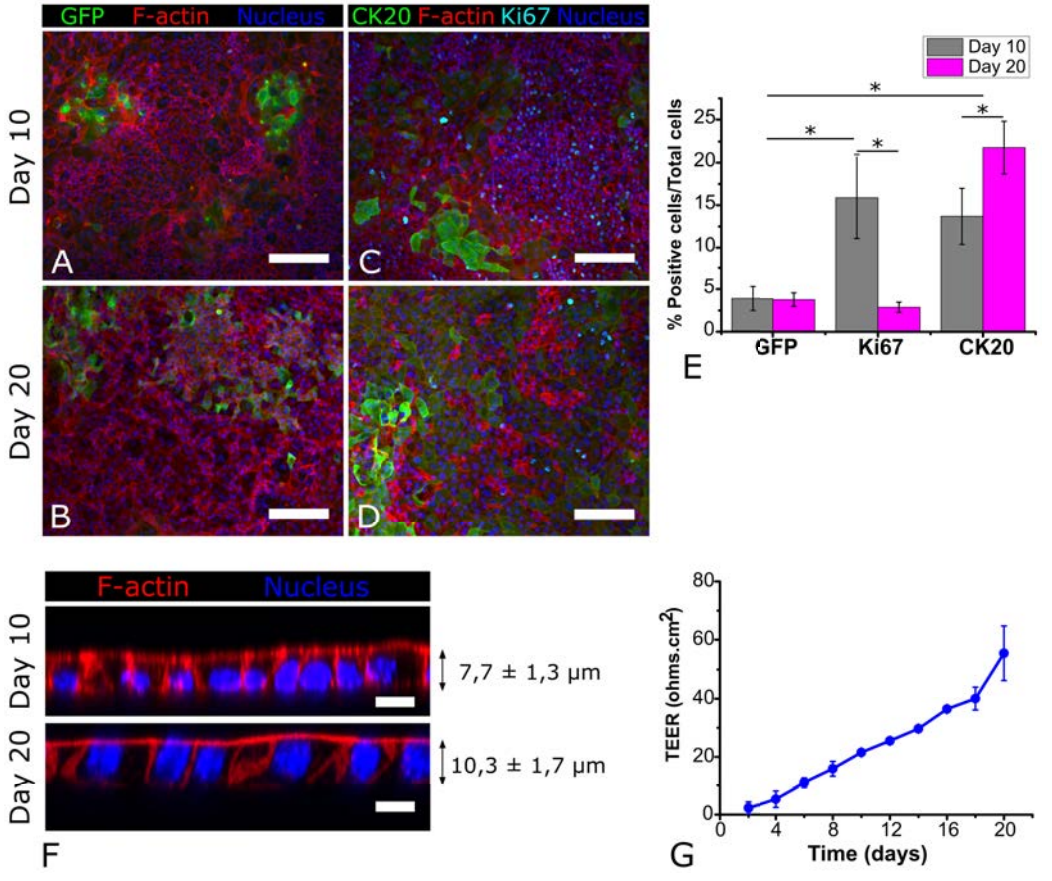

Figure 1.25: *Immunofluoresence for GFP after 10 (A), and 20 (B) days in culture. Immunofluoresence for Ki67 and CK20 after 10 (C) and 20 (D) days in culture. Intestinal cells were cultured under asymmetric administration of ISEMF_CM + Wnt3a + ENR_CV. Scale bars: 100 µm. Graph showing the quantification of the markers at day 10 (n = 3) and at day 20 (n = 2) (E). The data are presented as mean ± standard deviation. *p<0,05 by Student's t-test. Orthogonal sections of the epithelial monolayers stained for F-actin and nucleus at day 10 and 20 (F). Actin accumulation at the apical surface indicates proper apical basal polarity. The average cell height was calculated to be 7,7 ± 1,3 µm and 10,3 ± 1,7 µm at day 10 and day 20, respectively (n = 3). Scale bars: 10 µm. Graph showing the TEER profile of the monolayers cultured for 20 days (n=5) (G).*

1.4 Discussion

In vitro intestinal epithelial models are in demand in wide range of applications, including the studies of basic biology of intestinal epithelium, the accurate prediction of the *in vivo* absorption of orally administered drugs, and the development of patient-specific novel therapies. Traditional models based on human colon cancer-derived cell line (Caco-2) [9, 10] are limited in the accurate prediction of transport parameters of drug molecules due to their tight junctions being denser than those of the native small intestine [11, 12, 73], while the use primary human intestinal epithelial cells (hInEpCs) is hindered by the poor viability and short life span of these cells, and the availability of the donors [13]. The discovery of organoids, three-dimensional (3D) intestine-like structures derived from intestinal stem cell (ISC) containing intestinal crypts with self-renewal and self-organization capacities, made possible the long-term propagation of near-physiological intestinal epithelial tissue *in vitro* [15, 16]. Conventionally, organoids are cultured embedded in Matrigel® and cultured with biochemical factors mimicking the *in vivo* ISC niche environment [15, 16]. These 3D structures are comprised of crypt domains with ISCs and proliferative cells and villus domains with terminally differentiated absorptive and secretory cells very much like *in vivo*. Nowadays, organoid technology is considered as the gold standard of *in vitro* culture method in both basic and translational intestinal biology studies [74–76]. The major limitation of the organoid model is their 3D closed geometry that impedes direct access to the apical region of the epithelium, which is in contact with the dietary compounds, external antigens and microbial components present in the lumen. Therefore, the inaccessible organoid lumen limits routine use of organoids in studies of nutrient transportation, drug absorption and delivery, and microbe-epithelium interactions. To overcome this limitation, complicated techniques such as microinjection are required [26]. There is an increased interest in intestinal biology field to obtain intestinal epithelial monolayer cultures to overcome the sterical limitations of the 3D intestinal organoid, while maintaining their self-organization capacities and near-physiological phenotype.

Here we show that employing a thin film of Matrigel® (<20 μm in height) with an apparent stiffness [40] of the underlying hard substrate (tissue culture polystyrene ≈ 3 GPa [48]) it was possible to obtain epithelial monolayer derived from mouse intestinal organoids. Decreasing the bulk stiffness by using a thick layer (≈ 2 mm) of Matrigel® inhibited the formation of the epithelial monolayer

and favored the growth of intestinal organoids. The monolayers contained major intestinal epithelial cell types organized into proliferative crypt-like domains and differentiated villus-like regions. Our live imaging experiments, employing crypts derived from Lgr5-EGFP-ires-CreERT2 mouse demonstrate that intestinal cells first self-organized into ISC containing crypt-like domains from where cells migrate out to form the differentiated monolayer corresponding to the villus-like domain. These results showed that, like in 3D organoid cultures, intestinal crypts grown on 2D, are also capable to self-assemble into crypt-villus domains mirroring the *in vivo* epithelial physiology.

Although organoid-derived epithelial monolayers with crypt-villus domains generated on Matrigel® thin films was recently described [29], these monolayers failed to form effective barriers, likely due to the difficulty in expanding these cells, hampering their use in standard functional assays. Here we show that standard organoid medium supplemented with ISEMF_CM and Wnt3a boosted the intestinal cell growth allowing the generation of a functional and differentiated intestinal monolayer in Transwell® inserts with effective barrier function, as monitored by TEER. The monolayers show physiologically relevant TEER (40-100 $\Omega.cm^2$ for the native small intestine [30, 33, 34]) between day 16 and 20 of culture. The analysis of the cell composition of the monolayer along the culture time show that as time goes by the monolayer becomes less proliferative and more differentiated (also indicated by increasing TEER), while maintaining the ISC (GFP^+) population organized into crypt-like domains. Intestinal monolayers with tissue barrier properties derived from organoids/spheroids reported so far were devoid of such organization [22, 27, 35]. Moreover, they required the use of cell culture medium containing Wnt pathway inhibitors to achieve differentiation [22, 27, 35], as oppose to our epithelial model where the differentiation was achieved with prolonged culture times.

We believe that organoid-derived intestinal epithelial monolayer model we report here offers an up to date culture method and contributes to the current state-of-the art as it combines an *in vitro* intestinal epithelium that has *in vivo*-like crypt-villus organization and physiologically relevant tissue barrier function in a tissue culture format that allows access to both luminal and basolateral compartment. This culture format can be used in better prediction of the *in vivo* absorption of orally administered drugs, dietary compound screening, and studies of microbe-epithelium interactions. The model can be expanded to obtain human

intestinal organoid-derived epithelial monolayers, which can be used in screening for patient-specific novel therapies and in performing clinical testing to determine the efficacy of a particular therapy.

1.5 Conclusions

We have developed a new method to obtain intestinal epithelial monolayers from organoid-derived crypts. We have described the formation of the monolayers on hard substrates. We have characterized the cell-type composition and distribution and found that 2D intestinal epithelial model contained all major epithelial cell types organized into crypt-like and villus-like domains like *in vivo* intestine. We have shown that the use of cell culture media containing ISC niche biochemical factors to boost the proliferative capacity, increased the monolayer growth. We have transferred this culture system to the Transwell® setup and showed that, in a similar fashion, the intestinal cells were organized into crypt-like domains and non-proliferative regions. We have found that asymmetric administration of the ISC niche biochemical factors was also an important consideration to assure the formation of the monolayers. We have demonstrated that with the use of ISEMF_CM together with Wnt3a it was possible to obtain monolayers that mimic the function of epithelial barriers. We have monitored the monolayer tight junction integrity with TEER and shown that the 2D intestinal epithelial model had physiologically relevant TEER values, indicating a good maturation of the epithelial barrier. We have characterized the cell-type distribution and proportions and found that with prolonged culture times the monolayer had become less proliferative and more differentiated, in accordance with the TEER values that were increasing with time. Overall, the 2D intestinal epithelial model reported here faithfully reproduces the small intestine cell composition, cell positioning and physiology. We believe that this new model can complement the existing ones and offer a good alternative to the current 3D models for studies that require an accessible lumen compartment. The knowledge we acquired here on the optimal cell culture conditions and the method of delivery will be used in the following chapters.

References

[1] Nick Barker. "Adult intestinal stem cells: critical drivers of epithelial homeostasis and regeneration". In: (2013).

[2] Hans Clevers. "The intestinal crypt, a prototype stem cell compartment." In: *Cell* 154.2 (2013), pp. 274–84.

[3] Marc Leushacke and Nick Barker. "Ex vivo culture of the intestinal epithelium: Strategies and applications". In: *Gut* 63.8 (2014), pp. 1345–1354.

[4] Toshiro Sato and Hans Clevers. "Growing self-organizing mini-guts from a single intestinal stem cell: mechanism and applications." In: *Science (New York, N.Y.)* 340.6137 (2013), pp. 1190–4.

[5] Martyn D. Kirk et al. "World Health Organization Estimates of the Global and Regional Disease Burden of 22 Foodborne Bacterial, Protozoal, and Viral Diseases, 2010: A Data Synthesis". In: *PLoS Medicine* 12.12 (2015), pp. 1–21.

[6] Naiyana Gujral, Hugh J. Freeman, and Alan B.R. Thomson. "Celiac disease: Prevalence, diagnosis, pathogenesis and treatment". In: *World Journal of Gastroenterology* 18.42 (2012), pp. 6036–6059.

[7] J. Jasper Deuring et al. "The cell biology of the intestinal epithelium and its relation to inflammatory bowel disease". In: *The International Journal of Biochemistry and Cell Biology* 45.4 (2013), pp. 798–806.

[8] Alex Gregorieff et al. "Yap-dependent reprogramming of Lgr5+ stem cells drives intestinal regeneration and cancer". In: *Nature* 526.7575 (2015), pp. 715–718.

[9] I J Hidalgo, T J Raub, and R T Borchardt. "Characterization of the human colon carcinoma cell line (Caco-2) as a model system for intestinal epithelial permeability." In: *Gastroenterology* 96.3 (1989), pp. 736–49.

[10] P. Shah et al. "Role of Caco-2 Cell Monolayers in Prediction of Intestinal Drug Absorption". In: *Biotechnology Progress* 22.1 (2006), pp. 186–198.

[11] Y. Sambuy et al. "The Caco-2 cell line as a model of the intestinal barrier: influence of cell and culture-related factors on Caco-2 cell functional characteristics". In: *Cell Biology and Toxicology* 21.1 (2005), pp. 1–26.

[12] Huadong Sun et al. "The Caco-2 cell monolayer: usefulness and limitations". In: *Expert Opinion on Drug Metabolism and Toxicology* 4.4 (2008), pp. 395–411.

[13] Amanda L. Kauffman et al. "Alternative functional in vitro models of human intestinal epithelia". In: *Frontiers in Pharmacology* 4 (2013), p. 79.

[14] Adam J Ruben and Evolutionary Biology. "Hayflick , his limit , and cellular ageing". In: 1.October (2000), pp. 72–76.

[15] Akifumi Ootani et al. "Sustained in vitro intestinal epithelial culture within a Wnt-dependent stem cell niche." In: *Nature medicine* 15.6 (2009), pp. 701–6.

[16] Toshiro Sato et al. "Single Lgr5 stem cells build crypt-villus structures in vitro without a mesenchymal niche." In: *Nature* 459.7244 (2009), pp. 262–5.

[17] Toshiro Sato et al. "Long-term Expansion of Epithelial Organoids From Human Colon, Adenoma, Adenocarcinoma, and Barrett's Epithelium". In: *Gastroenterology* 141.5 (2011), pp. 1762–1772.

[18] Nick Barker et al. "Identification of stem cells in small intestine and colon by marker gene Lgr5." en. In: *Nature* 449.7165 (2007), pp. 1003–7.

[19] Chris S. Hughes, Lynne M. Postovit, and Gilles A. Lajoie. "Matrigel: A complex protein mixture required for optimal growth of cell culture". In: *PROTEOMICS* 10.9 (2010), pp. 1886–1890.

[20] Hiroyuki Miyoshi and Thaddeus S Stappenbeck. "In vitro expansion and genetic modification of gastrointestinal stem cells in spheroid culture". In: *Nature Protocols* 8.12 (2013), pp. 2471–2482.

[21] Hiroyuki Miyoshi et al. "Wnt5a potentiates TGF-β signaling to promote colonic crypt regeneration after tissue injury." In: *Science (New York, N.Y.)* 338.6103 (2012), pp. 108–13.

[22] Kelli L. VanDussen et al. "Development of an enhanced human gastrointestinal epithelial culture system to facilitate patient-based assays". In: *Gut* 64.6 (2015), pp. 911–920.

[23] Jason R. Spence et al. "Directed differentiation of human pluripotent stem cells into intestinal tissue in vitro". en. In: *Nature* 470.7332 (2010), pp. 105–109.

[24] Maria Helena Macedo et al. "iPSC-Derived Enterocyte-like Cells for Drug Absorption and Metabolism Studies". In: *Trends in Molecular Medicine* 24.8 (2018), pp. 696–708.

[25] Megan Aurora and Jason R. Spence. "hPSC-derived lung and intestinal organoids as models of human fetal tissue". In: *Developmental Biology* 420.2 (2016), pp. 230–238.

[26] S S Wilson et al. "A small intestinal organoid model of non-invasive enteric pathogen-epithelial cell interactions." In: *Mucosal immunology* 8.2 (2015), pp. 352–61.

[27] C. Moon et al. "Development of a primary mouse intestinal epithelial cell monolayer culture system to evaluate factors that modulate IgA transcytosis". In: *Mucosal Immunology* 7.4 (2014), pp. 818–828.

[28] Yuli Wang et al. "Self-renewing Monolayer of Primary Colonic or Rectal Epithelial Cells". In: *Cellular and Molecular Gastroenterology and Hepatology* 4.1 (2017), 165–182.e7.

[29] Curtis A. Thorne et al. "Enteroid Monolayers Reveal an Autonomous WNT and BMP Circuit Controlling Intestinal Epithelial Growth and Organization". In: *Developmental Cell* 44.5 (2018), 624–633.e4.

[30] Balaji Srinivasan et al. "TEER measurement techniques for in vitro barrier model systems." In: *Journal of laboratory automation* 20.2 (2015), pp. 107–26.

[31] Daniel H Elbrecht, Christopher J Long, and James J Hickman. "Transepithelial/endothelial Electrical Resistance (TEER) theory and ap- plications for microfluidic body-on-a-chip devices". In: *J Rare Dis Res Treat* 1.3 (2016), pp. 46–52.

[32] Mathieu Odijk et al. "Measuring direct current trans-epithelial electrical resistance in organ-on-a-chip microsystems". In: *Lab on a Chip* 15.3 (2015), pp. 745–752.

[33] P. Artursson, A. L. Ungell, and J. E. Lofroth. "Selective paracellular permeability in two models of intestinal absorption: cultured monolayers of human intestinal epithelial cells and rat intestinal segments." In: *Pharm. Res.* 10.8 (1993), pp. 1123–1129.

[34] Åsa Sjöberg et al. "Comprehensive study on regional human intestinal permeability and prediction of fraction absorbed of drugs using the Ussing chamber technique". In: *European Journal of Pharmaceutical Sciences* 48.1-2 (2013), pp. 166–180.

[35] Kenji Kozuka et al. "Development and Characterization of a Human and Mouse Intestinal Epithelial Cell Monolayer Platform." In: *Stem cell reports* 9.6 (2017), pp. 1976–1990.

[36] Francisco M. Barriga et al. "Mex3a Marks a Slowly Dividing Subpopulation of Lgr5+ Intestinal Stem Cells". In: *Cell Stem Cell* 20.6 (2016), 801–816.e7.

[37] Vanesa Fernández-Majada et al. "The tumour suppressor CYLD regulates the p53 DNA damage response". In: *Nature Communications* 7 (2016), p. 12508.

[38] Masaomi Koyanagi et al. "Inhibition of the Rho/ROCK Pathway Reduces Apoptosis During Transplantation of Embryonic Stem Cell-Derived Neural Precursors". In: *Journal of neuroscience research* 86 (2008), pp. 270–280.

[39] Xiaolei Yin et al. "Niche-independent high-purity cultures of Lgr5+ intestinal stem cells and their progeny." In: *Nature methods* 11.1 (2014), pp. 106–12.

[40] Cheng-Hwa R Kuo et al. "Complex stiffness gradient substrates for studying mechanotactic cell migration." In: *Advanced materials (Deerfield Beach, Fla.)* 24.45 (2012), pp. 6059–64.

[41] Alex Gregorieff et al. "Expression Pattern of Wnt Signaling Components in the Adult Intestine". In: *Gastroenterology* 129.2 (2005), pp. 626–638.

[42] Henner F. Farin, Johan H. Van Es, and Hans Clevers. "Redundant Sources of Wnt Regulate Intestinal Stem Cells and Promote Formation of Paneth Cells". In: *Gastroenterology* 143.6 (2012), 1518–1529.e7.

[43] Z. Kabiri et al. "Stroma provides an intestinal stem cell niche in the absence of epithelial Wnts". In: *Development* 141.11 (2014), pp. 2206–2215.

[44] Hassan Khalil et al. "Isolation of primary myofibroblasts from mouse and human colon tissue." In: *Journal of visualized experiments : JoVE* 80 (2013).

[45] Adrian Salic and Timothy J Mitchison. "A chemical method for fast and sensitive detection of DNA synthesis in vivo." In: *Proceedings of the National Academy of Sciences of the United States of America* 105.7 (2008), pp. 2415–20.

[46] Ziyad Jabaji et al. "Type I collagen as an extracellular matrix for the in vitro growth of human small intestinal epithelium." In: *PloS one* 9.9 (2014), e107814.

[47] Hynda K. Kleinman et al. "Isolation and Characterization of Type IV Procollagen, Laminin, and Heparan Sulfate Proteoglycan from the EHS Sarcoma". In: *Biochemistry* 21.24 (1982), pp. 6188–6193.

[48] Shengwei Deng et al. "Deformation and fracture of polystyrene polypropylene blends: A simulation study". In: *Polymer* 52.24 (2011), pp. 5681–5694.

[49] Muhammad H Zaman et al. "Migration of tumor cells in 3D matrices is governed by matrix stiffness along with cell-matrix adhesion and proteolysis." In: *Proceedings of the National Academy of Sciences of the United States of America* 103.29 (2006), pp. 10889–94.

[50] T Scholzen and J Gerdes. "The Ki-67 protein: from the known and the unknown." en. In: *Journal of cellular physiology* 182.3 (2000), pp. 311–22.

[51] Elizabeth McNeil, Christopher T Capaldo, and Ian G Macara. "Zonula occludens-1 function in the assembly of tight junctions in Madin-Darby canine kidney epithelial cells." In: *Molecular biology of the cell* 17.4 (2006), pp. 1922–32.

[52] Donald W. Nicholson et al. "Identification and inhibition of the ICE/CED-3 protease necessary for mammalian apoptosis". In: *Nature* 376.6535 (1995), pp. 37–43.

[53] Alastair J.M. Watson and Kevin R. Hughes. "TNF-α-induced intestinal epithelial cell shedding: implications for intestinal barrier function". In: *Annals of the New York Academy of Sciences* 1258.1 (2012), pp. 1–8.

[54] J. M. Blander. "Death in the intestinal epithelium – Basic biology and implications for inflammatory bowel disease". In: 283.14 (2016), pp. 2720–2730.

[55] Tim F. Bullen et al. "Characterization of epithelial cell shedding from human small intestine". In: *Laboratory Investigation* 86.10 (2006), pp. 1052–1063.

[56] S. M. Frisch and R. A. Screaton. "Anoikis mechanisms". In: *Current Opinion in Cell Biology* 13.5 (2001), pp. 555–562.

[57] W. W. Moll, R., Schiller, D. L., Franke. "Identification of protein IT of the intestinal cytoskeleton as a novel type I cytokeratin with unusual properties and expression patterns". In: *The Journal of Cell Biology* 111.2 (1990), pp. 567–580.

[58] Hans Clevers and Roel Nusse. "Wnt/β-catenin signaling and disease". In: *Cell* 149.6 (2012), pp. 1192–1205.

[59] Toshiro Sato et al. "Paneth cells constitute the niche for Lgr5 stem cells in intestinal crypts." In: *Nature* 469.7330 (2011), pp. 415–418.

[60] Nan Ye Lei et al. "Intestinal subepithelial myofibroblasts support the growth of intestinal epithelial stem cells". In: *PLoS ONE* 9.1 (2014).

[61] Kyung-Ah Kim et al. "R-Spondin family members regulate the Wnt pathway by a common mechanism." In: *Molecular biology of the cell* 19.6 (2008), pp. 2588–96.

[62] Nicholas Lahar et al. "Intestinal subepithelial myofibroblasts support in vitro and in vivo growth of human small intestinal epithelium". In: *PLoS ONE* 6.11 (2011), pp. 1–9.

[63] Manolis Roulis and Richard A. Flavell. "Fibroblasts and myofibroblasts of the intestinal lamina propria in physiology and disease". In: *Differentiation* 92.3 (2016), pp. 116–131.

[64] Alexis Desmouliere, Christine Chaponnier, and Giulio Gabbiani. "Tissue repair, contraction, and the myofibroblast". In: *Wound Repair and Regeneration* 13.1 (2005), pp. 7–12.

[65] R. C. Mifflin et al. "Intestinal myofibroblasts: targets for stem cell therapy". In: *American Journal of Physiology-Gastrointestinal and Liver Physiology* 300.5 (2011), G684–G696.

[66] John E Eriksson et al. "Introducing intermediate filaments: from discovery to disease." In: *The Journal of clinical investigation* 119.7 (2009), pp. 1763–71.

[67] La Ongthong Vajrabhaya et al. "The effect of age of refrigerated conditioned medium on cell survivability in vitro". In: *Dental Traumatology* 19.1 (2003), pp. 41–44.

[68] P de Santa Barbara, G R van den Brink, and D J Roberts. "Development and differentiation of the intestinal epithelium." In: *Cellular and molecular life sciences : CMLS* 60.7 (2003), pp. 1322–32.

[69] Magdalena Kasendra et al. “Development of a primary human Small Intestine-on-a-Chip using biopsy-derived organoids”. In: *Scientific Reports* 8.1 (2018), pp. 1–14.

[70] Xia Wang et al. “Cloning and variation of ground state intestinal stem cells”. en. In: *Nature* 522.7555 (2015), pp. 173–178.

[71] Anna Merlos-Suárez et al. “The Intestinal Stem Cell Signature Identifies Colorectal Cancer Stem Cells and Predicts Disease Relapse”. In: *Cell Stem Cell* 8.5 (2011), pp. 511–524.

[72] Andrew Scott et al. “Long-term renewable human intestinal epithelial stem cells as monolayers: A potential for clinical use”. In: *Journal of Pediatric Surgery* 51.6 (2016), pp. 995–1000.

[73] Staffan Tavelin et al. “Prediction of the oral absorption of low-permeability drugs using small intestine-like 2/4/A1 cell monolayers”. In: *Pharmaceutical Research* 20.3 (2003), pp. 397–405.

[74] Sabine Middendorp et al. “Adult Stem Cells in the Small Intestine Are Intrinsically Programmed with Their Location-Specific Function”. In: *STEM CELLS* 32.5 (2014), pp. 1083–1091.

[75] Norman Sachs and Hans Clevers. “Organoid cultures for the analysis of cancer phenotypes”. In: *Current Opinion in Genetics and Development* 24.1 (2014), pp. 68–73.

[76] Johanna F Dekkers et al. “A functional CFTR assay using primary cystic fibrosis intestinal organoids”. In: *Nature Medicine* 19.7 (2013), pp. 939–945.

Chapter 2

Poly(ethylene glycol) diacrylate based 3D villus-like scaffolds for organoid-derived intestinal epithelium

2.1 Introduction

The extracellular matrix (ECM) of tissues is a 3D network consisting of fibrous proteins, proteoglycans and other soluble factors [1]. It contains high amounts of water allowing diffusion of nutrients, oxygen and waste products and provides support for cell adhesion and tissue structure. The biophysical, mechanical and biochemical properties provided by ECM are able to regulate cell behavior [2] (Figure 2.1 A). The combination of composition, proportion and arrangement of the extracellular matrix is different for each specific tissue [3]. The ECM of the small intestinal epithelium, the basement membrane, contains collagens (predominantly type IV), laminins and other structural and adhesive proteins [4] forming a porous structure [5]. The basement membrane forms a continuous support layer along the walls of the crypt-villus units of the intestinal epithelium [6] (Figure 2.1 B) and controls the shape, gene expression, adhesion, migration, proliferation, and apoptosis of the epithelial cells [2, 7]. Therefore, an ideal engineered material for *in vitro* models of intestinal epithelium should reproduce key structural, compositional and mechanical features of this *in vivo* basement membrane.

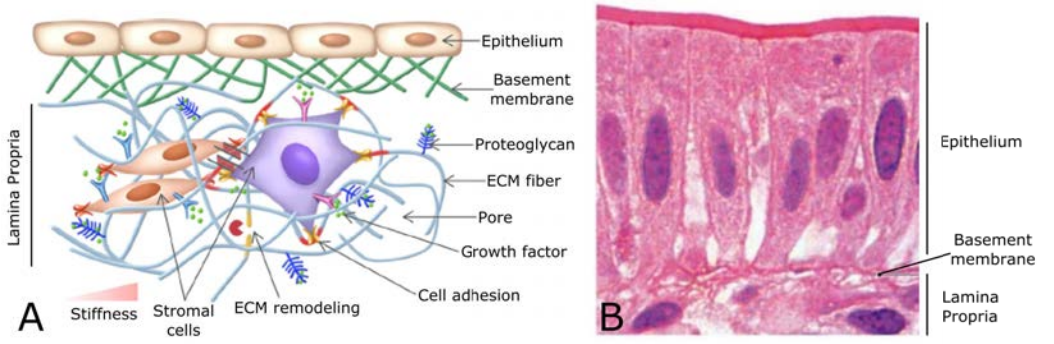

Figure 2.1: *Schematic representation of cues provided by ECM to the intestinal mucosal cells (A). Adapted from Huang et al. [8]. Histological section of intestinal epithelium showing the basement membrane and the underlying lamina propria (B). Adapted from Marieb et al. [9].*

Hydrogels have been widely used as support materials for *in vitro* tissue models due to their resemblance to native ECM of soft tissues [10–12]. Hydrogels are composed of hydrophilic polymers that form 3D networks upon chemical crosslinking or physical interaction of the polymer chains [13]. Hydrogels can imbibe great amounts of water (up to 900% increase in mass) without dissolving but rather increasing in volume, a phenomenon called swelling [14]. Their pore size can vary from couple of nanometers to hundreds of micrometers [15–17]. The pore size controls the mass transport characteristics of the hydrogels, meaning, the diffusion properties of the nutrient molecules and metabolic waste within the network. In addition, due to their high water content the elasticity of the hydrogels (Young's modulus varying from hundreds of Pa to hundreds of kPa) resembles very much that of the soft tissue [14, 17, 18]. For this reason, they are considered as good biomaterial candidates to be used in *in vitro* models of soft tissues [3].

Hydrogels can be made from a variety of materials both from natural and synthetic origins. The natural materials are commonly used in hydrogel fabrication due to their bioactivity and biocompatibility, since they are usually derived from ECM components. Among these, collagen and Matrigel® are the ones that are the most widely used as basement membrane substitutes for the cultures of intestinal epithelial cells [19–25]. Matrigel® is a mixture of ECM proteins, mainly laminin and collagen IV, and growth factors (not very well characterized) secreted by mouse tumor cells [26]. Main limitations of Matrigel® are batch-to-batch variability, immunogenicity due to its animal origin (complicating its approval for human use), difficulty in handling, high cost and poor mechanical properties [3,

14, 27]. Moreover, it is fast biodegradable therefore it is not suitable for long-term cultures. Even though natural-derived hydrogels (e.g. Matrigel® and collagen) are commonly used in intestinal epithelial cell cultures, their mechanical and chemical properties and degradation rates are difficult to tune.

Synthetic polymer-based hydrogels have emerged as a better alternative to their natural counterparts to mimic ECMs since they can be designed in a more precise way. Their exact chemical composition is known explicitly and their chemical and mechanical properties can be tailored to match the tissue-defined functionality [28]. Moreover, they are cost efficient and easy to process [29]. Synthetic hydrogels are used in variety of applications, such as tissue engineering scaffolds, drug delivery devices, and pharmacological formulations [30]. Some examples of synthetic hydrogels are poly(acrylic acid) (PAA), poly(ethylene glycol) (PEG), poly(vinyl alcohol) (PVA), polyacrylamide (PAAm), and polypeptides [31]. However, synthetic hydrogels are usually bioinert and need to be bioactivated with natural based cell adhesion ligands [28, 29].

Among the synthetic polymers used for hydrogels, poly(ethylene glycol) (PEG) is the most extensively utilized material in biomedical applications (Figure 2.2). These include surface modification, drug delivery and tissue engineering applications [3, 29, 32]. This is due to its unique properties, such as high hydrophilicity, biocompatibility, nonimmunogenicity and low protein adhesion [3, 29, 32]. In addition, it has been approved by the US Food and Drug Administration (FDA) for clinical usage due to its nontoxic and nonimmunogenic properties. In clinical applications, it is mainly used as drug delivery carriers and wound dressing material [33, 34]. PEG hydrogels can be fabricated with a wide range of elastic modulus values ($E \approx 3$–1000 kPa [18]) to better mimic the elasticity of soft tissues [35]. PEG molecule has a simple structure with hydroxyl end groups, known as PEG diol, and as it lacks functional sites able to interact directly with cells. The hydroxyl end groups, however, can easily be converted into other functional groups (e.g. acrylates, methacrylates, maleimides, thiols, azides) (Figure 2.2) that can react with each other to form a 3D crosslinked mesh [36–38]. Some of the crosslinking methods for PEG hydrogel formation are click chemistry, free radical polymerization and enzymatic reactions [31, 39, 40]. Moreover, these groups (e.g. acrylates, thiols, azides) can be used for conjugation of biomolecules that provide cell adhesion [31, 32]. Modified PEG compounds can be synthesized in house but also a wide range of PEG derivatives are commercially available.

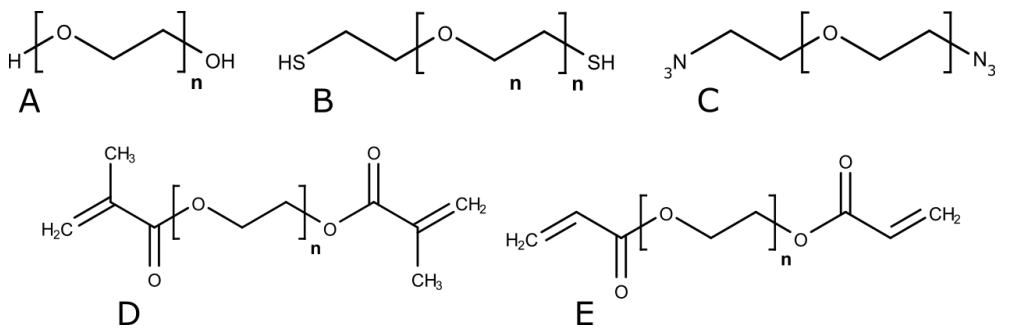

Figure 2.2: *Molecular structures of poly (ethylene glycol) (PEG) (A), poly (ethylene glycol) dithiol (B), polyoxyethylene bis(azide) (C), poly (ethylene glycol) dimethacrylate (D), and poly (ethylene glycol) diacrylate (PEGDA) (E).*

One of the most common variants of PEG molecule is poly(ethylene glycol) diacrylate (PEGDA), which has an acrylate group at each end of the linear chain. Due to the presence of carbon-carbon double bond at each end, PEGDA chains can be crosslinked by UV-initiated free radical polymerization in the presence of a photoinitiator to form covalently cross-linked networks or hydrogels [31] (Figure 2.3). Free radical polymerization is the formation of the polymer chains by the addition of radical building blocks. It is initiated by the UV irradiation of a photoinitiator (PI) molecule present in the prepolymer solution. The PI absorbs the irradiation energy and decomposes to form free radicals with unpaired electrons that attack the carbon-carbon double bonds in acrylate groups forming free radical monomers. The reaction propagates as free radical monomers attack unreacted double bonds and the polymer chain elongates. The reaction terminates when two radical chains react [41].

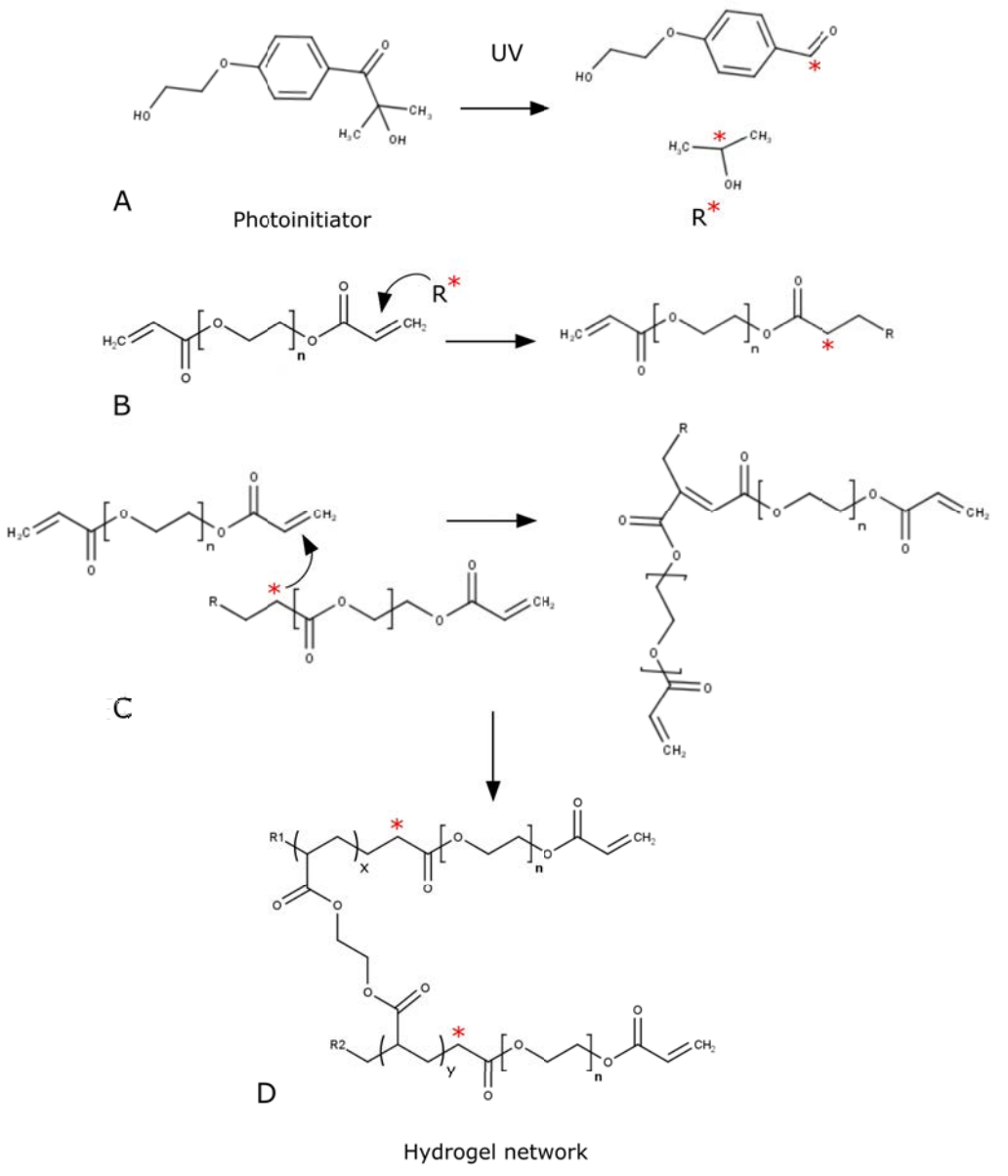

Figure 2.3: *Free radical polymerization of PEGDA by the activation of photoinitiator I2959. The polymerization reaction is initiated by the cleavage of I2959 into radicals (R^*) (A), and the radicalization of the PEGDA chains (B). The reaction propagates as the radical monomers attack new chains of PEGDA (C) to form the hydrogel network (D). Red dots indicate the unpaired electrons, x and y show the poly(acrylate) domains and n the size of the PEG domains. Adapted from Yanez Soto et al. [42].*

In most of the biomedical applications, PEGDA hydrogels are formed using

2-hydroxy-1-[4-(2-hydroxyethoxy) phenyl]-2-methyl-1-propanone, known as Irgacure 2959 or I2959 (Ciba® Irgacure®) as the PI (Figure 2.3). PEGDA hydrogels using I2959 have been used in many applications to fabricate hydrogel tissue substitutes [18, 43, 44]. However, for the polymerization to take place efficiently, the absorbance spectrum of the photoinitiator should overlap with the emission spectrum of the irradiation source. In most of the cases, the emission of the UV light source used is centered at 365 nm. The molar absorptivity of I2959 is limited to wavelengths up to 370 nm with a value of 4 $M^{-1}.cm^{-1}$ at 365 nm [45]. Consequently, the polymerization efficiency can be decreased depending on the light source used and this has to be considered in adjusting hydrogel scaffold fabrication parameters. Free radical polymerization is mainly controlled by the photoinitiator-related characteristics [41, 46]. In addition, the polymerization reaction is inhibited in the presence of molecular oxygen as it scavenges the radicals formed by the PI [47]. By adjusting the oxygen present in the experimental setup and the PI related parameters such as, its concentration and molar absorptivity, polymerization reaction can be controlled. The main advantage of the free radical polymerization is its relatively longer reaction times. Compared to click chemistry reactions that are spontaneous [40], free radical polymerization occurs relatively slow, which allows spatial and temporal control over the hydrogel formation. Moreover, it can take place under mild reaction conditions: in aqueous media at physiological temperature and pH [31, 48].

PEGDA hydrogels can be tailored to obtain materials with varying mechanical and swelling properties. The mechanical and swelling properties of PEGDA hydrogels can be adjusted by varying the molecular weight or the concentration of PEGDA in the prepolymer solution (E varying from couple of kPa up to MPa) [18, 49, 50]. Due to its inert nature PEGDA itself does not support cell culture and it has to be functionalized with biomolecules to promote cell adhesion. Biofunctional PEGDA hydrogels can be obtained by copolymerizing it with acrylated biomolecules, such as peptide monoacrylates or diacrylates, to incorporate cell adhesive peptides or proteins into the PEGDA network [32]. A variety of ECM proteins, e.g. fibronectin, laminin, collagen and elastin or their peptide derivatives can be used for this purpose [32]. Due to its highly tunable nature, PEGDA hydrogels have been extensively used as scaffolds for biomimetic tissue models such as, capillary tubes [51], cornea [42], vascular grafts [44], cartilage [18] and bone [43].

Hydrogels are usually fabricated as films or as bulk pieces. However, the functionality of many epithelial tissues *in vitro* is related to their complex 3D architecture including cysts, folds, invaginations [52]. For instance, the small intestinal epithelium has a characteristic crypt-villus 3D architecture, which is relevant to its physiology. Therefore, it would be desirable to include this 3D architecture in *in vitro* models. In fact, a number of studies have shown that the use of scaffolds mimicking the 3D intestinal architecture modify the barrier function, permeability, gene expression profiles and phenotypes of human colon cancer cell line (Caco-2) epithelial monolayers, approaching better the properties of native intestine [53–56]. Therefore, it is of interest recapturing the key morphological features of the native tissues in the bioengineered models.

Numerous methods have been developed to fabricate hydrogels with finely tuned microarchitectures. These methods are mainly classified as, micromolding, 3D bioprinting, microfluidics and photolithography [57, 58].

Micromolding is based on creating microstructures on soft hydrogels using a hard mold, previously fabricated by photolithography, etching or laser ablation [59]. The most common approach is to produce first an elastomeric mold made of polydimethylsiloxane (PDMS) using the hard molds as templates in a process called soft lithography. Then, the hydrogel precursor solution fills in the PDMS molds and after crosslinking, microstructures that are the negative of that of the molds are patterned on the material. This technique is used to microstructure numerous hydrogel materials [60, 61] including PEGDA [62]. Its main advantages are low cost, short processing times and easy-to-use procedures. However, microstructures can be deformed or even broken at the demolding step, since the hydrogels are soft materials. To overcome this limitation, molds can be coated with anti-sticking layers [63] or sacrificial molds that can be dissolved by water-based solutions are needed [64, 65]. Therefore, making the full fabrication process quite complex. Micromolding technique, in combination with laser ablation and sacrificial molds, was used to produce scaffolds with villus-like geometries for *in vitro* models of intestine [66] (Figure 2.4). These models were used in studies of drug permeability [53] and assessment of therapeutic potential of probiotics [67]. 3D villus-like architecture was shown to improve the correlation between *in vitro* models and native human small intestine [53]. However, these models were tested with intestinal epithelial cell lines. Recently, there has been some efforts in incorporating intestinal cells obtained from intestinal crypts [54] or from organoids [68] into these models to better represent the cellular diversity of the native intestine. The main disadvantage of this fabrication strategy is the need for

several molding and demolding steps (Figure 2.4). Moreover, these procedures require complex equipment.

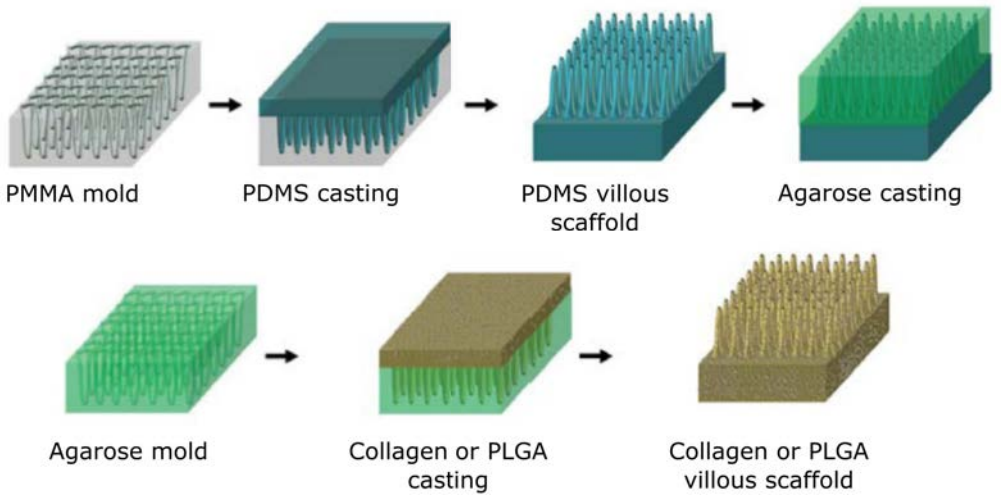

Figure 2.4: *Micromolding strategy developed by March and colleagues to fabricate scaffolds with high aspect ratio villus-like 3D structures from collagen [66] or PLGA [54]. PMMA mold was fabricated by laser ablation and agarose was used as sacrificial mold. Note that several molding and demolding steps were required. Adapted from Costello et al. [54].*

3D printing is a technique for fabricating scaffolds of complex 3D geometries by the precise deposition of biomaterials at the desired locations [69]. This technique also enables printing of the cells that are previously diluted in precursor polymer solutions to produce well defined cell-laden 3D structures [58]. PEGDA-based materials can be printed alone [70] or in combination with other types of biocompatible materials for improved properties [71]. In addition, due to its photocrosslinkable nature, the microstructuring of the PEGDA hydrogel can be done using a technique called digital micromirror device projection printing [72]. Although this strategy is ideal to fabricate complex shapes, it is limited in resolution, and require the use of sacrificial materials for fabricating soft structures [73, 74].

Microfluidics technology aims at the manipulation of fluid flows within micron scale devices that allows the use of small reagent volumes and miniaturization of the fabrication processes. This technology is mainly used for fabricating micron size tissue building blocks and microfibers that can further by assembled into more complex 3D hydrogel structures [58]. The advantage of this system is

that it provides a precise control over the size and the shape of the fabricated microstructures [57]. For instance, microfluidics can be combined with *in situ* photopolymerization to obtain monodispersed PEGDA microbeads [75]. Moreover, microfluidics technology allowed the development of specific devices, called lab on chip devices, with highly controlled microenvironments for the culturing of cells. These devices are designed to incorporate *in vivo* like fluid flows [76–79] and mechanical signaling [78, 79]. Usually, they are also equipped with integrated sensors that permit online monitoring of the tissue function [76, 80–82]. Specifically, *in vitro* gut models developed by this technology have proven to be useful in drug screening and toxicity testing [76, 77, 80], and in the development of co-cultures including microbial flora [78] or immune cells [81] (Figure 2.5 A, B). These gut-on-chip devices were tested with intestinal epithelial cell lines (e.g. Caco-2). However, very recently Kasendra *et al.* incorporated cells obtained from intestinal organoids to better represent gut cell populations [83]. These devices are suitable to be used in high throughput screening of drug molecules or nutrients [77, 80, 81, 83]. However, they have limitations in terms of limited space available for cells to grow and cells being cultured in a monolayer format, similar to 2D cell culture, without a 3D support matrix. Especially in the case of the intestinal epithelium where the 3D morphology of the tissue affects its function [55, 84], use of a mimetic cell support matrix (e.g. microstructured hydrogels) is desired.

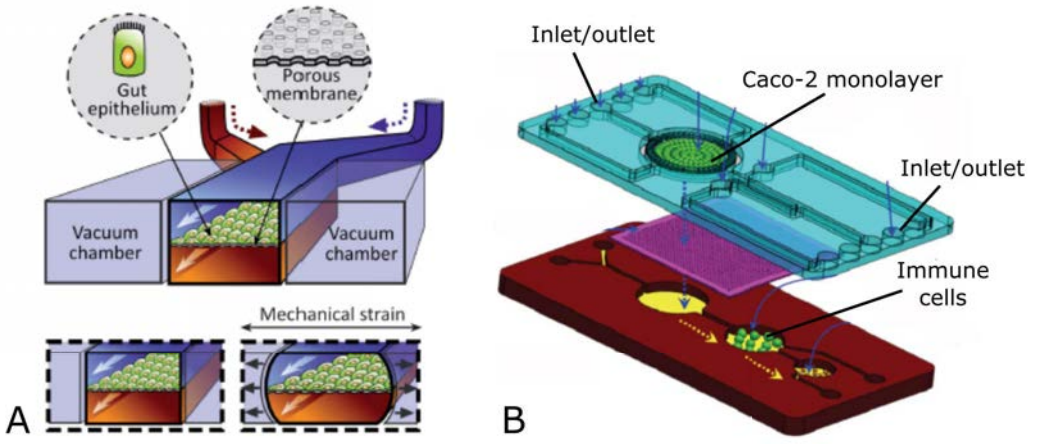

Figure 2.5: *Gut-on-chip model composed of two perfusion channels separated by a Caco-2 monolayer grown on a flexible, porous ECM-coated membrane (A). Vacuum chambers apply cyclic mechanical strain mimicking the peristaltic motion. Adapted from Kim et al. [78]. Another example of a gut-on-chip device that permits the co-culture of epithelial (Caco-2) and immune cells (B). Adapted from Ramadan et al. [81].*

Photolithography is another technique for microstructuring of materials, based on patterning of a precursor using photopolymerization, often by UV light. It can be performed with a digital or a physical photomask. Digital light projection stereolithography and laser-based stereolithography are the techniques that do not require the use of a physical photomask [58]. Stereolithographic methods are based on layer-by-layer irradiation of the material to create precise 3D shapes [85]. This technique is used to fabricate PEGDA hydrogels with controlled 3D structures for tissue engineering applications [86–88]. However, we will focus the review on photomask-based photolithography since it was the methodology adapted here. Photomask-based conventional photolithography method is as follows; first a light-sensitive chemical 'photoresist' is deposited on top of the material to be microstructured. Then, a photomask consisting of light transparent and opaque patterns, is placed on top of the photoresist and it is exposed to UV irradiation. Depending on the type of the photoresist, the illuminated region becomes either crosslinked (negative photoresist) or degraded (positive photoresist) and it is further developed with a solvent to reveal the pattern that will act as a mask. An etching step is then performed to etch the regions of the underlying material non-protected by the mask and finally the photoresist is removed [89] (Figure 2.6 A). The photomasks can be fabricated from glass, metal or high quality acetate sheets (only for microstructures with

micron scale dimensions). Microstructuring of photocrosslinkable hydrogels via photolithography is much more straight forward. The photomask is placed on top of the hydrogel precursor solution and it is exposed to UV. The parts illuminated with UV get polymerized/crosslinked, replicating the negative of the pattern of the photomask (Figure 2.6 B).

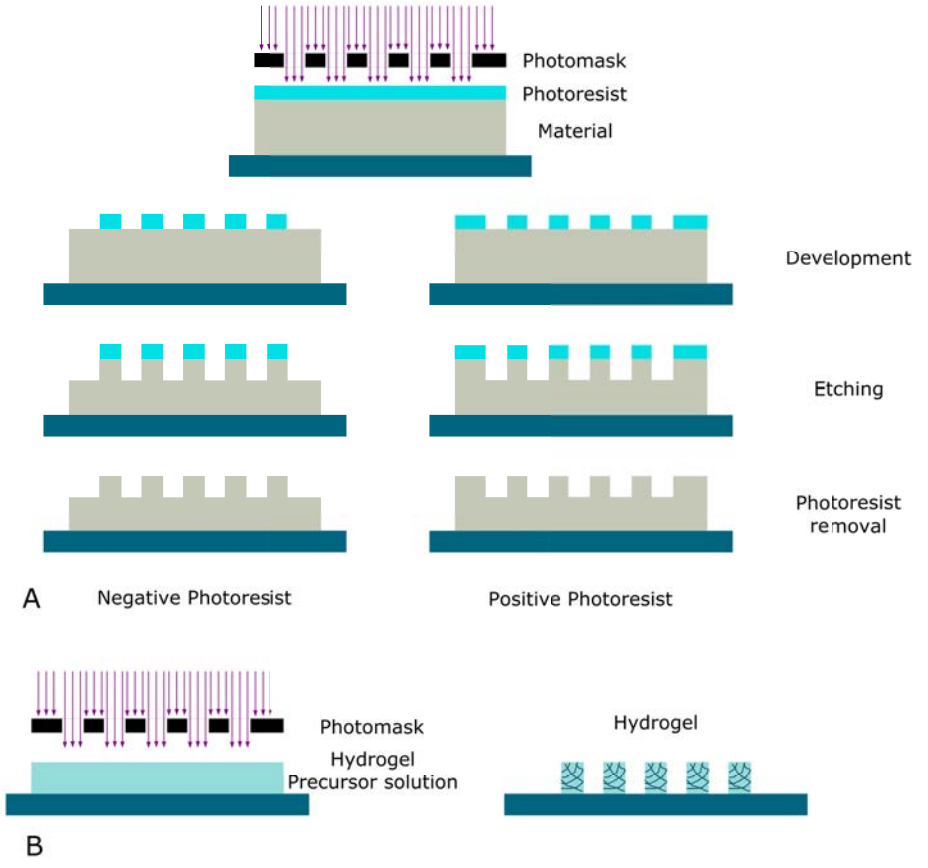

Figure 2.6: *Scheme depicting the conventional photolithography (A). Direct photopolymerization of a hydrogel using a photomask permitting the formation of microstructure patterns (B).*

The simplicity of the photolithography method allows facile fabrication of microstructured hydrogels. For that the hydrogel material has to have photocrosslinkable functional groups. Some of the photocrosslinkable hydrogel materials are: methacrylated hyaluronic acid, gelatin methacrylate, acrylate and methacrylate derivatives of PEG, e.g. PEGDA [90, 91]. Apart from acrylates, there are other functional groups (e.g. thiol-ene reactions) that are photocrosslinkable [92]. Microstructured PEGDA hydrogels have been used in a wide range of applications; some of which are cell and protein encapsulation studies [38, 93],

as tissue engineering scaffolds [42, 94], and platforms for cell guidance and migration [95, 96]. Photolithography is a simple and low-cost technique that can be easily implemented. It has been proven useful in producing simple forms on synthetic hydrogels such as poly(2-phenoxyethyl acrylate) and PEGDA [97–99]. However, creating complex 3D geometries with high aspect ratio and curvature on hydrogels is not straightforward. Shim *et al.* demonstrated the suitability of the photolithography technique for producing complex 3D geometries on hard photocrosslinkable resins that undergo free radical polymerization by establishing controlled oxygen gradients within the polymerization setup [100, 101]. They have defined a parameter, the Damköhler number (Da), the ratio of characteristic oxygen diffusion to oxygen depletion times, which was shown to control the polymerization reaction. It was possible to produce objects with conical shapes when Da ≈ 1, which can be achieved by including a source of oxygen in the polymerization system [100, 101]. Studies in the literature reporting the fabrication of 3D conical geometries on PEGDA were carried out with pure or highly concentrated solutions [98, 100, 102]. Yielding microstructures with hard mechanical properties were used either for microindentation [102] or as molds [98]. In a very recent work from our group, it has been demonstrated that scaffolds with self-standing high aspect ratio conical structures could be formed on soft hydrogels using diluted solutions of PEGDA [103]. These scaffolds were tested with intestinal epithelial cell lines (e.g. Caco-2). However, they have not been tried with a cell model that better represents intestinal cell populations.

The advances in microfabrication techniques allow fabricating physiologically relevant *in vitro* intestinal models that better mimic the native 3D tissue architecture of the intestine [104].

Wang *et al.* demonstrated the utility of photolithography in producing substrates with crypt-like microwell topography on PDMS [105] and collagen membranes [106]. Caco-2 cells grown on these substrates showed lower levels of differentiations marker expression [105] and Transepithelial electrical resistance (TEER) values [106]. These results suggested that crypt-like topography induced crypt-like cellular phenotype and tight junction permeability on Caco-2 cells. Substrates with villus-like architecture have been produced by combining photolithographic and molding techniques and shown to support successful engraftment of Caco-2 cells [54, 56, 66, 107, 108] (Figure 2.7 A, B, C). 3D villus-like collagen scaffolds, fabricated combining laser ablation and sacrificial molding [66] had high aspect ratios (close to 5) and were shown to improve the drug permeability correlation between the Caco-2 cell model and human native small intestine [53]

(Figure 2.7 B). Moreover, 3D architecture was shown to induce the expression of differentiation markers in Caco-2 cells [55]. As an alternative to collagen scaffolds that degrade to almost half of its original size through the course of the cell culture, which is typically 21 days for Caco-2 cells [66], the same group developed porous poly-lactic-glycolic acid (PLGA) scaffolds with 3D villi-like structures using the same fabrication strategy [54, 67] (Figure 2.7 C). The platform supported successful co-cultures of Caco-2 cells with both commensal and pathogenic bacteria [67], and with mucus producing cell line HT29-MTX [54]. As a proof-of-concept this 3D platform was also shown to support the growth of intestinal cells derived from mice crypts [54]. The 3D architecture was shown to induce location differential adhesion for specific types of bacteria [67] and position-specific expression of differentiation markers (more differentiation at the tips than the base) [54] (Figure 2.7 C) proving the significance of implementing *in vivo*-like 3D architecture in *in vitro* models. Altogether, these findings emphasizes the idea that 3D architecture induces changes in the cellular phenotypes better representing *in vivo* situation. However, complex fabrication design to obtain villus-like morphology that require multiple molding and demolding steps and sophisticated equipment [66, 107], hampers the routine implementation of these models. Moreover, immortalized cancer cell line model used in most of these studies does not faithfully represent *in vivo* intestinal cell populations.

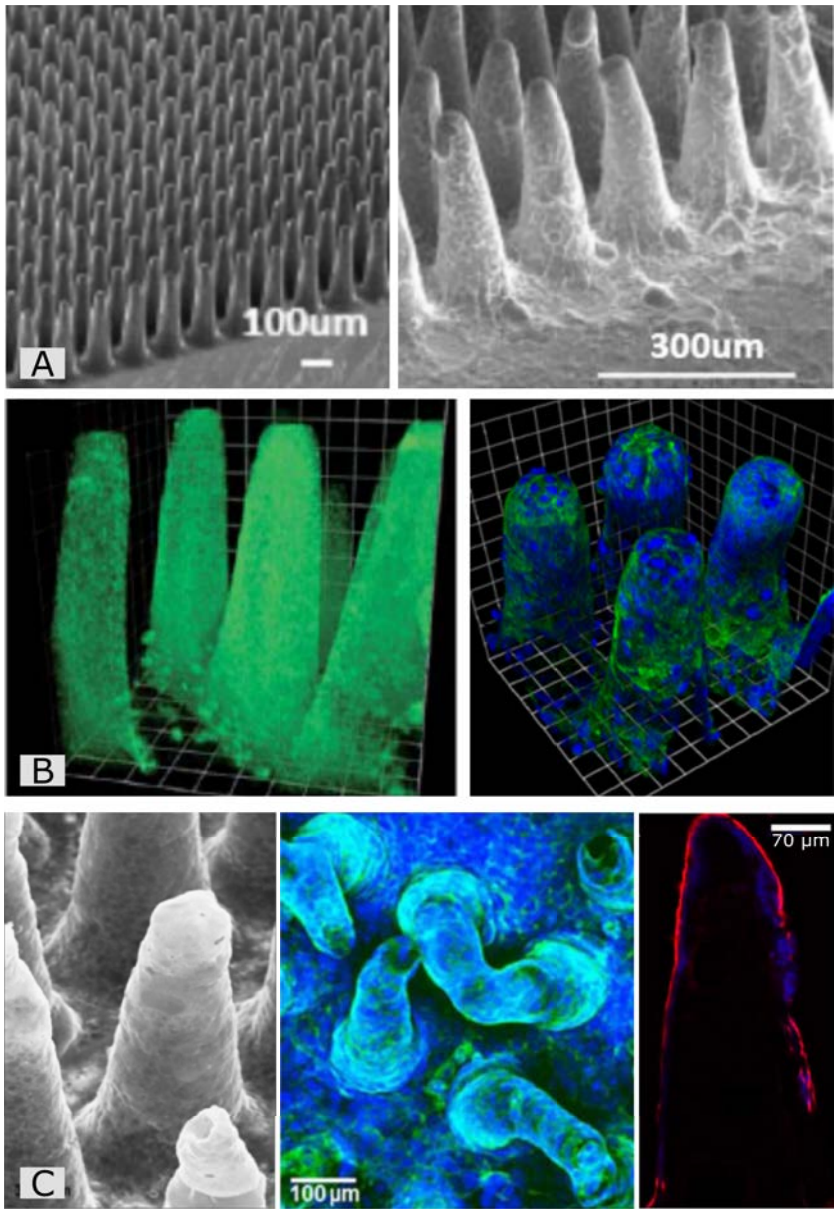

Figure 2.7: *Villus-like architecture reproduced on poly(lactic acid) using photolithography and replica molding (A, left panel), successfully engrafted with Caco-2 cells (A, right panel). Adapted from Yang et al. [107]. Collagen (green) villus-like scaffolds fabricated by combining laser ablation and sacrificial molds (B, left panel). Caco-2 cells cultured on these scaffolds (B, right panel) showed improved drug permeability. Adapted from Sung et al. and Yu et al., respectively [53, 66]. Villus-like porous PLGA scaffolds fabricated with the same strategy (C, left panel), successfully co-cultured with Caco-2 and mucus producing cell line HT29-MTX (C, middle panel). Position-specific expression of mucin (red) (more at the tips than the base) as induced by the 3D architecture (C, right panel). Adapted from Costello et al. [54].*

Self-renewal and self-organization abilities of organoid technology made it possible to culture primary, non-transformed intestinal epithelial cells including all cell types of the epithelium for prolonged periods of time [19, 20]. Conventionally, organoids are grown embedded in Matrigel® [19, 109] or collagen [20, 21] hydrogels. These matrices, which are from natural origin, have complex and variable compositions [26, 110] and their mechanical and biochemical properties can not be modified in a controlled manner. Moreover, since these materials are animal-derived they might raise immunogenic reactions, making them unsuitable for organoid expansion in clinical applications. Synthetic hydrogels are promising alternatives to the natural ones due to their highly tunable, inert nature. Recently, Gjorevski *et al.* reported PEG-based mechanically dynamic hydrogels that supported the growth of organoids embedded in such matrices. Functinalization of the PEG hydrogels with fibronectin protein was sufficient for intestinal stem cells (ISCs) survival and proliferation [111]. For ISC differentiation and organoid formation, cells needed to be embedded in hydrolytically degradable PEG variants functionalized with laminin [111]. This was the first time that a synthetic material was shown to support organoid growth. Although the use of PEG-based synthetic hydrogels overcomes the limitations of the use of animal-derived natural matrices in conventional organoid cultures, the fact that organoids present a 3D closed geometry embedded in the matrix is a major disadvantage. This closed geometry prevents access to the apical region of the epithelium (lumen), making them unsuitable for standard functionality assays that are typically done on monolayers. Complicated techniques such as microinjection are required to deliver the drug molecules to the lumen-like regions [112]. Therefore; it would be ideal culturing the ISCs on synthetic matrices in an opened-up format, forming monolayers.

Very recently, a couple of studies were published reporting microfabricated scaffolds with native-like topographical features that supported the growth of intestinal epithelial cells derived from organoids [113, 114]. Chen *et al.* reported silk-based porous tubular scaffolds with a screw pattern supported the growth of human intestinal cells derived from organoids [113]. Human intestinal subepithelial myofibroblasts (ISEMFs) were seeded inside the tubes and the organoid-derived cells were grown on the ISEMFs. The epithelium was shown to have all major cell types and presented proper microvilli polarization, tight junction formation and digestive enzyme secretion [113]. However, the ridge-like structures (400 μm in size) do not represent well the 3D morphology of the villi. Moreover, the tubular form of these scaffolds are not suitable for conventional *in vitro*

functional assays such as TEER, which requires two distinct compartments separated by the tissue construct. In an alternative approach, collagen scaffolds with crypt-villus architecture were fabricated from PDMS molds [114]. The structures had realistic dimensions and biomimetic round villus tips, and supported the growth of intestinal cells derived from spheroids [114]. The *in vitro* epithelium with an accessible lumen contained all major intestinal cell types. The system was adapted to a custom-made cell culture insert, which permitted the access to both apical and basolateral sides [114]. In addition, the compartmentalization of stem/progenitor cell and differentiated cell zones were achieved by delivering the ISC niche factors from the basolateral side [114]. However, the fabrication of collagen scaffolds with crypt-villus architecture required complicated microfabrication strategies; sequential photolithographic procedures, two step replica molding in PDMS and a final casting of collagen. Moreover, although the degradation of the collagen was slowed down by chemical crosslinking, its mechanical and biochemical properties and porosity can not be modified in a controlled manner. In addition, collagen-based scaffolds are not suitable for the permeability assays of rapidly absorbed hydrophobic drugs [53].

Overall, microfabrication techniques have proven useful in recapitulating the *in vivo* 3D architecture of the intestine for the development of better *in vitro* epithelial models. However, to be of practical use, the fabrication strategy should be easy to implement, and compatible with conventional cell culture and characterization techniques. On the other hand, the use of synthetic materials, such as PEG, allows better control over the material properties as oppose to their natural counterparts.

In this chapter, we describe fabrication of 3D villus-like scaffolds on PEGDA-based hydrogels using a simple photolithographic approach that doesn't require the use of a mold. The mechanical and swelling properties (crosslinking density) of the hydrogels could be adjusted by changing the PEGDA concentration. Bioactive hydrogels were obtained by copolymerizing PEGDA with acrylic acid and further anchoring cell adhesion proteins to the flanking carboxyl groups of the acrylic acid via carbodiimide-mediated amine coupling reaction. Intestinal organoid-derived crypts adhered and grew to cover the surface of the 3D villi-like scaffolds functionalized with collagen. In chapter 1, the beneficial effects of cell culture medium rich in ISC niche biochemical factors derived from ISEMFs were demonstrated. The proliferative capacity and surface coverage of the monolayers grown on 3D villus-like PEGDA scaffolds were also improved with the use of cell culture medium derived from ISEMFs. These results demonstrate that

3D villus-like biomimetic scaffolds fabricated by a simple, moldless photolithographic technique successfully supports the engraftment of intestinal cells derived from organoids, providing cells with a more realistic microenvironment, including proper chemical, mechanical, and topographical signaling.

2.2 Materials and Methods

2.2.1 Fabrication of 3D villus-like PEGDA scaffolds

The hydrogel formation was based on UV-initiated free radical photopolymerization of poly(ethylene glycol) diacrylate (PEGDA). Detailed experimental set-ups for the hydrogel formation and microstructuring are explained in the following subsections.

2.2.1.1 PEGDA hydrogel formation set-up

The hydrogel precursor solution was prepared by dissolving 6000 Da molecular weight PEGDA (P6000) (Sigma) and the photoinitiator, 2-hydroxy-1-[4-(2-hydroxyethoxy) phenyl]-2-methyl-1-propanone (I2959) (Sigma), in phosphate buffered saline (PBS) (Gibco) at pH 7,4. The concentration range of P6000 studied was 5%-10% w/v. I2959 was used at 1% w/v concentration. The solutions were mixed in glass vials (VWR), previously cleaned with 96% ethanol (PanReac Applichem), at 65°C for 1 hour, filtered by a 0,22 μm filter (Merck-Millipore), and used immediately. The solutions were protected from light at all times.

The experimental set-up used for PEGDA polymerization was developed by our group and described elsewhere [46, 103]. Briefly, a chip was designed to facilitate the formation of the hydrogel. For that, first a container of polydimethylsiloxane (PDMS) (Sylgard 184 Silicon Elastomer, Dow Corning) was made. The PDMS prepolymer was mixed with the curing agent in 10:1 w/w ratio and degassed under vacuum for at least 1 h. Then, it was casted to 4 well culture dishes (ThermoFisher Scientific) and the weight of prepolymer added was adjusted to obtain a PDMS slab 1 mm thick (≈ 2,5 g/well). The PDMS prepolymer was cured overnight at RT and for at least 1 h at 65°C. A pool of 10 mm in diameter was made with the help of a 10 mm punch (Acuderm) and two inlets were cut out by a 1,5 mm punch (Harris Uni-Core, GE Healthcare Life Sciences) to facilitate the introduction of the hydrogel precursor solution. To be able to recover and further manipulate the hydrogels, a glass coverslip of 12 mm in diameter (VWR) was used. The chip was assembled by placing the PDMS container on top of a plastic microscope slide (ThermoFisher Scientific), covering the pool area with the glass coverslip, and introducing the hydrogel precursor solution to the pool. All the pieces were washed with 96% v/v ethanol prior to use. A detailed scheme of the PDMS chip and the experimental set-up is depicted in figure 2.8.

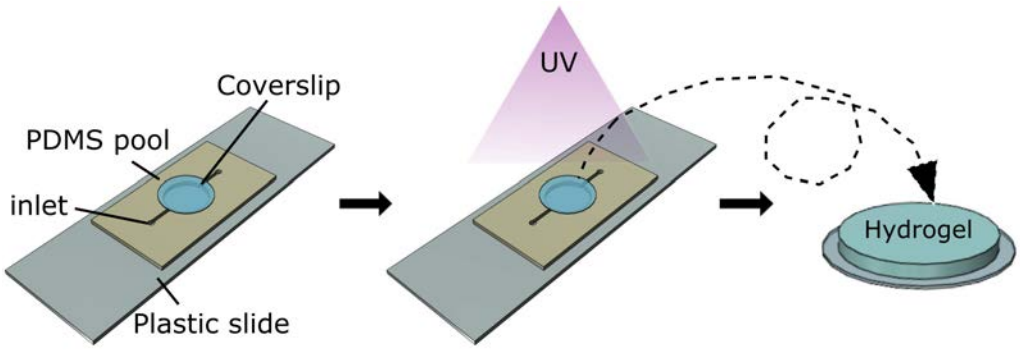

Figure 2.8: *Detailed scheme of the PDMS chip and the fabrication procedure. The PDMS pool is filled with the hydrogel precursor solution through the inlets and the chip is exposed to UV light. The disc shaped hydrogel is recovered on the coverslip.*

Even though the hydrogels were sticking to the glass coverslips initially, after prolonged incubation periods in liquid, they were lifting off of the substrate. In order to overcome this problem, the glass coverslips were silanized with 3-(Trimethoxysilyl)propyl methacrylate (Sigma), prior to use. Silanization is a method to coat the surface of a material (usually glass or silicon oxides) with a thin layer of self-assembling functional alkoxysilane molecules [115]. This particular silane was chosen because it has a vinyl functional group at its flanking end, which forms a covalent bond with the PEGDA chains upon UV initiated free radical polymerization. This assures the covalent attachment of the hyrogel to the glass coverslip surface. First, the coverslips were cleaned by sonicating 5 minutes in acetone and 5 minutes in 2-propanol (Isopropanol) and dried under nitrogen air flow. Then, they were placed into a glass petri dish making sure that they were flat and uncovered, and surface activated by exposing to UV for 15 minutes by a UV cleaner equipment (UV/ozone ProCleaner, Bioforce Nanoscience). In the meanwhile, the silane solution was prepared by diluting 2% v/v 3-(Trimethoxysilyl)propyl methacrylate and 3% v/v dilute acetic acid (10:1 glacial acetic acid:water) in absolute ethanol. The acetic acid was added just before use. Right after the UV activation of the surface, the silane solution was added onto the coverslips and incubated for one to two hours at RT. Then, the coverslips were washed thoroughly with 96% v/v ethanol to remove residual reagents, dried under nitrogen air flow and stored under vacuum until further use. All the solvents were purchased from Panreac Applichem unless stated otherwise.

For the crosslinking of the PEGDA hydrogel, a Mask aligner instrument (SUSS

MicroTec MJB4) equipped with a mercury short arc lamp (OSR HBO 350 W/S) present at the IBEC MicroFabSpace, was used. The UV intensity used was 25 $mW.cm^{-2}$. A plastic petri dish bottom (Fisher scientific) was used as a support to make sure that the samples were always at the same distance with respect to the UV light source. The plastic support (petri dish bottom) was covered with an opaque adhesive tape (Aironfix) to avoid the reflected light interfere with the reaction. Varying UV exposure times were used depending on the conditions and given in the corresponding experimental sections. After the UV exposure, the hydrogels recovered on coverslips (Figure 2.8) were washed thoroughly with PBS to remove all unreacted PEGDA chains and photoinitiator. Then, they were placed into a 24-well plate (ThermoFisher Scientific) and swollen in PBS to constant weight (see Section 2.2.4 for swelling studies) during which the PBS was a changed couple of times to ensure the removal of any unreacted species.

2.2.1.2 Microstructuring of PEGDA hydrogel scaffolds

In order to obtain 3D villus-like forms, a photomask was used during the photopolymerization of the hydrogels. The photomask design was consisted of a 0,8 x 0,8 mm^2 array of circular transparent regions with a diameter and a pitch of 100 μm, which had a density of 25 transparent $windows.mm^{-2}$. These values were selected to better mimic the anatomical dimensions of the human villi (diameter $\approx$ 125 μm) at the density (20-40 $villi.mm^{-2}$) that they are found in native intestine [116, 117]. The photomasks were designed in AutoCAD software (Autodesk) and printed on acetate films (CAD/Art Services).

The 3D villus-like structures were formed by a two step UV exposure. In an initial approach, first exposure was performed without the photomask to form a thin film of hydrogel that we called the base, and the second exposure was performed with the photomask that allowed the formation of the microstructures that we called pillars [46]. However, with this strategy partial gelling of the material at the unexposed regions was observed. As an improvement, the method was slightly changed. First, the hydrogel precursor solution was exposed to form the pillars followed by a washing step both with PBS and the hydrogel precursor solution. Then, it was exposed again, without the photomask, to form the base holding pillars together. This step was needed to create a homogeneous hydrogel surface. Microstructures of varying dimensions were fabricated by using exposure times ranging from 70 s to 170 s for pillar formation and either 10 s or 15 s

for base formation. A simplified scheme of the optimized fabrication protocol for microstructuring of PEGDA is given in figure 2.9.

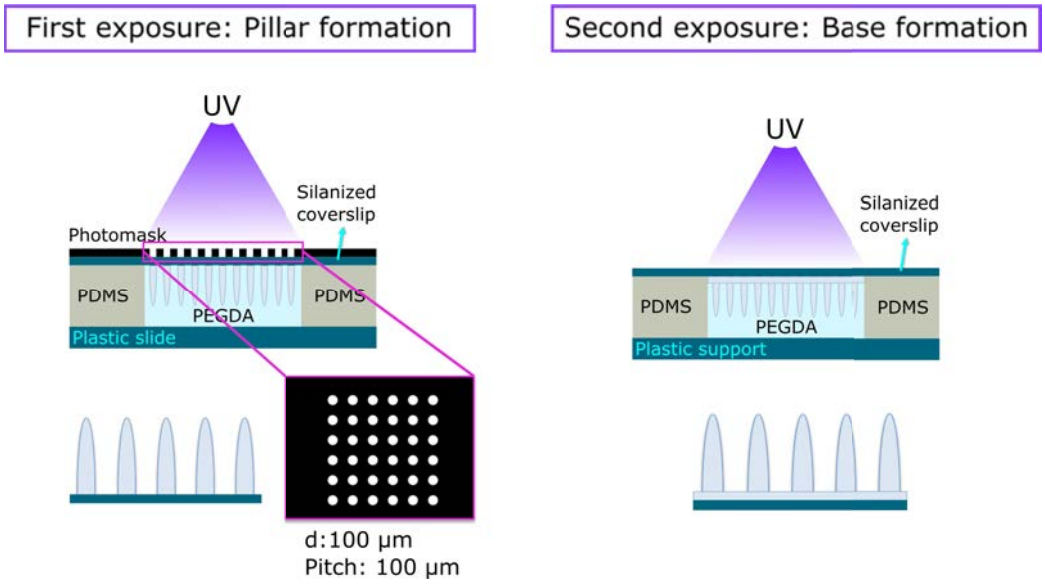

Figure 2.9: *Simplified scheme of the optimized fabrication protocol of the 3D villus-like PEGDA scaffolds. In the first exposure, the pillars are formed using a photomask consisting of an array of circular transparent windows with a diameter and a pitch of 100 µm. In the second exposure, the photomask is removed and the base is formed at the size of the diameter of the PDMS pool. This step is needed to create a homogeneous hydrogel surface.*

2.2.1.3 Copolymerization of PEGDA and acrylic acid

Although PEGDA hydrogel is a good candidate as a scaffold because of its high water uptake capacity and soft tissue like elasticity, due to its bioinert nature PEGDA alone cannot support cell adhesion and growth [31]. Therefore, its functionalization with bioactive species is essential for cell culture applications. However, in the PEGDA backbone there are no functional groups that would permit the addition of peptides and proteins to the structure. For that reason, acrylic acid was added to the hydrogel precursor solution and allowed to copolymerize with PEGDA. Acrylic acid (AA) is a molecule that has a vinyl and a carboxylic group. When copolymerized with PEGDA, it gets incorporated into the structure due to the presence of its vinyl group (Figure 2.10). The flanking carboxylic groups can then be further functionalized by a carbodiimide-mediated amine coupling [118] (Figure 2.10).

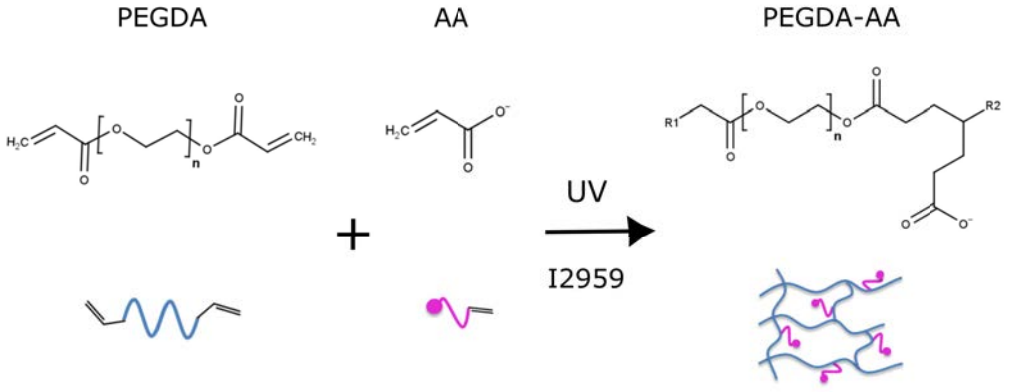

Figure 2.10: *Scheme showing the copolymerization reaction of acrylic acid (AA) and PEGDA. Vinyl groups (carbon-carbon double bonds) take part in the UV initiated free radical polymerization in the presence of the photoinitiator, I2959. The resulting PEGDA-AA hydrogel has flanking carboxylic groups that can further be biofunctionalized by a carbodiimide-mediated amine coupling [118].*

The incorporation of acrylic acid into the PEGDA backbone was well characterized in a previous study reported by our group [46, 103]. The hydrogel precursor solutions were prepared as explained in Section 2.2.1.1, acrylic acid was added to the solutions and they were mixed for 1 h at 65°C. The solution were filtered by a 0,22 μm filter, and used immediately. The solutions were protected from light at all times. The acrylic acid concentrations used in this study were 0,06% w/v (8,3 mM) and 0,3% w/v (41,6 mM). A wider range of acrylic acid concentrations (0% to 2,4% w/v) and the effects of their incorporation into the PEGDA backbone, microstructure morphology, material elasticity, swelling properties, and functionalization has been well described in a previous study carried out in our laboratory [46, 103].

2.2.2 Morphological assessment of 3D villus-like hydrogel scaffolds

After the scaffolds were fabricated, they were kept in PBS until equilibrium swelling (see Section 2.2.4 for the detailed protocol). After swelling they were visualized by optical microscopy or scanning electron microscopy (SEM) to assess their morphology and calculate the dimensions of the pillars.

2.2.2.1 Optical microscopy

The samples at equilibrium swelling were visualized either by a stereo microscope (Leica MZ10) or a bright field microscope (Nikon Eclipse Ts2). The pillars were cut out of the scaffolds with the help of a surgical blade (Didactic) or a 27 G 3/4 " needle (BD Microlance 3), and tilted horizontally to be able to visualize the cross-sections. The samples were kept submerged in PBS at all times. The images were analyzed with ImageJ free software (http://rsb.info.nih.gov/ij, National Institutes of Health) and the heights of the pillars were measured as the distance between the base and the tip of the pillars. At least three samples were analyzed for each condition ($n \geq 3$).

2.2.2.2 Scanning electron microscopy

Alternatively, SEM was also used to assess the morphology and calculate the heights of the pillars. SEM samples have to be dehydrated, since, this technique works under vacuum, and water molecules disturb the vacuum and with it the imaging. Air drying destroys the morphology of the samples as water has a high surface tension to air. Therefore, to dry the samples, first, they were washed thoroughly with MilliQ water to remove the salts, and then, the water was removed by immersing them sequentially in graded ethanol solutions diluted in MilliQ water. The steps were: 50% v/v 1 wash, 70% v/v 2 wash, 90% v/v 3 wash, 96% v/v 3 wash, and 100% 3 wash, each washing step being 10 minutes of incubation in the ethanol solution indicated. The samples were then, placed into a critical point dryer equipment (K850, Quorum technologies), sealed and cooled. Critical point drying is based on the complete replacement of ethanol with liquid CO_2 and then heating the CO_2 (35°C) at high pressure ($\approx$ 83 bar) to liquid-gas phase equilibrium where all the liquid phase eventually disappears. The dried samples were imaged by ultra high-resolution scanning electron microscopy (Nova^{TM} NanoSEM 230, FEI Company) under low vacuum conditions (< 2 mbar). No conductive coating was necessary for the imaging of the PEGDA-AA samples. Two samples were analyzed for the hydrogels fabricated with 5% w/v P6000, 0,06% w/v (8,3 mM) AA, and at least three images were taken at randomly selected regions. The sample holder was tilted by an angle (α) of 66° during image acquisition to be able to visualize the 3D structures of the pillars. The images were analyzed with ImageJ free software and the heights of the pillars were calculated correcting for the tilt angle (α = 66°) (Eqn. 2.1).

$$h_{real} = h_{measured}/cos(\alpha) \tag{2.1}$$

2.2.3 Characterization of the mechanical properties of the PEGDA-AA hydrogels

Mechanical properties of the hydrogels were analyzed by a compression test. The gels were casted as discs, 10 mm in diameter and $\approx$ 1 mm in height, and swollen to constant weight. The concentrations characterized were: 5%, 7,5%, and 10% w/v P6000 prepared in PBS with 1% w/v I2959 and 0,06% w/v (8,3 mM) AA. The UV exposure time used for the fabrication of the hydrogels was 200 s. After swelling, the hyrogels with increased diameters were punched with a 10 mm punch to make sure that all the samples had the same diameter. Stress-strain curves were obtained in compression mode with a dynamic mechanical analyzer equipment (Q800 Dynamic Mechanical Analyzer, TA Instruments). The samples of 1 mm height and 10 mm diameter were placed in between the compression clamps (Figure 2.11 A, B) and deformed by applying a constant strain rate of 1,20%.min^{-1} under unconfined compression up to a maximum strain of 10%, in agreement with similar works reported in the literature [119, 120]. A small preload of 100 mN was used to promote an adequate contact between the hydrogels and the apparatus. At the initial testings, the same samples were measured twice to make sure that no permanent deformation was being caused by the 10% maximum strain. Certain parameters, such as the cross-sectional area, A, of the hydrogels and the Poisson ratio had to be introduced to the operational software of the equipment (TA Instruments) to determine the compression modulus. The Poisson ratio was selected to be 0,5, in accordance with previously published reports [14, 121, 122]. The stress, σ, was calculated by the normal force applied, F, divided by A; and the strain, ϵ, as the ratio of the change in the hydrogel height to the original height, all of which was automatically calculated by the software from the empirical data recorded by the apparatus. Then, the stress-strain curves were plotted and from the slope of the linear part of the curves, where samples showed elastic behavior, Young's modulus (E) was calculated (Figure 2.11 C). At least three different samples were analyzed for each condition. The data were plotted as mean $\pm$ standard deviation with OriginPro 8.5 software. The statistical comparison was performed using two tailed, unequal variances Student's t-test and $p<0,05$ was considered significant.

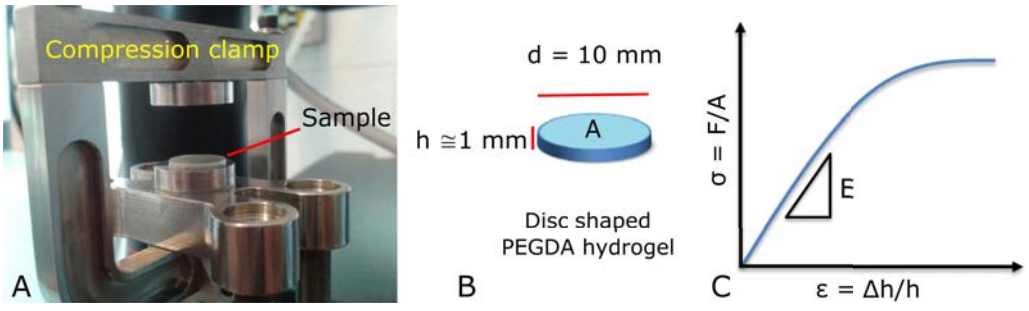

Figure 2.11: *Image showing the compression clamp of the Q800 Dynamic Mechanical Analyzer equipment and a disc-shaped hydrogel sample placed at the center of the compression plates (A). Drawing showing the dimensions of the disc-shaped hydrogel samples used in the compression tests (B). Typical stress-strain curve, where stress and strain are defined by σ and ϵ, respectively (C). The Young's modulus (E) is determined from the slope of the linear part of the curve, where the samples show elastic behavior.*

2.2.4 Characterization of the swelling properties of the PEGDA-AA hydrogels

The swelling behavior of the PEGDA-AA hydrogels was characterized as an indicator of their degree of crosslinking and also to determine the time of equilibrium swelling, the point after which the hydrogels do not imbibe more water. Determining the time of equilibrium swelling was important in designing the experiments following the hydrogel fabrication since during swelling, the properties of the material were changing. For example, their dimensions and mechanical properties vary. All the experiments, including morphological assessments, functionalization, mechanical characterization, and cell culture were done after letting the hydrogels swell to constant weight in PBS.

The hydrogels were casted as discs, 10 mm in diameter and $\approx$ 1 mm in height, at 5%, and 10% w/v P6000 concentrations in PBS with 1% w/v I2959 and 0,06% w/v (8,3 mM) AA. Hydrogels were fabricated either by 150 s or 200 s of UV exposure. The polymer concentrations were chosen to mark the lower and the upper limits of the working range. The equilibrium volume swelling ratios (Q) were calculated from the weights measured at three different time points i.e. after fabrication, at equilibrium swelling and at dry state, following well established protocols [14, 30, 123, 124]. The PEGDA-AA hydrogels were weighed right after fabrication (also called after curing), and the value was referred as m_c. Then, the hydrogels were swollen in a petri dish submerged in PBS and weighed at different time points: 15 min, 30 min, 1 h, 2 h, 1 day, 2 day, 3 day, and 4 day, 5 day and

7 day after fabrication. The weight of the hydrogel was increasing until a certain point after which it was maintaining constant. This is the weight at equilibrium swelling and it was referred as m_s. In order to avoid contamination, after each measurement the petri dish was changed and fresh, filtered PBS was added, and the swelling was performed at 4°C. Otherwise, the hydrogels were getting contaminated by microorganisms. The time required to reach the constant weight was also noted and it was ensured that in the following experiments, the gels were swollen sufficiently before further use. After swelling, the gels were dried overnight at RT and the next day in the oven at 65°C to constant weight to make sure that all the remaining water was eliminated. The weight of the hydrogel at dry state was referred as m_d. Once these values were obtained, weight fractions of the hydrogels after fabrication (q_F) and at equilibrium swelling (q_W) were calculated by the following equations 2.2 and 2.3, respectively.

$$q_{\mathrm{F}} = \frac{m_{\mathrm{c}}}{m_{\mathrm{d}}} \tag{2.2}$$

$$q_{\mathrm{W}} = \frac{m_{\mathrm{s}}}{m_{\mathrm{d}}} \tag{2.3}$$

Then, the polymer volume fraction of the hydrogel in swollen state ($V_{2,s}$) and the volume fraction in the relaxed state ($V_{2,r}$) were calculated by the following equations 2.4 and 2.5, respectively.

$$V_{2,s} = [1 + \frac{(q_W - 1) * \rho_p}{\rho_{swel}}]^{-1} \tag{2.4}$$

$$V_{2,r} = [1 + \frac{(q_F - 1) * \rho_p}{\rho_{sol}}]^{-1} \tag{2.5}$$

where ρ_p is the density the PEG (1,12 g.cm^{-3}) [14, 125], ρ_{swel} is the density of swelling agent used and ρ_{sol} is the density of the solvent used in the fabrication of hydrogel. In our set-up, both the swelling agent and the solvent were PBS and its density was taken as 1,01 g.cm^{-3} (calculated from the product datasheet). With the previous data, the volume swelling ratio (Q) of the hydrogels was calculated by the following equation 2.6.

$$Q = \frac{V_{2,r}}{V_{2,s}} \tag{2.6}$$

These calculations were based on previously published reports [14, 124, 126]. Four different samples were analyzed for each condition. The data were

plotted as mean ± standard deviation with OriginPro 8.5 software. Calculations of weight and volume fractions and volume swelling ratios were done with MATLAB R2015a software. The statistical comparison was performed using two tailed, unequal variances Student's t-test and p<0,05 was considered significant.

Hydrogel network parameters, such as, molecular weight between crosslinks (Mc), and the mesh size (ξ), were also estimated using volume swelling ratios. Detailed methods and the results are presented in the following chapter 3, as we consider these data to be more relevant in the context of chapter 3.

2.2.4.1 Determination of the gel fraction of the PEGDA-AA hydrogels

In order to determine the percentage of the PEGDA chains reacted to form the hydrogel, gel fraction values were determined following previously published protocols [14, 127]. For that, disc shaped hydrogels with a diameter of 10 mm and a thickness of $\approx$ 1 mm were fabricated. After manufacturing the hydrogels, they were dried overnight at RT and the next day in the oven at 65°C to constant weight to make sure that all the remaining water was eliminated. This constant weight obtained in this step is known as M. In this step, all the unreacted species and reaction residues were contributing to the dry weight of the hydrogel since they weren't swollen in an aqueous solution allowing the unreacted components to diffuse out. Then, the hydrogels were submerged into MilliQ water and were washed several times by refreshing the MilliQ water at various time points (1 h, 2 h, 3 h, 4 h, 5 h, 1 day, 2 days, 3 days and 4 days) until the time of equilibrium swelling was reached. Then, the gels were dried to constant weight as explained above. The constant weight obtained in this second step is called M'. Once the weights of the hydrogels before and after removing all the unreacted components were obtained, the percentage of gel fractions were calculated by the formula given in equation 2.7.

$$Gel\ fraction = \frac{M'}{M} * 100 \tag{2.7}$$

PEGDA solutions prepared in MilliQ at 5%, and 10% w/v P6000 with 1% w/v I2959 and 0,06% w/v (8,3 mM) AA were used, and the UV exposure times tested were 150 s and 200 s. MilliQ water was used to avoid the salt crystals adding up to the polymer mass. Four different samples were analyzed for each condition. The data were plotted as mean ± standard deviation with OriginPro 8.5 software. The statistical comparison was performed using two tailed, unequal variances Student's t-test and p<0,05 was considered significant.

2.2.5 Protein functionalization of the PEGDA-AA hydrogels

In order to render the scaffolds bioactive, ECM proteins were coupled to the PEGDA-AA hydrogels taking the advantage of the exposed carboxylic groups, by using N-(3-Dimethylaminopropyl)-N′ -ethylcarbodiimide (EDC) (Sigma) and N-Hydroxysuccinimide (NHS) (Sigma) as activators [118]. Carbodiimide-mediated protein coupling is a method commonly used in conjugating proteins to hydrogels for their functionalization [128–130]. The reaction is depicted in the figure 2.12.

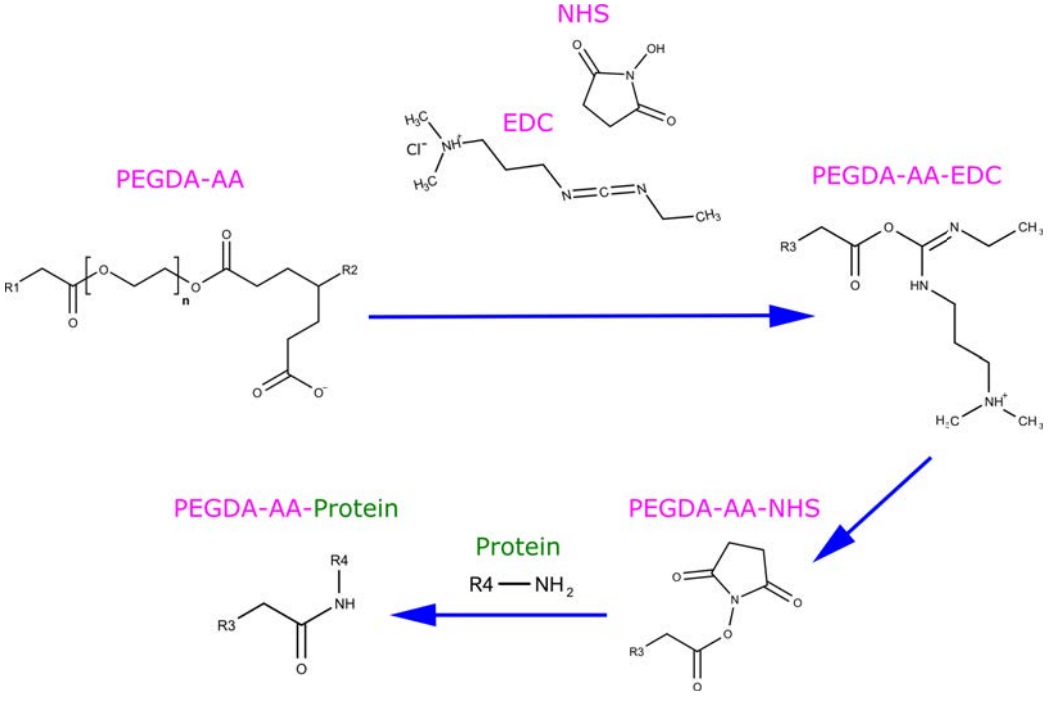

Figure 2.12: *Scheme showing the EDC/NHS mediated protein coupling to the PEGDA-AA hydrogels. First, the carboxyl groups of the hydrogel are activated with EDC, which is displaced by NHS forming a semi-stable NHS-ester. Subsequently, it is replaced by a primary amine (protein) forming a covalent bond (amide bond) between the PEGDA-AA hydrogel and the protein.*

Briefly, the hydrogels were swollen in PBS to the equilibrium swelling, during which the PBS was changed couple of times to make sure that all the non-reacted species were removed. EDC and NHS were dissolved in 2-(N-morpholino)ethanesulfonic acid (MES) buffer (0,1 M, pH 4,7) (ThermoFisher Scientific) at 25 mM and 50 mM, respectively. The hydrogels were submerged in EDC/NHS solutions and incubated for 30 min shaking at RT. After that, the hydrogels were washed three times with PBS and incubated with the protein

solution prepared in PBS. Several proteins or protein mixtures, e.g. Matrigel® were tested. To validate the successful incorporation of the proteins to the structure, Streptavidin Texas Red® (SA_TxRED) (Life Technologies) was used. As controls, samples that were not activated by EDC/NHS and hydrogels formed by P6000 homopolymer (without AA) were also incubated with SA_TxRED. For cell culture experiments, laminin (Sigma), Matrigel® (BD Biosciences), and collagen type I (Sigma) were used to functionalize the PEGDA-AA hydrogels. Matrigel® and collagen type I were used 10% diluted and laminin and SA_TxRED were used at 100 $\mu g.mL^{-1}$ and 50 $\mu g.mL^{-1}$ concentrations, respectively. For streptavidin functionalization, 1-2 hours of incubation at RT was enough. The scaffolds prepared for cell culture experiments were incubated with the protein solutions overnight at 4°C in order to avoid possible gelling of Matrigel® and collagen, which happens at RT and the incubation time was increased to maximize coupling efficiency. After that, the scaffolds were washed with PBS and kept in 10% v/v Penicillin/streptomycin until further use. To confirm the efficiency of the functionalization, immunostaining for collagen and laminin (major component of Matrigel®) was performed. The immunostaining protocol is given in the following section 2.2.7. As a comparison, direct physical adsorption of a Matrigel® drop to the 3D villus-like scaffold surfaces, another strategy reported [54], was also tested. A 10 μL drop of Matrigel® was added onto the scaffolds and they were briefly (<1 minute) centrifuged at 700 rpm. Then, they were incubated at 37°C for at least 15 minutes. This process was repeated 1-2 times to increase the amount of the Matrigel® layer deposited on top of the hydrogel. The protocol followed to visualize the deposited Matrigel® layer, is explained in the section 2.2.7.

2.2.6 Intestinal organoid-derived crypt seeding onto 3D villus-like PEGDA-AA scaffolds

Organoid-derived crypt suspension was prepared as explained in chapter 1 section 1.2.2. The total crypt number in the suspension was estimated by counting the number of crypts in a sample volume (see Chapter 1 Section 1.2.3.2 for details). After fabrication, PEGDA-AA hydrogels were swollen to equilibrium weight and functionalized with cell adhesion proteins as explained in Section 2.2.5. Later, the hydrogels were sterilized by storing them in 10% v/v penicillin/streptomycin in

PBS until use. UV sterilization was not suitable as it could damage the cell adhesion proteins. Before use, the scaffolds were transferred to a new sterile 24 well-plate (ThermoFisher Scientific). Two cell culture media were used to grow the intestinal epithelial cells on PEGDA-AA hydrogel scaffolds: 1) ENR_CV medium, and 2) ISEMF_CM supplemented with ENR_CV (see Chapter 1 Sections 1.2.2 and 1.2.4.1).

2.2.6.1 Cell seeding strategies

Two strategies were explored for the seeding of the PEGDA-AA hydrogel scaffolds: 1) with a drop of crypt suspension (Figure 2.13 A), and 2) using a pipette tip bottom as a container (Figure 2.13 B, C).

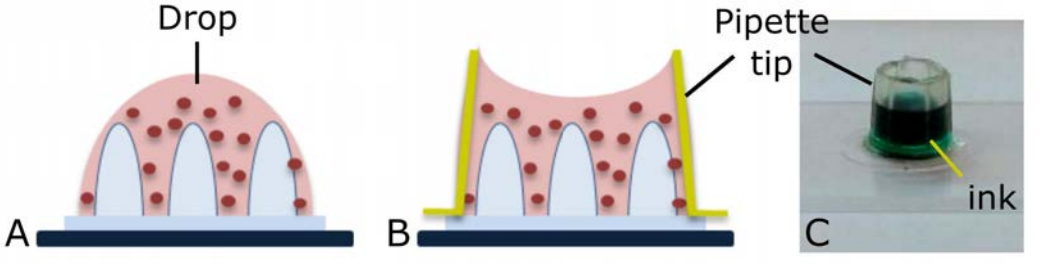

Figure 2.13: *Scheme showing the seeding of the hydrogel scaffolds with a drop of organoid-derived crypt suspension (A), or by using a pipette tip as a container (B). Image showing the pipette tip placed on top of a hydrogel scaffold (C). The pipette tip was filled with an ink to show that it could carry increased volumes of liquid without leakage.*

In the first case, the hydrogels were left to slightly dry for about 30 minutes under the cell culture hood just prior seeding, paying attention that they weren't drying out totally. This step was necessary to let evaporate the excess water, so that the crypt suspension drop would stay on top of the scaffold. After that, $\approx$ 30 μL of crypt suspension was added on top of the scaffolds and then the plates were carefully placed into the cell culture incubator to let the cells adhere. After 1-2 hours, 300 μL of organoid growth media or ISEMF_CM supplemented with ENR_CV was added. However, sometimes the drop was spreading out to the whole surface of the well causing an inhomogeneous seeding. In the second strategy, a sterile pipette tip bottom was used as a container. This permitted the use of increased crypt suspension volumes (up to 100 μL) and also assured that the suspension would stay on top of the scaffold. As in the first strategy, after 1-2 hours of seeding, culture medium was added but the pipette tip bottom wasn't removed

until the other day to ensure maximum cell adhesion. The seeding area of a 30 μL drop was estimated to be 0,79 cm^2 (the area of a 10 mm diameter disc dictated by the PDMS pool dimension). On the other hand, the seeding area was reduced to 0,31 cm^2 when the pipette tip was used (calculated using the dimensions of the inner diameter of the pipette tip). The seeding densities were calculated taking into account this variation in the area depending on which strategy was used. Approximately, the seeding densities used were 2500, and 3500 crypts.cm^{-2} for drop and pipette tip seeding, respectively. Pipette tip seeding allowed to have higher seeding densities for similar total crypt numbers. After seeding, cell culturing times differed from 6 to 9 days and are indicated in the figure captions of the corresponding experiments.

2.2.7 Immunofluorescence characterization

The cells were fixed with 10% neutralized formalin (Sigma), permeabilized with 0,5% v/v Triton X-100 (Sigma), and blocked with a blocking buffer containing 1% w/v BSA (Sigma), 3% v/v donkey serum (Millipore), and 0,2% v/v Triton X-100 in PBS for at least two hours. The primary antibodies used were: rabbit anti-Ki67 (1:100, abcam), and mouse anti-cytokeratin 20 (CK20) (1:100, Dako). Ki67 marks the proliferative and CK20 the differentiated intestinal epithelial cells. All samples were incubated with the primary antibody overnight at 4°C followed by 1 h incubation at RT with secondary antibodies: Alexa Fluor® 488 donkey anti-mouse, and Alexa Fluor® 647 donkey anti-rabbit (Jackson ImmunoResearch), diluted at 1:500. Cell nuclei were stained with 4',6-diamidino-2-phenylindole (DAPI) (1:1000). Alexa Fluor® 568 phalloidin was used to stain filamentous actin (F-actin). The samples were mounted with Fluoromount-G® (SoutherBiotech). For the visualization of collagen and Matrigel® functionalization, primary antibodies of mouse anti-collagen type I (1:200, ThermoFisher Scientific), and rabbit anti-laminin (1:500, abcam) were used, respectively. The secondary antibodies used were Alexa Fluor® 488 donkey anti-mouse, and Alexa Fluor® 488 donkey anti-rabbit diluted at 1:500. The immunostaining protocol was as explained above except the permeabilization step, which was not needed. All the reagents were obtained from Invitrogen unless stated otherwise.

2.2.8 Image acquisition, analysis and statistics

The fluorescence images were acquired using confocal laser scanning microscopy (CLSM) (TCS SP5, Leica) with 10x dry (N.A. = 0,40), and 20x dry (N.A. = 0,70)

objectives at randomly selected locations. The laser excitation and emission light spectral collection were optimized for each fluorophore. For the four color scans the emission bands were adjusted to avoid overlapping of the channels. The pin hole diameter was set to 1 Airy Unit (AU). For images acquired at 10x and 20x, z-steps of 1,5 μm and 5 μm were used for stacks of epithelial monolayers and bare scaffolds functionalized with collagen, respectively. Bright field microscopy images were obtained by an inverted microscope (Eclipse Ts2, Nikon) equipped with a low N.A. 4x objective to ensure an extended field and depth of view. The surface coverage of the epithelial monolayers on the PEGDA-AA scaffolds was estimated from the bright field microscopy images either by manually delimiting the areas or by running a trained WEKA pixel classifier (Trainable WEKA segmentation plugin from ImageJ) using ImageJ free software. The area covered with tissue was normalized to the total area of the image and expressed as percentage. The base and the pillars were homogeneously covered at the regions where there was monolayer, making it possible to estimate the percent surface coverage of the 3D surface from 2D projected bright field microscopy images. The quantification of the Ki67 marker, to determine the amount of proliferative cells with respect to the total cell number was estimated by a custom ImageJ macro provided by the Advanced Digital Microscopy (ADM) Unit of Institute for Research in Biomedicine (IRB) (See Appendix B for the macro code). 4 to 5 randomly selected regions of each sample were analyzed for surface coverage determination and CLSM stacks were obtained at 5 different positions among the areas covered with cells for Ki67 quantification. The error bars in the figures represent the standard deviations of at least three independent experiments. The statistical comparison was performed using two tailed, unequal variances Student's t-test and $p<0,05$ was considered significant. The data were processed and plotted with OriginPro 8.5 software.

2.3 Results

2.3.1 Morphological assessment of the 3D villus-like microstructured hydrogels

3D villus-like microstructured hydrogels can be obtained by free-radical polymerization of PEGDA using a 2D photomask as demonstrated previously [46]. PEGDA solution is introduced into a container made out of PDMS (PDMS pool), the photomask is placed on top of the pool and the solution is exposed to UV. Photomasks with transparent windows of 100 μm in diameter were used to fabricate microstructures with dimensions close to those of native intestinal villi. A PDMS container of 1 mm in height was used not to limit the polymerization in the vertical axis. A working range of 5% w/v to 10% w/v P6000 concentration was chosen in order to obtain a soft material. Mechanical characterization of P6000 revealed that the Young's modulus (E) of the material was ranging between 3 kPa to 11 kPa (see Section 2.3.2 for results) in agreement with previously published data (20% w/v P6000 $\approx$ 15 kPa) [49]. The use of high concentrations of PEGDA lead to very hard materials (E in the range of MPa [18, 50]) poorly mimicking *in vivo* mechanical properties of soft epithelial tissues. PEGDA photopolymerization is initiated by the activation of the photoinitiator (I2959) under UV light. Fractional monomer conversion is mainly controlled by photoinitiator related parameters, such as its concentration [41]. Meanwhile, its solubility is limited to 1% w/v in aqueous media (as reported in the datasheet). In order to obtain an optimal monomer conversion the maximum possible I2959 concentration, 1% w/v, was chosen. Figure 2.14 A and B show representative stereo microscopy images of the microstructures obtained from 5% w/v P6000 with two different UV exposure times: 150 s and 170 s. The hydrogel base was formed by a previous flood exposure of 15 s. The heights of the pillars were estimated from stereo microscope images and were found to be 600,6 $\pm$ 51,3 μm and 591,3 $\pm$ 27,6 μm for 150 s and 170 s, respectively. The pillars had an aspect ratio (height:diameter) of $\approx$ 4,5. SEM image in figure 2.14 C shows the array of individial, high aspect ratio pillars formed on a hydrogel base. The microstructures displayed biomimetic rounded tips (Figure 2.14 D) like those found in the small intestine. The heights of the microstructures were estimated from the SEM images, taking into account the tilt angle (see Section 2.2.2.2 for the calculation method), and found to be 348,3 $\pm$ 17,1 μm. This value is lower than the heights calculated from the stereo microscope images. This might be explained by a shrinkage that might have occurred during sample dehydration. SEM is an effective technique to assess the morphology

but the final dimensions seem to be affected by sample preparation; therefore, in what follows the heights of the pillars were estimated from the stereo microscope analysis.

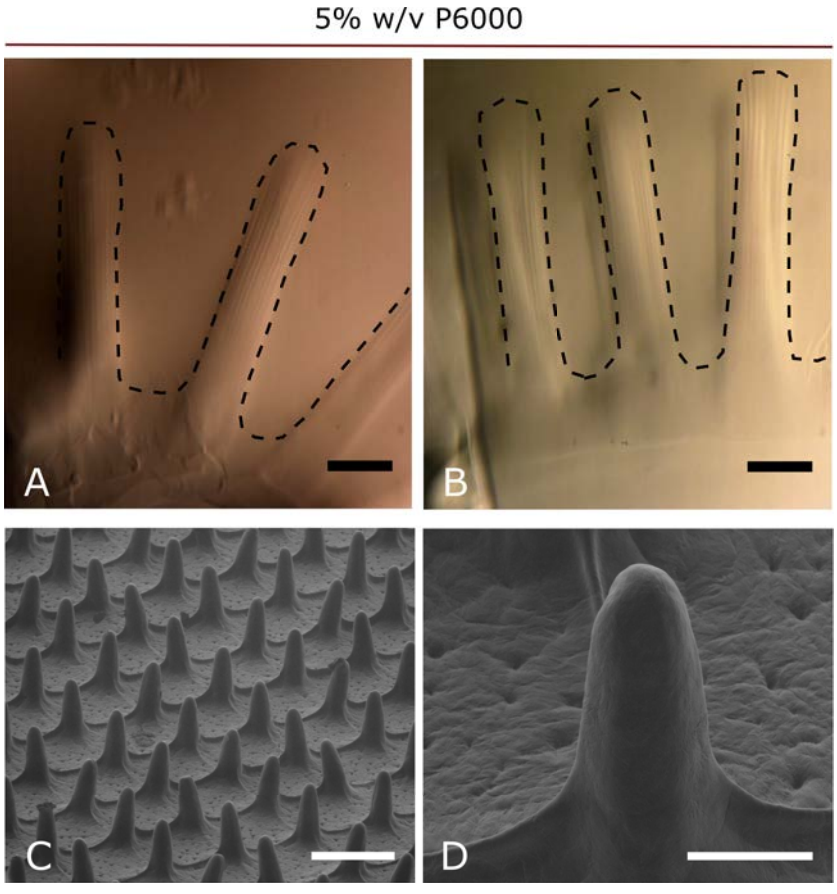

Figure 2.14: *Stereo microscope images of microstructured 5% w/v P6000 hydrogels fabricated with 150 s (A), and 170 s (B) of UV exposure. A flood exposure of 15 s was performed to create a hydrogel base that holds the microstructures together. Black dashed lines mark the border of the microstructures. Scale bars: 150 μm. SEM images of microstructured 5% w/v P6000 hydrogels fabricated with 150 s of UV exposure at low (C) and high magnification (D). Scale bars (C): 200 μm, D: 50 μm*

.

The heights of *in vivo* villi vary from 0,2 mm to 1 mm [117, 131]. The heights of the microstructures obtained are within this range. This assessment of the morphology demonstrates that with our fabrication protocol it is possible to produce microstructured hydrogels mimicking the shape and dimensions of the small intestine villi. There are some examples of high aspect ratio structures produced from PEGDA reported in the literature [98, 100, 102]. Dang *et al.* fabricated

PEGDA pillars of 1 mm height and 500 μm in diameter to be used as molds [98], Dardano *et al.* produced PEGDA microneedle arrays with heights larger than 1 mm for potential applications in microelectronic devices [102]. However, in these works 100% w/v or highly concentrated solutions of PEGDA were used, leading to microstructures with elastic modulus values in the range of MPa [50] far from the mechanical requirements of soft tissue models. Here, we demonstrate that it is possible to fabricate self-standing pillars with high aspect ratio on soft hydrogels, using diluted PEGDA solutions (5%-10% w/v), compatible with the requirements of epithelial tissues. It is remarkable that these microstructures with a complex 3D geometry (bullet-like) can be formed with a simple photolithographic technique without the need of a mold.

It is possible to obtain these complex bullet-like structures due to the interplay between the free-radical photopolymerization reaction dynamics and the formation of oxygen gradients within the fabrication setup [99, 100]. Molecular oxygen diffused in the solution scavenges the free-radicals and inhibits the polymerization reaction [47]. Therefore, the polymerization takes place only when the oxygen is depleted locally. When timescale of oxygen diffusion is comparable with that of oxygen depletion the polymerization is very sensititive to the oxygen concentration and can be controlled spatially by creating oxygen gradients [47, 132]. Shim *et al.* described the so-called Damköhler number, Da, which is a ratio between the timescales of oxygen diffusion and oxygen depletion processes to account for the relevance of the oxygen diffusion [100]. Damköhler number, Da, can be calculated as:

$$Da = \frac{\tau_{diff}}{\tau_{depl}} = \frac{R^2/D_0}{[O_2]_0/\phi\epsilon[PI]I} \tag{2.8}$$

Where R is the radius of the transparent windows of the 2D photomask, D_0 is the diffusion coefficient of oxygen in the polymer solution, $[O_2]_0$ is the molar concentration of oxygen initially dissolved in the polymer solution, ϕ is the quantum yield of the photoinitiator, ϵ is the molar extinction coefficient of the photoinitiator, [PI] is the molar concentration of the photoinitiator and I is the intensity of the UV light. According to Da values, three polymerization regimes are defined. When Da » 1 oxygen diffusion is slow and polymerization can occur. When Da « 1 oxygen diffusion is fast and it never depleted enough from the system so polymerization is inhibited. When Da $\approx$ 1, and the experimental setup is permissive to oxygen, microstructures were shown to grow in conical forms [100]. In our experimental setup, on top of the oxygen present in the prepolymer solution, oxygen

can diffuse through the walls of the PDMS pool [133] and through the air-liquid interface of the inlets. Therefore, oxygen diffusion has a role in the dynamics of the microstructure fabrication. Detailed characterization of the growth dynamics of the bullet-like microstructures has been previously reported in a work done in our group [46, 103]. Garcia Castaño *et al.* computed Da taking into account the features of our experimental setup: the radius of the transparent windows of the 2D photomask (d = 100 μm, R = 50 μm) and the light absorbance by the photoinitiator along the vertical axis of UV irradiation, z, which can be estimated by the Beer-Lambert law (Equation 2.9).

$$Da = \frac{\tau_{diff}}{\tau_{depl}} = \frac{R^2/D_0}{[O_2]_0/\phi\epsilon[PI]I.exp(-2,303\epsilon[PI]z)} \tag{2.9}$$

They found that Da was significantly changing with z. The diameter of the microstructures obtained was consistent with the dimensions of the photomask windows and heights could be controlled with the UV exposure time. Nevertheless, the microstructure heights were never reaching the full height of the PDMS pools, probably because for z greater than 800 μm Da was lower than 1 [46]. The findings of Garcia Castaño *et al.* broadly describe the mechanisms governing the fabrication process used here.

Once we showed that in our experimental setup fabrication of villus-like microstructures was possible, we have tested the effect of varying concentrations of the PEGDA macromer solution on the morphology of the microstructures. The P6000 concentrations tested were 5% w/v, 7,5% w/v and 10% w/v and the microstructures were fabricated with two different exposure times: 150 s and 170 s. The main observation was that with increased polymer concentrations, polymerization was also occuring at the unexposed regions (Figure 2.15 A-C). At higher PEGDA concentrations, unexposed regions fully polymerized. Because of this uncontrolled polymerization, the effective heights of the microstructures were reduced dramatically (Figure 2.15 D). Regarding the effects of UV exposure time, for 5% w/v P6000 increasing the UV exposure from 150 s to 170 s decreased the effective heights from 657,0 $\pm$ 24,0 μm to 368,5 $\pm$ 30,2 μm, showing that increasing the exposure time was also increasing the uncontrolled polymerization. Overall, these findings suggested that PEGDA concentration and UV exposure time both affect the shape and dimensions of the microstructures and both parameters should be tuned to obtain the proper morphologies.

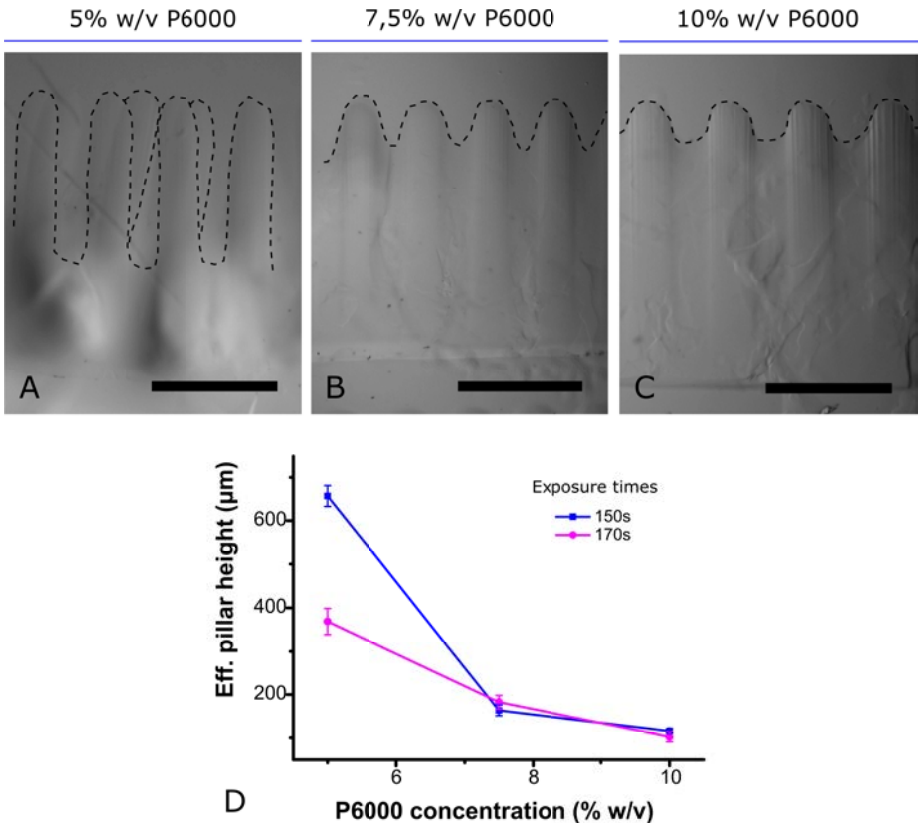

Figure 2.15: *Bright field microscopy images of microstructured P6000 hydrogels at 5% (A), 7,5% (B), and 10% (C) w/v concentrations fabricated with 150 s UV exposure. A second exposure of 15 s was performed to create a hydrogel base that holds the microstructures together. Black dashed lines mark the border of the microstructures. Graph showing the change in the effective height of the pillars with increased concentrations, fabricated with 150 s and 170 s of UV exposure (D). 4 samples were measured for each condition and the data were presented as mean ± standard deviation. Scale bars (A, B): 500 µm, C: 400 µm.*

The interstitial polymerization at the unexposed regions might have numerous explanations and reviewed in detail by Garcia Castaño *et al.* [46]. It is mainly attributed to the diffusion of radicals and monomers causing irregular polymerization at the illumination interface resulting in structures not faithfully reproducing the photomask pattern [134, 135]. Moreover, diffusion is a time and concentration dependent process, meaning with increasing exposure times and monomer (or building block) concentrations, the amplitude of interstitial polymerization should be more pronounced. This is in accordance with the results presented in figure 2.15. Viswanathan *et al.* also reported structural deviations compared to the photomask pattern with increasing UV exposure time [135]. In addition, the polymerized material (crosslinked hydrogel) produces scattering effects [136]. In

our fabrication protocol, the hydrogel base formed initially might have caused the scattering of the UV light in the following exposure performed for the formation of the pillars.

As an improvement, the fabrication protocol was revised [103]. In the modified protocol, first, the microstructures were formed (first exposure), then the pillars were washed with PBS and PEGDA macromer solution in order to remove any unreacted species. Finally, a short second exposure was performed to form the base that connected the microstructures. Microstructures with a variety of dimensions and P6000 concentrations were fabricated with the improved protocol (Figure 2.16). In all the conditions villus-like rounded forms were obtained. Longer exposure time yielded higher structures. Even with the more concentrated solutions, 6,5% and 10% w/v, with 120 s and 100 s exposure time, respectively, large high aspect ratio structures and a base holding them together could be obtained without any polymerization at the unexposed regions.

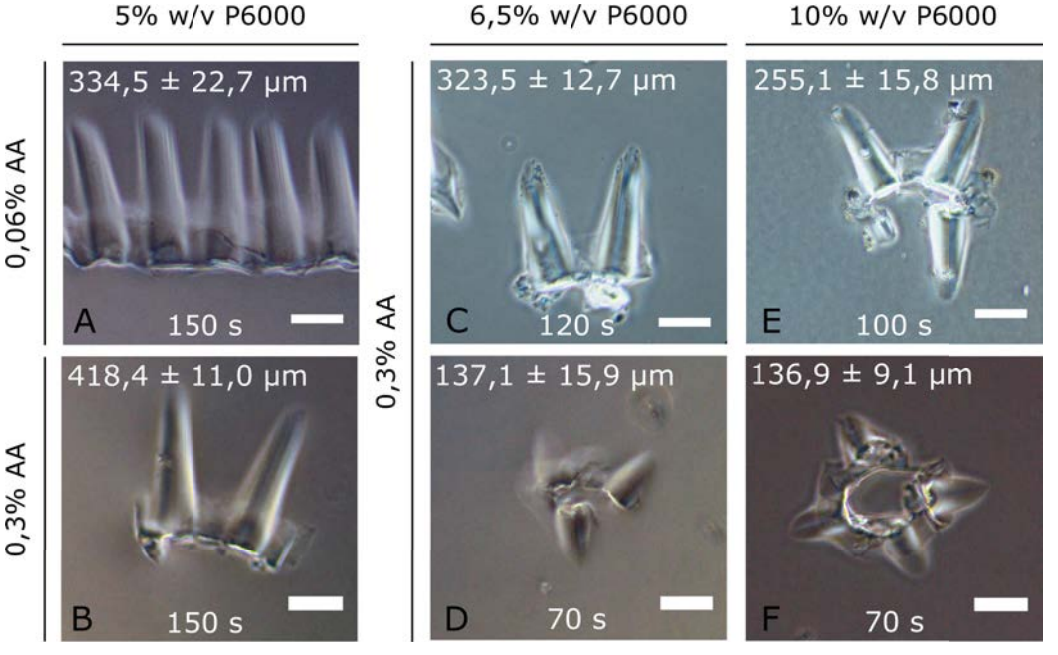

Figure 2.16: *Bright field microscopy images of microstructured hydrogel samples fabricated under different conditions; 5% w/v P6000 at 150 s of UV exposure with 0,06% w/v AA (A), or 0,3% w/v AA (B), 6,5% w/v P6000 with 0,3% w/v AA at 120 s (C) or 70 s (D) of UV exposure, 10% w/v P6000 with 0,3% w/v AA at 100 s (C) or 70 s (D) of UV exposure. A second exposure of 15 s (A, B, C) and 10 s (D, E, F) was performed to create the hydrogel base. Scale bars: 200 µm.*

With this configuration, the heights of the microstructures can be controlled

with a single parameter, the exposure time. The effective heights of the microstructures were estimated from bright field microscopy images and are given in figure 2.16. Microstructures with villus-like realistic dimensions [117, 131] could be obtained by exposure times 100 s or above and with different PEGDA concentrations (5% w/v, 6,5% w/v and 10% w/v). Overall, these results show that complex 3D microstructures of high aspect ratio and roundish geometries can be obtained by a moldless, simple photolithography-based process in an experimental setup permissive to oxygen. The dimensions of the microstructures can be easily tuned by modifying the UV exposure time.

2.3.2 Mechanical properties of the PEGDA-AA hydrogels

The Young's modulus of PEGDA-AA hydrogels prepared at different concentrations after swelling were determined with a compression test. Disc-shaped P6000 hydrogels at concentrations 5% w/v, 7,5% w/v, and 10% w/v were studied. The concentration range selected is the same range used for microstructured hydrogel fabrication. The acrylic acid concentration used in the prepolymer solution was 0,06% w/v and the time of polymerization was 200 s. The effect of the PEGDA concentration was studied.

Figure 2.17 A shows a representative stress-strain curve of 5% w/v P6000 hydrogel obtained by a compression test. The Young's modulus (E) was calculated from the slope of the linear region of the curve, as indicated by the red line. In a similar fashion, E was determined for all the samples analyzed. The Young's modulus of the PEGDA hydrogels significantly increased with increasing concentrations ($p<0,05$) (Figure 2.17 B). This result suggests that the E can be tuned by changing the total amount of PEGDA macromers. Bryant *et al.* showed that the compression modulus of the poly (ethylene glycol) dimethacrylate gels were increased with increasing concentration [38]. Other studies also adopted a similar strategy, changing PEG concentration in the hydrogel precursor solution, to obtain gels of varying stiffnessess [137, 138]. It is important to note that the mechanical characterizations were done with PEGDA hydrogels containing 0,06% w/v AA concentration; nevertheless, Garcia Castaño *et al.* showed that increasing AA concentrations up to 1,2% w/v did not significantly altered the Young's modulus of the PEGDA-AA hydrogels [46, 103].

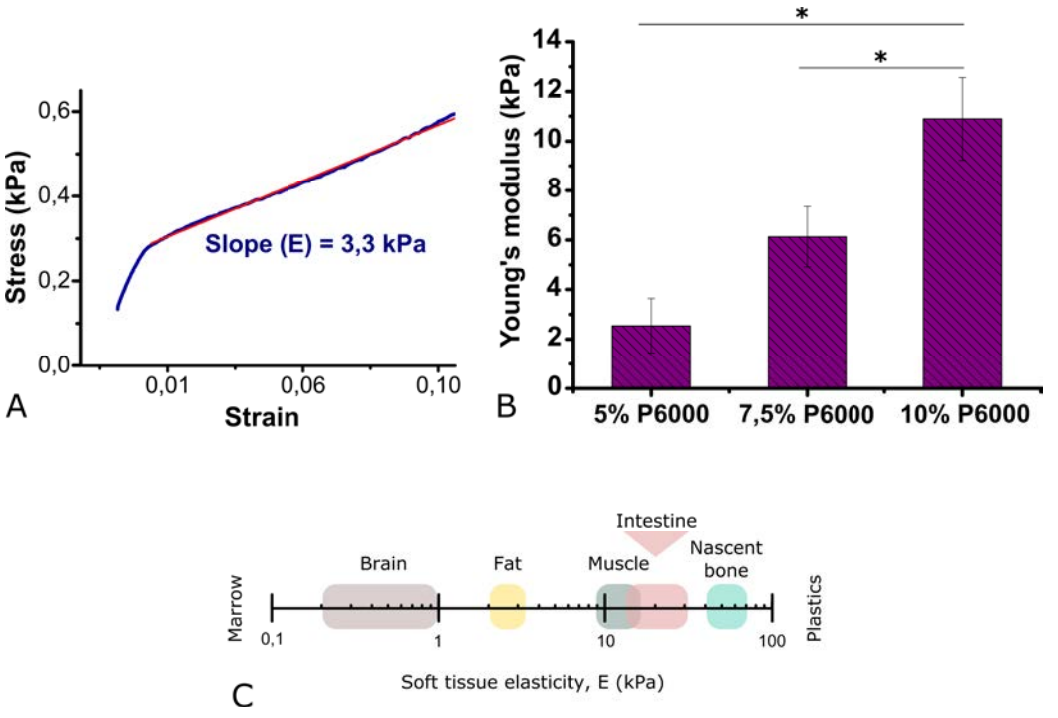

Figure 2.17: *Stress-strain curve of a 5% w/v P6000 hydrogel obtained by a compression test (A). The Young's modulus (E) was calculated from the slope of the linear part of the stress-strain curves. Graph showing the Young's modulus of P6000 hydrogel at different concentrations (mean ± standard deviation, Student's t-test, *p<0,05) measured after swelling (B). The concentration of AA used was 0,06% w/v. At least three different discs were characterized for each condition (n = 3). Scale showing soft tissue elasticity ranging from brain [139], fat [140], muscle [141], intestine [142, 143] to nascent bone [141] (C). Adapted from Discher et al. and Huang et al. [144, 145].*

The Young's modulus values determined varied from 2,5 ± 1,1 kPa to 10,9 ± 1,7 kPa, comparable with the values published in a previous study, where E of 20% P6000 was calculated to be ≈ 15 kPa [49]. In another work, Munoz-Pinto *et al.* reported a modulus value of 31 kPa for 10% P6000; however, the gels were crosslinked for 6 minutes [44], as oppose to 200 sec of exposure that was used in our experimental setup. Overall, the E values we have obtained are in accordance with the values reported in the literature, the variations observed can be attributed to the differences in the fabrications conditions. The mechanical properties of *ex vivo* small intestine tissue has also been characterized in some works. In one study, the elastic modulus of whole small intestinal segments from rats were found in the range of 20-30 kPa [142] (Figure 2.17 C). In another study, Sotres *et al.* reported the elasticity of freshly sectioned small intestine from adult pigs to be in the range of 14–22 kPa [143] (Figure 2.17 C). The Young's modulus values

obtained here were in the range of 3-11 kPa, similar to the findings of Sotres *et al.*, suggesting that the mechanical properties of our material were comparable to that of native small intestine.

2.3.3 Swelling properties of the PEGDA-AA hydrogels

To swell the hydrogels to equilibrium before performing further experiments is relevant, as swelling affects pore size and mechanical properties. We tested PEGDA concentrations of 5% and 10% w/v P6000, fabricating hydrogels with both 150 s and 200 s UV exposure times to determine the equilibrium volume swelling ratio (Q) depending on the PEGDA concentration and the exposure time. First, the change in hydrogel weight was followed by a gravimetric method, then from the weight values the Q was calculated (see Section 2.2.4 for the calculations). To calculate Q it was necessary to know the weight of the hydrogels right after fabrication (m_c), at the equilibrium swollen state (m_s) and at the dry state (m_d). Figure 2.18 A-C show the images of 5% w/v P6000 hydrogels fabricated with 200 s of UV exposure right after fabrication (A), at the equilibrium swollen state (B), and at the dry state (C). The hydrogel images show significant changes in the water content and, consequently, in the dimensions of the hydrogel. The graphs given in figure 2.18 D-G show how the weight of the hydrogels increases with time due to swelling for several replicas (hydrogel 1 to 4). The swelling of the hydrogels occurred more steeply during the first hours and subsequently, started to stabilize until it reached a point where it didn't show significant changes. For 5% w/v P6000 hydrogels fabricated with 150 s of UV exposure, swelling was performed up to 7 days to provide sufficient amount of time for swelling but it was found that 4 days were enough to reach the equilibrium swelling (Figure 2.18 D). For 5% w/v P6000 hydrogels fabricated with 200 s of UV exposure 4 days was also sufficient to reach the equilibrium swelling (Figure 2.18 E). Before any further use, 5% w/v P6000 hydrogels were assured to be swollen 4 days. The hydrogels fabricated with 10% w/v have shown a similar swelling behavior but the time to reach the equilibrium state was shorter (Figure 2.18 F, G). In fact, about 30 h was enough to reach the equilibrium swelling for the gels prepared with both 150 s and 200 s. However, for the sake of convenience 10% w/v P6000 hydrogels were assured to be swollen 48 h (2 days) before any further use. As an initial qualitative assessment, no difference was observed in equilibrium swelling times of hydrogels fabricated with different exposure times (150 s *vs.* 200 s).

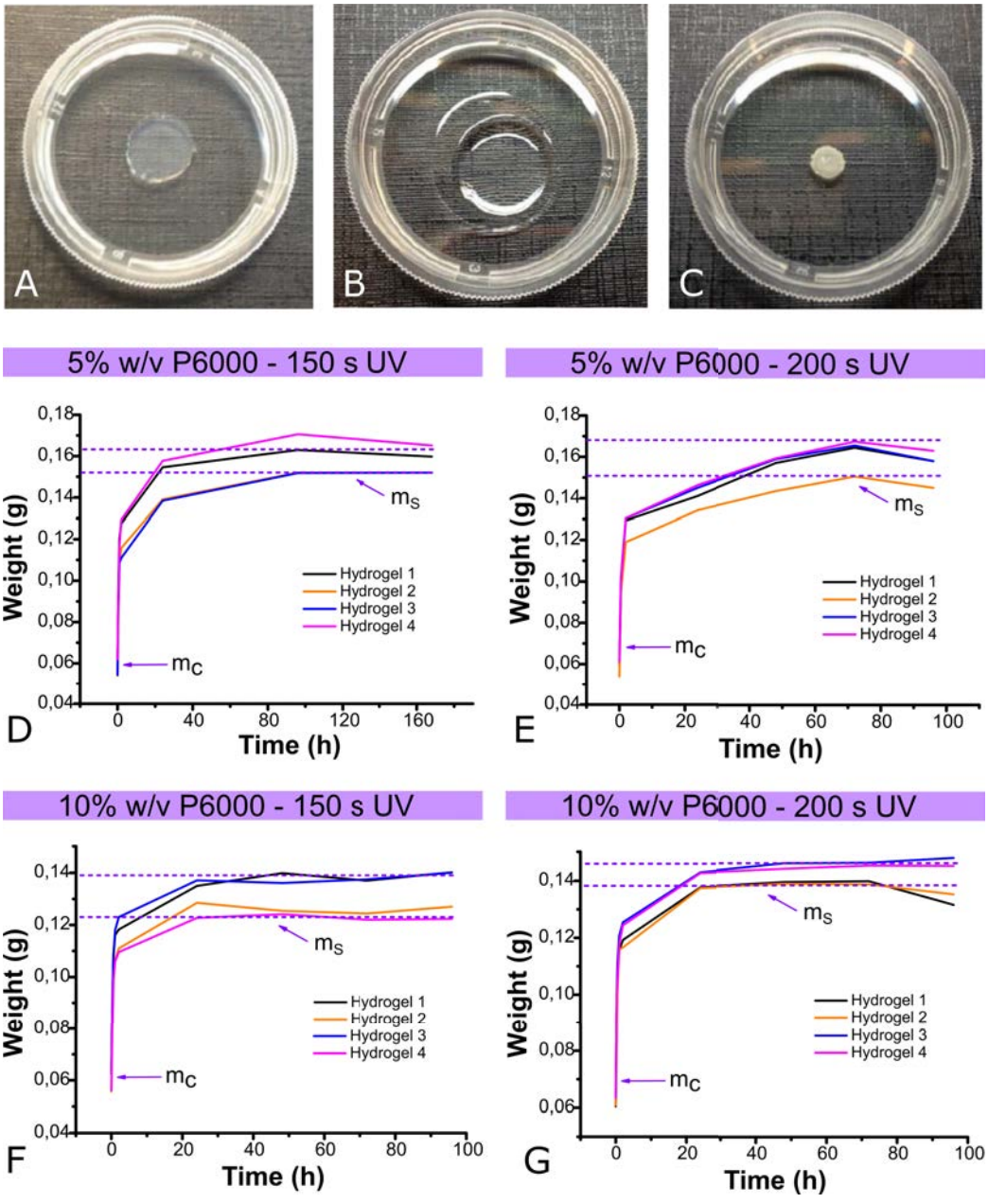

Figure 2.18: *Images of disc-shaped 5% w/v P6000 hydrogel fabricated with 200 s of UV exposure right after fabrication (A), at the equilibrium swollen state (B), and at the dry state (C). Graphs showing the change in weight of the hydrogels with time for 5% w/v P6000 (D, E) and for 10% w/v P6000 hydrogels (F, G) fabricated at 150 s (D, F) and 200 s (E, G) of UV exposure. The concentration of AA used was 0,06% w/v. The m_c, and m_s are indicated in the graphs.*

Table 2.1 lists m_c and m_s values for all the hydrogels together with the weight

of the dry hydrogels (m_d), which were obtained after drying the gels until constant weight. The average increase in weight ((m_s-m_c)/m_c*100) was calculated to be 174,5% ± 6,6% and 123,4% ± 6,0% for 5% w/v and 10% w/v P6000, respectively. It is important to mention that we have done the calculations for each hydrogel and then averaged the values, in order to eliminate initial weight variations coming from the fabrication step. These might be the break of the hydrogel when it was unmolded, pipetting variations or any other external factors.

Exposure time (s)	**150**				**200**			
Measured weights of 5% w/v P6000								
Hydrogels	1	2	3	4	1	2	3	4
m_c (g)	0,062	0,054	0,062	0,054	0,060	0,054	0,062	0,061
m_s (g)	0,163	0,152	0,171	0,152	0,164	0,151	0,166	0,167
m_d (g)	0,004	0,004	NA	0,004	0,004	0,003	0,004	0,004
Measured weights of 10% w/v P6000								
Hydrogels	1	2	3	4	1	2	3	4
m_c (g)	0,062	0,056	0,064	0,056	0,061	0,061	0,064	0,063
m_s (g)	0,140	0,127	0,140	0,122	0,131	0,135	0,148	0,145
m_d (g)	0,006	0,006	0,006	0,006	0,007	0,007	0,007	0,007

Table 2.1: *The weights of the hydrogels after fabrication (m_c), at the equilibrium swollen state (m_s), and at the dry state (m_d). These values were used to calculate the polymer volume fraction in the swollen state ($V_{2,s}$) and the equilibrium volume swelling ratio (Q). The m_d of one of the 5% w/v P6000 hydrogels is not available (NA) because it was broken during handling.*

From the swelling data presented above, the polymer volume fractions in the swollen state ($V_{2,s}$) and the volume swelling ratio (Q) values were calculated for all the fabrication conditions and listed in Table 2.2 (see Section 2.2.4 for the calculations). $V_{2,s}$ values were significantly higher (Student's t-test, p<0,001) and Q values were significantly lower (Student's t-test, p<0,01) for 10% w/v P6000 than for 5% w/v P6000 in a pairwise comparison for the same exposure times. $V_{2,s}$ and Q parameters are inversely related as given in equation 2.6 and it is well established that the Q decreases with increasing polymer concentrations [146–148], in accordance with our findings. The solution with higher PEGDA macromer concentration has more diacrylate reactive groups, which produces an increase in crosslinking density. This increase in crosslinking density hinders the mobility of the polymer chains and thereby decreases swelling (measured by the Q), which in turn also limits particle diffusivity [3, 149]. Overall, these results demonstrate

that the swelling of the hydrogels can be controlled by increasing PEGDA concentrations in the hydrogel precursor solution. It is important to note that the swelling characterizations were done with PEGDA hydrogels containing 0,06% w/v AA concentration; nevertheless, Garcia Castaño *et al.* showed that AA concentrations up to 0,6% w/v did not significantly influenced the swelling ratio of the PEGDA-AA hydrogels [46, 103].

	5% w/v P6000		**10% w/v P6000**	
Exposure time (s)	150	200	150	200
$V_{2,s}$	0,021 ± 0,001	0,021 ± 0,000	0,043 ± 0,001	0,044 ± 0,002
Q	2,76 ± 0,11	2,75 ± 0,05	2,23 ± 0,05	2,26 ± 0,08

Table 2.2: *The polymer volume fraction in the swollen state ($V_{2,s}$) and the volume swelling ratio (Q) calculated for all the different conditions studied. The data are represented as mean ± standard deviation (n = 4).*

On the other hand, there was no statistically significant differences (Student's t-test, p>0,05) between the Q values of the gels prepared with 150 s and 200 s of UV exposure. We can, therefore, conclude that the UV exposure time range we had chosen does not affect the crosslinking density of the hydrogels. This suggests that in our experimental fabrication conditions the crosslinking is saturated and the hydrogel network cannot incorporate more chains into the structure even though exposure time is increased. To test this hypothesis, we have also determined the gel fraction of the hydrogels for the all the conditions studied.

2.3.3.1 Gel fraction determination

In order to evaluate the amount of PEGDA chains crosslinked depending on the initial PEGDA concentration and the UV exposure time, the gel fraction was determined. Dry hydrogels were weighted right after fabrication (M), and after the removal of the unreacted species and reactional residues (M'), and the corresponding gel fractions were calculated (see Section 2.2.4.1 for calculations). Table 2.3 lists the percentage gel fraction values calculated.

	5% w/v P6000		10% w/v P6000	
Exposure time (s)	150	200	150	200
Gel fraction (%)	74,3 ± 1,2	73,9 ± 2,0	83,4 ± 1,4	83,5 ± 0,9

Table 2.3: *The average gel fraction values calculated for all conditions studied. The data are represented as mean ± standard deviation (n = 4).*

The gel fraction percentages ranged from 74% to 84% for the conditions tested. As it can be seen from these values, the polymerization efficiency wasn't maximal. Submaximal final double bond conversions of multi-acrylates have been reported in numerous studies [150–152]. This phenomenon is attributed to autoacceleration kinetics and formation of a glassy polymer leading to an attainment of a maximum conversion after which no significant reaction can occur even though there remain unreacted initiator and polymer chains and for extended times [150, 151]. In addition, gel fractions were not significantly changed (Student's t-test, p>0,05) with increased exposure times for a given concentration, suggesting that at the time points chosen, the maximum possible conversion had already been achieved. This also explains the insignificance of increasing UV exposure time on volume swelling ratios (Q). Overall, these results suggest that after 150 s no more PEGDA chains are incorporated to the hydrogel network and consequently the crosslinking density stays unaffected. On the other hand, gel fraction was significantly higher (p<0,001) for 10% w/v than for 5% w/v P6000 hydrogels. This shows that the amount of material affects the reaction percentage, which is in agreement with the previous finding that, with increased PEGDA macromer concentrations, the crosslinking density increases and the swelling ratio (Q) decreases. Altogether, the results of gel fraction determination support the findings of the swelling characterizations.

2.3.4 Characterization of protein functionalization of PEGDA-AA scaffolds

PEGDA-AA hydrogels present flanking carboxylic groups in their network structure that can further be used to attach biomolecules for cell adhesion, such as extracellular matrix proteins and peptides. Carbodiimide mediated reaction couples amino group bearing biomolecules to the carboxylic groups of the PEGDA-AA hydrogels. The EDC/NHS mediated bioactive functionalization reaction and associated protocol were explained in detail in figure 2.12 and section 2.2.5, respectively. Briefly, first, PEGDA and AA are copolymerized.

Then, the AA carboxylic groups are activated by EDC/NHS and, lastly, the functional biomolecules (e.g. cell adhesion proteins) are incorporated into the hydrogel structure. In order to test successful protein binding, microstructured 5% w/v P6000 hydrogels were fabricated either by copolymerizing it with AA or homopolymerization without AA. The hydrogels were all activated with EDC/NHS and incubated with a fluorescent protein Streptavidin_TexasRED (SA_TxRED). As a control, microstructured hydrogels that weren't activated with EDC/NHS were also incubated with SA_TxRED. Figure 2.19 shows confocal microscopy images of P6000 microstructures functionalized with the protein, fabricated by either P6000 homopolymerization (A, B) or copolymerizing it with AA (C, D). Both the hydrogels that were previously activated by EDC/NHS (Figure 2.19 A, C) and that were not (Figure 2.19 B, D), were tested. Only the P6000 hydrogels copolymerized with AA and activated with EDC/NHS showed a red SA_TxRED signal (Figure 2.19 C). The fluorescent intensity was found to be significantly higher ($p<0,001$) in the P6000-AA hydrogels activated with EDC/NHS (Figure 2.19 E) compared to the other negative controls. The low fluorescence signal in the negative controls can be explained by the trapping of some of the SA_TxRED molecules within the pores of the hydrogels. This result, already pointed out by Garcia Castaño *et al.* [46], proves the selectivity of the addition and EDC/NHS activation for the successful incorporation of proteins to the hydrogel structure. Moreover, the covalent nature of this protein binding strategy results in its resistance to washing steps and storage time as demonstrated by Garcia Castaño *et al.* [46]. It is noteworthy that the incorporation was homogeneous.

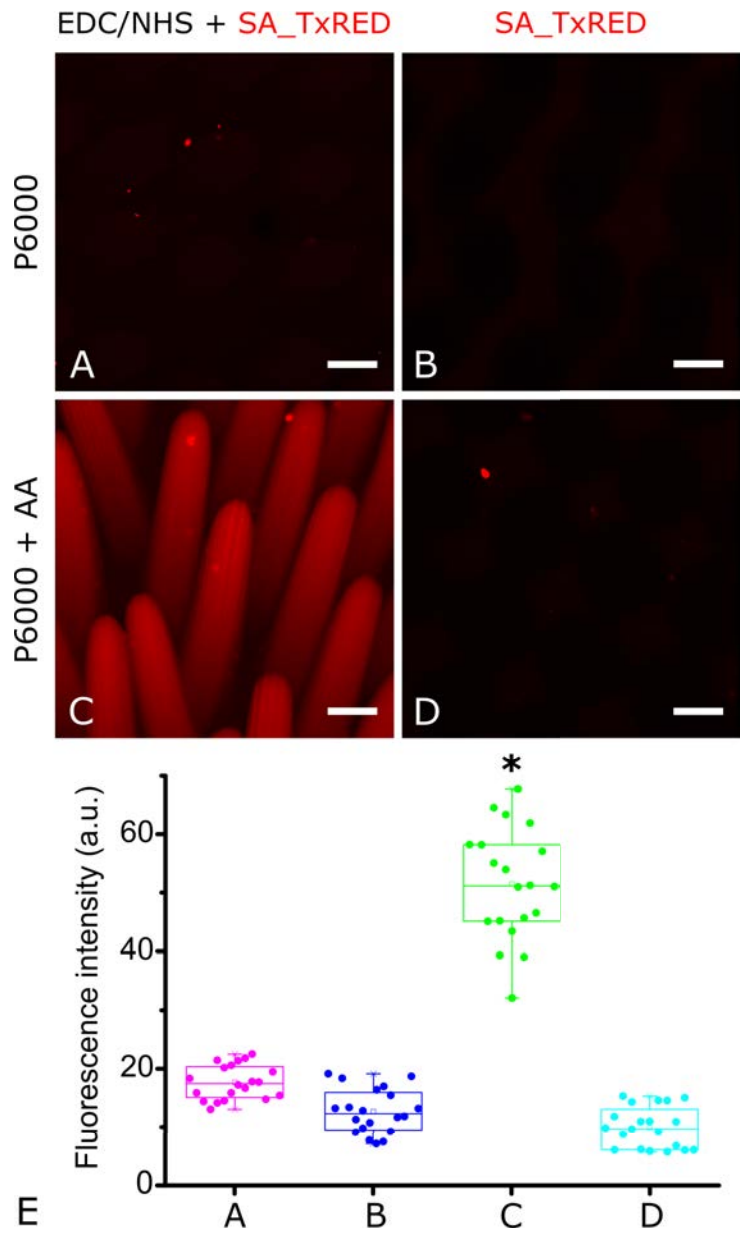

Figure 2.19: *Fluorescence images of the microstructured 5% w/v P6000 hydrogels functionalized with SA_TxRED, fabricated without (A,B) or with (C,D) AA, and with (A,C) or without (B,D) previous activation with EDC/NHS. The microstructures were fabricated with 150 s of UV exposure and the concentration of AA used was 0,06% w/v. The graph showing the fluorescence intensities quantified for each condition, within a selected circular area of 60 μm in diameter at 10 different regions (E). The regions were selected within the pillars for the condition C, and for the rest of the conditions at random locations. The fluorescent intensity was found to be significantly higher (Student's t-test, *p<0,001) for the condition C (green). For each condition, images acquired from two technical replicas were analyzed. Scale bars: 100 μm.*

The most common support matrix for primary intestinal epithelial cell culture is a laminin and collagen rich protein mixture, called Matrigel® [19, 109, 153]. Therefore, as an initial approach, the microstructured hydrogels were covalently functionalized with 3% and 10% diluted Matrigel® solutions. Alternatively, a drop of undiluted Matrigel® was physically adsorbed in a modification of a previously reported protocol [54] (see Section 2.2.5). In both cases, the Matrigel® functionalization was visualized by immunofluorescence using an antibody against laminin. Figure 2.20 shows the top views (A-C) and the 3D reconstructed views (A'-C') acquired by confocal microscopy. In the case of physical adsorption, the proteins were accumulated at the valleys of the microstructured hydrogels creating an unhomogeneous distribution (Figure 2.20 A, A'). Whereas, in the case of covalent attachment, the proteins were anchored more homogeneously to the microstructure surface (Figure 2.20 B-C'). The surface of the pillars was entirely covered with the proteins in the case of high Matrigel® concentration (Figure 2.20 C, C'). As this would be desired in order to present cells with a homogeneous coating of cell adhesion proteins. However, the stacks acquired did not reach the base of the microstructures as the effective height of the microstructures (657,0 $\pm$ 24,0 μm) was greater than the working distance of the lowest magnification objective available in confocal equipment.

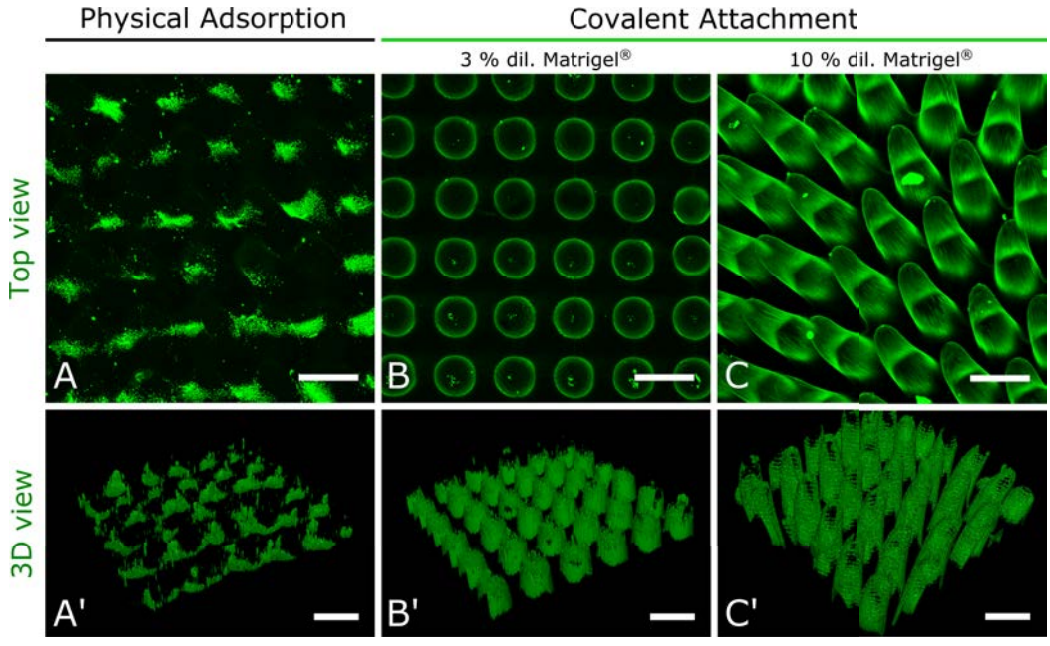

Figure 2.20: *Immunoflourescence for laminin showing the microstructured 5% w/v P6000 hydrogels functionalized with physical adsorption of a Matrigel® drop (A, A') and with covalent attachment by EDC/NHS amine coupling of 3% diluted (dil.) (B, B'), and 10% diluted (dil.) Matrigel® (C, C'). The images show the top (A, B, C) and 3D reconstructed views (A', B', C') of the microstructured hydrogels. The UV exposure times used were 150 s and 15 s for the microstructure and base formation, respectively. The concentration of AA used was 0,06% w/v. Scale bars: 200 μm.*

Collagen type I is one of the most predominant protein found in the extracellular matrix and can be used as support matrix in intestinal organoid cultures as an alternative to Matrigel® [20, 22]. The microstructured hydrogels were also functionalized with collagen type I (10% diluted) to demonstrate the versatility of the functionalization technique and to be further used in cell culture experiments alongside the hydrogels functionalized with Matrigel®. Figure 2.21 showing top and 3D reconstructed view of collagen type I functionalized microstructured hydrogels reveals that the pillar surfaces were homogeneously covered. However, as above, the stacks acquired did not reach the base of the microstructures that had an effective height of 418,4 $\pm$ 11,0 μm due to working distance limitations of the objective available in confocal equipment. Protein anchorage to the base could not be visualized by using the equipments that were available due to the

microstructure height. Nevertheless, the vertical sections (obtained by a protocol that we developed and presented in Appendix A) of the microstructured hydrogels functionalized with a fluorescent protein (SA_TxRED) revealed homogeneous protein anchorage both to the pillars and to the base region (Appendix A Figure A.2).

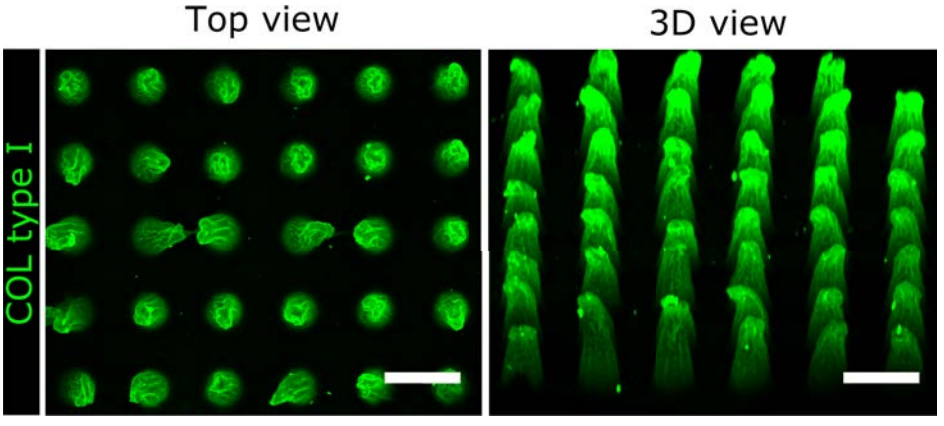

Figure 2.21: *Immunofluorescence for collagen type I functionalized microstructured hydrogels. The images show the top (left panel) and 3D reconstructed views (right panel) of the functionalized microstructured hydrogels. The UV exposure times used were 150 s and 15 s for the microstructure and base formation, respectively. The concentration of AA used was 0,3% w/v. Scale bars: 200 μm.*

These evaluations demonstrate that PEGDA-AA hydrogels can be bioactive functionalized with the protein of interest (depending on the application), proving the versatility of the material. It also shows the relevance of the right protein concentrations to be used. As oppose the epithelial cell lines (e.g. MDCK, Caco-2) that can grow on these microstructured PEGDA hydrogels functionalized with laminin [46], intestinal organoid-derived cells might require a different type of ligand for attachment and growth. Matrigel® and collagen type I are good candidates since they are used as support matrices for the organoid cultures. For the cell culture experiments regarding the ligand type, 10% diluted Matrigel® and 10% diluted collagen type I were used to functionalize the hydrogels. The selection of the ligand type optimal for the growth of intestinal organoid-derived cells is reported in the following section 2.3.5.1.

2.3.5 Screening for optimal conditions for intestinal organoid-derived cell growth on 3D villus-like PEGDA-AA scaffolds

PEGDA-AA hydrogels with villus-like 3D architecture biomimicking the native tissue were tested as scaffolds to culture the organoid-derived crypts. In a previous work performed in our group, these scaffolds, functionalized with basement membrane protein laminin, were shown to support the growth of colorectal adenocarcinoma (Caco-2) cells [103]. We studied parameters to optimize the PEGDA-AA material for the growth of intestinal epithelial cells such as cell adhesion ligand type, effects of pillar morphology, mechanical properties and cell culture medium composition.

2.3.5.1 Selecting the cell adhesion ligand type

To determine which ligand promoted better the intestinal epithelial cell growth, laminin, Matrigel®, and collagen type I were selected to functionalize the villus-like hydrogels. Laminin is the major non-collagenous component of the basement membrane of epithelial tissue [4] and a key protein in cell anchorage to the extracellular matrix [154]. Matrigel®, mainly composed of laminin and collagen, was selected as it is the most commonly used 3D support matrix for organoid growth [19, 109, 155]. Collagen type I was also tested as a potential cell adhesion ligand since it is the major component of the extracellular matrix and has been shown to support intestinal stem cell growth [20, 22, 114]. Microstructured PEGDA-AA hydrogels were prepared using two different AA concentrations: 0,06% and 0,3% w/v. The concentration of AA added to the prepolymer solution modulates the amount of proteins anchored to the hydrogel following a linear relationship [46, 103]. However, AA also has a major effect on the morphology of the microstructures; increased concentrations (values above 0,3%) causing smaller total heights and tip diameters; hence not desired [103]. The microstructures fabricated with 0,3% w/v AA concentration were shown to have realistic sizes and support the growth of Caco-2 cells [46, 103]. Therefore, microstructured hydrogels prepared with 0,3% w/v AA were tested to see if they allowed intestinal organoid-derived cell growth, along with hydrogels prepared with a much lower AA concentration (0,06% w/v) as an extreme condition to better illustrate the effect of very low ligand amounts, while minimally affecting the morphology. The different scaffolds were then functionalized with laminin, Matrigel® (10% diluted), and collagen type I (10% diluted) and organoid-derived crypts were cultured for 5 days. Among the conditions studied, intestinal organoid-derived cells grew to form

a monolayer only on collagen type I functionalized microstructured hydrogels that were fabricated with 0,3% w/v AA (Figure 2.22). However, neither laminin nor Matrigel® functionalization allowed intestinal cell adhesion (Figure 2.22). Laminin is extensively used for cultures of epithelial cell lines [156–158]. In fact, Caco-2 cells were successfully grown on these microstructured PEGDA hydrogels functionalized with laminin [46, 103]. Moreover, Gjorevski *et al.* showed that $Lgr5^+$ stem cells grew to form organoids when embedded into PEG hydrogels functionalized with laminin [111]. However, with the AA and laminin concentrations tested in this work, it was not sufficient to promote organoid-derived cell adhesion presumably due to sub-optimal ligand densities. Similarly, although Matrigel® is extensively used for organoid growth, Matrigel® functionalized microstructured hydrogels failed to support organoid-derived cell adhesion. This can be explained by the differences in the amounts of ligands presented to the cells. In our material, only the surface is functionalized with Matrigel® (Figure 2.21) and the amount added is limited by the AA concentration, as oppose to the undiluted material used for organoid growth. Collagen type I, however, successfully promoted organoid cell adhesion when the AA used was 0,3% w/v. Therefore, collagen type I was chosen to functionalize the microstructured hydrogels, fabricated with 0,3% w/v AA, for further cell culture experiments.

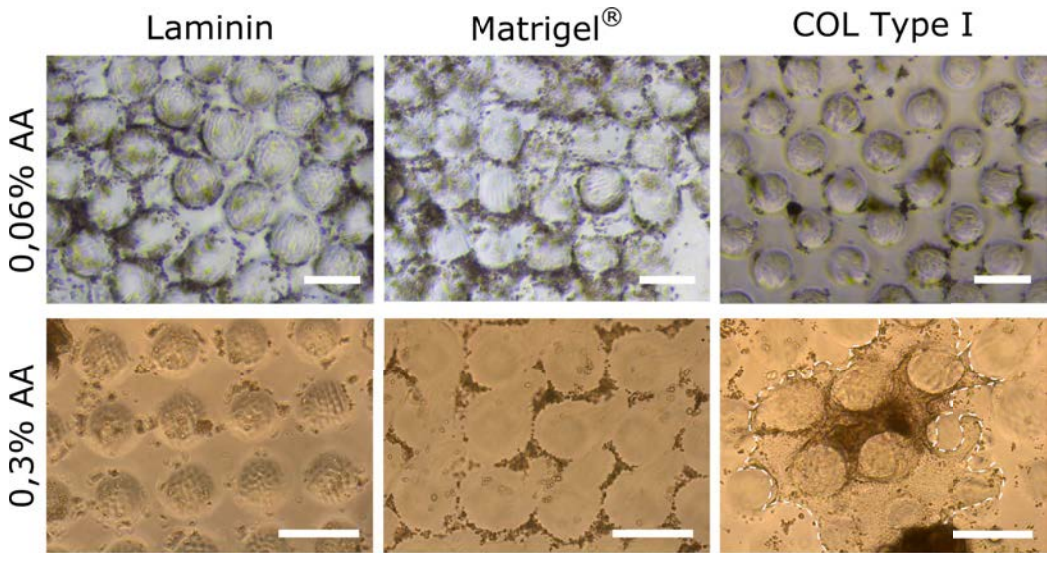

Figure 2.22: *Bright field microscopy images of intestinal organoid-derived crypts cultured on the microstructured PEGDA hydrogels fabricated with 0,06% or 0,3% AA w/v, functionalized with laminin, Matrigel® or collagen type I (COL Type I) after 5 days of culture. The seeding density used was 2500 crypts.cm^{-2}. Note that only when the AA concentration was 0,3% and the hydrogels were functionalized with collagen type I, the intestinal cells grew to form a monolayer. The white dashed line marks the epithelial border.*

2.3.5.2 Effects of seeding density

The seeding density is an important factor to be considered in cell-based assays, and the use of high seeding densities has shown to improve *in vitro* cell viability [159] and even affect stem cell lineage commitment [160]. However, seeding density is limited when working with primary cells. In the case of intestinal epithelial cells derived from organoids, the availability of the organoid stocks is limited since the maintenance and expansion of these cultures are expensive. Therefore, there is a trade off between the cell viability and the cost. To address this problem, we thought of decreasing the seeding area from 0,79 cm^2 for the entire microstructured hydrogel to 0,31 cm^2 (see Section 2.2.6.1). We did that by confining cells at the seeding with the use of a pipette tip (see Figure 2.13). In this manner, it was possible to increase seeding densities from 1400 crypts.cm^{-2} to 3500 crypts.cm^{-2} while using the same total organoid-derived crypt number. Figure 2.23 shows the growth of organoid-derived cells on microstructured hydrogels seeded at different seeding densities. In fact, when the seeding density was low ($\approx$ 1400 crypts.cm^{-2}) (Figure 2.23 A) the intestinal cells didn't grow on the material surface. Whereas, when the seeding density was $\approx$ 2500 crypts.cm^{-2}

and higher, the intestinal cells successfully colonized the surface (Figure 2.23 B, C). The total amount of crypts used in figure 2.23 A and C were the same, nevertheless, the seeding density was increased by decreasing the seeding area. This qualitative assessment demonstrates that high seeding densities are necessary for intestinal epithelial monolayer growth and there appears to be a critical density threshold below which the cells do not grow.

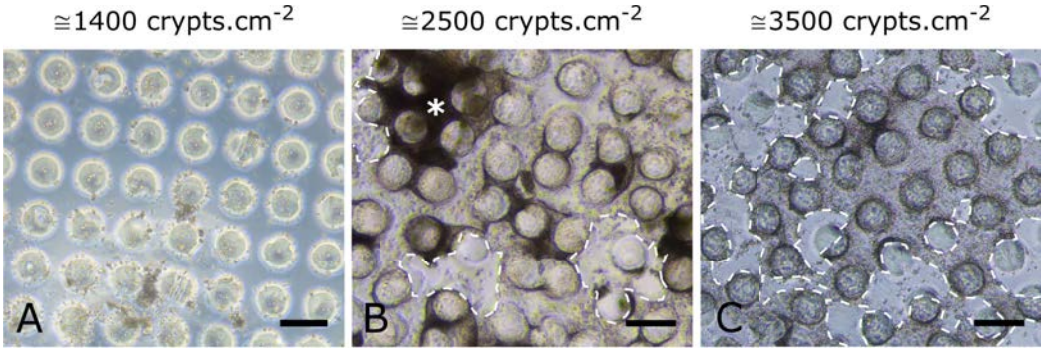

Figure 2.23: *Bright field microscopy images of intestinal organoid-derived crypts cultured on the microstructured PEGDA hydrogels at ≈ 1400 crypts.cm^{-2} (A), ≈ 2500 crypts.cm^{-2} (B), and ≈ 3500 crypts.cm^{-2} (C) seeding densities. The fabrication conditions of the microstructured hydrogels were: 6,5% w/v P6000 and 120 s of UV exposure for A and C and 5% w/v P6000 and 150 s of UV exposure for B (a second exposure 15 s was used to hold the microstructures together). The images were taken at day 6 of the cultures. Scale bars: 200 μm.*

2.3.5.3 Effects of microstructure height and mechanical properties on the growth of intestinal epithelial monolayers

A screening of organoid-derived epithelial cell growth on villus-like microstructured PEGDA-AA hydrogels with different heights and mechanical properties was performed by assessing the surface coverage. For that, microstructures with two very different heights, 418,4 ± 11,0 μm and 137,1 ± 15,9 μm were used for the assessment of the effect of the microstructure height. Also, microstructures with the same height were fabricated using the same exposure time (70 s) at different P6000 concentrations (6,5% w/v and 10% w/v) to assess the effect of the mechanical properties, which depend on the P6000 concentration as we have demonstrated in section 2.3.2 (E values ranging 3 kPa to 11 kPa). The morphologies and the fabrication conditions of the hydrogels are given in figure 2.24 (reproduced from Figure 2.16 for visualization purposes). The hydrogels fabricated in the first condition (Figure 2.24 A) have realistic sized villus-like features (*in vivo* villus heights range between 0,2 to 1 mm [117, 131]); however, scaffolds with much

shorter microstructures can also be useful in *in vitro* modeling of diseases such as celiac disease, in which the size of the villi are severely reduced [161, 162].

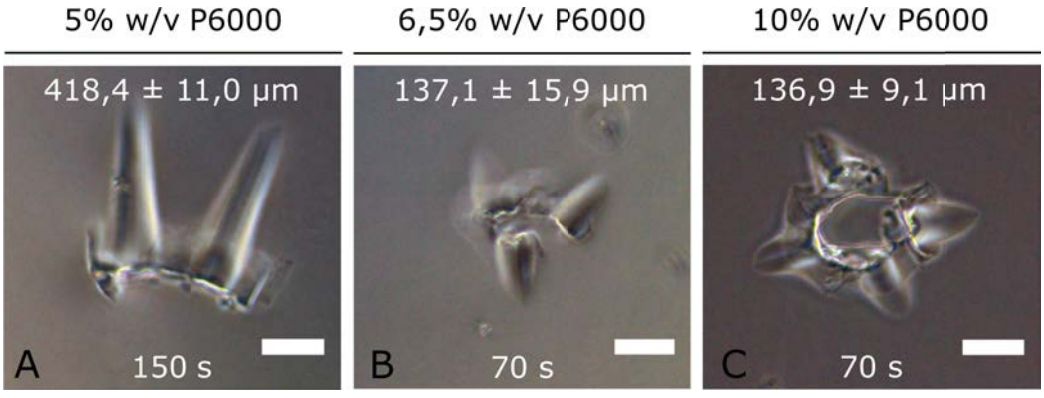

Figure 2.24: *Bright field microscopy images of the microstructured hydrogels fabricated under different conditions; 5% w/v P6000 and 150 s of UV exposure (A), 6,5% w/v P6000 and 70 s of UV exposure (B), and 10% w/v P6000 and 70 s of UV exposure (C). The base of the hydrogels were formed by a second exposure of 15 s (A) and 10 s (B,C). Images (A-C) are reproduced from Figure 2.16 for visualization purposes. Scale bars: 200 µm.*

The microstructured hydrogels were functionalized with collagen type I and cultured with organoid-derived crypts for 9 days. In all of the conditions studied, the intestinal crypts colonized the surface of the material suggesting that once the right cell adhesion ligand (collagen type I) and AA amount (0,3% w/v) were determined, the intestinal cells adhere and spread to form a monolayer on the material surface independent of microstructure heights and varying mechanical properties by varying P6000 concentration (6,5% w/v to 10% w/v) (Figure 2.25 A-C). The surface coverage was quantified for each condition from bright field images acquired as an indication of the monolayer growth (Figure 2.25 D). The surface coverage was ranged between 60% to 69% and there was no statistically significant difference (Student's t-test, $p>0,05$) among the conditions studied. These findings suggest that the microstructure height and the varying mechanical properties within the range studied do not have a significant effect on the growth of the monolayers on the hydrogel surface.

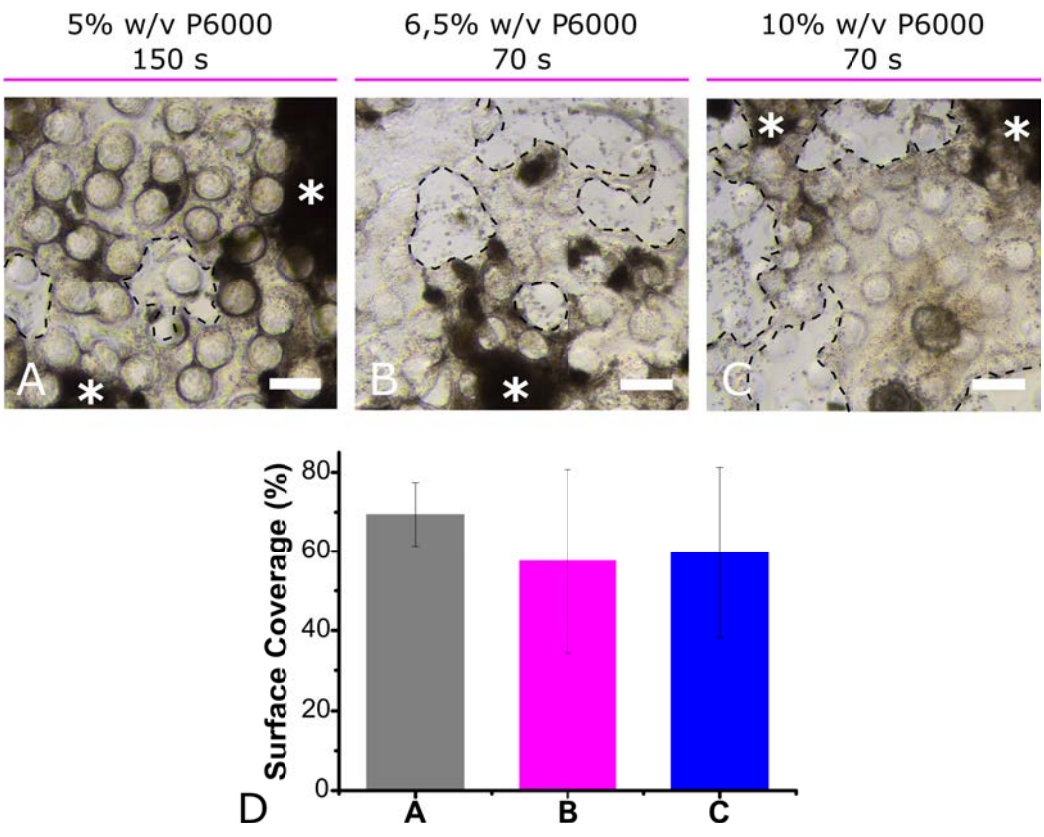

Figure 2.25: *Bright field microscopy images of the intestinal organoid-derived crypts cultured on the microstructured P6000 hydrogels characterized in Figure 2.24 at day 7 of culture (A-C). White asterisk marks accumulated cell clumps, presumably death cells coming from the non-viable organoid pieces that were present at the initial seeding. Scale bars: 200 μm. Graph showing the % surface coverage of the monolayers after 9 days of culture (D). The images were acquired at 4 different locations for each condition (n = 4). The data are presented as mean $\pm$ standard deviation. The error bars represent intra-sample variations.*

2.3.5.4 Effects of conditioned cell culture medium (ISEMF_CM) on the growth of intestinal epithelial monolayers

Intestinal subepithelial myofibroblasts (ISEMFs) produce biochemical factors that promote the stem and transit-amplifying cells' proliferation in the intestinal epithelium [163–165]. Here, we studied the effects of the factors secreted by ISEMFs on the epithelial monolayer surface coverage and the amount of proliferative cells by using conditioned cell culture medium produced by ISEMFs (ISEMF_CM) (see Chapter 1 section 1.2.4.1 for methods). The microstructured hydrogels (given in Figure 2.24) were functionalized with collagen type I and cultured with organoid-derived crypts for 9 days with either ISEMF_CM (supplemented with ENR_CV)

or standard ENR_CV medium. The surface coverage was estimated from bright field microscopy images (Figure 2.26 A) and found to range between 42% to 69%. Among the conditions tested (cell culture media and microstructure type), no statistically significant difference (Student's t-test, p>0,05) was observed.

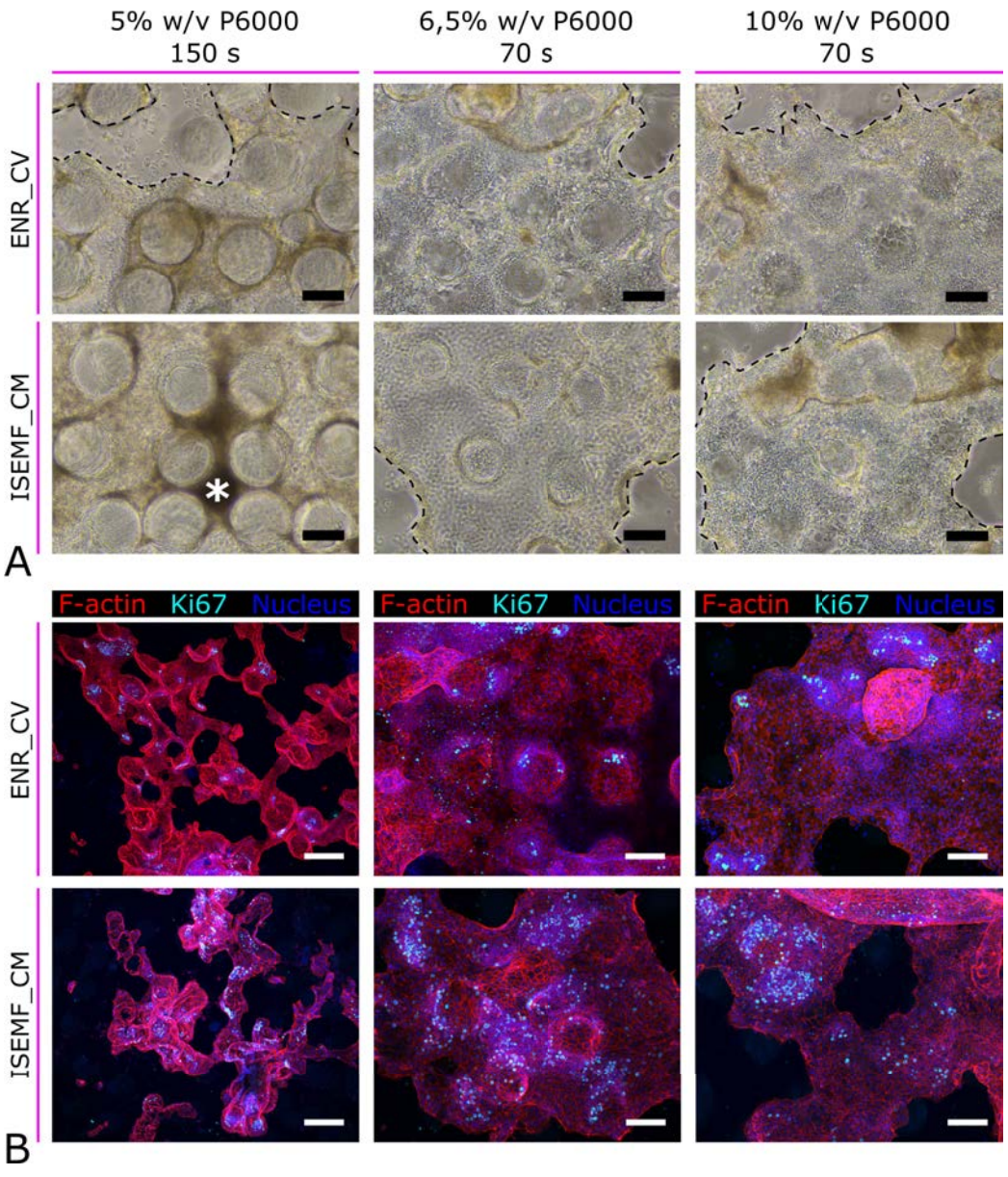

Figure 2.26: *Bright field microscopy images of the intestinal organoid-derived crypts cultured on the microstructured P6000 hydrogels either with ENR_CV medium or ISEMF_CM (supplemented with ENR_CV) at day 7 of culture (A). White asterisk marks accumulated cell clumps, presumably death cells coming from the non-viable organoid pieces that were present at the initial seeding. Scale bars: 100 μm. Immunofluorescence for Ki67 of the intestinal monolayers grown on microstructured P6000 either with ENR_CV medium or ISEMF_CM after 9 of culture (B). Counterstaining was performed for F-actin and nucleus. Scale bars (left panel): 200 μm, (middle and right panel): 100 μm.*

% Ki67$^+$ cells/Total cell #			
	5% w/v P6000	**6,5% w/v P6000**	**10% w/v P6000**
ENR_CV	5,0 ± 2,8	9,3 ± 6,1	7,5 ± 3,5
ISEMF_CM	16,5 ± 0,7	19,7 ± 4,4	14,6 ± 3,0

Table 2.4: *The % Ki67$^+$ cells, normalized to the total cell number, calculated for all the conditions studied that were presented in figure 2.26. The images were acquired at 4 different locations for each condition (n = 4). The data are presented as mean ± standard deviation. The error bars represent intra-sample variations.*

The immunofluorescence for Ki67 revealed that the Ki67$^+$ proliferative cells were found both at the base region and along the pillars. Occasionally, we observed spheroid-like formation on the monolayer as seen in figure 2.26 (right panel). This can be due to a crypt piece growing as a spheroid instead of spreading as monolayer on the material surface. We have also observed that in some regions the tips of the pillars were joined (Figure 2.26, left panel) and this was more pronounced in the case of hydrogels with larger pillars (5% w/v P6000, 150 s UV exposure). One possible explanation for this observation is that the cells at the tips join to form tubular structures, presumably due to the proximity. In a study by Sachs *et al.*, it was shown that the intestinal organoids embedded in collagen gels were contracting the gel and self-organizing to form tubular structures [166]. In a previous study, it was also shown that in close proximity, organoids were fusing to form larger structures [22]. Occasionally, similar observation were made in the cultures of Caco-2 cells grown on the microstructured PEGDA-AA hydrogels [46]. On the other hand, one can appreciate the cobblestone morphology characteristic of the epithelial cells.

The % Ki67$^+$ cells, normalized to the total cell number, were estimated for all the conditions studied and listed in table 2.4. The amount of proliferative cells was significantly higher (Student's t-test, p>0,05) in the monolayers culture with ISEMF_CM compared to ENR_CV on the same type of microstructure. ISEMFs secrete ISC niche factors that drive the proliferation of the Lgr5$^+$ stem cells [163–165]. Therefore, increased amounts of Ki67$^+$ proliferative cells found in the monolayers grown with ISEMF_CM (supplemented with ENR_CV) can be explained by these ISC niche factors found in the conditioned medium. Among these two culture media, ISEMF_CM was selected as it improves the proliferative capacity of the monolayers. Since we haven't observed any preference over the polymer concentration, previously established optimal condition for Caco-2 model [46] i.e.

6,5% w/v P6000 was selected. However, microstructured 6,5% w/v P6000 fabricated with 70 s of UV exposure was not enough to obtain villus-like features with anatomically realistic heights. For that reason, the exposure time was increased to 120 s. The morphology of the microstructures used in the following cell culture experiments can be seen in figure 2.27. The height of the pillars was estimated to be 272,3 $\pm$ 19,0 μm. On these samples, organoid-derived crypts were then cultured using ISEMF_CM as cell culture medium.

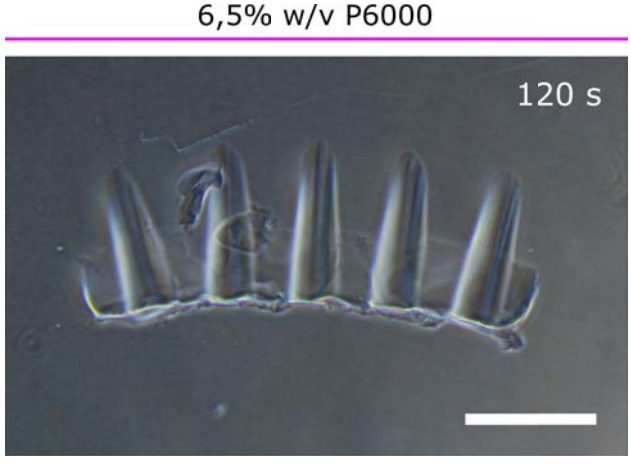

Figure 2.27: *Bright field microscopy image of the microstructured P6000 hydrogel fabricated with the selected fabrication conditions. A second exposure of 15 s was performed to create the hydrogel base. Scale bar: 400 μm.*

2.3.6 Growth of organoid-derived intestinal epithelial monolayers on 3D PEGDA-AA scaffolds

After the initial screening reported in section 2.3.5, the following conditions were selected: 6,5% w/v P6000 with 0,3% w/v AA fabricated by 120 s (pillar formation) + 15 s (base formation) UV exposure times. The scaffolds were functionalized with collagen type I and seeded with intestinal organoid-derived crypts at a density of 3500 crypts.cm^{-2}. The cells were cultured for 6 days with a cell culture medium composed of ISEMF_CM (supplemented with ENR_CV), as it was found beneficial in improving proliferative capacity of the intestinal cells. For comparison, standard ENR_CV medium was also studied as control. The monolayer was more continuous when the culture media was composed of ISEMF_CM supplemented with ENR_CV as oppose to only ENR_CV (Figure 2.28 A, B). The surface coverage was quantified and found to be 55,3% $\pm$ 3,8% and 40,7% $\pm$ 6,6% for ISEMF_CM and ENR_CV, respectively. The surface coverage of the monolayer

was significantly higher (Student's t-test, *p<0,01) when the organoid-derived crypts cultured with ISEMF_CM (Figure 2.28 C). Lei *et al.* reported similar enhancing effects of ISEMF_CM on the growth of intestinal organoids [167]. However, in none of the conditions studied 100% surface coverage was attained. We believe that sub-optimal surface coverage can be improved by increasing the seeding density, or seeding single sorted $Lgr5^+$ stem cells to assure homogeneous cell population. The committed progeny of the stem cells have a life span of 4-5 days. Depending on the composition of the cell pool, the efficiency of the surface coverage can vary. Figure 2.28 D and E shows the immunofluorescence for Ki67 for ENR_CV and ISEMF_CM, respectively. In accordance with the previous findings, the $Ki67^+$ proliferative cells were found both at the base region and along the pillars suggesting that there was no *in vivo* like cellular organization. The percent $Ki67^+$ cells were quantified and found to be 4,3% $\pm$ 3,3% and 7,5% $\pm$ 3,1% for ENR_CV and ISEMF_CM, respectively. The percentage of $Ki67^+$ cells was significantly higher (Student's t-test, *p<0,01) in the monolayers cultured with ISEMF_CM (Figure 2.28 F). Increased surface coverage for the cultures of ISEMF_CM can be explained by the presence of increased amounts of $Ki67^+$ proliferative cells promoting the monolayer expansion, while increased amounts of $Ki67^+$ cells for cultures of ISEMF_CM can be explained by the Wnt pathway activators and enhancers found in the medium [164, 167].

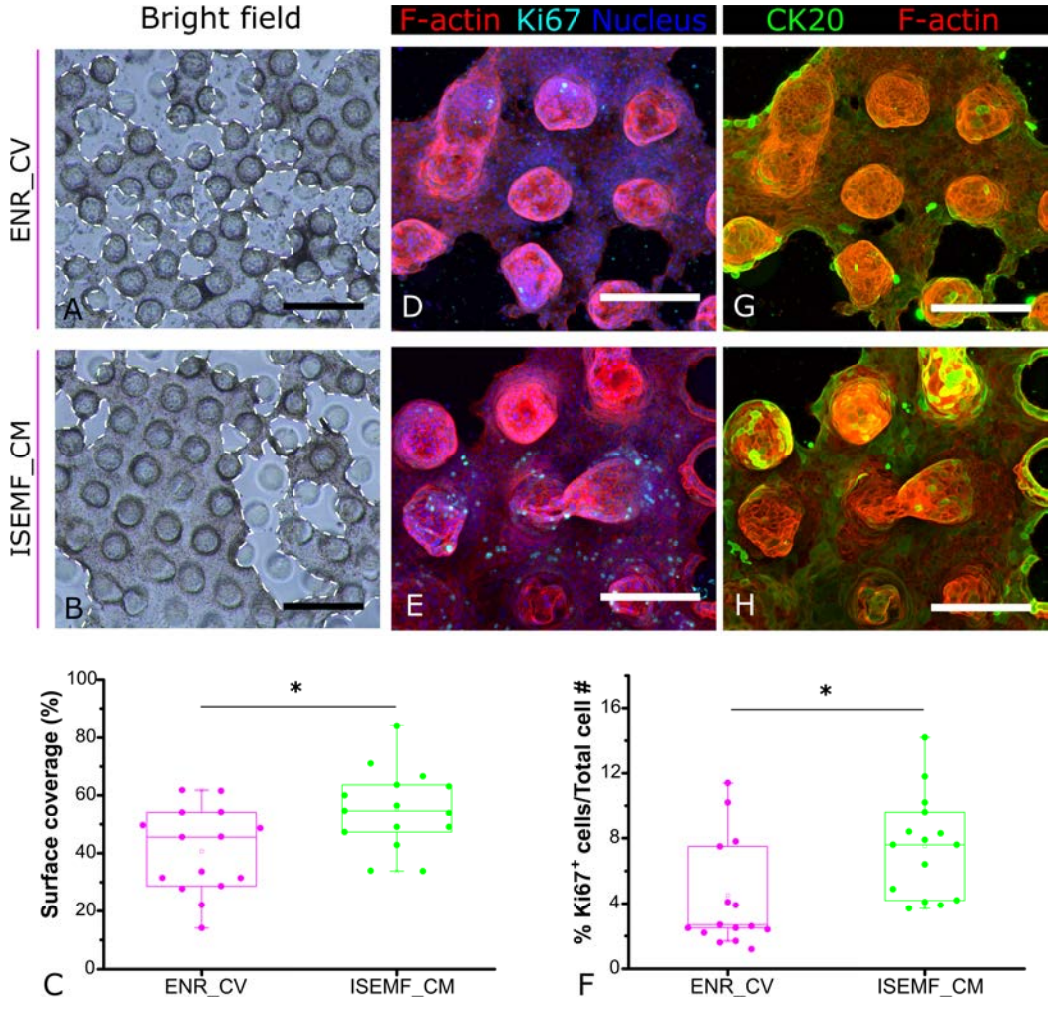

Figure 2.28: *Bright field microscopy images of intestinal organoid-derived crypts cultured on microstructured P6000 hydrogels after 6 days of culture, grown with standard ENR_CV medium (A), and ISEMF_CM supplemented with ENR_CV (B). White dashed line marks the epithelial border. Graph showing the % surface coverage of the monolayers (C). Co-immunofluorescence for Ki67 (D, E) and CK20 (G, H) grown with ENR_CV medium (D, G), and ISEMF_CM supplemented with ENR_CV (E, H). Graph showing % Ki67$^+$ cells normalized to the total cell number (F). The data are presented as mean ± standard deviation (Student's t-test, *p<0,01) of three independent experiments (n = 3). Scale bars (A-B): 400 μm, (D, E, G, H): 200 μm.*

Immunofluorescence for CK20 showed that terminally differentiated cells were found both at the epithelial border and the pillar tips for ENR_CV and ISEMF_CM, respectively. *In vivo*, terminally differentiated cells are found at the villi while the proliferative cells (Lgr5$^+$ stem and transit-amplifying cells) are at the crypts. Co-immunofluorescence for Ki67 and CK20 shows that on our 3D villus-like microstructured hydrogels *in vivo* like compartmentalization of

proliferative and differentiated cells was not present. This might be explained by the apical delivery of the intestinal stem cell niche factors (ENR_CV and ISEMF_CM) as oppose to *in vivo*, where the epithelial cells receive most of the niche factors from the underlying mesenchyme [168, 169]. Cell culture medium containing Wnt pathway activator, Wnt3a, (apical delivery in 2D tissue culture plate setup) was shown to cause the proliferative cells to scatter throughout the entire monolayer [170], disrupting the characteristic crypt-villus organization of the *in vitro* intestinal epithelial monolayers. To overcome this, Transwell® setup, which permits the physical separation between the apical and basolateral compartments of the culture, can be adopted. In the next chapter, we will report the strategies we have developed to adapt our 3D villus-like scaffolds to cell culture setups (Transwell®) permitting the basolateral delivery of intestinal stem cell niche factors.

Altogether, these results suggests that 3D villus-like PEGDA-AA hydrogels appear to be a good candidate to support the growth of intestinal organoid-derived cells that form a monolayer. Photolithography-based simple, moldless fabrication strategy can be easily implemented in *in vitro* models of organoid-derived intestinal epithelium. Moreover, PEGDA hydrogels can be easily tailored to have desired mechanical and swelling properties and bioactive functionality.

2.4 Discussion

It is well established that engineered *in vitro* tissue models that provide cells with a more physiologically representative microenvironment including cell-to-cell and cell-to-matrix interactions together with proper biochemical and mechanical signaling, improve the functionality of such tissue equivalents [171, 172]. Specifically, the functionality of many *in vitro* epithelial tissue is related to their complex 3D forms including cyts, folds, and invaginations [52], one of which is the small intestinal epithelium. Small intestinal epithelium has a complex 3D architecture, formed of finger-like protrusions called villi and invaginations called crypts. This architecture not only increases the absorptive surface area but also is important in the spatial distribution of different cell populations present in the intestinal epithelium. Intestinal stem cells (ISCs) and proliferative progeny resides within the crypt domains, while differentiated absorptive and secretory cells are found in the villus domains. ISC proliferation, migration and differentiation are tightly regulated by biochemical gradients along the crypt-villus axis [168]. In correlation these findings, the tight junction leakiness [173] and the distribution of laminin isoforms [174] vary along the crypt-villus axis. Therefore, mimicking the 3D architecture of the native tissue is expected to be important in the *in vitro* models of the intestinal epithelium. Most of the existing models neglect the characteristic 3D structure of the intestinal epithelium and based on the use of colon cancer cell lines (Caco-2), which fail to recapitulate normal small intestine cell populations and function.

Organoid technology made it possible to culture primary, non-transformed intestinal epithelial cell for prolonged periods of time [19, 20]. Conventionally, organoids are grown embedded in Matrigel® [19, 109] or collagen [20, 21]. These matrices have complex and variable compositions [26, 110], their mechanical and biochemical properties can not be modified in a controlled manner and their microstructuring is not straightforward. Moreover, the closed 3D geometry of the organoids do not allow access to the lumen, hampering their potential applications. In the previous chapter 1, we have developed 2D intestinal epithelium derived from organoids with *in vivo*-like crypt-villus cellular organization and tissue barrier function. In the effort of developing a more complex *in vitro* model of intestinal epithelium we used a photolithographic approach to produce synthetic hydrogel based scaffolds with 3D villus-like architecture and optimized the conditions to permit the growth of primary intestinal epithelial cells derived from organoids.

PEG-based hydrogels have been extensively used as synthetic scaffolds in *in vitro* tissue equivalents due to their highly tunable nature [32]. Gjorevski *et al.* showed its utility as support matrix, as an alternative to Matrigel®, in the organoid cultures [111]. Acrylate derivatives of PEG, e.g. PEGDA, photocrosslink in aqueous solutions, forming hydrogels. The photocrosslinkable nature of PEGDA allows the use of photolithographic techniques for the microstructuring of it. Because of these desirable properties, PEGDA was chosen as the scaffold material.

The formation of 3D bullet-like complex shapes was achieved by photolithography based dynamic polymerization of PEGDA in the presence of oxygen gradients, as previously established in our laboratory [46, 103]. The use of diluted solutions of PEGDA led to soft tissue like mechanical properties (E = 3-11 kPa). Methods such as 3D printing and micromolding can also be used to produce these complex geometries on hydrogels. However, 3D printing are limited in resolution, and require the use of sacrificial materials for manufacturing soft structures [74], while micromolding also requires the use of sacrificial molds and multiple fabrication steps to avoid destruction of the soft hydrogels at the demolding step [54, 66]. Photolithography, on the other hand, is a simple, low cost fabrication technique which only requires a UV lamp and inexpensive acetate photomasks, making it easily implementable in any laboratory. Through this process microstructures with heights similar to that of the small intestine villi could be obtained.

The material to be used as the basement membrane substitute must have the appropriate mechanical properties that resemble those of the basement membrane (3-30 kPa [142, 175]), especially when considering the relevance of the substrate stiffness on the epithelial cell phenotype [176]. Here, we show that the elastic modulus (E) can be easily tailored by changing the PEGDA concentration and the Young's modulus values of the PEGDA-AA hydrogels used (3-11 kPa), presented mechanical properties in the physiological range of the native small intestine [143]. The microstructured PEGDA-AA hydrogels favored the formation of intestinal epithelial monolayers, as oppose to the much softer Matrigel® matrix (having an E ranging from tens to hundreds of Pa [177]) that promoted formation of organoids as we have demonstrated in chapter 1.

The water content (the swelling ratio) of the basement membrane substitute is also crucial as it determines the diffusivity of metabolites, biomolecules and waste products across the synthetic construct. The diffusivity of molecules within the hydrogel is particularly relevant in *in vitro* models of intestinal epithelium as the

substrate should not interfere with the permeability and TEER measurements. Models with villus-like architecture that were successfully engrafted with intestinal epithelial cells, were obtained with materials such as PDMS, and poly(lactic acid) [107, 108]; however, these materials do not allow the diffusion of molecules. Here, we show that the PEGDA-AA hydrogels contained a high amount of water and the swelling ratio (Q) can also be tailored easily by changing the PEGDA concentration. It is well known that the hydrogel stiffness (E) and Q are inversely related [178]. In accordance with this fact, we demonstrated that increasing E by increasing the PEGDA concentration, led to a decrease in Q.

PEG-based hydrogels are naturally inert, so they are functionalized with extracellular matrix proteins or their peptide derivatives to allow for cell adhesion and growth. Copolymerizing PEGDA with AA to produce PEGDA hydrogels with flanking carboxyl groups is an easy route to introduce cell adhesion proteins via EDC/NHS mediated amine coupling [179–181]. Using this method, we have shown successful functionalization of the 3D villus-like PEGDA-AA hydrogels with different proteins demonstrating its versatility. Among the ligand types screened, laminin, Matrigel® and collagen type I, only collagen type I supported the growth of organoid-derived intestinal epithelial cell monolayers. The AA amount was also important. The density of protein ligands incorporated to the hydrogel can be controlled by the acrylic acid amount as we demonstrated previously [46, 103]. Here, we showed that the use of 0,3% w/v AA was necessary for intestinal cell growth and lower AA concentration was not enough to provide the cells with sufficient amount of protein ligands.

In vitro models of the human small intestinal epithelium are useful in many applications such as in vitro drug screening, studies of intestinal epithelial physiology and host/pathogen interactions, and disease modeling. Most of the current models lack either the characteristic 3D architecture of the tissue or native intestinal cell populations and function due to the use of cell lines. Lately, these has been some efforts in combining microfabrication techniques and the use of primary intestinal stem cells. Porous poly(lactic-co-glycolic) acid (PLGA) scaffolds have been micromolded into 3D villus-like geometries [54, 67]. These scaffolds have been shown to support the growth of cells derived from mouse intestinal crypts [54]. However, PLGA is a much harder substrate (E $\approx$ 1-2 GPa) than the native basement membrane. Silk-based porous tubular scaffolds with a screw pattern (ridge-like structures of 400 μm in size) were produced using PDMS replica molding [113]. These scaffolds were engrafted with organoid-derived intestinal epithelial cells, which formed epithelial tissue with all major epithelial cell types.

However, the tubular form of these scaffolds are not suitable for standard *in vitro* functional assays; therefore, can not be implemented easily. Moreover, the ridge-like forms do not represent the characteristic finger-like forms of the intestinal villi. In addition, mechanical properties of the silk material is out of the physiological range (E in the range of GPa) [182]. On the other hand, softer collagen hydrogels with realistic villus dimensions and biomimetic round tips were produced by combining photolithography and molding techniques [114]. The scaffolds were incorporated into custom-made cell culture inserts permiting access to both apical and basolateral sides. With the basolateral delivery of ISC niche factors, an *in vitro* epithelium all major cell types and their correct positioning was achieved. However, the fabrication method requires several photolithographic procudures and replica molding; therefore, it is not straightforward. The mechanical and biochemical properties and porosity can not be tailored in an easy, controlled way. In addition, collagen-based scaffolds interferes with the rapidly absorbed hydrophobic drugs [53], hampering their use in the permeability assays of such molecules. We overcome these limitations by using synthetic PEGDA-AA hydrogels that are inert in nature and their mechanical and swelling properties (porosity) can be tuned easily. Besides, due to the photocrosslinkable nature of PEGDA-AA, the formation of 3D villus-like anatomical models can be done by a simple photolithographic approach without the need of a mold. Moreover, carboxylic groups of acrylic acid can be used to attach desired extracellular matrix protein such as collagen type I, to promote cell adhesion. With all these good properties, PEGDA-AA hydrogels offer great versatility to match the cellular requirements of different epithelial tissues. Indeed, we demonstrated that PEGDA-based hydrogels (functionalized with collagen type I) successfully supported the growth of intestinal cells derived from organoids. In addition, we showed that cell culture medium enriched for ISC niche biochemical factors secreted by intestinal subepithelial myofibroblasts (ISEMFs) improved the proliferative capacity and the surface coverage of the epithelial monolayers. ISEMFs are found in the stroma of the intestinal epithelium and shown to play a critical role in the epithelial homeostasis by secreting key factors of the $Lgr5^+$ stem cell niche [169]. ISEMFs are included in numerous *in vitro* models to improve the functionality of the tissue construct [113, 167, 183, 184]. Here, we demonstrated to effect of the media containing the niche factors secreted by ISEMFs (ISEMF_CM) on the monolayer growth. Altogether, microstructured PEGDA-AA hydrogels appear as excellent basement membrane substitute for the growth primary intestinal cell monolayers providing cells with a more realistic microenvironment,

including proper biochemical, mechanical, and topographical signaling. The epithelial monolayer growth can be improved by using a cell culture medium rich in ISC niche biochemical factors.

2.5 Conclusions

Here, we have described the fabrication of 3D villus-like scaffolds on soft PEGDA-based hydrogels using a simple photolithographic approach that doesn't require the use of a mold. For the bioactive functionalization of otherwise inert PEGDA, hydrogels were fabricated by copolymerizing PEGDA with acrylic acid (AA). Microstructures with varying heights could be fabricated by controlling the UV exposure time. It was demonstrated that the mechanical and swelling properties (crosslinking density) of the PEGDA-AA hydrogels could be tuned by changing the PEGDA concentration. The Young's modulus of the PEGDA-AA hydrogels were similar to that of native small intestine. Calculation of volume swelling ratio (as an indicator of crosslinking density) and gel fraction showed that the within the fabrication times assayed crosslinking density was corresponding to the maximum monomer conversion. Cell adhesion proteins were anchored to the flanking carboxyl groups of the PEGDA-AA hydrogels via carbodiimide-mediated amine coupling reaction. Among the cell adhesion ligands tested, collagen type I at relatively high surface densities (controlled by the AA amount) supported the growth of intestinal organoid-derived crypts. On collagen type I functionalized materials, organoid-derived intestinal cells colonized the villus-like hydrogel surface independently of the microstructure heights and PEGDA concentrations (5%-10%) used to fabricate them. Medium derived from intestinal subepithelial myofibroblasts improved the proliferative capacity and surface coverage of the cultures. However, *in vivo* like cellular organization was absent. This can be improved by the basolateral delivery of the media containing stem cell niche factors, which will be addressed in the following chapter. The 3D villus-like scaffold model reported here, developed using a simple photolithographic approach with biomimetic material properties can have a great potential to routinely incorporate 3D architectures in cell culture systems of primary intestinal epithelial cells.

References

[1] Bruce Alberts. *Molecular biology of the cell*. 4th. New York: Garland, 2002.

[2] Francesca Gattazzo, Anna Urciuolo, and Paolo Bonaldo. "Extracellular matrix: A dynamic microenvironment for stem cell niche". In: *Biochimica et Biophysica Acta (BBA) - General Subjects* 1840.8 (2014), pp. 2506–2519.

[3] Cole a DeForest and Kristi S Anseth. "Advances in bioactive hydrogels to probe and direct cell fate." In: *Annual review of chemical and biomolecular engineering* 3 (2012), pp. 421–44.

[4] A C Y Li and A Li. "Basement membrane components". In: *Journal of Clinical Pathology* 56.12 (2003), pp. 885–887.

[5] Takashi Takeuchi and Tatsuo Gonda. "Distribution of the pores of epithelial basement membrane in the rat small intestine." In: *The Journal of veterinary medical science / the Japanese Society of Veterinary Science* 66.6 (2004), pp. 695–700.

[6] Inga C. Teller et al. "Laminins in the developing and adult human small intestine: Relation with the functional absorptive unit". In: *Developmental Dynamics* 236.7 (2007), pp. 1980–1990.

[7] Raghu Kalluri. "Angiogenesis: Basement membranes: structure, assembly and role in tumour angiogenesis". In: *Nature Reviews Cancer* 3.6 (2003), pp. 422–433.

[8] Guoyou Huang et al. "Functional and Biomimetic Materials for Engineering of the Three-Dimensional Cell Microenvironment". In: *Chemical Reviews* 117.20 (2017), pp. 12764–12850.

[9] Elaine N. Marieb, Patricia Brady Wilhelm, and Jon Mallatt. *Human Anatomy, Sixth Edition Media Update*. 2012. ISBN: 9780321753274.

[10] Kuen Yong Lee and David J. Mooney. "Hydrogels for Tissue Engineering". In: *Chemical Reviews* 101.7 (2001), pp. 1869–1880.

[11] N.-A. Peppas et al. "Hydrogels in Biology and Medicine: From Molecular Principles to Bionanotechnology". In: *Advanced Materials* 18.11 (2006), pp. 1345–1360.

[12] Hikmet Geckil et al. "Engineering hydrogels as extracellular matrix mimics". In: *Nanomedicine* 5.3 (2010), pp. 469–484.

[13] Syed K. H. Gulrez, Saphwan Al-Assaf, and Glyn O. "Hydrogels: Methods of Preparation, Characterisation and Applications". In: *Progress in Molecular and Environmental Bioengineering - From Analysis and Modeling to Technology Applications*. InTech, 2011. Chap. 5, pp. 117–150.

[14] Ting Yang. "Mechanical and Swelling properties of Hydrogels". PhD thesis. 2012, p. 67. ISBN: 9789175014715.

[15] Nasim Annabi et al. "Controlling the porosity and microarchitecture of hydrogels for tissue engineering." In: *Tissue engineering. Part B, Reviews* 16.4 (2010), pp. 371–83.

[16] Mohammad Ali Al-Ameen and Gargi Ghosh. "Sensitive quantification of vascular endothelial growth factor (VEGF) using porosity induced hydrogel microspheres". In: *Biosensors and Bioelectronics* 49 (2013), pp. 105–110.

[17] Ya Li Yang, Stéphanie Motte, and Laura J. Kaufman. "Pore size variable type I collagen gels and their interaction with glioma cells". In: *Biomaterials* 31.21 (2010), pp. 5678–5688.

[18] Quynhhoa T. Nguyen et al. "Cartilage-like mechanical properties of poly (ethylene glycol)-diacrylate hydrogels". In: *Biomaterials* 33.28 (2012), pp. 6682–6690.

[19] Toshiro Sato et al. "Single Lgr5 stem cells build crypt-villus structures in vitro without a mesenchymal niche." In: *Nature* 459.7244 (2009), pp. 262–5.

[20] Akifumi Ootani et al. "Sustained in vitro intestinal epithelial culture within a Wnt-dependent stem cell niche." In: *Nature medicine* 15.6 (2009), pp. 701–6.

[21] Ziyad Jabaji et al. "Use of collagen gel as an alternative extracellular matrix for the in vitro and in vivo growth of murine small intestinal epithelium." In: *Tissue engineering. Part C, Methods* 19.12 (2013), pp. 961–9.

[22] Ziyad Jabaji et al. "Type I collagen as an extracellular matrix for the in vitro growth of human small intestinal epithelium." In: *PloS one* 9.9 (2014), e107814.

[23] Andrew Scott et al. "Long-term renewable human intestinal epithelial stem cells as monolayers: A potential for clinical use". In: *Journal of Pediatric Surgery* 51.6 (2016), pp. 995–1000.

[24] C. Moon et al. "Development of a primary mouse intestinal epithelial cell monolayer culture system to evaluate factors that modulate IgA transcytosis". In: *Mucosal Immunology* 7.4 (2014), pp. 818–828.

[25] Kenji Kozuka et al. "Development and Characterization of a Human and Mouse Intestinal Epithelial Cell Monolayer Platform." In: *Stem cell reports* 9.6 (2017), pp. 1976–1990.

[26] Chris S. Hughes, Lynne M. Postovit, and Gilles A. Lajoie. "Matrigel: A complex protein mixture required for optimal growth of cell culture". In: *PROTEOMICS* 10.9 (2010), pp. 1886–1890.

[27] Monica A. Serban, Yanchun Liu, and Glenn D. Prestwich. "Effects of extracellular matrix analogues on primary human fibroblast behavior". In: *Acta Biomaterialia* 4.1 (2008), pp. 67–75.

[28] M P Lutolf and J A Hubbell. "Synthetic biomaterials as instructive extracellular microenvironments for morphogenesis in tissue engineering". In: *Nature Biotechnology* 23.1 (2005), pp. 47–55.

[29] Junmin Zhu and Roger E Marchant. "Design properties of hydrogel tissue-engineering scaffolds." In: *Expert review of medical devices* 8.5 (2011), pp. 607–26.

[30] Anushree Datta. "Characterization of polyethylene glycol hydrogels for biomedical applications". PhD thesis. 2007.

[31] Junmin Zhu. "Bioactive modification of poly(ethylene glycol) hydrogels for tissue engineering". In: *Biomaterials* 31.17 (2010), pp. 4639–4656.

[32] T Ipek Ergenç and Seda Kızılel. "Recent Advances in the Modeling of PEG Hydrogel Membranes for Biomedical Applications". In: *Biomedical engineering, trends in materials science*. 2011, pp. 307–345. ISBN: 978-953-307-513-6.

[33] Enrica Caló and Vitaliy V. Khutoryanskiy. "Biomedical applications of hydrogels: A review of patents and commercial products". In: *European Polymer Journal* 65 (2015), pp. 252–267.

[34] Anisha A. D'souza and Ranjita Shegokar. "Polyethylene glycol (PEG): a versatile polymer for pharmaceutical applications". In: *Expert Opinion on Drug Delivery* 13.9 (2016), pp. 1257–1275.

[35] April M. Kloxin, Julie A. Benton, and Kristi S. Anseth. "In situ elasticity modulation with dynamic substrates to direct cell phenotype". In: *Biomaterials* 31.1 (2010), pp. 1–8.

[36] Amarpreet S. Sawhney, Chandrashekhar P. Pathak, and Jeffrey A. Hubbell. "Bioerodible hydrogels based on photopolymerized poly(ethylene glycol)-co-poly(.alpha.-hydroxy acid) diacrylate macromers". In: *Macromolecules* 26.4 (1993), pp. 581–587.

[37] Jason A. Burdick and Kristi S. Anseth. "Photoencapsulation of osteoblasts in injectable RGD-modified PEG hydrogels for bone tissue engineering". In: *Biomaterials* 23.22 (2002), pp. 4315–4323.

[38] Stephanie J. Bryant and Kristi S. Anseth. "Hydrogel properties influence ECM production by chondrocytes photoencapsulated in poly(ethylene glycol) hydrogels". In: *Journal of Biomedical Materials Research* 59.1 (2002), pp. 63–72.

[39] Martin Ehrbar et al. "Biomolecular hydrogels formed and degraded via site-specific enzymatic reactions." en. In: *Biomacromolecules* 8.10 (2007), pp. 3000–7.

[40] Cole A. DeForest, Brian D. Polizzotti, and Kristi S. Anseth. "Sequential click reactions for synthesizing and patterning three-dimensional cell microenvironments". In: *Nature Materials* 8.8 (2009), pp. 659–664.

[41] K. (Krzysztof) Matyjaszewski and Thomas P. (Thomas Paul) Davis. *Handbook of radical polymerization*. Wiley-Interscience, 2002. ISBN: 0471461571.

[42] B. Yañez-Soto et al. "Biochemically and topographically engineered poly(ethylene glycol) diacrylate hydrogels with biomimetic characteristics as substrates for human corneal epithelial cells". In: *Journal of Biomedical Materials Research - Part A* 101 A.4 (2013), pp. 1184–1194.

[43] Fei Tan et al. "Fabrication of positively charged poly(ethylene glycol)-diacrylate hydrogel as a bone tissue engineering scaffold". In: *Biomedical Materials* 7.5 (2012), p. 055009.

[44] Dany J. Munoz-Pinto et al. "Characterization of sequential collagen-poly(ethylene glycol) diacrylate interpenetrating networks and initial assessment of their potential for vascular tissue engineering". In: *Biomaterials* 40 (2015), pp. 32–42.

[45] Benjamin D. Fairbanks et al. "Photoinitiated polymerization of PEG-diacrylate with lithium phenyl-2,4,6-trimethylbenzoylphosphinate: polymerization rate and cytocompatibility". In: *Biomaterials* 30.35 (2009), pp. 6702–6707.

[46] Albert Garcia Castaño. "Engineering poly (ethylene glycol) diacrylate-based microstructures to develop an in vitro model of small intestinal epithelium". In: *TDX (Tesis Doctorals en Xarxa)* (2018).

[47] Christian Decker and Aubrey D. Jenkins. "Kinetic approach of oxygen inhibition in ultraviolet- and laser-induced polymerizations". In: *Macromolecules* 18.6 (1985), pp. 1241–1244.

[48] Christopher N. Bowman and Christopher J. Kloxin. "Toward an enhanced understanding and implementation of photopolymerization reactions". In: *AIChE Journal* 54.11 (2008), pp. 2775–2795.

[49] Chaenyung Cha et al. "Tuning the dependency between stiffness and permeability of a cell encapsulating hydrogel with hydrophilic pendant chains." In: *Acta biomaterialia* 7.10 (2011), pp. 3719–28.

[50] Ozlem Yasar and Serkan Inceoglu. "Compressive Evaluation of Polyethylene (Glycol) Diacrylate (PEGDA) for Scaffold Fabrication". In: *Volume 2: Materials; Biomanufacturing; Properties, Applications and Systems; Sustainable Manufacturing*. ASME, 2016. ISBN: 978-0-7918-4990-3.

[51] Mojun Zhu, Maria Z. Lerum, and Wei Chen. "How To Prepare Reproducible, Homogeneous, and Hydrolytically Stable Aminosilane-Derived Layers on Silica". In: *Langmuir* 28.1 (2012), pp. 416–423.

[52] T. Mammoto and D. E. Ingber. "Mechanical control of tissue and organ development". In: *Development* 137.9 (2010), pp. 1407–1420.

[53] Jiajie Yu et al. "In vitro 3D human small intestinal villous model for drug permeability determination." In: *Biotechnology and bioengineering* 109.9 (2012), pp. 2173–8.

[54] Cait M Costello et al. "Synthetic small intestinal scaffolds for improved studies of intestinal differentiation." In: *Biotechnology and bioengineering* 111.6 (2014), pp. 1222–32.

[55] Si Hyun Kim et al. "Three-dimensional intestinal villi epithelium enhances protection of human intestinal cells from bacterial infection by inducing mucin expression." en. In: *Integrative biology : quantitative biosciences from nano to macro* 6.12 (2014), pp. 1122–31.

[56] Ying Chen et al. "Robust bioengineered 3D functional human intestinal epithelium". In: *Scientific Reports* 5 (2015), p. 13708.

[57] Ali Khademhosseini and Robert Langer. "Microengineered hydrogels for tissue engineering". In: *Biomaterials* 28.34 (2007), pp. 5087–5092.

[58] Fumiki Yanagawa, Shinji Sugiura, and Toshiyuki Kanamori. "Hydrogel microfabrication technology toward three dimensional tissue engineering". In: *Regenerative Therapy* 3 (2016), pp. 45–57.

[59] Dong Qin, Younan Xia, and George M Whitesides. "Soft lithography for micro-and nanoscale patterning". In: *Nature Protocols* 5.3 (2010), pp. 491–502.

[60] Megan L. McCain et al. "Micromolded gelatin hydrogels for extended culture of engineered cardiac tissues". In: *Biomaterials* 35.21 (2014), pp. 5462–5471.

[61] Daniel E. Heath et al. "Regenerating the cell resistance of micromolded PEG hydrogels". In: *Lab on a Chip* 15.9 (2015), pp. 2073–2089.

[62] Ali Khademhosseini et al. "Micromolding of photocrosslinkable hyaluronic acid for cell encapsulation and entrapment". In: *Journal of Biomedical Materials Research Part A* 79A.3 (2006), pp. 522–532.

[63] Halil Tekin et al. "Responsive microgrooves for the formation of harvestable tissue constructs". In: *Langmuir* 27.9 (2011), pp. 5671–5679.

[64] Andrew P. Golden and Joe Tien. "Fabrication of microfluidic hydrogels using molded gelatin as a sacrificial element". In: *Lab on a Chip* 7.6 (2007), pp. 720–725.

[65] Jong Hwan Sung et al. "Microscale 3-D hydrogel scaffold for biomimetic gastrointestinal (GI) tract model". In: *Lab Chip* 11.3 (2011), pp. 389–392.

[66] Jong Hwan Sung et al. "Microscale 3-D hydrogel scaffold for biomimetic gastrointestinal (GI) tract model." en. In: *Lab on a chip* 11.3 (2011), pp. 389–92.

[67] Cait M Costello et al. "3-D intestinal scaffolds for evaluating the therapeutic potential of probiotics." In: *Molecular pharmaceutics* 11.7 (2014), pp. 2030–9.

[68] Shahab A Shaffiey et al. "Intestinal stem cell growth and differentiation on a tubular scaffold with evaluation in small and large animals." In: *Regenerative medicine* 11.1 (2016), pp. 45–61.

[69] Sean V Murphy and Anthony Atala. "3D bioprinting of tissues and organs". In: *Nature Biotechnology* 32.8 (2014), pp. 773–785.

[70] Xiaolong Tu et al. "3D printed PEGDA microstructures for gelatin scaffold integration and neuron differentiation". In: *Microelectronic Engineering* 158 (2016), pp. 30–34.

[71] Duo Hu et al. "3D bioprinting of cell-laden scaffolds for intervertebral disc regeneration". In: *Materials Letters* 223 (2018), pp. 219–222.

[72] Maggie S. Chen, Yue Zhang, and Liangfang Zhang. "Fabrication and characterization of a 3D bioprinted nanoparticle-hydrogel hybrid device for biomimetic detoxification". In: *Nanoscale* 9.38 (2017), pp. 14506–14511.

[73] Sean V. Murphy and Anthony Atala. "3D bioprinting of tissues and organs". In: *Nature Biotechnology* 32.8 (2014), pp. 773–785.

[74] Christopher S. O'Bryan et al. "Three-dimensional printing with sacrificial materials for soft matter manufacturing". In: *MRS Bulletin* 42.8 (2017), pp. 571–577.

[75] Peng Xue et al. "Microfluidic synthesis of monodisperse PEGDA microbeads for sustained release of 5-fluorouracil". In: *Microfluidics and Nanofluidics* 18.2 (2015), pp. 333–342.

[76] Aaron Sin et al. "The Design and Fabrication of Three-Chamber Microscale Cell Culture Analog Devices with Integrated Dissolved Oxygen Sensors". In: *Biotechnology Progress* 20.1 (2004), pp. 338–345.

[77] Gretchen J. Mahler et al. "Characterization of a gastrointestinal tract microscale cell culture analog used to predict drug toxicity". In: *Biotechnology and Bioengineering* 104.1 (2009), pp. 193–205.

[78] Hyun Jung Kim et al. "Human gut-on-a-chip inhabited by microbial flora that experiences intestinal peristalsis-like motions and flow." In: *Lab on a chip* 12.12 (2012), pp. 2165–74.

[79] Hyun Jung Kim and Donald E Ingber. "Gut-on-a-Chip microenvironment induces human intestinal cells to undergo villus differentiation." en. In: *Integrative biology : quantitative biosciences from nano to macro* 5.9 (2013), pp. 1130–40.

[80] Hiroshi Kimura et al. "An integrated microfluidic system for long-term perfusion culture and on-line monitoring of intestinal tissue models". In: *Lab on a Chip* 8.5 (2008), p. 741.

[81] Qasem Ramadan et al. "NutriChip: nutrition analysis meets microfluidics". In: *Lab Chip* 13.2 (2013), pp. 196–203.

[82] Olivier Henry et al. "Organs-on-Chips with integrated electrodes for Trans-Epithelial Electrical Resistance (TEER) measurements of human epithelial barrier function". In: *Lab Chip* (2017).

[83] Magdalena Kasendra et al. "Development of a primary human Small Intestine-on-a-Chip using biopsy-derived organoids". In: *Scientific Reports* 8.1 (2018), pp. 1–14.

[84] Amy E. Shyer et al. “Bending Gradients: How the intestinal stem cell gets its home”. In: *Cell* 161.3 (2015), pp. 569–580.

[85] Shelby A. Skoog, Peter L. Goering, and Roger J. Narayan. “Stereolithography in tissue engineering”. In: *Journal of Materials Science: Materials in Medicine* 25.3 (2014), pp. 845–856.

[86] Vincent Chan et al. “Three-dimensional photopatterning of hydrogels using stereolithography for long-term cell encapsulation”. In: *Lab on a Chip* 10.16 (2010), p. 2062.

[87] Hyein Seo et al. “Preparation of PEG materials for constructing complex structures by stereolithographic 3D printing”. In: *RSC Advances* 7.46 (2017), pp. 28684–28688.

[88] Jaclyn A.Shepard Neiman et al. “Photopatterning of hydrogel scaffolds coupled to filter materials using stereolithography for perfused 3D culture of hepatocytes”. In: *Biotechnology and Bioengineering* 112.4 (2015), pp. 777–787.

[89] B Ziaie and Babak Ziaie. “Hard and soft micromachining for BioMEMS: review of techniques and examples of applications in microfluidics and drug delivery”. In: *Advanced Drug Delivery Reviews* 56.2 (2004), pp. 145–172.

[90] Pilnam Kim et al. “Fabrication of non-biofouling polyethylene glycol micro- and nanochannels by ultraviolet-assisted irreversible sealing”. In: *Lab on a Chip* 6.11 (2006), p. 1432.

[91] Aleksander Skardal et al. “Photocrosslinkable Hyaluronan-Gelatin Hydrogels for Two-Step Bioprinting”. In: *Tissue Engineering Part A* 16.8 (2010), pp. 2675–2685.

[92] Ruben F. Pereira and Paulo J. Bartolo. “3D bioprinting of photocrosslinkable hydrogel constructs”. In: *Journal of Applied Polymer Science* 132.48 (2015).

[93] Soah Lee, Xinming Tong, and Fan Yang. “Effects of the poly(ethylene glycol) hydrogel crosslinking mechanism on protein release.” In: *Biomaterials science* 4.3 (2016), pp. 405–11.

[94] Lin Lin et al. “Extracellular matrix-mimetic poly(ethylene glycol) hydrogels engineered to regulate smooth muscle cell proliferation in 3-D”. In: *Acta Biomaterialia* 10.12 (2014), pp. 5106–5115.

[95] M Hahn et al. “Photolithographic patterning of polyethylene glycol hydrogels”. In: *Biomaterials* 27.12 (2006), pp. 2519–2524.

[96] Chin-Lin Guo et al. “Long-range mechanical force enables self-assembly of epithelial tubular patterns.” In: *Proceedings of the National Academy of Sciences of the United States of America* 109.15 (2012), pp. 5576–82.

[97] Dinesh Chandra and Alfred J. Crosby. “Self-wrinkling of UV-cured polymer films”. In: *Advanced Materials* 23.30 (2011), pp. 3441–3445.

[98] Trung-Dung Dang et al. “A novel simple preparation method of a hydrogel mold for PDMS micro-fluidic device fabrication”. In: *Journal of Micromechanics and Microengineering* 22.1 (2012), p. 015017.

[99] K. Krutkramelis, B. Xia, and J. Oakey. “Monodisperse polyethylene glycol diacrylate hydrogel microsphere formation by oxygen-controlled photopolymerization in a microfluidic device”. In: *Lab on a Chip* 16.8 (2016), pp. 1457–1465.

[100] Tae Soup Shim, Seung-Man Yang, and Shin-Hyun Kim. "Dynamic designing of microstructures by chemical gradient-mediated growth". In: *Nature Communications* 6 (2015), p. 6584.

[101] Ju Hyeon Kim et al. "Reaction-Diffusion-Mediated Photolithography for Designing Pseudo-3D Microstructures". In: *Small* 13.17 (2017), pp. 1–11.

[102] Principia Dardano et al. "A Photolithographic Approach to Polymeric Microneedles Array Fabrication". In: *Materials* 8.12 (2015), pp. 8661–8673.

[103] Albert Garcia Castaño et al. "Single-step dynamic polymerization photolithography produces complex microstructures on hydrogels to generate a 3D intestinal tissue model". In: *Manuscript* (2018).

[104] Jiajie Yu et al. "Three dimensional human small intestine models for ADME-Tox studies". In: *Drug Discovery Today* 19.10 (2014), pp. 1587–1594.

[105] Lin Wang et al. "Influence of micro-well biomimetic topography on intestinal epithelial Caco-2 cell phenotype". In: *Biomaterials* 30.36 (2009), pp. 6825–6834.

[106] Lin Wang et al. "Synergic effects of crypt-like topography and ECM proteins on intestinal cell behavior in collagen based membranes". In: *Biomaterials* 31.29 (2010), pp. 7586–7598.

[107] Wen-Cheng Yang et al. "Engineering a Biomimetic Villus Array for In Vitro Three-Dimensional Culture of Intestinal Epithelial Cells". In: *Journal of Microelectromechanical Systems* 21.6 (2012), pp. 1418–1425.

[108] Julie Salomon et al. "Contractile forces at tricellular contacts modulate epithelial organization and monolayer integrity". In: *Nature Communications* 8 (2017), p. 13998.

[109] Jason R. Spence et al. "Directed differentiation of human pluripotent stem cells into intestinal tissue in vitro". en. In: *Nature* 470.7332 (2010), pp. 105–109.

[110] Slobodan Vukicevic et al. "Identification of multiple active growth factors in basement membrane matrigel suggests caution in interpretation of cellular activity related to extracellular matrix components". In: *Experimental Cell Research* 202.1 (1992), pp. 1–8.

[111] Nikolce Gjorevski et al. "Designer matrices for intestinal stem cell and organoid culture". In: *Nature* 539.7630 (2016), pp. 560–564.

[112] S S Wilson et al. "A small intestinal organoid model of non-invasive enteric pathogen-epithelial cell interactions." In: *Mucosal immunology* 8.2 (2015), pp. 352–61.

[113] Ying Chen et al. "In vitro enteroid-derived three-dimensional tissue model of human small intestinal epithelium with innate immune responses". In: *PLoS ONE* 12.11 (2017), pp. 1–20.

[114] Yuli Wang et al. "A microengineered collagen scaffold for generating a polarized crypt-villus architecture of human small intestinal epithelium". In: *Biomaterials* 128 (2017), pp. 44–55.

[115] Y. Han et al. "Surface activation of thin silicon oxides by wet cleaning and silanization". In: *Thin Solid Films* 510.1-2 (2006), pp. 175–180.

[116] M N Marsh and J A Swift. "A study of the small intestinal mucosa using the scanning electron microscope". In: *Gut* 10 (1969), pp. 940–949.

[117] Paul Kelly et al. “Responses of small intestinal architecture and function over time to environmental factors in a tropical population”. In: *Am. J. Trop. Med. Hyg.* 70 (2004), pp. 412–419.

[118] Naoki Nakajima and Yoshito Ikada. “Mechanism of Amide Formation by Carbodiimide for Bioconjugation in Aqueous Media”. In: *Bioconjugate Chemistry* 6.1 (1995), pp. 123–130.

[119] Keila B Fonseca et al. “Injectable MMP-sensitive alginate hydrogels as hMSC delivery systems.” In: *Biomacromolecules* 15.1 (2014), pp. 380–90.

[120] Huiyuan Wang et al. “Hybrid Elastin-like Polypeptide-Polyethylene Glycol (ELP-PEG) Hydrogels with Improved Transparency and Independent Control of Matrix Mechanics and Cell Ligand Density.” In: *Biomacromolecules* 15.9 (2014), pp. 3421–8.

[121] Adam Engler et al. “Substrate Compliance versus Ligand Density in Cell on Gel Responses”. In: *Biophysical Journal* 86.1 (2004), pp. 617–628.

[122] Mark Ahearne et al. “Characterizing the viscoelastic properties of thin hydrogel-based constructs for tissue engineering applications.” In: *Journal of the Royal Society, Interface* 2.5 (2005), pp. 455–63.

[123] N. Ch. Padmavathi and P. R. Chatterji. “Structural Characteristics and Swelling Behavior of Poly(ethylene glycol) Diacrylate Hydrogels †”. In: *Macromolecules* 29.6 (1996), pp. 1976–1979.

[124] Demet Melekaslan et al. “Swelling and elasticity of hydrogels based on poly(ethylene oxide) macroinimer”. In: *Polymer International* 53.3 (2004), pp. 237–242.

[125] Valentin Hagel, Tamás Haraszti, and Heike Boehm. “Diffusion and interaction in PEG-DA hydrogels”. In: *Biointerphases Biointerphases Hagel et.al. Biointerphases* 8.8 (2013).

[126] N. A. Peppas and E. W. Merrill. “Crosslinked poly(vinyl alcohol) hydrogels as swollen elastic networks”. In: *Journal of Applied Polymer Science* 21.7 (1977), pp. 1763–1770.

[127] Kittichin Plungpongpan et al. “Preparation of PVP/MHEC Blended Hydrogels via Gamma Irradiation and Their Calcium ion Uptaking and Releasing Ability”. In: *Energy Procedia* 34 (2013), pp. 775–781.

[128] A.J Kuijpers et al. “In vitro and in vivo evaluation of gelatin–chondroitin sulphate hydrogels for controlled release of antibacterial proteins”. In: *Biomaterials* 21.17 (2000), pp. 1763–1772.

[129] Mehrdad Rafat et al. “PEG-stabilized carbodiimide crosslinked collagen–chitosan hydrogels for corneal tissue engineering”. In: *Biomaterials* 29.29 (2008), pp. 3960–3972.

[130] Eric Y. Liu, Sukwon Jung, and Hyunmin Yi. “Improved Protein Conjugation with Uniform, Macroporous Poly(acrylamide- co -acrylic acid) Hydrogel Microspheres via EDC/NHS Chemistry”. In: *Langmuir* 32.42 (2016), pp. 11043–11054.

[131] G. J. Tortora and B. H. Derrickson. *Principles of Anatomy and Physiology*. 14th ed. Wiley Global Education, 2014.

[132] Samuel Clark Ligon et al. “Strategies to Reduce Oxygen Inhibition in Photoinduced Polymerization”. In: *Chemical Reviews* 114.1 (2014), pp. 557–589.

[133] Dhananjay Dendukuri et al. “Modeling of Oxygen-Inhibited Free Radical Photopolymerization in a PDMS Microfluidic Device”. In: *Macromolecules* 41.22 (2008), pp. 8547–8556.

[134] Burcu Gumuscu et al. “Photopatterning of Hydrogel Microarrays in Closed Microchips”. In: *Biomacromolecules* 16.12 (2015), pp. 3802–3810.

[135] Priyalakshmi Viswanathan et al. “Mimicking the topography of the epidermal–dermal interface with elastomer substrates”. In: *Integr. Biol.* 8.1 (2016), pp. 21–29.

[136] Nermin Orakdogen and Oguz Okay. “Correlation between crosslinking efficiency and spatial inhomogeneity in poly(acrylamide) hydrogels”. In: *Polymer Bulletin* 57.5 (2006), pp. 631–641.

[137] P M Gilbert et al. “Substrate elasticity regulates skeletal muscle stem cell self-renewal in culture.” en. In: *Science (New York, N.Y.)* 329.5995 (2010), pp. 1078–81.

[138] Emi Y Tokuda, Jennifer L Leight, and Kristi S Anseth. “Modulation of matrix elasticity with PEG hydrogels to study melanoma drug responsiveness.” In: *Biomaterials* 35.14 (2014), pp. 4310–8.

[139] Lisa A Flanagan et al. “Neurite branching on deformable substrates.” In: *Neuroreport* 13.18 (2002), pp. 2411–5.

[140] Parul Natvar Patel, Connie Kathleen Smith, and Charles W. Patrick. “Rheological and recovery properties of poly(ethylene glycol) diacrylate hydrogels and human adipose tissue”. In: *Journal of Biomedical Materials Research Part A* 73A.3 (2005), pp. 313–319.

[141] Adam J Engler et al. “Matrix elasticity directs stem cell lineage specification.” In: *Cell* 126.4 (2006), pp. 677–89.

[142] D. Liao et al. “The effect of epidermal growth factor on the incremental Young’s moduli in the rat small intestine”. In: *Medical Engineering and Physics* 25.5 (2003), pp. 413–418.

[143] Javier Sotres et al. “Ex-Vivo Force Spectroscopy of Intestinal Mucosa Reveals the Mechanical Properties of Mucus Blankets”. In: *Scientific Reports* 7.1 (2017), p. 7270.

[144] Dennis E Discher, David J Mooney, and Peter W Zandstra. “Growth factors, matrices, and forces combine and control stem cells.” In: *Science (New York, N.Y.)* 324.5935 (2009), pp. 1673–7.

[145] Guoyou Huang et al. “Engineering three-dimensional cell mechanical microenvironment with hydrogels”. In: *Biofabrication* 4.4 (2012), p. 042001.

[146] Silviya P Zustiak, Hacene Boukari, and Jennie B Leach. “Solute diffusion and interactions in cross-linked poly(ethylene glycol) hydrogels studied by Fluorescence Correlation Spectroscopy.” en. In: *Soft matter* 6.15 (2010), pp. 3609–3618.

[147] Deena A Rennerfeldt et al. “Tuning mechanical performance of poly(ethylene glycol) and agarose interpenetrating network hydrogels for cartilage tissue engineering.” In: *Biomaterials* 34.33 (2013), pp. 8241–57.

[148] Larry J Millet et al. “Characterization of mass and swelling of hydrogel microstructures using MEMS resonant mass sensor arrays.” In: *Small (Weinheim an der Bergstrasse, Germany)* 8.16 (2012), pp. 2555–62.

[149] E.H. Nafea, L.A. Poole-Warren A. Marson, and P.J. Martens. “Immunoisolating semipermeable membranes for cell encapsulation: Focus on hydrogels”. In: *Journal of Controlled Release* 154.2 (2011), pp. 110–122.

[150] Christopher N. Bowman and Nikolaos A. Peppas. "Initiation and termination mechanisms in kinetic gelation simulations". In: *Journal of Polymer Science Part A: Polymer Chemistry* 29.11 (1991), pp. 1575–1583.

[151] Devdatt L Kurdikar and Nikolaos A Peppas. "A kinetic study of diacrylate photopolymerizations". In: *Polymer* 35.5 (1994), pp. 1004–1011.

[152] Robert A. Scott and Nicholas A. Peppas. "Compositional effects on network structure of highly cross-linked copolymers of PEG-containing multiacrylates with acrylic acid". In: *Macromolecules* 32.19 (1999), pp. 6139–6148.

[153] Peter Jung et al. "Isolation and in vitro expansion of human colonic stem cells". In: *Nature Medicine* 17.10 (2011), pp. 1225–1227.

[154] Hynda K. Kleinman et al. "Isolation and Characterization of Type IV Procollagen, Laminin, and Heparan Sulfate Proteoglycan from the EHS Sarcoma". In: *Biochemistry* 21.24 (1982), pp. 6188–6193.

[155] Hiroyuki Miyoshi and Thaddeus S Stappenbeck. "In vitro expansion and genetic modification of gastrointestinal stem cells in spheroid culture". In: *Nature Protocols* 8.12 (2013), pp. 2471–2482.

[156] Tuomas Pakkala et al. "Function of Laminins and Laminin-Binding Integrins In Gingival Epithelial Cell Adhesion". In: *Journal of Periodontology* 73.7 (2002), pp. 709–719.

[157] Claudia Drewniok et al. "Molecular interactions of B-CAM (basal-cell adhesion molecule) and laminin in epithelial skin cancer". In: *Archives of Dermatological Research* 296.2 (2004), pp. 59–66.

[158] Azusa Hotta et al. "Laminin-based cell adhesion anchors microtubule plus ends to the epithelial cell basal cortex through LL5α/β". In: *The Journal of Cell Biology* 189.5 (2010), pp. 901–917.

[159] Mona Dvir-Ginzberg et al. "Liver Tissue Engineering within Alginate Scaffolds: Effects of Cell-Seeding Density on Hepatocyte Viability, Morphology, and Function". In: *Tissue Engineering* 9.4 (2003), pp. 757–766.

[160] Rowena McBeath et al. "Cell Shape, Cytoskeletal Tension, and RhoA Regulate Stem Cell Lineage Commitment". In: *Developmental Cell* 6.4 (2004), pp. 483–495.

[161] E. V. Marietta, C. S. David, and J. A. Murray. "Important lessons derived from animal models of celiac disease". In: *International Reviews of Immunology* 30.4 (2011), pp. 197–206.

[162] Naiyana Gujral, Hugh J. Freeman, and Alan B.R. Thomson. "Celiac disease: Prevalence, diagnosis, pathogenesis and treatment". In: *World Journal of Gastroenterology* 18.42 (2012), pp. 6036–6059.

[163] Alex Gregorieff et al. "Expression Pattern of Wnt Signaling Components in the Adult Intestine". In: *Gastroenterology* 129.2 (2005), pp. 626–638.

[164] Henner F. Farin, Johan H. Van Es, and Hans Clevers. "Redundant Sources of Wnt Regulate Intestinal Stem Cells and Promote Formation of Paneth Cells". In: *Gastroenterology* 143.6 (2012), 1518–1529.e7.

[165] Z. Kabiri et al. "Stroma provides an intestinal stem cell niche in the absence of epithelial Wnts". In: *Development* 141.11 (2014), pp. 2206–2215.

[166] Norman Sachs et al. "Intestinal epithelial organoids fuse to form self-organizing tubes in floating collagen gels." In: *Development* 144.6 (2017), pp. 1107–1112.

[167] Nan Ye Lei et al. "Intestinal subepithelial myofibroblasts support the growth of intestinal epithelial stem cells". In: *PLoS ONE* 9.1 (2014).

[168] Toshiro Sato and Hans Clevers. "Growing self-organizing mini-guts from a single intestinal stem cell: mechanism and applications." In: *Science (New York, N.Y.)* 340.6137 (2013), pp. 1190–4.

[169] Manolis Roulis and Richard A. Flavell. "Fibroblasts and myofibroblasts of the intestinal lamina propria in physiology and disease". In: *Differentiation* 92.3 (2016), pp. 116–131.

[170] Curtis A. Thorne et al. "Enteroid Monolayers Reveal an Autonomous WNT and BMP Circuit Controlling Intestinal Epithelial Growth and Organization". In: *Developmental Cell* 44.5 (2018), 624–633.e4.

[171] Melinda C. Cushing and Kristi S. Anseth. "Hydrogel cell cultures". In: *Science* 316.5828 (2007), pp. 1133–1134.

[172] Alison Abbott. "Biology's new dimension". In: *Nature* 424.6951 (2003), pp. 870–872.

[173] BrittMarie M. Fihn, Anders Sjoqvist, and Mats Jodal. "Permeability of the rat small intestinal epithelium along the villus-crypt axis: Effects of glucose transport". In: *Gastroenterology* 119.4 (2000), pp. 1029–1036.

[174] Jean-Francois Beaulieu. "Differential expression of the VLA family of integrins along the crypt-villus axis in the human small intestine." In: *Journal of cell science* 102 (1992), pp. 427–36.

[175] Laura A. Johnson et al. "Matrix stiffness corresponding to strictured bowel induces a fibrogenic response in human colonic fibroblasts". In: *Inflammatory Bowel Diseases* 19.5 (2013), pp. 891–903.

[176] Ovijit Chaudhuri et al. "Extracellular matrix stiffness and composition jointly regulate the induction of malignant phenotypes in mammary epithelium". In: *Nature Materials* 13.10 (2014), pp. 970–978.

[177] Shauheen S Soofi et al. "The elastic modulus of Matrigel as determined by atomic force microscopy." In: *Journal of structural biology* 167.3 (2009), pp. 216–9.

[178] Cole A. DeForest and Kristi S. Anseth. "Advances in Bioactive Hydrogels to Probe and Direct Cell Fate". In: *Annual Review of Chemical and Biomolecular Engineering* 3.1 (2012), pp. 421–444.

[179] P.D. Drumheller and J.A. Hubbell. "Polymer Networks with Grafted Cell Adhesion Peptides for Highly Biospecific Cell Adhesive Substrates". In: *Analytical Biochemistry* 222.2 (1994), pp. 380–388.

[180] Yoko Matsumoto et al. "Hydrogel based 2D-photonic crystal including acrylic acid for biosensing application". In: (2014).

[181] Woojin Lee, Tae Gyu Lee, and Won-Gun Koh. "Grafting of Poly(acrylic acid) on the Poly(ethylene glycol) Hydrogel Using Surface-initiated Photopolymerization for Covalent Immobilization of Collagen". In: *J. Ind. Eng. Chem* 13.7 (2007), pp. 1195–1200.

[182] Leng Duei Koh et al. “Structures, mechanical properties and applications of silk fibroin materials”. In: *Progress in Polymer Science* 46 (2015), pp. 86–110.

[183] Frédéric G Sala et al. “A multicellular approach forms a significant amount of tissue-engineered small intestine in the mouse.” In: *Tissue engineering. Part A* 17.13-14 (2011), pp. 1841–50.

[184] Nicholas Lahar et al. “Intestinal subepithelial myofibroblasts support in vitro and in vivo growth of human small intestinal epithelium”. In: *PLoS ONE* 6.11 (2011), pp. 1–9.

Chapter 3

Development and characterization of spatio-chemical gradients on 3D villus-like PEGDA hydrogels to modulate ISC behavior

3.1 Introduction

Biomolecular gradients control many important biological processes such as tissue development [1], migration of immune cells [2], and cancer metastasis [3]. Biomolecular gradients are key in biological processes that take place in the intestinal epithelium. The intestinal epithelium is continuously renewed due to the presence of intestinal stem cells (ISCs) [4]. ISCs reside within the crypts of the crypt-villus units of the intestinal epithelium [4]. ISCs divide every 24 h and give rise to all other cell types. The transit amplifying daughter (TA) cells migrate up along the villi, differentiate, and eventually shed off at the villi tips [4, 5]. The major cell types that derive from the stem cells are: terminally differentiated absorptive cells (enterocytes) and secretory cells (Goblet and enteroendocrine cells) that are found in the villi, and neigboring Paneth cells that provide ISCs with essential niche signaling [6]. This homeostasis is regulated by the tightly controlled spatio-chemical gradients of well-characterized signaling pathways: epidermal growth factor (EGF), Wingless/Int (Wnt) and bone morphogenetic protein (BMP) signaling [5]. These factors create biochemical gradients along the vertical axis of the intestinal villi and control the growth, migration and differentiation of the intestinal stem cells [5] (Figure 3.1). While EGF and Wnt are essential for the stemness state (proliferation of the cells without reaching the differentiation), BMP

negatively regulates this process [5].

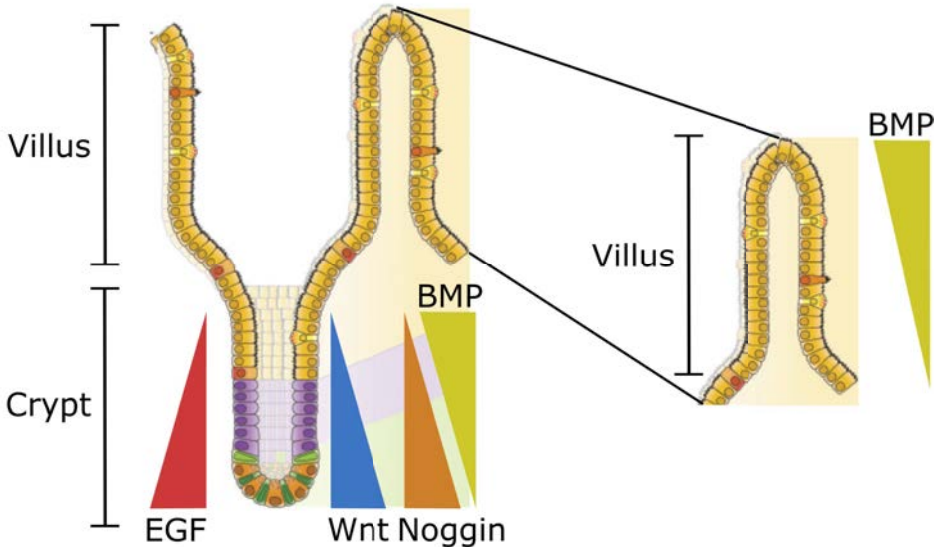

Figure 3.1: *Gradients of factors reported to be related to ISC maintanence, migration and differentiation. Adopted from Carulli et al.[7].*

Wnt pathway is the main pathway controling ISC proliferation. The activators of Wnt pathway are secreted by Paneth cells that reside side by side with the ISCs in the crypts [8] and the mesenchymal cells such as intestinal subepithelial myofibroblasts that are found beneath the crypts [9–11]. The subepithelial myofibroblasts were also shown to produce the enhancers of the Wnt pathway, e.g. R-Spondins [11, 12]. EGF signals exert strong mitogenic effects on ISCs. Finally, BMP signals are active in the villus compartment (Figure 3.1), but its inhibitor Noggin is routinely used in ISC cultures. Another necessary signaling for the ISC maintenance is the Notch lateral inhibition provided by the Paneth cells through membrane bound proteins [5]. However, there are no soluble factors involved in this pathway.

In an ideal *in vitro* model of intestinal epithelium derived from ISCs, *in vivo*-like spatio-chemical gradients of key niche factors should be considered.

Synthetic hydrogels are 3D hydrophilic matrices which are extensively used in regenerative medicine applications due to their unique biocompatibility, flexible methods of synthesis, range of constituents, and tunable physicochemical and mechanical properties [13]. They can serve as tissue engineering scaffolds, drug and protein delivery constructs, and adhesives or barriers between tissue and material surfaces [13]. These 3D matrices are capable of imbibing large amounts of

water and biological fluids without dissolving due to their chemically or physically crosslinked networks [14]. The network structure of the hydrogels is determinant in solute transport within the hydrogel; therefore, has to be considered as one of the most important design parameters. The network properties of the hydrogels, such as their degree of crosslinking, directly influence their water content and pore (mesh) size (Figure 3.2). These, in turn, dictate the diffusivity of molecules through their networks, and their mechanical properties [15]. As a rule of thumb, as the crosslinking density increases, the water content and the molecule diffusivity within the hydrogel decrease, while the stiffness of the hydrogel increases [15]. The most important parameters used to characterize the network structure of hydrogels are the polymer volume fraction in the swollen state ($V_{2,s}$), the molecular weight of the polymer chains between two neighboring crosslinking points (M_c), and the corresponding mesh size (ξ) [14].

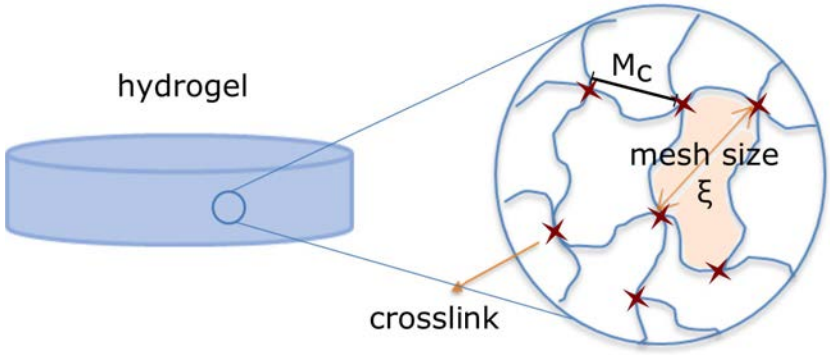

Figure 3.2: *Schematic representation of the mesh size (ξ) and the average molecular weight between two adjacent crosslinks (M_c).*

The $V_{2,s}$ is the amount of polymer in the gel, in other words, is a measure of the amount of liquid imbibed and retained by the hydrogel. The M_c is a measure of the degree of crosslinking of the polymer and the ξ is the distance between two adjacent crosslinks, which provides a measure of the space available between the macromolecular chains (e.g. relevant for diffusion studies). It is important to note that only average values of M_c and ξ can be calculated due to the random nature of the polymerization [14]. All these parameters are related to one another, and can be determined by various theoretical models and experimental techniques, all of which assume that the polymer network parameters follow a Gaussian distribution.

The two most common theories used to describe the network structure of hydrogels and to determine network parameters are rubber elasticity theory and equilibrium swelling theory [13, 14]. Rubber elasticity theory calculates the M_c by taking advantage of the description of the elastic properties of hydrogels. When hydrogels are subjected to tensions, they respond elastically if the deformation is usually less than 20% [14, 16]. To be able to analyze the structure and properties of hydrogels using this theory, it is necessary to know their shear modulus (G) [17]. Subsequently, the average molecular weight between crosslinks M_c, will be calculated with the following equation:

$$\frac{1}{M_c} = \frac{GQ^{1/3}}{RT'C_{2,r}} + \frac{2}{M_n} \tag{3.1}$$

where Q is the volume swelling ratio of hydrogel, R is the ideal gas constant, T' is the absolute temperature at which the shear modulus was measured, $C_{2,r}$ is the polymer concentration in the solution before crosslinking and M_n is the average molecular weight of the polymer [17].

Equilibrium swelling theory, on the other hand, is based on the swelling behavior of hydrogels. The principle of swelling is characterized by a thermodynamic balance between the internal energy changes of the extending polymer chains and the entropy change due to the diffusing solvent molecules. Hydrogels imbibe the solvent until reaching the equilibrium point when the potential difference is 0 [18]. Flory-Rehner equilibrium swelling model [19] calculates M_c by using the following equation:

$$\frac{1}{M_c} = \frac{2}{M_n} - \frac{\frac{v}{V_1} * [ln(1 - V_{2,s}) + V_{2,s} + \chi * V_{2,s}^2]}{(V_{2,s})^{1/3} - \frac{V_{2,s}}{2}} \tag{3.2}$$

where v is the specific volume of the polymer, V_1 is the molar volume of the solvent and finally, χ is the value of the polymer-solvent interaction parameter [20].

The mesh size (ξ) is a function of M_c and $V_{2,s}$ [21] (Eqn. 3.3) and once M_c is determined using either of the theories, ξ can be calculated using this relation (see Section 3.2.1 for detailed calculations).

$$\xi = f(M_c * V_{2,s}) \tag{3.3}$$

Both equilibrium swelling theory and rubber elasticity theory rely on experimentally determined gel properties to estimate M_c. However, hydrogels used

in regenerative medicine can also be formed by physical crosslinks, hydrogen-bonded structures or physical entanglements, in addition to chemical crosslinks. Moreover, due to the random nature of polymerization, network imperfections, such as loops and entanglements, can be formed. Though, these theories treat all types of junctions as tie points with equivalent behavior as the covalent crosslinks [13].

Due to the fact that hydrogels are very good in facilitating solute diffusion, they are good candidates as bioactive scaffolds that deliver critical biological factors in controlled fashion [22, 23]. Moreover, as their mechanical properties resemble that of the soft tissue, and their chemical structure can be functionalized to resemble the extracellular matrix, they have been increasingly used as *in vitro* microenvironments mimicking *in vivo* stem cell niches [24]. However, to recapitulate the spatial and temporal characteristics of the complex stem cell niches it is crucial to incorporate the gradients of key biomolecular factors in the design of such systems [25]. For the creation of such gradients, the microfluidic technology, which permits manipulation of nanoliters and picoliters of liquid with precise control over the deposition of the biomolecules, has been widely used [25]. Such gradients can be generated either by flow-based or by free-diffusion based approaches, and can be formed both in two-dimensional (2D) and three-dimensional (3D) cellular microenvironments [26].

Flow-based gradient generators produce biomolecular concentration gradients by bringing together streams of fluids composed of different chemical species or different concentrations of the same species in a microfluidic channel where the solutes are allowed to diffuse across the interface as they flow down the microchannel [2, 26, 27]. Embryonic stem cell colonies grown on gelatin films stimulated by spatially controlled gradients generated in this fashion were differentiated successfully [27]. In other studies, PEG hydrogel films were patterned with gradients of cell adhesion proteins using a flow-based gradient generator and they were used in single-cell migration studies [28, 29]. Although these 2D approaches were proven to be useful they omit the third dimension, an important factor of the stem cell fate.

The biomolecular gradients can also be generated in 3D artificial niches to better mimic the cellular microenvironments. In most of these approaches, the gradients were generated by the free-diffusion of soluble molecules through the hydrogel network [26]. Typically, hydrogel precursors are loaded and crosslinked between two parallel fluidic channels, which are perfused to act as a source and a sink of biomolecules diffusing through the hydrogel to establish a stable gradient

[25, 26, 30–32]. In the free-diffusion based gradient generators there is a component with high fluidic resistance such as porous or semi-permeable membranes, or hydrogels (e.g. collagen, agarose or Matrigel®). These obstacles provide physical barriers to avoid convective flows and gradient formation is solely based on diffusion [26]. Saadi *et al.* described a 'Ladder Chamber' to create gradients in collagen gels (Figure 3.3) and demonstrated its utility in the study of migration behavior of netrophils [30]. Using the same setup, Kunze *et al.* demonstrated that B27 (neuronal cell culture supplement) concentration gradients created within agarose-alginate gels enhanced neurite outgrowth of primary cortical neurons [32]. In another study, a similar diffusion-based gradient device was used to generate stable gradients of morphogen concentrations across a 3D collagen matrix to stimulate embryoid bodies towards neural differentiation [33].

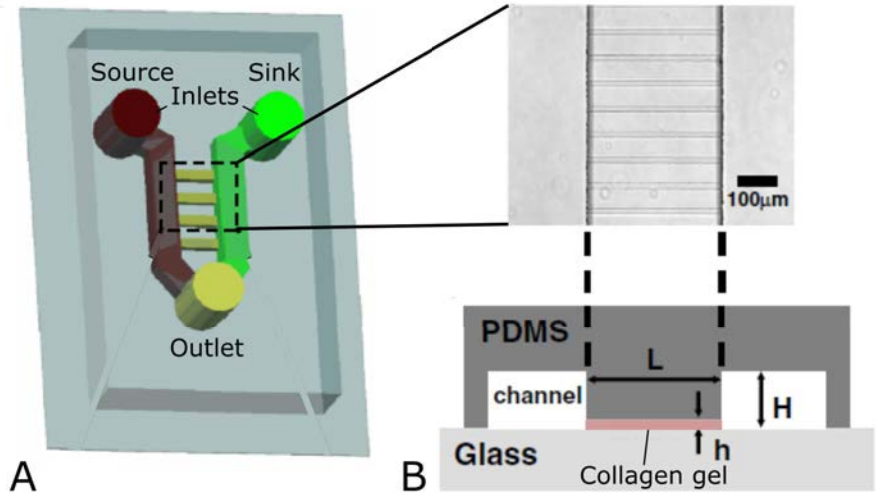

Figure 3.3: *Scheme depicting the design of the 'Ladder Chamber' for generating concentration gradients across microgrooves (A). Phase microscopy image and scheme showing cross-sectional view of the chamber, indicating where the collagen gel is loaded (B). Adapted from Saadi et al. [30].*

In free-diffusion based gradient generators since the transport of molecules occurs only by diffusion, the concentration gradient evolves over time until a steady state is achieved when influx and outflux transport are balanced [26]. To maintain constant concentrations at the source and the sink (infinite source/sink concept), continuous perfusion at the boundaries is needed [2, 30, 32]. Abhyankar *et al.* demonstrated that it is also possible to approximate infinite sources/sinks by using finite volume reservoirs that are periodically replenished [34, 35]. In

this way, linear gradients of biological factors were generated within a 3 mm long straight microchannel filled with 3D collagen matrix and these gradients could be maintained up to ten days. This device was used to study the invasion and migration of metastatic rat mammary adenocarcinoma as a response to a stable gradient of EGF [35].

In a study published by Cosson and Lutolf, diffusion-based gradients were created within agarose and gelatin-based hydrogel chips by delivering biomolecules from microchannels embedded in the hydrogel [36] (Figure 3.4 A). The biomolecules diffusing out radially formed gradients on the hydrogel surface. Long-term stable gradients were generated by dispensing biomolecules periodically in accordance with the findings of Abhyankar *et al.* (Figure 3.4 B). This platform was validated in the spatially controlled induction of neurogenic differentiation of the embryonic stem cell aggregates seeded on the hydrogel surface with a controlled gradient of retinoic acid [36] (Figure 3.4 C).

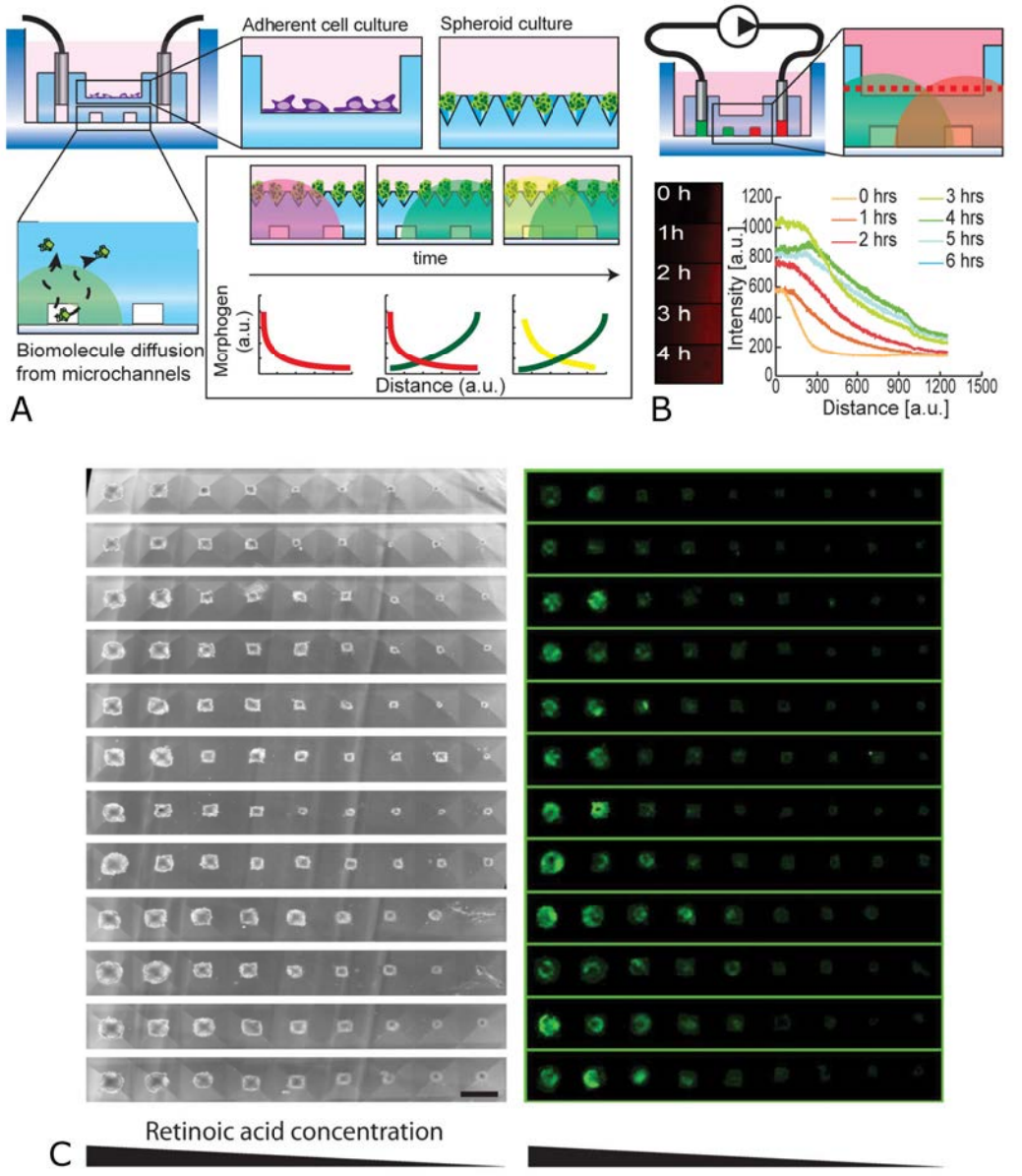

Figure 3.4: *Scheme depicting hydrogel chip for cell-based assay applications. Adherent culture on flat or spheroid-based culture on topographically structured gels can be performed. The delivery of biomolecules is achieved by molding microchannels at the bottom of the hydrogel chip for diffusion through the gel (A). Scheme depicting hydrogel chip and the gradient generation with a syringe pump (top). Characterization of stable fluorescently labelled BSA gradient generated by intermittent perfusion (periodic replenishment) (bottom) (B). Bright field microscopy and GFP fluorescence images of the embryonic stem cell aggregates exposed to retinoic acid gradients after four days of culture (C). GFP probes Sox1, neural differentiation marker. Scale bar: 400 μm. Adapted from Cosson and Lutolf [36].*

Although there are number of studies using hydrogels with biomolecular gradients to modulate stem cell behavior [25, 26, 33, 36], the applications of such systems to intestinal stem cell cultures are limited to a couple of articles. Allbritton and colleagues reported a simple linear gradient-generating device to screen for the optimal concentrations of Wnt3a and R-Spondin 1 on the growth of organoids derived from colon tissue [37]. The device consisted of a source and a sink chambers, similar in design to previously published reports [30, 35], separated by a Matrigel® loaded microchannel (Figure 3.5 A). Crypts isolated from colon tissue were mixed with Matrigel® prior to loading. The source and the sink were filled with standard organoid growth media. However, Wnt3a and R-Spondin 1 were only added to the source chamber. These proteins diffused through the gel towards the sink generating the gradients. The growth of colonic organoids in response to the varying concentrations of Wnt3a and R-Spondin 1 led to the determination of minimum necessary concentrations of these proteins for stem cell renewal and colonic expansion [37] (Figure 3.5 B). In a follow-up study, this device was used to study the organization of colonic organoids [38]. They showed that the colonic organoids cultured under Wnt3a and R-Spondin 1 gradients were highly polarized with proliferative cells localized at the region of the highest morphogen concentrations (Figure 3.5 C). These findings suggested that a linear gradient of Wnt signaling factors was sufficient to direct patterning of the proliferative units of the organoids in culture [38]. This simple gradient generating device provided useful information demonstrating that biochemical gradients generated *in vitro* can actually be used to guide self-organization in organoids. Indeed, in a very recent study, basolateral delivery of ISC niche factors was shown to lead to *in vivo*-like crypt-villus cellular distribution along microstructured collagen scaffolds [39].

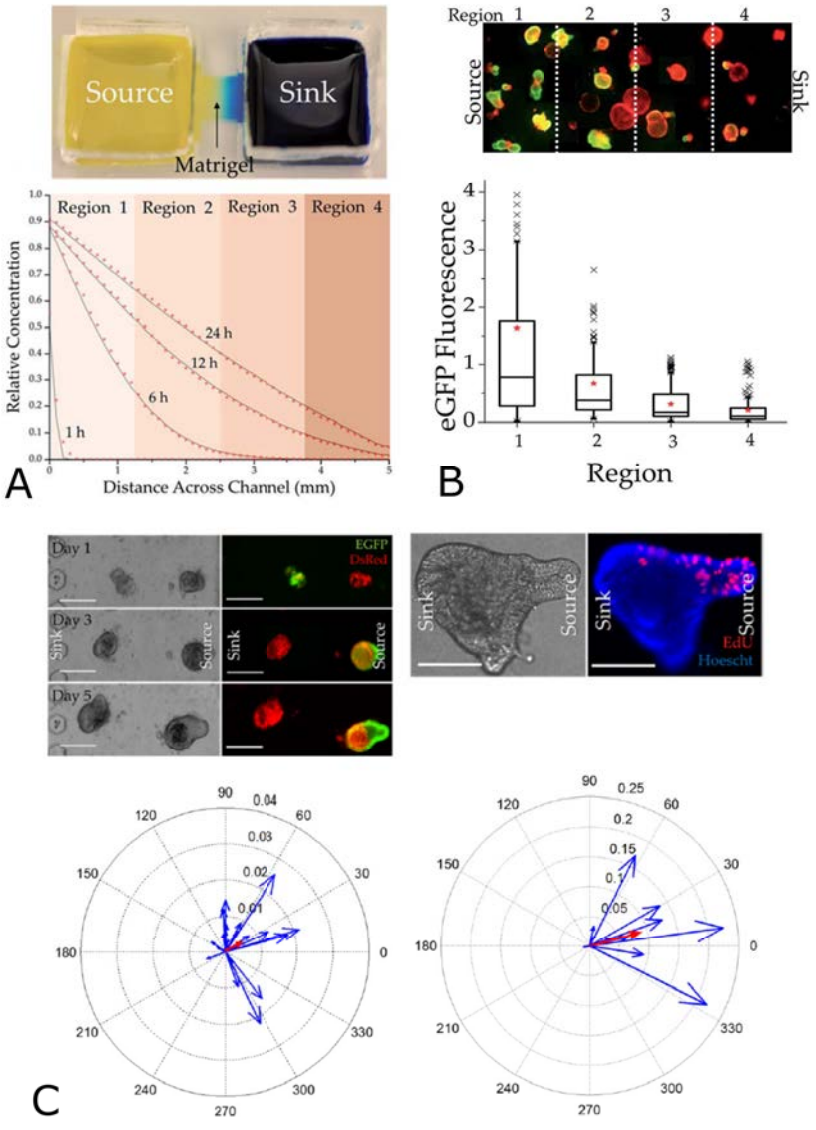

Figure 3.5: *Photograph of the gradient-generating device (top) and the characterization of the gradient by the diffusion of 40 kDa FITC-dextran through the channel (bottom) (A). Culture of colonic organoids in the presence of a combined R-Spondin 1 and Wnt-3a gradient (top). Green fluorescence marks the proliferative and Red fluorescence marks all of the cells. Quantification of the GFP fluorescence (bottom) per colonic organoid within different regions of the gradient (B). Adopted from Ahmad et al. [37]. Bright field and overlaid red/green fluorescence images of colonic organoids cultured under a Wnt3a and R-Spondin 1 gradient in the microchannel (top left). Scale bar: 250 μm. Colonic organoids pulse-labeled with EdU (red) for 2 h for proliferative cells after 5 days in culture (top right). Scale bar: 50 μm. Compass plots displaying the GFP (bottom left) and EdU polarization (bottom right) magnitude and angle for individual colonic organoids (blue) cultured under the Wnt3a and R-Spondin 1 gradient. The average vector can be seen in red. Adopted from Attayek et al.[38].*

In this context, we hypothesized that it is possible to modulate organoid-derived ISC behavior through gradients of ISC niche biochemical factors generated along the vertical axis of our PEGDA-based 3D villus-like hydrogel scaffolds. The 3D architecture would not only provide native tissue-like topography, but also a template to create spatio-chemical gradients as *in vivo*.

In this chapter, we describe the strategies adopted for the generation and characterization of spatio-chemical gradients of ISC niche biochemical factors within PEGDA-based 3D villus-like hydrogel scaffolds. First, the network properties of PEGDA hydrogels were experimentally determined to assess their suitability for the diffusion of the relevant biochemical factors and could be further adjusted by changing the PEGDA concentration. Finite element method was used to simulate the spatio-chemical gradients of ISC niche biochemical factors formed within the hydrogels and determine the characteristics of the gradients formed on the vertical axis of the microstructures with dimensions corresponding to villus *in vivo*. Then, the gradients were aimed to be characterized experimentally by microscopic techniques. For that, custom-made PEGDA hydrogel incorporated fluidic device was designed and fabricated. The chip was designed such that it allowed physical access to the hydrogel from the sides and the top for imaging. The gradient of fluorescently labelled model protein was visualized with light-sheet fluorescence microscopy (LSFM). Stable profiles were observed as predicted by the *in silico* model demonstrating that the gradients could be formed and maintained within PEGDA hydrogels in the experimental setup designed. Then, it was aimed to generate such gradients in standard cell culture platforms that permitted access to both sides of the hydrogel that can be used as the source and sink. PEGDA-based microstructured hydrogel platforms were succesfully adapted to Transwell® setup. Spatio-chemical gradients created in this setup were shown to compartmentalize the differentiated epithelial cells derived from organoid pieces preferentially at the tips of the villus-like microstructures. Here, we have successfully developed methods to generate spatio-chemical gradients of ISC niche factors within the PEGDA hydrogels. Finally, we have shown that these gradients influence cellular distribution on the microstructured hydrogels.

3.2 Materials and Methods

3.2.1 Estimation of the mesh size of PEGDA-AA hydrogels

In order to have a better insight into the diffusion properties of the proteins of interest within the PEGDA-AA hydrogels fabricated as explained in chapter 2, the mesh size (ξ) of the hydrogels was estimated using Flory-Rehner equilibrium swelling theory [16, 17, 19]. Peppas and Merrill modified the original Flory-Rehner model for hydrogels prepared in the presence of water [22, 40]. Since the presence of water modifies the thermodynamic balance of swelling, a term must be introduced that accounts for the volume fraction of the chains after crosslinking. This term is referred as volume fraction at the relaxed state ($V_{2,r}$). To estimate the mesh size first the molecular weight between crosslinks (M_c) has to be computed with the following equation.

$$\frac{1}{M_c} = \frac{2}{M_n} - \frac{\frac{v}{V_1} * [ln(1 - V_{2,s}) + V_{2,s} + \chi * V_{2,s}^2]}{V_{2,r} * [(\frac{V_{2,s}}{V_{2,r}})^{1/3} - \frac{V_{2,s}}{2V_{2,r}}]} \tag{3.4}$$

where M_n is the average molecular weight of the polymer, which is 6000 Da (P6000) in our case, v is the specific volume of bulk PEGDA (0,893 $cm^3.g^{-1}$) [41], V_1 is the molar volume of the solvent which is approximated to the molar volume of water (18 $cm^3.mol^{-1}$) [41] and finally, χ is the value of the polymer-solvent interaction parameter (0,426 as determined by Merill *et al.*) [20]. The values obtained in the swelling studies performed and reported in chapter 2 section 2.3.3 were used to calculate the weight fractions of the hydrogels after fabrication (q_F) and at equilibrium swelling (q_W), as explained in section 2.2.4. The polymer volume fraction of the hydrogel in swollen state ($V_{2,s}$) and the volume fraction in the relaxed gel ($V_{2,r}$) were calculated using these values (see chapter 2 section 2.2.4 for the calculations). After finding M_c, the mesh size (ξ) of the hydrogel network was determined by the equation that was described by Canal and Peppas [21]. In order to use this equation, first, we needed to obtain the root mean square of the end to end distance of the unperturbed state ($(r_0^{-2})^{1/2}$) of the PEGDA chain:

$$(r_0^{-2})^{1/2} = l * {C_n}^{1/2} * n^{1/2} \tag{3.5}$$

where Cn, the characteristic ratio for PEG, is 4 [16], l, the weighed average bond length of the PEG backbone, is 0,15 nm [41], and n is the number of repeating

units in the crosslink. It depends on M_c and on Mr, the molecular weight of the PEG repeating unit (44 g.mol^{-1}) [41]. The equation for calculating n is:

$$n = 2\frac{M_c}{M_r} \tag{3.6}$$

Finally, the mesh size (ξ) can be calculated by using the following equation:

$$\xi = (r_0^{-2})^{1/2} * V_{2,s}^{-1/3} \tag{3.7}$$

PEGDA concentrations and UV exposure times studied were: 5% w/v and 10% w/v P6000, and 150 s and 200 s, respectively, as established in chapter 2. The AA content was 0,6% w/v. Four different samples were analyzed for each condition. MATLAB software was used for the calculations and the data was plotted as mean $\pm$ standard deviation with OriginPro 8.5 software. The statistical comparison was performed using two tailed, unequal variances Student's t-test and p<0,05 was considered significant.

3.2.2 Determination of the protein diffusion coefficients in PEGDA-AA hydrogels

With the purpose of calculating the diffusion coefficients (D_g) of the proteins within the swollen hydrogels, a simple diffusion chip was designed and fabricated taking as an example the experimental setups described in previously published reports [42, 43]. Bovine serum albumin (BSA) (Thermo scientific) was selected as model protein, as its diffusion behavior and properties are extensively studied and reported in the literature. Also, its hydrodynamic diameter, 7,2 nm [44], is smaller than the mesh size estimated for both 5% w/v and 10% w/v P6000 hydrogels considered (see following section 3.3.1 for mesh size values); therefore, making diffusion possible. The designed diffusion chip consisted of a completely sealed donor (source) and a receiver (sink) chambers separated by the hydrogel (Figure 3.6 A). The chip was made of three layers of polydimethylsiloxane (PDMS) (Dow Corning) cut in 20 mm (width) x 30 mm (length) rectangles. The first and the third layers were $\approx$ 4 mm in thickness and had a central pool of 6 mm in diameter. The second layer was 1 mm in thickness and had a central pool of 10 mm in diameter (Figure 3.6 B). The pools were made by cutting PDMS out by punches of respective diameters (Harris Uni-Core, GE Healthcare Life). The PDMS preparation and curing was performed as explained in Section 2.2.1.1. The second layer was designed to include the hydrogel sandwiched between two

PDMS layers with central pools, creating a donor chamber both at the bottom and a sink chamber at the top of the hydrogel.

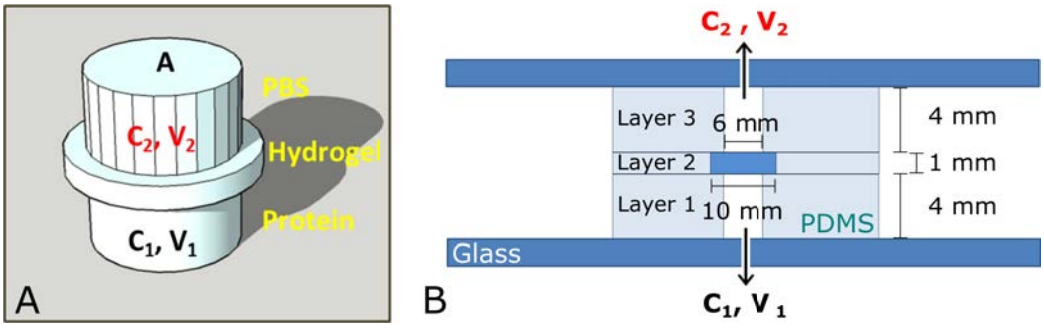

Figure 3.6: *Scheme of the hydrogel incorporated PDMS chip with a donor chamber (source) below and a receiver chamber (sink) above the hydrogel (A). V_1 and V_2 are the volumes of the two chambers, C_1 and C_2 are the concentrations of protein in the two chambers and A is the area of the aperture. Scheme showing the side view of the chip with its real dimensions denoted (B).*

The chip fabrication steps were as follows: 1) PDMS layers were cut into above mentioned diameters and washed with ethanol; 2) the first and the second layers were plasma bonded by activating the surface with a plasma cleaner (PDC-002, Harrick Scientific) for 30 s at high RF (18 W); 3) 10% w/v disc-shaped P6000 hydrogels fabricated with 165 s UV exposure (the concentration was chosen for the ease of manipulation) swollen to equilibrium were cut into discs of 10 mm in diameter right before use; 4) the surface of the bonded first and the second layer, 10 mm pool facing up, and the third layer were activated by plasma as above; 5) right after plasma exposure, the 10 mm diameter hydrogel was placed into the 10 mm PDMS pool and the activated third layer was placed onto the hydrogel, this step had to be performed as quickly as possible; 6) to completely seal the upper and lower chambers a glass slide was plasma bonded to both sides. The glass slides were perforated by a drill to have a hole of 2 mm in diameter right below the chambers to allow the delivery of the solutions. During the time course of the experiment these holes were plugged by a piece of PDMS. After the assembly of the chip, it was let sit for a few minutes to allow complete bonding, and the chambers were filled with PBS to re-swell the hydrogel that was partially dehydrated. Once the hydrogel was re-swollen, it completely occupied the 10 mm central pool and the transport of protein occured only across the hydrogel from the source to the sink. Particular attention was paid during filling of the chambers to avoid introducing air bubbles, which would impede the flow of the liquid and consequently the diffusion of the solute. The volume added to each chamber was 114,8 μL. The

diffusion experiments were started by replacing the PBS in the source chamber with 5 mg.ml^{-1} BSA and, immediately the first sampling was done by taking 10 µL of volume from the sink chamber. The removed volume was replaced by an equal amount of PBS to keep the total solution volume constant. The sampling was done at different time points: 0 h, 0,5 h, 24 h, 48 h, and 120 h for BSA and 0 h, 1 h, 2 h, 3 h, 28 h, 48 h, 72 h, and 96 h for laminin. The chip was maintained in a humidified chamber at 37°C throughout the experiment to avoid evaporation. As a control, a protein with a much larger diameter than the mesh size of the 10% w/v P6000 hydrogel network was tested. Laminin, high molecular weight protein of extracellular matrix with a hydrodynamic diameter of $\approx$ 40 nm [45], was chosen for that purpose. Laminin (Sigma) concentration used was 0,5 mg.ml^{-1}. In order to quantify the total amount of the proteins in the solution, a commercial BCA^{TM} Protein Assay Kit (Thermo Scientific) was used. The mechanism of action of this commercial kit is based on the reduction of the Cu_2^+ ion by proteins, which gives a unique color to the compound called bicinchonic acid (BCA). This color is then detected by absorbance at 562 nm [46]. For absorbance measurements, an Infinite M200 Pro multimode microplate reader (Tecan) was used. For the quantification of the unknown amounts of proteins, a calibration curve for BSA was constructed (Figure 3.7). A linear fit was made to relate the known concentrations of the total protein to their corresponding absorbance values.

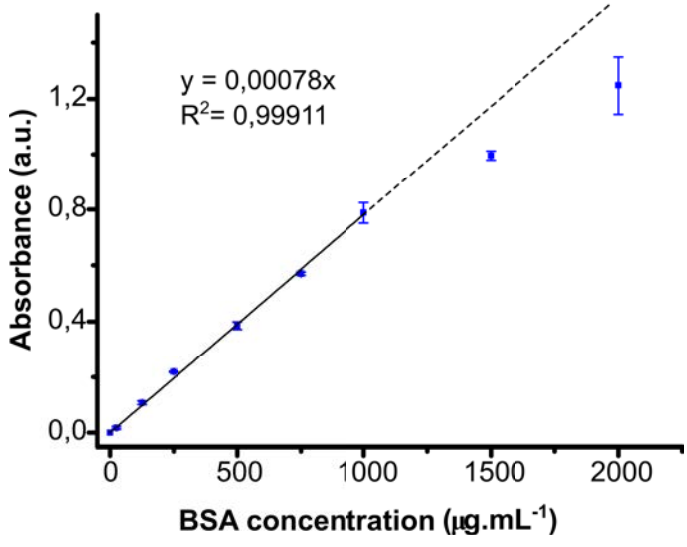

Figure 3.7: *Calibration curve for BSA.*

Total mass released at a given time point (M_i) was calculated by the following equation [42, 47].

$$M_i = C_i * V + \sum C_{i-1} * V_s \tag{3.8}$$

where C_i is the concentration of protein released in the solution at time i, V is the total volume of the solution in the sink (receiver) chamber and V_s is the sampled volume.

The diffusion coefficient of BSA, on the other hand, was calculated using a previously published method [42, 43]. Several assumptions were made to apply this method: 1) the solutions are well mixed (no concentration gradients in the wells), 2) the time it takes for the concentration in the hydrogel to stabilize to a linear profile is much shorter than the diffusion time (quasi-steady state), 3) no protein accumulation occurs at the hydrogel interfaces, and 4) radial diffusion is negligible (protein diffusion is one-dimensional through the gel). All of these assumptions apply to the geometric configuration and measurement timescales of our system. The initial condition at the sink (receiver) chamber was $C_{2,0}$ = 0 mg.ml^{-1} at t_0 = 0, hence the diffusion can be evaluated in the following form and D_g can be extracted [42, 43]. The detailed derivation of the following equation is given by Lee *et al.* [42].

$$-ln(1 - \frac{C_2}{\frac{N}{V}}) = \frac{D_g}{h}(\frac{t}{\tau}) \tag{3.9}$$

where N is the total solute mass in the system (0,57 mg), h is the hydrogel thickness (1 mm) and V and τ describe the geometric parameters of the system and can be computed by the following equations:

$$V = V_1 + Ah + V_2 \tag{3.10}$$

$$\tau = \frac{(V_1 + \frac{Ah}{2})(V_2 + \frac{Ah}{2})}{AV} \tag{3.11}$$

where V_1 and V_2 are the volumes of the source and the sink chambers (both 114,8 μL), respectively, and A is the area of the aperture (0,28 cm^2) over which diffusion occurs. C_2 values were experimentally determined at each time point as explained above. Then, equation 3.9 was used to determine D_g since it is the

only unknown variable. The D_g was calculated for each experimental point and averaged.

This setup was used to validate the chip fabrication, but not to systematically compute D_g of all proteins due to the technical challenges in the fabrication. The D_g of a variety of model proteins, in similar PEG-based hydrogel networks, are available in the literature [44, 48]. Also, there are commercially available blind-well chambers (NeuroProbe, Inc.) that can be possibly used instead of the diffusion chip developed here. And finally, spectroscopic techniques such as fluorescence correlation spectroscopy (FCS) can be used for the same purpose [49].

3.2.3 *In silico* modeling of protein diffusion on PEGDA-AA hydrogels

In order to be able to modulate the growth and differentiation of ISCs, it was aimed to form spatio-chemical gradients of EGF, R-Spondin 1, Noggin, Wnt3a biomolecules on 3D microstructured PEGDA hydrogels. For that, we decided to model these gradients on hydrogels using finite element method (FEM) through COMSOL Multiphysics® software.

The diffusion of proteins can be described by Fick's second law:

$$\frac{\partial c}{\partial t} = D\nabla^2 c \tag{3.12}$$

where c is the protein concentration as a function of time and space, and D is the diffusion coefficient. By using this equation we are making some assumptions: D is a constant value, there are no chemical reactions, there is no convection, the specie c is diluted and there is mass conservation.

The diffusion coefficient of the proteins in aqueous solution, D_0, can be calculated using Stokes-Einstein equation for diffusion of a spherical particle through a liquid:

$$D_0 = \frac{k_B T}{3\pi\eta d_H} \tag{3.13}$$

where k_B is the Boltzmann's constant (1,38.10^{-23} J.K^{-1}), T is the absolute temperature (37°C = 310 K), η is the viscosity of the solvent (6,915.10^{-4} N.m.s^{-2} for water at 37°C [48]) and d_H is the protein hydrodynamic diameter. Calculated D_0 values represent the diffusion coefficients of spheres with equivalent sizes.

For FEM simulations, model proteins with sizes similar to each of the ISC niche factors were selected (Table 3.1), since the values for hydrodynamic radius and D_g of these model proteins in similar PEG-based hydrogel networks can be

easily found in the literature. D_g of these proteins could be experimentally determined using the chip reported in the previous section 3.2.2. However, due to the technical difficulties in its fabrication, it was not used.

Stemness factor	Molecular mass (kDa)	Model protein	Molecular mass (kDa)	Diameter (nm)
EGF	6,0	Insulin	5,7	3,00 [48]
R-Spondin 1	25,6	CA	28,0	4,80 [48]
Wnt3a	37,0	Ovalbumin	42,7	6,96 [48]
Noggin	46,4	BSA	66,5	7,20 [44]

Table 3.1: *ISC niche biochemical factors and their corresponding model proteins with their molecular mass and the hydrodynamic diameters of the model proteins.*

For simulations, the 'Transport of diluted species' module of COMSOL Multiphysics® software was used. We assumed axial symmetry and that made it possible to reduce the 3D forms to 2D geometries. The geometry was composed of two media: the PEGDA hydrogel and the aqueous solution. For each medium the corresponding diffusion coefficient values of each species (i.e. D_0 for aqueous solution, D_g for PEGDA hydrogel) was used (Table 3.2). D_0 values for each of the diffusing biomolecule were calculated using Stokes-Einstein equation (Eqn. 3.13). D_g values of model proteins were obtained from literature in which PEGDA hydrogels with similar network structures (mainly determined by PEGDA concentration and chain length) were used.

Protein	D_0 x10^{-10} ($m^2.s^{-1}$)	D_g x10^{-10} ($m^2.s^{-1}$)	Concentration ($ng.mL^{-1}$)	Molarity x10^{-6} ($mol.m^{-3}$)
Insulin	2,19	1,27 [48]	100	17,50
CA	1,37	0,16 [48]	200	3,45
Ovalbumin	1,09	0,20 [48]	50	1,17
BSA	0,91	0,13 [50]	100	1,50

Table 3.2: *Values for the diffusion coefficients in the aqueous solution at 37°C, D_0, calculated using Stokes-Einstein equation for each of diffusing species; diffusion coefficients in the PEGDA gel, D_g; and the source concentrations for each protein.*

In the experimental setup the gradients are created using a source chamber located below the hydrogels and a sink chamber over the hydrogels. Therefore, the model geometry was designed accordingly. Initially, in a simplified approach, constant source concentrations (assuming infinite source condition) at the bottom boundary of the hydrogel and an open boundary at the hydrogel - sink interface was designed. No flux boundary was selected for the rest of the boundaries found

at the edges of the geometry. The initial concentration was set to zero in the entire geometry except the bottom boundary of the hydrogel. The source concentrations selected were the typical concentrations used in a standard organoid culture and given in table 3.2. Note that, even though the mass concentrations are the same or similar, the molarities are different due to differences in protein size.

We developed models with two different geometries: a rectangle model and a microstructure model (Figure 3.8 A). The aim of doing these two models was to characterize the diffusion profiles within the two hydrogel geometries with which we were working. In the rectangle model, PEGDA hydrogel height was set to 1 mm, corresponding to the experimental height of disc-shaped hydrogels. In the microstructure model, we implemented the villus-like microstructure geometry with a base height of 150 μm, and the villus-like microstructures with a semi-major axis of 75 μm (half-width) and a semi-minor axis of 300 μm (height) being considered as semi ellipses. The center-to-center spacing was set to 250 μm and an array of microstructures were constructed. In both of these models, the sink medium was represented as a rectangular form. The FEM mesh for the aqueous medium was set to "finer" in both models (1.10^{-2} mm < FE_{size} < 1 mm) and the "extra fine" mesh (1.10^{-3} mm < FE_{size} < 2.10^{-2} mm) was selected for the gel medium. The objective of the simulation was to determine the gradient profiles along the 2D cross-sections in the rectangle model and the concentrations along the curve contouring microstructure surface as a function of the vertical position (z) in the microstructure model (Figure 3.8 A). The simulations were performed up to 24 h of diffusion time, which is a convenient cell culture medium change frequency.

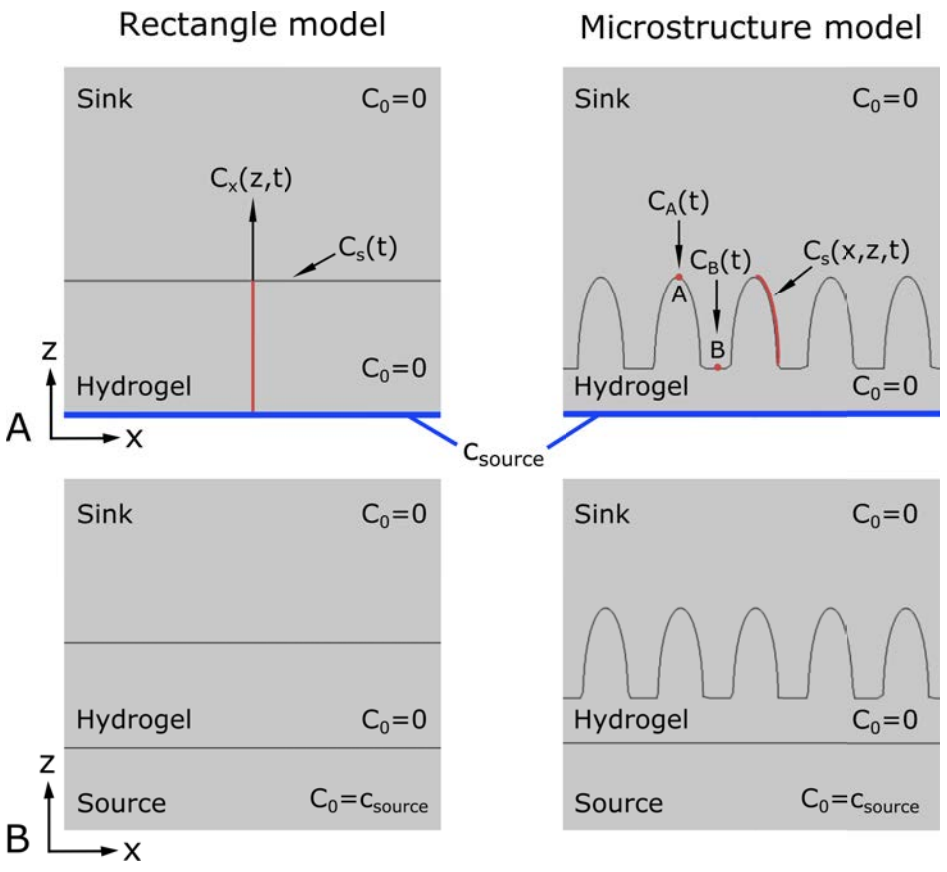

Figure 3.8: *Scheme showing the rectangle and microstructure geometries and the initial conditions used in the FEM simulations (A). Constant source concentrations are set at the bottom boundary of the hydrogel. The concentration gradients along a vertical axis in the 2D cross-sections (C_x) and along the surface of the microstructure (C_s) were determined in the rectangle and microstructure model, respectively. Also, the change in concentration as a function of time at the hydrogel-sink interface were determined (C_s in the rectangle model, C_A-tip and C_B-base in the microstructure model). Scheme showing the geometries of the improved model with a rectangular source compartment added to the bottom boundary of the hydrogel, simulating the finite source condition (B). The initial conditions are indicated. The sink and source sizes are not to scale for visualization purposes.*

In an improved simulation to be closer to experimental conditions, certain revisions were made to the *in silico* model. First, another rectangular geometry was added to the bottom boundary of the hydrogel as the source and the initial concentration within the entire source geometry was set to the values used in the experimental setup (Figure 3.8 B). This change simulated a finite source condition instead of the infinite source condition used in the initial approach (by setting the source concentration constant). Then, the medium change cycles were implemented to the model by running sequential simulations each time keeping

the hydrogel gradient profiles from the last time point and using them as the initial condition for the hydrogel in the following simulation; while resetting the source and the sink to their initial values. The aim of doing this was to simulate the effect of the medium change on the gradient profiles. Finally, the initially neglected material accumulation at the interfaces was simulated by adding a thin diffusion barrier. Nominal values for the diffusion barrier were selected taking into account the experiments performed (Section 3.3.3.2). Also, to better simulate the experimental conditions, D_0 and D_g values for BSA at 25°C were used. Again, D_0 at 25°C (6,8.10^{-11} $m^2.s^{-1}$) was calculated using Stokes-Einstein equation (Equation 3.13) and D_g at 25°C (1,0.10^{-11} $m^2.s^{-1}$) was taken from a previously published work [50].

3.2.4 Characterization of the protein gradients on PEGDA-AA hydrogels by using light-sheet fluorescence microscopy

3.2.4.1 Fabrication of a microfluidic chip allocating a hydrogel sample for diffusion studies

A PDMS chip with a microfluidic channel and a chamber allocating a hydrogel sample for the generation and visualization of gradients was designed. For the fabrication of the microfluidic channel a SU-8 resist master mold on silicon wafer (Si(111), 1-side polished, n-type) (MicroChemicals) was prepared using photolithography (Figure 3.9 A). Silicon wafers were cut into required sizes (30 x 40 mm) with a diamond tip cutter paying attention to the crystal orientation and the polished side facing down. The wafer pieces were rubbed with acetone and rinsed with acetone and isopropanol. The wafer surfaces were further cleaned by an expanded plasma cleaner (PDC-002, Harrick Scientific) for 20 min at low RF (6.8 W). Then, they were placed onto a hot plate at 95°C to remove the excess of humidity and were cooled down under nitrogen air flow. SU-8 2100 negative photoresist (Microchem) was selected to create the master mold. A 100 μm thick layer of SU-8 was produced by spin-coating SU-8 resist on silicon wafers. Briefly, the substrates were placed onto the stage of the spin coater (WS-650MZ-23NPP/LITE, Laurell Technologies) and immobilized by the vacuum applied. Approximately 1 mL of the resist was dispensed onto the wafer and spun first at 500 rpm for 5 sec with an acceleration of 100 rpm/sec, and then at 3000 rpm for 30 sec with an acceleration of 300 rpm/sec. The velocity of the second spin cycle was selected to be 3000 rpm to be able to obtain a layer of 100 μm, following the instructions provided in the manufacturer's datasheet. The film was baked

for 5 min at 65°C and 20 min at 95°C to evaporate the solvent. To produce the microchannel shape, the SU-8 film was exposed to UV light (25 mW.cm^{-2}) through a photomask using a mask aligner instrument (MJB4, SUSS MicroTec). The photomask used consisted of a single rectangular transparent window, 200 μm in width and 20 mm in length. It was designed using Inkscape software and printed on acetate films (CAD/Art Services) (Figure 3.9 A).

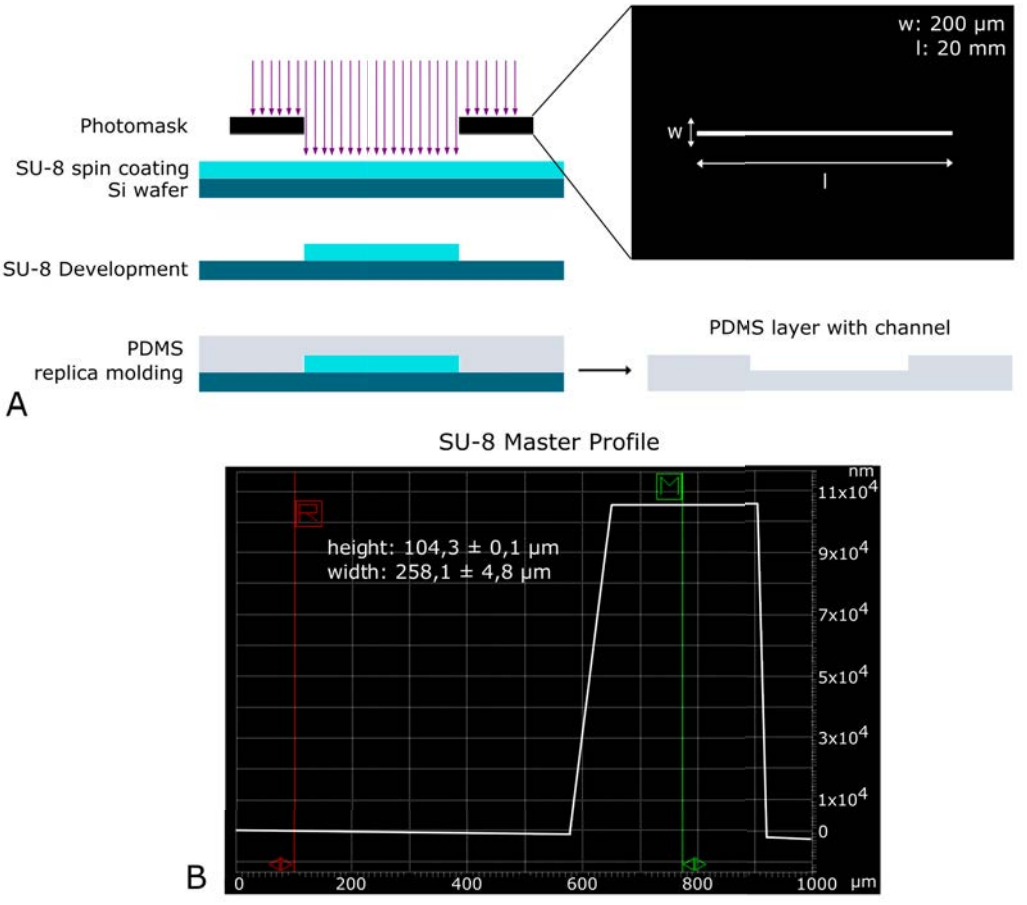

Figure 3.9: *Scheme depicting photolithographic procedure used to fabricate PDMS layer with a single channel (A). The dimensions of the transparent rectangular window in the photomask were 200 μm in width and 20 mm in length. A representative profile obtained by a profilometer showing the dimensions of the SU-8 master fabricated by photolithography (B).*

The exposure time necessary to obtain a structure of specific height is calculated by dividing the exposure energy needed to the power density of the mask aligner equipment. For structures of 100 μm in height the exposure energy needed was 240 mJ.cm^{-2} as provided in the manufacturer's datasheet. The power density

of the UV lamp being 25 $mW.cm^{-2}$ (25 $mJ.s^{-1}.cm^{-2}$), the exposure time for proper crosslinking was calculated to be 9,6 sec. After the exposure, the film was baked for 5 min at 65°C and 10 min at 95°C and was developed until there was no uncrosslinked residue left using the SU-8 developer provided by the manufacturer (Microchem). The efficiency of the development was checked by inspection after rinsing with isopropanol after 8 min, and development was extended up to 12 min. Finally, the masters were rinsed with the developer and isopropanol and dried under nitrogen air flow. Right after fabrication, the dimensions of the channel were confirmed using a profilometer (DEKTAK 6M, Veeco Instruments) (Figure 3.9 B). The height and width (calculated from the top portion) of the channel were calculated to be 104,3 $\pm$ 0,1 μm and 258,1 $\pm$ 4,8 μm, respectively.

The surface of the SU-8 masters was silanized with an anti-sticking silane, (Tridecafluoro-1,1,2,2-tetrahydrooctyl)trichlorosilane (ABCR GmbH & Co. KG), in vapor phase. The silanization helps with demolding and extends the master molds lifespan. A couple of drops of the silane solution were added into a container, and the container together with the masters were placed into a vacuum chamber. For proper silanization, the masters were left under vacuum for at least 1 h. These master molds were then used to produce PDMS negative replicas (Figure 3.9 A).

The fabrication protocol designed to produce a microfluidic chip allocating a hydrogel sample is depicted in figure 3.10. The steps are as follows: 1) A thin membrane of PDMS (250 μm thick) with a central opening of 5 mm in diameter was stamped onto a very thin layer of uncured PDMS and, immediately after, a silanized porous polycarbonate membrane (Tracketch®, 5 μm pore size and 13 mm diameter, Nuclepore) was stuck on it. Then, this assembly was cured at 65°C for at least two hours to assure the total adherence of the porous membrane to the PDMS layer. 2) Disc-shaped hydrogels were fabricated (see Chapter 2 Section 2.2.1.1) on top of the PDMS-membrane assembly with a PDMS pool of 4 mm in diameter, so that there was enough margin for the hydrogel to swell. 3) The PDMS layer containing the microfluidic channel (Figure 3.9 A) was punched with a 0,75 mm punch (Harris Uni-Core, GE Healthcare Life Sciences) at each end of the channel, and with a 4 mm punch at the center to form the chamber below the hydrogel. Then the PDMS layer with the microfluidic channel is plasma bonded to a 1 mm thick PDMS slab. 4) The hydrogel-PDMS-membrane assembly was bonded to the construct with the microfluidic channel by a thin layer of uncured PDMS, which is cured overnight at room temperature. Then, the channel and the bottom chamber were filled with PBS and the hydrogel is let swollen in PBS. Prior

to use, PBS was exchanged with protein solution.

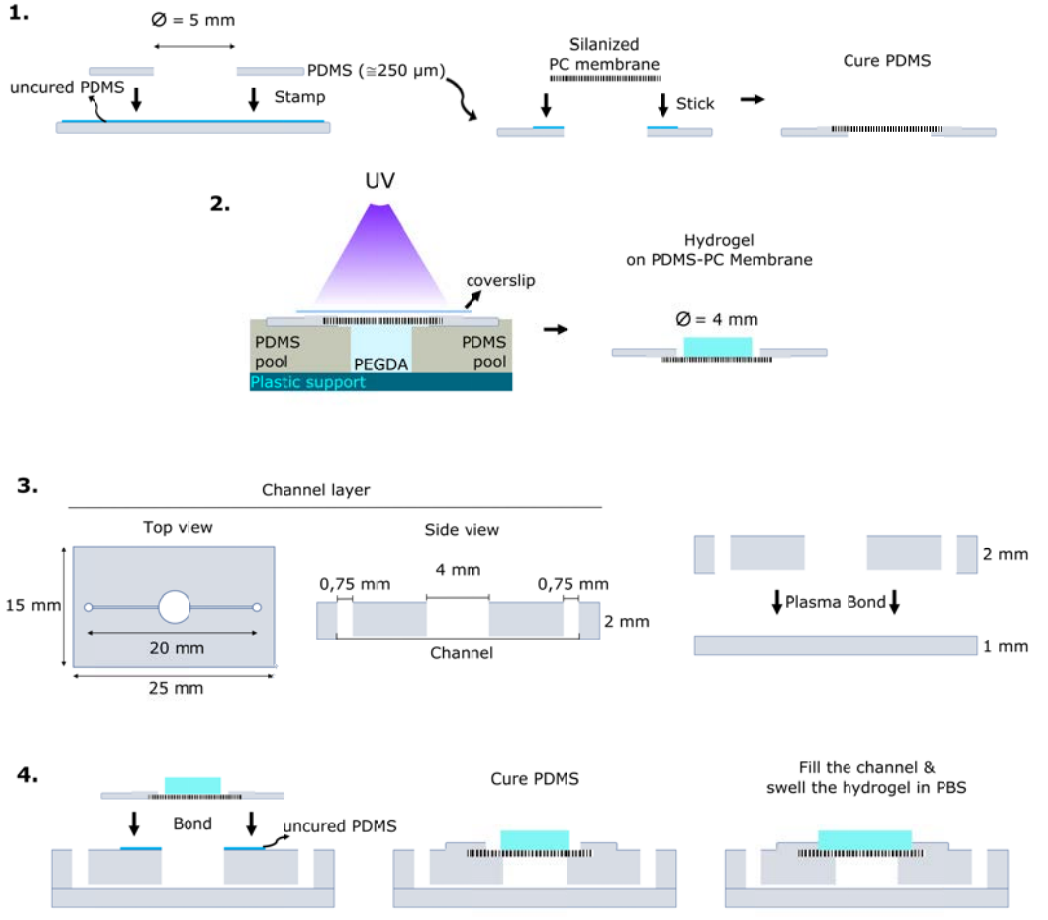

Figure 3.10: *Scheme showing the protocol for fabrication of a hydrogel disc incorporated PDMS chip. 1. Formation of PDMS-membrane assembly. 2. Fabricating disc-shaped hydrogels on PDMS-membrane assembly. 3. Preparation of PDMS layer with the channel e.g. inlet, outlet and chamber carving and then sealing the bottom with a PDMS slab. 4. Assembly of the whole chip. Then, channel filling and hydrogel swelling.*

3.2.4.2 In-chip diffusion studies on PEGDA hydrogels using light-sheet fluorescence microscopy

Light sheet fluorescence microscopy (LSFM) is a technique that uses a plane of light for optical sectioning and visualization of tissues with subcellular resolution (Figure 3.11 A) [51]. LSFM technique has intermediate to high optical resolution, but good optical sectioning capabilities and high speed [52, 53]. The photobleaching is minimized compared to wide-field fluorescence, confocal, or

multiphoton microscopy, since the samples are exposed to only a thin sheet of light and scanned fast [51]. It allows flexible sample access and mounting as it decouples the illumination and detection light paths, with an angle of 90° (Figure 3.11 A) [52, 53]. This permits the visualization of large-size samples requiring special mounting setup that would otherwise not be possible with other fluorescence microscopy techniques.

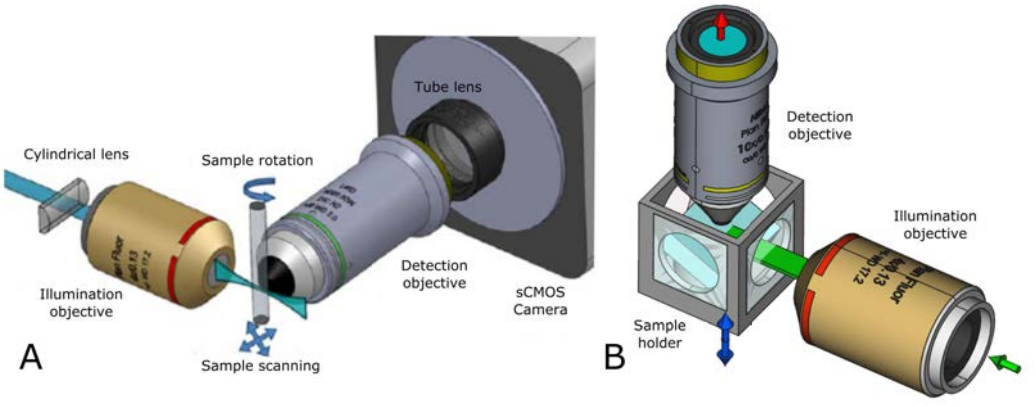

Figure 3.11: *Scheme depicting the light-sheet fluorescence microscopy concept (A). Adapted from Gualda et al. [54]. Scheme showing the setup we used where detection was performed in an up-right configuration (B).*

The hydrogel samples used in this study had large dimensions, discs of 1 mm thick and 5 mm in diameter, and the hydrogel allocated microfluidic chip had to be mounted in upright position, submerged in a chamber filled with liquid (PBS) to allow diffusion. For that reason, we have decided to use LSFM for the characterization of in-chip protein diffusion. LSFM analysis was performed in collaboration with Dr. Emilio Gualda at Super-resolution Light Microscopy & Nanoscopy Facility at The Institute of Photonic Sciences (ICFO). A custom-made light-sheet microscope developed at ICFO was used for these experiments. Continuous-wave (CW) laser with a wavelength of 561 nm (DPL 100mW, Cobolt) was used for excitation. The light sheet was created by a pair of galvanometric mirrors (GVSM002, Thorlabs), conjugated with the illumination objectives (Plan-Fluor 4x, NA 0,13, Nikon), through a pair of achromatic doublets (AC254-050-A-ML (f= 50 mm) and AC254-200-A-ML (f= 200 mm), Thorlabs), creating a flat top Gaussian beam profile to assure the homogeniety of the light-sheet [55]. Detection was performed in an up-right configuration, using water dipping objectives

(PlanFluor 10x, NA 0,3, Nikon) (Figure 3.11 B). An achromatic doublet (AC254-200-A-ML, Thorlabs) formed an image onto a Hamamatsu Orca Flash 4.0 CMOS camera chip. Emission filter of 620/ 52 (Texas red) (Semrock) was selected using a motorized filter wheel (FW102C, Thorlabs). A special sample holder (Figure 3.12 A) was designed using FreeCAD software and 3D printed (Hephestos 2, BQ) using poly(lactic acid) (PLA) as printing material (Figure 3.12 B). It consisted of a square swimming pool with open access on the top for sample insertion and imaging, and glass windows on the sides for proper light-sheet illumination. The chamber included a glass covered pedestal (oriented 25° from the optical table) where the microfluidic chip allocating the hydrogel was glued (Loctite), which also allowed bright-field illumination with a LED for sample positioning. With this inclination, the sample was illuminated and imaged transversally, to avoid any barrier on the path of the light-sheet illumination. Laser scanning for imaging of the chips was performed by vertical translation of the sample holder using a motorized vertical stage (PI M-501.1DG, Physik Instrumente), through a fixed horizontal light sheet plane. All the components of the microscope were controlled using a custom-made software (LabView).

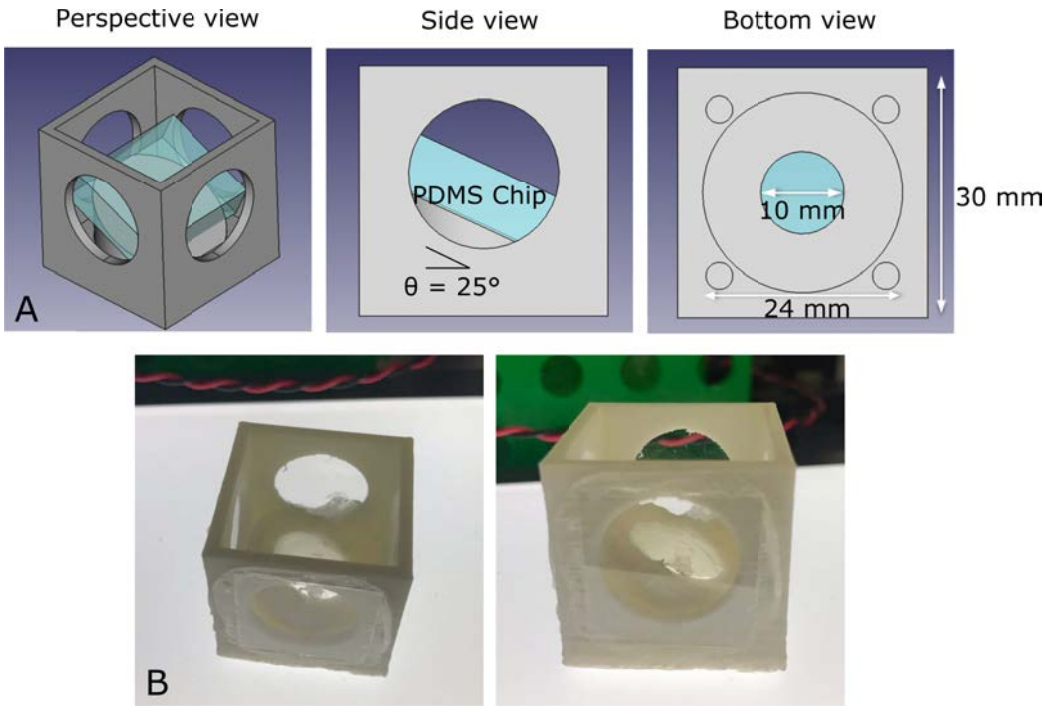

Figure 3.12: *Schemes showing the perspective, side and bottom view of the LSFM holder design (A). It's dimensions and the tilt angle of the pedestal are denoted in the schemes. Images showing the 3D printed LSFM holder (B).*

We imaged the stable gradients formed by the diffusion of BSA fluorescently labelled with Texas Red (BSA_TxRED) within PEGDA-based hydrogel, by performing a time-lapse acquisition of a 3D volume of 1,33 x 1,33 x 2,3 mm, over two hours with a frame interval of 5 min, and a stack step of 5 μm. The hydrogel was loaded 43 h prior to visualization with BSA_TxRED at a concentration of 10 $\mu g.mL^{-1}$ and the source and the sink chambers were replenished 24 h after loading and before acquisition. In order to reduce the data load, we binned the image by a factor of 4. Then, the overall lateral pixel size was 2,6 μm. The image processing was carried using ImageJ software. First, the stacks were resliced (ImageJ function) to obtain a vertical view of the source, the hydrogel and the sink. Then, a plane in the middle of the stack was chosen where the radial diffusion could be neglected. A linear ROI of 10 pixels in size was drawn on the perpendicular axis of the hydrogel (Figure 3.13). The relative fluorescence intensity (RFI) values along that line were obtained for all the time points acquired.

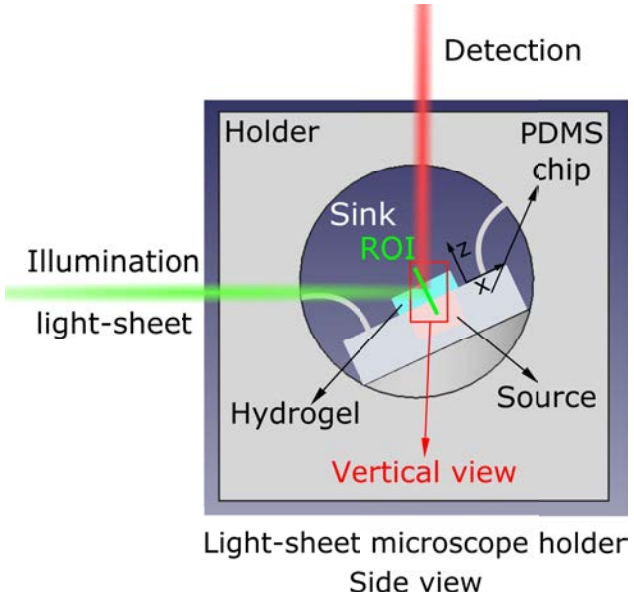

Figure 3.13: *Scheme depicting the LSFM holder with the PDMS chip placed inside. Illumination (with a horizontal light-sheet) and detection light paths are shown. Source and sink chambers as well as the linear ROI used for image analysis, taken perpendicular to the hydrogel axis, are indicated.*

The measured RFI values of the profiles along the perpendicular axis of the hydrogel were converted to concentrations by, first, constructing a calibration curve. For that, the fluorescence intensity of solutions with different BSA_TxRED concentrations were measured using the LSFM equipment. For each concentrations 21 measurements were made. The ROIs of 200 x 150 pixels in size were selected at the center of the stacks acquired in each measurement and the mean fluorescence intensity values were calculated. The background intensity value was determined from blank PBS. A calibration curve was plotted and fitted with a second degree polynomial function to relate measured RFI values to known concentrations using MATLAB software (Figure 3.14).

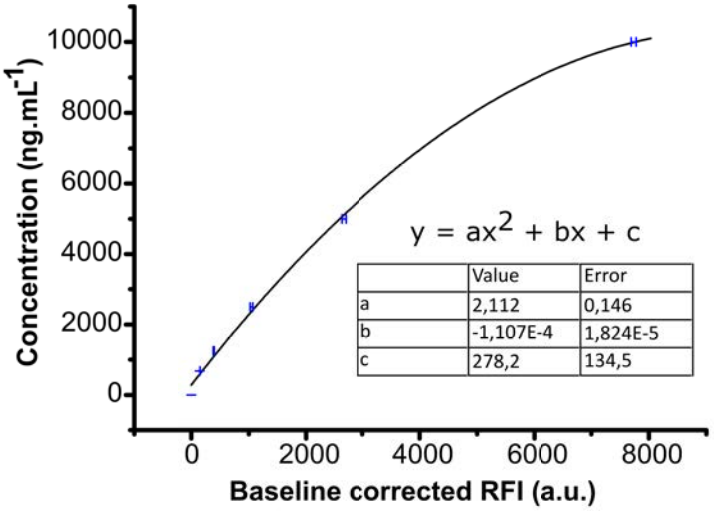

Figure 3.14: *Calibration curve constructed with the known concentrations of BSA_TxRED. 21 measurements were made for each concentration (n = 21).*

3.2.5 Experimental setup allowing protein diffusion in PEGDA-AA hydrogels with 3D villus-like microstructures

Standard Transwell® cell culture setup can also be used to form gradients as it separates the cell culture well into two compartments: apical (upper) and basolateral (bottom). These compartments can then be used as the source (bottom) and the sink (upper). As creating gradients in this standard cell culture setup is quite straightforward, we utilized this strategy. Note that the volumes of the source and the sink in Transwell® setup is different than those of the microfluidic chip; therefore can not be compared directly. For that, the microstructured hydrogels had to be fabricated on porous membranes to allow the diffusion of the biomolecules from the basolateral side and also to facilitate the mounting of the scaffolds onto the Transwell® inserts. In what follows, we explain experimental protocols used to achieve that.

3D villus-like microstructured hydrogels were fabricated on porous Tracketch® PET membranes following the method explained in section 2.2.1 with slight modifications. PDMS pools of 8 mm in diameter were used to have the whole surface of the hydrogel covered with microstructures (the photomask used had dimensions of 0,8 cm x 0,8 cm). The PET membranes were reduced in size by a 10 mm punch (Harris Uni-Core, GE Healthcare Life Sciences). The porous PET membranes were placed on top of the PDMS pools and glass coverslips of 12 mm

in diameter (VWR) were placed on top of the membrane as protective layer. The hydrogel precursor solution was introduced to the pool through the inlets and the photomask was placed on top of the pool. After the first exposure to form the villus-like microstructures, the hydrogels were washed with PBS and then with the hydrogel precursor solution. Afterwards, the above steps were repeated but this time without a photomask to form the base. Hydrogel precursor solution used had the following composition: 6,5% w/v P6000, 0,3% w/v AA, and 1% w/v I2959, as it was selected in the previous chapter. The exposure time ranges tested were 120-200 s and 0-10 s for the first (microstructures) and second (base) exposure, respectively. Hydrogels were swollen in PBS for at least 3 days and kept in 10% w/v Penicillin/streptomycin (in PBS) until further use.

Even though the hydrogels were sticking to the Tracketch® porous polyethylene terephthalate (PET) membranes initially, after prolonged incubation periods in liquid, they were lifting off of the substrate. To overcome this problem, the membranes, like the coverslips, were silanized with 3-(Trimethoxysilyl)propyl methacrylate (Sigma), prior to use. This particular silane was chosen because it has a vinyl functional group at its flanking end, which forms a covalent bond with the PEGDA chains upon UV initiated free radical polymerization. This assures the covalent attachment of the hydrogel to the membrane surface. The silanization protocol was optimized by modifying the silane manufacturer's protocol in the light of a previously published work reporting the silanization of polycarbonate membranes [56].

First, the Tracketch® PET membranes of 5 μm pore size and 13 mm diameter (Sabeu GmbH & Co) were dried in an oven at 65°C for 30 min. Then, they were placed into a glass petri dish making sure that they were flat, and were surface activated by exposing them to UV cleaner for 15 minutes (UV/ozone ProCleaner, Bioforce Nanoscience). In the meanwhile, the silane solution was prepared by diluting 2% v/v 3-(Trimethoxysilyl)propyl methacrylate and 3% v/v dilute acetic acid (10:1 glacial acetic acid:water) in absolute ethanol. The acetic acid was added just before use. Right after UV activation, the silane solution was added onto the membranes and incubated for one to two hours at RT. Then, the membranes were washed thoroughly with 96% v/v ethanol to remove residual reagents, dried under nitrogen air flow and in an oven at 65°C for 30 min. They were stored under vacuum until further use. All the solvents were purchased from Panreac Applichem unless stated otherwise.

To confirm their proper silanization, XPS analysis was performed by a Perkin-Elmer PHI 5500 Multitechnique System (Physical Electronics Inc.) with a

monochromatic X-ray source (Aluminium K α line of 1486,6 eV energy and 350 W), placed perpendicular to the analyzer axis and calibrated using the 3d5/2 line of Ag with a full width at half-maximum of 0,8 eV. The sampling area was 0,8 mm in diameter, and each sample was analyzed at several locations. C1s, O1s, N1s, Si1s and Si2p core level scan spectra were recorded for each location. The resolution selected for the spectra was 187,85 eV of pass energy and 0,8 eV/step for the general spectra and 23,5 eV of pass energy and 0,1 eV/step for the spectra of the different elements. A low energy electron gun (less than 10 eV) was used in order to discharge the surface when necessary. All measurements were made in a ultra-high vacuum chamber with a pressure between 5.10^{-9} and 2.10^{-8} torr. No sample degradation due to UH vacuum or X-rays was observed. Data processing was performed using MultiPak V6.0A software (Physical Electronics, Inc.) and the spectra were plotted with OriginPro 8.5 software. Figure 3.15 shows the survey spectra (A) and the high resolution spectra for Si1s and Si2p (B) of silanized and non-silanized PET membranes. PET molecule does not contain silicon atoms. Therefore, the presence of Si1s and Si2p peaks in the silanized samples demonstrated successful silanization of the PET membranes.

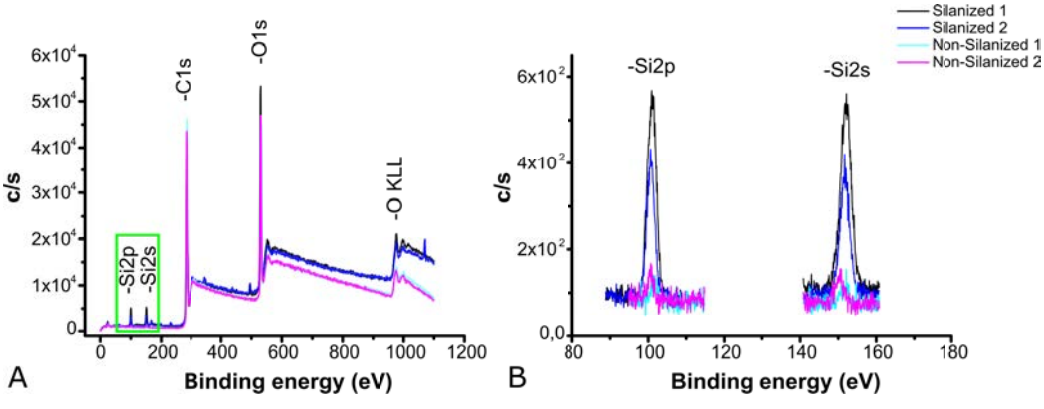

Figure 3.15: *Surface chemical composition characterization of silanized and non-silanized PET membranes by XPS analysis: survey spectra (A), and high resolution spectra for -Si2p and -Si2s peaks (B).*

The use of porous membranes as supports onto which microstructured hydrogels are fabricated causes light to scatter and induces morphological changes (the membrane effect) as oppose to the microstructures fabricated on glass coverslips. For the morphological assessment of the microstructures fabricated on membranes, another set of samples were fabricated on coverslips simulating "the

membrane effect" by placing the membrane between the coverslip and the photomask (Figure 3.16 A). In this way, the hydrogels were recovered on the coverslips and easily cut and visualized under an inverted bright field microscope (Nikon Eclipse Ts2). Different exposure times for the microstructure and base formation were tested and the morphology of the structures were assessed by a bright field microscope. The dimensions of the microstructures were measured using ImageJ free software (http://rsb.info.nih.gov/ij, National Institutes of Health). The effective microstructure height was taken as the distance from the hydrogel base to tip and the diameters were measured at a position closer to the base of the microstructures. The diameters of the microstructures were measured close to the base. At least three samples were analyzed for each condition ($n \geq 3$).

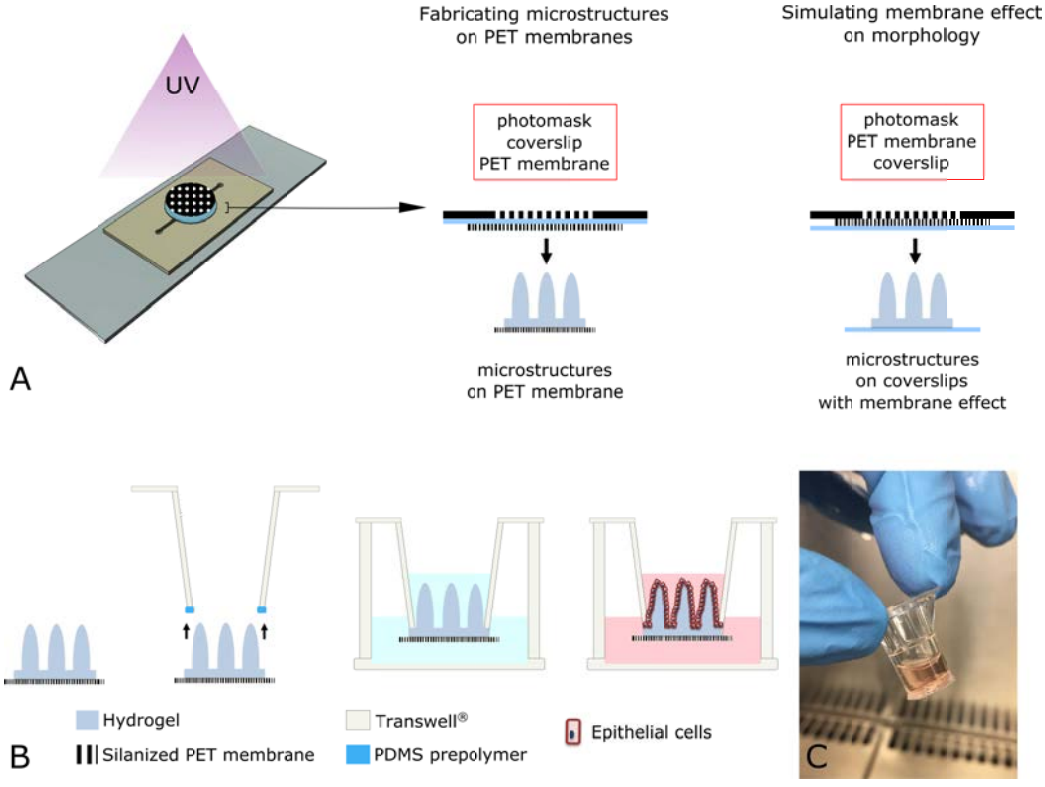

Figure 3.16: *Scheme showing the fabrication of microstructured hydrogels on porous PET membranes and on coverslips with membrane effect for morphological analysis (A). Scheme showing how microstructured hydrogels fabricated on porous PET membranes are mounted on Transwell® inserts for cell culture experiments (B). Image showing a mounted Transwell® insert (C). Note that it sustains the cell culture medium suggesting good sealing.*

For cell culture experiments, hydrogels fabricated on porous PET membranes were mounted on standard 24-well Transwell® filter inserts (Corning Costar) by

the following protocol (Figure 3.16 B). First, the polycarbonate membranes of the commercial Transwell® inserts were removed completely. Then, the inserts were cleaned with bleach and 70% ethanol and rinsed with distilled water. The inserts were further sterilized with UV irradiation for 15 min under the cell culture hood. The hydrogels fabricated on the silanized PET membranes were removed from the swelling solution in which they were kept and left out to let the excess liquid evaporate under the cell culture hood. In the meanwhile, a very thin layer of PDMS prepolymer mixture was spread onto a standard plastic petri dish. The inserts were stamped onto the PDMS prepolymer, and immediately, the PET membrane with the hydrogel on were placed on top of the stamped PDMS prepolymer. Mild pressure was applied at the ridges to assure contact between the membrane and the insert walls. Then, the inserts were let rest upside down to allow the curing of PDMS. As an initial approach, the mounted inserts were let dry overnight to allow the curing of the PDMS. However, the microstructures were drastically deformed due to this drying procedure. The morphological changes caused by drying was assessed by dehydrating and then rehydrating the microstructures and visualizing by a bright field microscope. As an improvement, the inserts were mounted and after 10-15 minutes, 10 μL of PBS was added on top of the microstructure region, just enough to keep the scaffolds wet but not to interfere with the curing of PDMS. Every couple of hours PBS was replenished and before overnight incubation, a 10 μL pipette tip bottom (matching the dimensions of the transwell insert walls) was cut and placed on top of the mounted inserts. The pipette tip bottom allowed the addition of more volume of PBS for the overnight incubation. The following day, 200 μL of PBS was added to the inserts to test the efficiency of the bonding by assessing the liquid leakage visually (Figure 3.16 C). All the manipulations explained above were performed under sterile conditions.

3.2.6 Organoid-derived crypt culture on 3D villus-like PEGDA-AA hydrogels allowing protein diffusion

To allow protein diffusion along the vertical axis of the villus-like microstructures, we adopted Transwell® setup as explained in the previous section. Organoid-derived crypt suspensions were prepared as explained in Section 1.2.2. The total crypt number in the suspension was estimated by proportioning the number of crypts counted in 5 μL to the total crypt suspension volume. PEGDA hydrogels

were fabricated, swollen to equilibrium weight, and mounted on Transwell® inserts as explained in the previous section 3.2.5. Later, the hydrogels were sterilized by storing them in 10% v/v penicillin/streptomycin in PBS until use. Before use, the hydrogels were functionalized with collagen type I as explained in section 2.2.5. The hydrogels were seeded with a density of 1500 crypts/sample and the cells were cultured for 6 days. Two conditions of cell culture were studied; only basolateral delivery (asymmetric administration) of ISC niche biochemical factors and both basolateral and apical delivery (uniform administration) of such factors. As ISC niche biochemical factors to be diffused through the hydrogel, EGF, Noggin, R-Spondin 1, Wnt3a and conditioned medium obtained from the culture of intestinal subepithelial myofibroblasts were used. These cell culture conditions were determined as the optimal to promote the growth of intestinal cells in previous chapters 1 and 2. In asymmetric administration condition, this cell culture medium was added only to the bottom compartment (source) and standard organoid growth medium without the ISC niche biochemical factors was added to the upper compartment (sink). For the uniform administration, the same ISC niche biochemical factors were added to both chambers. The gradient generation was started 24 h before seeding and both of the compartments were replenished with fresh media daily (approximately every 24 h) during cell culture in order to maintain the gradient profiles formed.

3.2.6.1 Immunofluorescence characterization

After 6 days of culture, the cells were fixed with 10% neutralized formalin (Sigma), permeabilized with 0,5% v/v Triton X-100 (Sigma), and blocked with a blocking buffer containing 1% w/v BSA (Sigma), 3% v/v donkey serum (Millipore), and 0,2% v/v Triton X-100 in PBS for at least two hours. Primary antibodies used were; rabbit anti-Ki67 (1:100, abcam), and mouse anti-cytokeratin 20 (CK20) (1:100, Dako). All samples were incubated with the primary antibody overnight at 4 °C followed by 1 h incubation at RT with secondary antibodies; Alexa Fluor® 488 donkey anti-mouse (invitrogen), and Alexa Fluor® 647 donkey anti-rabbit (Jackson ImmunoResearch), diluted at 1:500. Nuclei were stained with 4',6-diamidino-2-phenylindole (DAPI) (1:1000). Rhodamine phalloidin (Cytoskeleton) was used to stain filamentous actin (F-actin). The samples were mounted with Fluoromount-G® (SoutherBiotech).

3.2.6.2 Image acquisition, analysis and statistics

Fluorescence microscopy images of the immunostained cell samples were acquired using confocal laser scanning microscopy (TCS SP5, Leica) with 20x dry (N.A. = 0,70) objective at randomly selected locations. The laser excitation and emission light spectral collection were optimized for each fluorophore. For the four color scans the emission bands were adjusted to avoid overlap of the channels. The pin hole diameter was set to 1 Airy Unit (AU). A z-step of 2 μm was used for the stacks. Tile scans of the entire surface of the samples were acquired by Axio Observer 7 epifluorescence inverted microscope (Zeiss) with a low N.A. 5x objective. Rhodamine channel was used to acquire F-actin fluorescence images. The 3D reconstructions of the images were done using IMARIS software. The percentage of surface coverage could be calculated from the 2D projected areas only when the microstructure and the base regions were homogeneously covered. This is the situation in most of the cases, as reported in the previous chapter. However, in one of the samples, uniform administration condition, we have observed the otherwise. To be able to calculate the surface coverage correctly, we have performed necessary calculations to obtain true surface area. For that, first the surface area of one microstructure was estimated using the area of a truncated cone (ATC), which is equal to the sum of the lateral surface and the area of the upper circle as given in equation 3.14.

$$ATC = \pi(r + R)\sqrt{(R - r)^2 + h^2} \; + \; \pi r^2 \tag{3.14}$$

where r is the upper and R is the lower radius of the cone, as shown in figure 3.17 A. Afterwards, the total number of microstructures in a given area was estimated. For that, first the area occupied by a given number of microstructures (1 entire, 4 half, and 4 quarter microstructures: 4 in total) was calculated by selecting a square ROI in F-actin fluorescence images (Figure 3.17 B).

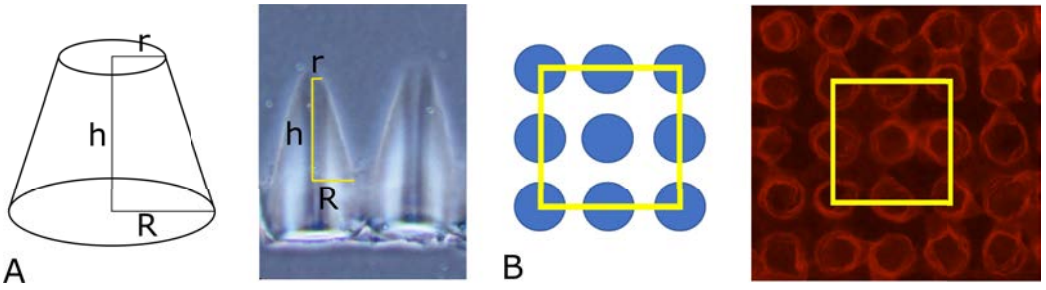

Figure 3.17: *Drawing of a truncated cone used to estimate the true surface area of one microstructure (A). Corresponding dimensions are indicated in both images. A rectangular ROI, crossing 9 microstructures to a total of 4 entire microstructures, as shown in the scheme and in the fluorescence image was used to calculate the area occupied by 4 microstructures, which then proportioned to the total surface area (B).*

Then, this number was proportioned to the 2D projected surface area of the microstructured hydrogels to obtain the total number of microstructures, p, in that given area. The true surface area (TSA) can then be calculated as follows;

$$TSA = 2D\,projected\,area - p(\pi R^2) + p * ATC \tag{3.15}$$

For the calculation of the true surface coverage, first the 2D projected surface area covered was measured using thresholding function of ImageJ free software. For the sample of uniform administration, uncovered parts were determined subtracting this value from the total area (Transwell® area). Then, the total TSA (for the entire sample surface) was calculated as explained above and the area of uncovered regions (as calculated by ImageJ thresholding function) was subtracted. For the sample of asymmetric administration, the coverage was estimated directly from the 2D projected covered surface area normalized to the total sample area (Transwell® area) by thresholding function of ImageJ software.

The quantification of Ki67 marker, used to determine the amount of proliferative cells, with respect to the total cell number was done by a custom-made ImageJ macro provided by the Advanced Digital Microscopy (ADM) Unit of Institute for Research in Biomedicine (IRB) (See Appendix B for the source code). Confocal microscopy stacks were obtained at least at 4 different positions among the areas covered with cell monolayer for Ki67 quantification. The statistical comparison was performed using two tailed, unequal variances Student's t-test and $p<0,05$ was considered significant.

The spatial distribution of CK20 signal along the surface of the microstructures was estimated by another custom-made ImageJ macro developed by the

ADM Unit of IRB (See Appendix C for the source code). The script quantifies the mean fluorescence intensity in the corresponding reporter channel within a binary mask limiting the measurements to the extension of the monolayer (F-actin signal). The measurements are performed slice by slice in the z-stacks to capture the intensity profile along the height of the microstructures (oriented perpendicularly to the image acquisition plane). The binary mask limiting the extension of the measurements is estimated by filtering (3D Gaussian filter) and thresholding (user defined level) the actin channel. In each slice, 2D connected particles smaller than 500 pixels were removed from the binary mask to discard spurious bits and only keep relevant sections. The accuracy of the segmentation was validated from summary images overlaying the masks over the original image stacks. As a complementary measurement, the integrated fluorescence intensity was also estimated within the same regions. For each sample, at least 4 stacks were acquired at randomly selected locations within the monolayer and quantified for spatial distribution of CK20 along the microstructures. To account for slight variations in microstructures heights (due to monolayers joining at the tips of the microstructures and sample preparation for imaging) and since some microstructures were not covered completely from tip to base, we limited the quantification to the first 175 μm from the microstructure tips. Maximum mean CK20 signal intensity and their corresponding positions along the microstructures were estimated from the profiles. As a measure of CK20 signal spread for each condition, widths at 50% of the maximum mean intensity were estimated from the profiles. Also, the cumulative sum of CK20 integrated intensity was computed and the height cut-off (from tip) at 75% of the total CK20 signal was determined for each condition from the cumulative profiles. The error bars in the figures represent the intra-sample variations. The data was processed and plotted with OriginPro 8.5 software.

3.3 Results

3.3.1 Mesh size of the PEGDA-AA hydrogels

In order to have a better insight into the network properties of the PEGDA hydrogels and consequently, the protein diffusivity through them, their mesh size (ξ) was using Flory-Rehner equilibrium swelling theory [16, 17, 19] as modified by Peppas and Merrill for hydrogels prepared in the presence of water [22, 40]. For that, the polymer volume fractions of the hydrogels in swollen and in relaxed states calculated from the swelling data presented in section 2.3.3 were used to first calculate the average molecular weight between crosslinks (M_c) (Section 3.2.1 Eqn. 3.4) and, then, the mesh size (Section 3.2.1 Eqn. 3.7) (Figure 3.18 A). To understand the dependence of the hydrogel network characteristics with the polymer concentration and UV exposure time two concentrations, 5% and 10% w/v P6000, and two UV exposure times, 150 s and 200 s, were selected. The concentrations tested mark the lower and upper limits of the range used to fabricate microstructured P6000 hydrogels (see Chapter 2 Section 2.2.1.1).

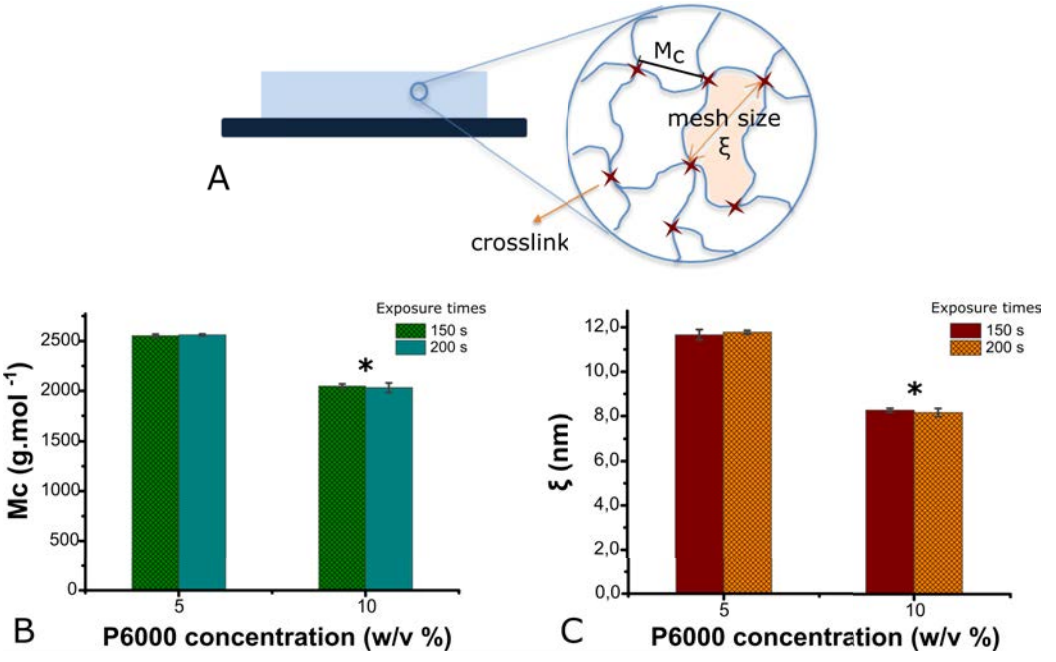

Figure 3.18: *Scheme of the network structure of a hydrogel showing crosslinks (red stars), mesh size (ξ), and molecular weight between crosslinks (M_c). Graphs showing estimated M_c (B) and mesh size (ξ) (C) for 5% and 10% w/v P6000 fabricated with 150 s and 200 s of UV exposure. Data are represented as mean ± standard deviation (Student's t-test, *p<0,001) of four technical replicas (n = 4).*

M_c values of hydrogel discs varied with PEGDA concentration and they ranged between 2030 g.mol^{-1} to 2560 g.mol^{-1} (Figure 3.18 B). Although one can expect the M_c values to be similar to the molecular weight of a single chain of PEGDA, that is 6000 g.mol^{-1}, since crosslinking is an end-linked reaction, we found that this is not the case. For all the conditions studied, M_c was by 58%-66% lower than 6000 (Figure 3.18 B). Similar findings, estimated M_c being less than molecular weight of single PEGDA chains, have been reported in number of studies [16, 41, 57]. It is well known that hydrogel networks are far from being ideal. They might contain number of defects, such as intra-chain cyclizations, chain entanglements, physical junctions and dangling ends (Figure 3.19). This is particularly true in poorly controllable chain growth polymerization processes such as free-radical polymerization of bifunctional acrylate derivatives like PEGDA [13, 50]. These imperfections that can occur during crosslinking cause a decrease in the apparent average molecular weight between crosslinks and consequently, in calculated M_c values. The M_c values depended on PEGDA concentration with 10% w/v hydrogels having significantly lower M_c than 5% w/v hydrogels (Student's t-test, p<0,001). The solution with higher concentration of PEGDA has more diacrylate reactive groups, which produces an increase in crosslinking density (see Section 2.3.3 for swelling ratios). Also, the likelihood that loops or imperfections occuring increases with higher PEGDA macromer concentrations, decreasing M_c.

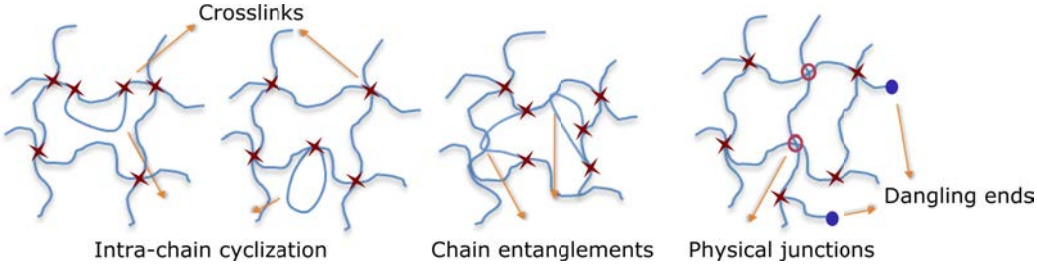

Figure 3.19: *Scheme depicting possible network defects. Adopted from Nafea et al. and Slaughter et al. [13, 58].*

As expected, a similar trend is observed in the mesh sizes. The mesh sizes of 5% w/v hydrogels were estimated to be 11,7 $\pm$ 0,2 nm and 11,8 $\pm$ 0,1 nm for 150 s and 200 s of UV exposure, respectively (Figure 3.18 C). Meanwhile, the mesh sizes of 10% w/v hydrogels were computed as 8,3 $\pm$ 0,1 nm and 8,2 $\pm$ 0,2 nm for 150 s and 200 s of UV exposure, respectively (Figure 3.18 C). In literature, comparable values were reported for PEGDA hydrogels, confirming the accuracy of

our results. Durst *et al.* obtained a mesh of 14 nm and 10 nm for 5% and 10% w/v P6000 hydrogels, respectively [57]. Al-Ameen *et al.* reported mesh sizes of 10% w/v P6000 hydrogels to be 7 nm [59]. As with M_c, the mesh of 10% w/v hydrogels was significantly lower than that of 5% w/v hydrogels (Student's t-test, p<0,001), indicating higher crosslinking densities. That is, higher the concentration, lower the M_c and therefore, lower the mesh size. This demonstrates that in our system the structural properties of the hydrogel can be regulated by varying the polymer concentration.

On the other hand, there was no statistically significant differences (Student's t-test, p>0,05) between the M_c and ξ of the hydrogels prepared with 150 s and 200 s of UV exposure. We can conclude that the UV exposure time range (150-200 s) we had chosen does not affect the crosslinking density of the hydrogels. This suggests that within our experimental setup and range of exposure time, the hydrogel network is saturated and cannot incorporate more chains into the structure even though the exposure times were increased from 150 s to 200 s. The results of gel fraction determination, reported in section 2.3.3.1, supported the hypothesis that in this time range (150-200 s) the maximum possible PEGDA macromer conversion (74%-84%) had already been achieved.

Our results clearly demonstrate that the network parameters (M_c and ξ) of the PEGDA hydrogels, depends on the PEGDA concentration. Regulating the network properties of hydrogels by altering the concentration of polymer precursors is well established [15, 41, 50, 57, 59]. Depending on the application of interest; e.g. tissue engineering scaffolds, drug delivery vehicles, tissue barriers, cell encapsulation medium, network properties (appropriate polymer concentrations) have to be adjusted [13]. For diffusion studies, it is relevant to remember that a decrease in the average mesh size hinders the mobility of the polymer chains, and thereby decreases swelling, limiting the transport of substances (diffusivity) through the hydrogel [58]. For proper diffusion of the biomolecules, the mesh of the hydrogel network has to be equal to or greater than the diameter of the biomolecules. Taking into account that most biomolecules such as proteins, growth factors and others that allow cell survival have a diameter of 5-15 nm [60], both 5% and 10% w/v P6000 hydrogels would allow the diffusion of these biomolecules. More importantly, the hydrodynamic diameters of main ISC niche biochemical factors (EGF, R-Spondin 1, Noggin, Wnt3a) range from 3 to 7,2 nm (see Section 3.2.3 Table 3.1). Therefore, both 5% and 10% P6000 hydrogels are suitable for the diffusion of these proteins through their network.

3.3.2 Determination of the diffusion coefficient of BSA protein in PEGDA-AA hydrogels

We have designed and fabricated a simple diffusion chip, on the bases of previously published reports [42, 43], to calculate the diffusion coefficients of proteins within the swollen P6000 hydrogel network (D_g). The diffusion chip consisted of a hydrogel sandwiched between a completely sealed source and sink chamber (Figure 3.20 A). The protein solution was introduced to the source chamber and the total mass diffused with time was quantified as explained in section 3.2.2. A protein with a hydrodynamic diameter smaller than the mesh estimated for P6000 hydrogels, BSA [44], and a protein much larger than the mesh, laminin [45], were selected for the diffusion studies. A proof-of-concept study was performed to validate the functionality of the fabricated diffusion chip.

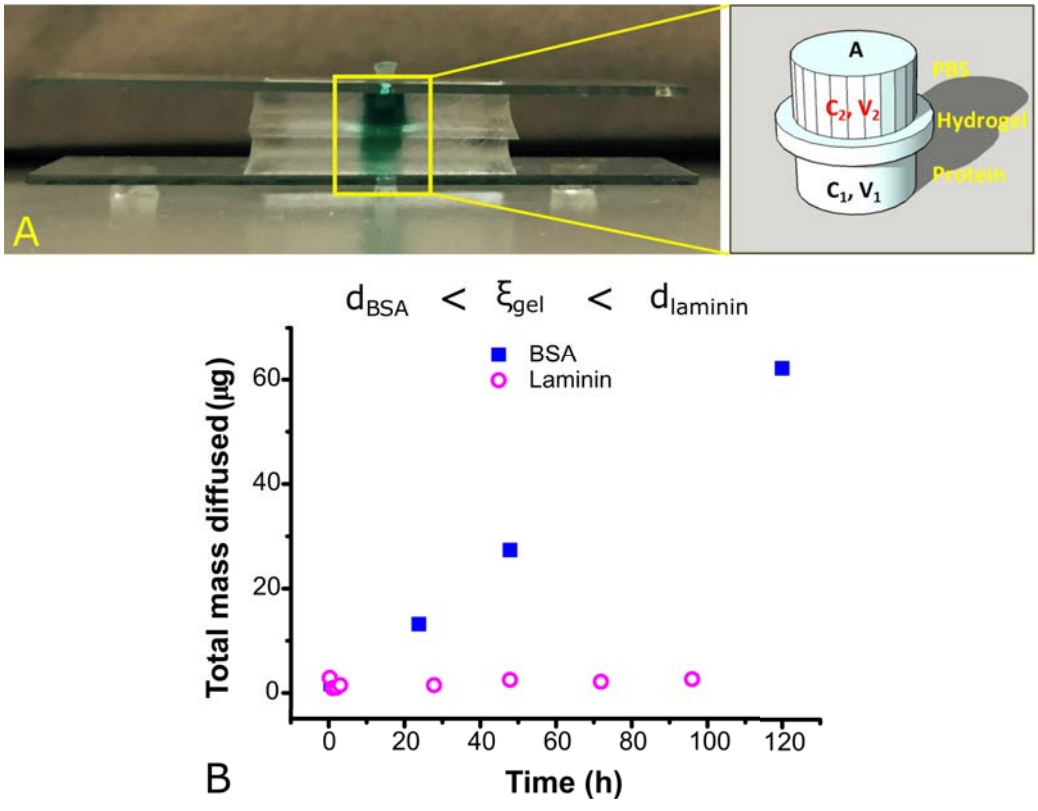

Figure 3.20: *Image of the hydrogel incorporated diffusion chip (A). Scheme indicated corresponding components. Graph showing the total mass of BSA and laminin diffused as a function of time (B).*

The successful fabrication of completely sealed chip suitable for the diffusion

studies was achieved (Figure 3.20 A). Nevertheless, the fabrication had some challenges, especially at the bonding step of the glass slides to PDMS to seal the donor and the receiver chambers, which required plasma activation of the PDMS surfaces with the hydrogel sandwiched in between. Although, we covered the openings to avoid exposing the hydrogel surface to plasma, the structural integrity of the hydrogel could get affected in this step. Until obtaining a completely sealed chip with the hydrogel unharmed, numerous trials had to be made. Only the ones that were assured to be completely sealed were used for the following diffusion experiments.

Figure 3.20 B shows the plot of the total mass diffused to the sink chamber for BSA and laminin proteins as a function of time for 10% w/v P6000 hydrogel. The total mass of BSA that diffused to the sink chamber incremented with time. However, the laminin concentrations measured in the sink chamber were at the baseline levels and didn't change over time. This suggests that laminin does not significantly penetrate the network of the tested hydrogel, presumably due to its diameter, $\approx$ 40 nm [45, 61], being much larger than the mesh of the studied hydrogel, 8 nm (see Section 3.3.1 for mesh size values). For BSA, a linear relationship between the diffused protein and time was observed. Because the diffusion chip is a closed system, the diffusion of proteins into the sink chamber would eventually slow down and come to an equilibrium. However, within the working time range (up to 120 h) we were still in the linear diffusion regime. Then, these collected data points were used to determine the diffusion coefficient of BSA (D_g) through the hydrogel (Section 3.2.2 Eqn. 3.9). The D_g value of BSA through 10% w/v P6000 was calculated to be 1,40 $\pm$ 0,02 x 10^{-12} $m^2.s^{-1}$. In previously published studies, D_g values for BSA within the same order of magnitude were reported for similar hydrogels. Peret and Murphy calculated D_g to be 1,40 x 10^{-12} $m^2.s^{-1}$ within 15% w/v P8000 at 25°C [62]. Engberg and Frank calculated D_g to be 1,87 x 10^{-12} $m^2.s^{-1}$ within 33% w/v P8000 at 37°C [43] and Lee *et al.* reported the diffusivity of BSA to be 5 x 10^{-12} $m^2.s^{-1}$ within 10% w/v P3000 at 25°C [50]. This validates the accuracy of our result and the functionality of the diffusion chip.

Peppas *et al.* described the molecular diffusivity within the hydrogel network as:

$$D_g = D_0(1 - \frac{r_s}{\xi})e^{-Y\frac{Q}{Q-1}} \tag{3.16}$$

where D_0 is the diffusivity of the molecule in pure solvent (BSA in aqueous media), r_s is the hydrodynamic radius of the diffusing molecule (3,6 nm for BSA

[44]), ξ is the mesh size of the network, Q is the swelling ratio, and Y is the ratio of the critical volume required for the translational movement of the encapsulated particle to the average free volume per molecule of solvent, which is usually taken as 1 [15]. We calculated D_g of BSA in 10% w/v P6000 using the above equation and previously measured values of the mesh size, 8,2 nm as reported in the previous section 3.3.1, and the Q, 2,2 as reported in section 2.3.3. D_0 was calculated as 9,1 x 10^{-11} $m^2.s^{-1}$ using Stokes-Einstein equation (Section 3.2.3 Eqn. 3.13). D_g estimated in this fashion was found to be 8,47 $\pm$ 0,29 x 10^{-12} $m^2.s^{-1}$, which is about 6 times more than the experimentally measured value. The discrepancy between estimated and experimentally measured D_g values might be due to possible variations of mesh size within the hydrogel. The mesh size estimated by Flory-Rehner equilibrium theory is an average value. In our hydrogel fabrication method, the light is attenuated in the vertical axis of the UV irradiation [63, 64], which most probably causes the layers closest to the light source get more crosslinked. Highly crosslinked regions would have a smaller mesh limiting the diffusion of the protein.

Overall, D_g value determined experimentally was comparable with the values reported in the literature for BSA in similar hydrogels [43, 62]. Importantly, BSA diffuses through the P6000 hydrogel network, while laminin does not due to the size restriction, demonstrating the functionality of the chip.

3.3.3 Characterization of the spatio-chemical gradients of ISC niche biochemical factors on PEGDA-AA hydrogels

In our system we aimed to generate the spatio-chemical gradients of ISC niche biochemical factors based on free diffusion of the proteins from a source to a sink. For the characterization of the gradients created in this fashion, first we developed an *in silico* model to determine the gradient profiles of each ISC niche factor formed within the hydrogels in our experimental setup (Section 3.3.3.1). Then, we visualized the gradients of fluorescently labelled BSA with light-sheet fluorescence microscopy (Section 3.3.3.2). Finally, based on these experimental findings, the *in silico* model was revised to better reflect the experimental conditions for the cell culture experiments (Section 3.3.3.3).

3.3.3.1 *In silico* modeling of the spatio-chemical gradients of ISC niche biochemical factors

Finite element method (FEM) simulations were performed to predict the spatio-chemical gradients of ISC niche biochemical factors formed within our PEGDA hydrogels. Mainly, we were interested in predicting the diffusion of Noggin, R-Spondin 1, Wnt3a and EGF. Initially, the *in silico* diffusion model was developed considering constant source concentrations (simulating an infinite source) at the hydrogel bottom boundary, and with a large finite sink. Two geometries for the hydrogels were implemented; 1) rectangle and 2) microstructure (see Section 3.2.3 Figure 3.8). Simulations were run considering the diffusion coefficients of biomolecules on our PEGDA material. Diffusion coefficients of model proteins were used for this purpose (see Section 3.2.3). The simulations were run up to 24 h, which was the cell culture medium change frequency set for convenience. Concentration of proteins in cross-sections of the hydrogels were obtained as a function of the height in the hydrogel (Figure 3.21 Color maps) and diffusion time (Figure 3.21 Graphs). In the rectangle model, at the initial time points these axial profiles exhibited an exponential decay for all proteins. At 24 h all the proteins had reached linear profiles, suggesting that the characteristic time (setup time) of diffusion of proteins to reach a pseudo equilibrium within the hydrogel geometry is shorter than 24 h [35]. In a system, where the concentration is only constrained at one end (source), it is expected that the steady state is reached for $c = c_{source}$ at all points. However, in practice, we observe that a pseudo steady state establishes within less than 24 h, with linear concentration profiles in the hydrogel. From that point, the concentration is expected to rise very slowly at the gel-sink interface (as a consequence of the large sink filling up). However, since this happens at a time scale $> > >$ 24 h (confirmed by FEM simulation), we consider the state reached at 24 h as a pseudo steady state of the system. One could then predict that medium change every 24 h would lead to the stabilization of the concentration profiles.

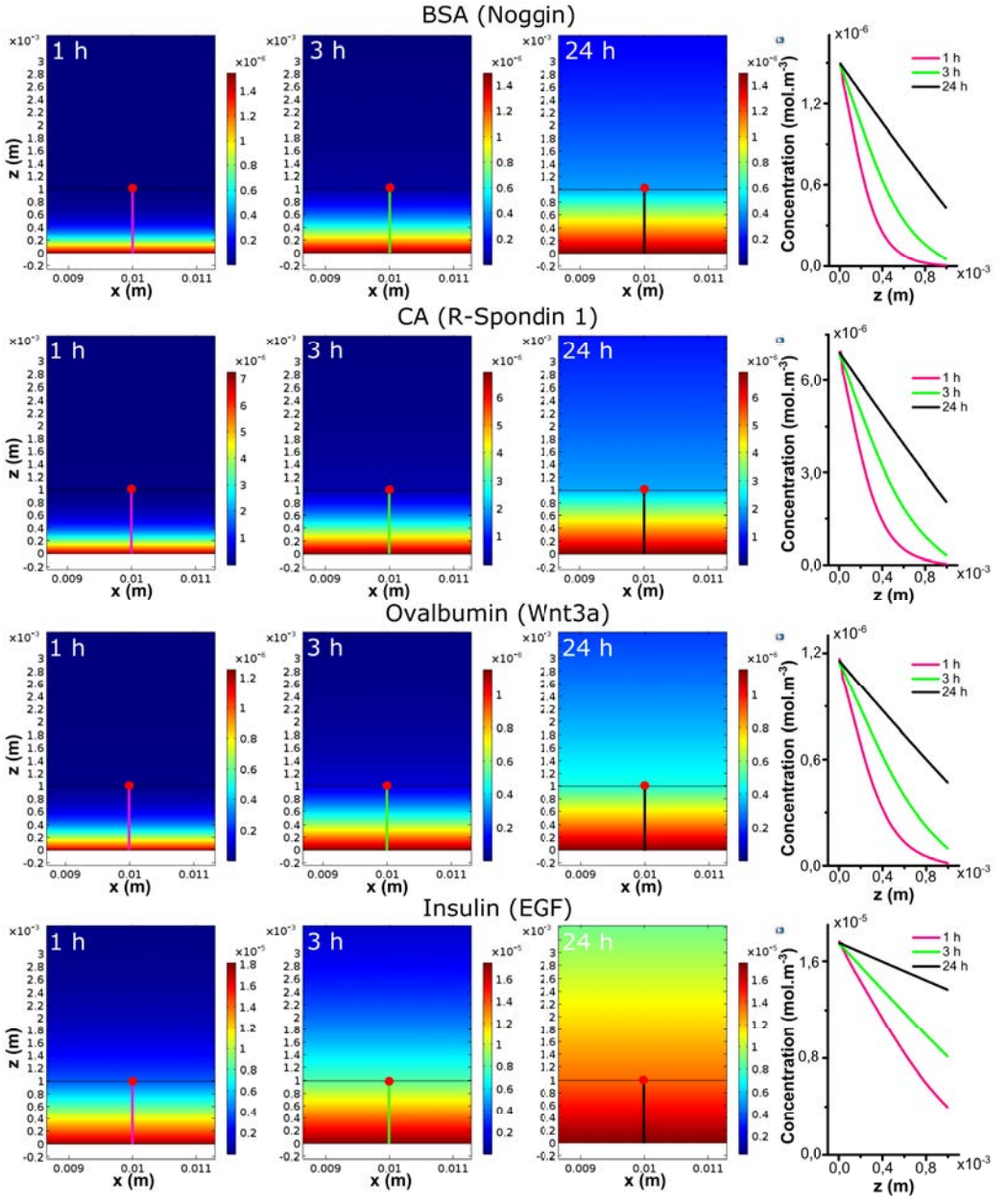

Figure 3.21: *Solutions of the 2D FEM simulations of the rectangle model for BSA, CA, Ovalbumin, and Insulin at 1 h, 3 h, and 24 h (left panels). Graphs showing the change in concentrations as a function of position along the z-axis at 1 h, 3 h, and 24 h (right panel). Profiles were taken along the lines indicated on 2D color maps and the red dot represents a point at the hydrogel - sink interface.*

Insulin (EGF) had loaded the hydrogel much faster than the rest of the proteins (Figure 3.21 Color maps). This is because Insulin is much smaller in size

than the other proteins (5,7 kDa *vs.* 28,0-66,5 kDa) and therefore, the D_g for Insulin is much larger that the others, and it has a higher source concentration. The slopes of the linear profiles at 24 h were calculated to be -1,1.10^{-3} mol.m^{-4}, -4,9.10^{-3} mol.m^{-4}, -6,9.10^{-4} mol.m^{-4}, and -3,8.10^{-3} mol.m^{-4} for BSA, CA, Ovalbumin, and Insulin, respectively. This, led to concentrations that differed from the source to the hydrogel surface (z = 1 mm) by 73% for BSA (Noggin), 70% for CA (R-Spondin 1), 58% for Ovalbumin (Wnt3a), and 20% for Insulin (EGF). These differences in relative concentration drops reflect the differences in diffusion coefficients of the proteins. The change in concentration as a function of time at the hydrogel - sink interface (z = 1 mm) revealed that the concentrations at the interface increased fast at the initial hours of diffusion and then slowed down significantly especially for BSA, Ovalbumin, and CA, reaching pseudo equilibrium at 24 h (Figure 3.22). However, a complete equilibrium could not be achieved as the sink continues to fill with time. Nevertheless, this increase is quite insignificant as the sink volume is much larger than that of the hydrogel. Therefore, we consider that the pseudo steady state is reached at 24 h.

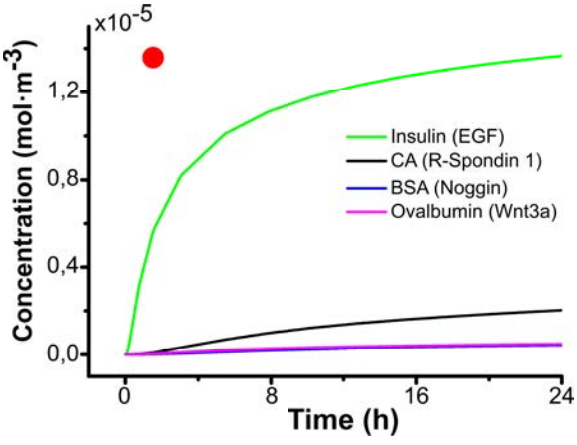

Figure 3.22: *Graph showing the change in concentration of proteins as a function of time at the hydrogel - sink interface (z = 1 mm). Measurement point represented by the red dot in the 2D color maps given in figure 3.21.*

We then have implemented the microstructure geometry in the *in silico* model, as we were interested in the concentration gradients generated along the surface (contour) of the microstructures. The microstructure heights were set to 300 μm, matching the heights of the microstructures of the PEGDA hydrogels used for the following cell culture experiments. As previously, simulations were run considering the diffusion coefficients of model proteins (see Section 3.2.3) on the

PEGDA hydrogel, up to 24 h. Concentration of proteins along the contour of the microstructures were obtained as a function of vertical position (z) (Figure 3.23 Color maps) and diffusion time (Figure 3.23 Graphs). In the microstructure model, the hydrogels were loaded much faster than in the rectangle model (Figure 3.23 Graphs), due to the dimensions of the microstructures that were 300 μm in height, smaller than 1 mm height rectangles. The concentration profiles along the z-axis were linear at 24 h for all the proteins, suggesting again that a pseudo equilibrium was attained [35]. Although, gradients were much less pronounced compared to those of the rectangle model. The slopes of the linear gradient profiles at 24 h were computed to be $-4{,}8.10^{-4}$ mol.m^{-4}, $-1{,}8.10^{-3}$ mol.m^{-4}, $-3{,}4.10^{-4}$ mol.m^{-4}, and $-2{,}2.10^{-3}$ mol.m^{-4} for BSA, CA, Ovalbumin, and Insulin, respectively. This, led to concentrations that differed by 17% for BSA (Noggin), 9% for CA (R-Spondin 1), 10% for Ovalbumin (Wnt3a), and 6% for Insulin (EGF) from the hydrogel base (z = 150 μm) to the tip (z = 450 μm). The steepest gradients in terms of concentration differences were predicted for BSA (Noggin), CA (R-Spondin 1), and Ovalbumin (Wnt3a). The gradient of Insulin (EGF) was insignificant.

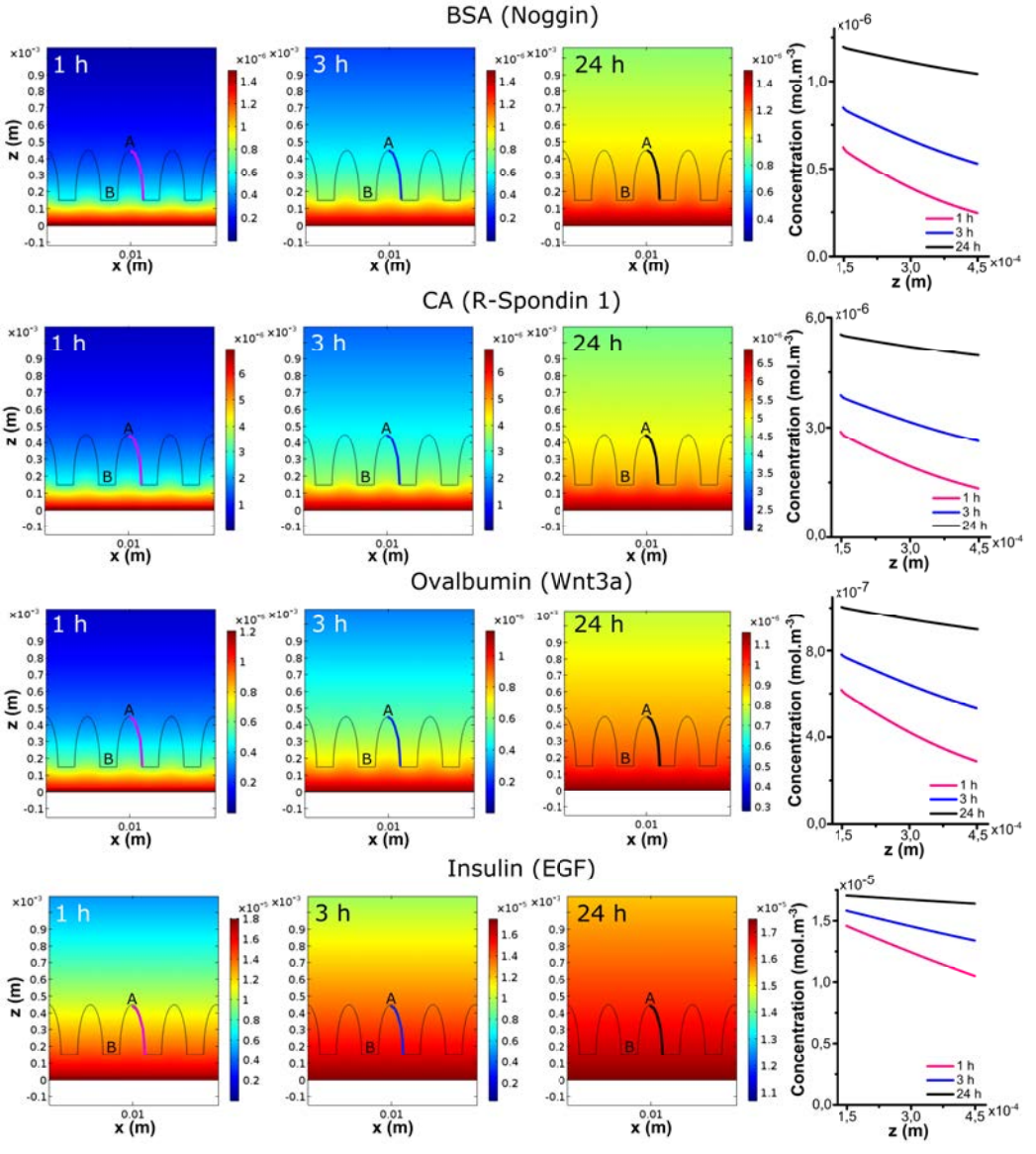

Figure 3.23: *Solutions of the 2D FEM simulations of the microstructure model for BSA, CA, Ovalbumin, and Insulin at 1 h, 3 h, and 24 h (left panels). Graphs showing the change in concentrations as a function of position on the microstructure surface along the z-axis, at 1 h, 3 h, and 24 h (right panel). Profiles were taken along the curves indicated on 2D color maps. Two points at the hydrogel interface at the tip (A) and at the base (B) were defined.*

The concentrations at the interfaces increased fast at the initial hours and then slowed down significantly (Figure 3.24), a behavior also observed in the rectangle model. However, in the microstructure model, the concentrations of all proteins

both at the base and the tip stabilized faster already reaching the pseudo equilibrium point at 24 h. This suggests that within this geometry, the time scale at which media is typically refreshed (24 h) during routine cell culture is sufficient to provide the cells with stable concentrations. The concentrations at the base were higher than the concentrations at the tip due to the proximity to the source.

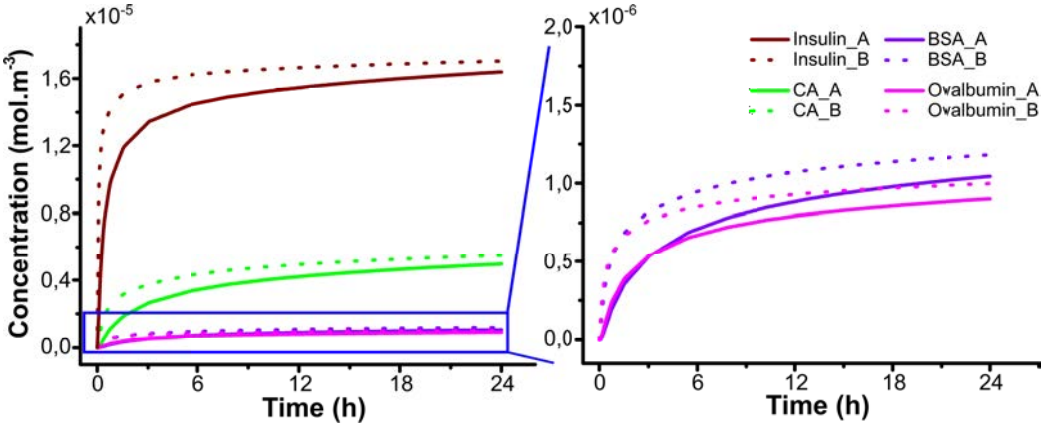

Figure 3.24: *Graphs showing the change in concentration of proteins as a function of time at the hydrogel - sink interface at the tip (z = 450 μm) and at the base (z = 150 μm), represented by points A and B in the 2D color maps (figure 3.23)*

In silico modeling of protein diffusion through PEGDA hydrogels with rectangular and microstructured cross-sections revealed that within the experimental setup that fulfills the boundary conditions set in these models (constant source concentrations), EGF (modeled with Insulin) almost does not form gradients. The gradients computed for the other proteins were more prominent, with the percentage concentration change from the base to the tip of the microstructures ranging from 16,7% to 9%. Although, more than the slope of the gradients, threshold concentrations necessary for the maintenance of ISCs might be more significant in controlling the growth and differentiation of ISCs. For instance, Ahmad *et al.* demonstrated that the minimum necessary concentration of R-Spondin 1 for ISC renewal was 88 $ng.mL^{-1}$ [37], lower than the R-Spondin 1 concentrations used in standard organoid cultures (typically 500 $ng.mL^{-1}$) [65, 66].

Overall, we have set up an *in silico* model to predict the gradients of ISC niche biochemical factors formed within the PEGDA hydrogel. Knowing the concentration gradients of these factors along the microstructure surface of the hydrogels provides valuable information in correlating the outcomes of cell cultures experiments with the gradient profiles.

3.3.3.2 Visualization of spatio-chemical gradients with light-sheet fluorescence microscopy

In order to create gradients of ISC niche factors within hydrogels and allow their characterization by microscopy techniques, a custom-made microfluidic device that allowed allocating the PEGDA hydrogel was designed and fabricated. One of the most critical design constraints for imaging was the physical access to the entire hydrogel from the sides and the top. In other words, the light path had to be free of obstacles, such as PDMS. To this end, the chip was designed in a way that the hydrogel would stick out allowing proper physical access, as it can be seen in figure 3.25 A. For that, the hydrogel was fabricated on a porous membrane supported by a layer of PDMS (250 μm) much thinner than the hydrogel disc (h = 1 mm) and, then, bounded to PDMS layer composing the microfluidic channel. An added technological challenge was to obtain a totally sealed source chamber with an inlet and outlet to deliver the proteins to the source compartment placed below the hydrogel. The fabrication procedure developed (described in Section 3.2.4.1), reached these requirements. For the visualization of protein gradients on the hydrogels, a fluorescently labelled model protein BSA_TxRED was selected. Fluorescently labelled protein gradients were visualized in-chip by light-sheet fluorescence microscopy (LSFM). LSFM technique was selected as it permits fast imaging at large working distances with fine axial resolution, a trade-off difficult to achieve by traditional confocal microscopy [52, 53]. By decoupling the illumination and detection light paths, LSFM allows a flexible sample access and mounting (not necessarily a flat coverslip) (see Section 3.2.4.2 Figure 3.11) [52, 53]. This is especially important to image large samples extended in all three dimensions. Additionally, LSFM offers high signal-to-noise ratios, high efficiency (minimal bleaching and photo-damage), and high imaging speed [52, 53], all important to this application. To fit the sample in the microscope a custom-made sample holder was designed and fabricated (Figure 3.25 B), which had transparent walls permitting the access of the light-sheet to the sample and a pedestal with 25° inclination to have better access to the hydrogel and the source chamber.

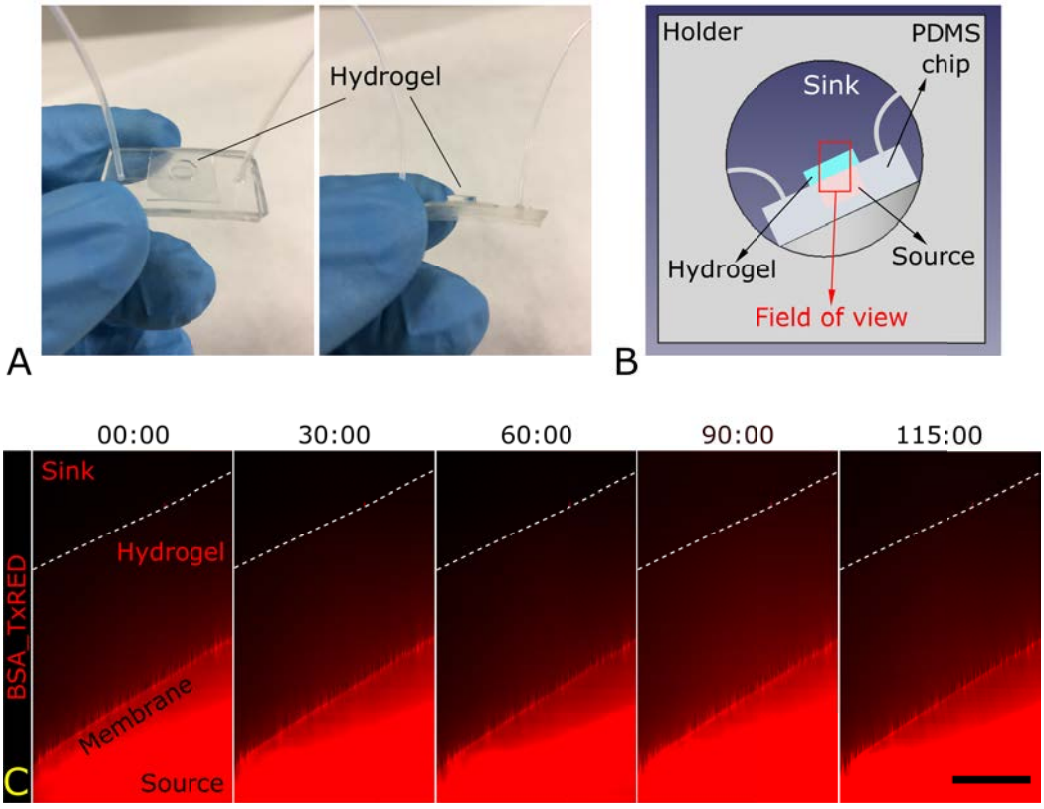

Figure 3.25: *Microfluidic chip allocating the hydrogel disc (A). The protein solution is delivered through the tubes to the chamber below the hydrogel. Scheme depicting the LSFM holder with the PDMS chip (B). Cross sectional fluorescence images acquired by LSFM spanning the source, hydrogel and the sink at different time points showing the stable gradient of BSA_TxRED (C). Scale bar: 500 μm.*

As an initial trial, we decided to measure the gradient profiles of fluorescently labelled BSA (BSA_TxRED). For that, it was aimed to visualized the gradients formed within the hydrogel along the z-axis after 24 h of diffusion, as it is done in the FEM simulations (Section 3.3.3.1). However, due to logistic limitations the hydrogel was loaded with the protein 43 h prior to the experiment and both the source and the sink chambers were refreshed with initial concentrations 24 h after loading and right before performing the LSFM experiment. The chip was placed in the custom-made holder and imaged acquiring stacks at intervals of 5 minutes intervals up to 115 minutes in total. The gradient profiles of BSA_TxRED acquired are shown in figure 3.25 C. These images show that within the time frame tested no significant change in the fluorescence intensities was observed.

To perform quantitative analysis, the fluorescence intensity profiles were measured along the z-axis and spanning the source, the hydrogel and the sink, as indicated by the white arrow in figure 3.26 A, at selected 5 time points (0 min, 30 min, 90 min, 115 min) and were plotted with respect to vertical position (z) (Figure 3.26 B). As seen in the fluorescence intensity profiles, the gradients formed within the hydrogel were linear and unchanging throughout the time of acquisition demonstrating that we were at pseudo steady state within the time frame of the acquisition. This finding supports the hypothesis that the steady state can be maintained by implementing a periodical medium replenishment (as performed here) when finite source and sink volumes are used [35]. The slope of the linear fit was computed to be $-4{,}4.10^{-2}$ $mol.m^{-4}$ (Figure 3.26 C, Hydrogel), which led to a change in protein concentration from the hydrogel bottom to top by 60%.

In figure 3.26 C the intensity profiles measured within the source, hydrogel and the sink regions are presented separately. In the source chamber, a stable concentration coinciding with the protein solution concentration added ($15{,}0 \times 10^{-5}$ $mol.m^{-1}$) was observed for the regions away from the hydrogel interface, while a decay was observed closer to the hydrogel boundary. This decay in the source concentration is probably due to the formation of gradients in unmixed solutions [67], as mixing wasn't implemented in the experimental setup. This gradient can be avoided by designing the microfluidics and the source chamber in such a way that allows mixing of the solution. In addition, the protein solution wasn't perfused continuously, in other words the source was finite, and the overall protein concentration in the source was decreasing slightly with time (Figure 3.26 C, Source).

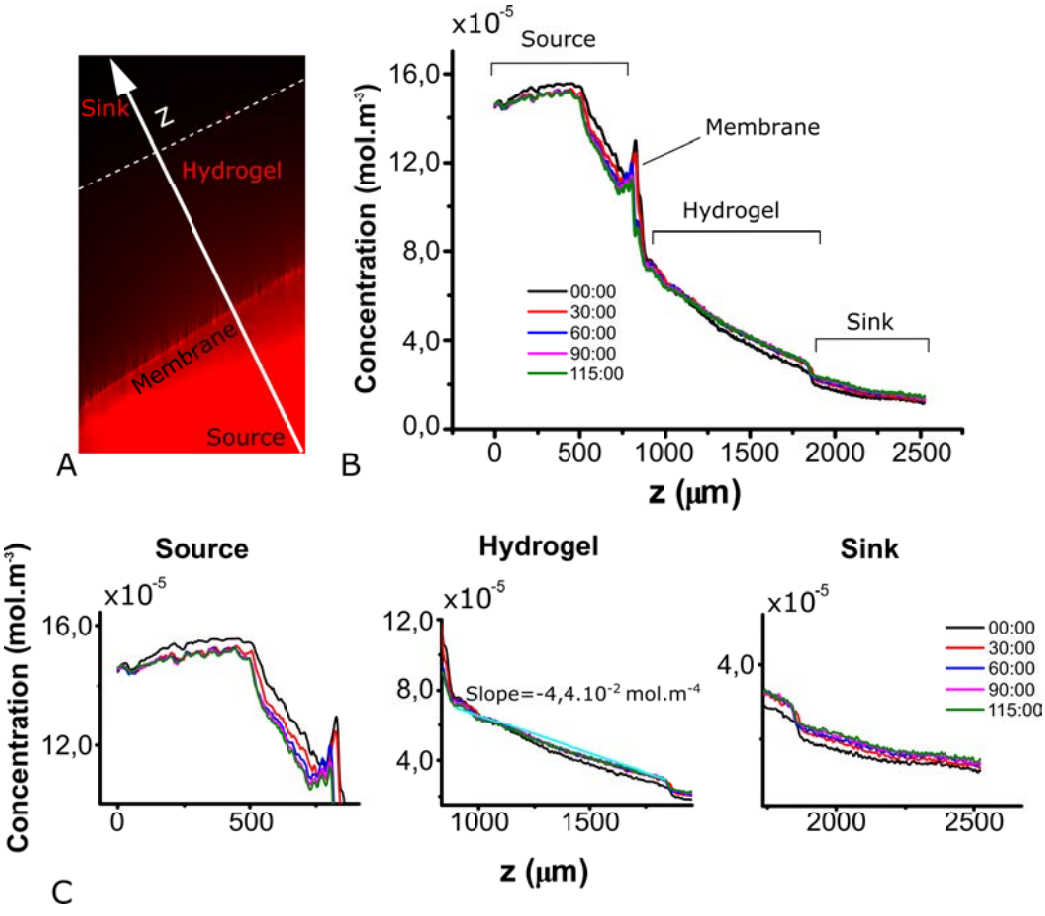

Figure 3.26: *Cross sectional fluorescence image spanning the source, hydrogel and the sink of BSA_TxRED diffusion (A). The white arrow marking the line at which the fluorescence intensity profiles were measured. Graph showing the intensity profiles at different time points (B). Magnification of the graph given in B at source, hydrogel and sink regions (C). The slope of the linear fit performed on the gradient profile within the hydrogel at t = 115 min (R^2 = 0,985) was computed to be -4,4.10^{-2} mol.m^{-4}.*

On the other hand, protein accumulation was observed both at the membrane - hydrogel (z = 750 µm) and at the hydrogel - sink (z = 1830 µm) interfaces (Figure 3.26 B, C). The protein concentrations dropped by 30% and 20% at the membrane - hydrogel and the hydrogel - sink interface interface, respectively. Most of the time, the material accumulation at the interfaces is considered negligible [42, 43] or not even considered [34, 35, 37]. On the contrary, our experimental results revealed that the accumulation at the interfaces was significant, especially at the membrane-hydrogel interface.

Taking all these observations into account, the *in silico* model was revised including: 1) finite source geometry and 2) gel loading and medium change cycles, and 3) the effect of material accumulation at the interfaces was simulated by adding thin diffusion barrier effects (nominal values were selected taking into account the percent decrease observed experimentally). Figure 3.27 shows the changes in the concentration profiles predicted with *in silico* model along the perpendicular axis of the hydrogel, spanning the source, the hydrogel and the sink with respect to time. During the gradient formation, finite volume source depletes as the protein diffuses from the source into the hydrogel, eventually reaching a pseudo steady state with linear profiles. However, since finite volume compartments are used, the source concentration depletes with time and the solutions in the compartments have to be refreshed (the time of the medium change is important in defining the gradient profiles). Implementing the medium change cycles into the *in silico* model proved this assumption. The frequency of the medium change (in this case 24 h) determined the initial gradient concentration range and further changes only stabilized more these profiles (Figure 3.27). After the first medium change, there was a slight shift to higher concentration. This is because after 24 h the source has already depleted to a new concentration C_s which is less than the initial source concentration C_0. Replacing the solution with a concentration C_0 perturbs the equilibrium and the concentration in the hydrogel increases then re-stabilizes until a shifted pseudo-steady state is reached [35]. If desired, this can be avoided by refreshing the source solution with C_s, which can be deduced from the *in silico* model. The disruption of the gradient at the initial time points were much more significant when the barrier effects were not implemented. This demonstrates that the high fluidic resistance provided by the porous membrane (simulated by diffusion barrier effects) helps to minimize disruption to the developed profiles during medium change cycles.

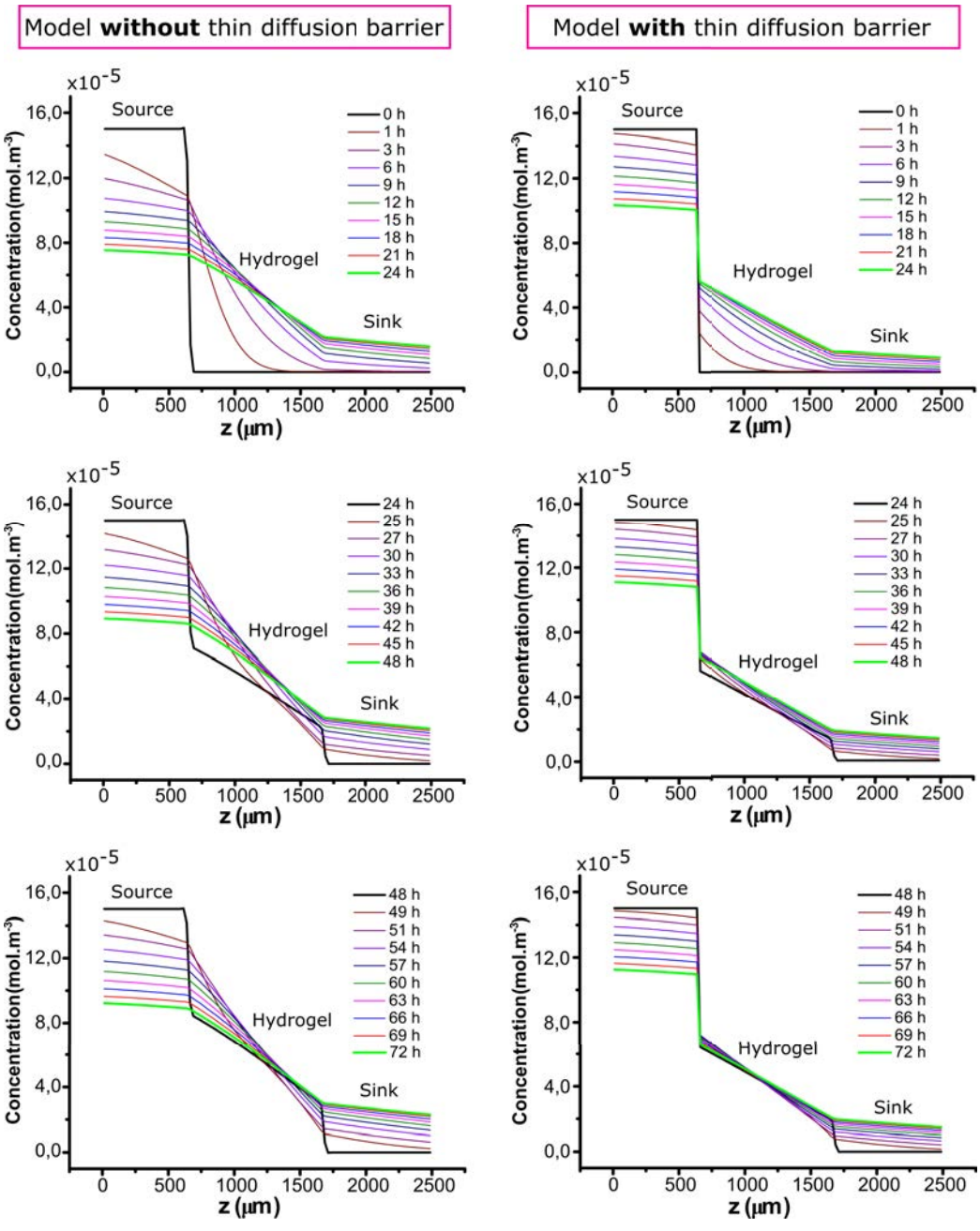

Figure 3.27: *Graphs showing the intensity profiles taken along a perpendicular line spanning the source, hydrogel and the sink of FEM simulations with medium change cycles of 24 h implemented without (left panel) and with thin diffusion barrier (right panel) at the hydrogel - membrane interface. BSA was used as the model protein for these simulations.*

Once the necessary changes were implemented to better simulate the experimental conditions, *in silico* model predicted similar stable gradient profiles as seen

in the 2D solutions of FEM simulation (Figure 3.28 A). The concentration profiles measured in the simulations (Figure 3.28 B) and the slope of the concentration gradient formed within the hydrogel, -5,9.10^{-2} mol.m^{-4}, were in good agreement with the concentration profiles and the gradient slope calculated experimentally (-4,4.10^{-2} mol.m^{-4}) (Figure 3.26 B, C). These findings validate the *in silico* model that we have developed.

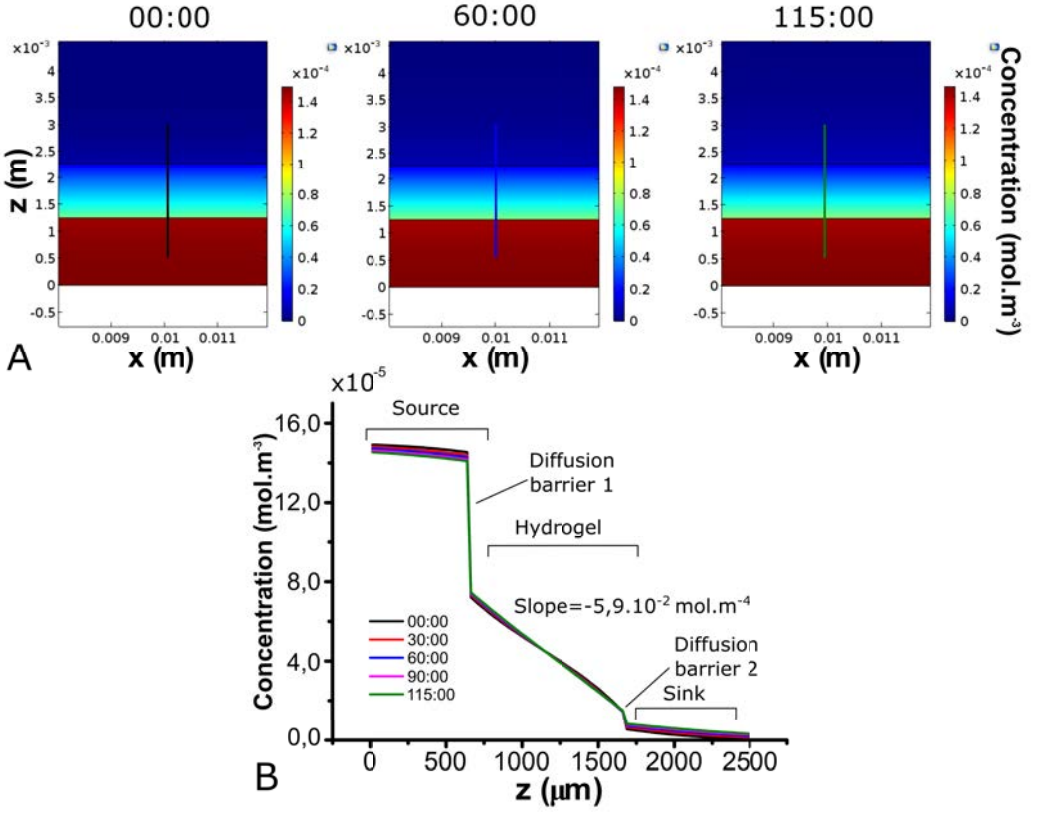

Figure 3.28: *2D solutions of FEM simulation at 0 min, 60 min, and 115 min (A). Intensity profiles predicted by the FEM model after the medium change cycles and the observed diffusion barriers were implemented (B). The profiles were taken along the lines indicated in A. The slope of the linear fit performed on the gradient profile within the hydrogel at t = 115 min (R^2 = 0,999) was computed to be -5,9.10^{-2} mol.m^{-4}.*

3.3.3.3 *In silico* modeling of the spatio-chemical gradients formed along microstructured surface in Transwell® setup

In order to be able to create gradients along the vertical axis of the villus-like hydrogels access to both upper and bottom side of the hydrogel is essential. Hydrogel incorporated microfluidic chip presented in the previous section 3.3.3.2

can be one strategy to form the gradients. On the other hand, a simplified setup that would permit facile testing of the complex biological system is desirable. For that reason, we decided to use standardized Transwell® setup, which consists of a semipermeable filter inserts that create two separate compartments (upper and lower compartment). The lower compartment was the source and the upper compartment was the sink. As oppose to the hydrogel incorporated PDMS chip, in the Transwell® setup the source chamber is much larger than the sink chamber. In order to estimate the nature of the expected gradients in the Transwell® setup, the *in silico* model with microstructure geometries and an infinite source (presented in Section 3.3.3.1) was revised, in the light of the findings of LSFM characterization. Finite source volume and thin diffusion barrier effects at the interfaces were added to the model. Then, the concentrations of the diffusing factors along the microstructured surface with respect to the position in the vertical axis were determined and plotted. Figure 3.29 shows the estimated gradient profiles for each protein along the microstructured surface at 1 h, 3 h, and 24 h after loading (24 h was selected as the maximum time since it is the typical/convenient medium change time interval). The protein concentrations differed from the hydrogel base (z = 150 μm) to the tip (z = 450 μm) by 21% for BSA (Noggin), 19% for CA (R-Spondin 1), 17% for Ovalbumin (Wnt3a), and 5% for Insulin (EGF). Similar to the predictions of the previous model, the most marked gradients were observed for BSA (Noggin), CA (R-Spondin 1), and Ovalbumin (Wnt3a) and the gradient of Insulin (EGF) was insignificant. However, with the exception of the Insulin (EGF), the concentration change of the factors from the base to the tip of the microstructures was greater in the revised model compared to those of the previous version (see Section 3.3.3.1). It is noteworthy to mention that the gradient profiles were non-linear (Figure 3.29). To check whether this change in the gradient profiles was due to the diffusion barrier effects or the finite source volumes we removed the diffusion barrier from the model and ran the simulation. Indeed, that was the explanation and without the barriers at the hydrogel interface linear gradient profiles were obtained at 24 h, similar to the findings of the previous model. The percentage decrease values were also slightly affected. However, since at the present we lack the experimental data, LSFM characterization of the gradients formed within the microstructures rather than hydrogel discs, we consider the revised model as the more accurate one.

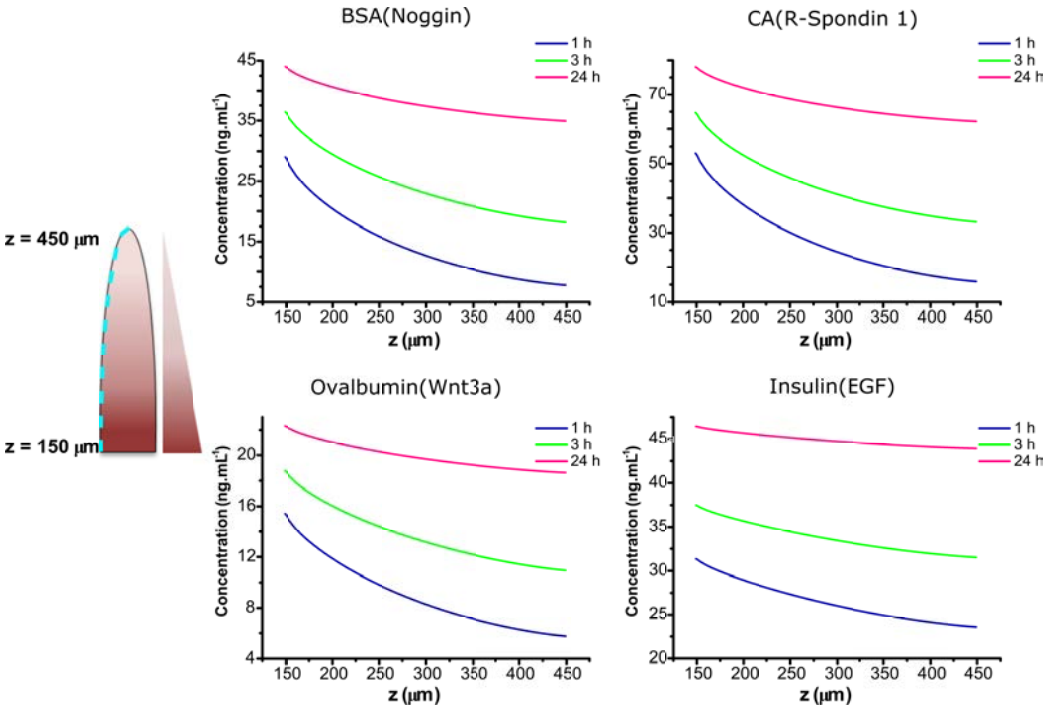

Figure 3.29: Concentrations as a function of position along the surface of one microstructure (as depicted in the drawing) at 1 h, 3 h and 24 h; represented by blue, green, and pink lines, respectively.

3.3.4 Adapting the fabrication setup to incorporate microstructured hydrogels into Transwell® inserts

The gradients of ISC niche biochemical factors can be generated in Transwell® setup by adding these factors only to the basolateral side (source compartment), as we have explained previously. However, the microstructured hydrogels fabricated by the experimental setup explained in chapter 2 section 2.2.1 cannot be placed directly inside Transwell® inserts since they are adhered on glass coverslips. To address this, we fabricated the microstructured hydrogels on porous PET membranes. In the following section we report the readjustment of the fabrication parameters accounting for the effects of the presence of the PET membrane in the photopolymerization process.

3.3.4.1 Morphological assessment of microstructures fabricated on PET membranes

Porous PET membranes were silanized to assure the covalent attachment of the hyrogel to the membrane surface (Section 3.2.5 Figure 3.15). Membranes with pore sizes of 5 μm diameter were used to minimize undesired absorbance and scattering effects interfering with the polymerization process. These effects were observed when using membranes with smaller pore sizes and/or other polymeric materials such as polycarbonate [63]. Even so, we have observed significant changes in the microstructure morphology compared to the samples fabricated on glass coverslips. Moreover, the use of these membranes caused the light intensity to reduce by 37-40% [64]. This attenuation of the UV light intensity also contributed to the changes in microstructure morphology. For that reason, we have reassessed the morphology to select the optimal fabrication conditions for obtaining microstructures with physiologically relevant dimensions.

The effect of UV exposure times on microstructure heights and diameters was studied. As hydrogel precurson solution recipe, 6,5% w/v P6000 with 1% w/v I2959 and 0,3% AA was used as it was selected to be optimal previously (Chapter 2). UV exposure times ranging from 120 s to 200 s were applied. The effect of the second exposure (base formation) on microstructure dimensions and the integrity of the whole sample was also assessed using UV exposure times ranging from 0 s (no base exposure) to 10 s. Figure 3.30 A shows the heights obtained for the microstructures fabricated in all the assayed conditions. The general trend was that the effective heights were increasing with increased UV exposure times but also the diameters as measured above the base. The microstructure shape was changing from bullet-like to pyramidal forms with increased exposure times (Figure 3.30 B), which compromised the objective of mimicking the roundish forms of native villi. The UV exposure time for base formation also affected the effective heights of the microstructures. We observed that with increased base exposure times the effective heights of the microstructures were decreasing (Figure 3.30 A). On the other hand, for shorter times (e.g. 0 s and 5 s) the base was not forming properly. In fact, the material formed in between microstructures was much softer, indicating loosely crosslinked network, barely holding the microstructures. This was also compromising the objective of presenting cells with a homogeneous hydrogel surface. To obtain an array with the microstructures hold together with a base the base exposure times had to be increased.

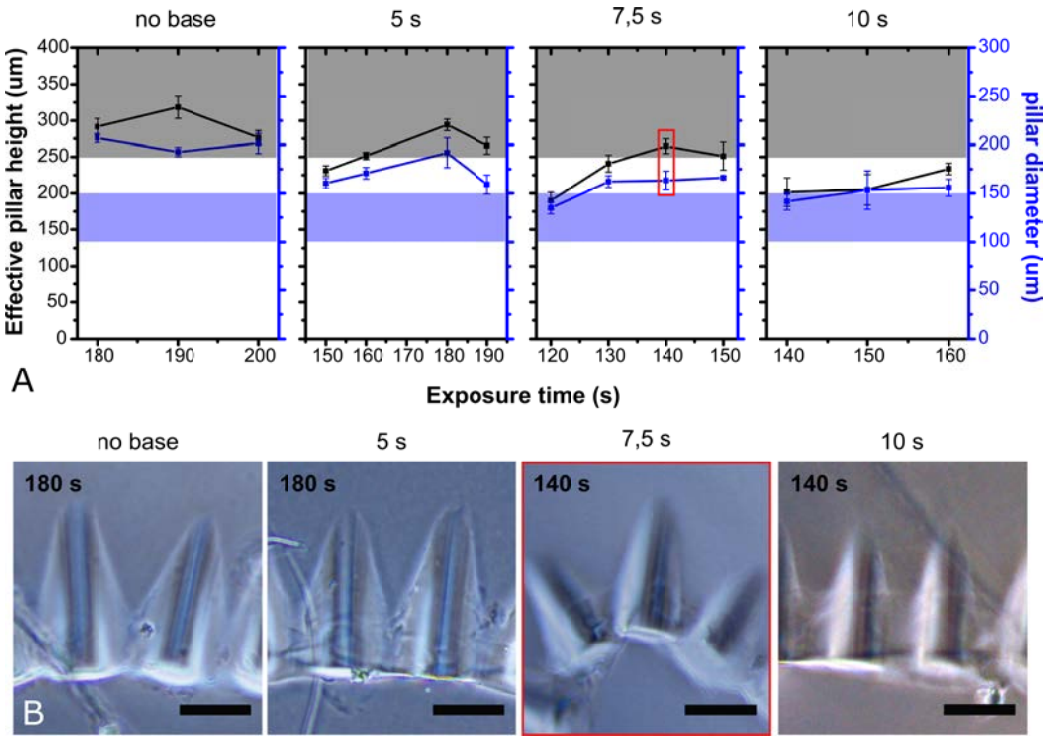

Figure 3.30: *Combined graphs of the effective heights and diameters of the microstructures as a function of the UV exposure time (A). The data is represented as mean ± standard deviation ($n \geq 3$). The regions of interest are represented in grey and blue for effective heights and diameters, respectively. Red frame marks the condition selected. Bright field microscopy images of microstructured P6000 hydrogels made of 6,5% w/v concentration with 0,3% AA with different first and second exposure times (B). Red frame marks the condition selected. Scale bars: 200 μm.*

In short, the exposure times for microstructure and base formation had to be selected in such a way that we would obtain an intact microstructured hydrogel array with microstructure dimensions comparable to that of native villi (0,2-1 mm in height, 100-150 in diameter [68, 69]). In figure 3.30 the regions of interest are represented in grey and blue for effective heights and diameters, respectively. With this in mind, UV exposure time of 140 s for microstructure formation and 7,5 s for the base formation were found most beneficial (red frames marks the condition selected in Figure 3.30 B). The effective height and diameter measured for this condition were 264,7 ± 10,2 μm and 163,2 ± 9,5 μm, respectively.

3.3.4.2 Mounting of microstructures fabricated on PET membranes on Transwell® inserts

Once the appropriate fabrication condition was selected we moved on to find the optimal conditions for mounting of microstructured hydrogels fabricated on PET membranes to Transwell® inserts. For that, we thought of using a thin layer of uncured PDMS to stick the PET membrane with the hydrogel on, to the inserts once their original membranes were removed. As an initial approach, hydrogel mounted inserts were let dry overnight to assure the curing of the PDMS layer. Once the PDMS was cured the hydrogels were rehydrated before the cell culture experiments. Unfortunately, this dehydration-rehydration cycle severely changed the morphology of the microstructures. Figure 3.31 shows the bright field microscopy images of the microstructures before dehydration and after rehydration. Black dashed line marks the contours of the microstructures. Drying of the hydrogels caused severe shrinkage in the sizes of the structures. Also, the shapes were deformed and wrinkling in the base region was observed. These observations suggested collapsing of the hydrogel network pores upon dehydration-rehydration cycle.

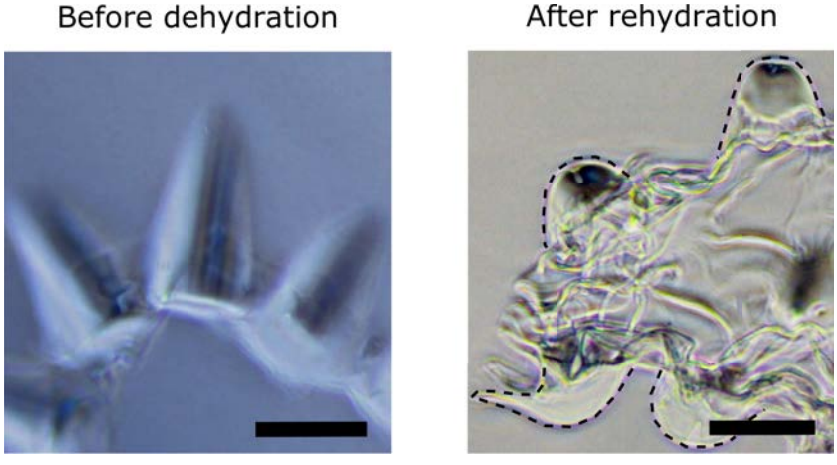

Figure 3.31: *Bright field microscopy images of the microstructured hydrogel selected to be used for cell culture studies before dehydration and after rehydration. Black dashed line marks the microstructures. Note the extreme deformation in the morphology upon the dehydration-rehydration cycle. Scale bars: 200 μm.*

In order to mimic the ISC niche biochemical gradients found *in vivo* in the Transwell® setup, we use the asymmetrical delivery of the factors from the basolateral side (lower compartment). Therefore, it is crucial that the microstructures

do not collapse during mounting process. For that reason, the mounting protocol was revised such that the hydrogels wouldn't dry out during the curing of PDMS (see Section 3.2.5 for the methods). Briefly, 10 μL of PBS was added only onto the hydrogel during curing and the efficiency of the sealing was checked by the capacity of the mounted Transwell® to hold media without leakage (Section 3.2.5 Figure 3.16 C). In this way, the microstructures and pore size of hydrogel was maintained. Once the mounting protocol was optimized we tested the effect of the gradients on the growth and differentiation patterns of intestinal organoid-derived cells.

3.3.5 Spatio-chemical gradients in Transwell® setup - a proof-of-concept study

As a proof-of-concept, microstructured hydrogels fabricated on porous PET membranes were mounted on Transwell® inserts, funtionalized with collagen type I and biomolecular gradients were formed prior to the seeding of organoid-derived crypt pieces. Two conditions were studied: basolateral delivery of ISC niche biochemical factors (asymmetric administration) and both basolateral and apical delivery of such factors (uniform administration). In the asymmetric case, gradients were generated 24 h before seeding, as estimated by FEM simulations (Section 3.3.3.3). Whereas, in the uniform condition there were no gradients within the gel, as the factors were also added to the sink chamber. The medium containing ISC niche factors was composed of medium secreted by intestinal subepithelial myofibroblasts (ISEMF_CM), ENR_CV, and Wnt3a (as optimized in the previous chapters). Note that ISEMF_CM contains mainly Wnts and R-Spondins [10–12]. Then, organoid-derived crypt pieces were seeded and cultured for 6 days and the cell culture media of both upper and lower compartments were changed every 24 h. This was especially important to maintain the gradients formed in the asymmetric condition as demonstrated in figure 3.27 section 3.3.3.2.

The surface coverage of the cell monolayers grown for 6 days in culture was quantified from F-actin fluorescence images as an indication of monolayer growth. Although full coverage of the microstructured scaffolds neither for the asymmetric nor for the uniform factor administration cases was attained, in both of the conditions the surface coverage was quite high with 76,1% and 95,3% of the substrate area covered by cells for asymmetric and uniform administration, respectively (Figure 3.32). These values were much higher than those obtained

for monolayers covering microstructured samples fabricated on glass coverslips and cultured with the same cell culture medium without the added Wnt3a, which was 55,3% ± 3,8% (Section 2.3.6 in Chapter 2). The overall improvement in the growth of the monolayer can be due to improved oxygen and nutrient diffusion in the Transwell® setup, where cells can receive these components from both apical and basolateral sides [70, 71]. Moreover, the exogenous Wnt3a added to the cell culture medium most probably improved the surface expansion of the monolayer through fueling the division of ISCs and transit amplifying cells. Similar growth enhancing effects were reported in the previous chapter 1. On the other hand, increased surface coverage in the sample of uniform administration can be explained by the fact that the cells receive higher amounts ISC niche factors since these factors are delivered both from basolateral and apical side. This could further fuel the proliferation of the ISCs or transit amplifying cells and lead to better expansion of the monolayer.

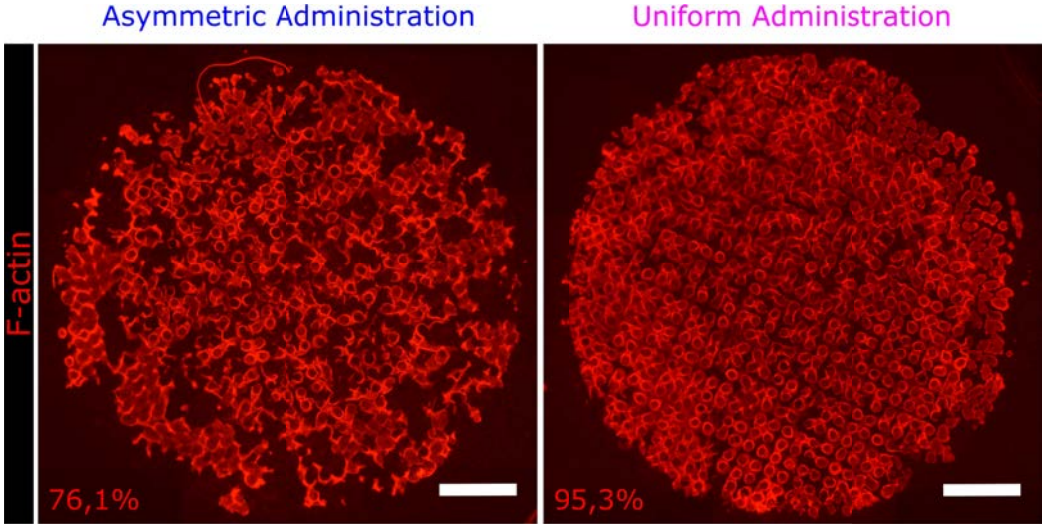

Figure 3.32: *Fluorescence of F-actin of the monolayers cultured on microstructured PEGDA hydrogels mounted on Transwell® inserts under asymmetric or uniform administration of ISC niche biochemical factors (ISEMF_CM + ENR_CV + Wnt3a) after 6 days of culture. Tile scans show the entire sample surface, which was used to calculate the surface coverage: 76,1% and 95,3% for asymmetric and uniform administration, respectively. Scale bars: 1 mm.*

On the contrary, immunofluorescence for Ki67 revealed that the amount of $Ki67^+$ proliferative cells (normalized to the total cell number) were quite low for

both conditions; 0,7% ± 0,4% and 0,6% ± 0,4% for asymmetric and uniform administration, respectively. In addition, there was no statistically significant difference (Student's t-test, p>0,05, n = 4) between these two conditions. Whereas, immunofluorescence for CK20 revealed that all the microstructure tips were covered with $CK20^+$ differentiated cells for both of the conditions as we can see in figure 3.33. This suggests that the cultures were highly differentiated. Then, the low amounts of proliferative cells can be attributed to two phenomena: 1) a negative feedback loop exerted by the BMP signaling generated by the differentiated cells inhibiting epithelial cell proliferation [72]; 2) upon cell-to-cell contact and cell cycle exit as a consequence of confluent epithelial cultures [73]. Since these cultures were almost confluent this might have caused cells to stop dividing.

Although high levels of CK20 expressing cells were observed in both of the conditions, the distribution of $CK20^+$ differentiated cells were significantly different. In figure 3.33 we represent the CK20 signal at three different heights from the tip of the microstructures. For that, we divided the entire CLSM stack acquired into three sub_stacks to evaluate the distribution of the CK20 signal along the vertical axis of the microstructures. Under asymmetric administration, CK20 signal was predominantly observed in the Sub_stack 1 (tips of villi); while under uniform administration it was present in all sub_stacks (along all the villi structure). $CK20^+$ differentiated cells were concentrated to the tip of the microstructures under asymmetric administration, while under uniform administration $CK20^+$ differentiated cells were more distributed along the microstructures. F-actin counterstaining was shown to point out that the absence of CK20 signal was not due to the absence of the cells. In other words, even though there was a cell monolayer, the cells were negative for CK20. After this initial qualitative assessment we quantified the mean CK20 intensity with respect to the vertical position along the microstructure to confirm our observations.

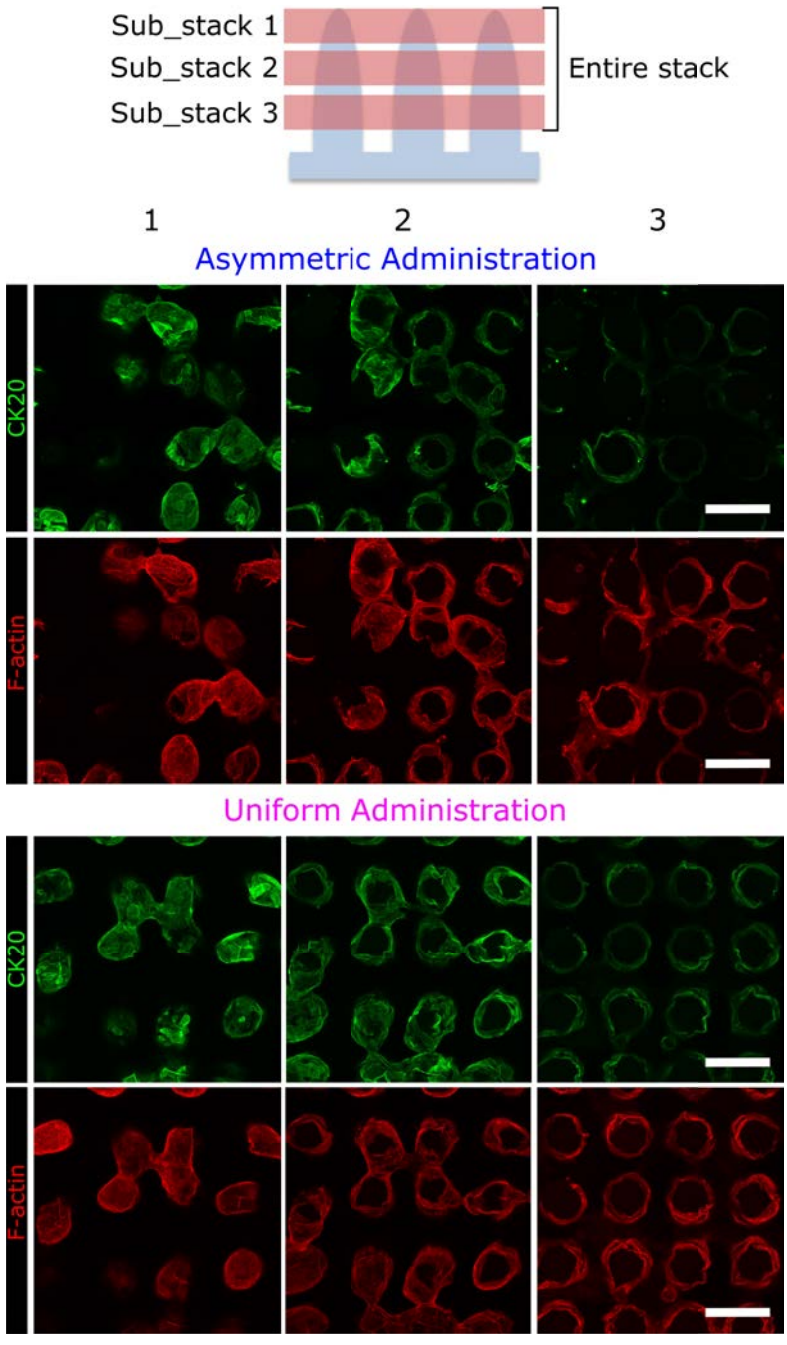

Figure 3.33: *Immunofluorescence for CK20 and F-actin staining of intestinal monolayers grown on the material under asymmetric or uniform administration of the factors. As depicted in the scheme at the top, the entire stack is divided into 3 sub_stacks to better visualize the distribution of the CK20 signal along the microstructure. Scale bars: 200 μm.*

Quantification of the mean CK20 intensity, within the monolayer, with respect

to the vertical position along the microstructures was performed from confocal microscopy stacks acquired at 4 randomly selected locations. Figure 3.34 A shows 3D views of representative CLSM stacks to better illustrate the CK20 signal distribution. As seen in figure 3.34 B, the distributions of CK20 are significantly different among the conditions. In the case of asymmetric administration (with gradients) of the ISC niche biochemical factors the differentiated cells were more compartmentalized to the tips of the microstructures. Whereas, in the case of uniform they were broadly distributed along the microstructure (Fig. 3.34 B). As a measure of CK20 signal spread for each condition, widths at 50% of the maximum mean intensity were estimated from the profiles and found to be 7,4 μm and 137,8 μm for asymmetric and uniform administration, respectively. Also, the cumulative sum of CK20 integrated intensity was computed and the height cut-off (from tip) at 75% of the total CK20 signal was determined (Fig. 3.34 E). In the case of asymmetric administration, 75% of the total CK20 signal was accumulated to the first 62 μm from the microstructure tip; whereas, in the case of uniform it was spread up to 114 μm from the tip. In fact at 62 μm from the microstructure tip under uniform administration, only 31,7% of the total signal was accumulated. This quantitative analysis clearly demonstrates that these two distributions are different suggesting that the hydrogels with gradients (asymmetric administration) promotes better the compartmentalization of the differentiated cells towards the tip of the microstructures similar to what happens *in vivo* intestine.

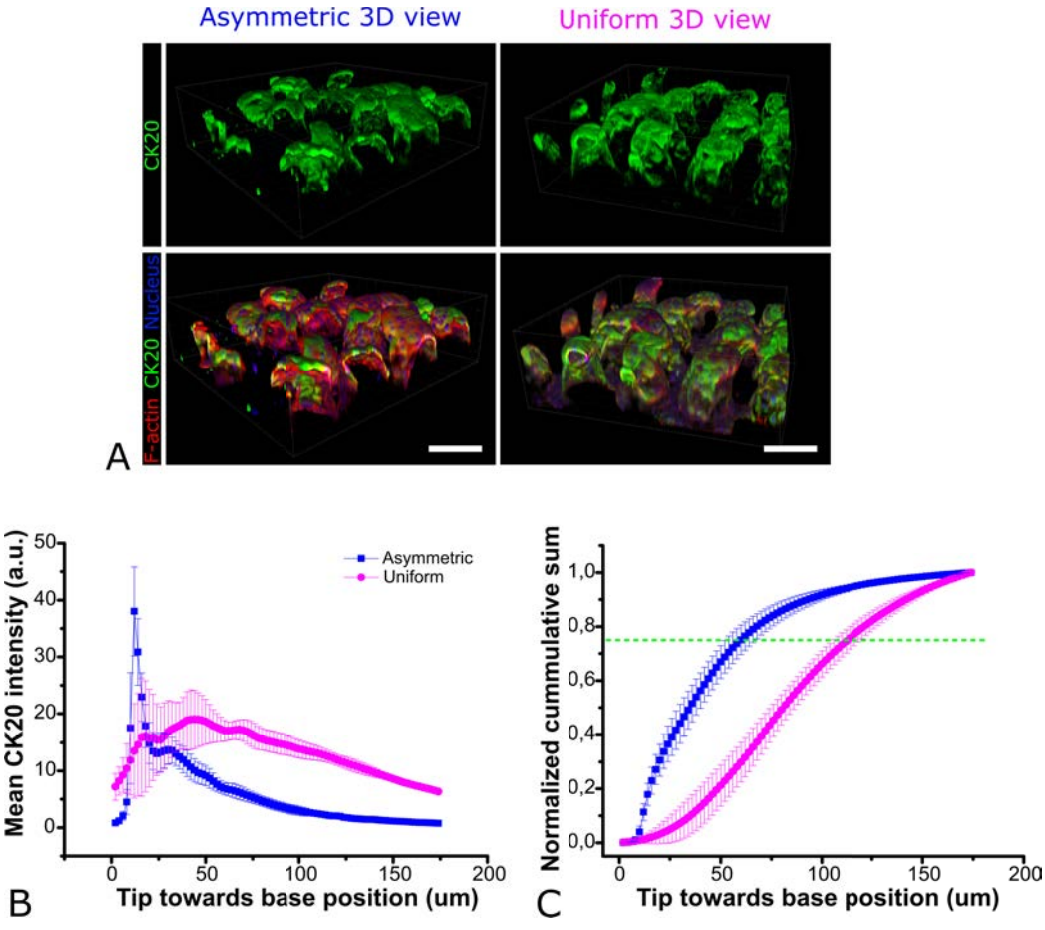

Figure 3.34: *3D views of immunofluorescence for CK20 of intestinal monolayers grown on the material under asymmetric or uniform administration of the factors (A). Counterstaining was done for F-actin and nucleus. Scale bars: 200 μm. Graph showing the mean CK20 intensity distribution (normalized to the F-actin area) along the microstructures for different conditions (B). Graph showing the normalized cumulative sum of CK20 signal along the microstructures (C). Green dotted line marks the 75% cut off line. The images were acquired at 4 different locations (n = 4) and the data are presented as mean ± standard deviation of intra-sample variations.*

This proof-of-concept experiment suggests that the spatio-chemical gradients generated in our biomimetic 3D villus-like hydrogels can be used for the compartmentalization of the proliferative and the differentiated cells in a similar fashion to that found in the *in vivo* tissue.

3.4 Discussion

The ISC proliferation, migration and differentiation along the 3D crypt-villus architecture of the intestinal epithelium are mainly governed by the spatio-chemical gradients of ISC niche factors: BMP, Wnt and EGF pathway modulators, generated along the crypt-villus axis [5]. Thus, we hypothesized that a microengineered system able to mimic the 3D crypt-villus architecture of the small intestine and the biochemical gradients generated along the vertical crypt-villus axis might lead to cell distribution similar to that found *in vivo*.

Standard Transwell® setup, based on the culture of primary intestinal epithelial cell monolayers on porous membranes separating the culture well into two compartments [74–76], does not allow control over the gradients as the system only consists of a cell monolayer formed on a porous membrane. To be able to generate gradients in a physiologically relevant way, along the vertical crypt-villus axis, a support matrix with 3D villus-like microstructures is needed. For that, we have developed PEGDA-based hydrogels with villus-like 3D as a support matrix for intestinal epithelial cells (as reported in Chapter 2). PEGDA hydrogels were chosen because, in addition to their easily tunable mechanical and biochemical properties (discussed previously in Chapter 2), their physicochemical properties such as the mesh size, crucial for the diffusion of biomolecules, can be tuned in a controllable manner [50]. Moreover, PEGDA hydrogels can be easily microstructured by photocrosslinking [77, 78] and the resulting microstructures with heights of few hundreds of microns provide the necessary template for the generation of gradients along the vertical axis of the villus like forms.

There has been some attempts to deliver gradients through hydrogels to direct intestinal stem cell behavior. Attayek *et al.* demonstrated that the Wnt3a and R-Spondin 1 gradients generated across the Matrigel® embedded colonic organoids led to the polarization of proliferative cell containing crypt domains towards the region of the highest morphogen (Wnt3a and R-Spondin 1) concentrations [38]. These findings demonstrated that the gradients of key ISC niche factors can actually be used to guide self-organization in organoids. Nevertheless, this model lacked the 3D architecture of the small intestine and the gradients were generated across the organoids embedded within the Matrigel®, far away from the *in vivo* scenario, where the gradients of ISC niche biochemical factors are present along the vertical crypt-villus axis. In a very recent study, Wang *et al.* mimicked crypt-villus architecture on collagen scaffolds and demonstrated that basolateral delivery of ISC niche biochemical factors led to *in vivo*-like crypt-villus cellular

distribution of spheroid-derived intestinal epithelial cells on these scaffolds [39]. The main disadvantage of the use of collagen material in a platform for diffusion of biomolecules is that its physicochemical properties such as its mesh size can not be modified in a controlled manner [79]. Moreover, the scaffold becomes the limiting barrier for rapidly absorbed hydrophobic drugs [80], which might also cause non-specific adsorption of diffusing proteins. In contrast to collagen, we have used PEGDA-based synthetic hydrogels that have numerous advantages over their natural counterparts like collagen. These are: their antifouling property that repels non-specific protein adsorption, which would otherwise interfere with the diffusion of the biomolecules and efficient tuning of diffusivity within the hydrogel network by simply varying its crosslinking density, which in effect controls the porosity (mesh size) of the hydrogel [81, 82].

As stated, the crucial factor determining the diffusivity of the biomolecules within the hydrogels is its mesh size. Here, we determined the mesh size of the PEGDA-based hydrogels to be between 8 to 12 nm and it could be tuned by simply changing the PEGDA concentration. Taking into account that the diameters of principle ISC niche factors; EGF, R-Spondin 1, Noggin, Wnt3a range from 3 to 7,2 nm (Section 3.2.3 Table 3.1), PEGDA hydrogels fabricated at the concentrations reported here have a porosity large enough to permit the diffusion of ISC factors. It is important to note that, the hydrogels fabricated on porous membranes compared to the ones fabricated on glass coverslips have larger mesh sizes for the same time of UV exposure, since porous membranes attenuate the UV light around 40% [64], which in return decreases the crosslinking density. However, this does not pose any challenge on the formation of the gradients since it would further increase the diffusivity of the proteins.

The diffusion studies through the PEGDA-based hydrogels revealed that material would be a barrier for large proteins such as laminin but it would allow the effective diffusion of smaller proteins such as BSA. The *in silico* modeling demonstrated that spatio-chemical gradients of ISC niche biochemical factors (proteins smaller in size than laminin) could be generated along the vertical axis of the hydrogels. The visualization of the gradients formed based on the diffusion of the biochemical factors within the hydrogels with large dimensions (h = 1 mm, d = 5 mm) was a technical challenge. For this purpose, a microfluidic chip allocating the hydrogel scaffold that permitted both the gradient formation and visualization, was designed and fabricated. The gradients of fluorescently labelled BSA were successfully visualized using light-sheet fluorescence microscopy (LSFM). The linear gradient profiles obtained by periodical replenishment of the medium

demonstrated both experimentally by LSFM and by *in silico* modeling, proved that pseudo steady state could be reached by using this methodology in accordance with previously published reports [34, 35].

LSFM technique allows fast imaging at large working distances and permits a flexible sample access and mounting by decoupling the illumination and detection light paths with an angle of 90° [51, 53]. This is especially important for the visualization of large-size samples that require a special mounting setup, as in our case, that would otherwise not be possible with other fluorescence microscopy techniques. LSFM is commonly used in the developmental studies of model organisms such as the zebrafish and the fruit fly [51]. Lately, there has been an increasing interest in utilizing LSFM for high-throughput screening of organoid cultures for analyzing both the morphology and dynamic processes [83, 84]. The microfluidic chip allocating hydrogel scaffold allowing LSFM analysis that we have developed, has a great potential in live imaging of 3D tissue mimics. Our 3D villus-like scaffolds can easily be incorporated into the microfluidic chip through which the gradients of ISC niche factors can be generated. The organoid-derived intestinal epithelial cells can be seeded onto the scaffolds and the monolayer formation and cellular organization dynamics can be visualized by LSFM. The live imaging of *de novo* tissue formation within a representative microenvironment, resembling anatomical villi, would provide useful information on the effect of such 3D architectures on the self-organization capacity of the ISC.

We have demonstrated the utility of the microfluidic chip allocating the hydrogel scaffold in creating biomolecular gradients. On the other hand, the complexity of the biological systems require a simplified setup that would permit facile testing. For that reason, we adapted our system standardized Transwell® setup. The microstructured hydrogels were successfully fabricated on PET membranes and mounted on Transwell® inserts. The gradients were formed in this setup by the basolateral delivery of the ISC niche biochemical factors and modeled with FEM simulations. *In silico* model predicted most pronounced gradients for Noggin, then for R-Spondin 1 and Wnt3a, while the gradient of EGF was insignificant. As a proof-of-concept, the effect of these gradients on intestinal epithelial cell growth and differentiation was assessed. Immunofluorescence characterization and image analysis revealed that the presence of gradients led to the compartmentalization of the terminally differentiated cells to the very tips of the microstructures. Whereas, in the absence of the gradients the differentiated cells were distributed along the height of the microstructures.

Our results suggest that these biomimetic PEGDA-based 3D villus-like hydrogels with spatio-chemical gradients of ISC niche biochemical factors can be used for the compartmentalization of differentiated epithelial cells in the monolayers derived from organoids. At this point, further efforts are required to systematically analyze the effects of different gradient profiles and concentration ranges of ISC niche factors on the growth and differentiation of the intestinal epithelial cells. Then, it would be possible to correlate the effects of such gradients to the cellular response and it would provide crucial information in an effort to control the growth, migration and differentiation of ISCs to obtain an *in vitro* intestinal epithelium with *in vivo* like cellular compositions and distributions.

3.5 Conclusions

In this chapter, we have demonstrated that it was possible to create spatio-chemical gradients of ISC niche biochemical factors on PEGDA hydrogels and showed that such gradients influenced the distribution of differentiated cells found in the epithelial monolayers along the villus-like microstructures. First, we have characterized the network structure of the PEGDA hydrogels and found that it can be controlled by the changing the PEGDA concentration. Then, a hydrogel incorporated PDMS chip was designed and fabricated to be used in the determination of the diffusion coefficients of proteins. We validated the functionality of the chip by a diffusion assay. FEM simulations performed to reveal the spatio-chemical gradients of ISC niche biochemical factors, formed within the disc-shaped and microstructured hydrogels. For the characterization of the gradients by microscopic techniques, a microfluidic chip allocating the hydrogel was designed and fabricated. The gradients of fluorescently labelled model protein BSA was visualized with light-sheet fluorescence microscopy (LSFM). Stable profiles were observed as predicted by the *in silico* model demonstrating that the gradients could be formed and maintained within PEGDA hydrogels in the experimental setup designed. PEGDA-based microstructured hydrogel platforms were succesfully adapted to standard cell culture platforms that permitted access to both sides of the hydrogel. Spatio-chemical gradients were created in this setup and organoid-derived crypts pieces were grown on these hydrogels with gradients. It was demonstrated that in the presence of these gradients the differentiated epithelial cells were compartmentalized more towards the tips of the microstructures. Overall, we have developed a novel 3D villus-like biomimetic hydrogel platform with spatio-chemical gradients of ISC niche biochemical factors that can be used to modulate the compartmentalization of the differentiated organoid-derived intestinal cells.

References

[1] Cornelis J. Weijer. "Collective cell migration in development". In: *Journal of Cell Science* 122.18 (2009).

[2] Christopher G Sip, Nirveek Bhattacharjee, and Albert Folch. "Microfluidic transwell inserts for generation of tissue culture-friendly gradients in well plates." en. In: *Lab on a chip* 14.2 (2014), pp. 302–14.

[3] Evanthia T. Roussos, John S. Condeelis, and Antonia Patsialou. "Chemotaxis in cancer". In: *Nature Reviews Cancer* (2011).

[4] Hans Clevers. "The intestinal crypt, a prototype stem cell compartment." In: *Cell* 154.2 (2013), pp. 274–84.

[5] Toshiro Sato and Hans Clevers. "Growing self-organizing mini-guts from a single intestinal stem cell: mechanism and applications." In: *Science (New York, N.Y.)* 340.6137 (2013), pp. 1190–4.

[6] Nick Barker. "Adult intestinal stem cells: critical drivers of epithelial homeostasis and regeneration". In: (2013).

[7] Alexis J Carulli, Linda C Samuelson, and Santiago Schnell. "Unraveling intestinal stem cell behavior with models of crypt dynamics." In: *Integrative biology : quantitative biosciences from nano to macro* 6.3 (2014), pp. 243–57.

[8] Toshiro Sato et al. "Paneth cells constitute the niche for Lgr5 stem cells in intestinal crypts." In: *Nature* 469.7330 (2011), pp. 415–418.

[9] R. C. Mifflin et al. "Intestinal myofibroblasts: targets for stem cell therapy". In: *American Journal of Physiology-Gastrointestinal and Liver Physiology* 300.5 (2011), G684–G696.

[10] Henner F. Farin, Johan H. Van Es, and Hans Clevers. "Redundant Sources of Wnt Regulate Intestinal Stem Cells and Promote Formation of Paneth Cells". In: *Gastroenterology* 143.6 (2012), 1518–1529.e7.

[11] Z. Kabiri et al. "Stroma provides an intestinal stem cell niche in the absence of epithelial Wnts". In: *Development* 141.11 (2014), pp. 2206–2215.

[12] Nan Ye Lei et al. "Intestinal subepithelial myofibroblasts support the growth of intestinal epithelial stem cells". In: *PLoS ONE* 9.1 (2014).

[13] Brandon V. Slaughter et al. "Hydrogels in Regenerative Medicine". In: *Advanced Materials* 21 (2009), pp. 3307–3329.

[14] N.-A. Peppas et al. "Hydrogels in Biology and Medicine: From Molecular Principles to Bionanotechnology". In: *Advanced Materials* 18.11 (2006), pp. 1345–1360.

[15] Cole a DeForest and Kristi S Anseth. "Advances in bioactive hydrogels to probe and direct cell fate." In: *Annual review of chemical and biomolecular engineering* 3 (2012), pp. 421–44.

[16] Anushree Datta. "Characterization of polyethylene glycol hydrogels for biomedical applications". PhD thesis. 2007.

[17] Ting Yang. "Mechanical and Swelling properties of Hydrogels". PhD thesis. 2012, p. 67. ISBN: 9789175014715.

[18] N. Ch. Padmavathi and P. R. Chatterji. "Structural Characteristics and Swelling Behavior of Poly(ethylene glycol) Diacrylate Hydrogels †". In: *Macromolecules* 29.6 (1996), pp. 1976–1979.

[19] P. J. Flory and J. Rehner. "Statistical Mechanics of Cross-Linked Polymer Networks II. Swelling". In: *The Journal of Chemical Physics* 11 (1943), pp. 521–526.

[20] Edward W. Merrill, Kathleen A. Dennison, and Cynthia Sung. "Partitioning and diffusion of solutes in hydrogels of poly(ethylene oxide)". In: *Biomaterials* 14.15 (1993), pp. 1117–1126.

[21] Tiziana Canal and Nikolaos A. Peppas. "Correlation between mesh size and equilibrium degree of swelling of polymeric networks". In: *Journal of Biomedical Materials Research* 23.10 (1989), pp. 1183–1193.

[22] N Peppas. "Hydrogels in pharmaceutical formulations". In: *European Journal of Pharmaceutics and Biopharmaceutics* 50.1 (2000), pp. 27–46.

[23] Chien Chi Lin and Andrew T. Metters. "Hydrogels in controlled release formulations: Network design and mathematical modeling". In: *Advanced Drug Delivery Reviews* 58.12-13 (2006), pp. 1379–1408.

[24] M P Lutolf and J A Hubbell. "Synthetic biomaterials as instructive extracellular microenvironments for morphogenesis in tissue engineering". In: *Nature Biotechnology* 23.1 (2005), pp. 47–55.

[25] Stefan Kobel and Matthias P. Lutolf. "Biomaterials meet microfluidics: Building the next generation of artificial niches". In: *Current Opinion in Biotechnology* 22.5 (2011), pp. 690–697.

[26] Sudong Kim, Hyung Joon Kim, and Noo Li Jeon. "Biological applications of microfluidic gradient devices." en. In: *Integrative biology : quantitative biosciences from nano to macro* 2.11-12 (2010), pp. 584–603.

[27] Wai To Fung et al. "Microfluidic platform for controlling the differentiation of embryoid bodies". In: *Lab on a Chip* 9.17 (2009), pp. 2591–2595.

[28] Steffen Cosson, Stefan A. Kobel, and Matthias P. Lutolf. "Capturing complex protein gradients on biomimetic hydrogels for cell-based assays". In: *Advanced Functional Materials* 19.21 (2009), pp. 3411–3419.

[29] Steffen Cosson and Matthias P. Lutolf. "Programmable microfluidic patterning of protein gradients on hydrogels". In: *Methods in Cell Biology* 121 (2014), pp. 91–102.

[30] Wajeeh Saadi et al. "Generation of stable concentration gradients in 2D and 3D environments using a microfluidic ladder chamber." In: *Biomedical microdevices* 9.5 (2007), pp. 627–35.

[31] Amy P. Wong et al. "Partitioning microfluidic channels with hydrogel to construct tunable 3-D cellular microenvironments". In: *Biomaterials* 29.12 (2008), pp. 1853–1861.

[32] Anja Kunze et al. "Micropatterning neural cell cultures in 3D with a multi-layered scaffold". In: *Biomaterials* 32.8 (2011), pp. 2088–2098.

[33] Ovid C. Amadi et al. "A low resistance microfluidic system for the creation of stable concentration gradients in a defined 3D microenvironment". In: *Biomedical Microdevices* 12.6 (2010), pp. 1027–1041.

[34] Vinay V Abhyankar et al. “Characterization of a membrane-based gradient generator for use in cell-signaling studies.” In: *Lab on a chip* 6.3 (2006), pp. 389–93.

[35] Vinay V. Abhyankar et al. “A platform for assessing chemotactic migration within a spatiotemporally defined 3D microenvironment”. In: *Lab on a Chip* 8.9 (2008), p. 1507.

[36] S Cosson and M P Lutolf. “Hydrogel microfluidics for the patterning of pluripotent stem cells.” In: *Scientific reports* 4 (2014), p. 4462.

[37] Asad A. Ahmad et al. “Optimizing Wnt-3a and R-spondin1 concentrations for stem cell renewal and differentiation in intestinal organoids using a gradient-forming microdevice”. In: *RSC Advances* 5.91 (2015), pp. 74881–74891.

[38] Peter J. Attayek et al. “In vitro polarization of colonoids to create an intestinal stem cell compartment”. In: *PLoS ONE* 11.4 (2016), pp. 1–23.

[39] Yuli Wang et al. “A microengineered collagen scaffold for generating a polarized crypt-villus architecture of human small intestinal epithelium”. In: *Biomaterials* 128 (2017), pp. 44–55.

[40] N. A. Peppas and E. W. Merrill. “Crosslinked poly(vinyl alcohol) hydrogels as swollen elastic networks”. In: *Journal of Applied Polymer Science* 21.7 (1977), pp. 1763–1770.

[41] Gregory M. Cruise, David S. Scharp, and Jeffrey A. Hubbell. “Characterization of permeability and network structure of interfacially photopolymerized poly(ethylene glycol) diacrylate hydrogels”. In: *Biomaterials* 19.14 (1998), pp. 1287–1294.

[42] Christina J Lee et al. “Determination of human lens capsule permeability and its feasibility as a replacement for Bruch’s membrane.” In: *Biomaterials* 27.8 (2006), pp. 1670–8.

[43] Kristin Engberg and Curtis W Frank. “Protein diffusion in photopolymerized poly(ethylene glycol) hydrogel networks”. In: *Biomedical Materials* 6.5 (2011), p. 055006.

[44] Sotirios Koutsopoulos et al. “Controlled release of functional proteins through designer self-assembling peptide nanofiber hydrogel scaffold.” In: *Proceedings of the National Academy of Sciences of the United States of America* 106.12 (2009), pp. 4623–8.

[45] Kazuo Onuma and Noriko Kanzaki. “Size Distribution and Intermolecular Interaction of Laminin-1 in Physiological Solutions”. In: *The Journal of Physical Chemistry B* 107.42 (2003), pp. 11799–11804.

[46] P. K. Smith et al. “Measurement of protein using bicinchoninic acid”. In: *Analytical Biochemistry* 150.1 (1985), pp. 76–85.

[47] Jennie B Leach and Christine E Schmidt. “Characterization of protein release from photocrosslinkable hyaluronic acid-polyethylene glycol hydrogel tissue engineering scaffolds.” In: *Biomaterials* 26.2 (2005), pp. 125–35.

[48] Laney M. Weber, Christina G. Lopez, and Kristi S. Anseth. “Effects of PEG hydrogel crosslinking density on protein diffusion and encapsulated islet survival and function”. In: *Journal of Biomedical Materials Research Part A* 90A.3 (2009), pp. 720–729.

[49] Zdenek Petrásek and Petra Schwille. “Precise measurement of diffusion coefficients using scanning fluorescence correlation spectroscopy.” In: *Biophysical journal* 94.4 (2008), pp. 1437–48.

[50] Soah Lee, Xinming Tong, and Fan Yang. "The effects of varying poly(ethylene glycol) hydrogel crosslinking density and the crosslinking mechanism on protein accumulation in three-dimensional hydrogels." In: *Acta biomaterialia* 10.10 (2014), pp. 4167–74.

[51] Peter A. Santi. "Light sheet fluorescence microscopy: A review". In: *Journal of Histochemistry and Cytochemistry* 59.2 (2011), pp. 129–138.

[52] A. H. Voie, D. H. Burns, and F. A. Spelman. "Orthogonal plane fluorescence optical sectioning: Three dimensional imaging of macroscopic biological specimens". In: *Journal of Microscopy* 170.3 (1993), pp. 229–236.

[53] Emmanuel G. Reynaud et al. "Light sheet-based fluorescence microscopy: More dimensions, more photons, and less photodamage". In: *HFSP Journal* 2.5 (2008), pp. 266–275.

[54] Emilio J. Gualda et al. "Three-dimensional imaging flow cytometry through light-sheet fluorescence microscopy". In: *Cytometry Part A* 91.2 (2017), pp. 144–151.

[55] Alexander Laskin and Vadim Laskin. "Beam shaping to generate uniform laser light sheet and linear laser spots". In: (2013), p. 88430C.

[56] Kadir Aslan, Patrick Holley, and Chris D. Geddes. "Metal-enhanced fluorescence from silver nanoparticle-deposited polycarbonate substrates". In: *Journal of Materials Chemistry* 16.27 (2006), p. 2846.

[57] Christopher a Durst et al. "Flexural characterization of cell encapsulated PEGDA hydrogels with applications for tissue engineered heart valves." In: *Acta biomaterialia* 7.6 (2011), pp. 2467–76.

[58] E.H. Nafea, L.A. Poole-Warren A. Marson, and P.J. Martens. "Immunoisolating semipermeable membranes for cell encapsulation: Focus on hydrogels". In: *Journal of Controlled Release* 154.2 (2011), pp. 110–122.

[59] Mohammad Ali Al-Ameen and Gargi Ghosh. "Sensitive quantification of vascular endothelial growth factor (VEGF) using porosity induced hydrogel microspheres". In: *Biosensors and Bioelectronics* 49 (2013), pp. 105–110.

[60] J K Armstrong et al. "The hydrodynamic radii of macromolecules and their effect on red blood cell aggregation." In: *Biophysical journal* 87.6 (2004), pp. 4259–70.

[61] Donna Phu. "The Effect of Entrapped Laminin-111 in Three-dimensional Polyethylene Glycol Gels on the Behavior of Nucleus Pulposus Cells from the Intervertebral Disc". PhD thesis. Duke University, 2010.

[62] Brian J. Peret and William L. Murphy. "Controllable Soluble Protein Concentration Gradients in Hydrogel Networks". In: *Advanced Functional Materials* 18.21 (2008), pp. 3410–3417.

[63] Albert Garcia Castaño. "Engineering poly (ethylene glycol) diacrylate-based microstructures to develop an in vitro model of small intestinal epithelium". In: *TDX (Tesis Doctorals en Xarxa)* (2018).

[64] Albert Garcia Castaño et al. "Single-step dynamic polymerization photolithography produces complex microstructures on hydrogels to generate a 3D intestinal tissue model". In: *Manuscript* (2018).

[65] Toshiro Sato et al. "Single Lgr5 stem cells build crypt-villus structures in vitro without a mesenchymal niche." In: *Nature* 459.7244 (2009), pp. 262–5.

[66] Xiaolei Yin et al. “Niche-independent high-purity cultures of Lgr5+ intestinal stem cells and their progeny.” In: *Nature methods* 11.1 (2014), pp. 106–12.

[67] Birger Brodin, Bente Steffansen, and Carsten Uhd Nielsen. “Passive diffusion of drug substances: the concepts of flux and permeability”. In: *Molecular Biopharmaceutics* (2010), pp. 135–151.

[68] Paul Kelly et al. “Responses of small intestinal architecture and function over time to environmental factors in a tropical population”. In: *Am. J. Trop. Med. Hyg.* 70 (2004), pp. 412–419.

[69] G. J. Tortora and B. H. Derrickson. *Principles of Anatomy and Physiology*. 14th ed. Wiley Global Education, 2014.

[70] Rebecca L Dimarco et al. “Integrative Biology Interdisciplinary approaches for molecular and cellular life sciences Engineering of three-dimensional microenvironments to promote contractile behavior in primary intestinal organoids Engineering of three-dimensional microenvironments”. In: *Integr. Biol. Integr. Biol* 6.6 (2014), pp. 103–234.

[71] Sojin Lee et al. “Construction of 3D multicellular microfluidic chip for an in vitro skin model”. In: *Biomedical Microdevices* 19.2 (2017), p. 22.

[72] Curtis A. Thorne et al. “Enteroid Monolayers Reveal an Autonomous WNT and BMP Circuit Controlling Intestinal Epithelial Growth and Organization”. In: *Developmental Cell* 44.5 (2018), 624–633.e4.

[73] Clara Mayo et al. “In vitro differentiation of HT-29 M6 mucus-secreting colon cancer cells involves a trychostatin A and p27KIP1-inducible transcriptional program of gene expression”. In: *Journal of Cellular Physiology* 212.1 (2007), pp. 42–50.

[74] C. Moon et al. “Development of a primary mouse intestinal epithelial cell monolayer culture system to evaluate factors that modulate IgA transcytosis”. In: *Mucosal Immunology* 7.4 (2014), pp. 818–828.

[75] Kelli L. VanDussen et al. “Development of an enhanced human gastrointestinal epithelial culture system to facilitate patient-based assays”. In: *Gut* 64.6 (2015), pp. 911–920.

[76] Kenji Kozuka et al. “Development and Characterization of a Human and Mouse Intestinal Epithelial Cell Monolayer Platform.” In: *Stem cell reports* 9.6 (2017), pp. 1976–1990.

[77] B. Yañez-Soto et al. “Biochemically and topographically engineered poly(ethylene glycol) diacrylate hydrogels with biomimetic characteristics as substrates for human corneal epithelial cells”. In: *Journal of Biomedical Materials Research - Part A* 101 A.4 (2013), pp. 1184–1194.

[78] Ju Hyeon Kim et al. “Reaction-Diffusion-Mediated Photolithography for Designing Pseudo-3D Microstructures”. In: *Small* 13.17 (2017), pp. 1–11.

[79] Ya Li Yang, Stéphanie Motte, and Laura J. Kaufman. “Pore size variable type I collagen gels and their interaction with glioma cells”. In: *Biomaterials* 31.21 (2010), pp. 5678–5688.

[80] Jiajie Yu et al. “In vitro 3D human small intestinal villous model for drug permeability determination.” In: *Biotechnology and bioengineering* 109.9 (2012), pp. 2173–8.

[81] Tony a Lin, a E Hosoi, and Daniel J Ehrlich. “Vertical hydrodynamic focusing in glass microchannels.” In: *Biomicrofluidics* 3.1 (2009), p. 14101.

[82] Mirae Kim and Chaenyung Cha. "Modulation of functional pendant chains within poly(ethylene glycol) hydrogels for refined control of protein release". In: *Scientific Reports* 8.1 (2018), pp. 1–12.

[83] Emilio J. Gualda et al. "Imaging of human differentiated 3D neural aggregates using light sheet fluorescence microscopy". In: *Frontiers in Cellular Neuroscience* 8.August (2014), pp. 1–10.

[84] Francesco Pampaloni, Bo Jui Chang, and Ernst H.K. Stelzer. "Light sheet-based fluorescence microscopy (LSFM) for the quantitative imaging of cells and tissues". In: *Cell and Tissue Research* 360.1 (2015), pp. 129–141.

General discussion

The small intestinal epithelium is a highly specialized organ formed of crypt-villus units. This 3D architecture is strongly related to its functions, including nutrient absorption, drug uptake, and formation of a tissue barrier to keep the pathogens and toxins away from the underlying tissue. The 3D architecture is also important in the spatial segregation of the diverse cell populations of the epithelium. Intestinal stem cells (ISC) residing in the crypts, divide and give rise to differentiated cells that migrate up and cover the villi surface. ISC proliferation, migration and differentiation are controlled by the gradients of biochemical factors along the crypt-villus axis. Experimental modeling of intestinal epithelial biology and physiology are restricted due to the lack *in vitro* platforms that recapitulate the key aspects of the small intestinal epithelium such as its distinct cell populations, 3D architecture and the gradients of ISC niche biochemical factors along the crypt-villus axis.

In this thesis, we have developed strategies to obtain improved *in vitro* models of small intestinal epithelium derived from organoids, aiming to overcome the limitations of the current models. Epithelial monolayers were generated both on flat surfaces and on scaffolds with 3D villus-like architecture in a cell culture setup that permitted access to both apical and basolateral side of the *in vitro* epithelium. The 2D intestinal epithelial model, faithfully reproduced the *in vivo*-like crypt-villus cellular organization and demonstrated physiologically relevant tissue barrier function (Chapter 1). 3D villus-like scaffolds were fabricated from PEGDA-based synthetic hydrogels that could be microstructured with a simple photolithographic technique and allowed facile tuning of biochemical and mechanical properties and diffusivity within the hydrogel (Chapter 2). Our final device included spatio-chemical gradients of ISC niche biochemical factors created along the villus axis of the microstructured hydrogels (Chapter 3). Their effect on differentiated intestinal epithelial cell distribution was demonstrated. This novel platform we have developed, anatomical villus model produced on synthetic hydrogels that bear spatio-chemical gradients of factors and suitable for the culture of intestinal cells derived from organoids, provide new opportunities in the field

of *in vitro* models of intestinal epithelium.

We expect this platform to be used as a physiologically relevant *in vitro* model to systematically study the role of gradients of ISC niche biochemical factors and their concentrations on the ISC proliferation, migration and differentiation. This would provide more information on the key signaling pathways that govern these processes for the maintenance of the epithelial homeostasis. Furthermore, the microfluidic chip allocating the hydrogel scaffold can be used to culture intestinal epithelial cells on the microstructured hydrogels. In this setup, live imaging can be performed combining appropriate mice model (e.g. Lgr5-EGFP-IRES-creERT2 mice) and microscopic techniques such as light-sheet fluorescence microscopy. This would reveal important information on the self-organization capacity of the ISC, previously demonstrated on 2D epithelial models [1], within a microenvironment resembling anatomical villi and the effect of such 3D architecture on *de novo* tissue formation.

The platform that we developed can further be improved to include nonepithelial cell types in an effort to achieve a more complex model of the intestinal mucosa. We have already incorporated biochemical signals provided by intestinal subepithelial myofibroblasts. Considering cell-cell contact interactions might also be relevant, intestinal subepithelial myofibroblast can be incorporated into the model by cultured them on the hydrogel scaffolds beneath the epithelial layer. Also, intraepithelial lymphocytes [2] can be co-cultured with the epithelial cells to incorporate part of the immune apparatus of the intestinal mucosa. This would allow screening for the immuno-modulatory effects of nutrients and toxins on the intestinal epithelium. Furthermore, mucus layer can be added either by implementing air-liquid interface culture technique or by using biopolymer-based synthetic mucins [3]. Air-liquid interface cultures were proven to induce better differentiation and the proper formation of the mucus layer in the monolayer cultures derived from ISC [4]. The cell culture format (Transwell®) we use permits the facile implementation of the air-liquid interface.

There has been substantial advances in human intestinal epithelial cell culture methods. Organotypic *in vitro* models of human intestine can be obtained from induced pluripotent stem (iPS) cells (induced organoid culture) [5] or from biopsy-derived adult intestinal crypts/stem cells (organoid or spheroid culture) [6, 7]. Our model can be adapted to include human intestinal stem cells by readjusting certain parameters, such as the cell culture medium [6, 8]. Moreover, the cell culture setup that we use permits facile implementation of the standard functional assays such as drug permeability. There is a great interest for such systems

in the field of personalized medicine. The use of patient's own intestinal epithelial cells allows defining susceptibilities, screening for the best treatment options and performing clinical testing to determine the efficacy of a particular treatment [9]. Moreover, in such systems host-microbe interactions can be defined [10].

The advances in the *in vitro* growth of the human intestinal tissue [6, 11] paved the way to better modeling of human diseases [12]. *In vitro* models of diseases such as colorectal cancer, cystic fibrosis and host-microbe interactions, have been established using organoid cultures [12]. These models have been useful in developing libraries from patient samples, and determining drug responsiveness, demonstrating their potential as diagnostic tools [12–15]. Also, intestinal organoids have been applied in studies of various types of host-microbe interactions, including studies of enteric viruses [16, 17], human protozoan parasites [10], and bacterial pathogens [18–20]. Although organoid model has been demonstrated as a powerful tool in modeling of number of diseases, it is not the most suitable one especially for studies that require easily accessible luminal surface. Specifically, the use of organoids in studies of host-microbe interactions dictates the use of labor-intensive microinjection technique [18–20]. Our intestinal epithelial model, on the other hand, by allowing access to the luminal surface, permits facile establishment of co-cultures of intestinal epithelium and enteric pathogens. In addition, probiotic organisms can be incorporated into these co-culture systems to assess their impact on inhibition of adhesion and invasion of the pathogenic organisms [21]. Furthermore, the 3D architecture appears to affect the adhesion and invasion patterns of pathogens [21]. In this respect, the accurate recreation of villus architecture, resulting in a more representative microenvironment for the intestinal epithelial cells, should provide important information on bacterial colonization during infections.

Inflammatory bowel disease (IBD) is an autoimmune-induced inflammatory condition affecting an important part of the world population, especially the westernized cultures [22]. Although conventional treatment strategies focus on readjusting the immune system that is locally or systemically deregulated [23], intestinal mucosal healing has gained importance in the clinical practice for improved long-term outcomes [24]. Our *in vitro* intestinal epithelial model can have potential advantages over current models in screening the effect of chemical compounds, bacterial components and drugs on *in vitro* epithelium derived from patient biopsy samples as it can be implemented easily and provides access to both luminal and basolateral sides, crucial for functional assays. In this way, how innate immunity is regulated in IBD patients can be understood and personalized

mucosal repair therapies can be developed. Moreover, the 3D villus-like architecture might have significance in the IBD patient's tissue response, and therefore, should be considered in the development of therapeutic strategies.

Gut-on-chip models reported up to date, include features for better mimicking of intestinal physiology such as fluid shear and cyclic mechanical loading resembling the peristaltic motion and allow tight regulation of the cellular microenvironment [25–28]. These devices have proven to enhance cell differentiation processes, allowed co-cultures of different epithelial cell lines [29], immune cells [30], commensal [25] and pathogenic bacteria [31]. Gut-on-chip devices provide high-throughput culturing and analysis, specifically in applications such as in high-throughput testing of drug efficacy and toxicity [28, 32], and nutrition analysis [30]. More complex 'human-on-chip' devices have been developed allocating other tissue types [33–35]. A chip including up to four different tissues i.e. small intestine, liver, skin and kidney equivalents has been succesfully achieved [36]. Very recently, primary intestinal epithelial cells from organoids were incorporated into gut-on-chip models in an effort of developing patient-based therapies [37]. However, these systems are similar to 2D cell cultures as the cells are grown in monolayer format lacking a support matrix that mimics the 3D architecture of the epithelial tissue. Our synthetic villus-like scaffolds, on the other hand, can be easily incorporated in such systems providing more realistic topographical cues for the cells. The strategies that we have developed to fabricate microfluidic chip allocating the hydrogel scaffold can be helpful in doing so. Alternatively, this chip itself, developed for in-chip diffusion characterization with microscopic techniques, can be used to culture intestinal epithelial cells on the hydrogels. This would not only present the cells with realistic topographical cues and gradients of ISC niche factors but also would allow live imaging of the *in vitro* tissue formation. Considering that villus-like topographies and gradients of ISC niche factors induce *in vivo*-like phenotypes [38], introducing scaffolds with such properties is relevant in the functionality of the *in vitro* tissue.

Altogether, the *in vitro* model of small intestinal epithelium reported here sets the foundations of a novel platform that can be potentially adopted in wide range applications from the studies of basic biology and physiology of intestinal epithelium to translational research.

References

[1] Curtis A. Thorne et al. “Enteroid Monolayers Reveal an Autonomous WNT and BMP Circuit Controlling Intestinal Epithelial Growth and Organization”. In: *Developmental Cell* 44.5 (2018), 624–633.e4.

[2] Maria Rescigno. “The intestinal epithelial barrier in the control of homeostasis and immunity”. In: *Trends in Immunology* 32.6 (2011), pp. 256–264.

[3] Sundar P. Authimoolam and Thomas D. Dziubla. “Biopolymeric mucin and synthetic polymer analogs: Their structure, function and role in biomedical applications”. In: *Polymers* 8.3 (2016).

[4] Xia Wang et al. “Cloning and variation of ground state intestinal stem cells”. en. In: *Nature* 522.7555 (2015), pp. 173–178.

[5] Jason R. Spence et al. “Directed differentiation of human pluripotent stem cells into intestinal tissue in vitro”. en. In: *Nature* 470.7332 (2010), pp. 105–109.

[6] Toshiro Sato et al. “Paneth cells constitute the niche for Lgr5 stem cells in intestinal crypts.” In: *Nature* 469.7330 (2011), pp. 415–418.

[7] Hiroyuki Miyoshi and Thaddeus S Stappenbeck. “In vitro expansion and genetic modification of gastrointestinal stem cells in spheroid culture”. In: *Nature Protocols* 8.12 (2013), pp. 2471–2482.

[8] Kelli L. VanDussen et al. “Development of an enhanced human gastrointestinal epithelial culture system to facilitate patient-based assays”. In: *Gut* 64.6 (2015), pp. 911–920.

[9] Anton Kuratnik and Charles Giardina. “Intestinal organoids as tissue surrogates for toxicological and pharmacological studies”. In: *Biochemical Pharmacology* 85.12 (2013), pp. 1721–1726.

[10] Christian Klotz, Toni Aebischer, and Frank Seeber. “Stem cell-derived cell cultures and organoids for protozoan parasite propagation and studying host-parasite interaction”. In: *International Journal of Medical Microbiology* 302.4-5 (2012), pp. 203–209.

[11] Peter Jung et al. “Isolation and in vitro expansion of human colonic stem cells”. In: *Nature Medicine* 17.10 (2011), pp. 1225–1227.

[12] Devanjali Dutta, Inha Heo, and Hans Clevers. “Disease Modeling in Stem Cell-Derived 3D Organoid Systems”. In: *Trends in Molecular Medicine* 23.5 (2017), pp. 393–410.

[13] Masayuki Fujii et al. “A Colorectal Tumor Organoid Library Demonstrates Progressive Loss of Niche Factor Requirements during Tumorigenesis”. In: *Cell Stem Cell* 18.6 (2016), pp. 827–838.

[14] Johanna F Dekkers et al. “A functional CFTR assay using primary cystic fibrosis intestinal organoids”. In: *Nature Medicine* 19.7 (2013), pp. 939–945.

[15] Johanna F. Dekkers et al. “Characterizing responses to CFTR-modulating drugs using rectal organoids derived from subjects with cystic fibrosis”. In: *Science Translational Medicine* 8.344 (2016).

[16] Stacy R. Finkbeiner et al. “Stem cell-derived human intestinal organoids as an infection model for rotaviruses”. In: *mBio* 3.4 (2012), pp. 1–6.

[17] Khalil Ettayebi et al. “Replication of human noroviruses in stem cell – derived human enteroids - SUPP”. In: *Science* 5211.August (2016).

[18] Jessica L. Forbester et al. “Interaction of salmonella enterica serovar Typhimurium with intestinal organoids derived from human induced pluripotent stem cells”. In: *Infection and Immunity* 83.7 (2015), pp. 2926–2934.

[19] Yong Guo Zhang et al. “Salmonella-infected crypt-derived intestinal organoid culture system for host–bacterial interactions”. In: *Physiological Reports* 2.9 (2014), pp. 1–11.

[20] Jhansi L. Leslie et al. “Persistence and toxin production by Clostridium difficile within human intestinal organoids result in disruption of epithelial paracellular barrier function”. In: *Infection and Immunity* 83.1 (2015), pp. 138–145.

[21] Cait M Costello et al. “3-D intestinal scaffolds for evaluating the therapeutic potential of probiotics.” In: *Molecular pharmaceutics* 11.7 (2014), pp. 2030–9.

[22] Natalie A. Molodecky et al. “Increasing incidence and prevalence of the inflammatory bowel diseases with time, based on systematic review”. In: *Gastroenterology* 142.1 (2012), 46–54.e42.

[23] William J. Sandborn. “Current Directions in IBD Therapy: What Goals Are Feasible With Biological Modifiers?” In: *Gastroenterology* 135.5 (2008), pp. 1442–1447.

[24] Guillaume Pineton De Chambrun et al. “Clinical implications of mucosal healing for the management of IBD”. In: *Nature Reviews Gastroenterology and Hepatology* 7.1 (2010), pp. 15–29.

[25] Hyun Jung Kim et al. “Human gut-on-a-chip inhabited by microbial flora that experiences intestinal peristalsis-like motions and flow.” In: *Lab on a chip* 12.12 (2012), pp. 2165–74.

[26] Hyun Jung Kim and Donald E Ingber. “Gut-on-a-Chip microenvironment induces human intestinal cells to undergo villus differentiation.” en. In: *Integrative biology : quantitative biosciences from nano to macro* 5.9 (2013), pp. 1130–40.

[27] Mandy Brigitte Esch et al. “On chip porous polymer membranes for integration of gastrointestinal tract epithelium with microfluidic ‘body-on-a-chip’ devices”. In: *Biomedical Microdevices* 14.5 (2012), pp. 895–906.

[28] Gretchen J. Mahler et al. “Characterization of a gastrointestinal tract microscale cell culture analog used to predict drug toxicity”. In: *Biotechnology and Bioengineering* 104.1 (2009), pp. 193–205.

[29] Gretchen J. Mahler, Michael L. Shuler, and Raymond P. Glahn. “Characterization of Caco-2 and HT29-MTX cocultures in an in vitro digestion/cell culture model used to predict iron bioavailability-”. In: *The Journal of Nutritional Biochemistry* 20.7 (2009), pp. 494–502.

[30] Qasem Ramadan et al. “NutriChip: nutrition analysis meets microfluidics”. In: *Lab Chip* 13.2 (2013), pp. 196–203.

[31] Hyun Jung Kim et al. “Contributions of microbiome and mechanical deformation to intestinal bacterial overgrowth and inflammation in a human gut-on-a-chip”. In: *Proceedings of the National Academy of Sciences* 113.1 (2016), E7–E15.

[32] Hiroshi Kimura et al. “An integrated microfluidic system for long-term perfusion culture and on-line monitoring of intestinal tissue models”. In: *Lab on a Chip* 8.5 (2008), p. 741.

[33] Aaron Sin et al. “The Design and Fabrication of Three-Chamber Microscale Cell Culture Analog Devices with Integrated Dissolved Oxygen Sensors”. In: *Biotechnology Progress* 20.1 (2004), pp. 338–345.

[34] Ilka Wagner et al. “A dynamic multi-organ-chip for long-term cultivation and substance testing proven by 3D human liver and skin tissue co-culture”. In: *Lab on a Chip* 13.18 (2013), pp. 3538–3547.

[35] Mandy B. Esch et al. “Modular, pumpless body-on-a-chip platform for the co-culture of GI tract epithelium and 3D primary liver tissue”. In: *Lab on a Chip* 16.14 (2016), pp. 2719–2729.

[36] Ilka Maschmeyer et al. “A four-organ-chip for interconnected long-term co-culture of human intestine, liver, skin and kidney equivalents”. In: *Lab Chip* 15.12 (2015), pp. 2688–2699.

[37] Magdalena Kasendra et al. “Development of a primary human Small Intestine-on-a-Chip using biopsy-derived organoids”. In: *Scientific Reports* 8.1 (2018), pp. 1–14.

[38] Yuli Wang et al. “A microengineered collagen scaffold for generating a polarized crypt-villus architecture of human small intestinal epithelium”. In: *Biomaterials* 128 (2017), pp. 44–55.

General conclusions

In **Chapter 1**, a method to develop functional intestinal epithelial monolayers from organoid-derived crypts was described. The method took the advantage of substrate stiffness to dictate the formation of monolayers rather than 3D organoids with a closed geometry. The 2D intestinal epithelial model contained all major epithelial cell types organized into crypt-like and villus-like domains like *in vivo* intestine. The use of cell culture medium rich in ISC niche biochemical factors boosted the proliferative capacity and monolayer expansion leading to the formation of monolayers with tissue barrier function. The monolayer differentiation was achieved with prolonged culture times, while maintaining the intestinal stem cell population organized into crypt-like domains. The monolayers had physiologically relevant TEER values, indicating proper tissue barrier formation. The 2D intestinal epithelial model reported here, contributes to the current state-of-the art as it demonstrates both *in vivo*-like crypt-villus organization and physiologically relevant tissue barrier function.

In **Chapter 2**, a more complex model of intestinal epithelium, incorporating a basement membrane substitute with the characteristic 3D villus-like architecture for the growth organoid-derived intestinal cell monolayers was described. 3D villus-like complex geometries on poly(ethylene glycol) diacrylate-based hydrogels with anatomical villus dimensions and biomimetic round tips were achieved by using a simple, moldless photolithographic approach. The mechanical and swelling properties of the hydrogels could be tuned by changing the polymer concentration to match the requirements of a tissue mimic. The bioactive functionalization of otherwise inert poly(ethylene glycol) diacrylate, was achieved by copolymerizing it with acrylic acid. In this way, the desired cell adhesion ligand could be covalently anchored to the hydrogel demonstrating the versatility of the method. The conditions affecting the growth of intestinal epithelial monolayers (ligand type, seeding density, microstructure height and mechanical properties) were studied and the cell culture medium composition optimal for the intestinal epithelial monolayer growth was established. Organoid-derived intestinal

epithelial cells successfully formed epithelial monolayers on collagen functionalized 3D villus-like hydrogels independently of the microstructure heights and mechanical properties (determined by polymer concentrations) within the range studied. The basement membrane substitute developed here provides the primary intestinal epithelial cells with a more realistic microenvironment including proper biochemical, mechanical, and topographical signaling. The simple fabrication procedure facilitates its implementation as a method to routinely incorporate 3D architecture mimicking the anatomical villi, in cell culture systems of primary intestinal epithelial cells.

In **Chapter 3**, a method to create spatio-chemical gradients of ISC niche biochemical factors on poly(ethylene glycol) diacrylate hydrogels, was described. The pore sizes of the hydrogels were sufficient to allow the diffusion of the biochemical factors through them and could be tuned by the changing the polymer concentration. *In silico* models were developed to gain an insight on the diffusion times, gradient profiles and surface concentrations of ISC niche biochemical factors within the experimental setups used. A microfluidic chip allocating the hydrogel scaffolds was designed and fabricated for in-chip diffusion of proteins that permitted microscopic characterization. The gradients were succesfully generated and visualized with light-sheet fluorescence microscopy. Stable profiles could be obtained by periodically replenishing the chambers. The platform was succesfully adapted to standard cell culture platforms that permitted access to both sides of the hydrogel. The spatio-chemical gradients generated in this setup using the basolateral compartment as the source and the apical compartment as the sink, led to the compartmentalization of differentiated cells more towards the tips of the villus-like microstructures.

Overall, a novel 3D villus-like biomimetic hydrogel platform with spatio-chemical gradients of ISC niche biochemical factors was developed. This *in vitro* platform can be potentially used to guide ISC migration and differentiation, to obtain an *in vitro* intestinal epithelial model with *in vivo* cell populations and their hierarchical distribution.

Appendix A

A simple embedding method for improved imaging of the polyethylene glycol based hydrogel scaffolds

A.1 Introduction

Hydrogel materials are widely used for tissue engineering and regenerative medicine applications [1]. Due to their network structure and mechanical properties, hydrogels can mimic well the extracellular matrix and their rich water content that facilitates the diffusion of biochemical factors and oxygen, enables long-term maintenance of mammalian cell cultures [2, 3]. Polyethylene glycol (PEG) is a synthetic biocompatible hydrogel material that is inherently non-fouling [4]. Yet, it can easily be functionalized with bioactive agents to stimulate the cell adhesion. The mechanical properties can also be adjusted to match those of the soft tissue [5]. Due to this adjustability the PEG hydrogels are commonly used as cell carriers and scaffold materials in tissue engineering [6–9].

Visualizing well the cell-cell and the cell-material interactions and monitoring the cell proliferation is very important for the evaluation of the success of the tissue engineered construct. Histological sections performed on the artificial tissue constructs provide crucial information on cytocompatibility, cell proliferation and differentiation [10]. Yet, due to their high water content, hydrogels do not withstand the routine tissue histology procedures. In standard paraffin processing, the exchange of tissue water with ethanol followed by a hydrophobic solvent (e.g. xylene) causes the hydrogel structures to collapse resulting in

poor preservation of the intricate forms of the hydrogels [10]. Cryosectioning is another method used when the antigen to be detected is sensitive to paraffin processing [11]. Cryosections are preferred over paraffin since water-based embedding media are used and therefore, the tissues and scaffolds are preserved closer to their original state [10]. However, the difference in the hardness of the embedding media and the hydrogel at sectioning temperatures (typically around - 20 °C) results in incomplete sections or total destruction of the hydrogel microstructure. Other embedding media such as; epoxy and acrylic resins are suitable for hard tissue histology and also require the dehydration of the tissue since they are immiscible with water [12, 13]. Water miscible embedding media, such as glycol methacrylate-based media, are useful in overcoming unwanted effects of dehydration; however, upon polymerization they form hard blocks since almost pure solutions of glycol methacrylate are used [14]. Hard blocks are necessary to be able to make very thin sections, for instance, for electron microscopy. However, polymerization of highly concentrated acrylates and the consequent shrinkage affect the complex microstructures of the soft hydrogels. Therefore, there is a need for an effective embedding and sectioning method that would preserve the water content, and consequently, the complex morphologies of microstructured soft hydrogel scaffolds.

Here, we present a simple embedding method for PEG based microstructured hydrogels to obtain undistorted sections without the need of dehydrating or freezing of the sample. For this purpose, diluted low molecular weight polyethylene glycol diacrylate (PEGDA) was used as embedding medium. For optimal immunofluorescence characterization several antigen retrieval conditions were examined.

A.2 Materials and Methods

Three dimensional (3D) villus-like PEGDA based hydrogel scaffolds were fabricated as explained in chapter 2 section 2.2.1. For the embedding medium, low molecular weight diluted PEGDA solution was prepared by dissolving 575 Da PEGDA (P575) (Sigma) in phosphate buffered saline (PBS) (Gibco) at 10% w/v concentration. The photoinitiator, 2-hydroxy-1-[4-(2-hydroxyethoxy) phenyl]-2-methyl-1-propanone (I2959) (Sigma) was added at 1% w/v concentration. The solution was mixed at 65°C for 1 hour, filtered and stored at 4°C until further use. Prior to embedding microstructured PEGDA scaffolds were acclimatized with 10% w/v P575 overnight at 4°C. Meanwhile, a container made out of

polydimethylsiloxane (PDMS) (Sylgard 184 Silicon Elastomer, Dow Corning) was made as explained previously (Chapter 2 Section 2.2.1). Briefly, a PDMS slab of 2 mm height was made and a pool of 10 mm in diameter was carved into PDMS using a 10 mm diameter punch (Acuderm). Then, the pool was placed on top of a 24 x 60 mm glass coverslip (Menzel-Glaser). All the pieces were washed with 96% v/v ethanol prior to use. The pool was filled with 10% w/v P575 solution and the microstructured hydrogels previously fabricated on glass coverslips were placed onto the pool upside down. For the crosslinking of P575, the container was exposed to UV by a Mask aligner instrument (SUSS MicroTec MJB4) equipped with a mercury short arc lamp (OSR HBO 350 W/S) present at the IBEC MicroFabSpace. The device was calibrated to a constant intensity of 25 mW.cm^{-2} by an UV intensity meter (SUSS MicroTec) equipped with a probe at 365 nm. First, the container was irradiated with UV for 100 s from the right side up and then it was flipped and exposed again for 100 s from upside down (Figure A.1). With this procedure we obtained translucent discs of P575 with the microstructured PEGDA scaffold inside. The samples were kept in PBS at 4°C until sectioning.

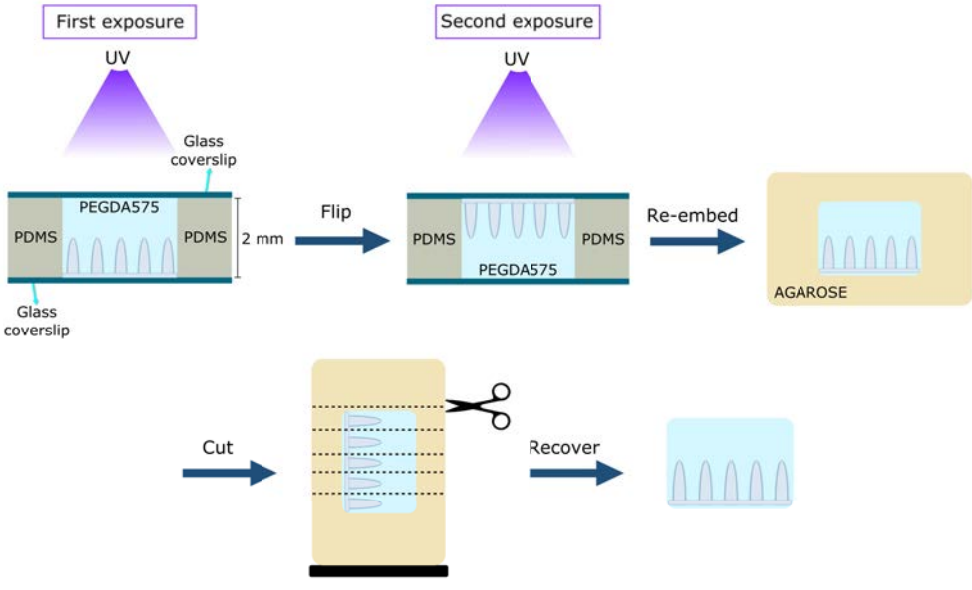

Figure A.1: *Scheme depicting the embedding and sectioning method.*

Prior to vibrotome sectioning, the P575 discs had to be re-embedded in agarose, which provided structural support. 8% w/v agarose (low melting point agarose D1, CONDA) was prepared in PBS by boiling two times in a microwave

oven and shaking at 65°C at least 30 min. A part of the agarose solution was added into a cryomold (Tissue-Tek) to fill halfway and the P575 disc was placed paying attention to the orientation of the microstructures. Then, more agarose solution was added until filling the mold and the block was solidified at 4°C for 4 min. A vibratome (Leica VT1000S) was used for the sectioning of the scaffold since it allows the sectioning of the tissues/scaffolds in wet conditions [15]. The block was fixed to the platform of the vibratome by superglue making sure that the microstructure tips were facing the blade. The bath was filled with ice cold PBS and ice was added to the chamber around the bath. The parameters were adjusted (0,075 $mm.s^{-1}$ advance rate, 81 Hz vibration and 1 mm amplitude) and sections of 350 μm were made. The cuts were recovered from the bath and kept in PBS at 4°C until further use.

The cuts were visualized with a bright field microscope (Nikon Eclipse Ts2). To further confirm that the microstructured PEGDA-acrylic acid (PEGDA-AA) hydrogel scaffolds stayed intact throughout the process we functionalized them with Streptavidin_TexasRED (SA_TxRED) (Life technologies) by using N- (3-Dimethylaminopropyl)-N'-ethylcarbodiimide (EDC) (Sigma) and N-Hydroxysuccinimide (NHS) (Sigma) molecules as activators (see Chapter 2 Section 2.2.5 for the method). The microstructured PEGDA-AA hydrogels described in chapter 2 have flanking carboxylic residues that allow protein coupling; while P575 hydrogel structure doesn't bear such groups. By anchoring SA_TxRED to carboxylic groups of microstructured PEGDA, it was possible to selectively visualize its morphology within the P575 structure.

In order to prove that the standard immunostaining protocols could be applied to the cuts obtained with this method, we used fixed cell samples of human epithelial colorectal adenocarcinoma cells (Caco-2) grown on microstructured PEGDA-AA (MW_{PEGDA} = 6000, P6000) scaffolds. The samples were prepared within the scope of a parallel study performed in our laboratory [16] and kindly given for the validations made here. The Caco-2 samples were fixed with 10% neutralized formalin (Sigma) and acclimatized with 10% w/v P575 overnight at 4°C. Then, embedding and sectioning were performed as explained above. After the cuts were recovered, the standard immunostaining protocol as given in chapter 2 section 2.2.7, was executed except with increased incubation times for primary and secondary antibodies. The readjusted incubation times were 72 h and 24 h for the primary and secondary antibodies, respectively. This allowed the necessary time for proper penetration of large antibody molecules into the P575 hydrogel structure. The primary antibodies and the dilutions

used were: mouse anti-villin (1:100) (abcam), rabbit anti-β-catenin (1:100) (abcam), and goat anti-*zona occludens 1* (ZO-1) (1:1000) (abcam). As secondary antibodies, Alexa Fluor® 488 donkey anti-mouse (Invitrogen), Alexa Fluor® 647 donkey anti-rabbit (Jackson ImmunoResearch), and Alexa Fluor® 568 donkey anti-goat (Invitrogen) diluted at 1:250, were used. Nuclei were stained with 4',6-diamidino-2-phenylindole (DAPI) (1:1000) (invitrogen). The cuts were mounted with Fluoromount G® (SoutherBiotech) and the fluorescence images were acquired using confocal laser scanning microscopy (CLSM) (TCS SP5, Leica) with 40x oil (N.A. = 1,25) objective. The laser excitation and emission light spectral collection were optimized for each fluorophore. The pin hole diameter was set to 1 Airy Unit (AU) and a z-step of 1 μm was used.

For the detection of villin it was necessary to perform antigen retrieval. To determine the optimal conditions, two different buffers were tested: PBS (pH 7,4) and citrate buffer (pH 6,0) at two different boiling times. The antigen retrieval was performed after embedding and sectioning. The cuts were submerged into the buffer and boiled in a microwave oven for 5 min or 10 min. After the antigen retrieval we proceeded with the standard immunostaining protocol (Chapter 2 Section 2.2.7).

A.3 Results

We have previously developed 3D villus-like anatomical models of the intestine on soft PEGDA hydrogels (Chapter 2). These hydrogels supported the growth of the human epithelial colorectal adenocarcinoma cells (Caco-2) that formed effective barrier colonizing the scaffold surface [17]. However, the microscopic inspection of these samples were limited to whole mount imaging since routine histology protocols were not compatible with these hydrogels that contained high amounts of water and had villus-like features of couple of hundreds of microns. The simple embedding method, based on the use of diluted low molecular weight PEGDA we propose here, overcomes this drawback.

The microstructured P6000 hydrogels were embedded in 10% w/v P575 by UV initiated crosslinking of P575. This provided a support for the microstructured hydrogel and enabled re-embedding in agarose, which was necessary for the vibratome sectioning. Vibratome cuts the tissues/scaffolds submerged in aqueous medium overcoming the need of the dehydration of the samples. In this way, minimum damage was made to the highly swollen hydrogels with complex forms. After sectioning, the recovered cuts were mechanically robust

enough that permitted further manipulation for immunostaining and imaging procedures (Figure A.2 A). Bright field microscopy image suggested that the procedure hadn't affected the morphology of the microstructures (Figure A.2 B). Selective labeling of the microstructured PEGDA by functionalizing with SA_TxRED confirmed that the villus-like features of the hydrogel was unaffected by the embedding procedure (Figure A.2 C).

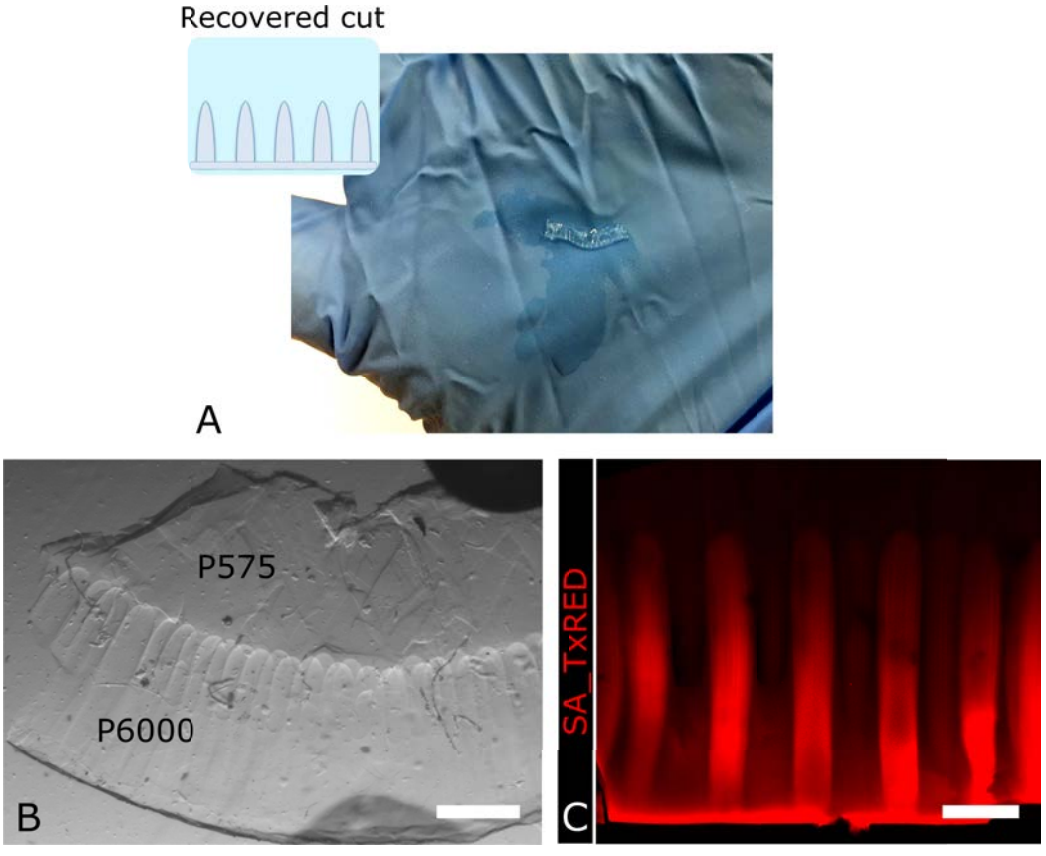

Figure A.2: *Image showing a recovered cut (A). Inset drawing depicts the microstructured PEGDA embedded in P575 within the cut. Bright field microscopy image of a single cut (B). Scale bar: 500 μm. Fluorescence image of SA_TxRED functionalized microstructured PEGDA hydrogel embedded in P575 (C). Scale bar: 200 μm.*

The immunostainings were performed on the sections of fixed cell samples prepared by our method. Epithelial markers such as β-catenin, localizes to cell-cell adhesion, and ZO-1, found at the tight junctions at the apical side, were expressed and located at the proper regions (Figure A.3). These markers did not required antigen retrieval prior to staining. Although, ZO-1 signal was only observed at some of the junctions and can possibly be improved by incorporating

this step. More importantly, the embedding and sectioning method permitted the visualization of microstructures of approximately 300 μm in height (Figure A.3 upper left panel) within the same focal plane at 40x magnification. This overcame the working distance limitations of high magnification objectives and revealed structural details such as the formation of multicellular layers, otherwise would have been diffucult to assess from the top view images of whole mounted samples. Note that the microstructures were not as high as the ones given in figure A.2 due to the fabrication parameters chosen for the microstructuring of the hydrogels. But also the sections can coincide to the base region of the scaffolds.

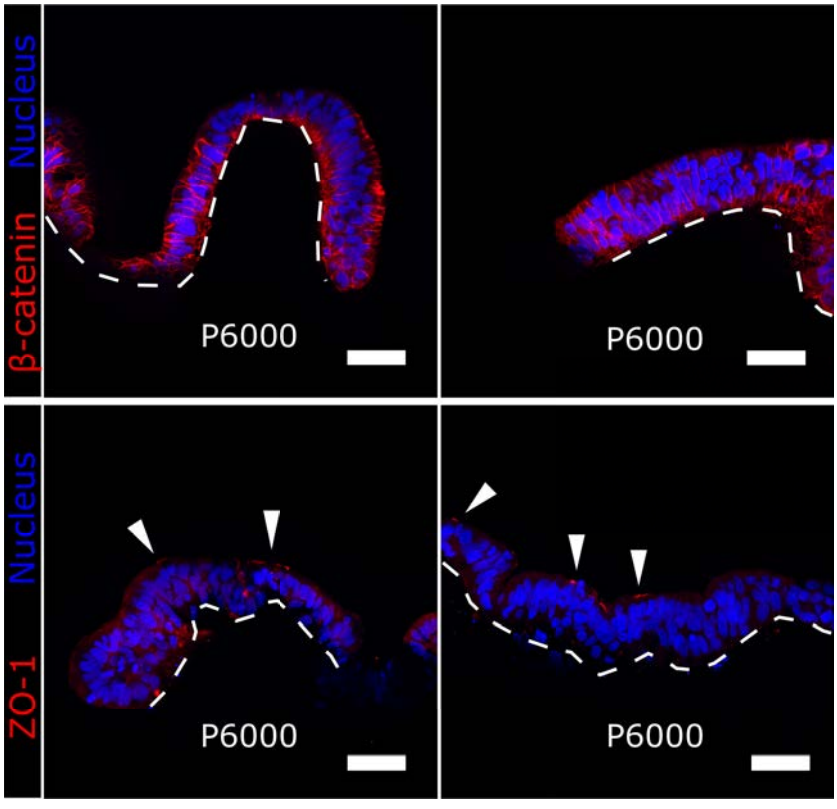

Figure A.3: *Immunofluorescence for β-catenin and ZO-1 of Caco-2 cells grown on microstructured P6000 hydrogels at day 21. White arrowheads indicate the ZO-1 signal. No antigen retrieval was performed on these cuts. Scale bars: 50 μm.*

For the detection of villin, an epithelial cell marker found at the apical side of the cells [18], it was necessary to perform antigen retrieval. We have tested both PBS and citrate buffer for retrieval times of 5 and 10 minutes. Increased times led to better detection of the villin protein both for PBS and citrate buffer (Figure A.4). As compared to PBS, the cuts retrieved with citrate buffer were stained

slightly better with a continuous villin-positive region at the apical side of the cell layer (Figure A.4 right panel). For that reason we propose the use of citrate buffer with a retrieval time of 10 minutes for the antigen retrieval of scaffold sections prepared in this fashion.

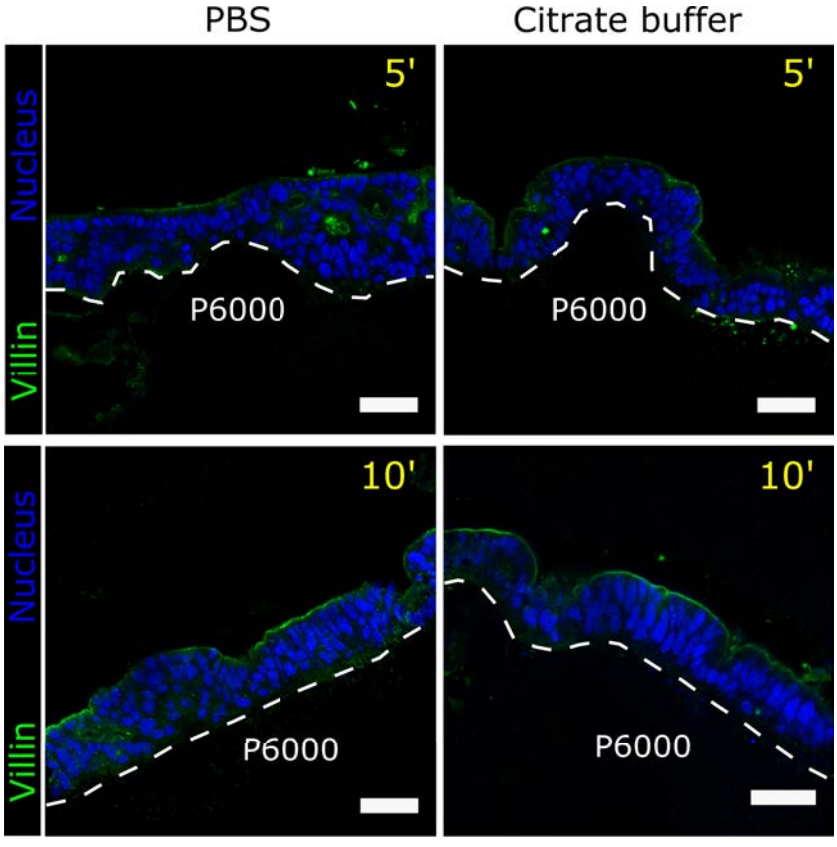

Figure A.4: *Immunofluorescence for villin of Caco-2 cells grown on microstructured P6000 hydrogels at day 21 for the assessment of antigen retrieval performed with either PBS (pH 7,4) or citrate buffer (pH 6,0) for 5 or 10 minutes. Scale bars: 50 μm.*

A.4 Discussion

The relative fragility of PEG-based hydrogels in routine tissue sectioning mainly depends on its high water content and soft mechanical properties. The processes that require the dehydration of the samples e.g. paraffin embedding, causes the hydrogel network to collapse and for that reason are not suitable. Alternatively in cryosectioning, water-based embedding media are used overcoming the need

of dehydration. Though, the formation of ice crystals upon freezing of the water left within the tissue/hydrogel is a problem, which is overcome by infiltrating the hydrogels with cryoprotectant solutions prior to embedding. The main problem that can occur in cryosectioning is the mismatch between the mechanical properties of the embedding media and the hydrogel. It was not possible to cut the microstructured PEGDA hydrogels by this technique because during cryosectioning the PEGDA scaffold remained more elastic compared to the surrounding embedding medium, which resulted in the compression of the scaffold by the blade. This then resulted in incomplete sections or squeezing of the hydrogel causing sections with distorted microstructures (data not shown). Although commercially available Optimal Cutting Temperature® (OCT) compound, used both as cryoprotectant and embedding medium, was proven useful in successful sectioning of PEG [10], collagen [19] and alginate hydrogel scaffolds [19], those materials were prepared in bulk with no complex topographical features. The most beneficial histological technique for examining microstructured hydrogels should enable optimal morphological evaluation.

The novel method presented here, makes use of diluted low molecular weight PEGDA (P575) as embedding medium. All the steps of this procedure; the crosslinking of P575, sectioning with vibratome, immunostainings, were performed in wet conditions (in aqueous media). This allowed the sectioning of the samples without the need of dehydration or freezing, which resulted in optimal preservation of the microstructure morphology. Fixed samples of Caco-2 cells cultured on microstructured PEGDA hydrogels were embedded and sectioned without affecting the cell layer integrity. Then, standard immunostaining protocol was succesfully performed on the sections with some adjustments on incubation times. Some of the epithelial markers were detected without the need of antigen retrieval; however, for villin it was necessary. Several antigen retrieval conditions were examined for optimal immunofluorescence detection. The most beneficial condition was using citrate buffer and boiling for 10 minutes. Also, the use of PEG, an inert material, as embedding medium resulted in minimal background staining in the sections.

The proper sectioning of PEGDA hydrogels with microstructures of couple of hundreds of microns permits the visualization of the entire microstructure within the same focal plane at relatively high magnifications (40x) overcoming the working distance limitations of high magnification objectives. This is particularly important to reveal structural details and the localization of certain markers that would otherwise be diffucult to assess from top views of fluorescently stained

samples. In addition, the method is simple, cost effective and can be easily implemented in any laboratory. Although here we demonstrated its use on PEGDA hydrogels, the method can be extended to the histological examination of other types of hydrogel scaffolds.

A.5 Conclusions

We have developed a simple and cost-effective embedding and sectioning method for microstructured PEGDA-based hydrogel scaffolds. The method made use of low molecular weight PEGDA to embed and cut microstructured scaffolds without the need of dehydration. This permitted the preservation of the microstructures that were couple of hundreds of microns in size. Moreover, it permitted the visualization of large size microstructures within the same focal plane at relatively high magnifications. Fixed cell samples were successfully cut and immunostained with minimal adjustments in standard protocols. For optimal immunofluorescence detection the best antigen retrieval condition was determined. This simple and effective embedding protocol can be used to better visualize cell-matrix interactions within PEG-based matrices as well as other hydrogel scaffolds that have large size features.

References

[1] Brandon V. Slaughter et al. “Hydrogels in Regenerative Medicine”. In: *Advanced Materials* 21 (2009), pp. 3307–3329.

[2] N.-A. Peppas et al. “Hydrogels in Biology and Medicine: From Molecular Principles to Bionanotechnology”. In: *Advanced Materials* 18.11 (2006), pp. 1345–1360.

[3] Cole a DeForest and Kristi S Anseth. “Advances in bioactive hydrogels to probe and direct cell fate.” In: *Annual review of chemical and biomolecular engineering* 3 (2012), pp. 421–44.

[4] T Ipek Ergenç and Seda Kızılel. “Recent Advances in the Modeling of PEG Hydrogel Membranes for Biomedical Applications”. In: *Biomedical engineering, trends in materials science*. 2011, pp. 307–345. ISBN: 978-953-307-513-6.

[5] Soah Lee, Xinming Tong, and Fan Yang. “The effects of varying poly(ethylene glycol) hydrogel crosslinking density and the crosslinking mechanism on protein accumulation in three-dimensional hydrogels.” In: *Acta biomaterialia* 10.10 (2014), pp. 4167–74.

[6] Christopher a Durst et al. “Flexural characterization of cell encapsulated PEGDA hydrogels with applications for tissue engineered heart valves.” In: *Acta biomaterialia* 7.6 (2011), pp. 2467–76.

[7] Mehrdad Rafat et al. “PEG-stabilized carbodiimide crosslinked collagen–chitosan hydrogels for corneal tissue engineering”. In: *Biomaterials* 29.29 (2008), pp. 3960–3972.

[8] Ho-Joon Lee et al. “Poly(ethylene glycol) diacrylate/hyaluronic acid semi-interpenetrating network compositions for 3-D cell spreading and migration.” In: *Acta biomaterialia* 14 (2015), pp. 43–52.

[9] B. Yañez-Soto et al. “Biochemically and topographically engineered poly(ethylene glycol) diacrylate hydrogels with biomimetic characteristics as substrates for human corneal epithelial cells”. In: *Journal of Biomedical Materials Research - Part A* 101 A.4 (2013), pp. 1184–1194.

[10] Jia-Ling Ruan et al. “An improved cryosection method for polyethylene glycol hydrogels used in tissue engineering.” In: *Tissue engineering. Part C, Methods* 19.10 (2013), pp. 794–801.

[11] Andrew H. Fischer et al. “Cryosectioning tissues”. In: *Cold Spring Harbor Protocols* 3.8 (2008).

[12] W. N. Eastham and W. B. Essex. “Use of tissues embedded in epoxy resin for routine histological examination of renal biopsies.” In: *Journal of clinical pathology* 22.1 (1969), pp. 99–106.

[13] S. Caropreso et al. “Thin sections for hard tissue histology: A new procedure”. In: *Journal of Microscopy* 199.3 (2000), pp. 244–247.

[14] Jakob Zbaeren, Daphne Zbaeren-Colbourn, and André Haeberli. “High-Resolution Immunohistochemistry on Improved Glycol Methacrylate—Resin Sections”. In: *Journal of Histotechnology* 30.1 (2007), pp. 27–33.

[15] Jonathan T Ting et al. “Improved methods for acute brain slice preparation from adult and aging brain (Part II): Glutathione depletion underlies rapid deterioration of adult brain slices”. In: *Society for Neuroscience* Part II (2012), p. 505.

[16] Albert Garcia Castaño. "Engineering poly (ethylene glycol) diacrylate-based microstructures to develop an in vitro model of small intestinal epithelium". In: *TDX (Tesis Doctorals en Xarxa)* (2018).

[17] Albert Garcia Castaño et al. "Single-step dynamic polymerization photolithography produces complex microstructures on hydrogels to generate a 3D intestinal tissue model". In: *Manuscript* (2018).

[18] Sudeep P. George et al. "Dimerization and actin-bundling properties of villin and its role in the assembly of epithelial cell brush borders". In: *Journal of Biological Chemistry* 282.36 (2007), pp. 26528–26541.

[19] C.-C. Yang, L. Jenkins, and K. J. L. Burg. "Adapted Cryosectioning Method for Hydrogels Used in Regenerative Medicine". In: *Journal of Histotechnology* 30.3 (2007), pp. 185–191.

Appendix B

Image analysis macro 1

In this Appendix, ImageJ macro used to quantify the intestinal epithelial cell markers is presented.

ImageJ Macro

```
Dialog.create("Tissue Cell");
Dialog.addNumber("Channel 1 (DAPI) pre-filter radius (pix)", 3);
Dialog.addNumber("Nuclei detection noise tolerance", 0.05);
Dialog.addNumber("DAPI intensity threshold", 30);
Dialog.addNumber("Chan 2 & 4 mean filter radius (pix)", 3);
Dialog.addNumber("Channel 2 positive intensity threshold", 7);
Dialog.addNumber("Channel 4 positive intensity threshold", 10);
Dialog.addNumber("Actin detection threshold", 5);
Dialog.addCheckbox("Remove nuclei outside detected actin tissue area?", false);
Dialog.show();
FltRad = Dialog.getNumber();
NoiseTol = Dialog.getNumber();
DapiIntThr = Dialog.getNumber();
MeanRad = Dialog.getNumber();
Chan2IntThr = Dialog.getNumber();
Chan4IntThr = Dialog.getNumber();
ActinIntThr = Dialog.getNumber();
RemoveOutside = Dialog.getCheckbox();
// Initialization
print("Image name: "+getTitle());
if(isOpen("ROI Manager"))
{
```

```
selectWindow("ROI Manager");
run("Close");
}
run("Point Tool...", "selection=Yellow cross=White marker=Small mark=0");
// Processing
run("Z Project...", "projection=[Max Intensity]");
rename("Proj");
run("Duplicate...", "title=Img duplicate");
run("Split Channels");
// Analyze actin channel (Channel 1)
selectImage("C1-Img");
run("Gaussian Blur...", "sigma=3");
// Use fixed filter radius for actin channel
setThreshold(ActinIntThr,255);
run("Create Selection");
run("Properties... ", "position=none stroke=yellow fill=none");
run("Add to Manager");
getStatistics(nPixels);
print("Projection actin tissue coverage area (pix): "+d2s(nPixels,0));
close();

// Analyze nuclei channel (Channel 3)
selectImage("C3-Img");
run("Grays");
run("FeatureJ Laplacian", "compute smoothing="+d2s(FltRad,2));
run("Invert");
if(RemoveOutside)roiManager("select",0);
run("Find Maxima...", "noise="+d2s(NoiseTol,2)+" output=[Point Selection]");
getSelectionCoordinates(Xpos,Ypos);
close();
selectImage("C3-Img");
run("Smooth");
Xposflt = newArray(lengthOf(Xpos));
Yposflt = newArray(lengthOf(Ypos));
cntValid = 0;
for(i = 0;i<lengthOf(Xpos);i++)
{
```

```
val = getPixel(Xpos[i],Ypos[i]);
if(val > DapiIntThr)
{
Xposflt[cntValid] = Xpos[i];
Yposflt[cntValid] = Ypos[i];
cntValid++;
}
}
Xposflt = Array.trim(Xposflt, cntValid);
Yposflt = Array.trim(Yposflt, cntValid);
makeSelection("point",Xposflt,Yposflt);
run("Properties... ", "position=none stroke=green fill=none");
run("Add to Manager");
print("Nuclei count: "+d2s(cntValid,0));
selectImage("C3-Img");
close();

// Analyze positive nuclei in channel 2 (Ki67 or other nuclear label)
selectImage("C2-Img");
run("Grays");
if(MeanRad>0)run("Mean...", "radius="+d2s(MeanRad,2));
cntPos = 0;
Xpospos = newArray(lengthOf(Xposflt));
Ypospos = newArray(lengthOf(Yposflt));
Ppospos = newArray(lengthOf(Xposflt));
for(i = 0;i<lengthOf(Xposflt);i++)
{
val = getPixel(Xposflt[i],Yposflt[i]);
if(val > Chan2IntThr)
{
Xpospos[cntPos] = Xposflt[i];
Ypospos[cntPos] = Yposflt[i];
Ppospos[i] = 1;
cntPos++;
}
}
Xpospos = Array.trim(Xpospos, cntPos);
```

```
Ypospos = Array.trim(Ypospos, cntPos);
makeSelection("point",Xpospos,Ypospos);
run("Properties... ", "position=none stroke=red fill=none");
run("Add to Manager");
print("Channel 2 positive nuclei count: "+d2s(cntPos,0));
print("Proportion of Channel 2 positive nuclei (%):
"+d2s(100*cntPos/cntValid,1));
selectImage("C2-Img");
close();

// Analyze positive nuclei in channel 4
selectImage("C4-Img");
run("Grays");
if(MeanRad>0)run("Mean...", "radius="+d2s(MeanRad,2));
cntPos = 0;cnt2Pos = 0;
Xpospos = newArray(lengthOf(Xposflt));
Ypospos = newArray(lengthOf(Yposflt));
for(i = 0;i<lengthOf(Xposflt);i++)
{
val = getPixel(Xposflt[i],Yposflt[i]);
if(val > Chan4IntThr)
{
Xpospos[cntPos] = Xposflt[i];
Ypospos[cntPos] = Yposflt[i];
if(Ppospos[i] == 1)cnt2Pos++;
cntPos++;
}
}
Xpospos = Array.trim(Xpospos, cntPos);
Ypospos = Array.trim(Ypospos, cntPos);
makeSelection("point",Xpospos,Ypospos);
run("Properties... ", "position=none stroke=yellow fill=none");
run("Add to Manager");
print("Channel 4 positive nuclei count: "+d2s(cntPos,0));
print("Proportion of Channel 4 positive nuclei (%):
"+d2s(100*cntPos/cntValid,1));
print("Channel 2+4 positive nuclei count: "+d2s(cnt2Pos,0));
```

```
print("Proportion of Channel 2+4 positive nuclei (%):
"+d2s(100*cnt2Pos/cntValid,1));
selectImage("C4-Img");
close();

// Overlay all results on projection selectImage("Proj");
for(i=1;i<=4;i++)
{
setSlice(i);
run("Enhance Contrast", "saturated=0.35");
}
roiManager("Show All");
roiManager("Deselect");
run("Brightness/Contrast...");
run("Channels Tool...");
```

Appendix C

Image analysis macro 2

In this Appendix, ImageJ macro used to quantify the spatial distribution of CK20 signal along the microstructure vertical axis is presented.

ImageJ Macro

```
// Assumptions: Chan1 (F-actin) used for masking, Chan2 (CK20) used for measurement
// Report Chan2 mean intensity within Chan1 mask for each Z slice
Chan1Thr = 12;
Chan1MinArea = 500;
Chan1Dil = 0;
// Processing OrigID = getImageID();
run("Duplicate...", "title=Copy duplicate");
if(isOpen("ROI Manager"))
{
selectWindow("ROI Manager");
run("Close");
}
setOption("BlackBackground", false);
rename("Stack");
run("Split Channels");
run("Set Measurements...", "area mean redirect=C2-Stack decimal=2");
selectImage("C1-Stack");
run("Grays");
run("Gaussian Blur 3D...", "x=1 y=1 z=1");
setThreshold(Chan1Thr, 255);
run("Analyze Particles...", "size="+d2s(Chan1MinArea,0)+"-Infinity show=
```

```
Masks in_situ stack");
run("Maximum...", "radius="+d2s(Chan1Dil,0)+" stack");
rename("Mask");
selectImage("C3-Stack");
close();
run("Clear Results");
selectImage("Mask");
xValues = newArray(nSlices);
yValues = newArray(nSlices);
aValues = newArray(nSlices);
for(i=1;i<=nSlices;i++)
{
setSlice(i);
xValues[i-1] = i;
run("Create Selection");
if(selectionType>-1)
{
run("Measure");
run("Add to Manager");
yValues[i-1] = getResult("Mean",i-1);
aValues[i-1] = getResult("Area",i-1);
}
else
{
run("Select All");
run("Measure");
run("Add to Manager");
yValues[i-1] = 0;
aValues[i-1] = 0;
}
}
selectImage("C2-Stack");
close();

// Display overlay on original image
selectImage(OrigID);
Stack.getDimensions(width, height, channels, slices, frames);
```

```
Stack.setSlice(round(slices/2));
for(i=1;i<3;i++)
{
Stack.setChannel(i);
run("Enhance Contrast", "saturated=0.35");
}
Stack.setChannel(1);
roiManager("Show All without labels");
run("Select None");

// Plot profiles
Plot.create
("Section area Z profile", "Slice", "Section area", xValues, aValues);
Plot.show();
Plot.create
("Intensity Z profile", "Slice", "Mean intensity", xValues, yValues);
Plot.show();
selectImage("Mask");
close();
```

Appendix D

Journal Articles

- 3D villus-like PEGDA-based hydrogels with spatio-chemical gradients to modulate intestinal epithelial stem cell behavior.
  G. Altay, E. Gualda, V. Fernández-Majada, S. Tosi, M. Garcia-Diaz, N. Torres, J. Folch, C. Insa, A. G. Castano, P. Loza, E. Batlle, E. Martínez.
  Manuscript under preparation.

- Self-organized intestinal epithelial monolayers in crypt-villus-like domains show effective barrier function.
  G. Altay, V. Fernández-Majada, E. Larrañaga, S. Tosi, F. Barriga, E. Batlle, E. Martínez.
  Manuscript to be submitted.

- Dynamic Photopolymerization Produces Complex Microstructures on Soft Hydrogels in a Moldless approach to Generate a 3D Intestinal Tissue Model.
  A. G. Castaño, M. García-Díaz, G. Altay, N. Torras, and E. Martínez.
  Biofabrication. Manuscript under review (no:BF-101695).

- Design and development of a microarray processing station (MPS) for automated miniaturized immunoassays.
  M. Pla-Roca*, G. Altay*, X. Giralt, A. Casals, and J. Samitier.
  *Shared first authorship
  Biomed Microdevices (2016) 18: 64. doi:10.1007/s10544-016-0087-6

Self-organized intestinal epithelial monolayers in crypt and villus-like domains show effective barrier function

Gizem Altay[1], Enara Larrañaga Carricajo[1], Sébastien Tosi[2], Francisco Barriga[3], Eduard Batlle[3], Vanesa Fernández-Majada[1], Elena Martinez[1,4,5*]

[1] *Biomimetic Systems for Cell Engineering Laboratory, Institute for Bioengineering of Catalonia (IBEC), The Barcelona Institute of Science and Technology (BIST), Baldiri Reixac 10-12, 08028 Barcelona Spain*

[2] *Advanced Digital Microscopy Unit, Institute for Research in Biomedicine (IRB), Baldiri Reixac 10-12, Barcelona 08028, Spain*

[3] *Colorectal Cancer Laboratory, Institute for Research in Biomedicine (IRB), Baldiri Reixac 10-12, Barcelona 08028, Spain*

[4] *Centro de Investigación Biomédica en Red (CIBER), Av. Monforte de Lemos 3-5, Pabellón 11, Planta 0, 28029 Madrid, Spain*

[5] *Department of Electronics and Biomedical Engineering, University of Barcelona (UB), Martí i Franquès 1, Barcelona 08028, Spain*

*Corresponding author contact information:

Biomimetic Systems for Cell Engineering Laboratory, Institute for Bioengineering of Catalonia (IBEC), Baldiri Reixac, 15-21, Barcelona 08028, Spain

E-mail address: emartinez@ibecbarcelona.eu

Tel: +34 934 037 177

Fax: +34 934 034 750

Abstract

Intestinal organoids technology has emerged as a powerful *in vitro* tool for studying intestinal biology. Organoids resemble many aspects of the intestine *in vivo,* including the presence of all intestinal cell types distributed along crypt-villus structures, essential cell-cell interactions and functions such as absorption and secretion. However, the sphere-like geometry of organoids prevents access to the apical side of the epithelium, making them unsuitable for standard functionality assays typically designed for cells grown as 2D monolayers. Here, we describe a simple method that permits the growth of mouse small intestinal organoids as monolayers that maintain the *in vivo* like cell-type composition and distribution and at the same time are suitable for functional tissue barrier assays. In our approach, organoid expansion on monolayers is driven by the mechanical properties of the substrate, while epithelial tissue barrier formation is promoted by the close-to-physiology basolateral delivery of stem cell niche factors. Through that combination, we obtained intestinal epithelial monolayers on Transwell® inserts. Such monolayers contain major intestinal epithelial cell types organized into proliferating crypt-like domains and differentiated villus-like regions, closely resembling the *in vivo* cell distribution. As a unique characteristic, organoid-derived monolayers form functional epithelial barriers with accessible apical surface and physiologically relevant transepithelial electrical resistance values. We believe that our technology offers an up-to-date non-existing culture method for intestinal epithelium, providing an *in vivo*-like cell structured model in a tissue culture format compatible with high-throughput drug absorption or microbe-epithelium interaction studies, where independent access to the luminal and basolateral compartment is needed.

Introduction

The surface of the small intestine is lined by a monolayer of tightly packed polarized epithelial cells organized into invaginations called crypts, and finger-like protrusions called villi (1,2). The intestinal epithelium is a rapidly renewing tissue sustained by the highly proliferative $Lgr5^+$ intestinal stem cells (ISCs) that reside at the crypt bases (3,4). ISCs undergo self-renewal and generate transit amplifying cells, which migrate up the long crypt-villus axis and gradually differentiate into absorptive enterocytes, mucus secreting goblet cells, hormone secreting enteroendocrine cells, and Wingless/Int (Wnt) secreting Paneth cells. After reaching the tips of villi, cells undergo apoptosis and are extruded into the lumen, being replaced by a new cell generation that ensures the intestinal homeostasis (1,2,4).

In vitro research on intestinal epithelium, including understanding its basic biology, investigating intestinal disorders and searching for new treatment options, has been traditionally hampered by the lack of appropriated cell culture systems. On the one hand, conventional intestinal models rely on 2D cultures of transformed cell lines, among which the Caco-2 cell line is vastly employed (5,6). However, those cell-line based models have several shortcomings based on their limited resemblance to the normal epithelium. This translates into significant non-physiological values of the parameters characterizing their functional properties when compared to the *in vivo* tissue: underestimated paracellular absorption, abnormally high transepithelial electrical resistance (TEER) and altered expression of metabolizing enzymes (7,8). On the other hand, cultures of primary intestinal epithelial tissues, although physiologically relevant, are hardly used *in vitro* due to the fast decrease of stem and proliferative cell populations, and the rapid onset of epithelial cell death when placed into culture (9,10).

In the last few years, though, technological advances in epithelial cell culture methods have permitted the long-term culture of primary intestinal epithelial cells (IECs), including ISCs with self-renewal and differentiation capacities. Sato *et al.* and Ootani *et al.* demonstrated that crypt cells isolated from mouse small intestines, which include $Lgr5^+$ ISCs, organize into three-dimensional (3D) intestine-like structures, termed intestinal organoids, when embedded in Matrigel® and cultured with biochemical factors mimicking the *in vivo* ISC niche environment (epidermal growth factor (EGF), Noggin and R-spondin) (11,12). Small intestinal organoids are spherical structures with numerous budding formations. Each of these buddings recapitulates the crypt intestinal structure, as it is composed of dividing cells with $Lgr5^+$ ISC and Paneth cells located at their crests. In between these buddings, the internal part of the spheres mimics the villus intestinal structures, composed of absorptive and secretory cells. The center of the organoids corresponds to the intestinal lumen, where differentiated cells are spelt upon death. Intestinal organoids can be cultured for several months without losing these characteristics and maintaining protein expression profiles highly similar to freshly isolated crypts (11,12). Specific modifications of the culture medium composition has also allowed for the long-term culture of intestinal organoids derived from other regions of the mouse intestinal tract (13) and from other species including humans (14,15). Undoubtedly, organoid culture technology has been a breakthrough in the field of *in vitro* cell culture, leading to significant improvements in the study of the intestinal epithelium. Nowadays, organoid technique has become the gold standard *in vitro* culture method in

both basic and translational intestinal biology studies (16,17), modelling of patient-specific epithelial diseases (18), as well as a source of tissue for autologous transplantation (19).

A major drawback of the intestinal organoid technology is that their 3D closed geometry impedes direct access to the apical region of the epithelium, making them unsuitable for some physiologically relevant studies. It is the apical epithelium that directly contacts the diet content, external antigens and microbial components present in the luminal region. Therefore, the non-accessibility to organoid-analog lumen limits organoid routinely use in studies of nutrient transportation, drug absorption and delivery, and microbe-epithelium interactions. To overcome this limitation, technically challenging methods such as organoid-microinjection are required (20). Alternatively, finding ways to open-up the spherical organoids into 2D epithelial monolayers appears as a suitable strategy to solve the problem of lumen inaccessibility and allow for epithelial functional studies. Lately, some efforts have been done in this direction. By culturing freshly isolated mouse intestinal crypts on substrates with the optimal mechanical properties, self-renewing 2D epithelial monolayers have been reported (21). These monolayers contained both proliferative and secretory lineage cell types. However, the proliferative cells were found evenly distributed at the epithelial borders, and the secretory Goblet cells were clustered at the center of the monolayer, in a cell-type distribution different of that found *in vivo* (21). Recently, intestinal epithelial monolayers with an improved, physiologically relevant cell distribution have been generated from mouse crypts. These contained proliferative foci and differentiated zones resembling cell organization found *in vivo* (22). Despite these benefits, the reported monolayers, grown onto Matrigel-coated well plates, neither completely covered the substrate nor allowed the access to cell basolateral side, thus preventing their use in functional tissue barrier assays (22). Such assays are usually performed in Transwell® systems, which provide apical and basolateral compartments separated by cell monolayers grown on porous membranes. Studies carried out with dissociated mouse and human organoids have demonstrated that epithelial monolayers can actually be also formed on Transwell® inserts (23–25). However, even though these monolayers were composed of differentiated polarized cells, formed tightly packed epithelia and expressed proper tight junction proteins, they show aberrantly high TEER values (from 400 up to 3000 $\Omega.cm^2$) compared to the native intestine (40 – 100 $\Omega.cm^2$) (26–28). Such non-physiological values of the monolayer tight junction integrity might be due to the loss of the stem and proliferative cells as Wnt pathway inhibitors were used at the later time points of these cultures (23,25). Indeed, in these studies no self-renewal capacities of the monolayers were reported. Therefore, although progress has been achieved in establishing primary intestinal epithelial monolayers, an optimal culture method that closely reproduces the *in vivo* intestinal cell composition and distribution while allowing for routine functional tissue barrier assays has not yet been defined. Altogether, these models are not representative of *in vivo* like cellular organization and transepithelial transport.

Here, we describe an experimental protocol that employs mouse-derived small intestinal organoids to obtain intestinal epithelial monolayers that self-organized in crypt and villus-like regions and show effective barrier function. Organoids are grown on substrates coated by thin films of Matrigel®, which provide the proper mechanical properties to induce the formation of epithelial 2D monolayers. Live-imaging experiments of green

fluorescent protein (GFP) cells obtained from *Lgr5-EGFP-ires-Cre ERT2* mice intestines (3) allowed the tracking of intestinal stem cells and demonstrated that organoid-derived cells first organize into stem cell-containing crypt-like domains. From these domains, cells migrate out to form non-proliferating and differentiated monolayers, resembling the villus-like regions. The formation of epithelial monolayers that fully cover the substrate is promoted by incorporating to the cell culture medium exogenous stem cell niche biochemical factors such as Wnt3a, and the ones produced by the intestinal subepithelial myofibroblast cell, which help maintaining the stem cell population within the crypt bases. Upon the basolateral delivery of these stem cell niche factors, epithelial monolayers are obtained on Transwell® inserts. Through this strategy, we found that organoid-derived intestinal epithelial monolayers show physiologically relevant TEER values, indicating a good maturation of the epithelial barrier. We believe that the technology we propose offers an original non-existing tool to obtain organoid-derived intestinal epithelial monolayers with *in vivo*-like structural and functional characteristics simultaneously. As such, our experimental set-up can fill in the existing gap between complex 3D organotypic cell culture systems and 2D formats needed for high-throughput testing.

Materials and methods

Mice model

Lgr5-EGFP-IRES-creERT2 mice have been previously described (3). Briefly, *Lgr5-EGFP-IRES-creERT2* mice were generated by homologous recombination in embryonic stem cells targeting the *EGFP-IRES-creERT2* cassette to the ATG codon of the stem cell marker *Lgr5* locus, allowing the visualization of $Lgr5^+$ stem cells with a green fluorescent protein (GFP).

Intestinal crypt isolation and culture

Intestinal crypts from *Lgr5-EGFP-IRES-creERT2* mice were isolated as previously described (29,30). Briefly, mice were sacrificed by cervical dislocation. Small intestines were dissected, flushed with PBS and cut longitudinally. Then, villi were mechanically removed. Intestinal crypts were isolated by incubating the tissue with PBS containing 2 mM EDTA (Sigma) for 30 minutes at 4ºC. The digestion content was filtered through a 70 µm pore cell strainer (Biologix Research Co.) to obtain the crypt fraction. Crypts were resuspended and plated in Matrigel® (BD Bioscience) drops and supplemented with basic organoid growth medium consisting of advance DMEM/F12 (Invitrogen) plus 1% Glutamax (Gibco), 1% HEPES (Sigma), Normocin (1:500, Invitrogen), 2% B27 (Gibco), 1% N2 (Gibco), 1,25 mM N-acetylcysteine (Sigma), supplemented with recombinant murine EGF (100 ng ml^{-1}, Gibco), recombinant human R-spondin 1 (200 ng ml^{-1}, R&D Biosystems), and recombinant murine Noggin (100 ng ml^{-1}, Peprotech) to obtain ENR-medium. The medium was changed every 2 to 3 days. The first 4 days of culture the Rho kinase inhibitor Y-27632 (Sigma) was added to avoid anoikis. Outgrowing crypts were passaged once a week. Organoid stocks were maintained in ENR-medium up to 3 to 4 months. After that time, fresh small intestinal crypts were isolated again from *Lgr5-EGFP-IRES-creERT2* mice.

Intestinal subepithelial myofibroblast isolation and culture

Intestinal subepithelial myofibroblasts (ISEMFs) were isolated from mouse colon using a modified version of a reported previously protocol (31). Briefly, left over tissue from the above explained crypt isolation procedure was further digested by incubation at 37°C for 60 min at 200 rpm with 2000 U of collagenase (Sigma). The digested tissue was pelleted and lysed at 47ºC for 5 minutes using ACK lysis buffer (Gibco). The pellet, containing lamina propria cells, was resuspended in Dulbecco's modified medium (DMEM) (Life Technologies) containing 10% fetal bovine serum (FBS) (Gibco), 1% Penicillin/streptomycin (Sigma), and 1% minimum essential medium non-essential amino acids (MEM-NEAA) (Gibco) and cultured in tissue culture plates (25 mm^2). After one week in culture only lamina propria fibroblasts, mainly myofibroblast, remained attached. Plates reached confluence after approximately 20 days in culture. Cell division of primary myofibroblast is limited, after 6-8 passages cells become senescent. Detection by immunofluorescence of α-smooth muscle actin (α-SMA) and vimentin expression as well as reduced desmin expression was used to determine the purity of the myofibroblast cultures. For harvesting the intestinal subepithelial myofibroblast condition medium (ISEMF_CM), plates at 60-80% of confluence were maintained in culture with the before mentioned medium for 6 days. Medium was harvested, centrifuged and filtered using a 22 µm pore strainer, and frozen until use. Medium harvested along several days from the same myofibroblast isolation was pooled to use the same medium in all experiments. ISEMF-CM was complemented with 1% Glutamax, 1% HEPES, Normocin (1:500), 2% B27, 1% N2, 1,25 mM N-acetylcysteine, EGF (100 ng ml^{-1}), human R-spondin 1 (200 ng ml^{-1}), Noggin (100 ng ml^{-1}), CHIR99021 (3 µM), and valproic acid (1mM) before use for organoids cultures.

Preparation and characterization of Matrigel©-coated substrates

Ibidi µ-Slides (ibidi GmbH) or Transwell® inserts (6,5 mm diameter, 0,4 µm pore size, Corning) were coated with Matrigel® to form thick (~ 2 mm in thickness) and thin (< 20 µm in thickness) films. Thick layers were formed by pipetting either 200 µL (on ibidi µ-Slides) or 80 µL (on porous membranes of Transwell® inserts). Thin films of Matrigel® were produced by pipetting 10 µL of Matrigel® solution and spreading it throughout the surface, followed by an incubation at 37°C for 1 hour for Matrigel® gelling. Matrigel® thin films were visualized by immunofluorescence using laminin antibodies, being laminin one of the major components of Matrigel® (32). To do that, after the coating process, the Matrigel® layer was fixed using 10% neutralized formalin (Sigma) for 30 min, blocked using a blocking buffer containing 1% BSA (Sigma), 3% donkey serum (Millipore), and 0,2% Triton X-100 in PBS for two hours, and incubated with the anti-laminin antibodies (abcam) diluted (1:500) overnight at 4°C, and with the secondary antibody Alexa Fluor® 488 (Invitrogen) diluted at 1:500 for 2 h. The images of the Matrigel® layers were acquired by a Leica SP5 confocal laser scanning microscope (CLSM) equipped with a 20x dry objective (NA = 0,7) and the thicknesses were estimated from the stacks using ImageJ software. The detailed explanation of the method used for the estimation of the thicknesses is given in the Supplementary Information.

Generation of organoid-derived intestinal epithelial monolayers

After coating the substrates with Matrigel®, digested crypts or single cells suspended in culture medium were added to each well. Before this step, organoid cultures were enriched for stem cells during 4-5 passages by supplementing the ENR-medium with CHIR99021 (3 µM) and valproic acid (1 mM) to obtain ENR_CV-medium (33). To obtain a preparation of crypt pieces with homogeneous size, full-grown organoids were subjected to a mild digestion protocol. Briefly, Matrigel® drops containing organoids were disrupted by pipetting using TrypLE Express1X (Gibco) and transferred to a Falcon tube at 4ºC, where mechanical disruption, using a syringe with a 23 G 1" needle (BD Microlance 3), was applied. Crypt pieces were seeded at a cell density of 1000 - 1500 crypts cm^{-2}, using an initial volume of 30-50 µl. We let crypt pieces to attach to the substrates for 3-4 hours and add more medium. To obtain organoid derived single cells, we applied a harsher digestion protocol. Matrigel® drops containing organoids were disrupted by pipetting using TrypLE Express 1X, transferred to a Falcon tube and incubated for approximately 5 minutes at 37ºC. After the digestion single cells o small clusters of cells were obtained. Cells were seeded at a cell density of 100.000 cell cm^{-2}, using an initial volume of 10-20 µl. We let cells attach to the substrate for 3-4 hours and then added more medium. Crypt- or single cells-derived epithelial monolayers were cultured up to varying time points ranging from 5 days to 4 weeks depending on the experiment. Culture times and culture medium composition are indicated for each experiment in the corresponding figure legends. For culture passaging experiments, epithelial monolayers were enzymatically digested every 6 to 8 days in culture. Epithelial monolayers were mechanically disrupted using a pipetted and digested by incubating them approximately 5 minutes at 37ºC with TrypLE Express 1X. Cells obtained from the digestion were reseeded on new Matrigel®-coated ibidi µ-slides. Following this protocol, we passaged the cultures up to 4 times, maintaining the cells in culture for more than one month. Further passages were not tested.

Immunostaining

Cells were fixed with 10% neutralized formalin (Sigma), permeabilized with 0,5% Triton X-100 (Sigma) and blocked with a blocking buffer containing 1% BSA (Sigma), 3% donkey serum (Millipore), and 0,2% Triton X-100 in PBS for at least two hours. Primary antibodies used were: anti-GFP (1:100, Life Technologies), anti-GFP (1:100, abcam), anti-Ki67 (1:100, abcam), anti-Ki67 (1:100, BD Biosciences), anti-lysozyme (1:100, Dako), anti- zonula occludens (ZO-1) (1:100, abcam), anti-cytokeratin 20 (1:100, Dako), anti-Cleaved Caspase-3 (1:200, Cell Signaling Technology), anti-EphB2 (1:200, R & D Systems). All samples were incubated with the primary antibody overnight at 4°C followed by 1 h incubation at RT with secondary antibodies, Alexa Fluor® 568 and Alexa Fluor® 488 donkey anti-goat, Alexa Fluor® 647 (Jackson ImmunoResearch) diluted at 1:500. Nuclei were stained with 4',6-diamidino-2-phenylindole (DAPI) (1:1000). Alexa Fluor® 568 phalloidin was used to stain filamentous actin (F-actin). For detection of mucus periodic acid-Schiff (PAS) (Sigma) was used. For the characterization of ISEMFs, antibodies against α-SMA (1:100, Sigma), and desmin (1:100, abcam), and anti-vimentin (1:100, Developmental Studies Hybridoma Bank) were used. All the antibodies before mentioned were obtained from Invitrogen unless stated otherwise. The fluorescence images were acquired using either a confocal laser scanning microscopy (TCS SP5,

Leica) or an epifluorescence microscope (Axio Observer 7, Zeiss). The bright field images were obtained by an inverted microscope (Eclipse Ts2, Nikon).

EdU pulse-chase experiment for evaluating the monolayer formation

5-ethynyl-2'-deoxyuridine (EdU) staining was performed following the manufacturer's protocol (Click-iT® Plus EdU imaging kit, Invitrogen). Briefly, crypts were cultured on ibidi µ-Slides coated with Matrigel®, as previously explained. After overnight in culture, cells were incubated with EdU (10 µM) for 2,5 h, washed with PBS and cultured with ENR_CV-medium. Samples were fixed with 3,7% formaldehyde (Electron Microscopy Sciences) immediately or 1 days after the EdU pulse. After fixation, samples were permeabilized with 0,5% Triton X-100 in PBS for 20 min and EdU was detected using Click-iT Plus EdU Alexa Fluor 488 imaging kit. Subsequently, the samples were washed with 3% BSA in PBS and incubated with primary antibodies anti-Ki67 (1:100) and anti-ZO-1 (1:200) overnight at 4°C, followed by incubation with the secondary antibodies, Alexa Fluor® 647 and Alexa Fluor® 568, for 1 h at RT. Nuclei were stained with Hoechst 33342 (10 µg mL^{-1}, Click-iT, Invitrogen) for 30 min at RT.

Image acquisition and analysis

The fluorescence images were acquired using either confocal laser scanning microscopy (TCS SP5, Leica) with 10x dry (N.A. = 0,40), 20x dry (N.A. = 0,70) and 40x oil (N.A. = 1,25) objectives at randomly selected locations. The laser excitation and emission light spectral collection were optimized for each fluorophore. For the four-color scans the emission bands were adjusted to avoid overlapping of the channels. The pinhole diameter was set to 1 Airy Unit (AU). For images acquired at 10x and 20x, a z-step of 1 µm, and for images acquired at 40x a z-step of 0,5 µm were used. The side view images of the monolayer were obtained from the orthogonal views of the confocal microscopy stacks acquired at 40x. The cell heights were measured from the orthogonal views of the stacks at 40x magnification at 10 randomly selected locations for each sample (n = 3). The quantification of the intestinal epithelial cell markers GFP (for stem cells), Ki67 (for proliferative cells), and cytokeratin 20 (CK20) (for terminally differentiated enterocytes and goblet cells), with respect to the total cell number was estimated by a custom-made ImageJ macro. The sequence of operations performed in the macro is as follows. 1) Compute maximum intensity in Z-projections (all channels). 2) Apply Laplacian of Gaussian filter to DAPI channel image. 3) Detect salient regional intensity minima in filtered DAPI image. 4) For each fluorophore, measure mean intensity in corresponding channel inside disks centered on detected minima; for disks with mean intensity above user defined threshold, count nucleus as positive for this fluorophore. All filtered radii were adjusted according to estimated nuclei size at the imaging magnification. Nuclei detection sensitivity (noise tolerance) was adjusted empirically to lead to most accurate detection. All thresholds were adjusted to local intensity estimates performed inside user selected regions (actin channel, inside tissue; weakest positive cell in label channels). The accuracy of the results was validated from summary images displaying colored markers at negative/positive nuclei positions overlaid over the projected image stacks.

For each sample, at least five randomly selected locations on the same monolayer were quantified using ImageJ software.

Time-lapse microscopy

Digested intestinal epithelial crypts and single cells were seeded on ibidi µ-Slides coated with Matrigel®, as previously explained. Formation of the epithelial monolayer was monitored by time-lapse microscopy experiments, conducted at 10x magnification with Axio Observer 7 epifluorescence inverted microscope (Zeiss) with temperature (37°C), humidity and CO_2 (5%) regulation. Phase contrast and EGFP channels were used and images were acquired every 5 minutes up to 96 hours of culture. The time-lapse videos and fluorescence images were processed with ImageJ software.

Transepithelial electrical resistance (TEER) measurements

To measure TEER values of the epithelial monolayers, Transwell® inserts (6,5 mm diameter, 0,4 µm pore size) were coated with thin layers of Matrigel® as explained above and seeded with crypts. In these experiments, 30-50 µl of crypt suspension leading to crypt seeding densities of 3000 - 3500 crypts cm^{-2} was used. ISEMF_CM supplemented with ENR_CV and Wnt3A (25 ng mL^{-1}) was added to the Transwell® compartment corresponding to the cell basolateral side, while basic organoid growth ENR-medium was added to the apical side. TEER was measured with an EVOM2 epithelial voltohmmeter with STX3 electrodes (World Precision Instruments) introduced at the apical and basolateral compartments of the inserts. The electrical resistance corresponding to cell epithelial monolayers was obtained by subtracting the intrinsic resistance (values measured on Transwells® with only the porous membranes and the Matrigel®-coated porous membranes) from the total resistance measured (this time including the cells) and corrected for surface area (0,33 cm^2) to be expressed as ohm cm^2.

Statistical analysis

The data were presented in the figures as mean ± standard deviation. The error bars represent the standard deviations of at least two independent experiments with three technical replicas. Statistical comparisons were performed using 2 sample Student's t-test. The data were processed and plotted with OriginPro 8.5 software.

Results

Mouse intestinal organoid-derived cells form epithelial monolayers with *in vivo*-like cell type composition and distribution on Matrigel®-coated hard substrates

Intestinal stem cells (ISCs) maintain their self-renewing and differentiation capacities to form 3D organoids with multicellular organization when embedded in Matrigel® drops and cultured with a medium containing specific growth factors (11). It has been recently shown that 3D organoids can form 2D epithelial monolayers when cultured on hard substrates coated with a thin layer of extracellular-matrix (ECM) proteins (22,24,25). These works acknowledged both matrix composition and substrate mechanical properties as key factors conditioning ISCs growth. We decided to employ Matrigel® as extracellular matrix substitute given its molecular composition, very similar to the intestinal epithelium basement membrane, and its suitability for ISCs growth (11,15,34). It has been shown that ISC expansion is favored within stiffer matrices (1,3 kPa) than on very soft matrices (300 Pa) (35). We then wondered whether the hard substrates needed for the formation of organoid-derived intestinal epithelial monolayers would provide an environment that does not hamper ISC proliferative and differentiation capacities and permits ISC self-organization as *in vivo*. To answer this question, we cultured intestinal organoid-derived crypts or single cells on hard tissue well plates coated with thin films of Matrigel®. Thin films were obtained by evenly spreading 10 µL of Matrigel® per cm^2 of substrate. For their characterization, we performed immunostainings against laminin, the Matrigel® major component. Confocal laser scanning microscopy analysis demonstrated a uniform coating (Supplementary Information Fig. S1) with an estimated thickness of 2,9 ± 0,1 µm (quantification details described in the Supplementary Information). The same substrates coated with thick Matrigel® layers were also prepared, which allowed to make comparisons with the thin films and unequivocally reveal the role of the mechanical properties of the substrate. Thick Matrigel® layers (~ 2 mm in thickness) were obtained by depositing 200 µL of Matrigel® per cm^2 of surface. It is reported that when gel thickness is less than 20 µm, the apparent stiffness of the material is reaching that of the underlying substrate (36). Since in our experimental setup the thin film thickness is below that value, the apparent stiffness for the cells seeded on Matrigel® thin films is that of the underlying tissue culture plate hard polymer bottom, presumably polystyrene (Young's modulus of ≈ 3 GPa) (37), and it will be referred as "hard substrate" in what follows. Whereas, on thick Matrigel® layers, the apparent stiffness for cells will be closer to that of the Matrigel® (Storage modulus ≈ 50 Pa) (38) and it will be referred as "soft substrate".

Intestinal organoids were digested using a mild or harsh digestion protocol to obtain either intestinal crypt pieces or intestinal single cells respectively. Both cells fractions were seeded on top of either "hard" or "soft" Matrigel®-coated substrates (Fig. 1A) and the cell growth behavior was analyzed in each case. Actin staining showed that after 5 days of culture both organoid-derived crypt pieces and intestinal single cells attached to the "hard" substrates and spread over it forming an epithelial monolayer (Fig. 1B). In contrast, organoid-derived crypt pieces and intestinal single cells on "soft" substrates failed to grow as spreading 2D epithelial layer and, instead, formed 3D organoids on the Matrigel® thick layers (Fig. 1B), very much resembling organoids growing within Matrigel® 3D matrices. These results indicate that it is the substrate stiffness, which dictates primary intestinal cell growth phenotype. In addition, we found that intestinal epithelial monolayers grown on hard Matrigel®-coated substrates contained proliferative (Ki67

positive) and non-proliferative cells distributed in a clear spatial segregated fashion. Samples were covered by foci of packed proliferating cells separated by non-proliferating areas in line with recently published results (Fig. 1B) (22).Therefore, hard Matrigel®-coated substrates provide a suitable environment that favors both ISC division and epithelial monolayer formation.

In order to characterize more precisely the cell composition of the different areas found on the epithelial monolayers, we checked for the expression of intestinal cell-type markers. We found that regardless the seeding units employed (crypts or single cells), the proliferative areas of the epithelial monolayers were formed by a pool of double positive cells for GFP and Ki67, which corresponds to actively dividing $Lgr5^+$ stem cells (Fig. 1C, left panel). We could also identify a population of $Ki67^+$, GFP^- cells, indicating that, in addition to $Lgr5^+$ stem cells, those cell-proliferative pools are composed of transit-amplifying proliferative cells (Fig. 1C, left panel). Furthermore, GFP^+ and $Lysozyme^+$ cells are in close proximity positioned at the crypt-like domains (Fig. 1C, middle panel), indicating that in our epithelial monolayers, Paneth cells form part of the stem cell niche, like in *in vivo* intestine (39). Cell composition and distribution of those proliferative areas very much resembles the in vivo intestinal crypts and therefore were referred to us as a crypt-like domains. On the one hand, expression of Cytokeratin 20 (CK20), a marker of mature enterocytes and goblet cells, was found in the non-proliferative areas of the monolayers, especially in cells close to the epithelial layer border (Fig. 1C, right panel). Periodic acid-Schiff (PAS) staining showed also the presence of mucus secreting Goblet cells scattered throughout the non-proliferative monolayer (Fig. 1D). On the other hand, accumulation of the tight junction protein ZO-1 at the apical inter-cellular membrane, (Fig.1E), and of the F-actin at the cell apical side (Fig. 1E) demonstrated the correct apical-basal cell polarization. All these are features corresponding to mature differentiated cells indicting that the non-proliferative areas of the epithelial monolayers correspond to villus-like regions. In addition, immunofluorescence against cleave caspase-3 (CC-3) showed that cells underwent apoptosis at the epithelial borders of the monolayer (Fig. S2A). Time-lapse microscopy experiments also supported this finding, as illustrated by a representative time lapse-image sequence where a cell undergoes cell death and sheds off near of the epithelial border (Fig. S2B and Supplementary Movie 1), resembling the physiological extrusion of apoptotic cells at the villus tips (40). Overall, the histological characterization of the epithelial monolayers demonstrated that hard Matrigel®-coated substrates promoted the formation of a 2D intestinal epithelium model composed of crypt-like domains containing $Lgr5^+$ stem, Paneth and proliferative transit-amplifying cells, and villus-like regions containing differentiated epithelial cells with the typical apical-basal polarization, resembling the cellular crypt-villus organization of the *in vivo* intestinal epithelium.

Cell division in the crypt-like domains fuels the formation of self-renewal organoid-derived intestinal epithelial monolayers

To investigate epithelial monolayer formation on Matrigel®-coated hard substrates, we employed cells derived from *Lgr5-EGFP-ires-CreERT2* intestinal organoids (3). These organoids express GFP under the control of the stem cell marker Lgr5, which allows for the ISC tracking. Time-lapse microscopy experiments showed that organoid-derived

crypt pieces, rapidly refolded on themselves to form crypt-like domains containing Lgr5^{+} ISCs, resembling the in *vivo* crypt base stem cell disposition (Fig. 2A, upper row, and Supplementary Movie 2). After the crypt-like domains were formed, intestinal epithelial cells spread on the substrate and migrated out of crypt-like domain, forming monolayers composed of GFP^{-} cells corresponding to villus-like regions (Fig. 2A, lower row, and Supplementary Movie 2). We then investigated whether the capacity of the intestinal epithelial cells to first self-organize into crypt-like domains and then originate villus-like regions is regulated intrinsically and is not due to the preservation of pre-established cell-type configuration. To do this, instead of seeding organoid-derived crypts we further digested the organoids to obtain intestinal single cells. Similar to the previous results, when organoids-derived single cells were seeded on Matrigel®-coated hard substrates they spontaneously self-assembled to form crypt-like domains containing Lgr5^{+} ISCs, similar to the *in vivo* crypt base stem cell arrangement in structures that very closely mimic the in vivo crypt morphology (Fig. 2B, insets). Also, in this case after crypt-like regions were formed, intestinal epithelial cells started to spread out generating an epithelial monolayer composed of GFP^{-} cells, resembling the intestinal villus (Fig. 2B). These results revealed the intrinsic capacity of ISCs to self-assemble and form *in vivo*-like domains when grown on 2D hard substrates. To further characterize the growth of such monolayers we then performed EdU pulse-chase experiments. Organoid-derived pieces cells were left to attach on Matrigel®-coated hard substrates overnight; then cells where pulsed with EdU (0 hours chase), which was incorporated into dividing cells and passed to their progeny. EdU positive cells were followed by a chase period of 1 day. Immunofluorescence analysis of both EdU and Ki67 showed that, right after the pulse, the forming crypt-like domains were mainly composed of proliferating cells (Ki67^{+}) (Fig. 2C, upper panel). After one day of chasing, those dividing cells had generated a non-dividing epithelial monolayer (Ki67^{-}, EdU positive). These non-proliferative cells express markers of epithelial maturation, such as the accumulation of the tight junction protein zonula occludens 1 (ZO-1) at the cell membranes (Fig. 2C, lower panel). Overall, both the time-lapse microscopy and EdU pulse-chase experiments demonstrated that by Matrigel®-coated hard substrates, organoid-derived intestinal cells self-organized first into proliferative, ISC-containing crypt-like domains, able to divide and generate a progeny. Later, this progeny migrates, differentiates, matures and dies, closely following the intestinal epithelial homeostasis that is described *in vivo*.

Furthermore, we demonstrated that the intestinal epithelial monolayer generated on Matrigel®-coated hard substrates possess self-renewing capacities. After approximately one week in culture (6 to 8 days), epithelial monolayers were enzymatically digested to single cells and cultured on freshly Matrigel®-coated hard substrates. These cells were able to regenerate epithelial monolayers maintaining the spatial cell segregation of proliferating foci and non-proliferating regions found in the original monolayer, at least up to four passages (Fig. 2D). The surface coverage by the epithelial monolayer was comparable throughout the passages, indicating the preservation of the stem cell capacities (data not shown). This indicated that epithelial monolayers generated on Matrigel®-coated hard substrates could be passaged and maintained in culture for an extended period without losing their regenerative and self-organizing capacities.

Epithelial monolayers maintain *in vivo*-like cell type composition and distribution on Matrigel®-coated Transwell® insert membranes

Although intestinal organoids are defined as functional mini-organs, in practice functional assays evaluating their intestinal barrier function are very limited. Currently, permeability and absorption assays using intestinal organoids are performed by delivering the tested compound through the epithelium basolateral side (41). In order to mimic physiological apical delivery, sophisticated techniques, such as intra-organoids microinjection, are needed (42). 2D monolayers of intestinal epithelium that maintain cell population and *in vivo*-like distribution found in organoids while making feasible tissue barrier functional assays are an elegant way to exploit organoid benefits and overcome their steric limitations. Epithelial functional assays are usually based in the standard Transwell® insert system, which separates the apical and basolateral compartments of the culture through a monolayer of cells cultured on a porous membrane. If a matured epithelial monolayer fully covers the membrane, a tissue barrier is formed. However, while the monolayer is not entirely covering the substrate and does not form an effective barrier, cells will be receiving biochemical inputs from both the apical and the basolateral sides, this situation very much resembles the experimental conditions provided by the 3D environment. Therefore, with this in mind, we tested if the mechanical signal provided by the hard-porous membrane (polycarbonate polymer, Young's modulus of ≈ 4 GPa) (43) was successful at generating monolayers in Transwell® inserts. In figure 3A we depict the adaptation of the experimental setup to an appropriated culture format for epithelial functional assessment. For this purpose, Lgr5^{+}-GFP Ires-CreERT2 organoid-digested crypts were seeded on Matrigel®-coated porous membranes of Transwell® inserts. Initially, to mimic the gradients of stem cell niche biochemical factors found *in vivo* (44), the basolateral compartment was filled with ENR_CV-medium and the apical compartment with basic organoid medium (non-supplemented with ENR-CV factors) (Fig. 3A). Under these culture conditions, we obtained intestinal epithelial monolayers that maintain the spatial cell-type segregation found on Matrigel®-coated hard substrates. The epithelial monolayers grown on Transwell® inserts showed proliferative crypt-like domains of Ki67^{+} cells (Fig. 3B), which contained Lgr5^{+} GFP^{+} stem cells (Fig. 3C), and a spreading monolayer of non-proliferative Ki67^{-} cells corresponding to the villus-like regions (Fig. 3B-C). To further prove the crypt-villus-like cell self-organization of these cultures, we checked for the expression of ephrin type-B receptor 2 (EPHB2). EPHB2 receptor is highly expressed in ISCs and becomes gradually silenced as the cells differentiate (45). We found high expression of EPHB2 restricted to specific cell clusters distributed throughout the epithelial monolayer (Fig. 3D), similarly to the Ki67 expression (Fig. 3B), defining the crypt-like domains. EPHB2 expression was gradually fading from the center of these domains (Fig. 3D), suggesting the differentiation of the intestinal cells as they moved out of the crypt-like domains, mirroring the *in vivo* crypt-villus-like cell organization (45). Altogether, our results showed that mechanical signal from the hard-porous membranes is driving the formation of intestinal epithelial monolayers that maintain the crypt-villus-like cell distribution in the Transwell® insert system. However, as it can be seen in the representative immunofluorescence images of figure 3 (Fig. 3B, C), the epithelial monolayers grew very rapidly for the first days of the culture but failed to cover the entire membrane even if extended cell culture periods were assayed up to 4 weeks (data not shown). Therefore, although the methodology presented here succeeds in recapitulating the main cellular and organizational beneficial features of 3D

organoids in 2D systems, it does not constitute a suitable method for forming epithelial monolayers with tissue barrier properties.

Biochemical factors produced by intestinal subepithelial myofibroblasts boost cell growth and result on intestinal epithelial monolayers fully covering Transwell® insert membranes

To obtain epithelial monolayers fully covering the membranes of Transwell® inserts, we focused our efforts on increasing the proliferative capacities of the ISCs. One key driver in ISCs maintenance and proliferation is the Wingless/Int(Wnt)/β-catenin signaling pathway (1,46). Paneth cells, which are interdigitated among the ISCs, provide an essential stem cell niche by the constant secretion of Wnt proteins, mainly Wnt3a (39,47). However, *in vivo* depletion of Paneth cells did not impair the normal intestine homeostasis (48,49), indicating the redundancy in the Wnt production within the intestinal crypts. Intestinal subepithelial myofibroblasts (ISEMFs) are considered as an important alternative non-epithelial source of Wnt pathway activators, including Wnt2, Wnt2b, Wnt4, Wnt-5a, Wnt9b and Wnt11 (47,50,51), and the enhancers of the Wnt pathway, R-spondin 2 and R-spondin 3 (51–53). Therefore, we postulated that ISEMF-derived signals might be a good strategy to enhance the proliferative capacities of the ISCs in our culture method. To test this hypothesis, ISEMF were isolated from mice colon and immunofluorescence staining was used to corroborate the expression of specific markers characterizing myofibroblasts. Cells stained positive for α smooth muscle actin (α-SMA) and vimentin, and negative for desmin, confirming the ISEMF phenotype (52,54) (Fig. S3). These freshly isolated ISEMFs were cultured to obtain ISEMF-conditioned medium (ISEMF_CM). We then compared the growth of epithelial monolayers on Matrigel®-coated hard substrates cultured with the following conditions: regular ENR_CV-medium, ENR_CV supplemented with ISEMF_CM, and ENR_CV supplemented with ISEMF_CM and recombinant Wnt3a. This last condition was included to further enhance the endogenous Wnt3a signal derived from the Paneth cells of the culture (Fig. 4A). The effects of the different cell culture mediums were qualitatively assessed by bright field microscopy (Fig. 4A) and quantitatively evaluated by computing the surface coverage of the monolayers (Fig. 4B). Our results show that, after 5 days in culture, ISEMF_CM increases by two-fold the surface coverage of the monolayers with respect to the regular crypt medium. On top of that, adding Wnt3a to this medium further boosts the intestinal epithelium growth, now being a three-fold increase in surface coverage with respect to regular crypt medium. In the light of these results, the culture medium composition was revised to include both ISEM_CM and Wnt3a in addition to ENR_CV.

To test the validity of this approach on the Transwell® insert system, crypt pieces derived from organoids were seeded on Matrigel®-coated porous membranes and were cultured using the new culture medium formulation, administrated through the basolateral side as in previous experiments. Representative pictures of cells stained with F-actin showing the full area of the Transwell® porous membranes (6,5 mm in diameter) demonstrated that after 10 days of culture, the intestinal epithelial monolayer is properly formed depicting a characteristic epithelial cell cobblestoned disposition (Fig. 4C, upper panel). Moreover, we found that 10 days were enough time for the epithelial monolayer to fully cover the whole surface (Fig. 4C, upper left panel and Fig. 4D). As a relevant parameter

for the potential applications of these monolayers, we evaluated their integrity and morphology for longer time periods (up to 20 days). Our data demonstrate that intestinal epithelial monolayer integrity is preserved (Fig. 4C, bottom left panel) and surface coverage is still complete (Fig. 4C, right bottom panel and Fig. 4D) after 20 days of culture. Note that a small portion of this particular sample was detached due to manipulation (the membranes have to be cut from the inserts to obtain good microscopy images). Thus, our results prove that adding exogenous stem cell niche-derived biochemical factors (derived from subepithelial myofibroblasts and added Wnt3a) to the regular crypt medium boosts intestinal epithelial cell proliferation. Such proliferation boosting allows for the formation of an epithelial monolayer that fully covers the Transwell® porous membranes. We determined that with this approach an area of 33 mm^2 is fully covered in approximately 10 days and the culture maintains its morphology and surface coverage for up to 20 days.

Epithelial monolayers self-organized in crypt-villus like domains show effective barrier function

We analyzed by immunostaining the cellular composition and distribution of the intestinal epithelial monolayers generated on Transwell® inserts with the cell culture medium described above. We found GFP^+ stem cells clustered in specific foci, indicating the formation of crypt-like domains containing $Lgr5^+$ ISCs both at day 10 and 20 of culture (Fig. 5A, left panel). Therefore, in these conditions, the stem cell distribution previously observed on Matrigel®-coated hard substrates and Transwell® inserts was maintained (Figs. 1C and 3C). In contrast, at day 10 of culture, proliferative $Ki67^+$ cells were not as clustered as GFP^+ stem cells, but rather dispersed throughout the monolayer (Fig. 5A, right panel). This difference can be attributed to the new culture medium used (ENR_CV, supplemented with ISEMF-CM and Wnt3a), which boosts cell proliferation and may cause the expansion of the transit-amplifying domain out of the GFP^+ foci. On the other hand, differentiated cells marked by CK20 accumulated in non-proliferative areas ($Ki67^-$) both at day 10 and 20 (Fig. 5A, right panel). Quantification of the different cell populations was performed on the basis of the immunostanings. It was found that the amount of GFP^+ cells remained constant throughout the culture time analyzed, indicating that the pool of $Lgr5^+$ stem cells is maintained over time (Fig. 5B). In contrast, the amount of proliferative $Ki67^+$ in the monolayer evolved over time. At day 10, from the total percentage of proliferative cells (15,8% ± 4,8%), only about 25% were Lgr5 ISCs (3,9% ± 1,4%), suggesting that the rest of the proliferative population was consisting of transit-amplifying cells. However, at day 20, the percentages of GFP^+ (3,8% ± 0,8%) and $Ki67^+$ cells (2,4% ± 1,2%) were not statistically different (Fig. 5B). Interestingly, this decrease on proliferative cells over time correlated with an increase of differentiated $CK20^+$ cells (Fig. 5B). In addition, this was accompanied by a significant increase in the cell height (Fig. 5C), which indicates an enhanced polarization of the epithelial cells forming the monolayer. These results suggest that the intestinal epithelial monolayer grown on Matrigel®-coated porous membranes with a basolateral administration of stem cell niche biochemical factors is highly proliferative in the initial stages, when the epithelial monolayer is forming, while after reaching confluency epithelial differentiation increases and cell proliferation attenuates.

Specifically, this culture set-up allows to register transepithelial electric resistance (TEER) measurements, to evaluate epithelial monolayer formation and tight junctions integrity, both indicators of epithelia barrier function (26,55). For instance, the presence of gaps in the epithelial monolayer using the before mention tissue culture method leads to TEER values near to background levels (data not shown). Interestingly, the increase of cell differentiation and polarization over time coincides with an increase of the TEER values along the culture time. During the initial stages of the culture, when epithelial monolayer is forming, and proliferation is still high, TEER values were found to be very low. From day 16 to day 20 of culture, correlating with an increase in intestinal differentiation and maturation of the monolayer, TEER values starting to fall into the physiologically relevant range found to be between 40 and 100 $\Omega.cm^2$ in the small intestine (26–28).
As opposed to other studies in which intestinal differentiation was accomplished by the removal of the activators and the addition of inhibitors of the Wnt pathway (23–25,56) or by the use of air-liquid interface (57), in our model levels of epithelial monolayer differentiation was achieved by prolonged culture times.

Discussion

The intestinal biology field has an increased interest to obtain intestinal epithelial cells monolayer cultures, to overcome the sterically limitations of the 3D intestinal organoid. Here we show that employing a thin film of Matrigel® (<20 µM in height) we obtained mouse organoid-derived epithelial monolayer that contain major intestinal epithelial cell types organized into proliferative crypt-like domains and differentiated villus-like regions, closely resembling the in vivo cell distribution. Decreasing the Matrigel® bulk stiffness inhibited the formation of the epithelial monolayer and favored the growth of intestinal organoids. Our results demonstrate that substrate stiffness dictates primary intestinal cell growth phenotype.
Our live imaging experiments, employing Lgr5-EGFP-ires-CreERT2 mouse derived-small intestinal cells demonstrate that first, intestinal cells reorganize into stem cell containing crypts-like domains, resembling *in vivo* stem cell distribution and morphology, from where cells migrate out to form a non-proliferative and differentiated monolayer corresponding to the villus-like region. These results showed that, like in Matrigel® 3D cultures, when stem cells are grown on 2D, are also capable to self-assemble and organize in Paneth cells-containing stem cell niches that give rise to proliferative cells which differentiate while migrate generating the differentiated epithelium, mirroring the *in vivo* epithelial physiology.
Although epithelial tissue organization in crypt-villus domains was recently described (22), it was proven that obtaining functional, mature monolayers using conventional culture formats for epithelial functional analysis remains still a challenge, likely due to the difficulty in expanding these cells. Here we show that supplementing the conventional crypt medium with ISEMF_CM and Wnt3a boosted the intestinal cell growth allowing for the generation of a functional and differentiated intestinal monolayer in Transwell® inserts with effective barrier function, as demonstrated by the physiological relevant TEER values obtained. Thus, the tissue culture conditions here described, allow for the expansion of the intestinal cells to obtain fully covering surfaces that permits the functional analysis of the epithelium maintaining the self-organization of the epithelial

monolayer in stem cell niche foci and non-proliferative differentiated regions. The analysis of the cell composition of the monolayer along the culture time show that as time goes by the monolayer becomes less proliferative and more differentiated without the need of any additional external signal such as Wnt inhibitors or Notch activators in contrast to the previously described (23–25). We attributed this effect to two phenomena; on the one hand epithelial differentiation is dependent upon cell-to-cell contact and confluent cultures lead to cell cycle exit (58), and on the other a negative feedback loop exert by the BMP signaling generated by the differentiated cells inhibit epithelial cell proliferation (22). Thus, the decrease of proliferative cells with time in our experimental set-up might be explained by the increase of BMP-producing differentiated cells. However, our results show that the levels of ISC (GFP^+) remained constant throughout the culture times analyzed, indicating that the described effect of the BMP signaling on cell proliferation does not affect the amount of stem cells in the culture.

We believe that organoid-derived intestinal epithelial monolayer model we report here offers an up to date novel culture method and contributes to the current state-of-the art in combining an *in vitro* intestinal epithelium with *in vivo*-like cellular organization with a tissue culture format compatible with studies where an access to both luminal and basolateral compartment is needed, such as in studies of drug absorption and microbe-epithelium interactions.

Acknowledgments

This project was founded by Biomedical Networking Research Centre on Bioengineering, Biomaterials and Nanomedicine (CIBER-BBN) and by the project of the Spanish Ministry of Economy and Competitiveness MINAHE5 (TEC2014-51940-C2-C-R). This work has been financially supported from the Commissions for Universities and Research of the Department of Innovation, Universities, and Enterprise of the Generalitat de Catalunya (2014 SGR 1442). The financial support of the European Research Council through the COMIET project (647863) is gratefully acknowledged. The authors gratefully acknowledge the Agència de Gestió d'Ajuts Universitaris i de Recerca (AGAUR) for the funding of Gizem Altay through FI-DGR 2014.

References

1. Clevers H. The intestinal crypt, a prototype stem cell compartment. Cell [Internet]. 2013 Jul 18;154(2):274–84.

2. Leushacke M, Barker N. Ex vivo culture of the intestinal epithelium: Strategies and applications. Gut. 2014;63(8):1345–54.

3. Barker N, van Es JH, Kuipers J, Kujala P, van den Born M, Cozijnsen M, et al. Identification of stem cells in small intestine and colon by marker gene Lgr5. Nature [Internet]. 2007 Oct 25;449(7165):1003–7.

4. Barker N. Adult intestinal stem cells: critical drivers of epithelial homeostasis and regeneration. 2013.

5. Hidalgo IJ, Raub TJ, Borchardt RT. Characterization of the human colon carcinoma cell line (Caco-2) as a model system for intestinal epithelial permeability. Gastroenterology [Internet]. 1989 Mar;96(3):736–49.

6. Shah P, Jogani V, Bagchi T, Misra A. Role of Caco-2 Cell Monolayers in Prediction of Intestinal Drug Absorption. Biotechnol Prog [Internet]. 2006 Feb 3;22(1):186–98.

7. Sambuy Y, De Angelis I, Ranaldi G, Scarino ML, Stammati A, Zucco F. The Caco-2 cell line as a model of the intestinal barrier: influence of cell and culture-related factors on Caco-2 cell functional characteristics. Cell Biol Toxicol. 2005 Jan;21(1):1–26.

8. Sun H, Chow EC, Liu S, Du Y, Pang KS. The Caco-2 cell monolayer: usefulness and limitations. Expert Opin Drug Metab Toxicol. 2008 Apr 23;4(4):395–411.

9. Aldhous MC, Shmakov AN, Bode J, Ghosh S. Characterization of conditions for the primary culture of human small intestinal epithelial cells. Clin Exp Immunol [Internet]. 2001 Jul 1;125(1):32–40.

10. Grossmann J, Walther K, Artinger M, Kiessling S, Steinkamp M, Schmautz W-K, et al. Progress on isolation and short-term ex-vivo culture of highly purified non-apoptotic human intestinal epithelial cells (IEC). Eur J Cell Biol. 2003;82(1):262–70.

11. Sato T, Vries RG, Snippert HJ, van de Wetering M, Barker N, Stange DE, et al. Single Lgr5 stem cells build crypt-villus structures in vitro without a mesenchymal niche. Nature [Internet]. 2009 May 14;459(7244):262–5.

12. Ootani A, Li X, Sangiorgi E, Ho QT, Ueno H, Toda S, et al. Sustained in vitro intestinal epithelial culture within a Wnt-dependent stem cell niche. Nat Med [Internet]. 2009 Jun;15(6):701–6.

13. Mahe MM, Aihara E, Schumacher MA, Zavros Y, Montrose MH, Helmrath MA, et al. Establishment of Gastrointestinal Epithelial Organoids. Current Protocols in Mouse Biology. 2013: 217-240.

14. Sato T, Stange DE, Ferrante M, Vries RGJ, Es JHVAN. Long-term Expansion of Epithelial Organoids From Human Colon, Adenoma, Adenocarcinoma, and Barrett's Epithelium. Gastroenterology. 2011;141(5):1762–72.

15. Jung P, Sato T, Merlos-Suárez A, Barriga FM, Iglesias M, Rossell D, et al. Isolation and in vitro expansion of human colonic stem cells. Nat Med. 2011 Oct 4;17(10):1225–7.

16. Middendorp S, Schneeberger K, Wiegerinck CL, Mokry M, Akkerman RDL, van Wijngaarden S, et al. Adult Stem Cells in the Small Intestine Are Intrinsically Programmed with Their Location-Specific Function. Stem Cells. 2014 May 1;32(5):1083–91.

17. Sachs N, Clevers H. Organoid cultures for the analysis of cancer phenotypes. Curr Opin Genet Dev. 2014;24(1):68–73.

18. Dekkers JF, Wiegerinck CL, de Jonge HR, Bronsveld I, Janssens HM, de Winter-de Groot

KM, et al. A functional CFTR assay using primary cystic fibrosis intestinal organoids. Nat Med. 2013 Jul 2;19(7):939–45.

19. Yui S, Nakamura T, Sato T, Nemoto Y, Mizutani T, Zheng X, et al. Functional engraftment of colon epithelium expanded in vitro from a single adult Lgr5+ stem cell. Nat Med. 2012 Apr 11;18(4):618–23.

20. Wilson SS, Tocchi A, Holly MK, Parks WC, Smith JG. A small intestinal organoid model of non-invasive enteric pathogen-epithelial cell interactions. Mucosal Immunol. 2015 Mar;8(2):352–61.

21. Wang Y, DiSalvo M, Gunasekara DB, Dutton J, Proctor A, Lebhar MS, et al. Self-renewing Monolayer of Primary Colonic or Rectal Epithelial Cells. Cell Mol Gastroenterol Hepatol [Internet]. 2017 Jul;4(1):165–182.e7.

22. Thorne CA, Chen IW, Sanman LE, Cobb MH, Wu LF, Altschuler SJ. Enteroid Monolayers Reveal an Autonomous WNT and BMP Circuit Controlling Intestinal Epithelial Growth and Organization. Dev Cell. 2018;44(5):624–633.e4.

23. Moon C, Vandussen KL, Miyoshi H, Stappenbeck TS. Development of a primary mouse intestinal epithelial cell monolayer culture system to evaluate factors that modulate IgA transcytosis. Mucosal Immunol. 2014;7(4):818–28.

24. VanDussen KL, Marinshaw JM, Shaikh N, Miyoshi H, Moon C, Tarr PI, et al. Development of an enhanced human gastrointestinal epithelial culture system to facilitate patient-based assays. Gut. 2015;64(6):911–20.

25. Kozuka K, He Y, Koo-McCoy S, Kumaraswamy P, Nie B, Shaw K, et al. Development and Characterization of a Human and Mouse Intestinal Epithelial Cell Monolayer Platform. Stem cell reports. 2017 Dec 12;9(6):1976–90.

26. Srinivasan B, Kolli AR, Esch MB, Abaci HE, Shuler ML, Hickman JJ. TEER measurement techniques for in vitro barrier model systems. J Lab Autom. 2015 Apr;20(2):107–26.

27. Artursson P, Ungell AL, Lofroth JE. Selective paracellular permeability in two models of intestinal absorption: cultured monolayers of human intestinal epithelial cells and rat intestinal segments. Pharm Res. 1993;10(8):1123–9.

28. Sjöberg Å, Lutz M, Tannergren C, Wingolf C, Borde A, Ungell A-L. Comprehensive study on regional human intestinal permeability and prediction of fraction absorbed of drugs using the Ussing chamber technique. Eur J Pharm Sci. 2013 Jan 23;48(1–2):166–80.

29. Barriga FM, Montagni E, Mana M, Mendez-Lago M, Hernando-Momblona X, Sevillano M, et al. Mex3a Marks a Slowly Dividing Subpopulation of Lgr5+ Intestinal Stem Cells. Cell Stem Cell. 2016;20(6):801–816.e7.

30. Fernández-Majada V, Welz P-S, Ermolaeva MA, Schell M, Adam A, Dietlein F, et al. The tumour suppressor CYLD regulates the p53 DNA damage response. Nat Commun. 2016;7:12508.

31. Khalil H, Nie W, Edwards RA, Yoo J. Isolation of primary myofibroblasts from mouse and human colon tissue. J Vis Exp. 2013 Oct 12;(80).

32. Hughes CS, Postovit LM, Lajoie GA. Matrigel: A complex protein mixture required for optimal growth of cell culture. Proteomics. 2010 Feb 16;10(9):1886–90.

33. Yin X, Farin HF, van Es JH, Clevers H, Langer R, Karp JM. Niche-independent high-purity cultures of Lgr5+ intestinal stem cells and their progeny. Nat Methods. 2014 Jan;11(1):106–12.

34. Spence JR, Mayhew CN, Rankin SA, Kuhar MF, Vallance JE, Tolle K, et al. Directed differentiation of human pluripotent stem cells into intestinal tissue in vitro. Nature. 2010 Dec 12;470(7332):105–9.

35. Gjorevski N, Sachs N, Manfrin A, Giger S, Bragina ME, Ordóñez-Morán P, et al. Designer matrices for intestinal stem cell and organoid culture. Nature. 2016 Nov

16;539(7630):560–4.

36. Kuo C-HR, Xian J, Brenton JD, Franze K, Sivaniah E. Complex stiffness gradient substrates for studying mechanotactic cell migration. Adv Mater. 2012 Nov 27;24(45):6059–64.

37. Deng S, Zhao X, Huang Y, Han X, Liu H, Hu Y. Deformation and fracture of polystyrene/polypropylene blends: A simulation study. Polymer (Guildf). 2011 Nov 10;52(24):5681–94.

38. Zaman MH, Trapani LM, Sieminski AL, Siemeski A, Mackellar D, Gong H, et al. Migration of tumor cells in 3D matrices is governed by matrix stiffness along with cell-matrix adhesion and proteolysis. Proc Natl Acad Sci U S A. 2006 Jul 18;103(29):10889–94.

39. Sato T, van Es JH, Snippert HJ, Stange DE, Vries RG, van den Born M, et al. Paneth cells constitute the niche for Lgr5 stem cells in intestinal crypts. Nature. 2011;469(7330):415–8.

40. Watson AJM, Hughes KR. TNF-α-induced intestinal epithelial cell shedding: implications for intestinal barrier function. Ann N Y Acad Sci. 2012 Jul 1;1258(1):1–8.

41. Xu P, Becker H, Elizalde M, Masclee A, Jonkers D. Intestinal organoid culture model is a valuable system to study epithelial barrier function in IBD. Gut. 2017;0(0):4–6.

42. Hill DR, Huang S, Tsai Y-H, Spence JR, Young VB. Real-time Measurement of Epithelial Barrier Permeability in Human Intestinal Organoids. J Vis Exp [Internet]. 2017;(130):1–10.

43. Larsson A, Dérand H. Stability of polycarbonate and polystyrene surfaces after hydrophilization with high intensity oxygen RF plasma. J Colloid Interface Sci. 2002;246:214–21.

44. Sato T, Clevers H. Growing self-organizing mini-guts from a single intestinal stem cell: mechanism and applications. Science. 2013 Jun 7;340(6137):1190–4.

45. Merlos-Suárez A, Barriga FM, Jung P, Iglesias M, Céspedes MV, Rossell D, et al. The Intestinal Stem Cell Signature Identifies Colorectal Cancer Stem Cells and Predicts Disease Relapse. Cell Stem Cell. 2011 May;8(5):511–24.

46. Clevers H, Nusse R. Wnt/β-catenin signaling and disease. Cell. 2012;149(6):1192–205.

47. Gregorieff A, Pinto D, Begthel H, Destrée O, Kielman M, Clevers H. Expression Pattern of Wnt Signaling Components in the Adult Intestine. Gastroenterology. 2005 Aug 1;129(2):626–38.

48. Garabedian EM, Roberts LJJ, McNevin MS, Gordon JI. Examining the role of Paneth cells in the small intestine by lineage ablation in transgenic mice. J Biol Chem. 1997;272(38):23729–40.

49. Durand A, Donahue B, Peignon G, Letourneur F, Cagnard N, Slomianny C, et al. Functional intestinal stem cells after Paneth cell ablation induced by the loss of transcription factor Math1 (Atoh1). Proc Natl Acad Sci. 2012;109(23):8965–70.

50. Farin HF, Van Es JH, Clevers H. Redundant Sources of Wnt Regulate Intestinal Stem Cells and Promote Formation of Paneth Cells. Gastroenterology. 2012 Dec 1 [cited 2017 Dec 15];143(6):1518–1529.e7.

51. Kabiri Z, Greicius G, Madan B, Biechele S, Zhong Z, Zaribafzadeh H, et al. Stroma provides an intestinal stem cell niche in the absence of epithelial Wnts. Development. 2014;141(11):2206–15.

52. Lei NY, Jabaji Z, Wang J, Joshi VS, Brinkley GJ, Khalil H, et al. Intestinal subepithelial myofibroblasts support the growth of intestinal epithelial stem cells. PLoS One. 2014;9(1).

53. Kim K-A, Wagle M, Tran K, Zhan X, Dixon MA, Liu S, et al. R-Spondin family members regulate the Wnt pathway by a common mechanism. Mol Biol Cell. 2008 Jun;19(6):2588–96.

54. Lahar N, Lei NY, Wang J, Jabaji Z, Tung SC, Joshi V, et al. Intestinal subepithelial myofibroblasts support in vitro and in vivo growth of human small intestinal epithelium. PLoS One. 2011;6(11):1–9.

55. Elbrecht DH, Long CJ, Hickman JJ. Transepithelial/endothelial Electrical Resistance (TEER) theory and ap- plications for microfluidic body-on-a-chip devices. J Rare Dis Res Treat. 2016;1(3):46–52.

56. Scott A, Rouch JD, Jabaji Z, Khalil HA, Solorzano S, Lewis M, et al. Long-term renewable human intestinal epithelial stem cells as monolayers: A potential for clinical use. J Pediatr Surg. 2016 Jun;51(6):995–1000.

57. Wang X, Yamamoto Y, Wilson LH, Zhang T, Howitt BE, Farrow MA, et al. Cloning and variation of ground state intestinal stem cells. Nature. 2015 Jun 3;522(7555):173–8.

58. Mayo C, Lloreta J, Real FX, Mayol X. In vitro differentiation of HT-29 M6 mucus-secreting colon cancer cells involves a trychostatin A and p27KIP1-inducible transcriptional program of gene expression. J Cell Physiol. 2007 Jul;212(1):42–50.

Figure legends

Figure 1. (A) Scheme depicting the experimental protocols used. (B) Representative images corresponding to immunofluorescence of filamentous actin (F-actin) and Ki67 from organoid-derived crypts and single cells cultured either on a thin film of Matrigel® (2,9 ± 0,1 µm height), referred as "Hard" or on a thick layer of Matrigel® (approx. 2mm height), referred as "Soft" after 5 days of culture. Scale bars: 100 µm. (C) Co-immunofluorescence for GFP and Ki67 (left panel), Lysozyme (Lyz) and GFP (middle panel), and Ki67 and cytokeratin 20 (CK20) (right panel) of 2D epithelial cultures derived from crypts (upper panel) or single cells (lower panel) grown on Matrigel®-coated hard substrates for 7 days. Scale bars: 100 µm. (D) Periodic acid-Schiff base (PAS) staining of 2D epithelial monolayers grown on Matrigel®-coated hard substrates for 7 days. Scale bar: 100 µm. (E) Immunostaining for zona occludens 1 (ZO-1) and F-actin of 2D epithelial monolayers grown on Matrigel®-coated hard substrates for 7 days. Upper and lower panels show the top view and the orthogonal sections of the 2D monolayers, respectively. Scale bars: 50 µm (upper panel); 10 µm (lower panel).

Figure 2. (A) Live-imaging sequence, of overlapped bright field and GFP channels, corresponding to the first 60 hours after seeding organoid-derived crypts and (B) first 96 hours after seeding organoid-derived single cells on a thin film of Matrigel®. Time of image acquisition is shown. White arrow heads indicate Lgr5-GFP^{+} cells. Scale bars: 50 µm (A upper panel and B); 100 µm (A bottom panel). (C) Immunofluorescence of EdU, Ki67 and ZO-1 of an EdU pulse-chase experiment. Representative images of 0h (upper panel) and 1 days (lower panel) after EdU chase are shown. Scale bars: 50 µm. (D) Immunofluorescence for Ki67 and F-actin of epithelial monolayers from passage 0 to passage 3 (P0, P1, P2, P3). Epithelial monolayers were passed by enzymatical digestion after every 6 to 8 days in culture. Scale bars: 50 µm.

Figure 3. (A) Scheme depicting the experimental setup used. Organoid-derived digested crypts were seeded on top of Matrigel®-coated polycarbonate porous membranes and cultured under asymmetric administration of ENR_CV medium**.** (B) Immunofluorescence of Ki67, (C) GFP, (D) EHPHB2 and (B-D) F-actin of epithelial monolayer on Matrigel®-coated polycarbonate membranes cultured for 10 days. Yellow arrowheads indicate crypt-like regions. The inset panel in B, C and D corresponds to zoomed images of the crypt-like regions. Scale bars: 100 µm.

Figure 4. (A) Representative bright field images of epithelial monolayers grown on Matrigel®-coated polystyrene plates and cultured with regular ENR_CV crypt medium, ISEMF_CM supplemented with ENR_CV, and ISEMF_CM supplemented with ENR_CV and Wnt3a after 5 days of culture. Black dashed line marks the epithelial border. Scale bars: 100 µm. (B) Graph showing the percent surface coverage for each condition. Mean values were calculated by measuring 12 randomly selected regions from bright field images obtained from three different samples for each condition (n = 3). The surface

coverage values were found to be 24,0% ± 4,1%, 50,0% ± 13,3%, and 69,6% ± 2,7% for media containing ENR_CV, ISEMF_CM + ENR_CV and ISEMF_CM + ENR_CV + Wnt3a, respectively. The data were represented as mean ± standard deviation (Student's t-test, *p<0,05). (C) Fluorescence of F-actin and nucleus of the monolayers cultured in transwell setup under asymmetric administration of ISEMF_CM + ENR_CV + Wnt3a medium at day 10 and day 20. Left panel shows the F-actin staining of the entire sample surface and right panel shows F-actin and nucleus staining at a higher magnification. Scale bars: 1 mm (left panel); 100 μm (right panel). (D) Graph showing the percent surface coverage calculated from the entire surface of the samples. Six samples were analyzed for day 10 (n=6) and four samples for day 20 (n=4). The surface coverage values were found to be 93,9% ± 1,8% and 96,6% ± 1,5% for day 10 and day 20, respectively. The data were represented as mean ± standard deviation (Student's t-test, *p<0,05).

Figure 5. (A) Immunofluoresence for GFP, Ki67 and CK20 after 10 and 20 days in culture. Scale bars: 100 μm. (B) Graph showing the quantification of the indicated markers expressed as % positive cells/ total cells at day 10 (n=3) and at day 20 (n=2) of culture. The data were represented as mean ± standard deviation (pairwise Student's t-test, *p<0,05). (C) Orthogonal sections of the epithelial monolayers stained for F-actin and nucleus at day 10 and 20. Scale bars: 10 μm. The average cell height was calculated to be 7,7 ± 1,3 μm and 10,3 ± 1,7 μm for day 10 and day 20, respectively. 10 cells were analyzed at randomly selected locations in a total of three independent samples (n=3) for each condition. The data were represented as mean ± standard deviation. (D) Graph showing the TEER profile of the epithelial monolayers throughout the first 20 days of culture. Samples from three independent experiments with technical replicas in a total of 5 independent samples were analyzed (n=5).

Figure 1.

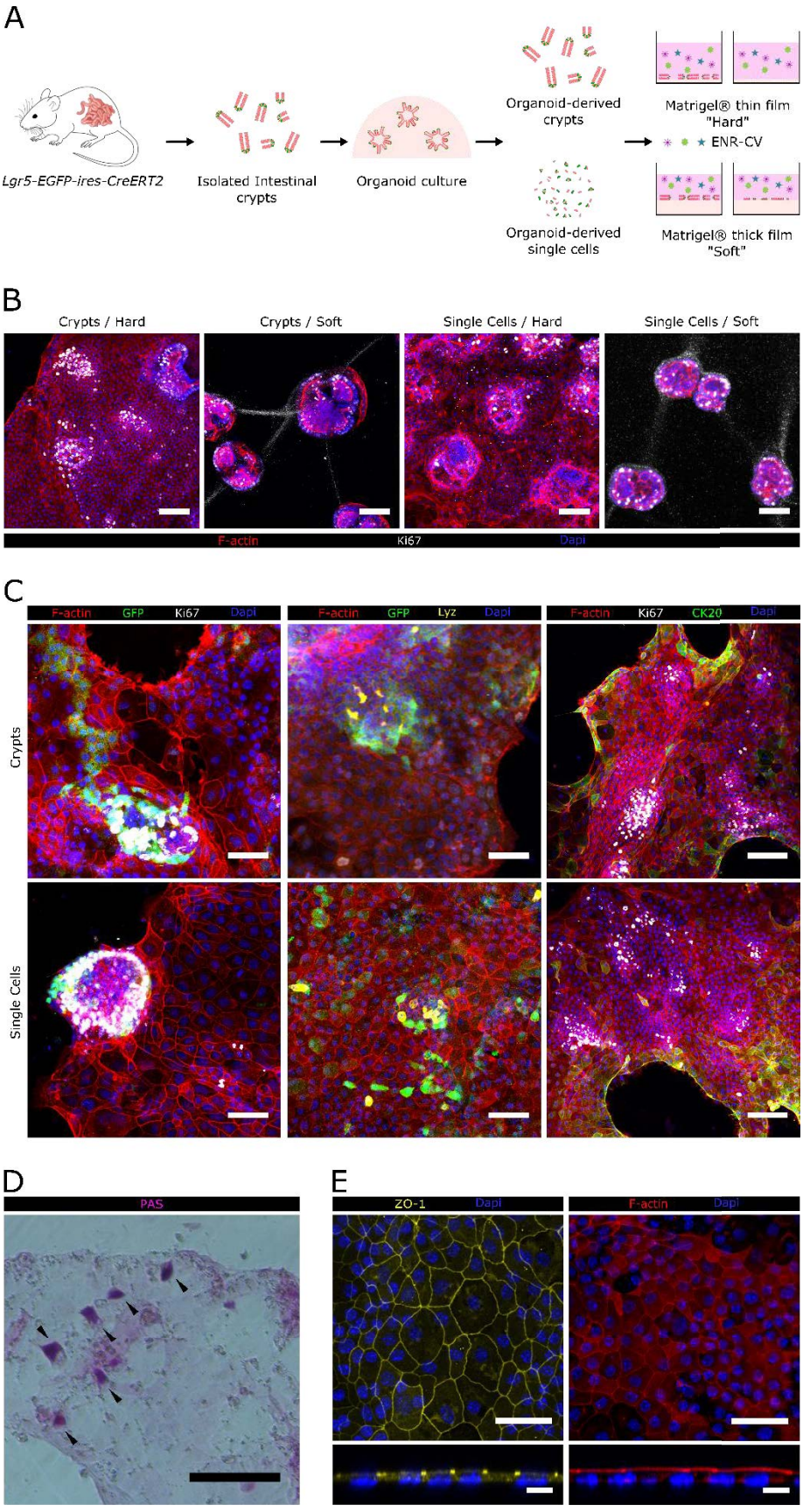
A
Lgr5-EGFP-ires-CreERT2
Isolated Intestinal crypts
Organoid culture
Organoid-derived crypts
Organoid-derived single cells
Matrigel® thin film "Hard"
ENR-CV
Matrigel® thick film "Soft"
B
Crypts / Hard
Crypts / Soft
Single Cells / Hard
Single Cells / Soft
F-actin
Ki67
Dapi
C
F-actin GFP Ki67 Dapi
F-actin GFP Lyz Dapi
F-actin Ki67 CK20 Dapi
Crypts
Single Cells
D
PAS
E
ZO-1 Dapi
F-actin Dapi

Figure 2.

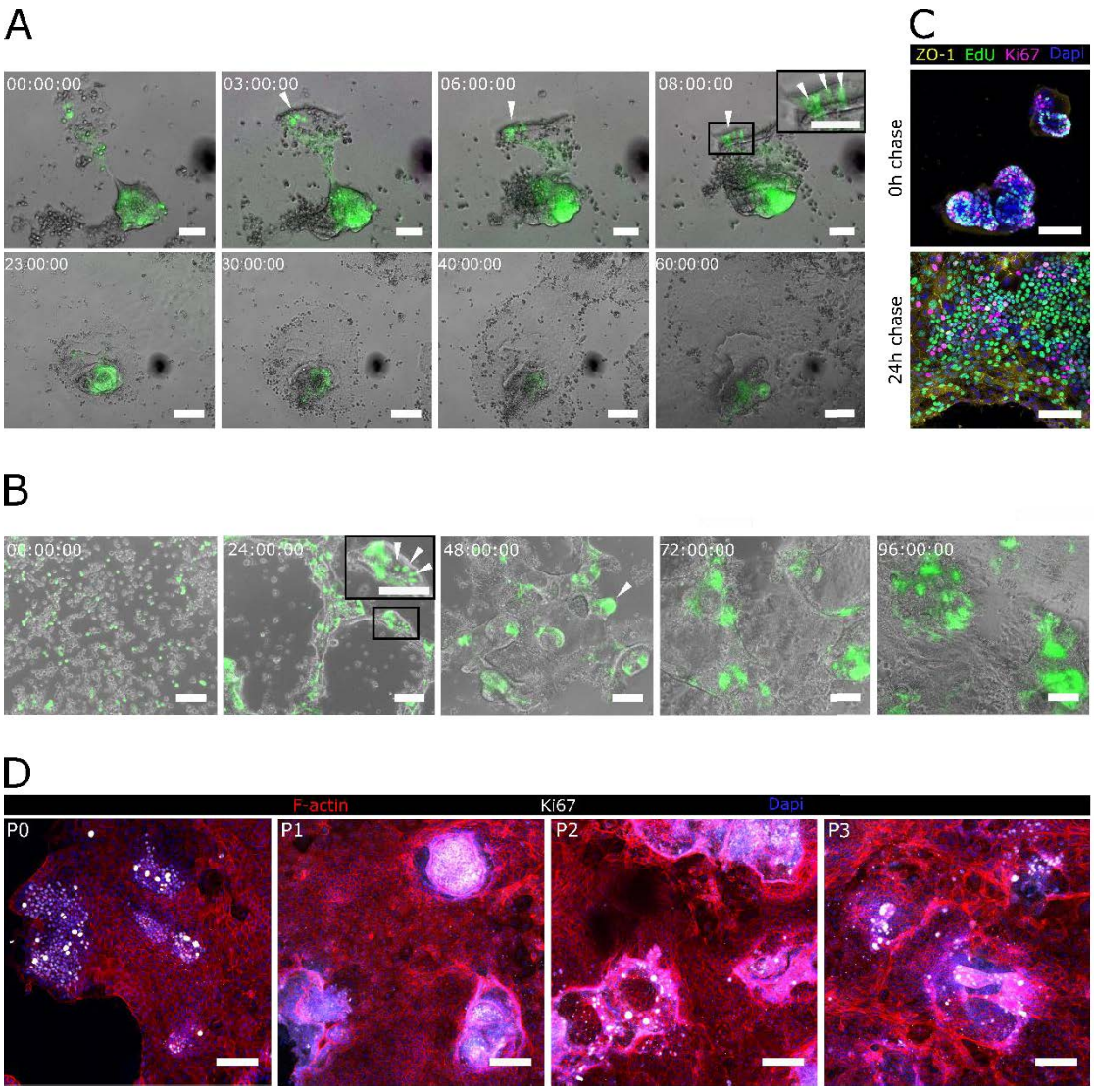
A
00:00:00
03:00:00
06:00:00
08:00:00
23:00:00
30:00:00
40:00:00
60:00:00
C
ZO-1 EdU Ki67 Dapi
0h chase
24h chase
B
00:00:00
24:00:00
48:00:00
72:00:00
96:00:00
D
F-actin
Ki67
Dapi
P0
P1
P2
P3

Figure 3.

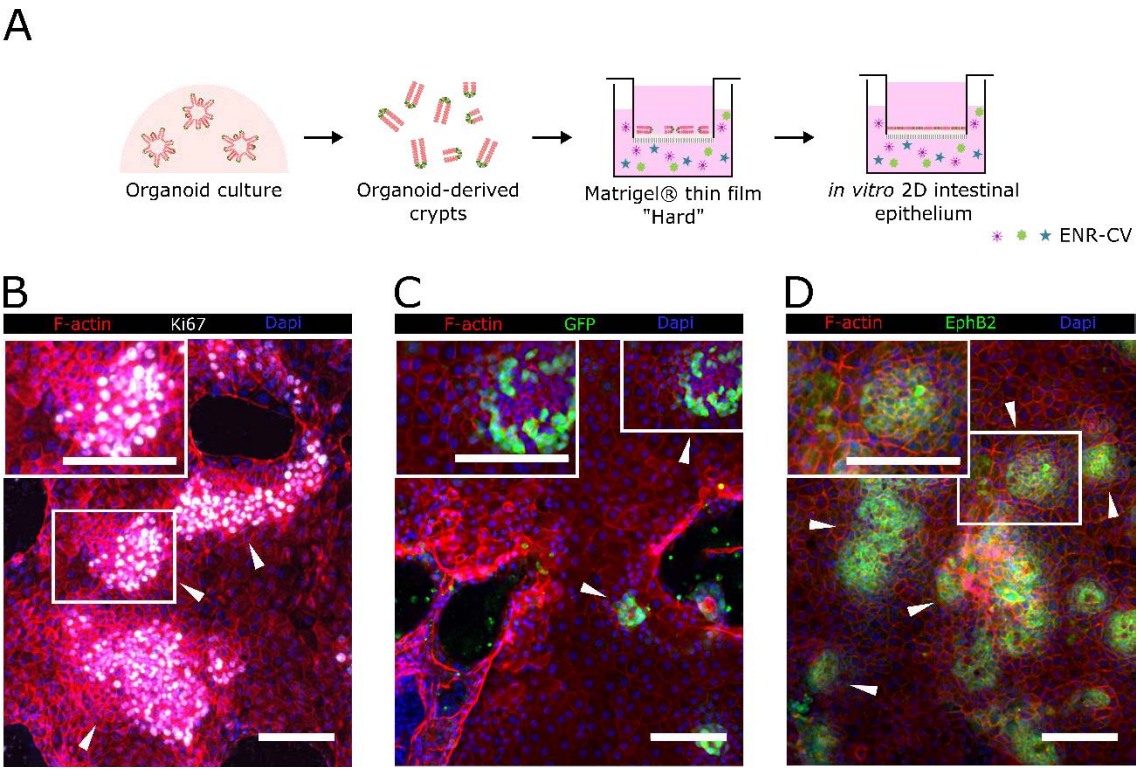
A
Organoid culture
Organoid-derived crypts
Matrigel® thin film "Hard"
in vitro 2D intestinal epithelium
ENR-CV
B
F-actin
Ki67
Dapi
C
F-actin
GFP
Dapi
D
F-actin
EphB2
Dapi

Figure 4.

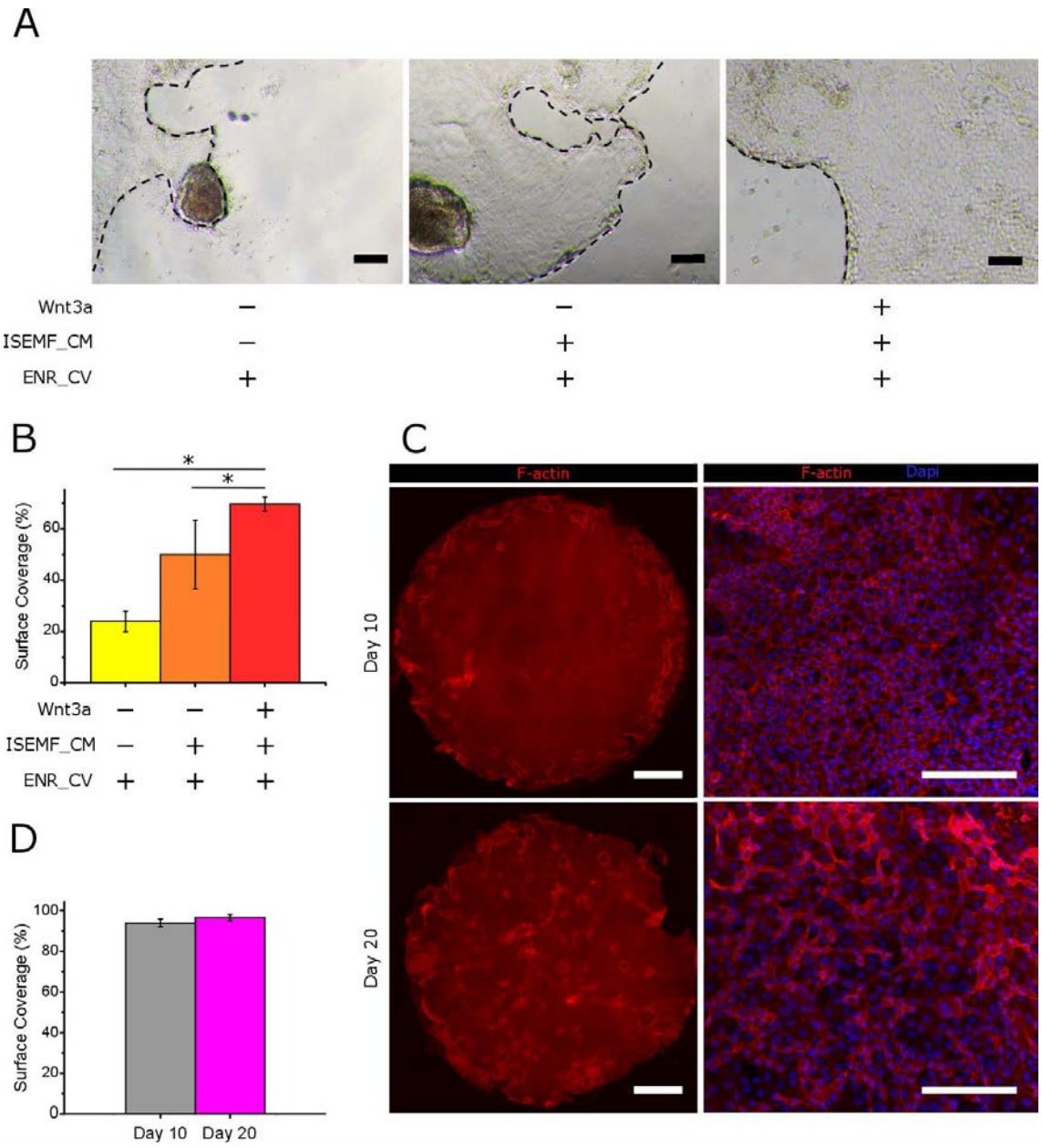
A
Wnt3a
ISEMF_CM
ENR_CV
B
Surface Coverage (%)
Wnt3a
ISEMF_CM
ENR_CV
C
F-actin
F-actin
Dapi
Day 10
Day 20
D
Surface Coverage (%)
Day 10
Day 20

Figure 5.

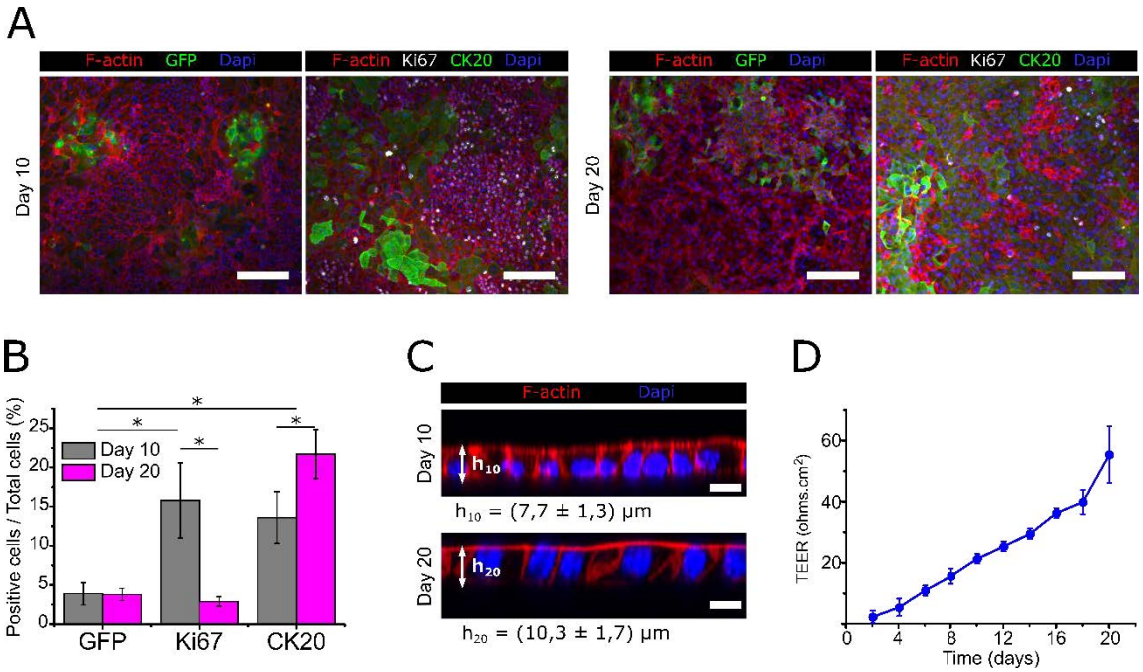
A
F-actin GFP Dapi
F-actin Ki67 CK20 Dapi
Day 10
Day 20
B
Positive cells / Total cells (%)
Day 10
Day 20
GFP
Ki67
CK20
C
F-actin Dapi
Day 10
Day 20
h10
h20
h10 = (7,7 ± 1,3) µm
h20 = (10,3 ± 1,7) µm
D
TEER (ohms.cm2)
Time (days)

Supplementary Information

Self-organized intestinal epithelial monolayers in crypt and villus-like domains show effective barrier function

Gizem Altay, Vanesa Fernández-Majada, Enara Larrañaga Carricajo, Sébastien Tosi, Francisco Barriga, Eduard Batlle, Elena Martinez

Characterization of Matrigel©-coated substrates

Matrigel® staining images were acquired by a Leica SP5 confocal laser scanning microscope (CLSM) equipped with a 20x dry objective (NA = 0,7) and hybrid detectors. The laser excitation and emission light spectral collection were both optimized for GFP. The pinhole was set to 1 Airy unit and a stack of 22 µm (z-step of 1 µm) was acquired for each sample. The CLSM stacks were then all post-processed by deconvolution by a theoretical model of the objective (Mediacy Autoquant X3, fixed PSF, constrained iterative, 10 iterations). This helped mitigating the axial spread of the point spread function of the instrument. We analyzed three technical replicas and the thicknesses were estimated using ImageJ software. To assess the sample uniformity and improve the estimates, for each sample we analyzed 20 randomly selected intensity axial profiles, each of them extracted along 32-pixel thick lines, covering the whole extension of the stack (ImageJ TransformJ Turn + Plot profile). Since the extracted intensity profiles closely resembled Gaussian functions, we fitted a Gaussian plus offset function to the observations to estimate both the level of the background and the standard deviation of the function (ImageJ Curve Fitting). For each intensity profile, an estimate of the layer thickness was obtained as the full width at half height of the fitted Gaussian function (FWHM ≈ 2,355 σ). The estimates of the layer thickness at different regions were averaged for each sample in a total of three samples and presented as mean ± standard deviation.

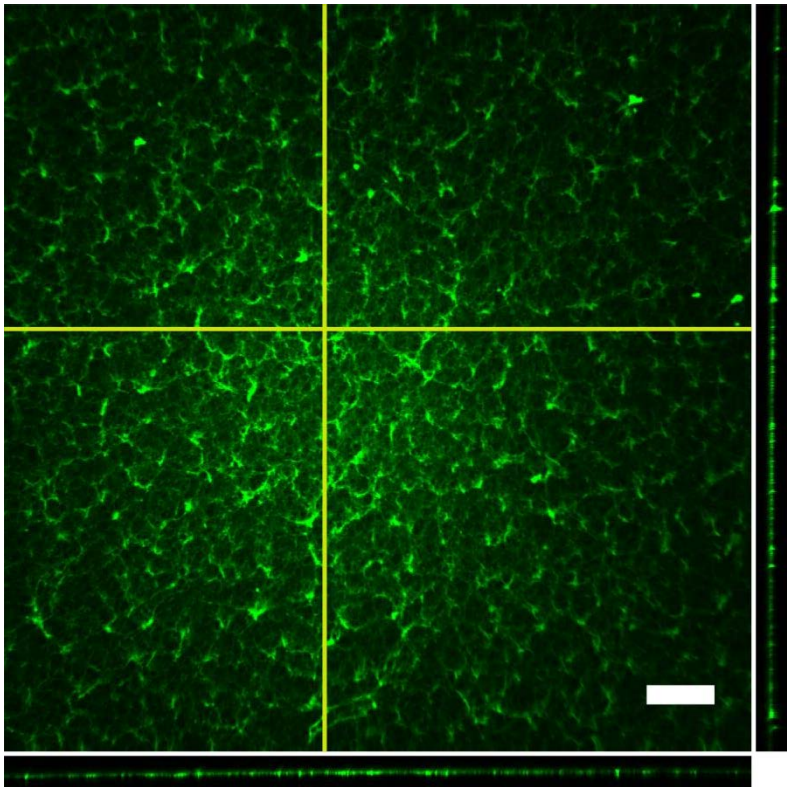

Figure S1. Immunofluorescence for laminin, one of the more abundant components of Matrigel®, of a thin layer of Matrigel® on polystyrene plates. One representative top and two orthogonal views are shown. Yellow lines indicate the position from where the orthogonal sections were taken. Orthogonal sections were used to calculate the thin film thickness. Thin film thickness value (2,9 ± 0,1 µm) corresponds to the mean ± standard deviation of measurements obtained from 20 different regions per each sample in a total of three technical replicas (n=3). Scale bar: 50 µm.

Characterization of cell death

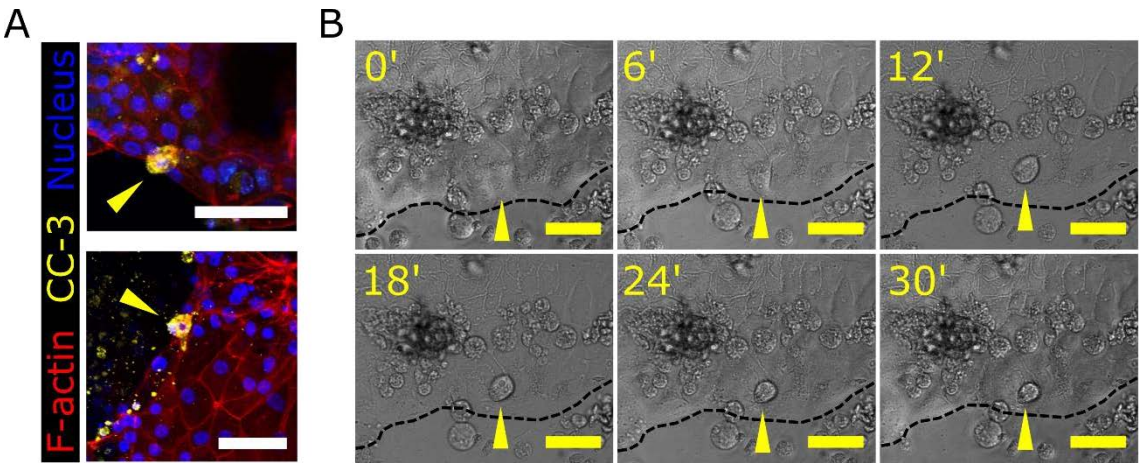

Figure S2. (A) Immunostaining for Cleaved caspase-3 (CC-3) of epithelial monolayers after 7 days in culture showing cell death at the epithelial border. Yellow arrowheads mark apoptotic cells. Scale bars: 50 µm. (B) Live image sequence at day 8 of culture showing a cell dying at the epithelial border. Yellow arrow head point to the dying cell. Black dashed line marks the epithelial border. Scale bars: 50 µm.

Characterization of intestinal subepithelial myofibroblasts

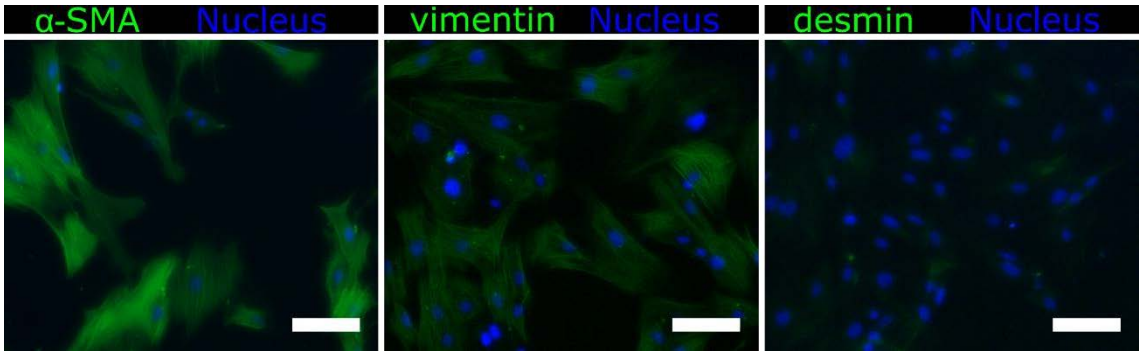

Figure S3. Immunofluorescence for α-smooth muscle actin (α-SMA), and vimentin, and desmin of intestinal subepithelial myofibroblasts (ISEMFs) isolated from mouse colon lamina propria. Counterstaining was done with Hoechst 33342. Scale bars: 50 µm.

Dynamic Photopolymerization Produces Complex Microstructures on Soft Hydrogels in a Moldless approach to Generate a 3D Intestinal Tissue Model

Albert G. Castaño[1], María García-Díaz[1], Gizem Altay[1], Núria Torras[1] and Elena Martínez[1,2,3]

[1] Institute for Bioengineering of Catalonia (IBEC), The Barcelona Institute of Science and Technology (BIST), Barcelona, Spain
[2] Centro de Investigación Biomédica en Red (CIBER), Madrid, Spain
[3] Department of Electronics and Biomedical Engineering, University of Barcelona, Barcelona, Spain

E-mail: emartinez@ibecbarcelona.eu

Received xxxxxx
Accepted for publication xxxxxx
Published xxxxxx

Abstract

Epithelial tissues contain three-dimensional (3D) complex microtopographies that are essential for proper performance. These microstructures provide cells with the physicochemical cues needed to guide their self-organization into functional tissue structures. However, most *in vitro* models do not implement these 3D architectural features. The main problem is the availability of simple fabrication techniques that can reproduce the complex geometries found in native tissues on the soft polymeric materials required as cell culture substrates. In this study reaction-diffusion mediated photolithography is used to fabricate 3D microstructures with complex geometries on soft poly(ethylene glycol)-based hydrogels in a single step and moldless approach. By controlling fabrication parameters such as the oxygen diffusion/depletion timescales, the distance to the light source and the exposure dose, the dimensions and geometry of the microstructures can be well-defined. In addition, copolymerization of poly(ethylene glycol) with acrylic acid improves control of the dynamic reaction-diffusion processes that govern the free-radical polymerization of highly-diluted polymeric solutions. Moreover, acrylic acid allows adjusting the density of cell adhesive ligands while preserving the soft mechanical properties of the hydrogels. The method proposed is a simple, single-step, and cost-effective strategy for producing models of intestinal epithelium that can be easily integrated into standard cell culture platforms.

Keywords: microengineered 3D tissue models, poly(ethylene glycol) hydrogels, photopolymerization, 3D microstructures, intestinal epithelium

1. Introduction

Three-dimensional (3D) microstructures such as compact folds, invaginations, evaginations, and wavy morphologies are common in invertebrate and vertebrate animals, particularly in epithelial tissues. These microstructures are formed during tissue development and are key to their proper functioning. In the small intestine, crypts and villi provide the tissue with a large surface area. This increases the volume and residence time of the fluids trapped between villi, improving its absorbance function. In addition, 3D microstructures provide an oxygen depleted microenvironment for the microbiota and compartmentalize the multiple cell types composing the

tissue. Villi are finger-like protrusions, 0.2-1 mm in height, 100-200 μm in diameter, and have a density of 20-40 villi mm^{-2} [1–3]. Despite its physiological relevance, this 3D complex architecture is omitted in standard *in vitro* models of the small intestine. Conventional models are based on flat monolayers of cell lines such as Caco-2 cells, grown on filter supports that provide separate access to the luminal and basolateral side of the monolayer. These conventional two-dimensional (2D) models have been essential as screening tools for drug development, but recent publications demonstrate that the predictive capacity of current preclinical assays is not optimal [4]. Improved *in vitro* models rely on providing cells with a more physiologically realistic environment, including tissue architecture, cell-matrix interactions and biomimetic chemical and mechanical signaling [4–8]. Hydrogels have been proposed as alternative cell culture substrates. They are hydrophilic polymers with high water content and they provide a friendly environment for cell growth and differentiation. They also have a broad range of mechanical properties compatible with soft tissue microenvironments (< 50 kPa). This level of softness, however, hampers 3D hydrogel shaping to simulate the topographies found at the tissue level. The main limitation is the difficulty in microfabricating soft materials with complex 3D geometries, high aspect ratio and curvature using efficient and simple methods which could be routinely implemented in standard assays. Microfabrication techniques such as conventional replica molding and direct printing are typically restricted to the fabrication of low to medium aspect ratio microstructures with perpendicular walls [9]. Several variations of replica molding techniques including the use of laser ablation and sacrificial molds can produce soft 3D microstructures [9,10]. These procedures use complex equipment and multiple fabrication steps to overcome the difficulties in demolding the soft microstructures. Photopolymerization-based microfabrication techniques such as photolithography, soft lithography or stereolithography are well established to produce microstructures without the need for molding and demolding steps. While stereolithography requires sophisticated optical set ups and it is based on layer-by-layer photopolymerization [11], conventional photolithography is a much more simpler technique that has been widely used for micropatterning in various fields. Typically, it is based on the crosslinking of a photoresist through a 2D photomask with a desired pattern upon exposure to collimated UV light. Photolithography has been traditionally used to produce microstructures with simple geometries on hydrogels of synthetic polymers such as poly(2-hydroxyethyl methacrylate) and polyethylene glycol (PEG) derivatives [12–14]. Shim *et al.* demonstrated the suitability of the photolithography technique for producing 3D microstructures with complex morphologies on hard photocurable resins that undergo free radical polymerization [15,16]. This was done by establishing controlled oxygen gradients within the polymerization set up. The Damköhler number, Da, (ratio of characteristic oxygen diffusion to oxygen depletion times) controls the polymerization reaction. When Da ~ 1, which can be achieved by including a source of oxygen in the polymerization system, objects with conical shapes can be formed [15,16].

In this study, we propose to exploit the potential benefits of reaction-diffusion mediated photolithography in the production of 3D cell culture substrates for biomedical applications. For this purpose, we demonstrate that by the proper tuning of the polymer composition and the fabrication parameters we can faithfully mimic the 3D architecture of the small intestinal epithelium in soft synthetic hydrogels. We used a system design in which the Damköhler number significantly changes with the distance to the polymerization light source. Through this strategy, we demonstrate that villi-like microstructures of anatomic and predictable dimensions can be easily fabricated using poly(ethylene glycol) diacrylate (PEGDA) polymer. The reaction-diffusion process is not straightforward when applied to create complex 3D structures on soft hydrogels from solutions with low polymer concentrations. In diluted solutions, the free radical polymerization proceeds longer, and the diffusion of the radicals into unexposed regions leads to uncomplete crosslinking at the boundaries between polymerized and unpolymerized material [17]. The crosslinking density affects the mechanical properties of the material, and therefore the cellular adhesion and response [18]. To gain control on cell-surface interactions, it is crucial to accurately control the properties at the boundaries. Copolymerization is an attractive technique as a route to functionalize polymers with tunable properties. The copolymerization of PEGDA with acrylic acid (AA) has been shown to tune hydrogel properties such as crosslinking density and swelling behavior [19,20]. In the presence of oxygen, AA affects the termination rate of the free radical polymerization [21], leading to a confinement of the crosslinking volume and therefore minimizing the tacky surfaces resulting from incomplete poplymerization. Moreover, the copolymerization of PEGDA with AA provides the material with carboxylic groups that allow the controlled immobilization of cell adhesive ligands. Synthetic polymers such as PEGDA have advantages over natural polymers. These include adjustable mechanical properties and non-biodegradability to withstand long term cell culture conditions [22]. However, PEGDA-based hydrogels are intrinsically nonadhesive for cells and their bioactive modification is essential for cell culture applications. Bioactive hydrogels are usually obtained by copolymerization with extracellular matrix (ECM)-based peptides or proteins that have been previously chemically modified with reactive groups such as acrylates [23,24]. In our approach, the copolymerization of PEGDA-AA allows the covalently immobilization of

unmodified ECM proteins and renders the material suitable for cell culture (Figure 1(a)). By adjusting the amount of AA, the ligand density on the material can be fine-tuned while preserving the soft mechanical properties of the hydrogels.

The 3D villi-like scaffolds were successfuly fabricated onto porous filter membranes allowing the monitoring standard functional properties of the intestinal cell barrier such as its integrity and permeability. Caco-2 cells seeded on the 3D scaffolds formed monolayers of differentiated enterocytes with transepithelial electrical resistance (TEER) values that were significantly closer to *in vivo* values than conventional cell monolayers. These results demonstrate that this moldless microfabrication technology is an easy-to-use tool that can faithfully replicate 3D microtopographies at the tissue level in soft hydrogels. It can provide cells with a more realistic microenvironment, including cell-to-matrix interactions and proper chemical and mechanical signaling, while remaining compatible with standard cell characterization techniques.

2. Materials and methods

2.1 Materials

Poly(ethylene glycol) diacrylate (PEGDA) (Mn 6000 g mol^{-1}), 2-Hydroxy-4′-(2-hydroxyethoxy)-2-methylpropiophenone (Irgacure D-2959) photoinitiator, (1-ethyl-3-(3-dimethylaminopropyl)carbodiimide hydrochloride) (EDC), N-Hydroxysuccinimide (NHS), Acrylic acid (AA) and Hank's Balanced Salt Solution (HBSS) were purchased from Sigma-Aldrich. Phosphate buffered saline (PBS) and BupH MES buffered saline were from ThermoFisher. Polydimethylsiloxane (PDMS) Sylgard 184 was from Dow Corning. Collagen type I, fibronectin and laminin were from Sigma-Aldrich. Fluorescein-isothiocyanate (FITC) dextran of 4 kDa (FD4) was from Sigma-Aldrich. Streptavidin Texas Red® was from ThermoFisher. Fluoromont-G mounting solution was from SouthernBiotech.

2.2 Fabrication of PEGDA-AA villi-like scaffolds

A chip fabricated with 1 mm thick PDMS stencil containing an array of pools on a black coated polystyrene support was used for hydrogel UV polymerization (Figure S1). Briefly, PDMS prepolymer was prepared at a ratio 10:1 w/w with the curing agent. The prepolymer solution was casted between two flat poly(methyl methacrylate) sheets spaced 1 mm apart and cured for 24 h at room temperature. Pools, either 6.5 or 10 mm in diameter, were punched, and two inlets and channels connecting them were carved, with a 1.5 mm punch and a scalpel, respectively, to introduce the hydrogel solution (Figure 1(b)). Silanized glass coverslips of 12 mm in diameter or Tracketch® polyethylene terephthalate (PET) membranes of 5 µm pore size (Sabeu GmbH & Co) were then used to cover the tops of the PDMS pools. Prepolymer solutions containing 6.5% w/v PEGDA, 0 to 1.2% w/v AA, and 1% w/v Irgacure D-2959 were dissolved in PBS at 65 ºC for 1 h, filtered and flown into the chip. Villi-like micropillars were fabricated by placing patterned photomasks on top of the glass coverslips or porous membranes. Photomasks had pattern designs consisting of arrays of circular UV-transparent windows 50 µm in radius at a density of 25 windows mm^{-2}. These were designed using AutoCAD software (Autodesk) and printed on acetate films (CAD/Art Services Inc.). Pattern dimensions were selected to match the structures found in small intestinal tissue [1,3]. UV light exposure was performed in a MJBA mask aligner (SUSS MicroTech), using a power density of 25 mW cm^{-2} measured at 365 nm wavelength (SUSS MicroTech). Prepolymer solutions were exposed for 60 to 220 s to form the micropillars. After UV exposure, unreacted polymer and photoinitiator were washed out with PBS. When required, hydrogel disc samples were also fabricated by light flood exposure, without photomask. Samples were kept submerged in PBS at 4 ºC for at least three days to reach equilibrium swelling. During the swelling period, PBS was exchanged every day to remove uncrosslinked polymer molecules. After swelling, cross-sections of microstructured hydrogels were obtained using a scalpel. Sample cross-sections were imaged by bright field microscopy using a Nikon Eclipse Ts2 instrument to determine their morphology and dimensions (Figure S2). The morphology of the microstructured scaffolds was also assessed by scanning electron microscopy (SEM). Samples were sequentially dehydrated in ethanol followed by critical point drying (K850, Quorum technologies). Samples were then imaged by SEM (NovaTM NanoSEM 230, FEI).

2.3 Assembly of PEGDA-AA hydrogels on modified Transwell® inserts

PEGDA-AA hydrogel scaffolds, fabricated on porous PET membranes, were mounted on standard 24-well polycarbonate Transwell® filter inserts (Corning Costar) using double-sided pressure-sensitive adhesive (PSA) rings (Adhesives Research) (Figure S3). The inserts form two compartments (apical and basolateral) that mimic the luminal and stromal parts of the intestinal tissue barrier. Briefly, the standard polycarbonate (PC) membrane from the Transwell® inserts was carefully removed with a scalpel and replaced by the PET membrane containing the hydrogel on top and then fixed by the double-sided PSA ring. Immediately after, pressure was applied for 15 min at RT to assure proper sealing. Then, a drop of sterile PBS buffer supplemented with 10% v/v penicillin/streptomycin and 1:500 Normocin (InvivoGen) was added on top of the hydrogels to prevent them from drying. Later, extra 200 µL and 600 µL of the same PBS buffer solution were added to the apical and basolateral Transwell® cavities, respectively, and the inserts were stored at 4 ºC until

further use. All the assembly process was performed under sterile conditions.

2.4 Characterization of PEGDA-AA hydrogels

The copolymerization of PEGDA-AA was characterized by Fourier-transform infrared spectroscopy (FTIR) in a Nicolet iS 10 instrument (ThermoFisher Scientific), using an ATR diamond and a DTGS detector. Hydrogel discs (12 mm diameter, 2 mm height.) were prepared from prepolymer solutions of 10% w/v PEGDA and AA concentrations ranging 0 to 1.2% w/v. Hydrogels were polymerized for 300 s to ensure full crosslinking. All samples were rinsed with Milli-Q water and allowed to dry for 24 h in a vacuum desiccator before being analyzed by FTIR. Scans in the range of 500-4000 cm^{-1} were performed with a resolution of 4 cm^{-1}. Spectra reported correspond to the average of 16 scans. To determine the effects of acrylic acid on the mechanical properties of the samples, hydrogel discs (10 mm diameter, 2 mm height) were obtained by polymerizing solutions of 6.5% w/v and AA concentrations ranging from 0 to 1.2% w/v for 150 s. Hydrogels were allowed to reach equilibrium swelling for 3 days in PBS. After swelling, sample diameters differed among them, so swollen hydrogels were punched to obtain 10 mm diameter samples. Stress-strain curves in compression were recorded with a Zwicki Z0.5TN machine (Zwick-Roell). To avoid drying of hydrogels, a few drops of PBS were added just before the beginning of each measurement. Stress-strain curves were obtained with a speed of 2 mm min^{-1}, limiting the strain rate to 1% min^{-1} and the maximum strain to 10% [25]. An initial load of 5 mN was applied to promote the adequate contact between the hydrogel and the compression plates. The Young's modulus of the samples was calculated as the slope of the linear part of the stress-strain curves. Since the height of each hydrogel was also recorded from the mechanical testing, this was used to determine the swelling ratio [23]. The height of each hydrogel after swelling was compared with its height immediately after fabrication.

2.5 Functionalization of PEGDA-AA villi-like scaffolds with cell adhesive proteins

After swelling, PEGDA-AA hydrogels were functionalized with laminin or collagen type I via a EDC/NHS mediated coupling. Specifically, the carboxylic groups of PEGDA-AA hydrogels were activated with a solution containing 25 mM EDC and 50 mM NHS in MES buffer (0.1 M, pH 4.7) for 30 min at room temperature. Hydrogels were then washed with PBS and further reacted with 0.01% w/v collagen type I or 50 µg mL^{-1} laminin solution overnight at 4ºC. The hydrogel activation and further protein functionalization were characterized by FTIR as previously described.

To determine the effects of AA concentration on the ligand density of the hydrogels, discs (10 mm diameter, 1 mm height) were prepared from solutions of 6.5% w/v PEGDA and AA

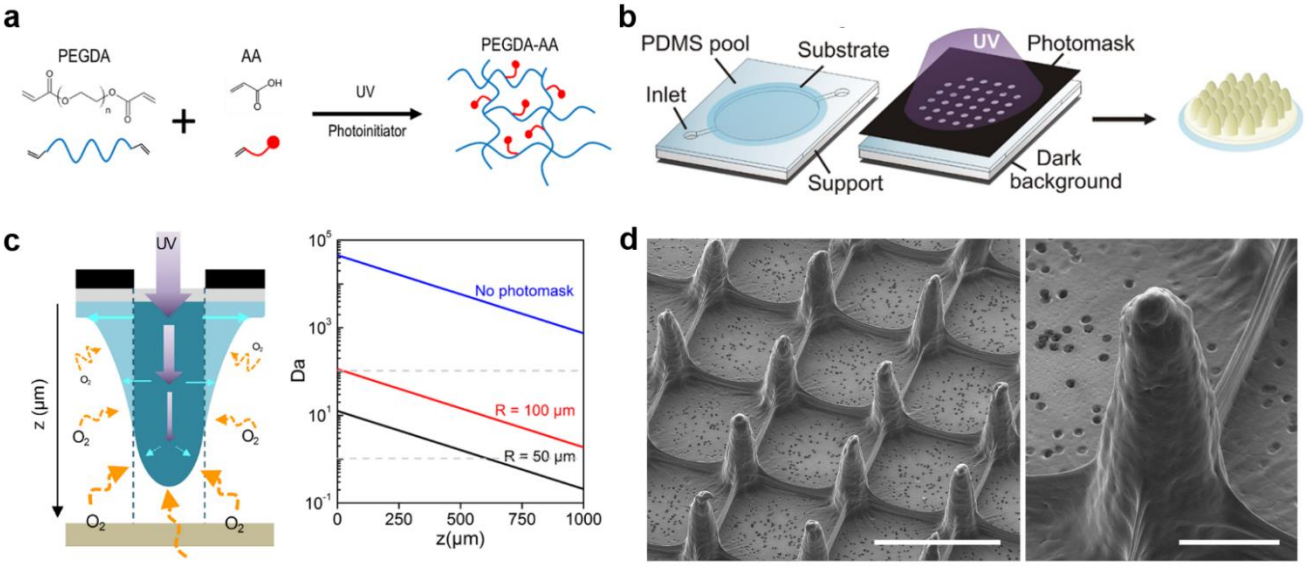

Figure 1. Dynamic photopolymerization approach for single-step, moldless microfabrication of villi-like hydrogel scaffolds. **(a)** Scheme for copolymerization of PEGDA and acrylic acid (AA) in the presence of the photoinitiator with UV radiation. **(b)** Schematic illustration of the single-step photolithography process. The substrate can be a cover glass or a porous membrane **(c)** Oxygen effects create dynamic polymerization conditions on the fabrication process. Left: Schematic illustration of the convolution of the attenuation of light (violet arrows) and the diffusion of oxygen along the vertical axis *z*. Dashed line indicates the boundary of the photomask window. Right: Plot of Damköhler number as a function of the vertical axis *z* varying the photomask window diameters. **(d)** SEM images of hydrogel microstructures fabricated on a porous membrane (pores are seen at the base due to sample preparation process). Left: Scale bar = 200 µm. Right: Scale bar = 100 µm.

concentrations ranging from 0 to 0.6% w/v upon 150 s of UV irradiation. Samples were activated with EDC/NHS as described above and functionalized with Streptavidin Texas Red® (0.05 mg mL^{-1}). Hydrogels were mounted with Fluoromont-G and imaged with a Leica TCS SPE confocal microscope. Discs prepared with a AA concentration of 0.9% w/v were used to test the stability of the protein functionalization to rinsing and storage time. Samples were rinsed one to 10 times and their fluorescence was evaluated by fluorescence microscopy. Analogously, samples were stored at 4 ºC in PBS for 1 to 7 days, exchanging PBS solution every day, and their fluorescence was monitored over the storage time.

2.6 Cell culture

Caco-2 cells (ATCC® HTB-37™) from passages 74 to 80 were expanded and maintained in 75 cm^2 flasks in high glucose DMEM (Gibco, Thermofisher), supplemented with 10% v/v fetal bovine serum (FBS) (Gibco, Thermofisher), 1% v/v penicillin/streptomycin (Sigma-Aldrich) and 1% v/v of non-essential amino acids (Gibco, Thermofisher). Cells were maintained in an incubator at 37ºC and 5% CO_2, changing medium every two days and passaged weekly. Cells were seeded either on the hydrogels fabricated on coverslips at a density of $5x10^5$ cells cm^{-2}, or on the hydrogels mounted on the modified insert at a density $2.5x10^5$ cells cm^{-2}. The surface area of the villi-like hydrogels was estimated using the formula for the area of a truncated cone without base (see Supporting Information). Control experiments were performed on cells cultured in standard 24-well polycarbonate Transwell® filter inserts (0.33 cm^2 growth area, 0.4 μm pore size) at a density of $1.5x10^5$ cells cm^{-2}. Cells were cultured for 21 days, exchanging media every other day.

2.7 Barrier integrity assessment

The intestinal epithelium forms a hihgly selective tissue barrier. The tissue barrier integrity formed by the Caco-2 cells cultured on the villi-like hydrogel scaffolds was monitored during cell culture using an standard approach. Hydrogel samples fabricated on porous membranes were mounted on Transwell® inserts and Caco-2 cells were cultured on them. The transepithelial resistance (TEER) between the two compartments formed by the inserts was measured every other day with a EVOM2 Epithelial voltohmmeter with STX3 electrode (World Precision Instruments). Measured resistance values were corrected by substracting the resistance of the membrane and the hydrogel. TEER values were normalized by the total surface area of the cell monolayer, which significanlty differ from 2D and 3D cell culture systems. After 21 days, drug permeability studies using FITC-dextran of 4.4 kDa (FD4) as a tracer were performed to monitor the paracellular transport through the tight junctions. Briefly, cells were carefully washed with HBSS buffer prior to adding 200 μL of test compound at a concentration of 0.5 mg mL^{-1} to the apical and 600 μL of HBSS buffer to the basolateral compartments. Throughout the experiment, cells were incubated at 37 ºC on a horizontal shaker at 50 rpm. Samples were withdrawn from the basolateral compartment at specific time points during 3 h followed by buffer replacement. Retrieved samples were then transferred to a 96-well black plate and their fluorescence was read on the Infinite M200 PRO Multimode microplate reader (Tecan) at 495 nm excitation and 520 nm emission wavelengths. The apparent permeability coefficient (P_{app}) was calculated by the following equation,

$$P_{app} = \frac{dQ}{dt} \cdot \frac{1}{A \cdot C_0}$$

where dQ/dt is the flux, A the area of the filter insert, and C_o the initial donor concentration of the test compound. The steady state flux was used for calculation of the P_{app} value. All experiments were done in triplicate. As a control, the flux through the hydrogels without cells was also measured to assure that the hydrogel was not limiting the permeability of the tracer.

2.8 Cell polarization assessment

Cells on the intestinal epithelium are characterized by their columnar shape and polarization, with the apical and basolateral compartments separated by tight junctions. Cell polarization was studied through the immunostaining of nuclei, filamentous actin (F-actin), and epithelial cell markers (ZO-1, β-catenin, and villin). After 21 days of culture, cells were fixed with 10% neutral buffered formalin solution (Sigma-Aldrich) at RT for 30 min, permeabilized with 0.5% Triton-X and blocked with 1% bovine serum albumin (BSA) and 3% donkey serum. Primary antibodies were used against ZO-1 (ab190085, Abcam, UK) (2 μg mL^{-1}), β-catenin (ab2365, Abcam) (5 μg mL^{-1}) and villin (ab201989, Abcam) (1 μg mL^{-1}). The incubation was performed for 2 h at RT and overnight at 4°C. Then, samples were incubated with secondary antibodies and/or Alexa Fluor® 568 Phalloidin (ThermoFisher Scientific) for 2 h at RT. Anti-goat Alexa 568 (A11057, ThermoFisher Scientific), anti-rabbit Alexa 647 (Jackson Immunoresearch) and anti-mouse Alexa 488 (A21202, ThermoFisher Scientific) were used at 2 μg mL^{-1}. Finally, samples were incubated with a 1:5000 dilution of DAPI (ThermoFisher Scientific) for 15 min.

Cell polarization was also assessed by analyzing nuclei elongation and orientation with respect to the surface of the villi-like microstructures. Confocal microscopy images of cells cultured for 21 days on either villi-like scaffolds or conventional Transwell® inserts were used for this purpose.

Results were compared with data obtained from images of histological cross sections of human small intestine [26]. Villi-like hydrogels were mounted on a 1 mm high PDMS holder to preserve microstructures morphology during image acquisition. Samples were imaged using confocal laser-scanning microscopes (TCS SPE or SP2, Leica Microsystems), acquiring z-stacks at 1 µm intervals. Images were processed by Image J software [27]. The image threshold was adjusted to individually identify cell nuclei and surface contour. Then, images were converted to binary values and nuclei were fitted to ellipses. Nuclei elongation was determined as the ratio between the major and the minor ellipse axis. Nuclei orientation with respect to the surface was computed by cell orientation index, which ranges between 1, when the major ellipse axis are normal to the surface (polarized cells), and -1, when they lay parallel to the surface (non polarized cells).

2.9 Data analysis and statistics

Graphs were plotted using OriginPro 8.5 software. In the case of normal distributions, differences between groups were compared using ANOVA. Non-parametric analyses were performed using the Mann-Whitney U and Kruskal-Wallis tests. The tests performed are specified in the respective figure legends. Differences were considered statistically significant when $p < 0.05$.

3. Results

3.1 Controlled growth of high-aspect ratio, villi-like microstructures on soft hydrogels

Free radical polymerization can produce polymeric microstructures with complex and well-defined shapes by controlling the dynamics of the polymerization reaction and establishing oxygen gradients within the system [14–16]. Molecular oxygen inhibits radical induced polymerization because of its high reactivity with radicals, forming peroxide molecules that terminate the reaction [28]. For polymerization to take place, the concentration of oxygen needs to be locally depleted, so monomers can successfully compete with molecular oxygen for the scavenging of the initiator radicals [28]. If the system has a source of oxygen, this will diffuse towards the regions with lowered concentrations. When the timescale of oxygen diffusion is comparable to that of oxygen depletion produced by the termination reaction, the photopolymerization will stop, even if it has already been initiated [29]. Because of high surface-to-volume ratios, the inhibition of photopolymerization reactions is aggravated on the microscale [14]. To account for the relevance of oxygen diffusion within such systems, the so-called Damköhler number, Da, can be used. Da accounts for the ratio between the characteristic timescales involved in oxygen diffusion and oxygen depletion processes [15,16]. The characteristic oxygen diffusion time, τ_{diff}, depends on the oxygen diffusion coefficient within the polymer, D_0, and the size of the microstructures to be fabricated, which is defined by the radius of the transparent windows of the 2D photomask, R. The timescale of oxygen depletion, τ_{depl} can be estimated from the initial oxygen molar concentration in the solution, $[O_2]_0$, and the rate of radical formation, which depends on the photoinitiator properties φ (quantum yield of radical production) and ε (molar extinction coefficient), the photoinitiator molar concentration [PI] and the intensity of UV light I [15]. Da can be then calculated as:

$$Da = \frac{\tau_{diff}}{\tau_{depl}} = \frac{R^2/D_0}{[O_2]_0/\varphi\varepsilon[PI]I}$$

Depending on the Da value, Shim *et al.* [15] identified three growth pathways for polymeric microstructures. When Da >>1, growth does not depend on oxygen diffusion, the diameter of the microstructures is always equal to the transparent windows of the photomask, and the height of the microstructures can be controlled by the UV light irradiation time. When Da ~ 1 and the system is closed to oxygen, the microstructures will grow in laterally along the central axis of the transparent windows while maintaining height during growth (limited to the thickness of the container of the polymer solution). When Da ~ 1 and the system is open to oxygen on one of its surfaces, conical microstructures that maintain their height during growth are obtained [15,16]. In our experimental set-up (Figure 1(b)), the height of the container is significant. Due to the absorbance of light intensity by the photoinitiator, which can be estimated from the Beer-Lambert law, Da will change along the vertical axis (distance to the ligth source), z, as:

$$Da\,(z) = \frac{R^2/D_0}{[O_2]_0/\varphi\varepsilon[PI]I \cdot exp(-2.303\varepsilon[PI]z)}$$

For masks of R = 50 µm, a value that matches the anatomic dimensions of small intestinal villi microstructures, PEGDA hydrogels (D_0 = 1 x 10^{-10} m^2s^{-1}, $[O_2]_0$ = 1 mol m^{-3}), [14] maximum light intensity (centered at λ = 313 nm), I = 9.75·10^{-4} mol $m^{-2}s^{-1}$, and 1% w/v of Irgacure 2959 solution as photoinitiator (φ = 0.29, and ε (λ = 313 nm) = 40 m^2 mol^{-1}) [30], Da significantly changes with *z* (Figure 1(c)). Because our set-up is open to oxygen due to the PDMS pools and polystyrene support, distinguishable growing pathways were expected for different *z* values. However, while the absence of photomask rapidly produced the full polymerization of the polymer solution (Da ~ 10^4 for containers 6 mm in diameter),

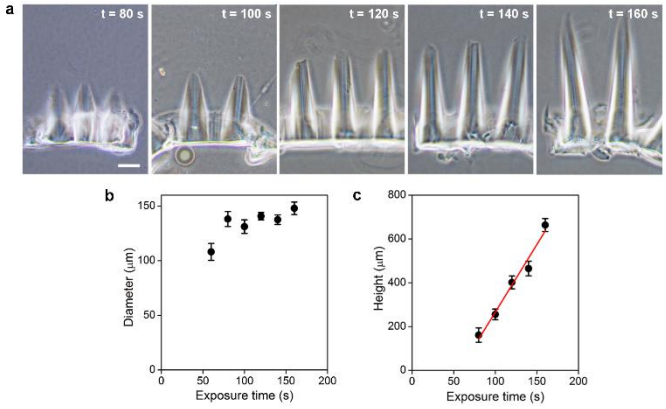

Figure 2. Effect of exposure time on microstructure base diameter, height and morphology. **(a)** Cross-sections of villi-like hydrogel scaffolds fabricated with 6.5% w/v PEGDA and 0.3% (w/v) AA and exposed for 80 to 160 s. For characterization purposes samples were produced on glass coverslips, so a flood exposure of 15 s was performed to hold them together. **(b,c)** Hydrogel total height and tip diameter as a function of exposure time. Mean ± SD, n > 12. Scale bar = 100 µm

the presence of the photomask with 50 µm radius light windows produced finger-like micropillars of high aspect-ratio (Figure 1(d)). The height of the micropillars can be controlled by tuning a single parameter, the exposure time and micropillars up to 600 µm, corresponding to aspect ratios 1:6 (width: height) can be obtained (Figure 2). The diameter of the microstructures obtained was consistent with the dimensions of the photomask windows, and the microstructures had blunt tips like those found in the small intestinal tissue. We attribute these complex geometries to a mixture of the growth pathways defined by Shim et al [15]. Bottom-to-top growth seems to dominate for distances close to the lamp (Da ~ 10), so the microstructures grow in height while keeping their lateral dimensions to the full extent of the transparent windows of the mask. At greater distances, Da ~ 1, and conical shapes appeared. For distances above 800 µm, polymerization was not experimentally observed, probably because Da < 1.

3.2 PEGDA-AA copolymers allow fine tuning of photopolymerization reaction and ligand density

Epithelial cells forming tissue barriers need to be polarized to exert their protective function. They possess an apical region facing the lumen, and a basolateral membrane facing the organ side. Cell polarity is guided by the structural features of the tissue and, in particular, by the epithelial basement membrane [31–34]. Collagen-coated membranes as well as collagen hydrogels are good supports for epithelial cell polarization [9,35]. However, collagen matrices degrade over time, do not allow long-term experiments [36], and are not photocrosslinkable. Synthetic hydrogels based on PEG acrylates are an attractive alternative to natural hydrogels. PEGDA hydrogel networks are biocompatible and chemically versatile, allowing the incorporation of cell adhesive proteins and peptides [14]. When copolymerized with AA, PEGDA-AA networks have been used in cell culture applications, forming composite hydrogels with collagen [37]. In addition, PEGDA-AA copolymers have also been employed as substrates in biosensing applications [38].

We copolymerized PEGDA with different amounts of AA ranging from 0 to 1.2% w/v. The incorporation of AA was assessed by the presence of a strong absorbance peak at 1576 cm^{-1} in the FTIR spectra, which is attributed to the asymmetric vibration of carboxyl groups, (Figure S4) [39]. Factors such as viscosity of the solution or the presence of oxygen may affect the kinetics of the reaction and the polymerization rate. The viscosity of PEGDA-AA solutions was not significantly different for solutions with increasing AA concentration (Figure S5). Therefore, we can presume that the diffusion of the species was not significantly altered. In the presence of oxygen, the termination rate for PEGDA was reported as 2.5 x 10^3 $m^3mol^{-1}s^{-1}$ [14], while the termination rate for AA polymerization was reported as 3.2 x 10^5 $m^3mol^{-1}s^{-1}$ [21]. This increase in the termination rate had an effect on the shape of the microstructures. With increasing AA concentration, significantly shorter microstructures were obtained for identical exposure times (Figure 3(a)).

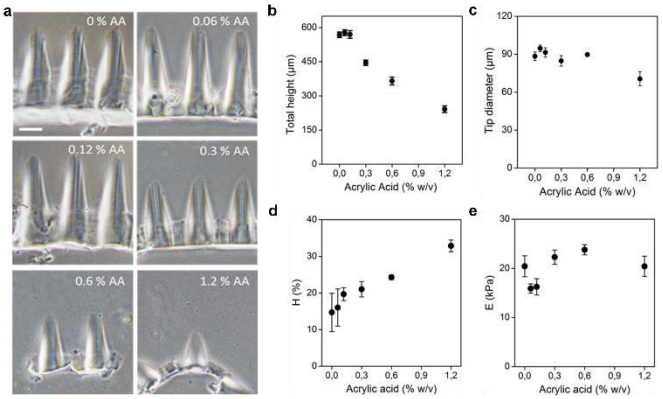

Figure 3. Effect of acrylic acid content on the polymerization reaction and the morphology of resulting microstructures. **(a)** Cross-sections of villi-like hydrogel scaffolds fabricated with 6.5% w/v PEGDA and varying concentrations of AA exposed for 120 s. For characterization purposes samples were produced on glass coverslips, so a flood exposure of 15 s was performed to hold them together. **(b,c)** Hydrogel total height and tip diameter as a function of AA concentration. **(d,e)** Hydrogel swelling ratio H and Young's modulus (E) of PEGDA-AA hydrogels as a function of AA content. Mean ± SD, n > 5. Scale bar = 100 µm.

The total height of the pillars decreased from around 600 μm to 240 μm when AA was increased to 1.2% (w/v) (Figure 3(b)). The finger-like shape of the structures was maintained, but the tip became sharper, especially with the highest AA concentration (Figure 3(c)). Then, the production of samples with microstructure dimensions compatible with those found in the villi of small intestinal tissue are conditioned by the concentration of AA.

The incorporation of AA allowed the fine tuning not only of the morphology but also of the physicochemical properties of the hydrogel [19]. The hydrogel swelling ratio increased significantly with the percentage of AA within the copolymer (Figure 3(d)). However, within the range of concentration assayed, no significant differences on the compression elastic modulus of the samples were observed (Figure 3(e)). All the elastic modulus values measured for the samples were consistent with values reported for intestinal mucosa [40,41]. Trends observed in both swelling and elastic modulus values are in agreement with those previously reported for PEGDA-AA copolymers [19,42]. The increased swelling can be related to the increased amounts of carboxyl groups with increased concentrations of AA. Carboxylic groups have higher polarity than the ester groups in PEGDA, and draw more water into the crosslinked polymer network [42].

Copolymerization with AA allowed for the covalent binding of extracellular matrix proteins to the hydrogel through a carbodiimide-mediated crosslinking reaction in the presence of carboxyl groups. Samples were activated by EDC/NHS and further incubated in a protein solution (Figure 4(a)). FTIR spectra show that, after activation, the carboxylate peak of the AA, located at 1576 cm^{-1}, disappeared due to the incorporation of NHS molecules through amide bonds (Figure 4(b)). Two peaks around 1800 cm^{-1} appeared and these corresponded to the presence of NHS [43].

After incubation with collagen I, amide bands centered at 1550 and 1650 cm^{-1} were visible [44], together with a significant decrease in the absorbance of the NHS peaks. Fluorescent measurements obtained after incubation with streptavidin Texas Red® revealed that the functionalization was homogeneous along the microstructures (Figure 4(c)). The amount of immobilized protein increased with the amount of AA in the polymer solution (Figure 4(d)), which agrees with previously published data [38]. Fluorescent measurements performed after repeated washing of the sample and during a 7 days storage period revealed the covalent nature of the protein binding, as no significant differences in the fluorescence intensity levels were found after both procedures (Figure S6). Therefore, this methodology allows tuning the ligand density of the hydrogel by use of a single parameter, the concentration of the AA in the initial polymer solution. As an added feature, within the concentration of AA investigated, ligand density can be finely tuned without significantly affecting the mechanical properties of the sample.

Taking these results altogether, we selected PEGDA-AA with an AA concentration of 0.3% w/v as the most suitable material to seed intestinal epithelial cells. This selection was based on the material that displayed the maximum number of covalent ligands while attaining the required dimensions for the villi microstructures (at least 400 μm in height).

3.3 Caco-2 cells form a polarized monolayer covering the villi-like microstructures fabricated in PEGDA-AA upon collagen functionalization

PEGDA-AA hydrogel scaffolds were fabricated on glass coverslips and were functionalized with either laminin or collagen, since these are the main components of the epithelial basement membrane. Caco-2 cells were then seeded on top of them. Both laminin and collagen scaffolds allowed cell growth, although only scaffold surfaces functionalized with collagen were consistently covered with a cell monolayer within 48 h of culture. Time-lapse videos recorded 4 h after seeding revealed that most of the cells were initially located at the base of the villi microstructures and they formed a

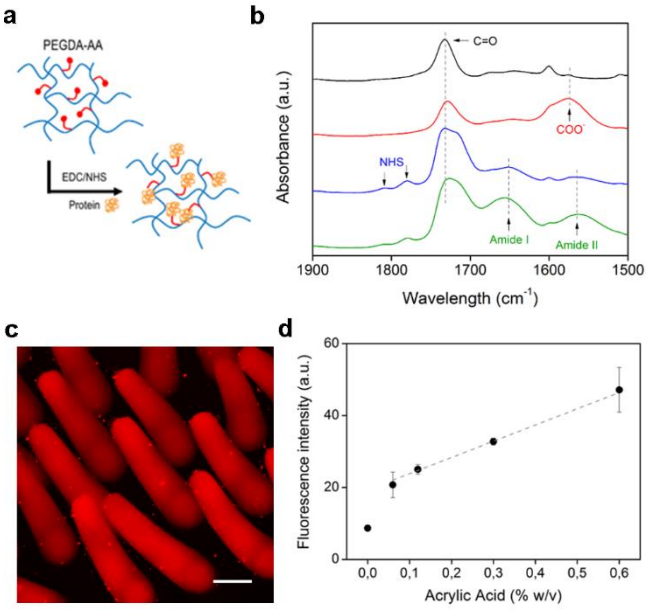

Figure 4. Functionalization of PEGDA-AA hydrogels with ECM proteins. **(a)** Scheme of the hydrogel functionalization through the EDC/NHS coupling reaction. **(b)** Detailed FTIR spectra acquired after each step of the functionalization process. PEGDA hydrogel in black, PEGDA-AA hydrogel in red, EDC/NHS activated hydrogel in blue, and collagen-functionalized hydrogel in green. **(c)** Confocal projection of microstructured PEGDA-AA hydrogel functionalized with Streptavidin-Texas Red. **(d)** Fluorescence intensity of hydrogels as a function of AA concentration after functionalization with Streptavidin-Texas Red. Mean ± SD, n = 5. Scale bar = 100 μm.

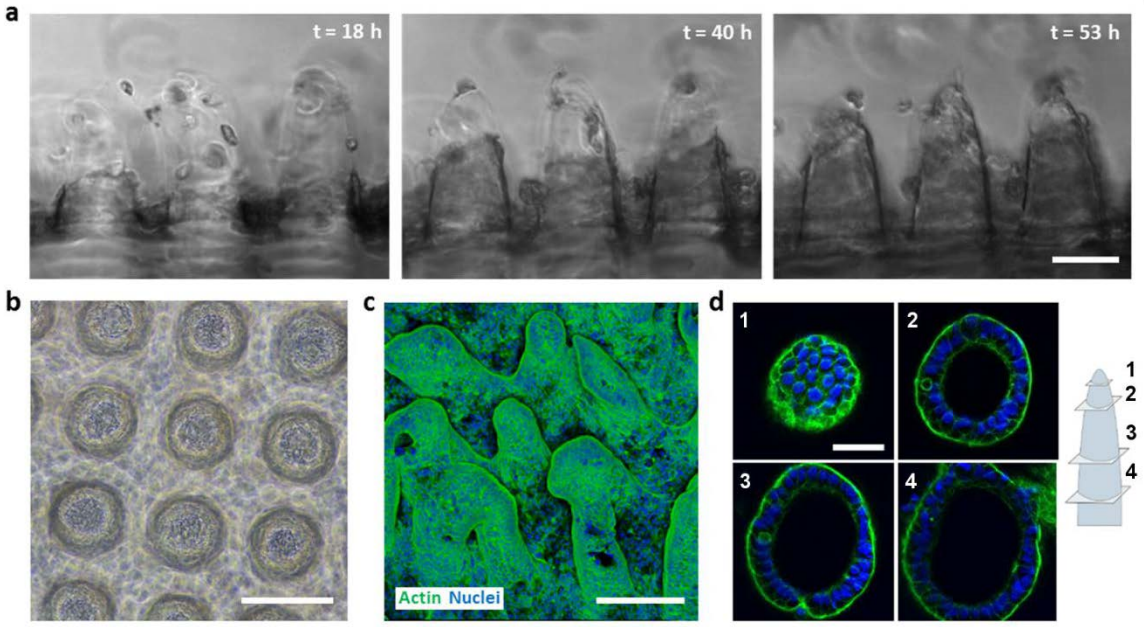

Figure 5. Caco-2 cell culture on PEGDA-AA villi-like 3D scaffolds. **(a)** Sequential frames from time-lapse microscopy of Caco-2 cells migrating upwards along the PEGDA-AA micropillars. **(b)** Top view brightfield image and **(c)** confocal projection of Caco-2 cells grown on the 3D scaffolds for 21 d. **(d)** Detailed cross-sections of a representative Caco-2 cell covered micropillar. Nuclei are shown in blue and F-actin is shown in green. Scale bars: a = 150 μm; b and c = 200 μm; d = 50 μm.

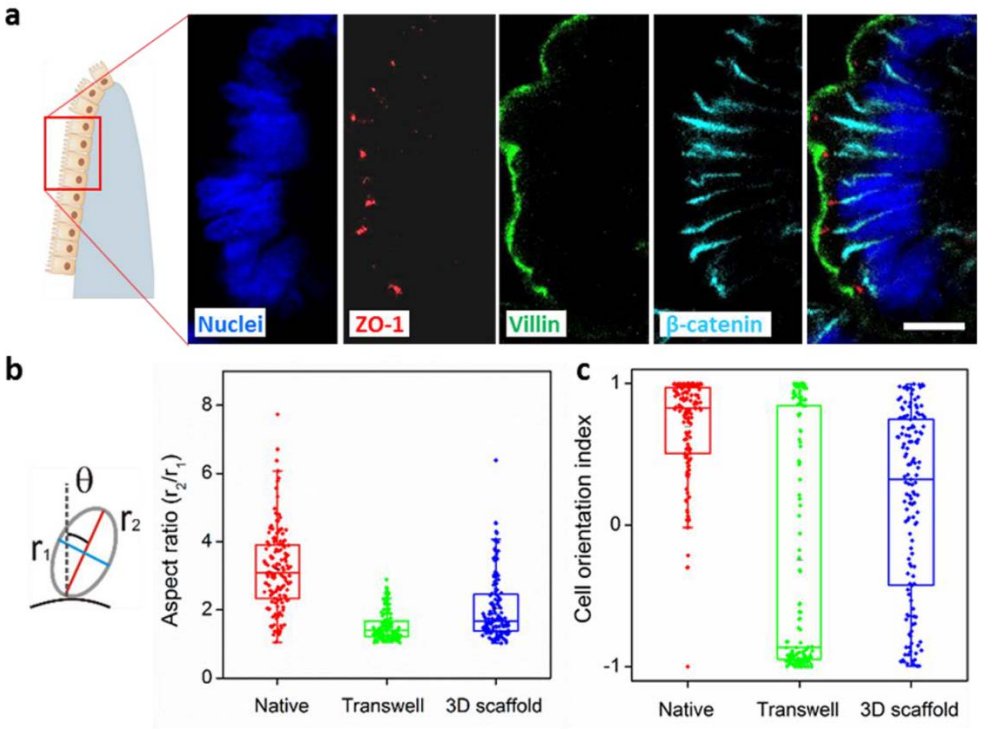

Figure 6. Caco-2 cell polarization characterization. (a) Confocal images of Caco-2 monolayer formed on the 3D scaffold showing the nuclei in blue, ZO-1 in red, villin in green and b-catenin in cyan. (b, c) Nuclei elongation and orientation analysis. The nuclei aspect ratio and cell orientation index from Caco-2 cells grown for 21 d in conventional Transwell® or in the PEGDA-AA villi-like 3D scaffolds are compared with the nuclei from a histological cross-section of a native small intestine [26]. For the boxplots, the bar shows the median, and the upper and lower boxes represent the 75% and 25% of the data, respectively. The whiskers extend to the 5% and 95%. n = 140. Scale bar = 10 μm.

migrating front that climbed up the walls of the villi until the structure was fully covered (Figure 5(a), Supplementary movie M1). After 14 days, cells displayed morphological characteristics of a polarized columnar epithelium along all heights of the villi microstructures, with the presence of F-actin accumulation at the apical-side of the cells (brush border) (Figure 5(b-d)). After 21 days of culture, cells expressed epithelial cell markers such as villin, which characterize microvilli formed in the apical side, zonula occludens-1 (ZO-1), found in tight junctions, and β-catenin, which is found in the basolateral cell membranes, at the proper locations (Figure 6(a)).

Polarized cells in columnar epithelia are also characterized by elongated cell nuclei, which are oriented perpendicular to the tissue surface.[1] Therefore, cell polarization was also assessed by analysis of nuclei morphology and nuclei orientation with respect to the surface of the microstructures. These data were then compared to data obtained from histological images of villi in human tissue and cells cultured on standard Transwell® membranes. Cell nuclei were significantly more elongated on the cells grown on the 3D scaffolds compared to the cells grown on porous polycarbonate membranes (Figure 6(b)). In addition, cell nuclei were also oriented closer to surface perpendicularity on the 3D scaffolds than on cells cultured on conventional substrates (Figure 6(c)). Overall, cells displayed improved polarization morphology on the 3D scaffolds when compared with standard culturing methodologies based on porous filter membranes in Transwells®. Similar experiments were performed with the MDCK cell line, which also successfully formed a monolayer after 14 d of culture (Figure S7), thus extending the usefulness of PEGDA-AA copolymers to other epithelial cell models.

3.4 Caco-2 cells form a functional tissue barrier on the synthetic PEGDA-AA villi-like microstructures

PEGDA-AA hydrogel scaffolds were fabricated on porous PET membranes and mounted on standard Transwells® (Figure S3). Membranes with pore sizes of 5 µm diameter were used to minimize undesired absorbance and scattering effects interfering with the polymerization process that were observed with membranes of smaller pore size and/or polycarbonate material. When using these membranes and comparing them to samples fabricated on glass coverslips used for characterization purposes, the light intensity through the membrane was reduced by 40%. This attenuation of the UV light intensity significantly affected the microstructure morphology. For the same exposure time, the micropillar height was reduced from 400 to 140 µm (Figure 7(a)).

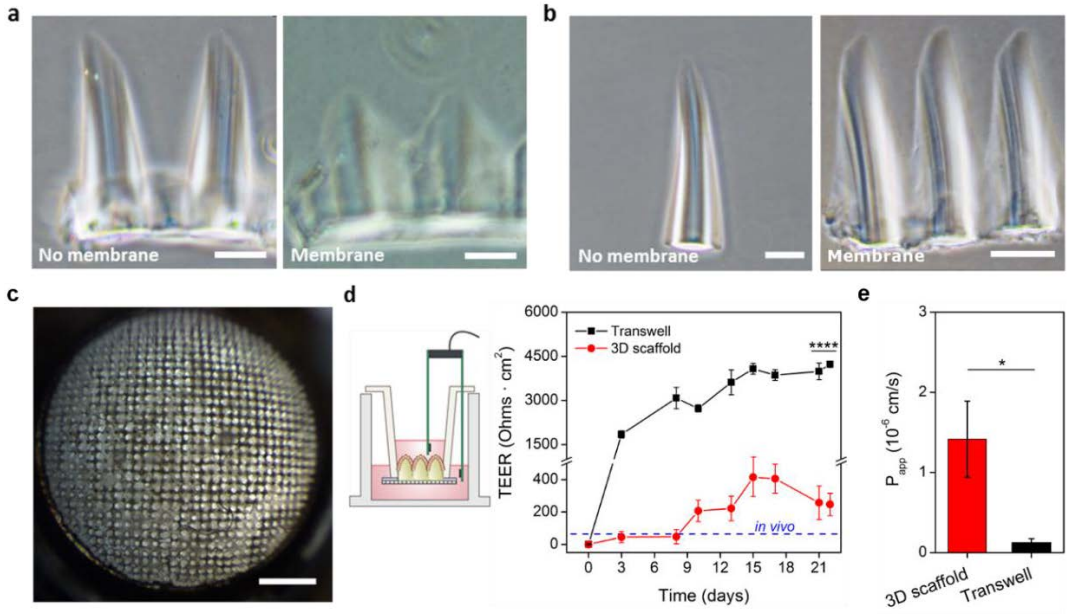

Figure 7. Assembly of 3D scaffolds on modified Transwell® inserts. (a, b) Effect of PET membrane absorption on microstructure morphology compared to glass coverslips used for characterization purposes. PEGDA-AA hydrogels were exposed (a) 120 s for the pillars (plus 15 s of flood exposure to hold pillars together), or (b) 205 s in a single exposure, with or without PET membrane. With the PET membranes, self-standing and joined pillars were obtained in a single fabrication step. (c) Top view of the Caco-2 cell culture on the PEGDA-AA villi-like 3D scaffold assembled on a modified Transwell® insert. (d, e) TEER measurements and permeability of FITC-dextran 4 kDa in epithelial monolayers grown on conventional Transwell® (black) or in PEGDA-AA villi-like 3D scaffolds (red). Mean ± SD, n = 4. Scale bars: a and b = 100 µm; c = 1 mm.

Therefore, the fabrication parameters were optimized to account for the membrane absorption. Due to the light scattering effects produced by the membrane, scaffolds containing micropillars 475 ± 23 μm high joined through a supporting base, were obtained in a single exposure process (Figure 7(b)).

TEER measurements provide information about the integrity of the monolayer of polarized cells and were recorded as a function of the cell culture time. TEER values steadily increased with culture time for both the cells seeded on the 3D scaffolds and the standard monolayers cultured on porous filter membranes (Figure 7(c-d)). This behavior is attributed to the proper formation of a monolayer that is functional as a tissue barrier. TEER values for the cells cultured on the 3D scaffolds were significantly lower than those for the Transwell® control for all of the time points tested. In particular, at 21 days of culture, TEER values of 3D scaffolds were reduced by 10-fold with respect to flat monolayers on porous filter membranes, suggesting that the tight junctions are affected by the 3D topography and on the 3D scaffolds their behaviour approaches *in vivo* measurements.. The permeability of the paracellular model compound FD4 was significantly higher in the 3D scaffolds (Figure 7(e)). The PEGDA hydrogel did not influence the Papp measurements. PEG-based hydrogel scaffolds are characterized by a high porosity and hydrophilicity. Specifically, hydrogels fabricated with 5% (w/v) PEGDA 6 kDa have an average mesh size of 14 nm [45], therefore the scaffold does not represent a barrier to diffusion of molecules such as FD4, with an average diameter of 2.8 nm.

These results are consistent with previous 3D models of the intestinal epithelium [36,46,47], where cells grown on 3D surfaces showed increased leakiness and had TEER values closer to those found *in vivo*.

4. Discussion

Tissue equivalents providing cells with a more physiologically relevant microenvironment are in demand for both clinical and *in vitro* testing applications. It is widely recognized that including cell-to-cell and cell-to-matrix interactions, together with proper chemical and mechanical signaling, would benefit the functionality of such constructs [4,5]. However, the complex 3D architectures found in tissues are neglected in most engineered tissues. One of the main reasons limiting the use of 3D tissue microtopography when studying epithelial tissues is the difficulty in producing 3D objects of complex shapes made of soft materials (E < 50 kPa). Conventional microfabrication techniques are ill suited to deliver structures with high aspect ratios and curvature, such as those forming natural epithelial tissues. Methods such as replica molding, 3D printing and photopolymerization have been used to produce scaffolds with 3D topographies for biomedical applications [48,49]. To obtain roundish geometries by replica molding requires complex fabrication design, while avoiding problems demolding soft hydrogels involves the use of intermediate molds and multiple fabrication steps [9]. 3D printing methods are ideal candidates to fabricate complex shapes but are limited in resolution, and require the use of sacrificial materials for manufacturing soft structures [50,51]. Photopolymerization can be used to produce 3D shapes in soft materials by methods such stereolithography or two-photon lithography, but it requires the use of expensive instrumentation [11,49]. Photolithography using 2D photomasks is a low-cost, single-step and parallel fabrication technique that is standardized in the microelectronics field. When applied to materials that undergo radical polymerization, complex shapes can be fabricated by controlling the dynamics of the polymerization reaction through oxygen gradients [15,16]. In this study, we explored this concept further and applied it to a biomedical setup. Through this process we obtained, in a single and moldless fabrication procedure, microstructures of very soft hydrogels (E ~ 20 kPa) with high aspect ratio (1:6), roundish tip contours, and the anatomical dimensions of small intestine villi. The simplicity and low-cost of the fabrication technique, which only requires a UV lamp and inexpensive acetate photomasks, makes it easily compatible with well-established cell culture systems such as Transwell® inserts. Furthermore, this fabrication process can be easily parallelized, obtaining multiple scaffolds in one single exposure.

PEG-based hydrogels have been extensively investigated as synthetic scaffolds in tissue engineering applications [22]. PEG acrylates photocrosslink in aqueous solutions, forming hydrogels. PEG-derived hydrogels do not withstand protein adsorption, so they are functionalized with peptides or extracellular matrix proteins to allow for cell adhesion and growth. Copolymerization with AA during the crosslinking reaction is an easy method to introduce anchoring groups for cell-adhesive biomolecules. Control of PEG and AA content on properties such as swelling, hydrophilicity and pH sensitivity can be precisely adjusted [19,20]. We observed that the amount of AA had a strong impact on the photopolymerization reaction and can be used as a parameter to modify the polymer growth regime and, ultimately, the shape and dimensions of the microstructures. We have also determined that, within the range of AA concentrations tested, the density of protein ligands incorporated into the hydrogel can be controlled by the AA concentration while leaving the mechanical properties of the structure unaltered. This provides an ideal platform to decouple the influence of mechanical and chemical cues on cell behavior.

In vitro models of the human small intestinal epithelium are routinely used to determine the absorption and metabolism of drugs and these models play a crucial role in preclinical drug

development. Conventional systems are based on 2D Caco-2 cell monolayers grown on permeable membranes, and these systems are accepted as standard by pharmaceutical companies and regulatory authorities. However, they lack physiological resemblance and this could lead to incorrect predictions about drug permeability [52]. Numerous attempts, using a variety of materials, have been made to diminish the gap between the conventional 2D models and human intestinal epithelium. Porous poly(lactic-*co*-glycolic) acid (PLGA) scaffolds have been micromolded into villus geometries with high aspect ratios [47,53]. These scaffolds promote epithelial differentiation and absorption [54] but PLGA has mechanical properties outside of the physiological range (E ~ 1-2 GPa). On the other hand, soft collagen hydrogels can be fabricated using a combination of laser ablation and sacrificial molding technique [9,36,46] or by micromolding using PDMS moulds [10]. However, these collagen scaffolds are degraded before the cell culture period needed for complete cell differentiation (usually 21 days for Caco-2 cells). In addition, collagen scaffolds are unsuitable for testing the permeability of rapidly absorbed hydrophobic drugs [36]. The use of synthetic PEG-based hydrogels overcomes limitations on cell culture time, so long-term cell culture experiments are feasible. In addition, photocrosslinkable PEGDA-AA hydrogels offer great versatility to match the cellular requirements of different epithelial tissues. PEGDA chain size and concentration can be used to tune the mechanical properties of the hydrogel within a wide range (E ~ 5 – 900 kPa) [55], while carboxylic groups of acrylic acid can be used to anchor other extracellular matrix proteins such as laminin, which is also a major component of the basement membrane of epithelia. Indeed, we demonstrated that MDCK cells can form a polarized monolayer when grown on laminin functionalized scaffolds. Therefore, PEGDA-AA copolymerized hydrogels appear to be excellent basement membrane surrogates for engineered epithelial tissues.

One of the major limitations of the standard Caco-2 cell model is its high level of resistance, with TEER values up to 1000 Ω cm^2 [56,57], compared to values reported for human intestine (12 to 69 Ω cm^2) [58]. Aberrantly increased TEER values in current *in vitro* models have been attributed to the colon origin of the Caco-2 cell line. While tight junctions of the human small intestine have average pore radius of 6-13 Å, Caco-2 cells display average porosities of only 5 Å [59–61]. However, our results, and those of other researchers, demonstrate that Caco-2 cell monolayers can improve their TEER barrier properties by adding the native tissue architecture [36]. This can modulate the tight barrier properties associated with the curvature of the structures. Theoretical models of epithelial folds are based on evaluation of intraepithelial stresses. These take into account tensions generated at cell-lumen, cell-cell and cell-basement membrane contacts and predict pronounced modulations in cell thickness and cell shape depending on their position along groove-to-crest structure axis [62]. However, *in vivo* leakiness of the tight junctions increases from the tip of the villi to the crypt regions in normal juvenile intestines [63]. Therefore, by including the 3D intestinal architecture, the functional barrier characteristics of standard cell lines can better mimic those found *in vivo* [36]

5. Conclusion

A photolithography-based process based on dynamic polymerization to fabricate 3D hydrogel microstructures of high-aspect ratio and roundish geometries resembling the villi structures of the small intestinal epithelium is described. Using a polymerization process that controls the timescales of oxygen diffusion and depletion along the irradiation pathway, we demonstrated the production of 3D complex microstructures in a moldless and single fabrication step. The dimensions of the microstructures can be easily adjusted by modifying fabrication parameters such as the polymer composition and irradiation time. In addition, by employing poly(ethylene) glycol diacrylate and acrylic acid copolymers, the ligand density of hydrogel microstructures can be tuned in a simple way without significantly affecting their soft mechanical properties. The resulting hydrogel microstructures effectively support the growth of epithelial cells until a mature and confluent monolayer is formed. The simple fabrication procedure facilitates its integration with standard characterization techniques. Microstructured hydrogel scaffolds were successfully integrated in a Transwell® system to assess the barrier properties of the biomimetic intestinal epithelium formed. The microfabrication technology described here shows great potential as a method to routinely incorporate 3D structures mimicking microtopographies at the tissue level in cell culture systems.

Acknowledgements

Funding for this project was provided by European Union's Horizon 2020 ERC grant agreement No 647863 (COMIET), the CERCA Programme/ Generalitat de Catalunya (2017-SGR-1079), and the Spanish Ministry of Economy and Competitiveness (TEC2014-51940-C2-2-R, TEC2017-83716-C2-1-R and the Severo Ochoa Program for Centers of Excellence in R&D 2016-2019). M. G.-D. thanks the BEST Postdoctoral Programme, funded by the European Commission under Horizon 2020's Marie Skłodowska-Curie Actions COFUND scheme (Grant Agreement no. 712754) and by the Severo Ochoa programme of the Spanish Ministry of Science and Competitiveness (Grant SEV-2014-0425 (2015-2019)). The collaboration of the MicroFabSpace from IBEC is gratefully acknowledged. Authors thank Raquel Martin-Venegas and Rut Ferrer from the Departament de Bioquímica i Fisiologia, Facultat de Farmàcia i Ciències de l'Alimentació, Universitat de Barcelona (UB) for providing the Caco-2 cells. The results presented here reflect only the views of the

authors; the European Commission is not responsible for any use that may be made of the information it contains.

References

[1] Tortora G J and Derrickson B H 2014 *Principles of Anatomy and Physiology* (Wiley Global Education)

[2] Marsh M N and Swift J A 1969 A study of the small intestinal mucosa using the scanning electron microscope *Gut* **10** 940–9

[3] Kelly P, Menzies I, Crane R, Zulu I, Nickols C, Feakins R, Mwansa J, Mudenda V, Katubulushi M, Greenwald S and Farthing M 2004 Responses of small intestinal architecture and function over time to environmental factors in a tropical population. *Am. J. Trop. Med. Hyg.* **70** 412–9

[4] Abbott A 2003 Cell culture: Biology's new dimension *Nature* **424** 870–2

[5] Cushing M C and Anseth K S 2007 Hydrogel cell cultures *Science (80-.).* **316** 1133–4

[6] Justice B A, Badr N A and Felder R A 2009 3D cell culture opens new dimensions in cell-based assays *Drug Discov. Today* **14** 102–7

[7] Elliott N T and Yuan F 2011 A review of three-dimensional in vitro tissue models for drug discovery and transport studies *J. Pharm. Sci.* **100** 59–74

[8] Yu J, Carrier R L, March J C and Griffith L G 2014 Three dimensional human small intestine models for ADME-Tox studies *Drug Discov. Today* **19** 1587–94

[9] Sung J H, Yu J, Luo D, Shuler M L and March J C 2011 Microscale 3-D hydrogel scaffold for biomimetic gastrointestinal (GI) tract model *Lab Chip* **11** 389–92

[10] Wang Y, Gunasekara D B, Reed M I, DiSalvo M, Bultman S J, Sims C E, Magness S T and Allbritton N L 2017 A microengineered collagen scaffold for generating a polarized crypt-villus architecture of human small intestinal epithelium *Biomaterials* **128** 44–55

[11] Raman R and Bashir R 2015 *Stereolithographic 3D bioprinting for biomedical applications* (Elsevier Inc.)

[12] Chandra D and Crosby A J 2011 Self-wrinkling of UV-cured polymer films *Adv. Mater.* **23** 3441–5

[13] Guvendiren M, Yang S and Burdick J A 2009 Swelling-Induced surface patterns in hydrogels with gradient crosslinking density *Adv. Funct. Mater.* **19** 3038–45

[14] Krutkramelis K, Xia B and Oakey J 2016 Monodisperse polyethylene glycol diacrylate hydrogel microsphere formation by oxygen-controlled photopolymerization in a microfluidic device *Lab Chip* **16** 1457–65

[15] Shim T S, Yang S-M and Kim S-H 2015 Dynamic designing of microstructures by chemical gradient-mediated growth *Nat. Commun.* **6** 6584

[16] Kim J H, Je K, Shim T S and Kim S H 2017 Reaction-Diffusion-Mediated Photolithography for Designing Pseudo-3D Microstructures *Small* **13** 1–11

[17] Viswanathan P, Guvendiren M, Chua W, Telerman S B, Liakath-Ali K, Burdick J A and Watt F M 2016 Mimicking the topography of the epidermal–dermal interface with elastomer substrates *Integr. Biol.* **8** 21–9

[18] Kloxin A M, Kloxin C J, Bowman C N and Anseth K S 2010 Mechanical properties of cellularly responsive hydrogels and their experimental determination *Adv. Mater.* **22** 3484–94

[19] Scott R A and Peppas N A 1999 Compositional effects on network structure of highly cross-linked copolymers of PEG-containing multiacrylates with acrylic acid *Macromolecules* **32** 6139–48

[20] Scott R A and Peppas N A 1999 Kinetics of copolymerization of PEG-containing multiacrylates with acrylic acid *Macromolecules* **32** 6149–58

[21] Li R J and Schork F J 2006 Modeling of the inhibition mechanism of acrylic acid polymerization *Ind. Eng. Chem. Res.* **45** 3001–8

[22] Zhu J 2010 Bioactive modification of poly(ethylene glycol) hydrogels for tissue engineering *Biomaterials* **31** 4639–56

[23] Xu K, Fu Y, Chung W, Zheng X, Cui Y, Hsu I C and John W 2012 Thiol – ene-based biological / synthetic hybrid biomatrix for 3-D living cell culture *Acta Biomater.* **8** 2504–16

[24] Pierce B F, Tronci G, Rößle M, Neffe A T, Jung F and Lendlein A 2012 Photocrosslinked Co-Networks from Glycidylmethacrylated Gelatin and Poly(ethylene glycol) Methacrylates *Macromol. Biosci.* **12** 484–93

[25] Fonseca K B, Gomes D B, Lee K, Santos S G, Sousa A, Silva E A, Mooney D J, Granja P L and Barrias C C 2014 Injectable MMP-Sensitive Alginate Hydrogels as hMSC Delivery Systems *Biomacromolecules* **15** 380–90

[26] Anon http://medcell.med.yale.edu/systems_cell_biology/gi_tract_lab.php

[27] Schneider C A, Rasband W S and Eliceiri K W 2012 NIH Image to ImageJ: 25 years of image analysis *Nat. Methods* **9** 671–5

[28] Decker C and Jenkins A D 1985 Kinetic Approach of O2 Inhibition in Ultraviolet and Laser Induced Polymerizations *Macromolecules* 1241–4

[29] Ligon S C, Husar B, Wutzel H, Holman R and Liska R 2014 Strategies to Reduce Oxygen Inhibition in Photoinduced Polymerization *Chem. Rev.* **114** 557–89

[30] Liu M, Li M De, Xue J and Phillips D L 2014 Time-resolved spectroscopic and density functional theory study of the photochemistry of Irgacure-2959 in an aqueous solution *J. Phys. Chem. A* **118** 8701–7

[31] O'Brien L E, Zegers M M P and Mostov K E 2002 Building epithelial architecture: Insights from three-dimensional culture models *Nat. Rev. Mol. Cell Biol.* **3** 531–7

[32] Klein G, Langegger M, Timpl R and Ekblom P 1988 Role of laminin a chain in the development of epithelial cell polarity *Cell* **55** 331–41

[33] Schuger L, Yurchenco P, Relan N K and Yang Y 1998 Laminin fragment E4 inhibition studies: Basement membrane assembly and embryonic lung epithelial cell polarization requires laminin polymerization *Int. J. Dev. Biol.* **42** 217–20

[34] Weaver V M, Petersen O W, Wang F, Larabell C A, Briand P, Damsky C and Bissell M J 1997 Reversion of the malignant phenotype of human breast cells in three-dimensional culture and in vivo by integrin blocking antibodies *J. Cell Biol.* **137** 231–45

[35] Hidalgo I J, Raub T J and Borchardt R T 1989 Characterization of the human colon carcinoma cell line (Caco-2) as a model system for intestinal epithelial permeability *Gastroenterology* **96** 736–49

[36] Yu J, Peng S, Luo D and March J C 2012 In vitro 3D human small intestinal villous model for drug permeability determination *Biotechnol. Bioeng.* **109** 2173–8

[37] Madaghiele M, Marotta F, Demitri C, Montagna F, Maffezzoli A and Sannino A 2014 Development of semi-

and grafted interpenetrating polymer networks based on poly(ethylene glycol) diacrylate and collagen *J. Appl. Biomater. Funct. Mater.* **12** 183–92

[38] Park S, Lee H J and Koh W-G G 2012 Multiplex Immunoassay Platforms Based on Shape-Coded Poly(ethylene glycol) Hydrogel Microparticles Incorporating Acrylic Acid *Sensors (Switzerland)* **12** 8426–36

[39] Wu Y, Liang J, Horkay F and Libera M 2016 Antimicrobial loading into and release from poly(ethylene glycol)/poly(acrylic acid) semi-interpenetrating hydrogels *J. Polym. Sci. Part B Polym. Phys.* **54** 64–72

[40] Liao D, Yang J, Zhao J, Zeng Y, Vinter-Jensen L and Gregersen H 2003 The effect of epidermal growth factor on the incremental Young's moduli in the rat small intestine *Med. Eng. Phys.* **25** 413–8

[41] Huang G, Wang L, Wang S, Han Y, Wu J, Zhang Q, Xu F and Lu T J 2012 Engineering three-dimensional cell mechanical microenvironment with hydrogels *Biofabrication* **4** 042001

[42] Browe D P, Wood C, Sze M T, White K A, Scott T, Olabisi R M and Freeman J W 2017 Characterization and optimization of actuating poly(ethylene glycol) diacrylate/acrylic acid hydrogels as artificial muscles *Polym. (United Kingdom)* **117** 331–41

[43] Wang W H, Dong J L, Baker G L and Bruening M L 2011 Bifunctional polymer brushes for low-bias enrichment of mono- and multi-phosphorylated peptides prior to mass spectrometry analysis *Analyst* **136** 3595–8

[44] De Campos Vidal B and Mello M L S 2011 Collagen type I amide I band infrared spectroscopy *Micron* **42** 283–9

[45] Durst C A, Cuchiara M P, Mansfield E G, West J L and Grande-Allen K J 2011 Flexural characterization of cell encapsulated PEGDA hydrogels with applications for tissue engineered heart valves *Acta Biomater.* **7** 2467–76

[46] Kim S H, Chi M, Yi B, Kim S H, Oh S, Kim Y, Park S and Sung J H 2014 Three-dimensional intestinal villi epithelium enhances protection of human intestinal cells from bacterial infection by inducing mucin expression. *Integr. Biol. (Camb).* **6** 1122–31

[47] Costello C M, Hongpeng J, Shaffiey S, Yu J, Jain N K, Hackam D and March J C 2014 Synthetic small intestinal scaffolds for improved studies of intestinal differentiation *Biotechnol. Bioeng.* **111** 1222–32

[48] Yanagawa F, Sugiura S and Kanamori T 2016 Hydrogel microfabrication technology toward three dimensional tissue engineering *Regen. Ther.* **3** 45–57

[49] Zorlutuna P, Annabi N, Camci-Unal G, Nikkhah M, Cha J M, Nichol J W, Manbachi A, Bae H, Chen S and Khademhosseini A 2012 Microfabricated biomaterials for engineering 3D tissues *Adv. Mater.* **24** 1782–804

[50] Murphy S V. and Atala A 2014 3D bioprinting of tissues and organs *Nat. Biotechnol.* **32** 773–85

[51] O'Bryan C S, Bhattacharjee T, Niemi S R, Balachandar S, Baldwin N, Ellison S T, Taylor C R, Sawyer W G and Angelini T E 2017 Three-dimensional printing with sacrificial materials for soft matter manufacturing *MRS Bull.* **42** 571–7

[52] Artursson P, Palm K and Luthman K 2001 Caco-2 monolayers in experimental and theoretical drug transport predictions of drug transport *Adv. Drug Deliv. Rev.* **46** 27–43

[53] Costello C M, Sorna R M, Goh Y, Cengic I, Jain N K and March J C 2015 3-D Intestinal Scaffolds for Evaluating the Therapeutic Potential of Probiotics *Mol. Pharm.* **11** 2030–9

[54] Shaffiey S A, Jia H, Keane T, Costello C, Wasserman D, Quidgley M, Dziki J, Badylak S, Sodhi C P, March J C and Hackam D J 2016 Intestinal stem cell growth and differentiation on a tubular scaffoldwith evaluation in small and large animals *Regen. Med.* **11** 45–61

[55] Nguyen Q T, Hwang Y, Chen A C, Varghese S and Sah R L 2012 Cartilage-like mechanical properties of poly (ethylene glycol)-diacrylate hydrogels *Biomaterials* **33** 6682–90

[56] Sun H, Chow E C, Liu S, Du Y and Pang K S 2008 The Caco-2 cell monolayer: usefulness and limitations. *Expert Opin. Drug Metab. Toxicol.* **4** 395–411

[57] Boegh M, Foged C, Müllertz A and Mørck Nielsen H 2013 Mucosal drug delivery: barriers, in vitro models and formulation strategies *J. Drug Deliv. Sci. Technol.* **23** 383–91

[58] Ferrec E, Chesne C, Artusson P, Brayden D, Fabre G, Gires P, Guillou F and Rousset M 2001 In Vitro Models of the Intestinal Barrier *Atla* **29** 649–68

[59] Calatayud M, Vázquez M, Devesa V and Vélez D 2012 In vitro study of intestinal transport of inorganic and methylated arsenic species by Caco-2/HT29-MTX cocultures *Chem. Res. Toxicol.* **25** 2654–62

[60] Han L, Zhao Y, Yin L, Li R, Liang Y, Huang H, Pan S, Wu C and Feng M 2012 Insulin-Loaded pH-Sensitive Hyaluronic Acid Nanoparticles Enhance Transcellular Delivery *AAPS PharmSciTech* **13** 836–45

[61] Tavelin S, Taipalensuu J, Söderberg L, Morrison R, Chong S and Artursson P 2003 Prediction of the oral absorption of low-permeability drugs using small intestine-like 2/4/A1 cell monolayers *Pharm. Res.* **20** 397–405

[62] Štorgel N, Krajnc M, Mrak P, Štrus J and Ziherl P 2016 Quantitative Morphology of Epithelial Folds *Biophys. J.* **110** 269–77

[63] Schulzke J-D, Bentzel C J, Schulzke I, Riecken E-O and Fromm M 1998 Epithelial Tight Junction Structure in the Jejunum of Children with Acute and Treated Celiac Sprue *Pediatr. Res.* **43** 435–41

Biomed Microdevices (2016) 18:64
DOI 10.1007/s10544-016-0087-6

Design and development of a microarray processing station (MPS) for automated miniaturized immunoassays

Mateu Pla-Roca[1] · Gizem Altay[1] · Xavier Giralt[2] · Alícia Casals[2,4] · Josep Samitier[1,3,5]

Abstract Here we describe the design and evaluation of a fluidic device for the automatic processing of microarrays, called microarray processing station or MPS. The microarray processing station once installed on a commercial microarrayer allows automating the washing, and drying steps, which are often performed manually. The substrate where the assay occurs remains on place during the microarray printing, incubation and processing steps, therefore the addressing of nL volumes of the distinct immunoassay reagents such as capture and detection antibodies and samples can be performed on the same coordinate of the substrate with a perfect alignment without requiring any additional mechanical or optical realignment methods. This allows the performance of independent immunoassays in a single microarray spot.

Mateu Pla-Roca and Gizem Altay contributed equally to this work.

Electronic supplementary material The online version of this article (doi:10.1007/s10544-016-0087-6) contains supplementary material, which is available to authorized users.

✉ Mateu Pla-Roca
mpla@ibecbarcelona.eu

[1] Nanobioengineering Laboratory, Institute for Bioengineering of Catalonia (IBEC), Baldiri Reixac, 10-12, 08028 Barcelona, Spain

[2] Robotics Laboratory, Institute for Bioengineering of Catalonia (IBEC), Baldiri Reixac, 10-12, 08028 Barcelona, Spain

[3] The Biomedical Research Networking Center in Bioengineering, Biomaterials and Nanomedicine (CIBER-BBN), Maria de Luna, 11, 50018 Zaragoza, Spain

[4] Center of Research in Biomedical Engineering, Universitat Politècnica de Catalunya, Jordi Girona, 1-3, 08034 Barcelona, Spain

[5] Department of Engineering: Electronics, University of Barcelona (UB), Martí i Franquès, 1, 08028 Barcelona, Spain

Keywords Automation · Microarrays · High-throughput screening · Immunoassays · Customization

1 Introduction

Immunoassays are powerful tools in detection of disease biomarkers, thus hold great importance in clinical diagnostics and prognostics (Rifai et al., 2006). Many biologically informative molecules such as cancer biomarkers and cytokines are present at very low concentrations (Lutz et al. 2008) in complex samples. This makes the sensitivity one of the major challenges. The enzyme-linked immunosorbent assay (ELISA) due to dual binding of capture (cAb) and detection antibody (dAb) to two different epitopes of the same protein better prevents non-specific bindings and is considered as the gold standard for biomarker validation and quantification. However, it is a single-plexed, labor intensive technique that requires large amounts of sample, and has an overall low throughput (Angenendt et al. 2003). Usually ELISAs are performed on well plates by manual delivery of samples and reagents and manual emptying, drying and washing of the wells after the corresponding incubation times.

Antibody microarrays has emerged as a high-throughput tool for detection of proteins in biological samples in reduced volumes and exhibit sensitivities comparable to the conventional ELISA (Yu et al. 2010; Cretich et al. 2014). The performance of miniaturized immunoassays with minimal sample consumption by means of incubation of small droplets of sample has been already demonstrated effective by Angenendt and coworkers (Angenendt et al. 2003). In this study 1 nL samples directly labeled with fluorescent dyes or enzymes were printed onto the capture Ab spots. Another approach is the so called antibody colocalization microarray (ACM) strategy, which demonstrates that cross reactivity

Published online: 12 July 2016

issue in multiplexed immunoassays could be overcome by spotting each cAb and each matched dAb to the same spot of the microarray (Pla-Roca et al. 2012; Li et al. 2015). Yet, all the processing steps i.e. blocking, washing were performed manually; therefore, alignment became a problem since the substrate had to be taken out each time for manual processing, with the consequent use of customized realignment systems.

Here we propose a new technology called microarray processing station (MPS) which allows automatic processing of microarrays and the addressing of nL amounts of reagents on the same location of a substrate in order to perform independent miniaturized immunoassays and thus increase the number of distinct immunoassay per substrate area. The use of the MPS in combination with a commercial microarrayer allows transforming a simple microarrayer to an immunoassay station where the assay can be processed with no human intervention. There are some commercial systems that perform the ELISA in an automated manner, for instance, EVOlyzer® workstation from TECAN (TECAN website, http://diagnostics.tecan.com/products/liquid_handling_and_robotics/freedom_evolyzer) and SOLO-based ELISA workstation from Hudson Robotics Inc. (Hudson Robotics Inc. website, http://www.hudsonrobotics.com/products/other-products/compact-solo-based-elisa-workcell/). However, they are expensive and massive systems, and therefore; they are required to be allocated in central labs. Moreover, since they perform ELISA on well plates, they require large amounts of samples and reagents.

On the contrary, once the MPS is allocated inside the microarrayer it holds the substrate in its place during the printing of the microarray spots and then it automatically performs all the routine processing steps that are present in any immunoassay, i.e. rinsing, washing, blocking and incubation with probing reagents. This allows us to automate the performing of miniaturized immunoassays. In this work, we describe the design, the assembly and the testing of this fluidic device.

2 Materials and methods

2.1 MPS components description

The microarray processing station (MPS) is comprised of a washing bowl with a washing mesa, washing and waste connections, waste aspiration area, drying nozzles and reagents and washing solutions' sources (Fig. 1a). The washing bowl is the recipient where the substrate is placed in order to perform the automatic washing and drying. The washing mesa is the area (25 mm × 25 mm) where the microarray substrate (25 mm × 25 mm or less) is positioned and fixed with a magnetic clamping system. The washing mesa has on both sides waste aspiration areas with 3 drains each allowing an efficient drain of the solutions used on the washing procedures. The apertures height is adjusted such that liquids' and gases' flow is directed to the substrate surface in order to ensure efficient washing and drying processes. The maximum height of the substrate that can be used is 1 mm (the standard thickness of microscope glass slides) although thinner substrates can be allocated. The washing bowl is made of acrylonitrile butadiene styrene (ABS) and fabricated with a conventional 3D printer. Fluids (the reagents and the washing solutions) are pumped and gases (for the drying processes) controlled thanks to peristaltic pumps and solenoid valves' manifolds respectively. The MPS controlling system actuates the peristaltic pumps and solenoid valves' manifolds, following previously programmed processing routines. Completely dried slides could be obtained after blowing gas during 2 min. This time is larger comparable with the time required when using microarrays spin dryers, which can be of few tens of seconds although thanks to this system substrate can be dried *in situ* without moving or touching the substrate.

Peristaltic pump tubing (Tygon® tubing, ID1/8″) is connected to the washing bowl using barbed connections. The maximum flow rate that can be achieved with each peristaltic pump (KCS peristaltic pump, Kamoer Fluid Tech) is 120 mL/min. The peristaltic pumps are based on step motors which allow a precise control on the peristaltic pump actuation. The electro valves' manifold (solenoid valves from Gems® normally close type) when actuated let the pressurized gas pass through and reach the drying nozzles. The gas used for the drying process can be pressurized nitrogen or pressurized air. Gas source can be either in-line, from a bottle or from an air compressor. The peristaltic pumps and the solenoid valves are controlled using a microprocessor (Arduino Mega®). Other electronic components such Arduino power shield (Sparkfun®), peristaltic pumps' drivers (Makerbot®), power supplies (5 V and 12 V), USB cable connections to the PC and cable connections to peristaltic pumps manifold and electro valves where required to construct the controlling electronics system. The detailed description of the distinct components of the MPS is given in Online Resource 1. The MPS can be fixed on a metallic support and placed into different models of contact microarrayers and inkjet printers.

Installation of the MPS on a microarrayer The MPS station is fixed to a metallic support that matches the slide tray area of the SpotBot microarrayer from Arrayit® (Fig. 1b). The bottom magnets of the MPS are used to fix the position of the MPS on the microarrayer. The overview of the integrated system can be seen in Fig. 1c. Once installed printing and washing routines can be performed inside the microarray chamber (See Online Resources 2 and 3). The programming of the MPS is explained in the next section and its coordination with the printing routine of the microarrayer is explained in section 2.4.

Programming the automated routines Arduino microprocessor was programmed using C++ language. The automated

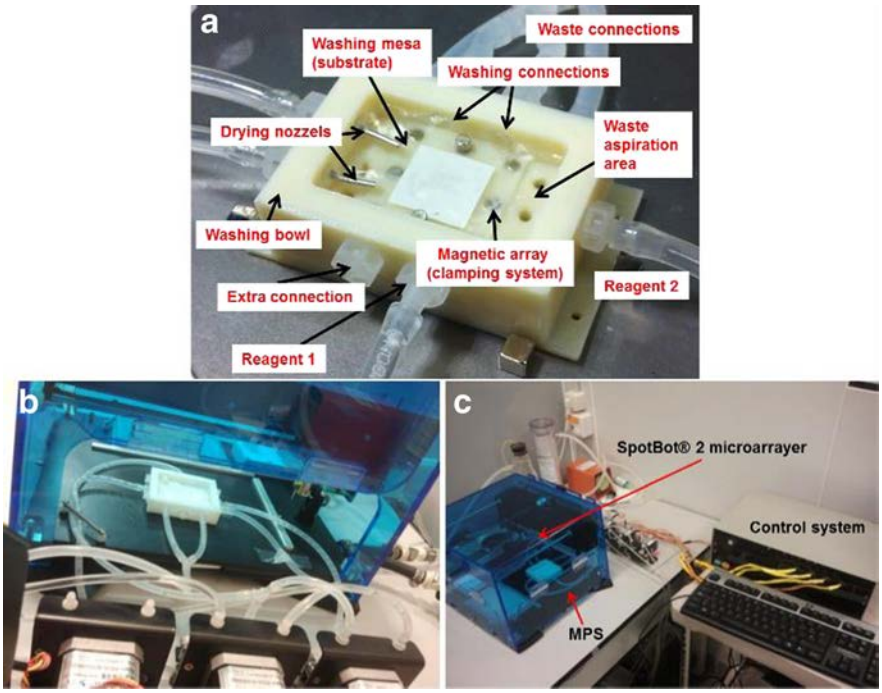

Fig. 1 Microarray processing station (MPS) description and installation. **a** MPS close view with the distinct parts indicated with labels. **b** Installation of the MPS on a commercial contact microarrayer (SpotBot® 2, Arrayit corporation, USA). **c** Overview of the integrated system showing the MPS, the microarrayer, the pumping system and the control unit

routines (steps) can be divided to: (i) system priming (filling of the tubes), (ii) system empting (empting of the tubes), (iii) wash and dry routines, and (iv) reagents loading and (v) mixing. The automated routines can be set by simply sending information of the velocity and the functioning time of the peristaltic pumps and the opening time of the drying nozzles (See Online Resource 4). The mixing routine is performed by changing peristaltic pumps' pumping sense repetitively in order to induce pulsations on the flow when operating. This pulse introduces agitations that increase the efficiency of the incubations such as, the blocking steps.

Coordination of the microarrayer software and the MPS actuation software Microarrayer software and MPS software run in coordination thanks to the use of Quickmacros®. This program coordinates both of the programs externally without the requirement of any modification of the microarray software (see Online Resource 1).

2.2 Testing of MPS performance

Alignment of repetitive addressing of micro spots Multiple deliveries of the nL solutions to the exact same micro spot was assessed by repetitive addressing of microarray coordinates without removing the substrate and realigning. For that, two rounds of printing performed first with AlexaFluor555-conjugated donkey anti-goat IgG (Invitrogen, CA, USA) and second with AlexaFluor647-conjugated goat anti-rabbit IgG (Invitrogen, CA, USA) with partially overlapping regions on Oncyte-Supernova nitrocellulose film slides (Grace Biolabs, USA). After each spotting round washing was performed with the MPS to remove the excess of the antibodies (assessment of the washing conditions are explained in the following section) and the surface was completely dried with the drying system. The antibodies were diluted at 100 μg/mL in phosphate buffer saline pH 7.4 (PBS) containing 10 % glycerol in order to avoid the evaporation of the spots (Optimized printing conditions are given in Online Resource 1). Printings were performed with SpotBot® 2 Personal microarrayer equipped with a 946MP4 series stainless steel contact pin (Arrayit Corp., CA, USA). Printing chamber was humidified up to ~60 % (small variations observed upon changes in ambient humidity) with the humidifier of the printer and was maintained at that value throughout the experiment in order to minimize evaporation of solutions while printing. The default factory settings of the microarray such as; substrate height and contact time were adjusted after the insertion of the MPS (Microarray Processing Station) module. All the chemicals were purchased from Sigma-Aldrich unless stated otherwise. The 946MP4 pins had a 100 μm × 100 μm foot print and used to deposit ~1.1 nL (as listed in the datasheet of the product) spots at 0 s contact time with a pitch of 500 μm. The slides were visualized with GenePix® 4000B microarray scanner (Molecular Devices, CA, USA) with AF555 and AF647 settings. In order to facilitate representation, false colors green and red were used for AF555 and AF647 respectively. The experiment was repeated at least at three different times.

Washing efficiency of the MPS In order to evaluate the material erosion upon washing with MPS, three replicate arrays of AlexaFluor555-conjugated donkey anti-goat IgG that was diluted at 100 μg/mL in PBS_10% glycerol were printed with

a pitch of 500 μm on Oncyte-Supernova nitrocellulose film slides (Grace Biolabs, USA) and SuperEpoxy slides (Arrayit Corp., CA, USA) each. The slides were incubated 1 h at room temperature and scanned with GenePix® 4000B microarray scanner (Molecular Devices, CA, USA) with AF555 settings just before washing. The washing routine implemented by the MPS (microarray processing station) included consecutive washing and aspiration steps first with PBS_0.5 % Tween (PBST) and then with MilliQ (Online Resource 1). After each minute of washing and drying cycle, the slides were scanned with GenePix® 4000B microarray scanner with the same laser power and gain settings. The GenePix® Pro Analysis and Acquisition software was used to quantify the spot fluorescence intensity from the scanned images. The experiments were repeated at two different times.

Assessment of spot-to-spot interference A special printing scheme was selected in order to evaluate the possibility of adjacent spots contaminating one another upon washing. Briefly, a spot of AlexaFluor555-conjugated streptavidin (Invitrogen, CA, USA) was printed into the central coordinate of an empty square array of biotinylated sheep anti-mouse IgG, Biot-IgG (Jackson ImmunoReseach Laboratories Inc., USA) with a pitch of 200 μm on Oncyte-Supernova nitrocellulose film slides (Grace Bio-labs, USA). The spot spacing was chosen lower than the one used in the rest of the experiments (300–500 μm) to have an idea of the necessary lower limit of the spot spacing in order to avoid spot-to-spot contamination. The protein solutions were prepared at 100 μg/mL in PBS_10% glycerol and the printing was performed at ~60 % humidity. The slides were incubated for 1 h at RT and later washed with the MPS following the optimized washing routine explained in the previous section. At least 5 arrays were printed in distinct regions of the nitrocellulose pad. The slides were visualized with Nikon E1000 Fluorescence Microscope (Japan). The images were analyzed using ImageJ software.

Validation of the MPS using a two-step assay The possibility of performing biochemical assays using nL volumes was first tested using a two-step assay. Biotinylated anti-mouse IgG (Biot-IgG) (100 μg/mL) in PBST was printed on a nitrocellulose coated slide and let incubate for 1 h. After 1 min of automatic rinsing with PBST using the MPS station, the substrate was dried using the *in situ* drying system for 2 min. Next, distinct dilutions of IRDye® 800CW streptavidin (LI-COR® Biosciences, USA), from 1000 ng/mL to 1 ng/ml, were addressed on the biotinylated antibody spots printed on the nitrocellulose substrate. Printing volume was approximately 1 nL for each reagent. Direct printing of the streptavidin onto spots that did not contain biotin was used as negative control. Odyssey® Infrared Imaging System (LI-COR® Biosciences, USA) was used to determine signal intensities. The images were analyzed using Image Studio V3.1 software.

3 Results and discussion

We have validated the MPS showing that both the commercial microarrayer and the pumping system function correctly, which makes it possible to perform miniaturized immunoassays. Several aspects have been evaluated such as the alignment of multiple spotting, efficiency of the washing process and performance of immunoassays with minute amounts of sample and reagents.

3.1 Alignment of spotting

The same microarray coordinates can be addressed as many times as required since the substrate stays on place during the washing and incubation steps. In order to demonstrate that two rounds of printing were performed first with AlexaFluor555-conjugated donkey anti-goat IgG (AF555) and second with AlexaFluor647-conjugated goat anti-rabbit IgG (AF647) on nitrocellulose film slides. Perfect overlapping between the two spotting rounds was achieved (Fig. 2) despite several washing and drying processes were performed between each spotting round. This result clearly shows that the substrate remains in the exact same position during the incubation, drying and washing steps and that the clamping system used was effective.

3.2 Protein wash-off profiles

In conventional protocols, after printing, the microarrays are washed for at least couple of minutes with a buffer and this step is repeat 2–3 times with a fresh buffer to make sure that all the unbound proteins wash off (Angenendt et al. 2003; Pla-Roca et al. 2012). Therefore, it was predicted that much shorted times of washing should have been enough. In order to assess this, we printed AF555 IgG and measured the RFI before and after numerous cycles of washing. Here, besides the nitrocellulose film slides on which the proteins are adsorbed by physical interactions, epoxy functionalized slides were also used. Epoxy groups form irreversible covalent bonds with amino functional groups of the proteins. It is observed that after the initial wash off, the amount of material deposited stabilizes for both of the surfaces (Fig. 3). To remove the unbound proteins from the surface 1 min of washing was enough. This

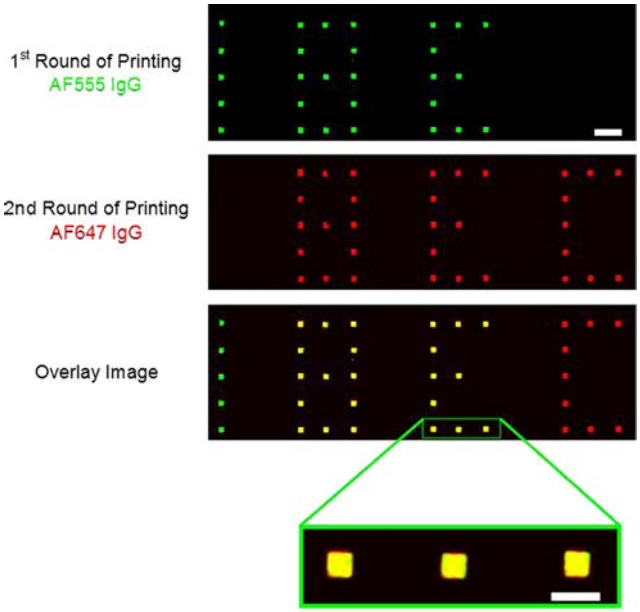

Fig. 2 Multi-spotting alignment. Fluorescent images showing that spotting several times to the exact same spot is possible. First spotting round was performed with AF555 IgG (Scale bar =500 μm) and the second with AF647 IgG. Between each spotting round a washing process was performed automatically. The zoomed image at the bottom shows the perfect alignment achieved between the spotting rounds. Scale bar =200 μm

value was fixed as the washing time in the processing routine.

Usually this process require the use of gaskets and the use of multichannel pipettes or washing automatic manifolds that implies using approximately 1 mL of washing buffer per similar substrate area and around 16 mL of washing buffer per processed microarray (if 16 well gaskets were used). Here we use an automatic pumping system that continuously delivers a fresh washing solution (PBST and MilliQ) with a velocity that also induces agitation due to the peristaltic pump pulsing. The volume of fresh washing solutions (PBST and MilliQ) used is 120 mL since the washings was performed for 1 min with a 120 mL/min pump. This volume is more than the one used per microarray in manual processing. Yet, the time of washing is much less and the process is automated. In a typical washing step, the slides are manually washed 3 to 5 times with 5 min of shaking each. Besides, by means of washing with MPS, substrate is kept in its position and all the expensive or scarce reagents such as capture and detection antibodies and samples can be printed to the exact same spot repetitively allowing us to perform immunoassays in a single microarray spot.

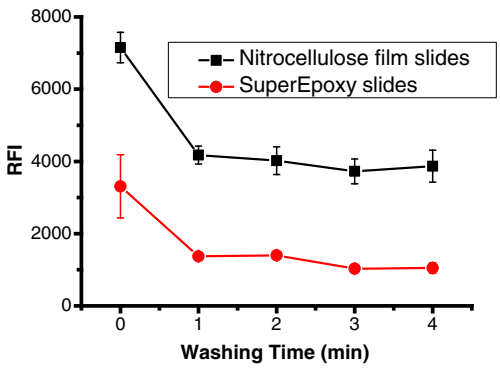

Fig. 3 Protein wash-off profile**.** Graph showing the change in relative fluorescence intensity (RFI) upon increased time of washing on different substrates. AF555 IgG were microarrayed on the nitrocellulose film slides (*black*) and SuperEpoxy slides (*red*) and scanned before (0 min) and after washing steps (from 1 to 4 min). After the first cycle of washing the signal remained stable indicating that the excess amounts of printed antibody was washed off during the first cycle of washing

3.3 Spot-to-spot interference

With this technology, an array of nL spots that are like miniaturized chambers where a different immunoassay takes place, are fabricated with a micron scale separation. This raises the question that upon a washing procedure the excess of biomolecules deposited at one spot could contaminate the adjacent spot during a washing procedure and consequently give a false signal.

In conventional methods, the capture antibodies are printed and the slides are incubated with the samples and a cocktail of detection antibodies, where the cross reactivity is an issue (Pla-Roca et al. 2012) but the spot-to-spot interference is irrelevant since the whole microarray is incubated with the sample and detection antibody solutions. Whereas in our case, since independent assays are performed in each spot of the microarray, spot-to-spot interference may become an issue. In order to address this question and validate the MPS washing procedure not only in terms of removing the unbound proteins but as well in terms of spot-to-spot interference AF555 labeled streptavidin (SA_AF555) was printed into the center coordinate of a square pattern of biotinylated anti-mouse IgG (Biot-IgG) spots. The spacing used was 200 μm, which is less than the spot spacing used for the immunoassays (i.e. 300 μm). Streptavidin-biotin recognition couple was selected because it is one of the strongest non-covalent interactions known in nature. This extreme scenario was tested in order to make sure that even under these circumstances there was no significant spot-to-spot contamination. In Fig. 4a the SA_AF555 spots are seen in red and the surrounding Biot-IgG spots are visible in the zoomed image (Fig. 4b). The intensity profile along the yellow line (Fig. 4c) crossing both the SA_AF555 and Biot-IgG spots clearly shows that the amount of protein that is captured by the adjacent Biot-IgG spots is not significantly higher than the background signal. The SA_AF555 spots presented variations in intensity due

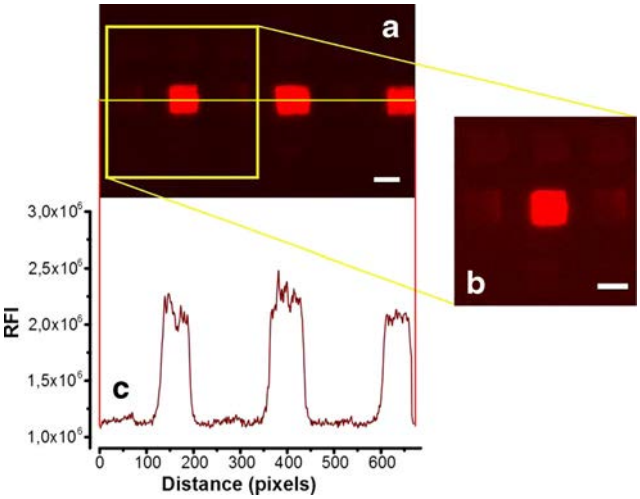

Fig. 4 Spot-to-spot interference. **a** Image showing fluorescent labeled streptavidin SA_AF555 spots printed at the center coordinate of a square pattern of Biot-IgG spots with 200 μm spacing; **b** Zoomed image of the indicated square area, where the surrounding Biot-IgG can be appreciated; **c** Intensity profile along the yellow line crossing both the SA_AF555 and Biot-IgG spots. Fluorescent labeled streptavidin (SA_AF555) captured by the adjacent Biot-IgG spots is not significantly higher than the background signal. Scale bars correspond to 100 μm

to the local adsorption inhomogeneities and the fact that the concentrations of the SA_AF555 printed where high.

3.4 Validation of two-step recognition assay

As a proof of concept we assessed the possibility of performing immunoassays with MPS, we performed a two- step recognition assay. First the biotinylated anti-mouse IgG (Biot-IgG) were printed and then the distinct dilutions of IRDye® 800CW labelled streptavidin, from 1000 ng/mL to 1 ng/ml, were addressed on the biotinylated antibody (Biot-IgG) spots. Direct printing of the streptavidin onto spots that did not contain biotinylated anti-mouse IgG was used as negative control. Both Biot-IgG and labelled streptavidin were printed by the microarrayer and processed by the MPS in a fully automated way. The volume of reagents (i.e. Biot-IgG and labelled streptavidin) used was 10 μL each, whereas the volume of washing solution (i.e. PBST and MilliQ) used was 120 mL each time the slide was washed after printing. The total volume of the washing buffer consumed is more than the one used per microarray in manual processing. However, by means of washing with MPS, the substrate was kept in its position and all the proteins used for the assay were printed to their corresponding spots on the slide allowing us to perform this two-step recognition assay on each microarray spots. Therefore, all the expensive or scarce reagents such as Biot-IgG and labelled streptavidin in this case, were used in minute amounts (i.e. 10 μL).

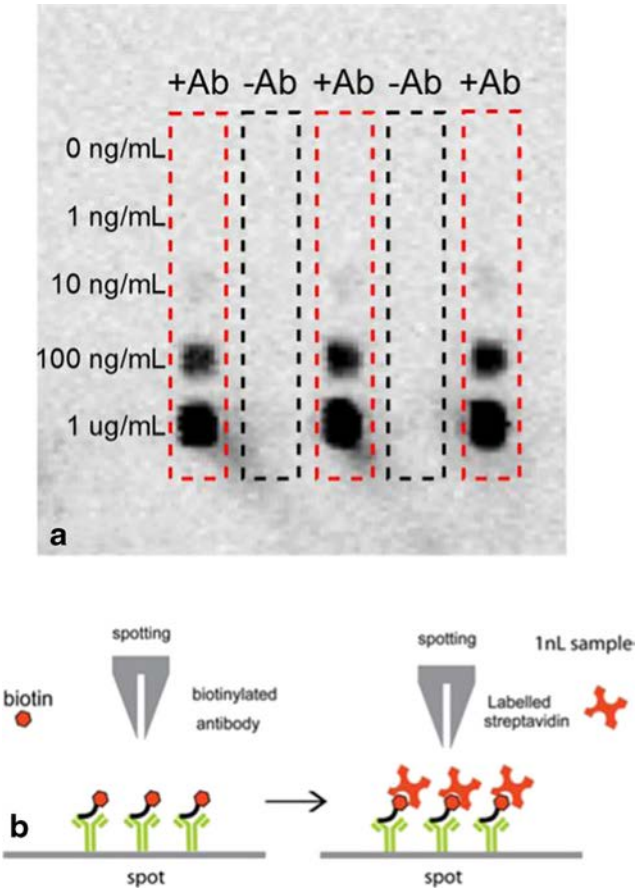

Fig. 5 Two-step recognition assay processed using a MPS. **a** Image of IRDye® 800CW labeled streptavidin (dilution from 1000 ng/mL to 1 ng/ml) printed on biotinylated antibody spots (+Ab). No signal was observed on the negative controls (−Ab). **b** Scheme depicting two-step protocol

As it is seen in Fig. 5 we were able to detect streptavidin at a concentration of 10 ng/mL. No signal was observed on the spots that didn't contain the Biot-IgG, which demonstrates the specific recognition. The limit of detection of this assay can be improved by using classical amplification methods (Miersch et al. 2013; Zhou et al. 2015). In any case the signal amplification protocols may be introduced to the automatic routine as well.

On this immunoassay performed by the MPS, five concentrations of reagents has been tested on an area of 3 mm × 2,5 mm (7.5 mm^2). This area can be smaller if the spot pitch is reduced. If this assay would have been performed on a classical 16-pad nitrocellulose slide we would have needed fifteen pads, which correspond to almost one whole slide (588 mm^2). Therefore; high throughput screening can be achieved with the MPS by using one single slide.

In Fig. 5 we can see the comets at the highest concentration spots (1 μg/mL) as a consequence of washing direction. The presence of comets is a common problem in microarray assays performed manually (Gonzalez et al. 2008). In order to minimize the effect of comets and consequently a possible spot-to-spot contamination, spots were printed from lower to higher

concentrations with respect to the washing direction and the highest possible flow rate was used.

4 Conclusion

We have developed a new device called microarray processing station (MPS) that enables performing miniaturized biochemical assays when integrated on a commercial microarrayer. It was shown that the repetitive addressing of distinct solutions on the same coordinate of an array becomes feasible without requiring complex realignment strategies. The MPS allows processing the microarrays at the same location where they are printed and thus no substrate realignment strategy is required. It was found that even if the mechanism of grafting of the desired protein was different (i.e. physical adsorption or covalent bonding) the excess of unbound proteins present after a printing process is effectively washed off with the MPS washing routines, and that due to the efficiency of the washing routines no spot-to-spot contamination was observed. Finally a two-step recognition assay was performed using the MPS in order to demonstrate that a commercial microarrayer can be converted to an automated immunoassay station when a MPS is integrated on it.

Acknowledgments This work was supported by Networking Biomedical Research Center in Bioengineering, Biomaterials and Nanomedicine (CIBER-BBN), Spain. The Nanobioengineering group at the Institute for Bioengineering of Catalonia (IBEC) receives support from the Commission for Universities and Research of the Department of Innovation, Universities and Enterprise of the Generalitat de Catalunya (No. 2014 SGR 1442). In addition, the research received support from the Spanish Ministry of Economy and Competitiveness, OLIGOCODES (MAT2012-38573-C02), and the Fundación Botín, Santander, Spain. M. Pla-Roca acknowledges a Beatriu de Pinos fellowship (2010 BP-B00180) from the Agència de Gestió d'Ajuts Universitaris i de Recerca (AGAUR).

Compliance with ethical standards

Conflict of interest The authors declare that they have no conflict of interest.s

Human and animal rights "This article does not contain any studies with human participants or animals performed by any of the authors."

References

P. Angenendt, J. Glökler, Z. Konthur, H. Lehrach, D. J. Cahill, Anal. Chem. **75**, 4368 (2003)

M. Cretich, F. Damin, M. Chiari, Analyst **139**, 528 (2014)

R. M. Gonzalez, S. M. Varnum, and R. C. Zangar, Methods Pharmacol. Toxicol. Biomark. Methods Drug Discov. Dev. 273 (2008).

H. Li, S. Bergeron, M. G. Annis, P. M. Siegel, D. Juncker, Mol. Cell. Proteomics **14**, 1024 (2015)

A. M. Lutz, J. K. Willmann, F. V. Cochran, P. Ray, S. S. Gambhir, PLoS Med. **5**, e170 (2008)

S. Miersch, X. Bian, G. Wallstrom, S. Sibani, T. Logvinenko, C. H. Wasserfall, D. Schatz, M. Atkinson, J. Qiu, J. LaBaer, J. Proteome Res. **94**, 486 (2013)

M. Pla-Roca, R. F. Leulmi, S. Tourekhanova, S. Bergeron, V. Laforte, E. Moreau, S. J. C. Gosline, N. Bertos, M. Hallett, M. Park, D. Juncker, Mol. Cell. Proteomics **11**, M111.011460 (2012)

N. Rifai, M. A. Gillette, S. A. Carr, Nat. Biotechnol. **24**, 971 (2006)

X. Yu, N. Schneiderhan-Marra, T. O. Joos, Clin. Chem. **56**, 376 (2010)

G. Zhou, S. Bergeron, D. Juncker, J. Proteome Res. **14**, 1872 (2015)